Technical Report

TR-10-23

THM-issues in repository rock

Thermal, mechanical, thermo-mechanical and hydro-mechanical evolution of the rock at the Forsmark and Laxemar sites

Harald Hökmark, Margareta Lönnqvist, Billy Fälth
Clay Technology AB

May 2010

Svensk Kärnbränslehantering AB
Swedish Nuclear Fuel
and Waste Management Co

Box 250, SE-101 24 Stockholm
Phone +46 8 459 84 00

ISSN 1404-0344
SKB TR-10-23

THM-issues in repository rock

Thermal, mechanical, thermo-mechanical and hydro-mechanical evolution of the rock at the Forsmark and Laxemar sites

Harald Hökmark, Margareta Lönnqvist, Billy Fälth
Clay Technology AB

May 2010

Summary

The present report addresses aspects of the Thermo-Hydro-Mechanical (THM) evolution of the repository host rock that are of potential importance to the SR-Site safety assessment of a KBS-3 type spent nuclear fuel repository.

The report covers the evolution of rock temperatures, rock stresses, pore pressures and fracture transmissivities during the excavation and operational phase, the temperate phase and a glacial cycle on different scales. The glacial cycle is assumed to include a period of preglacial permafrost with lowered temperatures and with increased pore pressures in the rock beneath the impermeable permafrost layer. The report also addresses the question of the peak temperature reached during the early temperate phase in the bentonite buffer surrounding the spent fuel canisters.

The main text is devoted exclusively to the projected THM evolution of the rock at the Forsmark site in central Sweden. The location and the geometry of the repository are assumed to be according to the Layout D2 underground design established for the Forsmark site. Material property data used as input are taken from the **Data report** based on Forsmark site descriptive models. The focus is on the potential for stress-induced failures, i.e. spalling, in the walls of the deposition holes and on changes in the transmissivity of fractures and deformation zones. All analyses are conducted by a combination of numerical tools (*3DEC*) and analytical solutions.

In addition to the main text, the report comprises a number of appendices. The numerical and analytical tools, by which the analyses are carried out, are described in Appendix A. The influence of steeply dipping deformation zones and choice of large-scale material properties on nearfield boundary conditions are analysed in Appendix B. Analyses regarding the influence of repository size and layout on thermally induced stresses are provided in Appendix C. A pore pressure model for the glacial phase is derived in Appendix D. Additional and complementary THM-analyses on all three scales to those presented in the main text are provided in Appendix E to Appendix H. Results corresponding to those given for Forsmark in the main text are provided in Appendix I for the Laxemar site. The Laxemar analyses are not given with same level of detail as those for Forsmark.

All phases are treated separately and independently of each other, although in reality construction will overlap with heat generation because of the step-by-step excavation/deposition approach with some 50 years between deposition of the first and last canisters. It is demonstrated here that the thermal and thermo-mechanical evolution of the near-field will be independent of heat generated by canisters that were deposited in the past, provided that deposition is made in an orderly fashion, deposition area by deposition area. Peak temperatures and near-field stresses can, consequently, be calculated as if all canisters were deposited simultaneously.

The canister and tunnel spacing is specified such that the peak buffer temperature will not exceed 100°C in any deposition hole, i.e. not even in the hottest ones. To account for uncertainties in the thermal calculations, the layout is established with a margin of about 5°C to the 100°C limit. It is demonstrated here that the spatial variability of rock heat transport properties means that there is considerable robustness in the design approach. An underestimate of the uncertainty margin by a few degrees appears to impact on very few canisters, even under the conservative assumption that all deposition holes are completely dry.

Spalling after excavation of a deposition hole excavation is not likely unless the major horizontal stress is aligned off the orientation of the tunnel axis by the largest angle given within the uncertainty range of the Forsmark *in situ* stress model. In case it happens, the spalling will be limited to the top 1 m of the deposition hole for the most likely Forsmark major stress magnitude and to the top 3 m for the upper bound stress magnitude.

Thermally-induced spalling is almost certain to occur after some time of heating, i.e. also for the most favourable conditions regarding stress orientation and magnitude. However, for the most favourable conditions the spalling will occur late and be limited to the top 5 m of the deposition hole.

All spalling risk estimates are based on the assumption that the spalling strength varies between 52% and 62% of the uniaxial compressive strength of the intact rock, as suggested by field experiments

performed in the Äspö Hard Rock Laboratory. It is also assumed that the deposition holes are completely dry, i.e. without any swelling pressure to support and stabilize the walls. These assumptions are all claimed to be conservative. The stress path for rock in the walls of KBS-3 deposition holes will be different from corresponding stress paths in the field experiments and a small support pressure, possibly sufficient to limit the extent of the spalling, will be found also in dry deposition holes.

Transmissivity effects on rock fractures are evaluated on different scales by use of stress-transmissivity models based on results from lab scale tests on rock joint samples from Forsmark. At distances of 1–2 metres from the repository openings, the proximity to the openings and the fracture geometry, e.g. the angle and location of fracture-opening intersections, are more important to the impacts on transmissivity than details in the description of the background stress evolution. Therefore, the results obtained for the region surrounding the openings in the SR-Can assessment are judged to be valid. At larger distances, the stress evolution and the pore pressure evolution during the thermal phase and following glacial cycles control how transmissivities change.

During the thermal phase the compression increases for most fractures, giving unchanged or just slightly reduced transmissivities. The largest relative systematic increase in transmissivity are found for horizontal fractures in non-heated regions between the deposition areas or just outside the repository and for vertical fractures close to the ground surface. The increases are modest though, about a factor of two at maximum.

The largest transmissivity effects during the glacial cycle, a factor of about seven, are found for vertical fractures during a period of preglacial permafrost with increased pore pressure coinciding with a forebulge type stress field. This increase is found just below the frozen ground and requires that the permafrost layer is impermeable and that lowered temperatures reduce the horizontal stresses. At repository depth the increase is a factor of three at maximum.

Contents

1 Introduction and background

1.1 General

Mechanical and thermo-mechanical processes in the geosphere are potentially important to performance and long-term safety. The present report addresses the impact on the hydraulic conditions of loads occurring during the different phases of the repository host rock considered within the 1 million year SR-Site safety assessment time frame. Other effects of rock mechanics processes of potential importance than changes in the hydraulic conditions are not addressed here. The risk of direct canister damage occurring in response to fracture shear displacements across deposition holes, for instance, is treated in a separate report /Fälth et al. 2010/.

This report is intended to provide background information for use in hydrological models and transport models analyzed within the SR-Site safety assessment. The conclusions are of the same character as those drawn in the corresponding report produced for the SR-Can assessment /Hökmark et al. 2006/. Some of the results obtained in that report are general enough to be quoted and utilized here without repeating the analyses.

Results and conclusions are provided for both sites included in the site investigation programme, i.e. the Forsmark and Laxemar sites, Figure 1-1. For both sites, site descriptive models as well as detailed layout plans have been established, whereas only the Forsmark site is part of the SR-site assessment. Therefore, the focus here is on the Forsmark site. The Laxemar results are found in Appendix I.

In the following chapters, short names will be used when citing the main supporting references for the safety assessment SR-Site. The references in question are listed in Table 1-1.

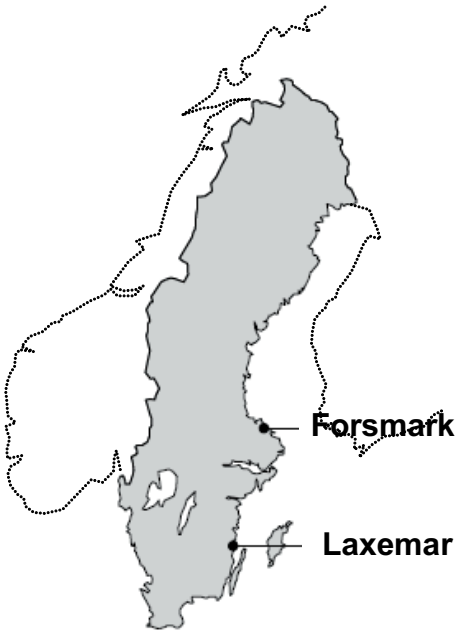

Figure 1-1. *Locations of Forsmark and Laxemar candidate sites.*

Table 1-1. List of short names of main supporting references for the safety assessment SR-Site used in this report.

Short name	Full name	In reference list
Climate report	Climate and climate related issues for the safety assessment SR-Site	/SKB 2010a/
Data report	Data report for the safety assessment SR-Site	/SKB 2010c/
Geosphere process report	Geosphere process report for the safety assessment SR-Site	/SKB 2010e/
Model summary report	Model summary report for the safety assessment SR-Site	/SKB 2010f/
Spent fuel report	Spent nuclear fuel for disposal in the KBS-3 repository	/SKB 2010h/
Underground openings construction report	Design, construction and initial state of the underground openings for operational and long-term safety	/SKB 2010d/

1.2 Thermal, mechanical, thermo-mechanical and hydro-mechanical evolution of the repository host rock

The mechanical evolution of the repository host rock starts with the transition from the pre-mining undisturbed initial state to a state characterized by the mechanical impact of the excavation activities and by stress redistribution effects around the repository openings. The groundwater pressure will be reduced from an initial value of about 5 MPa to atmospheric at the peripheries of the openings. The pressure reduction will increase the effective normal stress acting across fractures and increase the fracture shear strength.

After deposition, backfilling and closure, the mechanical evolution is controlled by the heat generation from the spent fuel, by the swelling pressure of the bentonite buffer in the deposition holes and by the gradual restoration of the groundwater pressure, which will reduce the effective stress and the fracture shear strength. The timescale for the thermal effects can be predicted accurately as demonstrated in numerous analyses of the thermal development of the repository /Thunvik and Braester 1980, Probert and Claesson 1997a, Ageskog and Jansson 1999, Ikonen 2003, Hökmark and Claesson 2005/. The time-scale for the development of the swelling pressure is more complicated and depends on the local permeability conditions around the individual deposition holes and on the general repository-scale restoration of the groundwater pressure.

After the thermal pulse, when the host rock temperatures have returned to, or approach, the natural geothermal values, the continued mechanical evolution of the repository is controlled by climate variations with projected glaciation/deglaciation cycles and periods of permafrost. During periods of glaciation, tectonic compression may generate additional horizontal stresses under the stabilizing ice cover and add to stresses caused by the direct elastic response to the ice-load and by crust bending. The scope, extent, time-scale and duration of future loads are much more uncertain than the repository-driven thermal load. In addition to the mechanical effects of the ice loading and unloading, there will be changes in temperature and changes in groundwater pressure during these glacial periods.

There are four time periods/climate domains to consider (cf. **Geosphere process report)**, each with different load scenarios:

- Excavation/operation period.
- Initial temperate period.
- Permafrost.
- Glaciation.

Figure 1-2 shows the approximate temporal evolution of conditions that control the THM behaviour of the repository rock mass during the 1 million year assessment time. Periods of potential importance, i.e. when stresses, or stresses in combination with pore pressure variations, may result in significant fracturing or significant fracture shear- or normal displacements, are specifically indicated. The excavation/operation period ends when the initial temperate period starts, i.e. when the last canister is deposited and the repository is closed.

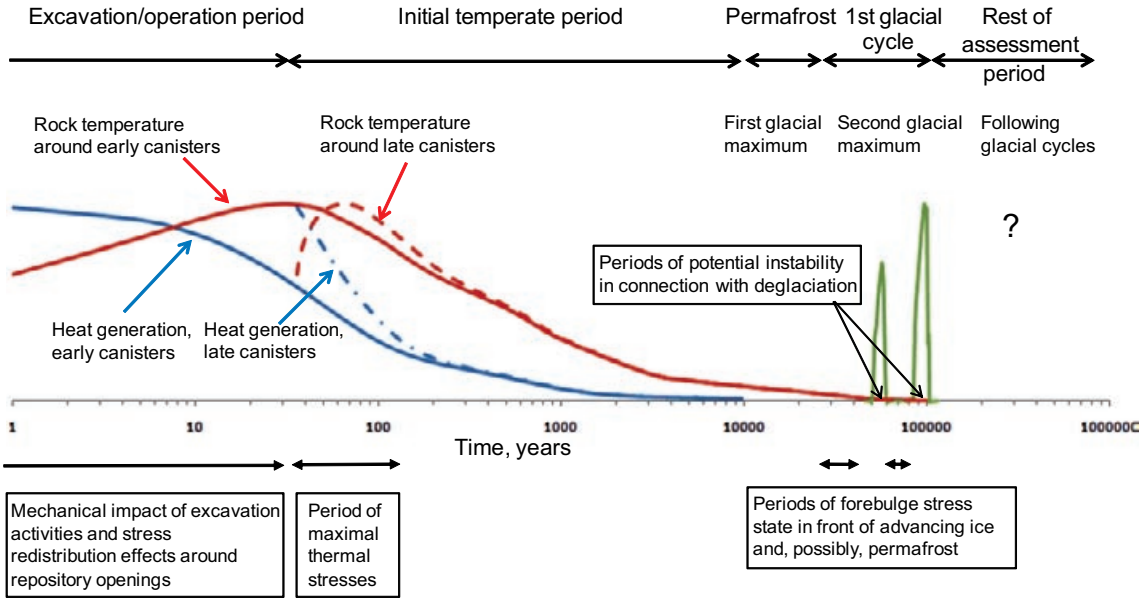

Figure 1-2. *Temporal evolution of conditions controlling the THM behaviour of repository rock mass: heat generation and ice loads. The assessment time frame is 1 million years.*

In addition to the load scenarios associated with the time frames, or climate periods, listed above, there is the possibility of earthquakes occurring close to the repository, with hydromechanical effects on the host rock and with possible mechanical effects on the engineered barriers. The shaking and the stress redistribution generated by an earthquake will propagate, shear, close or dilate fractures in the host rock. The extent of these deformations will depend upon the size, location and orientation of the individual fractures in relation to each other, to the earthquake generating fault and on the character of the earthquake. Some of these deformations will be permanent and result in increased or reduced transmissivities, depending on whether the fracture closed or opened in response to the earthquake, and on whether shear displacements took place under low or high normal stresses.

In contrast to other load scenarios, e.g. thermal load during the early temperate phase or glacial loads, for which the resulting deformations are systematic and, as demonstrated later in this report, possible to correlate to transmissivity changes, the net result of the impact of an earthquake close to the repository is judged to be a reorganization of the flow pattern, rather than a systematic increase or decrease of the overall transport capacity of the repository bedrock. This means that it is neither meaningful nor necessary to describe or quantify the bulk hydraulic changes in the host rock occurring as a response to earthquakes. The impact of earthquakes on the transport properties of the repository host rock is therefore not addressed in this report or in the safety assessment.

If, however, a canister is mechanically damaged as a result of an earthquake, the fractures connecting that particular deposition hole with the biosphere are assumed to short-circuit the hydraulic system. This is done without any attempts to quantify the actual mechanical and hydromechanical disturbances imposed upon the fracture system. The possibility of canisters being damaged mechanically as a result of earthquakes is treated in separate reports /Fälth et al. 2010, Munier 2010/.

1.3 Objectives

An evaluation of the potential impact of the different mechanical and hydro-mechanical processes on the hydraulic conditions within and around the repository was made for the SR-Can assessment /Hökmark et al. 2006/. The overall objective of this report is to produce a corresponding evaluation for the SR-Site assessment for the Forsmark site. The evaluation will be based on the layouts actually specified for SR-Site, updated rock mechanics data given in the **Data report** and updated models of the stress evolution, and the associated pore pressure evolution, during a projected glacial cycle.

Similar to the SR-Can assessment, the evaluation is made using combinations of numerical models and analytical solutions.

2 Scope

2.1 General

In this chapter, the modelling approach and the issues considered in the modelling for the different periods (excavation/operation period, initial temperate period, permafrost and glaciations, cf. Figure 1-2) are briefly described.

2.2 Modelling approach

2.2.1 Overview

The THM behaviour of the repository rock mass during the different periods is assessed on different scales in this report as summarized in Table 2-1. Note that there is no explicit H-modelling. Instead results from mechanical (M) and thermo-mechanical (T-M) models are used to estimate changes in transmissivities. Fracture pore pressures input to the models are either hydrostatic (construction/operational and temperate phases) or elevated (permafrost and glacial phases). Elevated pore pressures are derived from separate analyses (cf. Appendix D)

The main modelling tool is the three-dimensional distinct element code *3DEC* which is specifically developed for discontinuous media modelling /Itasca 2007/. For code verification, see the SR-Site **Model summary report**. In keeping with the sign convention used in *3DEC, c*ompressive rock stresses are negative whereas compressive fracture (effective) normal stresses are positive. The code has a built-in programming language, *FISH*, which enables the user to define new variables and functions. *FISH* functions are extensively used in the modelling presented here, for instance to automate temperature calculations and to control moving boundaries. The *3DEC* thermal logic allows for modelling of numerous discrete time-dependent heat sources that can be located within or outside the volume of rock that is actually being modelled, either individually or in regular arrays according to any given repository deposition layout.

3DEC models based on site data for Forsmark and Laxemar /**Data report,** SKB 2010b/ are analyzed on three different scales:

- Small scale one-tunnel near-field models with a detailed representation of the tunnel and a small number of deposition holes.
- Medium scale sized models with 5 tunnels and no deposition holes.
- Large scale models without explicitly modelled openings.

In all *3DEC* analyses of the temperate phase, the thermal impact of all canisters are included, regardless of the model scale and regardless of whether openings are explicitly modelled or not.

Table 2-1. Model type overview.

Phase	Small scale 40×40×40 m	Medium scale 200×200×200 m	Large scale 8×7.5×3 km	Very large scale >>> 8×7.5 ×3 km
Excavation/ Operation	3DEC (M) linear elastic	3DEC (M) fractured	–	
Intial temperate	3DEC (TM) linear elastic Analytical solutions (T)	3DEC (TM) fractured	3DEC (TM) linear elastic 3DEC and analytical solutions (T)	
Permafrost	–	3DEC (M) fractured		
Glaciation	3DEC (M) linear elastic	3DEC (M) fractured	–	

At the very large scale no numerical modelling is performed. Instead estimates of the scope and extent of pore pressure driven processes (e.g. hydraulic jacking) that potentially could be important during the glacial cycle are made. The pore pressure evolution during the glacial cycle is obtained from calculations presented in Appendix D.

The small scale *3DEC* models are generated mainly to analyze stress concentrations around the openings and do not include any fractures. The response of fractures small enough to be contained in the small near-field models is dominated by the way the fractures intersect or pass by the opening peripheries rather than by details in the stress field. The medium scale models are not sufficiently finely meshed to capture small scale local, near-opening, variations in shear and normal displacements. Therefore the assessment of the near-field behaviour of intersecting fractures is based on results obtained by /Fälth and Hökmark 2007/ using small scale *3DEC* models with a stylized fracture geometry defined specifically to cover the response of potentially important fractures.

2.2.2 Couplings

Figure 2-1 (left) shows the principles of THM couplings in a jointed rock mass. For the repository rock mass, the different interactions are not equally important. /Löfman 2005/ simulated the disturbances caused by heat to the hydraulic conditions around the Olkiluoto repository in Finland. He concluded that after the closure of the tunnels, the temperature rise induces an increasing upward groundwater flow, which for hundreds of years delays the recovery of the flow conditions towards the natural state and raises the salinity of groundwater in the vicinity of the repository. These T-H simulations did not address the question of thermally or chemically induced long term effects on the host rock permeability. The thermal disturbance was significant, but of relatively short duration in the safety assessment time perspective. Buoyancy and convection do contribute to the water transport and to heat transport, but the contributions are small compared with the contributions from the natural isothermal groundwater flow and from conductive heat transport, respectively, and are not included here. Similarly, the energy expended on, for instance, friction work is too small to have any measurable influence on the temperature.

Figure 2-1 (right) shows the couplings considered in this report. These are the T→M one (thermal stress), the H→M one (impact of pore pressure on effective stress) and the M→H coupling (change of fracture transmissivity because of shear and normal fracture displacements and permeability increases caused by fracturing). The M→H coupling is not explicitly modelled: instead the effects are estimated or calculated by comparison of the model results (stress concentrations, fracture shear displacements, change in fracture normal stress) with different permeability models (cf. Chapter 3).

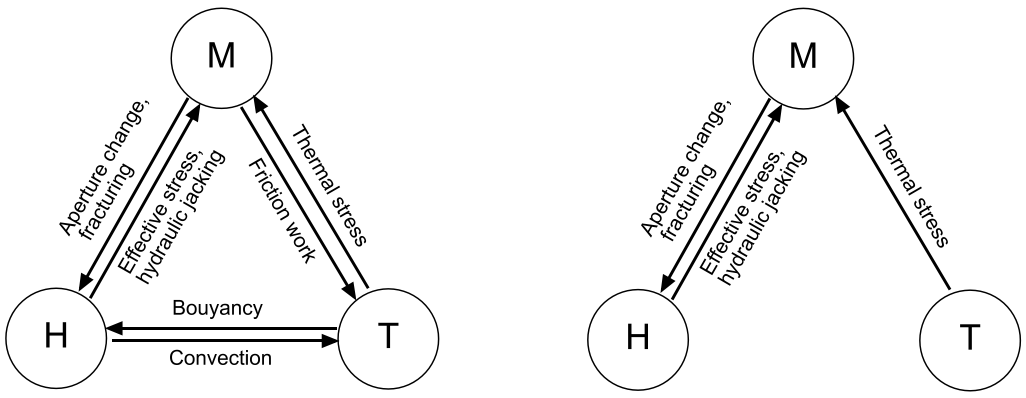

Figure 2-1. *Jointed rock mass couplings in general (left) and couplings relevant to the safety assessment (right).*

2.3 Operational phase – transition from in situ state to state at the time of closure

2.3.1 General description

During construction (excavation) there will be stress redistribution effects around the repository openings. Redistribution effects will not reach more than a couple of opening diameters away from the opening peripheries cf. /Brady and Brown 1993/. Given the spacing between tunnels and deposition holes specified for the different rock domains, this means that the possible impact on fractures transecting tunnels and deposition holes, for instance transmissivity disturbances caused by shear- or normal displacements will be very local. This means also that the effects are independent of how the excavation work is extended over time, and that local models are sufficient and adequate for analyzing excavation effects, at least as far as purely mechanical effects are concerned.

There is the theoretical possibility that the local *in situ* conditions are disturbed by thermal effects, i.e. that overlapping of phases might have to be considered. In case deposition has taken place in nearby parts of the repository and sufficient time has elapsed, thermal stresses may have been generated in the part where construction is going on. This possibility is considered and analyzed schematically by use of analytical solutions in a following chapter (cf. Section 6.2). The outcome justifies, with good margins, the approximation made here and in previous studies, i.e. that the excavation can be handled as a local process taking place in undisturbed rock.

The pore pressure will be reduced from about 5 MPa to atmospheric at the periphery of the openings. This will tend to increase the shear strength of fractures intersecting the near-field. The time scale for the local pore pressure reduction and the extent of the reduction will depend on the repository-scale pressure evolution, the excavation sequence and the local permeability conditions. For the modelling of the operational phase presented in this report, the pore pressure reduction is conservatively ignored.

2.3.2 Handling in this report

The operational phase is modelled on the small scale and on the medium scale. The cases evaluated during the operational phase are:

- Potential of stress induced failure following from stress concentrations around deposition holes and tunnels (Chapter 9).
- Local transmissivity disturbances of intersecting fractures (Chapters 8 and 9).

Naturally, the potential formation of an excavation damaged zone around the deposition tunnel would also be covered, but in the SR-Site project this has been assessed in other projects. The findings of that are summarised in Section 6.5 of the **Data report.**

2.4 Initial temperate period – impact of heat generation

2.4.1 General description

The temperatures in the rock mass surrounding the repository will start to change with the deposition of the first canister. Effects of disturbances such as excavation, ventilation and other activities in the tunnel before deposition and closure are uncertain. Experience from the thermal modelling of the Prototype Repository /Kristensson and Hökmark 2007/ is that the thermal evolution is completely governed by the canister power a few years after deposition and closure and indicates that early disturbances can be ignored. Here, the temperature changes generated by the nuclear fuel were evaluated by considering two main issues:

1. The thermal evolution itself, i.e. the way the temperatures in different regions within and around the repository change over time as a result of the heat emitted by the fuel.
2. The thermomechanical evolution, i.e. the way the heat expansion generates thermal stresses and fracture shear- and normal displacements. Stress concentrations around deposition holes are particularly important because of the risk of stress induced failure (spalling) in the walls of the deposition hole and the following change in the conditions for mass exchange between the buffer and fractures intersecting the deposition hole.

The thermal evolution in itself is of importance because of the 100°C design limit specified for the buffer temperature /SKB 2009a/. Ensuring that this temperature criterion is met for all canisters at all times is a matter of dimensioning the repository /Hökmark et al. 2009/, i.e. of determining the minimum canister spacing. This is dealt with in the Site Engineering Reports /SKB 2009b, 2010g/. The continued long term thermal evolution, after the peak buffer temperature has been reached some 5–15 years after deposition, has some importance to the temperature in repository components like shafts, access tunnels, top seals etc. but no direct impact on anything related to the safety assessment. There may also be some late effects of the residual heat on the projected permafrost development in connection with the next glaciation. Otherwise, the thermal evolution, which is described specifically in Chapter 5, is important only because it controls the thermo-mechanical (and thermo-hydro-mechanical) evolution.

The thermo-mechanical evolution is modelled on three different scales in this report (See Table 2-1). All canisters are assumed to be deposited simultaneously. The validity of this approximation is verified in Sections 5.6 (local temperature evolution) and 6.2 (local stress evolution) by use of analytical solutions. Fracture pore pressures are set to their initial undisturbed values, i.e. ignoring effects of drainage to the repository openings during the operational phase.

2.4.2 Handling in this report

The scenarios evaluated during the initial temperate phase were:

- Stress additions at different depths and accompanying transmissivity impact, cf. Chapters 6 (large-scale) and 8 (near-field);
- Shearing, cf. Chapters 6 (large-scale) and 8 (near-field);
- Heave of ground surface, cf. Chapter 6;
- Increased stress concentrations around deposition holes and associated risk of stress induced failure in the walls (Spalling) cf. Chapter 9.

2.5 Permafrost

The permafrost scenario is handled in connection with glaciation, see the following section.

2.6 Glaciation

2.6.1 General description

The safety assessment includes a projected glacial cycle, which is based on a reconstruction of the Weichselian glaciation, with ice loads advancing and retreating as shown in the left part of Figure 2-2, cf. **Climate Report.** At the time of the largest areal extent the height of ice sheet is assumed to be as in the right part. At the time preceding the arrival of the ice there may be periods of permafrost. The ice loads and the increased pore pressures generated at the ice-rock interface impacts on the stresses, on fracture transmissivities and, potentially, on the stability of fractures and fracture zones.

Stress impact of ice load

The vertical stress addition can be assumed to be equal to the ice load at all times, i.e. it appears and disappears as in Figure 2-2 (left). The horizontal stress additions and the temporal evolution of these also depend on the properties of the elastic crust, the duration and extent of the crust flexure, on the properties of the viscous mantle and on the mechanical crust-mantle interaction. The horizontal stress evolution assumed in this report is selected from a set of results of ice-crust-mantle simulations performed by /Lund et al. 2009/, all based on the ice load histories shown in Figure 2-2 (left). The differences between results obtained using the most relevant, best developed crust-mantle models are not large, meaning that uncertainties in the description of the crust and mantle are not

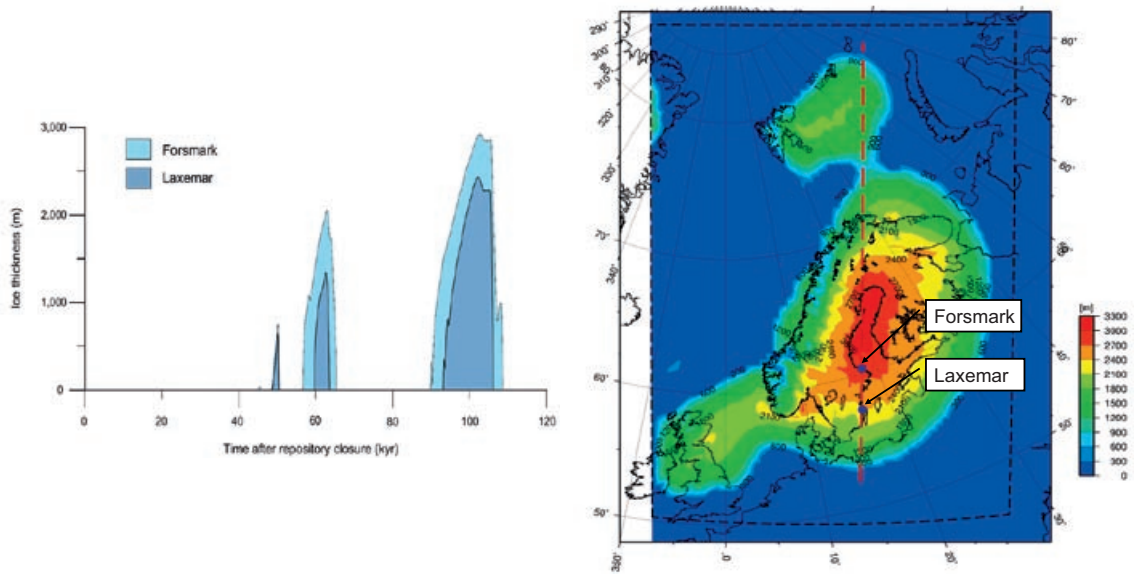

Figure 2-2. *Left: Projected evolution of the ice sheet thickness at Forsmark and Laxemar, from /SKB 2006a/. Right: Height of the latest, Weichselian, ice sheet at 18.4 kyr BP when the ice had its largest extent, modified from /Lund et al. 2009/.*

large, whereas there may be uncertainties related to the ice-load and the possible impacts of tectonic strain /Lund et al. 2009/. /Lund et al. 2009/ do not include the possible impact of the motion of the glacier in their ice/crust/mantle analyses. This is in agreement with the views presented by /Wu 2009/ who argues that basal drag is likely to be smaller than 1 MPa at the ground surface at the average, with shear stresses concentrated to areas where the basal coupling is controlled by subglacial sediments. The impact at larger depths would be well below this level and very small compared to the weight of the ice sheet and the horizontal bending stresses.

Instability

Figure 2-3 shows changes of instability quantity Coulomb Failure Stress (*CFS*) during the previous glacial cycle at 9,500 m depth at Forsmark and Laxemar for excess pore pressures in the range 50–100% of the weight of the ice as calculated by /Lund et al. 2009/ using best estimate crust-mantle models. *CFS* is defined as:

$$CFS = \tau - \mu(\sigma_n - P_f) - c$$

Here τ is the shear stress, μ the coefficient of friction, σ_n the normal stress, P_f the pore pressure and c the cohesion. Positive values of ΔCFS mean instability (regardless of the sign convention otherwise used for compressive stresses in this report). In these examples the *in situ* stresses are based on idealized synthetic stress fields, whereas the instability effective in models and estimates presented in following chapters of this report are based on *in situ* stresses given in Section 6.4 in the **Data report** and in /SKB 2010b/. The examples illustrate nevertheless how the instability may vary over time, with pore pressure and between places. In Forsmark, for instance, the instability is at maximum when the ice has just disappeared, meaning that this may be a period with potential for large-scale shear displacements.

Pore pressure evolution

The pore pressure will increase as an effect of the water pressure at the ice-ground interface. An upper bound estimate would be a pressure corresponding to the ice load, i.e. about 25 MPa for an ice thickness of about 2.8 km. This upper bound boundary pressure estimate (or rather 98% of the actual ice load) is used as basis for all calculations presented here involving pore pressures during the glacial cycle. The pore pressure in the rock, for instance at repository depth, will however lag behind the boundary pressure; the greater the depth and the lower the hydraulic pressure diffusivity,

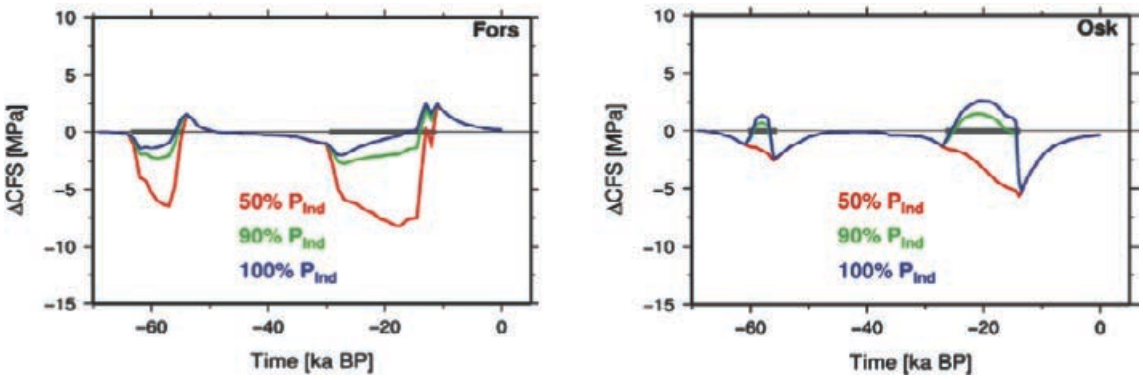

Figure 2-3. *Instability at Forsmark (left) and Laxemar (right) for the glacial stresses calculated by /Lund et al. 2009/. Glacially induced pore pressures correspond to 50–100% of the ice load. In situ stresses are from synthetic stress models.*

the greater the time lag /Lönnqvist and Hökmark 2010/. Glacial cycle rock pore pressures assumed in the models presented here are obtained from excess pore pressure calculations performed with account of the projected ice sheet advance speed and retreat speed (Appendix D). Here the excess pore pressure is taken to be that in the fractures rather than that within the intact rock. The fracture pore pressure contributes to determine fracture shear strengths and fracture transmissivities and may, depending on the large-scale rock permeability, change relatively quickly when the boundary conditions change. The intact rock pressure, which is likely to vary slower, is of less importance to the hydro-mechanical behaviour of the fracture system.

Permafrost

Permafrost conditions are assumed to prevail in a period preceding the arrival of an advancing ice cover (cf. Figure 1-2). Permafrost conditions may coincide with a period of forebulge stress regime, i.e. with a period of time when crustal flexure will tend to reduce the horizontal stresses outside the ice margin, cf. e.g. /Lund et al. 2009/. Additionally, the reduced temperatures during permafrost conditions /Hartikainen et al. 2010/ may reduce the horizontal stresses further. The pore pressure may potentially increase under the impermeable permafrost layer because of the high pore pressures found in the permafrost melt-zone under the ice some distance away from the ice front, cf. /Lönnqvist and Hökmark 2010/. The combined effects of forebulge stresses, thermally induced stress reductions and increased pore pressures may potentially increase the transmissivity of fractures and fracture zones within and around the repository.

2.6.2 Handling in this report

The scenarios evaluated during the permafrost and glacial periods were:

- Stress additions at different depths and accompanying transmissivity impact, cf. Chapters 7 (large-scale) and 8 (near-field);
- Shearing, cf. Chapters 7 (large-scale) and 8 (near-field);
- Pore pressure evolution;
- Thermally induced stress reductions (permafrost only);
- Hydraulic jacking, cf. Chapter 7;
- Spalling, cf. Chapter 9.

3 Approach to evaluating modelling results

3.1 General

The load scenarios described in the previous chapters will be evaluated with regard to:

- Spalling, i.e. stress-driven instability causing splitting/cracking in the periphery of openings.
- Transmissivity changes of existing fractures.

There are the following additional processes that potentially could influence the hydraulic conditions:

- Formation of an excavation disturbed zone (EDZ)
- Propagation and coalescence of existing water-bearing fractures.

The formation and evolution of an EDZ is not addressed in this report. The conceptual description, the experimental background material and the potential consequences for liquid flow in the near-field are described in Section 6.5 in the **Data report**.

Propagation and coalescence of existing fractures are not considered for reasons given in the following section.

3.2 Propagation and coalescence of existing fractures

The geometry of the fracture networks, as described by site-specific Discrete Fracture Network (DFN) models, i.e. the fracture frequency, the size and orientation of individual fractures and the connectivity between individual fractures, may potentially change because of fracture propagation and coalescence when the rock stresses change as a result of mechanical and thermo-mechanical loads. Fracture propagation and coalescence may occur close to the openings, but require high stress levels and high values of the major/minor remote principal stress ratio $\sigma1/\sigma3$. /Shen and Stephansson 1996/ analyzed effects of a number of loading events using the Displacement Discontinuity Method and found propagation and coalescence close to tunnels and deposition holes only if that stress ratio was 400% or larger, i.e. if $\sigma1/\sigma3 \geq 4$. The local and modest changes of the fracture network geometry found in their study are too small to be of importance to the DFN models and to the overall rock mass permeability.

The study of /Shen and Stephansson 1996/ did not address the possibility of fracture propagation far away from the openings, for instance because of tensile conditions near the ground surface appearing as a result of pore pressure variations. This possibility is considered in Chapter 7.

The possibility that the repository, i.e. the system of tunnels and deposition holes, may act as a plane of weakness can be discarded provided that the tunnel spacing is greater than about 20 m /Lönnqvist et al. 2010/.

There is also the possibility of time-dependent fracture growth, i.e. that fractures would propagate also under different and less anisotropic stress conditions than those considered by /Shen and Stephansson 1996/ because of stress corrosion, i.e. strength degradation at the tip of the fracture. /Damjanac and Fairhurst 2010/ demonstrated that confinement suppresses time-dependent fracture growth efficiently, since fracture growth requires tension at the tips of the propagating fracture. Confinement is effective also for the case of zero fracture toughness which represents the limiting state of time-dependent strength decay of a tensile crack. At some distance from the periphery openings the rock will be in compression at all times. After a few tens of years, when the swelling pressure of buffer and backfill has developed, there will be compression also close to the opening peripheries. This means that fracture propagation because of stress corrosion, if it occurs at all, is a process that will be limited in both time and space. For the overall permeability of the repository rock it will not be important. Effects close to the openings can be ignored compared with the uncertainties related to the properties of the tunnel EDZ and the spalled zone.

3.3 Spalling

3.3.1 General

Spalling, i.e. stress-driven instability causing extensional splitting/cracking, in the walls of deposition holes will change the conditions for mass exchange between the buffer and fractures intersecting the deposition hole /SKB 2006b/. In the most recent safety analysis of the KBS-3 repository /SKB 2006b/, spalling is recognized as an important rock mechanics safety analysis issue, although it is also shown that even if spalling occurs the consequences only marginally affect the calculated risk.

Spalling that takes place during the construction and operational phase, in still open deposition holes, is not necessarily of importance to performance and long-term safety. Detached rock fragments can be removed and cavities can be filled with, for instance, pieces of bentonite or with bentonite pellets before or during installation of the bentonite buffer. If the deposition holes remain intact during the construction and operational phase and the bentonite buffer has had time to take up water and begin to close the buffer-rock gap before the thermal stresses have reached levels that may cause spalling, then the bentonite support pressure will probably be sufficient to prevent spalling altogether, or to limit the growth of failed rock regions. /Cho et al. 2002/ and /Andersson and Eng 2005/, for instance, have concluded that confining stresses in the order of tens of kPa are sufficient to control spalling. In addition, if the bentonite-rock gap has closed at the time of the failure, there will not be any disturbances of the geometry and homogeneity of the bentonite buffer because of displaced rock fragments. Thus, the main concern will be spalling induced by thermal stresses in deposition holes with still open bentonite-rock gaps.

It will be demonstrated in Chapter 9 that the tangential stresses in the walls of the deposition holes begin to increase very soon after the canister and the bentonite buffer have been emplaced. Effects of cooling, caused for instance by tunnel ventilation, during the emplacement work are difficult to quantify, and are therefore conservatively ignored in the assessment of the early thermal and thermo-mechanical evolution.

Provided that the bentonite pellets, planned to fill out the annular buffer-rock space, are in place soon after canister deposition, there will not be any holes with open bentonite-rock gaps at the time when thermally induced spalling might be initiated. The support pressure provided by the loosely filled pellets is however not large and cannot, without relevant field evidence, be trusted to suppress the spalling process.

Spalling strength

For spalling to occur, the stresses in the periphery must exceed the spalling strength. The present view is that the spalling strength can be expressed as a fraction of the laboratory-determined uniaxial compression strength (UCS). The evaluation of the APSE project, conducted in the TASQ tunnel at Äspö HRL, suggest that the spalling strength should be about 57% of the UCS /Andersson 2007/. The APSE experiment included two deposition holes, both with dimensions approximately as KBS-3 deposition holes, separated by a 1 m pillar (cf. Figure 3-1, top left). In one of the holes a small support pressure was maintained on the walls by use of a water-filled and pressurized rubber bladder. No spalling was observed in the supported hole, whereas spalling took place in part of the open hole in direct response to the stress redistribution following excavation. During a subsequent heating phase the failure propagated downwards (cf. Figure 3-1, right) in reasonably good agreement with the 57% strength estimate as the thermal stresses slowly increased.

The 57% strength estimate seems to have been relevant for the non-heated phase as well as for the heated phases of the APSE test. Therefore, this estimate is used for assessing the spalling risk in the walls of unsupported deposition holes and tunnels in this report without regard to possible impact of stress path differences. It should however be recognized that the geometry of the APSE experiment was designed to maximize the stresses in the floor: the tunnel was oriented perpendicular to the major stress and the floor was rounded. The pillar was slender enough for the stress fields around the two holes to overlap. All this will have impacted on the stress path for points close to the walls of the two deposition holes, in particular the second, open one. The stress concentration found around the edge of the moving bottom of the hole during the excavation will be higher than for a KBS-3 deposition hole for which the geometry has been designed to keep the stresses in the floor region low.

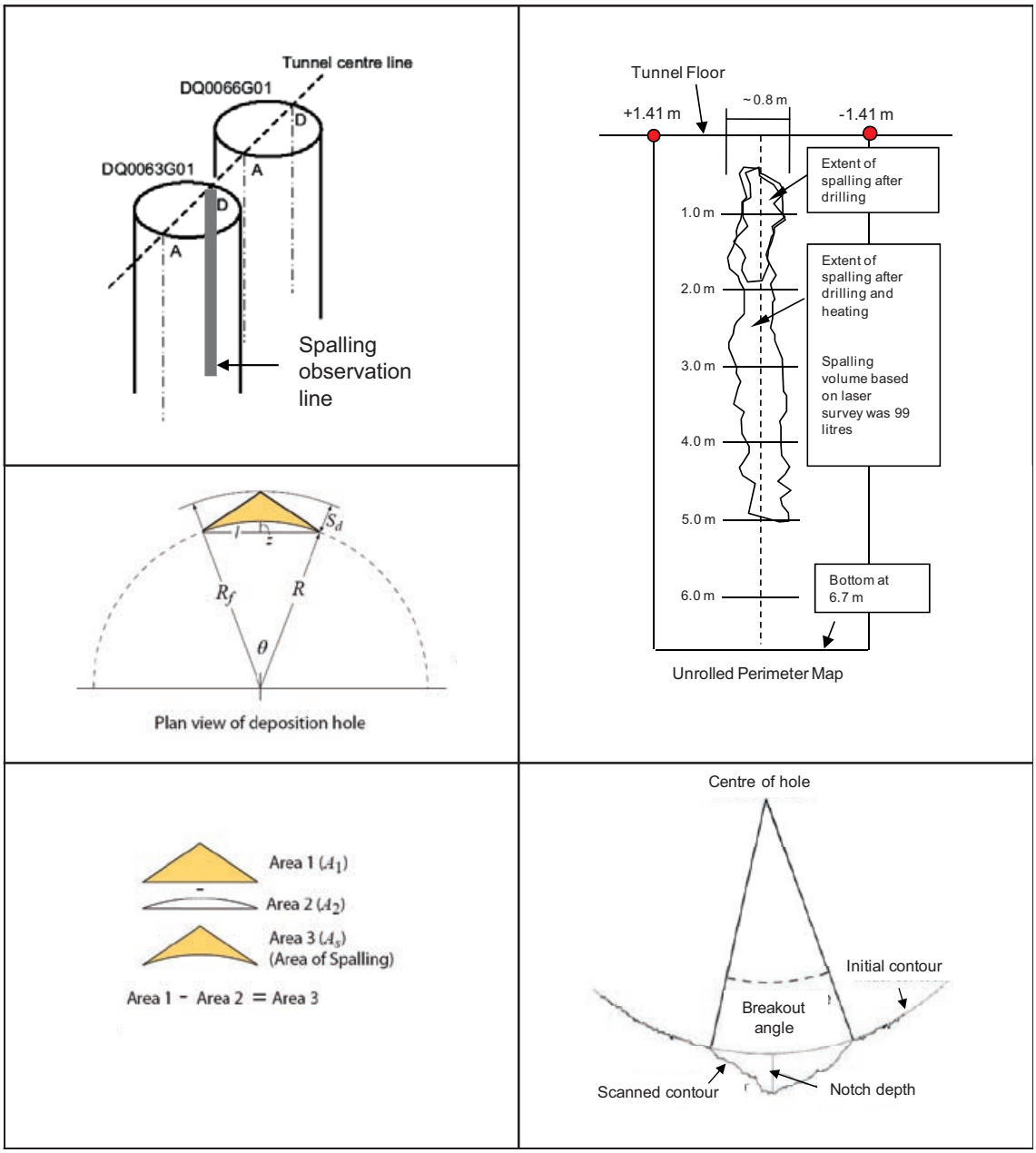

Figure 3-1. *Left: Schematics of APSE experiment and determination of spalled area. Right: Results of laser scan in unsupported APSE hole. From /Andersson and Eng 2005, Martin 2005, Andersson 2007/.*

There are no results from heated tests in KBS-3 type deposition holes performed with a safe margin to the spalling threshold during the initial excavation stage and where a following slow thermally-induced stress increase would push the rock wall stresses over the nominal spalling threshold. Therefore it is not possible to speculate on whether a more gentle stress path would leave the walls with less initial damage and increase the spalling strength. The 57% strength estimate is, however, probably conservative from the stress path point of view.

The CAPS experiment in the TASQ tunnel at Äspö HRL included eight holes (0.5 m diameter and 4 m deep) and was conducted primarily to explore the possible effects of very small support pressures on the scope and extent of thermally induced spalling (cf. following sections) by comparing spalling observations made in open and supported holes /Glamheden et al. 2010/. The spalling observations differed significantly, however, also among the open holes, apparently because of differences in hydraulic conditions. In deposition holes appearing as dry, minor spalling occurred (at the expected stress level) sporadically in a few small and separated regions, whereas more continuous zones of failure were

observed in holes appearing as wet. The differences in relative humidity are not necessarily the only causes of the differences in spalling observed among the open holes; also inhomogeneities may have contributed. At present, there is no final assessment of the importance of saturation and suction to the spalling strength. For the safety assessment, the main concern is spalling in deposition holes that are sufficiently dry that the bentonite buffer stays unsaturated, i.e. does not develop any supporting swelling pressure, for many months. These deposition holes are likely to exhibit spalling behaviour similar to that found in the dry CAPS holes, which means that the stresses may have to increase in excess of the 57% threshold to produce more than minor and sporadic spalling. The above suggests that the average spalling strength assumed in this report for dry deposition holes (57% of the UCS) is likely to be underestimated rather than overestimated.

Size and shape of failed zone

/Martin 2005/ proposed the following empirical formula to predict the depth of failure S_d in a circular opening of radius a:

$$S_d = a \cdot \left(0.5 \frac{\sigma_{\theta\theta}}{\sigma_{sm}} - 0.52 \pm 0.1 \right), \text{ for } \sigma_{\theta\theta} > \sigma_{sm} \qquad \text{Eq. 3-1}$$

Here $\sigma_{\theta\theta}$ and σ_{sm} are the maximum boundary stress and the rock mass spalling strength, respectively. The equation is a fit to data obtained from tunnels excavated in high stress rock masses around the world and does not necessarily apply for cases where the maximum boundary stress is the result of slow thermally induced stress increase. The relation is rewritten and pictured in Figure 3-2. Note that APSE data, obtained during different stages of the thermal stress evolution, do not plot on the best fit line.

Considering how the APSE data plot in the diagram, the failure depth in a slowly heated KBS-3 deposition hole is likely to increase much slower with increasing tangential stress than predicted by Equation 3-1. Instead it appears that the increasing thermal load did not increase the failure depth once a stable v-shaped notch, similar to the one shown in Figure 3-1 (left) had formed /Andersson and Eng 2005/. The vertical extension of the failure increased, however as shown in Figure 3-1, right. The findings seem to support the notion that the depth of failure is controlled by the tangential stress that prevailed locally when the failure started, and not by subsequent stresses. Note that the failure did not extend into the floor region, i.e. the tunnel EDZ.

In URL in Canada, brittle failures were found along nearly vertical lines in the walls of 0.6 m holes, drilled in the floor of a tunnel in fracture-free, highly stressed rock /Martino and Read 1995/. Spalling to a depth of about 50 mm from the walls occurred as a result of the excavation. In the top part of the hole, down to depth of about 0.5 m below the tunnel floor, no spalling was observed. During a subsequent heating phase, the failure propagated downwards such that the failure zone was continuous down to the bottom of the hole at the end of experiment, still with the exception of the top 0.5 m. However, similar to the APSE, the depth of the failure did not change much during the period of increasing thermal load.

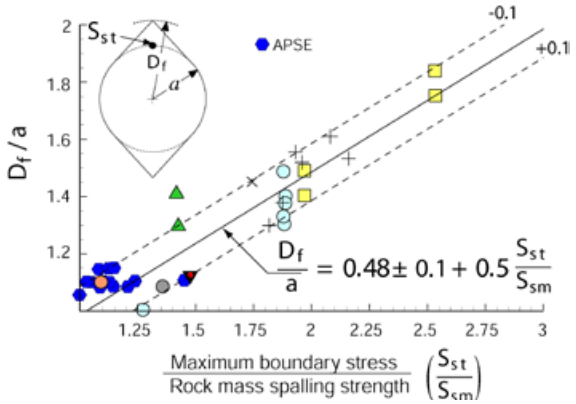

Figure 3-2. *Depth of failure measured in the APSE test does not appear to increase with the boundary stress as predicted by the stress-depth relation. From /Andersson 2007/.*

The area of the spalled zone can be estimated by the following expression /Martin 2005/, cf. Figure 3-1 (bottom, left):

$$A_S = \frac{1}{2} R\left(2(R + S_d)\sin\left(\frac{\theta}{2}\right) - R\theta \right) \qquad \text{Eq. 3-2}$$

Here, R is the radius of the deposition hole, S_d is the depth of failure and θ (radians) the breakout angle. In the APSE test the maximum depth of failure was about 0.13 m, whereas the average was about 0.07 m, say 0.1 m to be on the safe side. The width of the spalled zone was about 0.5 at the average. The total spalling volume was about 0.1 m^3 /Andersson 2007/.

3.3.2 Effects of support pressure

Spalling is known to be sensitive to small confining pressures, cf. e.g. /Diederichs 2007/. Theoretically this is a consequence of the nature of microcrack growth in crystalline rocks, which is a process of tensile rupture along grain boundaries oriented in the direction of the major (compressive) stress. Confining pressure, acting normal to the extending cracks, is very effective in suppressing the tensions induced at the crack tips, so that crack growth is inhibited, and the rock strength increases rapidly with confinement as the zone of tension is suppressed, cf. e.g. /Damjanac and Fairhurst 2010/.

In the unsupported hole in the APSE experiment spalling was observed for tangential stresses amounting to around 57% of the Uniaxial Compressive Strength (UCS) /Andersson 2007/. In the supported hole no spalling was observed, i.e. in qualitative keeping with the support pressure theory. The support pressure was, however, in the order of 100 kPa and more, i.e. significantly larger than the pressure that would be provided by loosely filled bentonite pellets.

The CAPS experiment was carried out particularly to establish whether or not the pressure provided by dry, loosely filled bentonite pellets would be sufficient to control the spalling. The experiment was carried out in a part of the tunnel previously used for the APSE test, meaning that the evaluation of the two tests could be based on the same set of rock mass parameter values. Figure 3-3 shows the outlines of the experiment. Four pairs of holes (0.5 m diameter and 4 m deep) were excavated

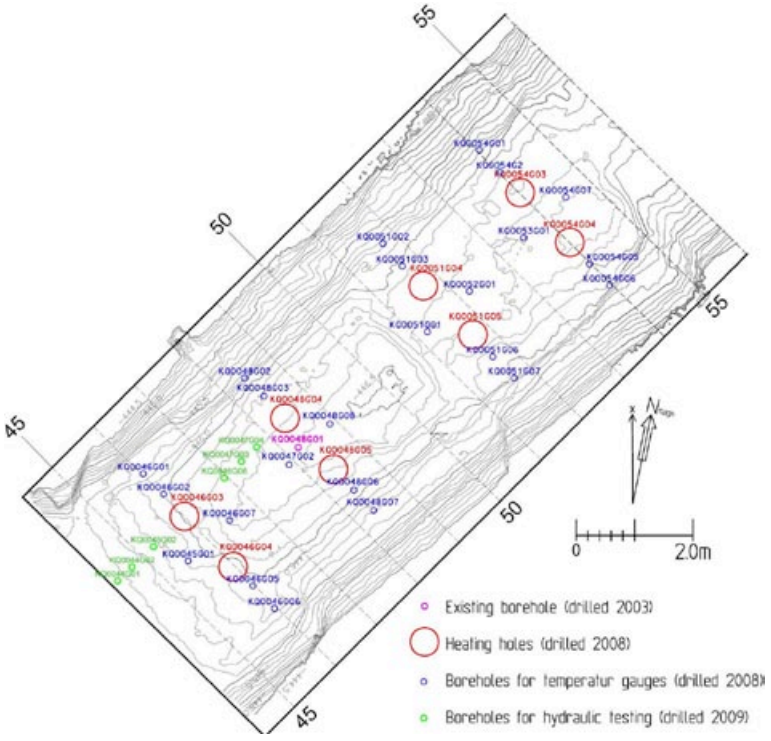

Figure 3-3. *CAPS holes, 0.5m in diameter in the floor of TASQ-tunnel at Äspö HRL. From /Glamheden et al. 2010/.*

in the tunnel floor. Similar to the APSE test the stresses in the floor were high enough that spalling took place in a limited height section in the upper part of the holes in direct response to the stress redistribution caused by excavation. Some of the holes were left open during the subsequent heating phase, whereas in some holes the space between rock wall and the heated central cylinder was filled with dried, non-swelling, clay pellets with mechanical properties similar to those of dry bentonite pellets /Glamheden et al. 2010/.

Noting that the results were highly variable and not totally consistent, presumably because of different saturation conditions and the rock inhomogeneity, /Glamheden et al. 2010/ yet concluded that the support pressure provided by the loosely filled pellets limited the growth and extension of the spalled zone very efficiently, even if it did not completely inhibit crack formation. Injection tests performed in the supported, potentially fractured, part of the wall indicated that no continuous zone of increased permeability had formed.

3.3.3 Models for assessment of hydraulic conductivity in spalled zone

The permeability in the spalled zone is estimated based on observations from the APSE and CAPS experiments in separate documents /Neretnieks and Andersson 2009/ and /Glamheden et al. 2010/.

3.4 Transmissivity effects on single fractures

The existing fracture network controls the hydraulic conditions on all scales larger than that of the individual deposition holes, which may be influenced also by spalling. The hydraulic transmissivity T of individual fractures depend on the hydraulic aperture e:

$$T = \frac{\rho g}{12\mu} e^3, \qquad \text{Eq. 3-3}$$

where g is the gravitational acceleration, ρ the fluid density and μ the dynamic viscosity of the fluid. The relation is known as the cubic flow law and is strictly valid for fluid flow between two perfectly parallel and smooth surfaces separated a distance e. For rock fractures with rough and irregular fracture surfaces the mechanical aperture, E, which is a measure of the real distance between the two surfaces, is larger than the effectively conducting hydraulic aperture e. The ratio E/e between the mechanical and hydraulic apertures depends on the roughness of the fracture surfaces and approaches unity when the apertures increase. /Hakami 1995/ found ratios between 1.1 and 1.7 for mechanical apertures in the 100–500 µm range. /Barton 1982/ suggested the model pictured in Figure 3-4. Here, JRC is the Joint Roughness Coefficient.

According to /Barton 1982/ the hydraulic aperture is thus given by:

$$e = \frac{E^2}{JRC^{2.5}} \qquad \text{Eq. 3-4}$$

Deformation zones and fractures located within and around the repository will be subject to mechanical and hydromechanical disturbances, i.e. shear displacements, changes in mechanical normal load and fluid pressure variations, during all repository phases. All these disturbances may potentially change the mechanical and hydraulic apertures. For the safety assessment, the issue is to estimate the accompanying transmissivity changes. The following discussion is based on models and views established mainly by use of results obtained from tests performed on laboratory-scale samples of single fractures. In Chapters 6, 7 and 8, the evolution of normal load and shear displacements on differently oriented and located fractures and deformation zones are calculated by use of numerical models and analytical solutions. The resulting impact on transmissivities are estimated using the transmissivity models described in this section, although they are not necessarily fully relevant for deformation zones containing multiple, connected and disconnected, fractures.

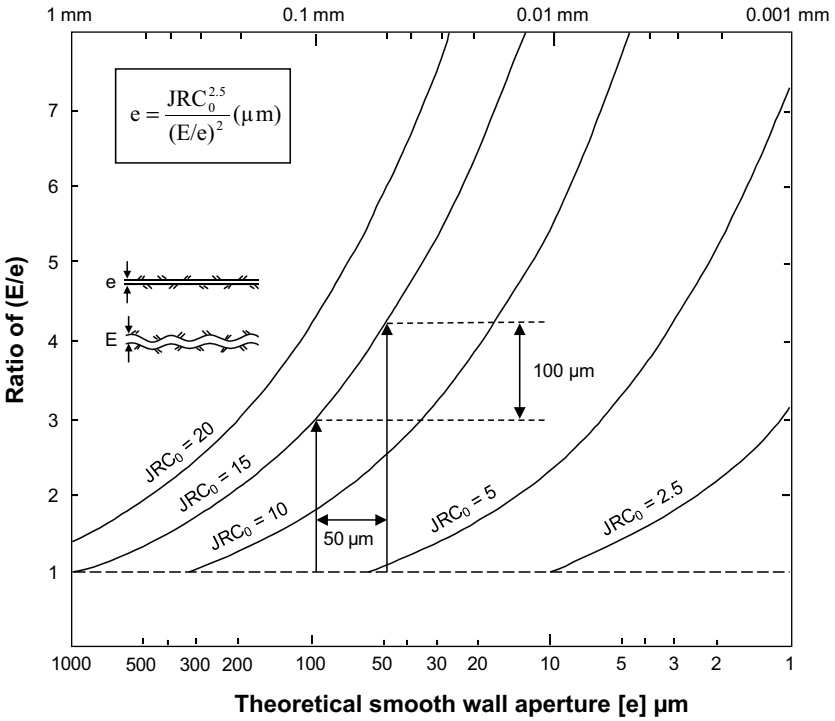

Figure 3-4. *Empirical relation between aperture ratio E/e and smooth wall aperture e for different values of the Joint Roughness Coefficient (JRC). For the example indicated by the arrows, a 50 µm increase in hydraulic aperture would require a mechanical opening of approximately 100 µm. Based on figure from /Barton 1982/.*

3.4.1 Transmissivity changes caused by normal stress variations

When the normal stress on an individual fracture changes as a result of loading or un-loading of the rock containing the fracture, the mechanical aperture E and the hydraulic aperture e will change, leading to decreased or increased transmissivity of the individual fracture. The mechanical response is controlled by the fracture normal stiffness K_n.

$$K_n = \frac{d\sigma_n}{dE},$$

where σ_n is the effective normal stress acting on the fracture. The effects on transmissivity depend on the stress-stiffness relation and on how mechanical apertures should be translated to hydraulic apertures.

Mechanical aperture changes

Stress-deformation relations for single fractures are non-linear with stiffnesses increasing strongly with increasing compression (cf. e.g. /Goodman 1976, Bandis 1980/). Most stress-closure models can be reasonably well described by the stress-stiffness relation contained in the continuously yielding (CY) joint model /Itasca 2007/ which approximates the hyperbolic relation in Barton-Bandis joint model /Barton 1982, Barton et al. 1985/. The CY normal stress-stiffness relation reads:

$$K_n = JKN\sigma_n^{JEN} \qquad \text{Eq. 3-5}$$

Here, K_n is the joint normal stiffness, σ_n the effective joint normal stress, and *JKN* and *JEN* model parameters. Figure 3-5 (left) shows a fit of stress-stiffness data, derived from results given by /Vik and Barton 1988/ to Equation 3-5. Note that *JKN* is the stiffness at 1 MPa of normal stress, while *JEN* is the slope of the curves in the double-logarithmic diagram. Figure 3-5 (right) shows, for comparison, stress-stiffness data compiled in a literature study by /Fransson 2009/. Qualitatively, i.e. with respect to the nature of the stress-stiffness relation, the literature data is in support of the CY model results. At a normal stress of 10 MPa, joint stiffnesses are about 1,000 GPa/m, whereas they range between 1,000 and 10,000 GPa/m for the specific joint sets considered in the Stripa study (left).

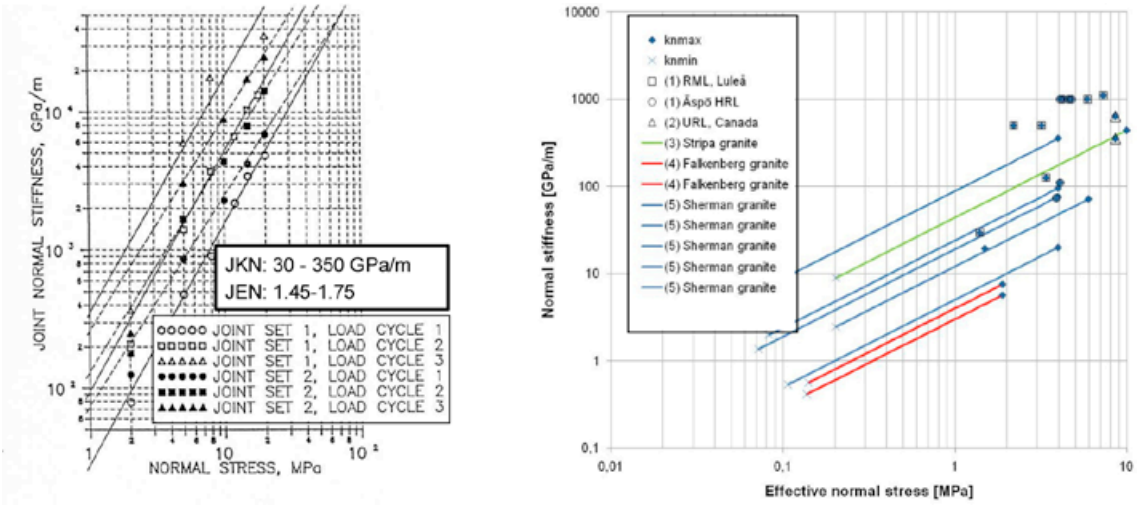

Figure 3-5. *Discrete plot symbols show data derived from /Vik and Barton 1988/, who determined parameter values of Barton-Bandis joint model for two sets of Stripa granite joints and generated stress-displacement relations by use of that model. The straight lines are fits of Equation 3-5 to the results. JEN is obtained as the slope of the straight lines and JKN as the intercept with the vertical axis. From /Hökmark 1990, Fransson 2009/.*

For the purpose of this report, it is suggested that the law given by Equation 3-5 captures the important aspects of stress-opening/closure behaviour of rock fractures sufficiently well (at least for the stress ranges indicated in Figure 3-5) to be used as point of departure for a general stress-transmissivity model. If the initial aperture at normal stress σ_0 is E_0, then Equation 3-6 gives the aperture E at stress σ as:

$$E = E_0 + \Delta E = E_0 - \frac{1}{JKN}\int_{\sigma_0}^{\sigma} \sigma'^{-JEN} d\sigma' \qquad \text{Eq. 3-6}$$

Values of parameters *JKN* and *JEN* are obtained from results of cyclic loading compression tests performed on core samples from the sites (cf. **Data report** and handling in Chapter 4). The parameter values are determined from the results of the second load cycle, observing that stiffness results obtained from the first cycle are likely to be influenced by the disturbances done to the fracture surfaces during sampling (cf. e.g. /Martin et al. 1990/).

Hydraulic aperture changes

Using site-values of the Joint Roughness Coefficient *JRC*, Equation 3-4 is used to convert the mechanical apertures given by Equation 3-6 to hydraulic apertures.

The law given by Equation 3-6 does not, however, account for the existence of a limiting residual aperture (as, for instance, hyperbolic laws do, cf. e.g. /Fransson 2009/) and may potentially overestimate joint closure at high normal stresses. For given values of *JKN, JEN* and *JRC,* the exponential expression, suggested by /Liu et al. 2003/, that was used in the SR-Can assessment of THM rock processes /Hökmark et al. 2006/ can be fitted to the hydraulic apertures obtained using Equations 3-4 and 3-6. The exponential expression is given by:

$$e = e_r + e_{max} \exp(-\alpha\sigma_n) \qquad \text{Eq. 3-7}$$

Here e_r is the residual aperture and σ_n the effective normal stress whereas e_{max} and α are model parameters. For the Forsmark site, values of the parameters *JKN, JEN, JRC* as well as values of e_r, e_{max} and α are given in Section 6.4 in the **Data report**. Figure 3-6 shows examples of exponential fits.

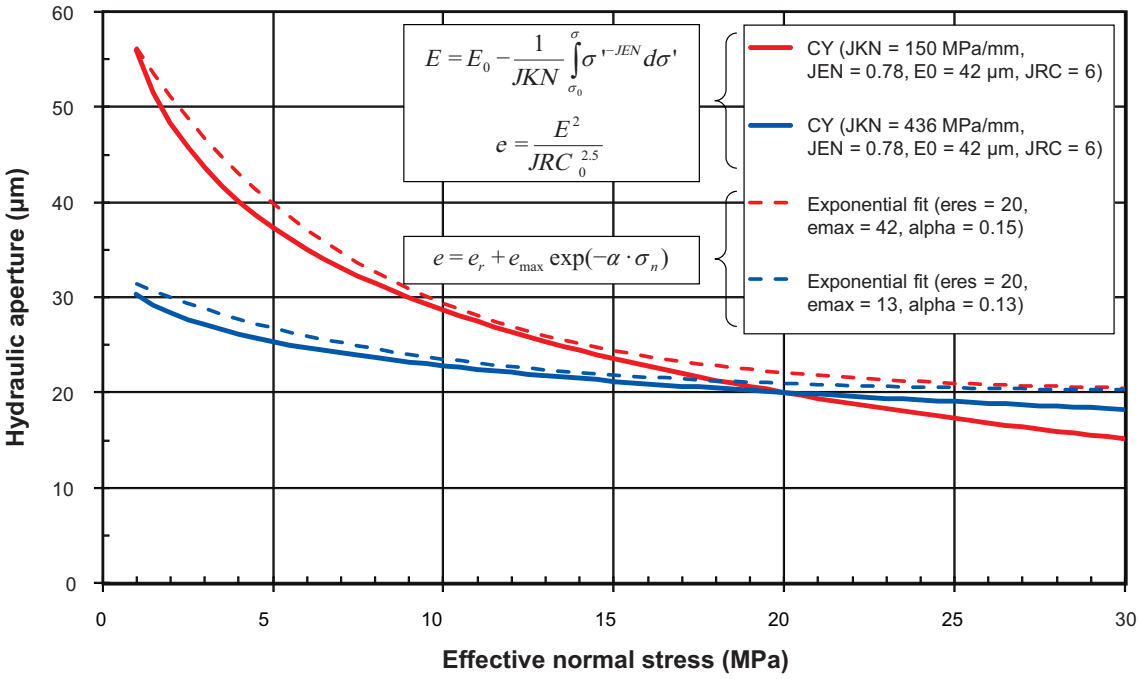

Figure 3-6. *Stress-aperture relations.*

Relative transmissivities

Once the stress-aperture relations are established, following the cubic flow law, the relative transmissivities are given by

$$T / T_0 = (e / e_0)^3 \qquad \text{Eq. 3-8}$$

Figure 3-7 shows examples of stress- relative transmissivity relation for two sets of parameter values. Here the relative transmissivities have been normalized to two different values of the initial normal stress: 10 MPa (left) and 20 MPa (right). The relations are compared with a direct, empirical stress-transmissivity law proposed by /Raven and Gale 1985/ and /Dershowitz et al. 1991/. Contrary to the stress-transmissivity results described above, there are no explicit assumptions regarding stiffness, flow laws or relation between mechanical and hydraulic apertures.

$$T / T_0 = (\sigma / \sigma_0)^{-\beta} \qquad \text{Eq. 3-9}$$

T and T_0 are the transmissivities at normal effective normal stresses σ and σ_0, respectively, and β is a model parameter. For rock joints samples of Stripa granite, /Dershowitz et al. 1991/ found that $\beta = 1$ would reproduce the measured results reasonably well. Figure 3-7 shows relative transmissivities calculated by use of Equation 3-9 compared with results obtained using the exponential fit and the cubic flow law.

Figure 3-7 illustrates the sensitivity to normal stress reductions. The basis for determination of parameter values used in the report is described in Section 6.4 in the **Data report**. The actual parameter values used for the site specific model are given in Chapter 4.

3.4.2 Shear displacements

During fracture shear movements, the mechanical aperture will change due to dilation, i.e. the two fracture surfaces are forced to separate because of surface irregularities. Dilation is, however, not an easily calculated quantity. Depending on the magnitude of the normal stress and on the joint wall strength, asperities can be sheared through or overridden. A compilation of models and concepts relevant to the problem of normal deformations and aperture changes during shear is given by /Olsson 1998/. Equation 3-10 below, for instance, is an approximation of the peak dilation angle d_n suggested by /Barton and Choubey 1977/ to be valid at low normal stresses.

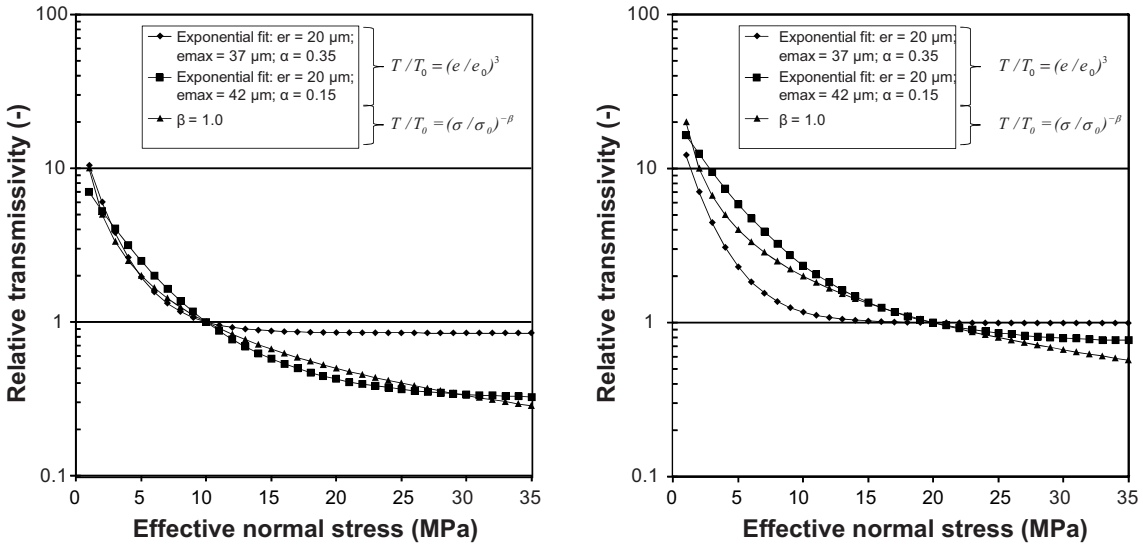

Figure 3-7. *Stress-transmissivity relations normalized to different values of the initial normal stress.*

$$d_n = JRC \cdot \log(JCS / \sigma_n) \qquad \text{Eq. 3-10}$$

Here, σ_n is the joint normal stress. *JRC* is the Joint Roughness Coefficient and *JCS* the effective Joint wall Compressive Strength (see e.g. /Barton and Choubey 1977, Bandis et al. 1983/). Here, "low normal stress" relates to the value of *JCS*. For *Ävrö granite* fractures, /Olsson 1998/ found that the equation reproduced peak dilation angles measured at normal stresses of 2–4 MPa. The equation can be found in the literature in different versions, for instance with coefficients that explicitly account for the more extensive damage of the fracture surfaces that would result from shearing under high compression, cf. /Fransson 2009/.

Figure 3-8 shows results of actual mechanical closure-opening measurements performed in shear box experiments on joint samples of *Ävrö granite* /Olsson 1998/. The hydraulic apertures, calculated from actual flow measurements, are shown along with the mechanical results. An increase in mechanical opening of about 0.7 mm resulted in 0.3 mm increase in hydraulic aperture in this shear test.

The shear tests pictured in Figure 3-8 were conducted under constant stiffness with a low (2 MPa) initial normal load. Higher loads will suppress joint opening and limit the increase in hydraulic aperture.

For shear movements, changes in transmissivity are determined not only by changes in the mechanical apertures, but also by possible gouge production, which would tend to reduce the transmissivity. For high normal stresses, there will be more asperity damage and less dilation. Figure 3-9 shows results of hydro-mechanical constant stiffness shear tests performed on samples of *Ävrö granite* fractures /Olsson 1998/.

/Olsson 1998/ gives two sets of results: one for 2 MPa of initial normal stress and one for 4 MPa. For the tests conducted at 4 MPa of initial normal stress, it took between 3 and 4 mm of shear displacement to arrive at any significant transmissivity increase, whereas the 2 MPa tests all showed transmissivity increases after one mm of shear displacement. For the 4 MPa experiment, the transmissivity increased by perhaps a factor of 20 after 5 mm of shear displacement and by two orders of magnitude after 15 mm.

/Koyama 2007/ presents results from shear-flow tests performed on plaster replicas of granitic rock joint samples. Similar to the results obtained by /Olsson 1998/, transmissivities increased by typically two orders of magnitude after about 5 mm of shear displacement. These tests were, however, performed under even lower normal stresses than those reported by /Olsson 1998/.

It is difficult to estimate corresponding transmissivity effects of shear displacements that take place at significantly higher normal stresses. Increasing the normal stress from 2 MPa to 4 MPa appeared to suppress the increase in transmissivity very efficiently in the experiments performed by /Olsson 1998/. /Esaki et al. 1999/, on the other hand, performed coupled laboratory scale shear-flow tests on artificially created granite fractures and observed transmissivity increases of between one and two

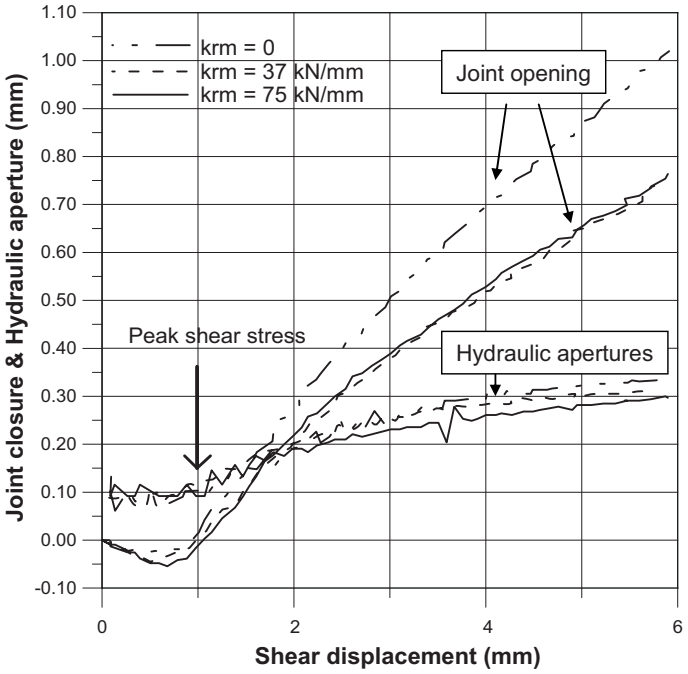

Figure 3-8. *Left: Measured mechanical displacements (openings) and calculated hydraulic apertures. Constant stiffness values were 0 GPa/m, 1 GPa/m and 2 GPa/m, respectively for the three experiments (spring constants krm 0, 37 and 75 kN/mm) From /Olsson 1998/. Note that "closure" is negative.*

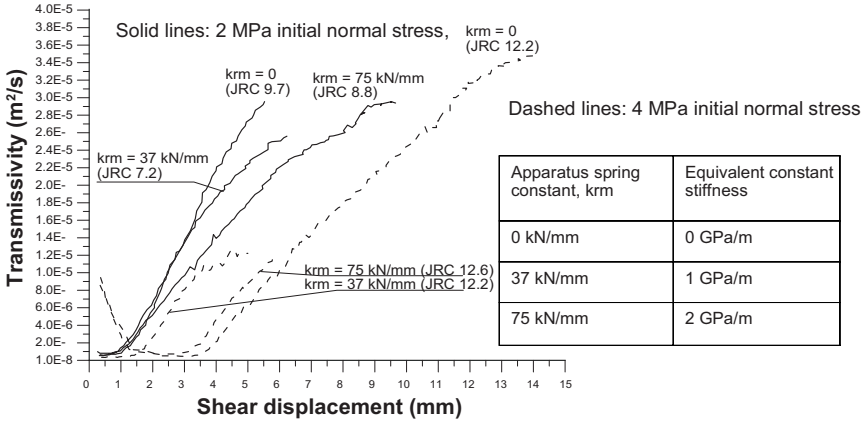

Apparatus spring constant, krm	Equivalent constant stiffness
0 kN/mm	0 GPa/m
37 kN/mm	1 GPa/m
75 kN/mm	2 GPa/m

Figure 3-9. *Measured transmissivities of Ävrö granite fractures as function of shear displacement. The hydro-mechanical shear tests were conducted under different normal stiffnesses. From /Olsson 1998/.*

orders of magnitude after about 5 mm of shear also for tests performed under high normal stresses. It is not clear, however, if the response of the fresh artificial fractures should count as representative of natural fractures. For a test performed under a normal stress of 20 MPa, a repeated movement in the reversed direction gave insignificant transmissivity effects for up to 10 mm of shear. In the following it is assumed that high normal stresses suppress transmissivity effects in a way similar to that found for the natural fractures tested by /Olsson 1998/.

At a distance of a few meters from the repository openings, effective normal stresses will be even larger: typically 10 MPa or more (cf. Chapter 8). The dilation, or mechanical joint separation, will be less than for low-stress fractures (such as those examined by /Olsson 1998/, cf. Figure 3-8) and the gouge production will influence the flow conditions such that the resulting effective transmissivity increase is likely to be very modest. Close to the repository openings where normal stresses may be low, at least locally, shear displacements exceeding about 4 mm may result in local transmissivity increases of between one and two orders of magnitude.

3.5 Evaluation approach – summary

The THM impacts of a damaged zone, EDZ, are not addressed in this report.

The possible THM impacts of the creation of new fractures or the coalescence of existing fractures, i.e. changes in the geometry of the water-bearing fracture system, are judged to too minor, in comparison with the loading-unloading effects on the existing fractures, to be addressed in the overall THM assessment of the repository host rock.

The issues requiring attention in this report are the possible impacts of spalling and transmissivity changes.

3.5.1 Spalling

The spalling strength is assumed to be 52–62% of the laboratory-determined uniaxial compressive strength. This range is used in Chapter 9 to assess the potential for spalling for different assumptions regarding conditions that determine the stress evolution in the walls of deposition holes in Forsmark and Laxemar (*in situ*-stresses, tunnel orientation, local heat transport properties etc.). The following should be observed:

- Exceeding the nominal spalling strength does not necessarily mean that spalling actually will occur:
  - The small support pressure provided by the pellets filling out the annular space between bentonite blocks and the rock wall in KBS-3 deposition holes may suppress the spalling.
  - The assumed spalling strength is likely to be an underestimate for KBS-3 deposition holes. The stress path will be gentler for KBS-3 holes than for the APSE holes. The CAPS test indicated that spalling may occur less systematically in dry deposition holes.
- The shape and the size of the spalled zone cannot be assessed from the calculations. Experience from the APSE /Andersson 2007/ indicates that the failures will be notch-shaped and that the notch will self-stabilize at some depth that depends on the stress that prevailed at the time of the failure. Once the notch is stable, subsequent increases in stress will not significantly increase the depth of the failure. The notch developed at APSE was typically 0.5 m wide and 0.1 m deep /Andersson 2007/.

None of these issues are, however, taken into account in the spalling potential estimates made in this report (Chapter 9).

3.5.2 Fracture transmissivity changes

Fracture transmissivities change because of effective normal stress variations and because of shear displacements.

In this report, effects of effective normal stress variations are estimated by use of the stress-transmissivity relation used in the SR-Can assessment /Hökmark et al. 2006/. Parameter values used in following chapters are based on mechanical data on fractures tested in the site investigations: normal stiffness data and joint roughness data, cf. Section 6.4 in the **Data report**. The stress transmissivity relation is given by Equation 3-7 as:

$$e = e_r + e_{max} \exp(-\alpha\sigma_n)$$

For shear displacements there are no corresponding quantitative relations. Laboratory-scale experiments indicate that transmissivities increase considerably for shear displacements exceeding a couple of millimetres. That transmissivity increase appears, however, to be sensitive to normal load variations. /Olsson 1998/ demonstrated that raising the initial normal stress from 2 MPa to 4 MPa may suppress the potential transmissivity increase almost completely for shear displacements of 4–5 mm (Figure 3-9). In the present report, it is assumed that transmissivity increases, caused by shear displacements taking place under effective normal stresses higher than around 6–7 MPa, are sufficiently small to be ignored. Contrary to the stress-transmissivity model (Equation 3-7), for which a rough reality check can be made by comparing with *in situ* stress-transmissivity correlations (cf. Section 6.4 in the **Data report**), there are no field data that can be used to validate this approach, cf. e.g. /Fransson 2009/

For transmissivity effects of shear displacements one should also note that shear displacements of the magnitudes produced in the laboratory, i.e. typically 5 mm and more, are only possible for very large fractures. This is demonstrated in following chapters. Close to the edges of any fracture, shear displacements are close to zero regardless of the fracture size.

None of the approaches, i.e. to apply stress-transmissivity relations of the type given by Equation 3-7 to account for normal stress variations or to disregard transmissivity effects of shear displacements under high normal stresses, take explicit account of the complex pattern of in-plane flow channels or how that pattern would be disturbed because of compression, separation, shear, dilation and gouge production. /Koyama 2007/ observes, for instance, that the flow fields perpendicular and parallel to the shear direction change differently and that the shear history influences the results of shear flow tests. For the purpose of this study, i.e. to provide order-of-magnitude estimates of potential systematic changes of the hydraulic conditions within and around the repository host rock occurring in response to the projected stress and pore pressure evolution, these schematic ways of handling the processes are judged to be adequate.

For the stress-transmissivity relation (Equation 3-7) results are shown for two sets of parameter values: one set giving a likely best estimate of the average sensitivity to stress changes and one giving an upper bound estimate of that sensitivity.

4 Data used in THM modelling

4.1 Introduction

The repository sites investigated by SKB – Forsmark and Laxemar – are located on the east coast of southern Sweden, cf. Figure 4-1 (left).

The repository for spent nuclear fuel will have a capacity of 6,000 canisters /SKB 2007/, which will be deposited at approximately 500 m depth /SKB 2009b, 2010g/ as shown schematically in Figure 4-1 (right). For each site, specific repository layouts have been designed based on local conditions, e.g. the thermal properties of the rock (that determine canister spacing) and intersections with major deformation zones that require respect distances. Note that the layouts presented for the sites (cf. Sections 4.3 and I.2.2) contain more potential canister positions than the required 6,000 in order to accommodate for any loss of canister positions. The bases for rejecting a deposition hole are outlined in the Site Engineering Reports /SKB 2009b, 2010g/:

- Canister positions will be rejected if a fracture or minor deformation is observed across the entire tunnel perimeter or intersects five or more deposition holes.
- A deposition hole will be rejected if the ground water inflow is more than 0.1 litres/min.
- Canisters may not be placed in rock with very low thermal conductivity (amphibolite) at Forsmark.

The modelling work conducted here is mainly focused on the THM evolution within the deposition areas, i.e. the near-field thermal evolution (Chapter 5), stress induced transmissivity changes of near-field fractures (Chapter 8) and spalling in the walls of depositions holes and tunnels (Chapter 9), although THM evolution on a larger scale is also considered (Chapters 5, 6 and 7). In the modelling work the following types of data are required:

- initial state of stress,
- orientations, mechanical and Mohr-Coulomb strength properties of fractures and fracture zones,
- thermal, thermo-mechanical and mechanical properties of the rock mass,
- spalling strength,
- hydraulic properties of the rock mass and fractures,
- glacial stress additions.

In the following sections site descriptions and a summary of the relevant data used in the THM modelling on different scales of the repository rock mass are given. More detailed descriptions of these data and discussions on uncertainties with regard to Forsmark can be found in Chapter 6 in the **Data report** and references therein.

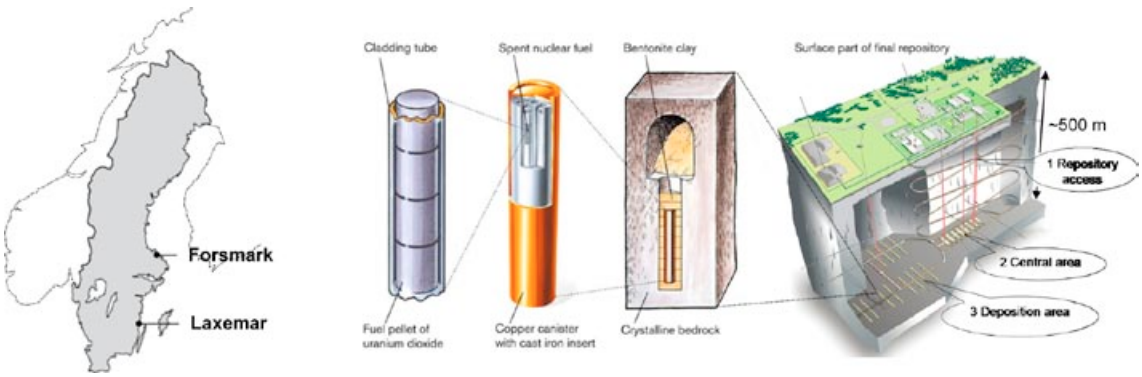

Figure 4-1. *Left: Map of Sweden with the locations of the sites investigated by SKB – Forsmark and Laxemar. Right: Schematic representation of a KBS-3 repository, modified from /SKB 2007, 2009b/.*

4.2 Overview of the Forsmark site

The rock in the candidate area at Forsmark is subdivided into rock domains and fracture domains as shown in Figure 4-2 (left), each with similar characteristics. Rock domain RFM029 is made up of fracture domains FFM01, FFM02 and FFM03, whereas rock domain RFM045 coincides with fracture domain FFM06 /Glamheden et al. 2007a/. The repository will be located within fracture domains FFM01 and FFM06 /SKB 2008/. Figure 4-2 (right) shows a schematic view of the rock mass characteristics at Forsmark.

4.3 Layout

There are several versions of Layout D2 for the Forsmark site depending on the expected loss of potential canister positions /SKB 2009c/. Since the thermal load is most concentrated for the layout with the smallest loss of positions, i.e. the version with 13% loss, the calculations in this report only consider this option. This version of Layout D2 is shown in Figure 4-3 superimposed on a map of the Forsmark area. The repository depth at Forsmark is prescribed such that the roof in any part of the deposition area is never above the elevation –450 m /SKB 2009b/. The deposition tunnels will be inclined for drainage purposes, which will result in a difference in elevation of about 25–30 m between the highest and lowest points of the repository /SKB 2009b/.

The layout version used in the modelling work contains approximately 6,900 potential canister positions /SKB 2009c/ of which about 80% are located within rock domain RFM029 and about 20% within rock domain RFM045. The canister spacing in each of the two rock domains is 6 m (RFM029) and 6.8 m (RFM045) /SKB 2009b/, respectively. To reduce the risk of spalling, the orientations of the deposition tunnels (for Layout D2) have been optimised with respect to the orientation of the major horizontal *in situ* stress /SKB 2009c/. In the layout version considered here, the tunnel orientation varies between approximately 123° and 142° with respect to North. For the purpose of the modelling work, the variations in repository elevation are not considered and an average repository elevation (tunnel floor level) of –460 m is used in all models. There are uncertainties associated with the spatial distribution of fracturing, which means that the rejected canister positions cannot be identified in the layout /SKB 2009b/. In the large-scale modelling (Chapters 5 and 6) every 8th canister is removed uniformly across the repository region order to achieve the given loss of canister positions, *i.e.* the average power density. In the near-field modelling (Chapters 5, 8 and 9) every potential canister position is assumed to be occupied.

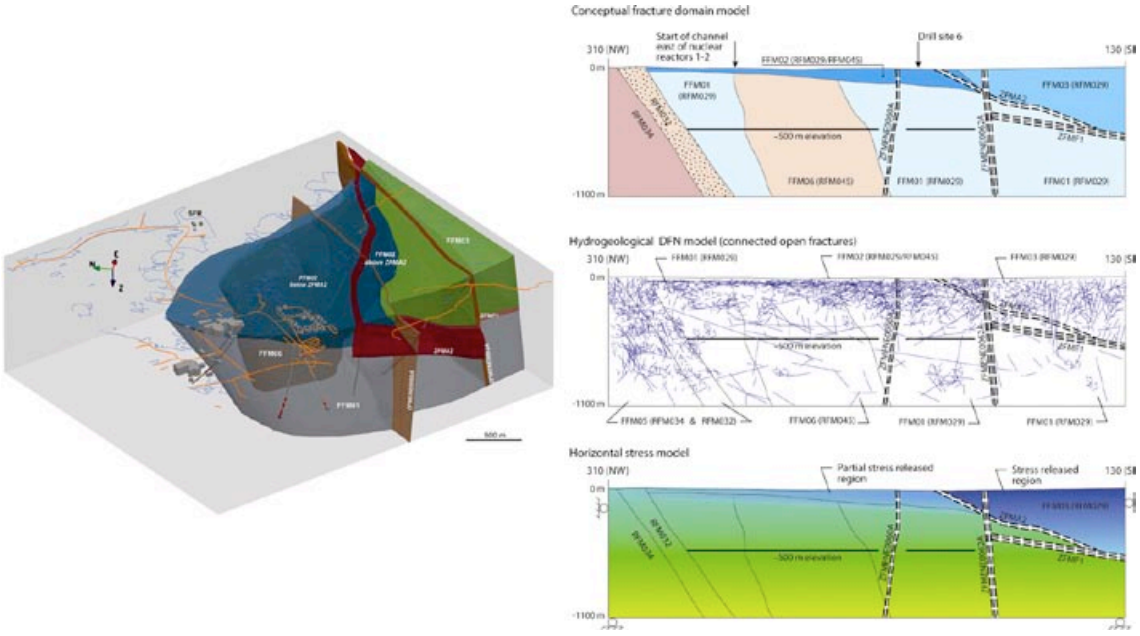

Figure 4-2. *Left: Three dimensional view of the rock domain model at Forsmark viewed towards the East-North-East, from /Olofsson et al. 2007/. Right: Schematic view of rock mass characteristics at Forsmark, from /SKB 2009b/.*

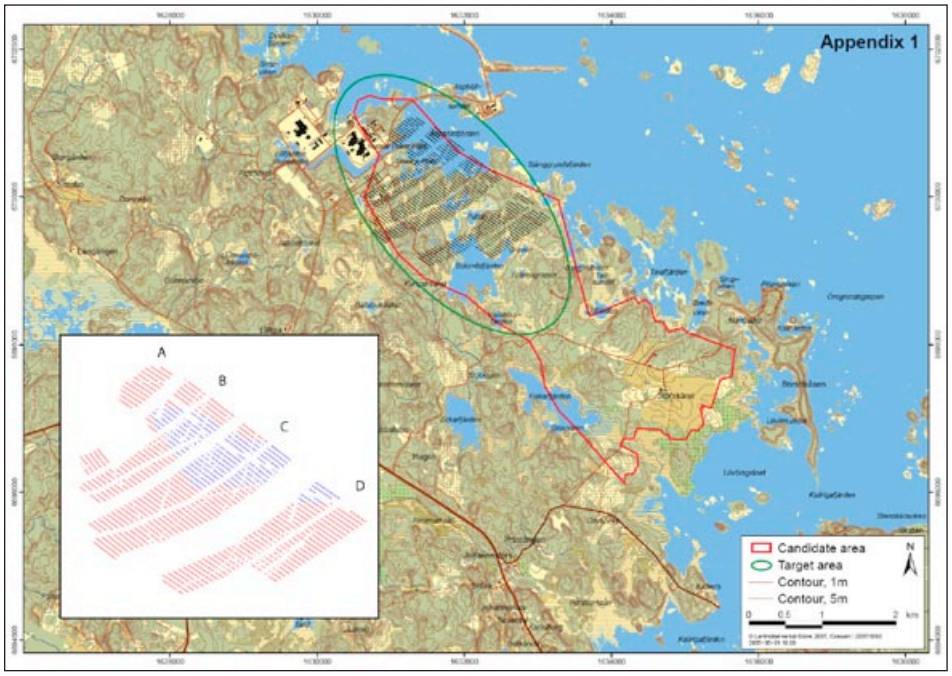

Figure 4-3. *Map of the Forsmark area with the repository layout, version with 13% loss of potential canister positions superimposed in black. Inset shows the layout with the two rock domains RFM029 (canister spacing 6 m) marked in red and RFM045 (canister spacing 6.8 m) marked in blue. Map of Forsmark area from /SKB 2008/.*

4.4 State of stress

Figure 4-4 shows the most likely stress-depth relations with uncertainty spans reported by /Glamheden et al. 2007a/ for the region around the target area at Forsmark, cf. Section 6.4 in the **Data report**. The major principal *in situ* stress appears to have a plunge of approximately 5° /Martin 2007/. Therefore, the stress components σ_H (major horizontal stress), σ_h (minor horizontal stress) and σ_v (vertical stress) are approximated to be principal stresses.

The stress-depth relations used in the large-scale modelling work are given in Section 6.4 in the **Data report**, cf. Table 4-1. These are equivalent with the most likely values of stress magnitudes and orientations shown in Figure 4-4. The stress model reported by /Glamheden et al. 2007a/ is valid to depths of around 600 m. However, in the present modelling work, it is assumed that the stress gradients provided for the depth-range 400–600 m are also valid at larger depths (~1 km). Note that *in situ* stresses are not explicitly included in the large-scale models. Where total stresses are required, the stresses presented in Table 4-1 are added to the modelled thermal stresses (Chapter 6) or glacial stresses (Chapter 7).

Table 4-1. Stress-depth relations used in large-scale modelling work for Forsmark, from Section 6.4 in the Data report. The orientation of the major horizontal in situ stress is given with respect to North.

Depth range	σH (MPa)	σH, orientation (°)	σh (MPa)	σv (MPa)
0–150 m	–19–0.008z	145	–11–0.006z	–0.0265z
150–400 m	–9.1–0.074z	145	–6.8–0.034z	–0.0265z
>400 m	–29.5–0.023z	145	–9.2–0.028z	–0.0265z

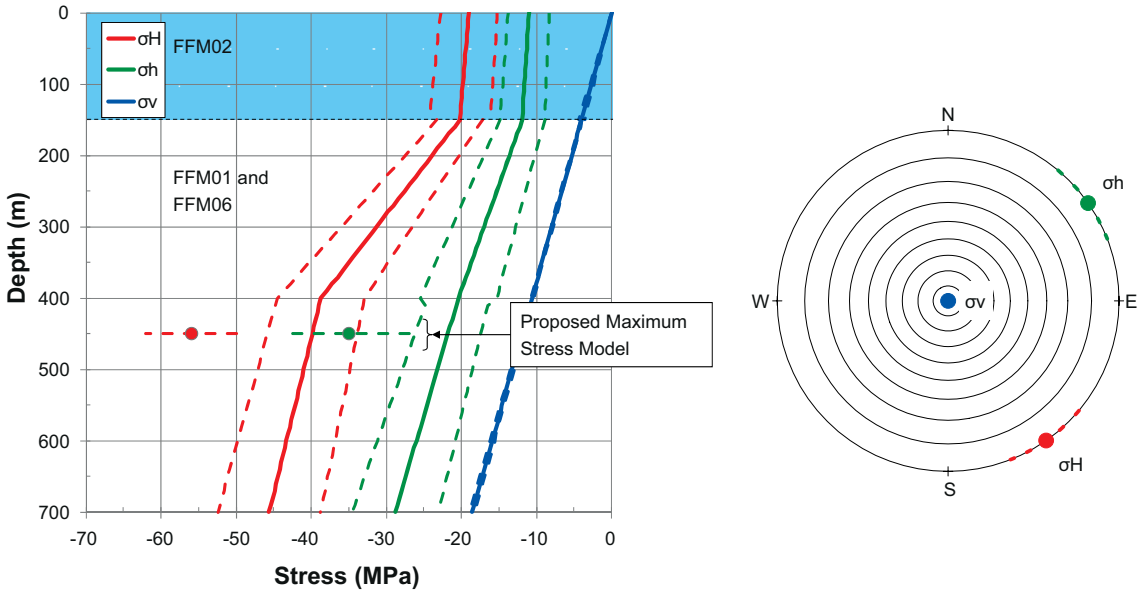

Figure 4-4. *Left: In situ stress model with associated uncertainty spans /Glamheden et al. 2007a/ for the region around the target area at Forsmark (fracture domains FFM01, FFM02 and FFM06). The stress ranges in a proposed Maximum Stress Model /SKB 2009b/ at repository level are marked with plot symbols. Right: Mean value orientations (plot symbols) and ranges in uncertainty (dashed lines) of the principal in situ stress components.*

For the medium-scale (Chapter 8) and small-scale (Chapter 9), the most likely values at repository depth (460 m) for *in situ* stresses and their orientations used, cf. Section 6.4 in the **Data report**. *In situ* stress variations with depth within the near-field models are judged to be sufficiently small not to be considered in the modelling work. A summary of the stress magnitudes and orientations are presented in Table 4-2 (top row). The orientation of the *in situ* stress tensor with respect to the deposition geometry is determined from the layout presented in Figure 4-3. For the near-field model locations considered here, the major horizontal *in situ* stress deviates by about 3–22° from the deposition tunnel axis.

In order to assess the influence of variations in *in situ* stress magnitudes and orientations on the potential for spalling (Chapter 9), five additional stress states (labelled I, II, III, IV and V) are provided in Section 6.4 in the **Data report**, cf. Table 4-2. Stress states I–III take uncertainty spans in the most likely stress model for Forsmark /Glamheden et al. 2007a/ into account. Stress states IV and V are based on a 'Proposed Maximum Stress Model' /SKB 2009b/, which should only be used to assess the risk of spalling due to elevated stress magnitudes at repository level. The five stress states are summarised below.

- I: Most likely stress magnitudes and most unfavourable orientation (about 33–37°) of the major horizontal *in situ* stress with respect to the tunnel orientation, cf. Figure 4-4 (left, solid lines).
- II: Lower limit stress magnitudes and most favourable orientation (about 0–3°) of the major horizontal *in situ* stress with respect to the tunnel orientation, cf. Figure 4-4 (left, dashed lines with lowest absolute magnitude).
- III: Upper limit stress magnitudes and most unfavourable orientation (about 33–37°) of the major horizontal *in situ* stress with respect to the tunnel orientation, cf. Figure 4-4 (left, dashed lines with highest absolute magnitude).
- IV: Mean value of 'Proposed Maximum Stress Model' and most unfavourable orientation (about 33–37°) of the major horizontal *in situ* stress with respect to the tunnel orientation, cf. Figure 4-4 (left, plot symbols).
- V: Upper limit of 'Proposed Maximum Stress Model' and most unfavourable orientation (about 33–37°) of the major horizontal *in situ* stress with respect to the tunnel orientation, cf. Figure 4-4 (left, horizontal dashed lines).

Table 4-2. Most likely in situ stress magnitudes and orientation (with respect to North) at repository depth (460 m) used in small and medium-scale near-field modelling work for Forsmark. Stress states I–V are alternatives used in the spalling assessment. Data compiled from Section 6.4 in the Data report.

Description	σH (MPa)	σH, orientation (°)	σh (MPa)	σv (MPa)
Most likely	–40.08	145	–22.08	–12.19
I	–40.08	130–160	–22.08	–12.19
II	–34.07	130–160	–17.66	–11.96
III	–46.09	130–160	–26.50	–12.42
IV	–56.00	130–160	–35.00	–12.42
V	–62.00	130–160	–43.00	–12.42

4.5 Fractures and fracture zones

The modelling work is based on data for fractures in fracture domain FFM01, cf. Section 6.4 in the **Data report**. There are no data for the mechanical or strength properties of fractures in fracture domain FFM06, but these are assumed to similar to those in fracture domain FFM01 /Glamheden et al. 2007a/.

Figure 4-5 (left) shows the pole orientations of the high and medium confidence deterministic deformation zones in the local model at Forsmark. Note that some of the deformation zones in the pole plot do not intersect the ground surface. The right part of the figure shows the fracture pole set orientations in fracture domains FFM01 and FFM06 /Fox et al. 2007/ on which the orientation model for these fracture domains are built.

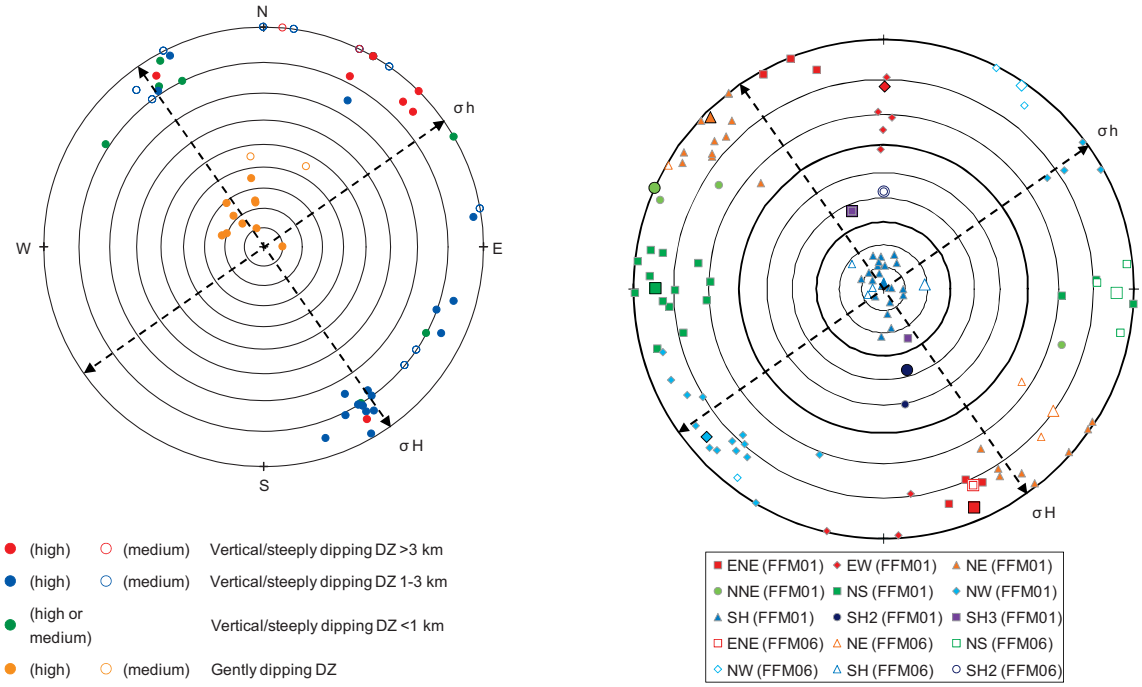

Figure 4-5. *Left: Pole plot of orientations (compiled from Table 5-2 in /Stephens et al. 2007/) of high and medium confidence deformation zones in the local model at Forsmark. Right: Fracture pole orientations in fracture domains FFM01 and FFM06 (compiled from Tables 4-10, 4-13 and 7-1 in /Fox et al. 2007/). Large plot symbols represent the mean orientations of fracture sets in the fracture domain models. The orientations of the present-day horizontal in situ stress components are marked with dashed arrow lines.*

In the large-scale modelling work (Chapters 6 and 7), fractures are not modelled explicitly. Instead, estimates of transmissivity changes and shear displacements are presented

- as functions of depth on hypothetical fracture planes with orientations perpendicular to the *in situ* stress components, i.e. vertical or horizontal planes (cf. Figure 4-5).
- at selected depths on fracture planes striking perpendicular to the major horizontal *in situ* stress and dipping 27.1° (= 45°–35.8°/2). This is the fracture orientation with the largest possible instability, given the Mohr-Coulomb fracture strength and the stress state, cf. Figure 4-6.
- in the form of contoured stereonet plots at selected depths.

Five fracture orientations are chosen for the modelling work on the medium scale, cf. Figure 4-7. Fractures no. 1–4 are based on the orientation model for Fracture Domain FFM01 (global set) /Fox et al. 2007/ and one fracture (no. 5) is specifically oriented such that the potential for shearing is large.

The mechanical and strength properties of the fractures chosen for the medium-scale near-field modelling work are provided in Section 6.4 in the **Data report**, cf. Table 4-3. These values are based on results from direct shear tests of fractures in fracture domain FFM01 reported by /Glamheden et al. 2007a/.

- The Mohr-Coulomb strength properties (cohesion and friction angle) used in the modelling work are obtained by taking the average value of their mean laboratory-determined peak and residual values.
- The normal stiffness is represented by its mean laboratory determined value.
- The shear stiffness is represented by its mean laboratory determined value obtained at a normal stress of 20 MPa.
- The dilatancy angle is represented by its mean laboratory determined value obtained at a normal stress of 20 MPa.

Table 4-3. Mean value fracture properties in fracture domain FFM01 at Forsmark used in the modelling work, cf. Section 6.4 in the Data report.

Fracture properties	Unit	FFM01
Cohesion (c)	MPa	0.5
Friction angle (φ)	°	35.8
Normal stiffness (k_n)	GPa/m	656
Shear stiffness (k_s)	GPa/m	34
Dilatancy angle (ψ)	°	3.2

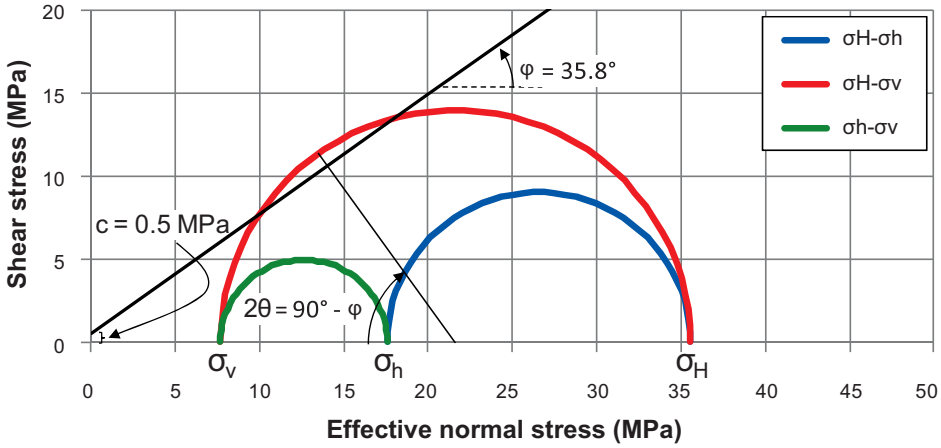

Figure 4-6. *Mohr circle representation of the in situ stress state at repository (460 m) depth (Table 4-2, top row). Given the Mohr-Coulomb fracture strength properties (Table 4-3) and the stress state, the fracture orientation with the largest possible instability dips 27.1° along the major horizontal stress.*

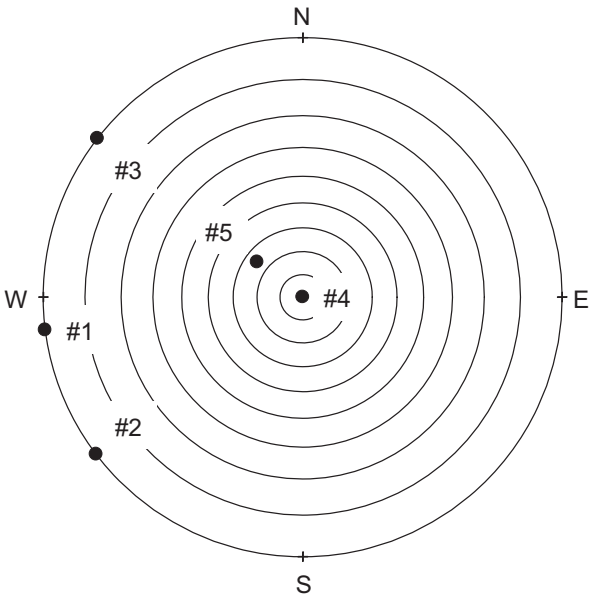

Fracture ID	Trend	Plunge
#1	262.8	0
#2	232.8	0
#3	307.8	0
#4	-	90
#5	307.8	65

Figure 4-7. *Fracture pole orientations used in the medium-scale near-field models for Forsmark. The orientations of fractures no. 1-4 are based on the orientation model for Fracture Domain FFM01 (global set) /Fox et al. 2007/, whereas the orientation of fracture no. 5 is chosen such that the potential for shearing is large.*

4.5.1 Relevance of data

All parameter values given here for the properties of rock fractures are based on results from laboratory-scale experiments. In the following chapters these values are taken to apply for fractures of all sizes. The implications of this are discussed in Chapter 10.

4.6 Thermal, thermo-mechanical and mechanical properties of the rock

The distribution of the thermal conductivity for rock domains RFM029 and RFM045 is presented in Figure 4-8.

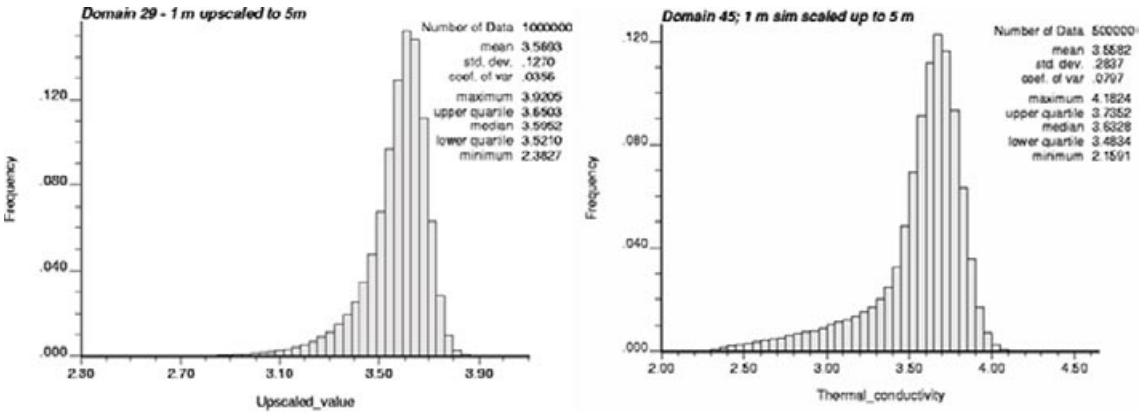

Figure 4-8. *Distribution of thermal conductivity at the 1 m scale upscaled to 5 m in rock domains RFM029 /Back et al. 2007/ (left) and RFM045 /Sundberg et al. 2008b/ (right), cf. Section 6.2 in the* ***Data report****.*

The *in situ* temperatures based on measurements in 8 boreholes at 400, 500 and 600 m depth at the Forsmark site are presented in Section 6.2 in the **Data report**, cf. Table 4-4. An approximate value for the *in situ* temperature at repository level (460 m), 11.2°C, is obtained by interpolation between the values given for the 400 m and 500 m levels. The *in situ* temperature does not influence the thermo-mechanical calculations and is only used in the temperature calculations presented in Chapter 5.

The reference thermal, thermo-mechanical and mechanical parameter values chosen for the modelling work are presented in Table 4-5:

- The heat capacity is represented by its mean value in each rock domain, cf. Section 6.2 in the **Data report**. Note that in the numerical (*3DEC*) thermo-mechanical modelling (on all scales) of the rock in rock domain RFM029 an alternative value of the heat capacity 2.15 MJ/(m^3·K) (based on the dominating rock type) /Back et al. 2007/ is used together with the mean thermal conductivity.
- Two values of the thermal conductivity are chosen: The mean value in each rock domain (cf. Section 6.2 in the **Data report**) and the dimensioning value (*i.e.* the effective thermal conductivity for the hottest canisters) in each rock domain. The latter value is obtained from the nomographic charts in Figure 5-4.
- The value presented for the rock mass density is a generic value used in all modelling work to be compatible with the vertical stress gradient, cf. e.g. Table 4-1 and Section 6.4 in the **Data report**.
- The rock mass is assumed to be isotropic /Glamheden et al. 2007a, p 136/. This means that only two values of the elastic rock mass properties (Young's modulus and Poisson's ratio) are required. These parameters are represented by their mean values in each fracture domain, cf. Section 6.4 in the **Data report**.
- The heat expansion coefficient is represented by the mean value of the dominating rock type (*Granite to granodiorite*, 101057), cf. Section 6.2 in the **Data report**.

The spalling strength of the rock is assumed to be in the range 52–62% of the laboratory determined uniaxial compressive strength (*UCS*) of intact rock, cf. Section 6.4 in the **Data report**. The reference parameter values chosen to represent the uniaxial compressive strength of intact rock are given in Section 6.4 in the **Data report**, cf. Table 4-6, where the given value for each rock domain is the mean value of the dominating rock type (*Granite to granodiorite*, 101057).

In order to assess the thermal and thermo-mechanical impact of uncertainties in thermal, thermo-mechanical and mechanical parameter values an additional set of parameter values are presented in Table 4-7:

- Variations of ±1 standard deviation (0.10 MJ/(m^3·K) in rock domain RFM029 and 0.15 MJ/(m^3·K) in rock domain RFM045 /Sundberg et al. 2008b/) from the mean value, cf. Section 6.2 in the **Data report**.
- Variations of ±1 standard deviation (8 GPa in FFM01 and 12 GPa in FFM06 /Glamheden et al. 2007a/) from the mean value of Young's modulus of the rock mass, cf. Section 6.4 in the **Data report**.
- Variations of ±1 standard deviation (0.03 in FFM01 /Glamheden et al. 2007a/) from the mean value of Poisson's ratio of the rock mass, cf. Section 6.4 in the **Data report**.
- Range of measured mean values of the heat expansion coefficient of the main five rock types in the target volume, cf. Section 6.2 in the **Data report**.

Table 4-4. Mean in situ temperatures at different depths at Forsmark /Sundberg et al. 2008b/, from Section 6.2 in the Data report.

400 m	500 m	600 m
10.5°C	11.6°C	12.8°C

Table 4-5. Reference thermal, thermo-mechanical and mechanical properties of the rock mass at Forsmark, compiled from Sections 6.2 and 6.4 in the Data report, subsection 6.3.2 in /Back et al. 2007/ and Figure 5-4.

Parameters	Unit	RFM029/FFM01	RFM045/FFM06
Heat capacity (C)	MJ/(m^3·K)	2.06 (2.15)	2.12
Mean thermal conductivity (λ_m)	W/(m·K)	3.57	3.56
Dimensioning thermal conductivity (λ_d)	W/(m·K)	2.9	2.55
Density (ρ)	kg/m^3	2,700	2,700
Young's modulus (E)	GPa	70	69
Poisson's ratio (v)	–	0.24	0.27
Heat expansion coefficient (α)	K^{-1}	$7.7 \cdot 10^{-6}$	$7.7 \cdot 10^{-6}$

Table 4-6. Reference values of the strength properties of intact rock at Forsmark, from Section 6.4 in the Data report.

Parameters	Unit	FFM01	FFM06
Uniaxial compressive strength (UCS)	MPa	226	373

Table 4-7. Parameter variations of the thermal, thermo-mechanical and mechanical properties of the rock at Forsmark, compiled from Sections 6.2 and 6.4 in the Data report.

Parameters	Unit	RFM029/FFM01	RFM045/FFM06
Heat capacity (C)	MJ/(m^3·K)	1.96–2.16	1.97–2.27
Young's modulus (E)	GPa	62–78	57–81
Poisson's ratio (v)	–	0.21–0.27	–
Heat expansion coefficient (α)	K^{-1}	$7.2 \cdot 10^{-6}$–$8.1 \cdot 10^{-6}$	–

4.7 Hydraulic properties

4.7.1 Stress-transmissivity relations

There are two potential sources to changes in transmissivity /e.g. Fransson 2009/, cf. Chapter 3.

1. Transmissivity changes due to normal stress variations.
2. Transmissivity changes due to shearing. There is no quantitative model to assess transmissivity changes due to shearing. The effective transmissivity increase is likely to be modest, with a local transmissivity increase of one to two orders of magnitude near repository openings, cf. Chapter 3.

As described in Section 6.4 in the **Data report**, variations in hydraulic aperture with effective normal stress are represented by an exponential relation, cf. Equation 4-1. The relative transmissivity is then calculated assuming the cubic law (Equation 4-2) to hold.

$$e = e_r + e_{max} \exp(-\alpha \cdot \sigma_n) \qquad \text{Eq. 4-1}$$

$$T/T_0 = \left(e/e_0 \right)^3 \qquad \text{Eq. 4-2}$$

Here, e is the total hydraulic aperture, e_r the residual aperture and σ_n is the effective normal stress acting across the fracture, whereas e_{max} and α are model parameters.

Two stress-transmissivity models (denoted Models A and B) are chosen to estimate stress-induced transmissivity changes. In both models, the residual aperture at high normal stress is based on reported transmissivities for fractures below 400 m depth in fracture domain FFM01 ($6.5 \cdot 10^{-9}$ m^2/s) /Follin et al. 2007/. Model A can be considered a "worst case" option based on lower bound fracture normal stiffness estimates and is therefore very sensitive to normal stress variations. Model B is

based on average fracture normal stiffness estimates and is less sensitive to variations in normal stress. Both models are more sensitive to normal stress variations than the most conservative *in situ* correlation reported for Forsmark by /Follin et al. 2008/, cf. Section 6.4 in the **Data report**. The parameter values for each stress-transmissivity model are given below.

- **Model A.** The residual aperture (e_r) is 20 µm, the maximum aperture increase (e_{max}) is 42 µm and α is 0.15.
- **Model B.** The residual aperture (e_r) is 20 µm, the maximum aperture increase (e_{max}) is 13 µm and α is 0.13.

4.7.2 Hydraulic diffusivity

Estimates of the hydraulic conductivity, based on data from /Follin et al. 2007/, at different depth intervals in fracture domain FFM01 are presented in Figure 4-10 (left). An estimate of the bulk hydraulic conductivity over the whole volume of rock is 10^{-9}–10^{-8} m/s /Follin et al. 2007, p 149/. The large-scale distribution of permeability at 465 m depth is shown in Figure 4-10 (right). Note that no hydraulic modelling is conducted; instead the data presented in Figure 4-10 are used to assess changes in transmissivity and the potential for hydraulic jacking at different depths.

The hydraulic diffusivity of the rock mass (κ) is expressed as the ratio between hydraulic conductivity (K) and the specific storage coefficient of the rock (S_S), cf. Equation 4-3. Inserting typical parameter values for the Forsmark site (E = 70 ± 15 GPa, v = 0.24 and n = 0.1–1%, cf. Figure 4-11 and Sections 6.4 and 6.8 in the **Data report**), the resulting value of S_S is in the range $1.0 \cdot 10^{-7}$–$1.6 \cdot 10^{-7}$ m^{-1}. Figure 4-11 shows the hydraulic diffusivity as functions of hydraulic conductivity for different assumptions regarding the properties of the rock mass.

$$\kappa = \frac{K}{S_S} = \frac{K}{\rho \cdot g\left(\frac{n}{K_w} + \frac{(1-2v)(1+v)}{E(1-v)}\right)} \qquad \text{Eq. 4-3}$$

Here, ρ is the density of water (1,000 kg/m3), g is the acceleration due to gravity (9.81 m/s2), n is the porosity of the rock mass, K_w is the bulk modulus of water (2.2 GPa), v is Poisson's ratio and E is Young's modulus.

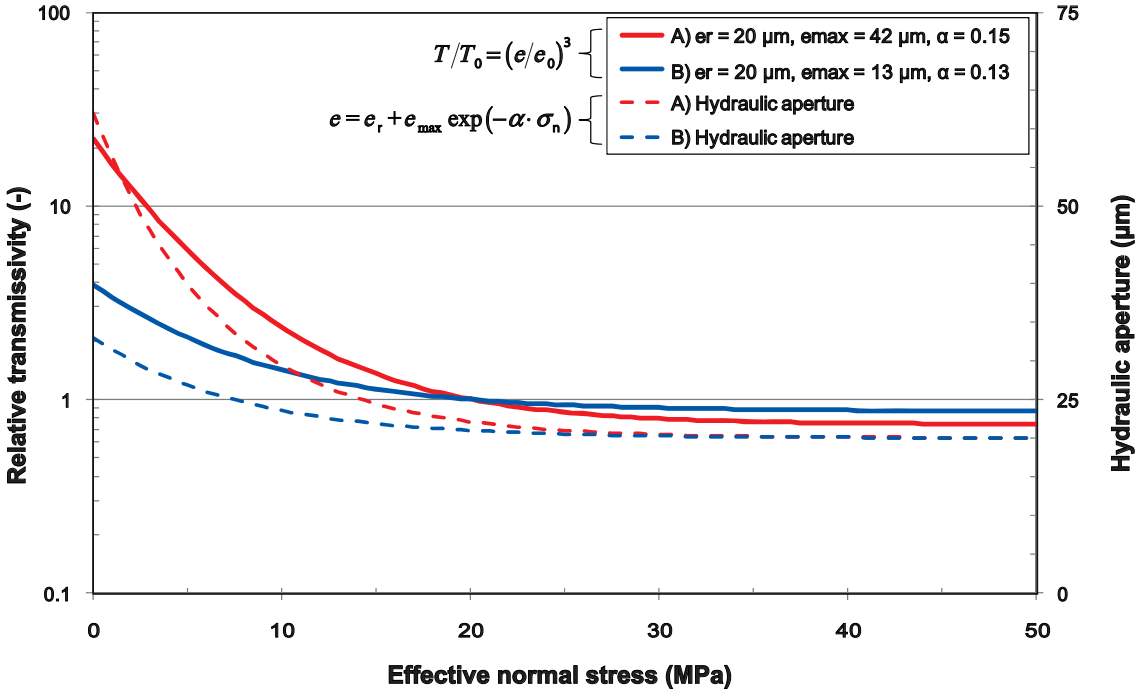

Figure 4-9. *Stress-transmissivity models adopted for the Forsmark site (cf. Equations 4-1 and 4-2). Here, the two models are normalised to a normal stress of 20 MPa. In the chapters presenting the modelling results (Chapters 6, 7 and 8), the relative transmissivity is normalised to in situ conditions.*

Depth range (m)	Bulk conductivity estimate (m/s)
100-200 m	1.44E-07
200-400m	5.18E-10
>400 m	6.31E-11

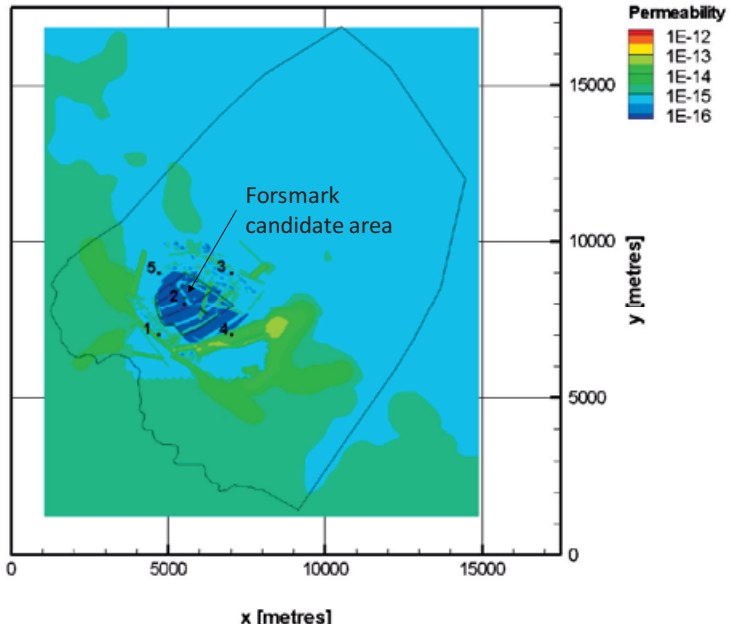

Figure 4-10. *Left: Estimates of the hydraulic conductivity in fracture domain FFM01 at different depths at Forsmark site. Compiled from Tables 10-22, 10-23 and 10-24 in /Follin et al. 2007/. Right: Permeability distribution at 465 m depth, from /Vidstrand et al. 2010/.*

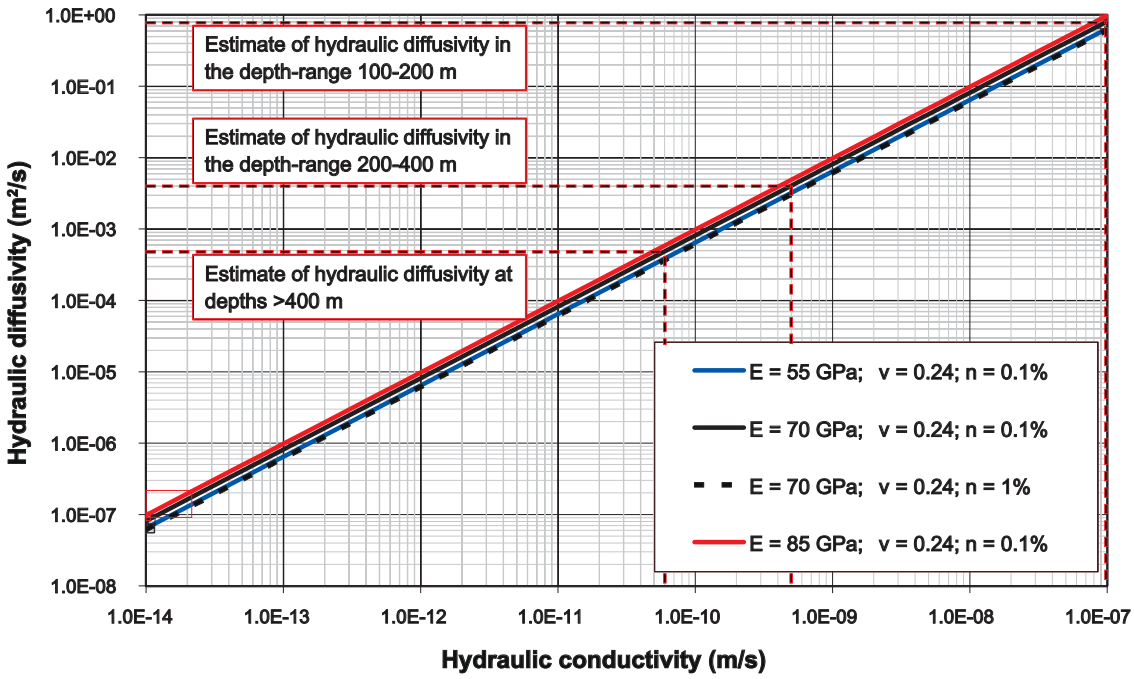

Figure 4-11. *Estimates of hydraulic diffusivity, by use of Equation 4-3, as functions of hydraulic conductivity, modified from /Lönnqvist and Hökmark 2010/.*

4.8 Glaciation

SKB's reference glacial cycle is based on a reconstruction of the Weichselian glaciation, cf. Figure 2-2 (left) and the **Climate report**. For the purpose of the modelling work, only the two major (*i.e.* the two latest) advance and retreat cycles are considered. Time zero denotes the time when the first mechanical effects of an approaching ice occur (cf. Figure 1-2). Therefore, the time-scale in figures showing the evolution of glacially induced stresses or ice sheet thickness in the following sections has no significance other than indicating the time-frame of the two major advance and retreat cycles, *i.e.* it does not represent time after present (or deposition of the canisters). In the following subsections, only data specific for the glacial phase are given. All other data used in the modelling of the glacial phase are the same as those in the previous sections.

4.8.1 Glacially induced stresses

Figure 4-12 shows the temporal development of the glacially induced principal stresses obtained from ice-crust-mantle analyses performed by /Lund et al. 2009/ at 500 m depth at Forsmark during this glacial cycle. Note that the horizontal stress additions are about one third of the vertical in the early phases (in keeping with the expected response according to the Poisson effect). Later, crustal flexure tends to increase the horizontal stress additions.

As shown in Section 6.4 in the **Data report**, there are only marginal variations in stress magnitudes with depth. For the purpose of the modelling work, the stress magnitudes given for 500 m depth are assumed to be valid at all depths in the upper 1 km of the rock.

Five points in time are selected from Figure 4-12 for modelling work: The first glacial maximum (12 ka), edge passing (15 ka), stress reduction due to forebulge (39 ka), second glacial maximum (54.5 ka) and edge passing (58 ka), cf. Figure 4-13 (left).

4.8.2 Temperatures during permafrost cover

Figure 4-14 (left) shows temperatures as functions of depth without considering heat from the repository during permafrost conditions (here evaluated at 70 kyr BP, *i.e.* when the ice sheet reaches Forsmark for the first time in the Weichselian reconstruction) and for *in situ* conditions. For the purpose of the present study, the temperature reduction shown in the right part of the figure is assumed to coincide with the forebulge associated with the second glacial cycle (at 39 kyr in Figure 4-12).

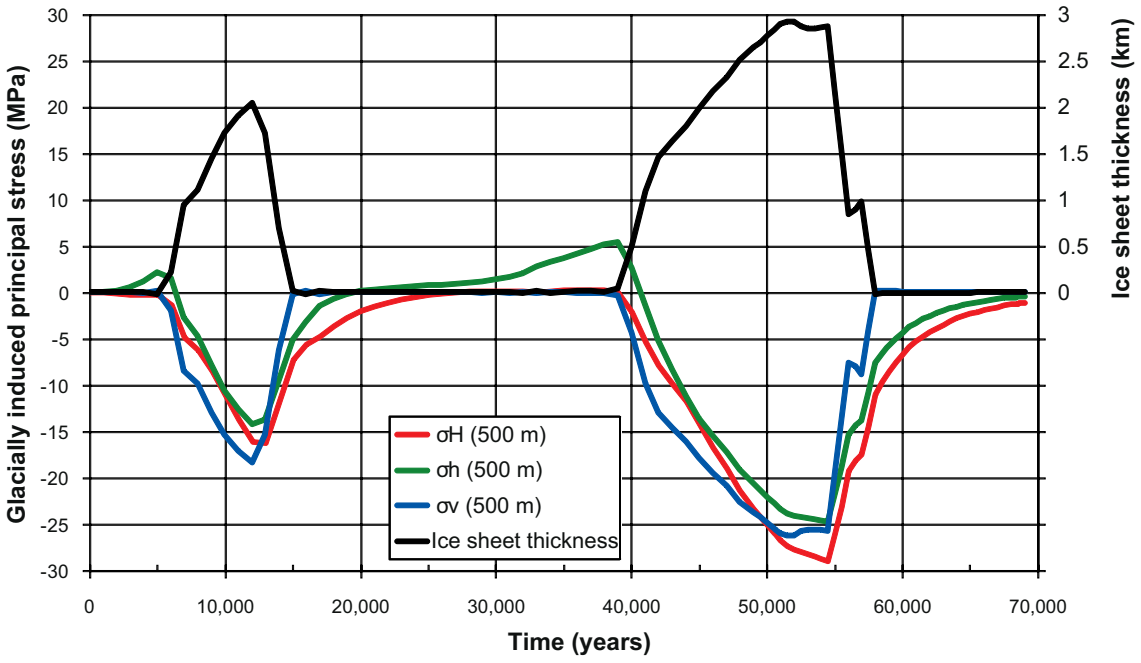

Figure 4-12. *Temporal development of the glacially induced principal stresses (in excess of in situ conditions) at 500 m depth based on data from ice-crust-mantle analyses performed by /Lund et al. 2009/ and estimate of the ice sheet thickness during the reference glacial cycle at Forsmark.*

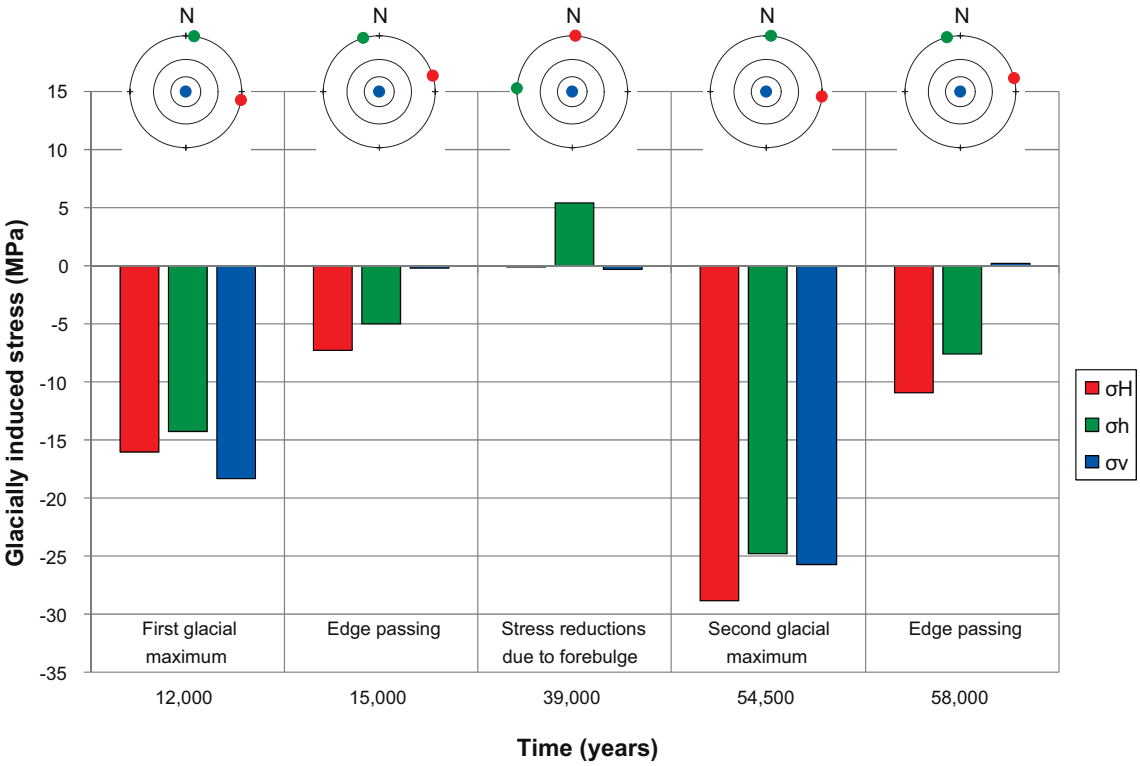

Figure 4-13. *Glacially induced principal stress magnitudes and orientations of horizontal principal stress components (used in the modelling work in the depth-interval 0–1 km). Data from Section 6.4 in the* ***Data report****.*

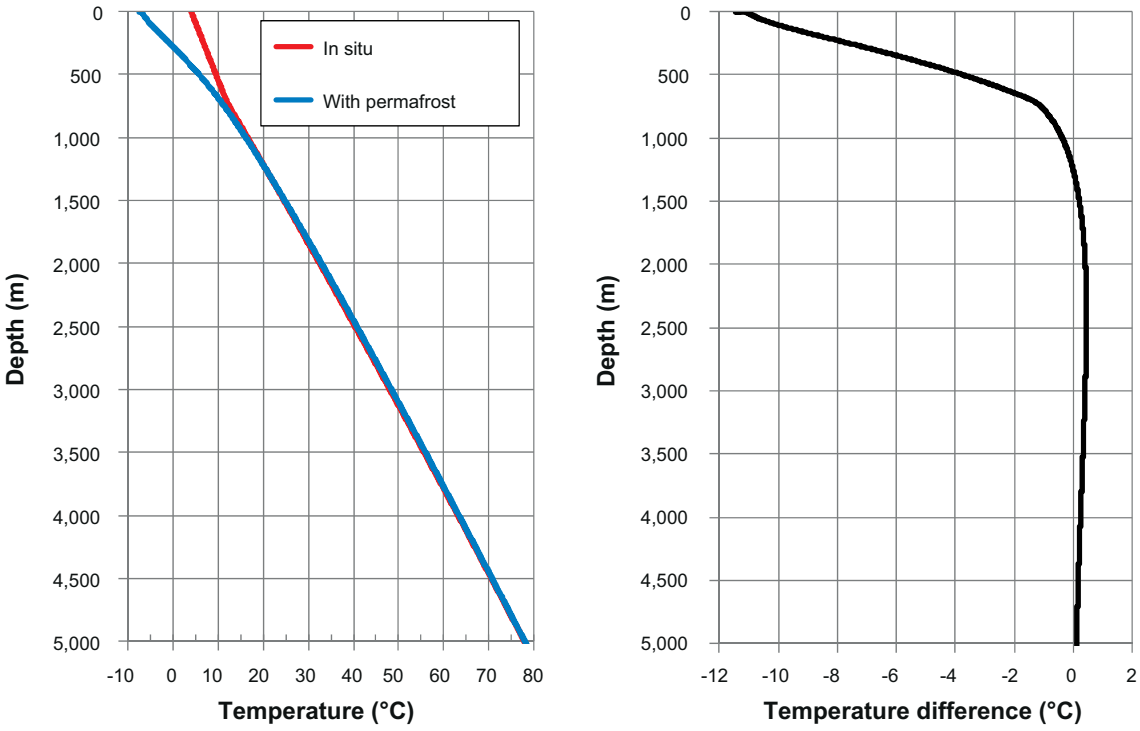

Figure 4-14. *In situ temperature and temperature during permafrost conditions (here evaluated at 70 kyr BP) as functions of depth based data from permafrost modelling by /Hartikainen et al. 2010/. Right: Corresponding temperature difference between permafrost conditions and in situ conditions as a function of depth.*

5 Thermal evolution

5.1 General

The thermal evolution of the repository depends on the site-specific thermal properties of the rock, the canister power and on the repository layout, *i.e.* the canister spacing and the tunnel spacing. For the thermal evolution in the interior of the deposition holes, e.g. for the peak buffer temperature, the properties of the bentonite buffer and of, possibly remaining, air-filled gaps are additional parameters. These properties depend strongly on the water supply, i.e. on the degree of buffer saturation and may differ from one deposition hole to another depending on the local hydraulic conditions.

The SR-site assessment of the thermal evolution is based on dimensioning guidelines and calculation schemes established in /Hökmark et al. 2009/ and on results in the Site Engineering Report /SKB 2009b/ regarding layout D2 for the Forsmark site obtained applying those guidelines /SKB 2009c/. The dimensioning guidelines, i.e. the rules for determining the spacing between canisters and between tunnels in the different rock domains, are formulated such that the calculated peak buffer temperature will be below 100°C with a margin of a few degrees for all canisters, also for the hottest. According to the Layout D2 design premises, the tunnel spacing should be set at 40 m and the canister power at 1,700 W at the time of deposition. The canister spacing should be fixed at one specific value within each rock domain, i.e. without any attempts to optimize the layout.

The peak temperature occurs some 5-15 years after deposition /Hökmark et al. 2009/. At this instance of time, the heat contribution from each individual canister dominates its own temperature evolution, although there are contributions from the overlapping temperature fields generated by nearby canisters. This means that the local heat transport properties control (although not completely) the peak temperature for the individual canisters. Therefore, the low tail of the conductivity distribution, the spatial variability and the scale of variation are important for the dimensioning issue, i.e. the temperature around the hottest canisters. In the dimensioning guidelines /Hökmark et al. 2009/ a numerical tool developed to handle the spatial conductivity variation within typical rock domains in numerical analyses of the thermal near-field evolution is described, demonstrated and verified. In the Site Engineering Report the numerical tool is applied to the rock domain data given in the Thermal Site Descriptive Model /Back et al. 2007, Sundberg et al. 2008b/ to establish the Layout D2 canister spacing with due account of the uncertainty margins prescribed in the dimensioning guidelines.

As far as demonstrating that the 100°C Safety Assessment requirement is met for all canisters, including the hottest ones, is concerned, the calculations in the Site Engineering Report are adequate and sufficient, provided that the margin applied to account for uncertainties and model simplifications cannot be shown to be insufficient. These calculations concern, however, only the first 20 years after deposition and apply only for canisters deposited in rock volumes dominated by low conductivity rock types. They cannot be used to estimate the number of canisters that actually will have peak temperatures close to the design threshold and they do not capture the overall large-scale and long-time thermal evolution of the repository host rock. Note, for instance, that the majority of the canisters will be deposited in rock with properties approximately equal to the domain mean values and consequently have lower peak temperatures. These issues are elaborated in this chapter using analytical and semi-analytical calculation tools described in the dimensioning guidelines /Hökmark et al. 2009/ along with the numerical tool used to establish the canister spacing.

5.2 Canister power and decay rate

The heat generation as function of time contributes to determine the thermal evolution. The power of each canister will decay at a rate that depends on the burn-up of the fuel and the interim storage time, i.e. the time between discharge of the fuel from the nuclear power plant and deposition, cf. Figure 5-1 (right). /Hökmark et al. 2009/ fitted an exponential expression to power decay data given for SKB fuel of different types, different burn-up and different interim storage times to give the normalized canister power $P(t)$, cf. Equation 5-1. This expression is used in the Site Engineering Report and throughout in this report to represent the power decay rate of the spent nuclear fuel.

$$P(t) = \sum_{i=1}^{7} a_i \exp(-t / t_i) \qquad \text{Eq. 5-1}$$

Here, t is time after deposition and t_i are time constants. The coefficients, a_i, are presented in Table 5-1. The exponential decay function is valid for 20,000 years or more /Hökmark et al. 2009/.

The normalized power, Equation 5-1, during the first 10,000 years after deposition is shown in Figure 5-1 (left). Figure 5-1 (right) shows the normalized power of fuel of different ages and different burn-up from Boiling Water Reactors (BWR) and Pressurized Water Reactors (PWR) compared with the exponential expression in Equation 5-1. The exponential relation holds sufficiently well also for the small amount of MOX fuel that will be included among the BWR fuel assemblies /Hökmark et al. 2009/.

Table 5-1. Decay-coefficients for SKB reference fuel /Hökmark et al. 2009/.

I	t_i (years)	a_i (–)
1	20	0.060147
2	50	0.705024
3	200	–0.054753
4	500	0.249767
5	2,000	0.025408
6	5,000	–0.009227
7	20,000	0.023877

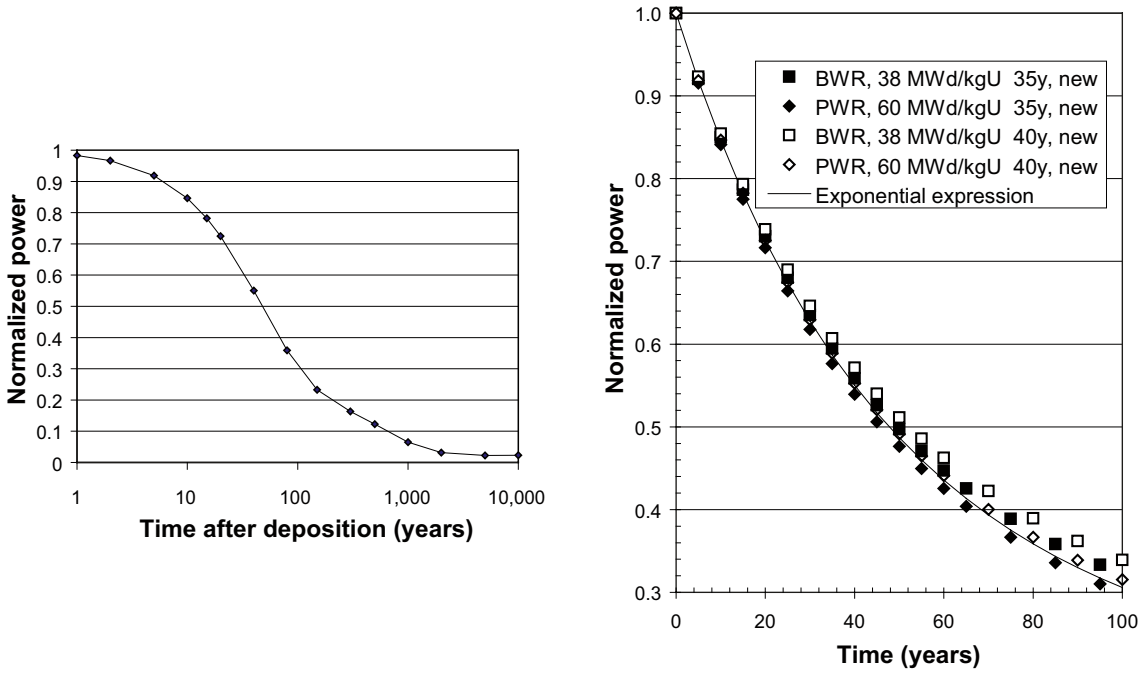

Figure 5-1. Left: Normalized power function, P(t), as function of time, cf. Equation 5-1. Right: Normalized power function compared with normalized heat power of BWR and PWR fuel of different ages and burn-up with power decay /SKBdoc 1198314/ based on radionuclide inventories given in the ***Spent fuel report.***

5.3 Principles of peak buffer temperature calculation

The peak buffer temperature is calculated as shown in Figure 5-2. The temperature at rock wall mid-height is added to the temperature difference, $\Delta T_{tot}(t)$, between rock wall and the hottest part of the canister surfaced being in contact with the buffer.

In dry deposition holes, the maximum buffer temperature is found at the top of the canister where the bentonite is in direct contact with the copper surface, cf. Figure 5-2 (left). Note that the hottest point on the canister surface (at canister mid-height) is not in contact with the buffer in dry deposition holes because of the insulating 10 mm air-filled annular gap. In wet deposition holes, the air-filled gap between the canister and bentonite blocks will soon close, and the bentonite will be in direct contact with the copper surface at canister mid-height. In this case, the maximum buffer temperature will coincide with the hottest point on the canister surface, cf. Figure 5-2 (right).

Expressions for the temperature drop across the bentonite buffer in dry and wet deposition holes are given by Equations 5-2 and 5-3, respectively.

$$\text{Dry holes: } \Delta T_{Tot}(t) = \phi \frac{Q(t)}{A \cdot \lambda_{b(eff)}} \cdot R_0 \cdot \ln(R_2 / R_1) + 16 \cdot \frac{Q(t)}{1700} \qquad \text{Eq. 5-2}$$

$$\text{Wet holes: } \Delta T_{Tot}(t) = \phi \frac{Q(t)}{A \cdot \lambda_{b(eff)}} \cdot R_0 \cdot \ln(R_2 / R_0) \qquad \text{Eq. 5-3}$$

The last term in the expression given for dry holes represents the effects of the heat transport resistance across the air-filled 10 mm gap between canister surface and the bentonite blocks.

Here, $R_0 = 0.525$ m is the radius of the canister, $R_1 = 0.535$ m is the inner radius of the surrounding bentonite blocks and $R_2 = 0.875$ m is the radius of the deposition holes. $Q(t)$ is the power function presented in Section 5.2 and $\phi = 0.87$ is a scale factor /Hökmark et al. 2009/. $A = 17.664$ m^2 is the canister's surface area. The effective heat conductivity of the bentonite, $\lambda_{b(eff)}$, is assumed to be 1.0 W/(m·K) for dry holes /Hökmark et al. 2009/ and 1.3 W/(m·K) for wet holes /Åkesson et al. 2010a, Table 12-5/, respectively.

The temporal evolution of the temperature drop, ΔT_{Tot}, for both dry and wet holes, is presented in Figure 5-3.

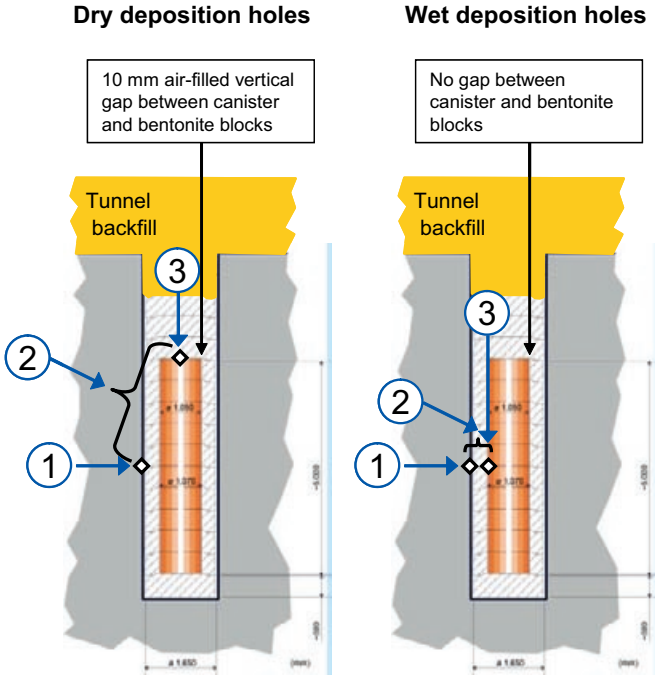

Figure 5-2. *Rock wall temperature (1), temperature drop across bentonite (2), maximum bentonite temperature (3) located at the top of the canister in dry deposition holes and at canister mid-height in wet deposition holes. Modified from /Hökmark et al. 2009/.*

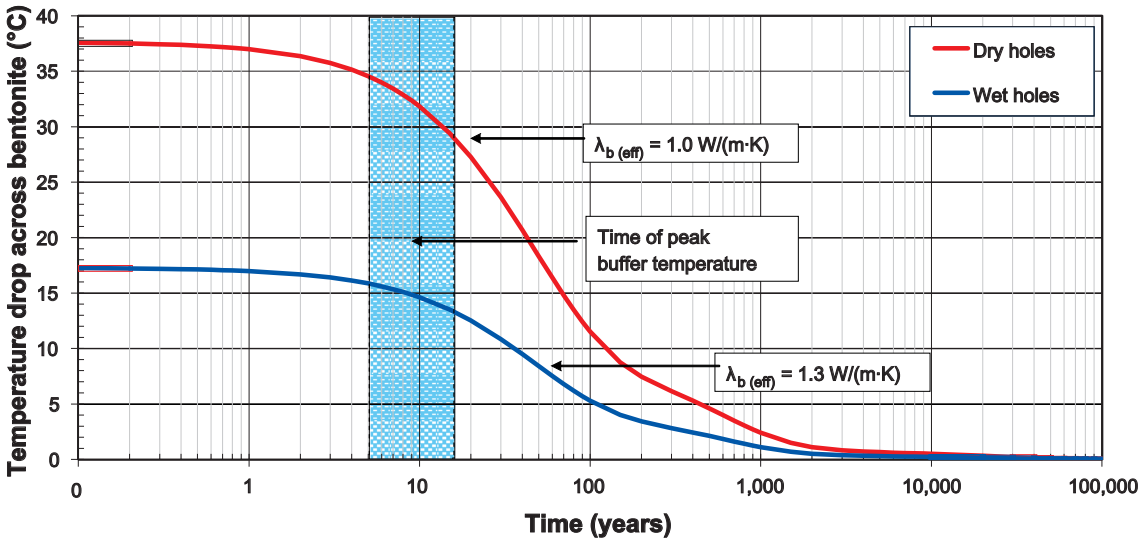

Figure 5-3. *Temperature drop ΔT_{Tot} for dry and wet holes, respectively. The main cause of the difference is the air-filled canister-bentonite gap present in dry, but not in wet, holes.*

The peak buffer (or canister surface) temperature is found by adding the rock wall temperature to the expressions for the temperature drop shown in Figure 5-3. In the dimensioning calculations in the Site Engineering Reports all deposition holes are conservatively assumed to be dry. The rock wall temperature can be calculated:

- as in the Site Engineering Reports, i.e. using the numerical scheme described in /Hökmark et al. 2009/ with explicit account of the spatial variability,
- with analytical solutions (e.g. the one described in /Hökmark et al. 2009/) that assume the rock thermal conductivity to be uniform and homogeneous.

In case analytical solutions are used, the effective rock thermal conductivity, i.e. the homogeneous global thermal conductivity that would give the same temperature evolution in the rock wall as the actual inhomogeneous, spatially varying conductivity found around the deposition hole being considered, must be estimated. For the majority of the canisters the effective conductivity is close to the mean conductivity. For canisters deposited in rock volumes dominated by low-conductivity rock types, the effective conductivity will be below the mean and vice versa for canisters in volumes dominated by high-conductive rock types. As time proceeds and temperature fields from an increasing number of canisters begin to overlap and the heat generation decreases, the effective conductivity tends to approach the mean conductivity for all canisters, regardless of the local conditions.

5.4 Dimensioning thermal conductivity

At the time of the peak temperature, which occurs around 10 years after deposition, cf. Figure 5-3, there is still a significant spread in effective conductivities. The effective conductivity of the rock surrounding the hottest canisters is called the dimensioning thermal conductivity here. However, the dimensioning conductivity is not actually used for determining the canister spacing. Once the spacing has been established, the dimensioning conductivity can be estimated using the analytical solution, i.e. as the homogenous rock thermal conductivity that gives (with account of the margin) the threshold peak temperature.

Figure 5-4 shows nomographic charts /Hökmark et al. 2009/ derived for the different rock domains in Forsmark. The dimensioning conductivity, i.e. the effective thermal conductivity for the hottest canisters in each domain, is found knowing the initial temperature, the spacing and the margin established in the Site Engineering Report /SKB 2009b/.

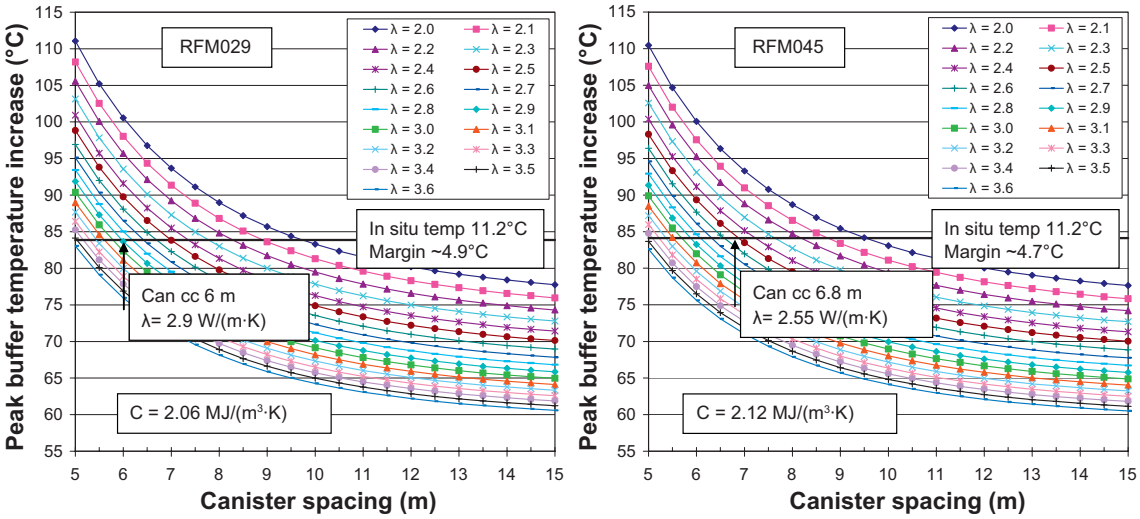

Figure 5-4. *Nomographic charts for rock domains RFM029 (left) and RFM045 (right) at Forsmark. The dimensioning thermal conductivity is defined as the effective thermal conductivity value that gives a peak buffer temperature of 100°C with account of in situ temperature and uncertainty margin for the canister spacing established for the rock domain. The uncertainty margin is estimated from /Hökmark et al. 2009/. Here the dimensioning conductivities are 2.9 and 2.55 W/(m·K) for rock domains RFM029 and RFM045, respectively.*

5.5 Distribution of peak buffer temperatures

As seen in Figure 5-5 (right), at the time of peak buffer temperature the local canister contributes about 45–60% to the total rock temperature increase, *i.e.* the temperature of hottest canisters that determine the spacing is not completely determined by the local conditions. This is one of the reasons why the dimensioning conductivity, i.e. the lowest effective conductivity that needs to be considered at the time of the peak temperature, is significantly higher than the lowest rock conductivity reported in the site descriptions. After about 100 years, the temperature contribution from the local canister is reduced to about 20% of the total temperature increase, which implies that a thermal conductivity relevant on a much larger scale determines the continued long-term evolution of the rock temperature around the local canister. Additionally, after that long period of time, the buffer in most deposition holes will be close to saturation, meaning that the variation in temperature among the canister will be small. At the time of the peak, however, the variation is considerable. An estimate of the distribution of peak buffer temperatures in dry deposition holes can be made by use of the analytical solution /Hökmark et al. 2009/ and the distributions of thermal conductivity in each rock domain /Back et al. 2007, Sundberg et al. 2008b/, cf. Section 6.2 in the **Data report**.

The analytical solution does not take spatial variations of the thermal properties into account, i.e. the thermal properties are assumed to be uniform everywhere. Therefore, peak buffer temperatures calculated using thermal conductivity values from the low end of the distribution are overestimated, whereas the corresponding temperatures at the high end of the distribution are underestimated. A temperature correction, T_{corr}, proposed by /Hökmark et al. 2009/ that accounts for the variability of the thermal properties is given by Equation 5-4. The temperature correction is equivalent to applying the analytical solution to a distribution of effective conductivities rather than to the actual distribution given in the thermal site reports. Without the correction, i.e. Equation 5-4, all canisters will get peak temperatures as if the local 5-m scale conductivity applied for the entire repository, which gives overestimated as well as underestimated temperatures. By construction, the correction is zero for canisters deposited in mean conductivity rock.

$$T_{corr}(\lambda) = 6.7 \cdot \left(\mathrm{abs}\left(\frac{\lambda - \lambda_{mean}}{2.0 - \lambda_{mean}} \right) \cdot \left(\left(\frac{100 - f(\lambda)}{100} \right)^{0.3} - \left(\frac{f(\lambda)}{100} \right)^{0.3} \right) \right) \qquad \text{Eq. 5-4}$$

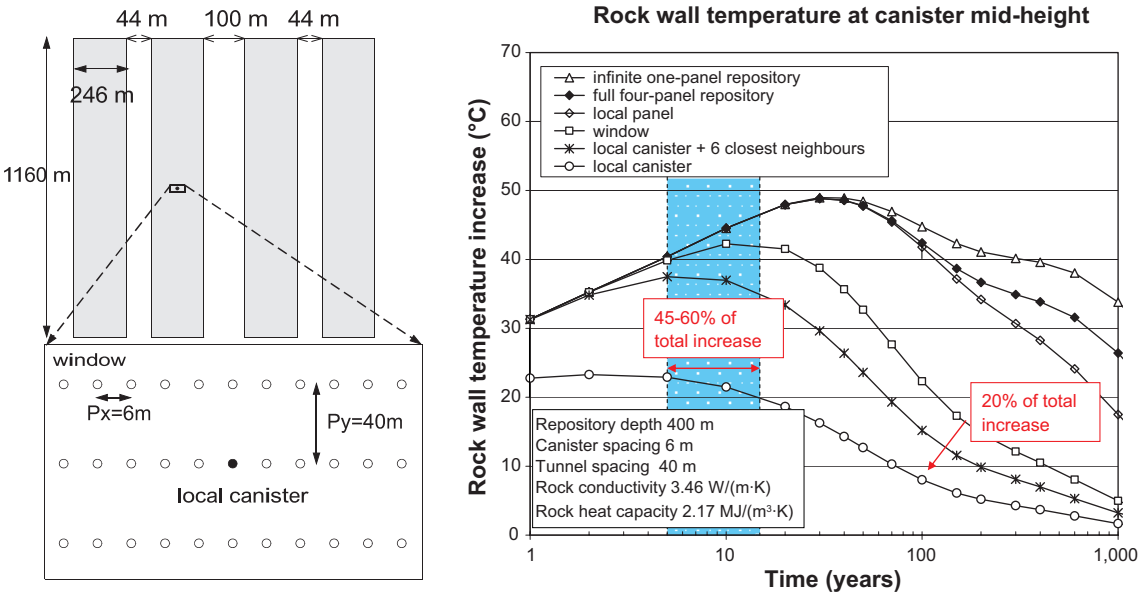

Figure 5-5. *Left: Schematic representation of repository. Right: Temporal evolution of the rock wall temperature increase at different scales. At the time of peak buffer temperature (marked in blue) the local canister contributes by 45–60% of the total temperature increase, whereas after 100 years the contribution is only about 20%. Modified from /Hökmark et al. 2009/.*

Figure 5-6 (top) shows the 5-m scale distributions of the thermal conductivity in rock domains RFM029 and RFM045 at Forsmark. The bottom part shows corresponding peak temperature distributions calculated for the canister spacing established in the Site Engineering Report /SKB 2009b/.

It should be noted that the temperature correction is an approximate way of accounting for the inhomogeneity in rock thermal properties. The method was, however, used by /Hökmark et al. 2009/ for different spacing assumptions to get a first estimate of the spacing required in the two Forsmark domains and was found to forecast the values established (by use of the numerical method) in the Site Engineering Report with good accuracy.

An estimate, based on the corrected temperature distributions, of the number of canisters in each rock domain with a given peak buffer temperature is presented in Figure 5-7. The total number of canisters in the repository has been set to 6,000. The ratio between canister positions in the rock domains has been taken from Layout D2 at Forsmark, i.e. around 80% in rock domain RFM029 and about 20% in RFM045.

As seen in Figure 5-7, less than one canister would have a peak buffer temperature larger than 95°C, meaning that the design requirement would be satisfied with a margin of 5°C. A very large majority of the canisters, about 98%, will have a margin of 10°C or more. Yet the peak temperatures are overestimated because of the following:

- All canisters are assumed to be deposited using the nominal canister spacing everywhere, whereas in Layout D2 the projected loss of deposition holes is at least 13% /SKB 2009c/. Canister neighbouring rejected positions will get lower temperatures.
- All canisters are assumed to be deposited in the central parts of the deposition areas whereas in reality about 1,000 canisters will be deposited close enough to the tunnel ends to get reduced peak temperatures.
- All canisters are assumed to be deposited in completely dry holes with a 10 mm air-filled gap between canister and bentonite, whereas in reality there will be a variation in the degree of saturation. A fraction of the holes will be sufficiently close to saturation that the wet hole model rather than the dry hole model applies (cf. Figure 5-2 and Figure 5-3). This will reduce the peak temperatures.

The peak temperature distribution can be used to check the robustness of the dimensioning approach. Figure 5-8 shows the number of canisters that would get peak temperatures above the 100°C threshold and how large that excess temperature would be if the margin applied in the dimensioning calculations should be insufficient, for instance because of changes or variations in details of the near-field design. A 5°C margin error would mean that altogether 131 canisters, out of 6,000, would get a buffer peak temperature above the threshold. The majority of these canisters would, however, get excess temperatures of not more 2°C. The results are based on the assumption that all canisters are placed in completely dry deposition holes. No account is taken of the temperature reduction that will be found for canisters deposited near tunnel ends. The number of canisters that actually would get temperatures above the threshold is therefore significantly smaller than the numbers indicated in Figure 5-8.

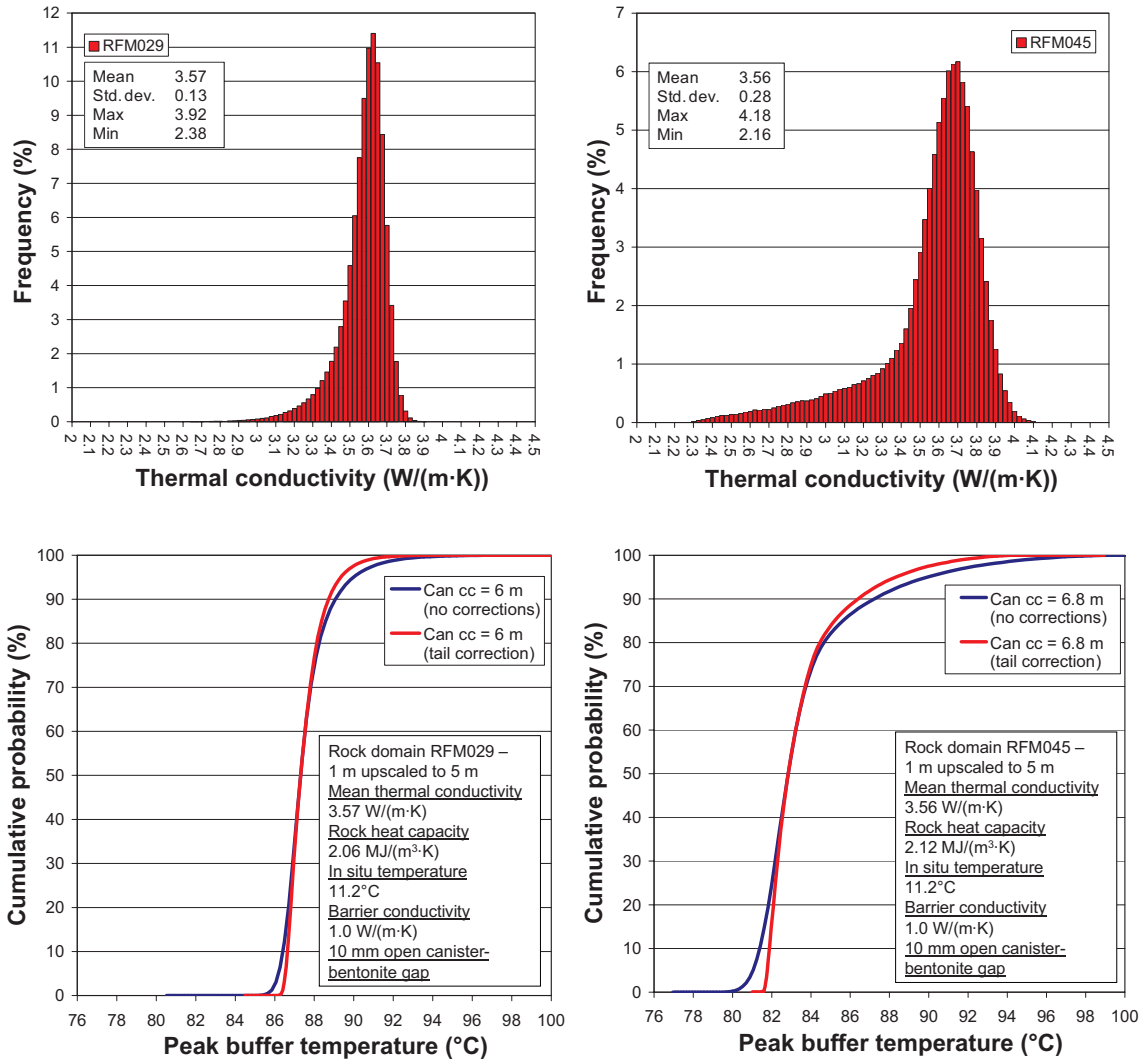

Figure 5-6. *Top: Distribution of thermal conductivity in rock domains RFM029 (left) and RFM045 (right) at Forsmark (cf. Section 6.2 in the* ***Data report****), modified from /Back et al. 2007/ and /Sundberg et al. 2008b/, respectively. Bottom: Corresponding effects on the temperature distribution due to the temperature correction in Equation 5-4.*

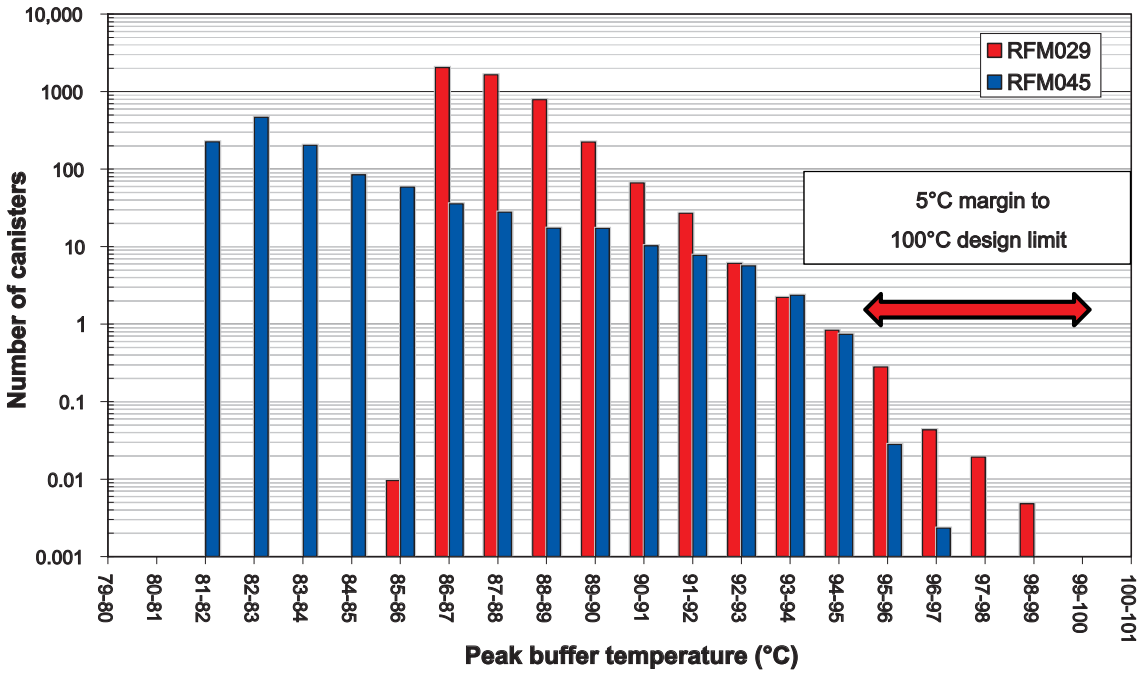

Figure 5-7. *Estimate of the number of canisters with given peak buffer temperature in rock domains RFM029 (canister cc 6 m) and RFM045 (canister cc 6.8 m) at Forsmark. The total number of canisters has been scaled to 6,000 canister with about 80% of canisters in RFM029 and about 20% in RFM045. All canisters are assumed to be located in dry deposition holes in the central parts of a deposition area.*

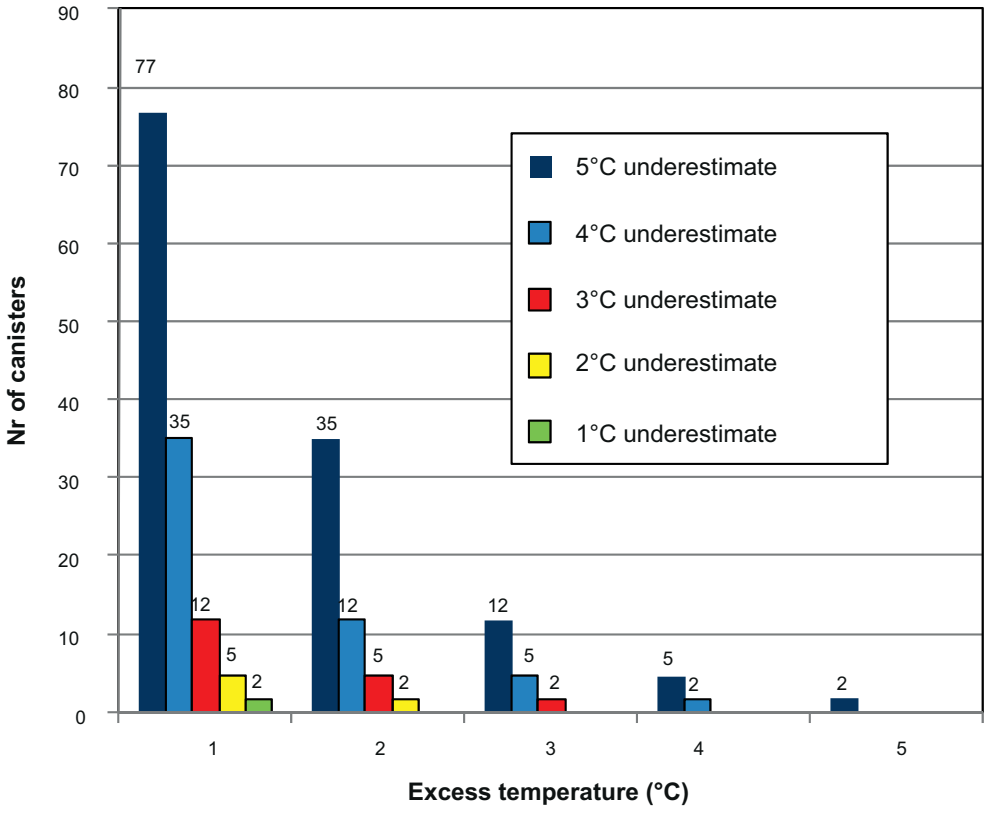

Figure 5-8. *Numbers of canisters with excess temperatures for different assumptions of hypothetical margin underestimate made in the dimensioning calculations.*

5.6 Deposition sequence – importance to the peak buffer temperature

It is assumed throughout the report (and in the Site engineering Reports) that all canisters are deposited simultaneously. Analytical temperature calculations by /Hökmark et al. 2009/ show that if the canisters are deposited in an orderly fashion (i.e. panel by panel) at a rate of 2 or 4 days per canister, the increase in temperature at the time of the peak buffer temperature is less than 0.2°C, cf. Figure 5-9. The 'worst case' deposition order (shown in the lower left part of the figure), where the local canister is deposited last, gives a significantly elevated temperature compared with simultaneous deposition.

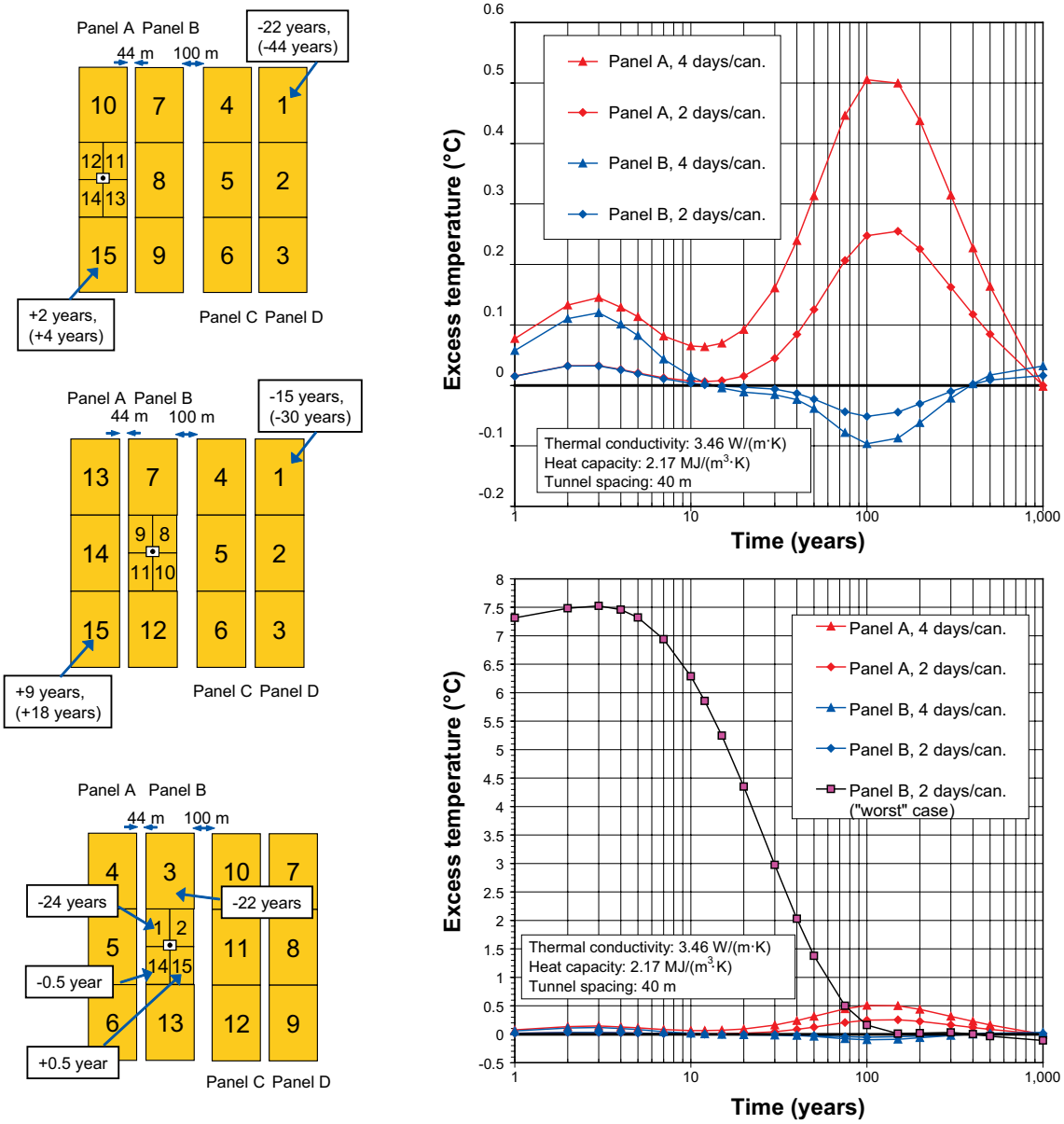

Figure 5-9. *Left column: Deposition panels (labelled Panel A through D) are subdivided into smaller units and deposited in the order shown in the figures at a rate of 2 days/canister or 4 days/canister (times in brackets). Time zero is defined as the time when the local canister (positioned at the centre of Panel A, top figure, or the centre of Panel B, middle and lower figures) is deposited. Right column: Excess rock wall temperature as compared with simultaneous deposition of all canisters. From /Hökmark et al. 2009/.*

5.7 Rock temperature calculations

The previous section dealt with the question of ensuring, or verifying, that the peak buffer temperature issue is adequately handled in Site Engineering Reports and in the D2 layout. Calculating buffer peak temperatures is largely a local problem with a time scale of less than 20 years, whereas the thermal evolution of the repository is of potential importance also on the large scale and for longer periods of time.

The distinct element code *3DEC* /Itasca 2007/ is used here to model the thermal evolution of the repository on all scales. The temperature at each gridpoint is calculated at every time-step using a built-in analytical solution similar to the one described in /Hökmark et al. 2009/. The *3DEC* thermal logic and the purely analytical solution described in previous sections are effectively equivalent and can be used interchangeably. Note that the *3DEC* models cannot capture effects of the spatial variability in heat transport properties reported in the site descriptions.

By use of the programming language *FISH* /Itasca 2007/, *3DEC* heat sources can be positioned at the exact locations given by the Layout D2 coordinate list for each site. Depending on the required level of detail, the heat sources can be represented by point sources, vertical line sources, or combinations of line sources, to better reflect the temperature distribution around the spent fuel canisters (cf. /Fälth and Hökmark 2007, Hökmark et al. 2009/).

The repository is at $z = 0$ and the ground surface at $z = H$. The ground surface is kept at 0°C by defining a mirror repository with negative power at $z = 2H$. However, at repository depth the temperature effect of the mirror repository is small, i.e. the cooling effects of the ground surface are not important to the thermal evolution, cf. Appendix H.

In large-scale temperature calculations all canisters are represented by point sources, each with initial power 1,700 W and decay-rate as described in Section 5.2.

In near-field temperature calculations, i.e. where the temperature at the wall of a given deposition hole needs to be accurately determined, the canisters are represented in the same way as in the large-scale calculations but the local, central, canister and its six nearest neighbours are replaced by more detailed representations of canisters. The local canister and its two nearest neighbours are represented by so-called compound line sources /Hökmark et al. 2009/, which have been calibrated to fit the thermal output at canister mid-height of a detailed numerical representation of a KBS-3V canister /Hökmark and Fälth 2003/. The other four neighbour canisters are represented by ordinary line sources.

5.8 Application to Forsmark

5.8.1 Layout, properties and initial conditions

Layout D2 for the Forsmark site contains 6,916 canister positions with an expected loss of 13%, cf. Figure 5-10. Variations in repository elevation are not considered here, cf. Section 4.3. In all temperature calculations, as well as subsequent thermo-mechanical calculations for Forsmark in Chapters 6, 8 and 9 the tunnel floor is set at an elevation of –460 m in all areas of the repository.

Canister spacing in fracture domain FFM01/rock domain RFM029 is set at 6 m and at 6.8 m in fracture domain FFM06/rock domain RFM045 in accordance with specifications in the Site Engineering Report (SER) for the Forsmark site /SKB 2009b/.

Interpolation between the values for the *in situ* temperature given at the 400 m and 500 m levels /Sundberg et al. 2008b/ results in an approximate value for the *in situ* temperature at repository level (460 m) of 11.2°C, cf. Table 4-4.

The mean and dimensioning values of the thermal properties in each rock domain are presented in Table 5-2, cf. Section 4.6. Nomographic charts showing the procedure to obtain the dimensioning value of the thermal conductivity are presented in Figure 5-4. Note that the values for the dimensioning thermal conductivities should be seen as conservative estimates.

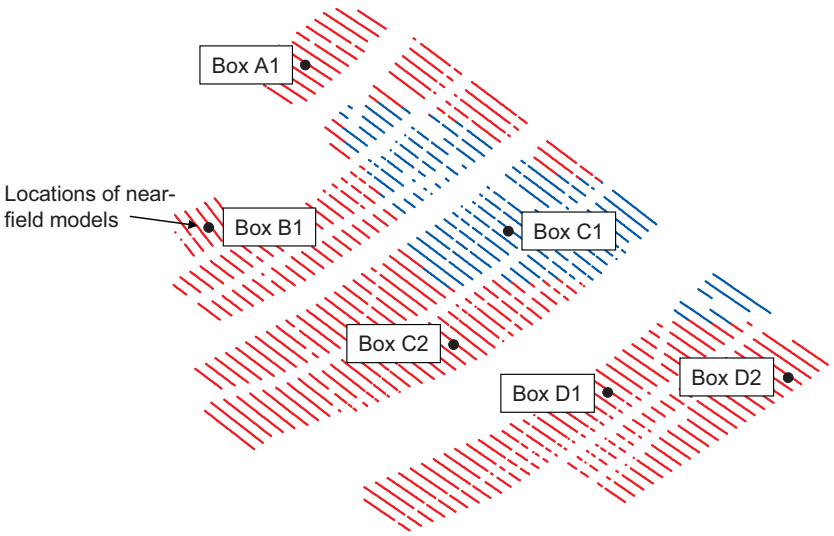

Figure 5-10. *Forsmark Layout D2 (version with 13% loss of canister positions) and locations of thermo-mechanical near-field models, cf. Chapter 9. Red colour represents parts of the repository region with 6 m canister spacing (FFM01/RFM029) and blue colour represents parts of the repository region 6.8 m canister spacing (FFM06/RFM045).*

Table 5-2. Thermal properties of the rock mass, cf. Section 4.6. Dimensioning value of the thermal conductivity is obtained from the nomographic charts in Figure 5-4.

Parameters	Unit	RFM029	RFM045
Heat capacity (C)	MJ/(m^3·K)	2.06	2.12
Mean thermal conductivity (λ_m)	W/(m·K)	3.57	3.56
Dimensioning thermal conductivity (λ_d)	W/(m·K)	2.9	2.55

5.8.2 Large-scale

As no information can be available at present regarding how the loss of canister position is distributed across the repository region, every 8th canister position is removed uniformly across the repository in order to achieve the approximate thermal load on a large scale. Point sources representing the heat generating canisters are positioned 5 m below the tunnel floor.

Figure 5-11 shows the increase in rock temperature along three vertical scanlines at Forsmark – A (between two deposition areas), B (through a deposition area) and C (in the central area). Here, the temperatures are calculated using mean value properties in rock domain RFM029, cf. Table 5-2. More detailed near-field temperature analyses are performed in subsection 5.8.3.

The scanline temperatures were calculated assuming all canisters to be deposited simultaneously. In reality, the deposition will be distributed over time with approximately one canister every 3rd day /Hansson et al. 2009/ and in a sequence as approximately indicated by the dashed arrows in the upper part of the figure. The lower right diagram shows the effects on Scanline B of distributing over time in this way. Here time $t = 0$ is when the closest canister is deposited. The difference between simultaneous deposition and sequential deposition is less than 0.1°C on the scanline. This is in keeping with the results shown in Figure 5-9 for the rock wall temperatures and verifies again that, provided that the deposition is made in a reasonably orderly fashion, the approximation of simultaneous deposition of all canisters is valid. The temperature around any individual canister develops in the local time-scale with $t = 0$ at the time of the local deposition as if all canisters were deposited simultaneously. The ground surface temperature is set to zero at all times, i.e. the cooling of the ground surface is assumed to be efficient enough that the heat generation will not have an impact on the ground surface temperature. The graphs show temperature increase due to the heat generating fuel only, i.e. ignoring any climate variations taking place during the early temperate phase. Climate induced temperature variations are, however, assumed to take place after 10,000 years. These are handled in the permafrost section of Chapter 7.

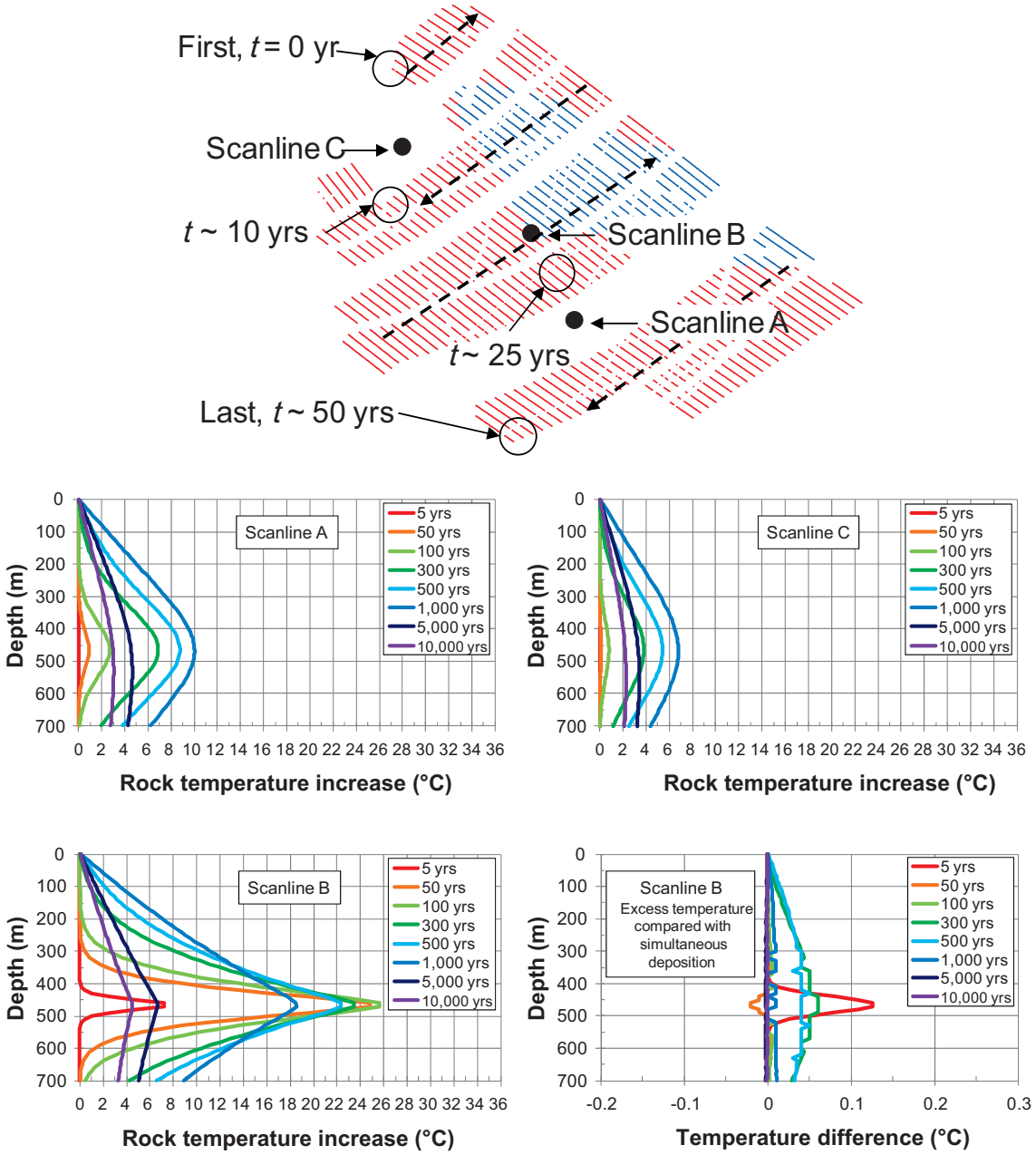

Figure 5-11. *Increase in rock temperature as functions of depth along the vertical scanlines marked in the uppermost figure (assuming simultaneous deposition of all canisters). The repository is at 460 m depth. For Scanlines A and C. the proximity to the cooled ground surface is, relatively seen, more important such that the the long time curves do not peak at the repository level. The bottom right diagram shows the effect on Scanline B temperatures of distributing the deposition over time in the way indicated in the uppermost figure.*

Figure 5-12 shows contour plots of the mean rock temperature increase at the repository level (5 m above canister mid-height) after 50, 200, 1,000 and 5,000 years. The left column shows contours obtained assuming simultaneous deposition of all canisters. The right column shows contours obtained assuming the deposition sequence illustrated in the upper part of Figure 5-11, i.e. with one canister every three days. Here time $t = 0$ is when the first canister is deposited. The differences between the 50-year contours in the two columns are obvious: 50 years after depositing the first canister, a number of canisters have only recently been deposited. After 200 years the differences are very small. Note that these contours are based on a grid that is too coarse to capture the details around the individual canisters and underestimate the real maximum temperature increases, which are around 50°C after 50 years and 35°C after 200 years, cf. Figure 5-5. After even longer, when the local temperature gradients around the canisters tend to disappear, there is a better agreement between the maximum temperature increases shown in the contours and the rock wall temperature increase shown in Figure 5-5.

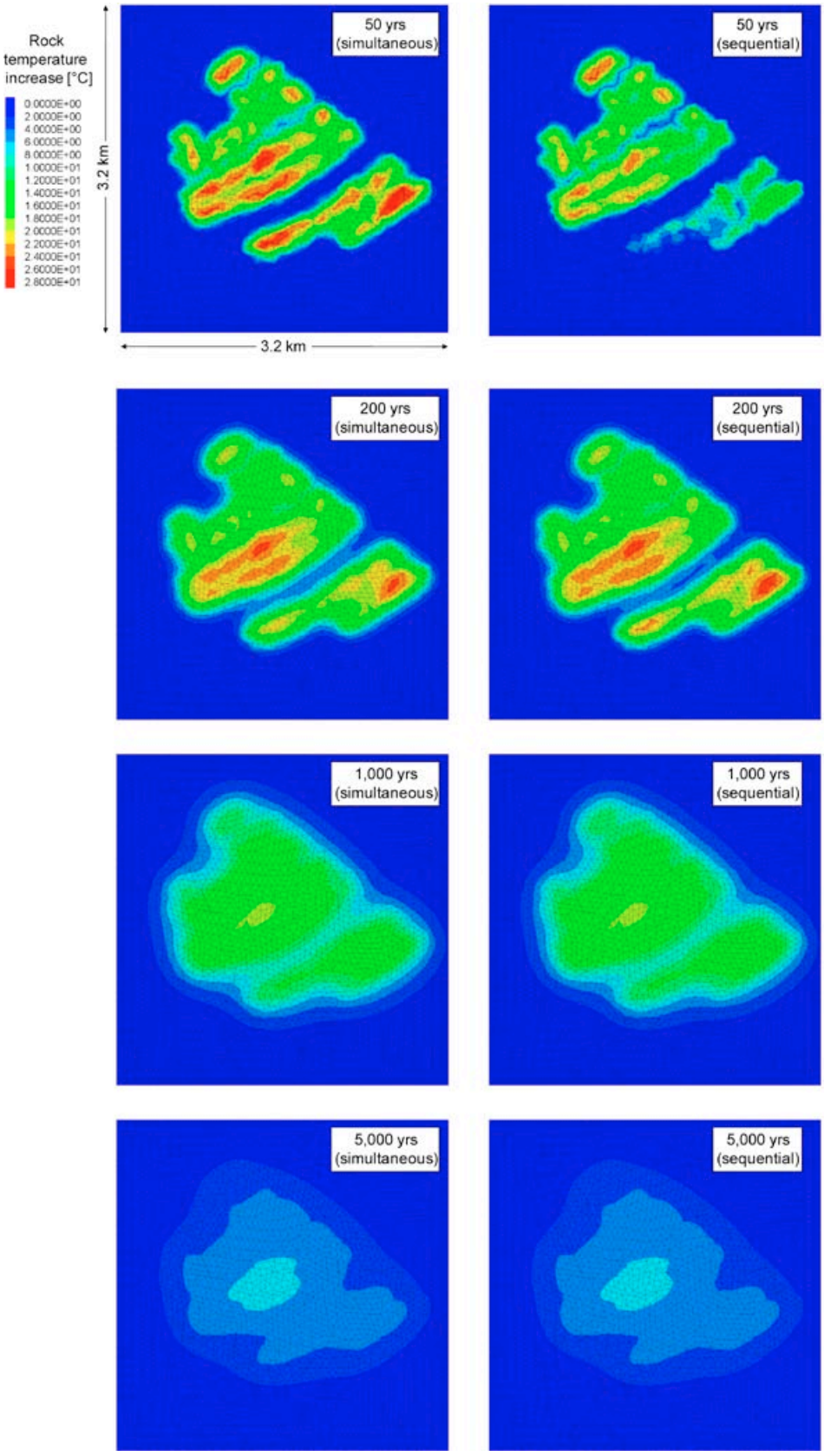

Figure 5-12. *Contour plots of the rock temperature increase at repository level (460 m) at Forsmark. Left: Simultaneous deposition. Right: Sequential deposition.*

5.8.3 Near-field

Similarly to the previous section, the tunnel floor is set at an elevation of –460 m in all areas of the repository. Compound line sources, line sources and point sources representing the heat generating canisters are positioned with their mid-height 5 m below the tunnel floor.

In the near-field temperature calculations, all available canister positions are assumed to be filled. Therefore, the total number of canisters at the Forsmark site is overestimated by about 900 canisters, which consequently may results in an overestimate in temperature. The peak buffer temperature occurs after approximately 5–15 years after deposition /Hökmark et al. 2009/ and the highest tangential stresses in the walls of a deposition hole coincide with the peak rock wall temperature (approximately 50 years after deposition), cf. Chapter 9.

Figure 5-13 shows the effect on the rock wall temperature increase at the point labelled 'Box C2' for two assumptions regarding loss of canister positions compared with the case where all available canister positions are filled:

- All available canister positions in Deposition area C are filled. The loss of canister positions in the remaining deposition areas is set to 20% such that the total number of canisters is 6,000. In this case there is no difference in the rock wall temperature increase at canister mid-height during the first 50 years after deposition.
- The loss of canister spacing is assumed to be 12.5% everywhere except in a 'window', containing 33 canisters, centred on the local canister where all canister positions are filled. In this case the rock wall temperature increase at canister 0–0.3°C lower at the time of peak buffer temperature and 0.9–1.4°C lower at the time of maximum tangential stresses.

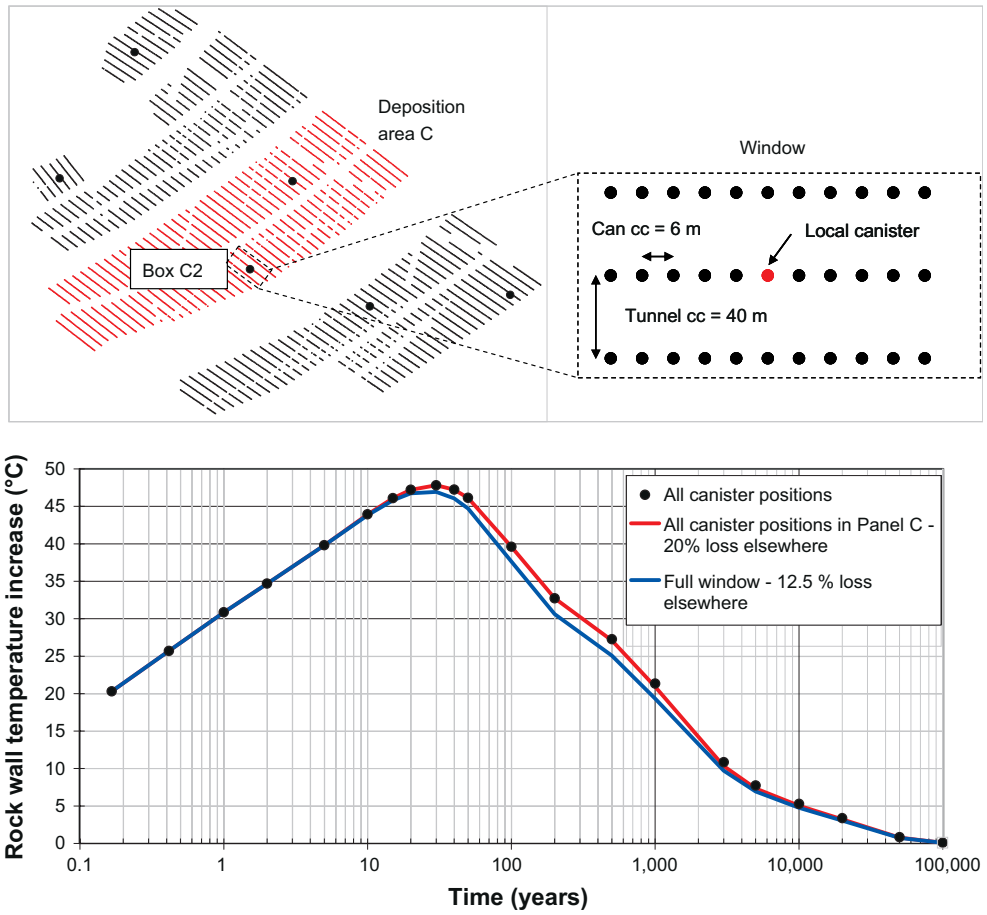

Figure 5-13. *Temporal evolution of the rock wall temperature increase at canister mid-height in Box C2 for two assumptions regarding the distribution of loss of canister positions compared with the case where all canister positions are filled.*

Figure 5-14 shows the rock wall temperature increase at canister mid-height at a number of locations within the repository region, cf. Figure 5-10. These positions correspond to the central canister in each thermo-mechanical near-field model in Chapter 9.

The rock wall temperature increase at the point labelled Box C1 is significantly lower than at the other positions. This is due to the fact that Box C1 is located in rock domain RFM045, which has similar mean value thermal properties but larger canister spacing.

Canisters, which are located in smaller deposition areas or close to the edges of the repository, i.e. Boxes A1, B1 and D2, cf. Figure 5-10 and Figure 5-14, have lower temperatures after a few hundred years than the more centrally located canisters in Boxes C1, C2 and D1.

The peak buffer temperature in dry and wet deposition holes is obtained as described in Section 5.3. Figure 5-15 shows a comparison of the rock wall temperature and peak buffer temperatures in dry and wet deposition holes in Box C1 (RFM045) and Box C2 (RFM029) for both the mean value of the thermal conductivity and the dimensioning value of the thermal conductivity. After about 200 years, the bentonite buffer can be assumed to be saturated in all deposition holes and the 10 mm initial gap between canister surface and buffer closed /Åkesson et al. 2010b/ meaning that the temperature drop across the bentonite will be that of 'Wet holes'.

Uncertainties

The effects on the rock wall temperature increase at canister mid-height due to variations of one standard deviation in heat capacity are presented in Figure 5-16. In rock domain RFM029 the mean heat capacity is 2.06 MJ/(m^3·K) with standard deviation 0.1 MJ/(m^3·K), whereas the mean in rock domain RFM045 is 2.12 MJ/(m^3·K) with standard deviation 0.15 MJ/(m^3·K), cf. Section 4.6, and Section 6.2 in the **Data report**.

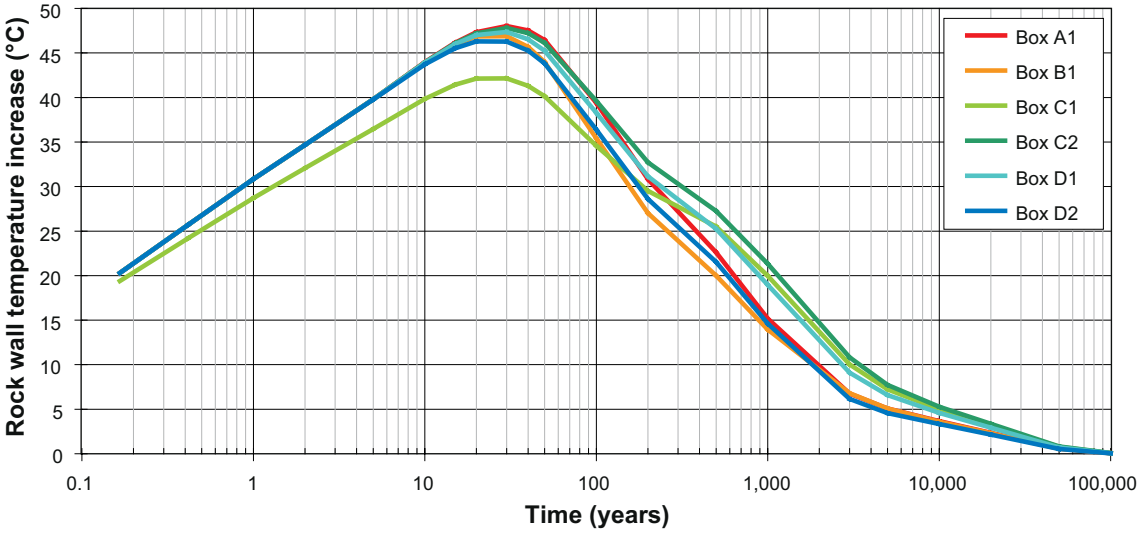

Figure 5-14. *Rock wall temperature increase (mean value thermal conductivity) in rock domain RFM029 (Box A1, B1, C2, D1 and D2) and rock domain RFM045 (Box C1).*

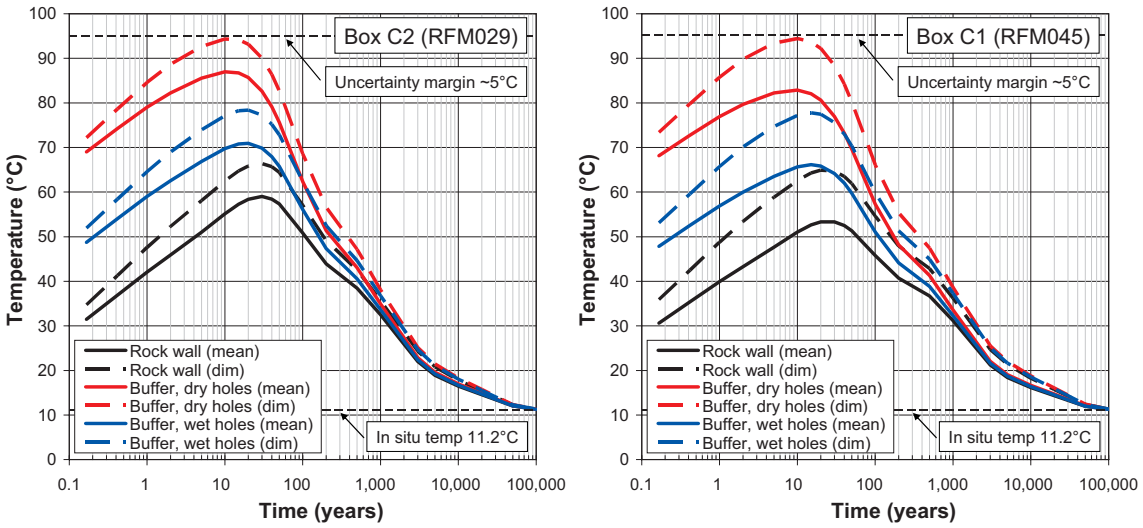

Figure 5-15. *Comparison between rock wall temperature at canister mid-height, peak buffer temperature in dry deposition holes and wet deposition holes in Box C2 in rock domain RFM029 (left) and Box C1 in rock domain RFM045 (right).*

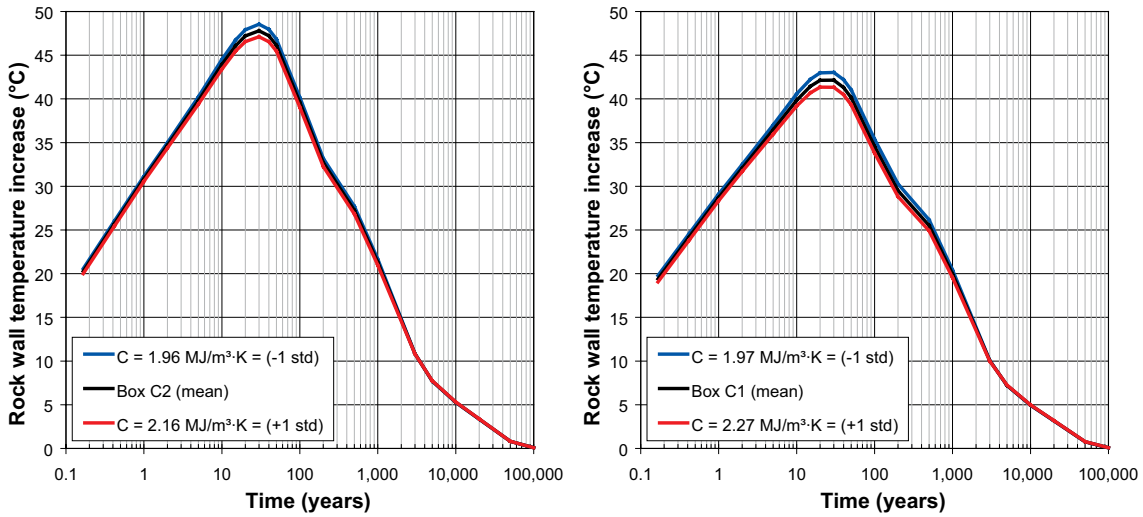

Figure 5-16. *Effects on the rock wall temperature increase at canister mid-height due to variations of 1 standard deviation from the mean of the heat capacity in each rock domain. Left: Box C2 situated in rock domain RFM029. Right: Box C1 situated in rock domain RFM045.*

5.9 Thermal evolution – conclusions

5.9.1 Buffer peak temperature

The canister spacing established in the Site Engineering Reports /SKB 2009b, 2010g/ for the different rock domains in Forsmark and Laxemar ensures that the buffer temperature will not exceed 100°C for any canister, provided that the margins defined to account for uncertainties and model simplifications are adequate. For the uncertainties the following observations are made:

- The largest uncertainty is in the heat transport properties in the interior of the deposition holes and relates mainly to the impact of dry conditions (i.e. uncertainty in the local solution given by Equation 5-2). The margin required for the local solution uncertainty ranges between 3.45°C (Laxemar rock domains RSMM01 and RSMA01) and 4.05°C Forsmark rock domain RFM029), depending on the different style of heat flux distribution applying for deposition holes in rock of different thermal conductivity /Hökmark et al. 2009/.

- Uncertainties in rock thermal properties have significantly smaller effects: between 1.05 and 1.85°C /SKB 2009b, 2010g/, depending on domain specific conditions (conductivity, anisotropy, documented spread in measured data, etc).
- Uncertainties related to the approximate assumption of simultaneous deposition of all canisters made in the dimensioning calculations are too small to impact on the margin. Provided that the deposition is made in an orderly fashion, the effect corresponds to less than 0.1°C at the time of the peak, even assuming the deposition to extend over 65 years (4 days/canister).

The simplifications made to improve computational efficiency in the numerical calculations performed to establish the canister spacing in the Site Engineering Report (meshing, boundary effects etc.) give a small buffer temperature overestimate. Accounting for uncertainties and model simplification gives the margin to the 100°C design limit finally applied in the numerical spacing calculations (4.5°C for both Forsmark domains, cf. /SKB 2009b/). For the analytical solution the uncertainties are approximately the same as for the numerical one, whereas the model simplifications are slightly different /Hökmark et al. 2009/, giving a margin of about 5°C. The analytical solution is however not intended for fine-tuning the spacing, meaning that the margin does not need to be established within fractions of degrees. The error in the results obtained when the analytical solution is applied to site data, i.e. to rock volumes with inhomogeneous heat transport properties, is dominated by the problem of defining relevant values of the effective conductivities. The scheme suggested in Equation 5-4 for transforming the 5 m scale conductivity distribution to a distribution of effective conductivities appeared to reproduce the Site Engineering Report results very satisfactory: the peak temperature exceeded the 95°C threshold for less than one canister when the spacing was set as proposed in the Site Engineering Report.

Given that all uncertainties are correctly assessed and accounted for, the agreement between the numerical and the analytical results supports the conclusion that the buffer temperature will not exceed 100°C for any canister, provided that deposition is made according to layout D2 and with a deposition sequence for which the assumption of simultaneous deposition of all canisters is a valid approximation, cf. Figure 5-9.

Looking at the peak temperature distribution in Figure 5-7, it appears that the margin to the 100°C limit is large, or very large, for the majority the canisters: the limit would be met for all but 5 canisters out of 6,000 even if the uncertainties would require the margin to be 2°C larger than the margin applied in the layout calculations. Table 5-3 illustrates the sensitivity to underestimates of the margin applied in the Forsmark layout. The table is based on the distribution shown in Figure 5-7.

Table 5-3 indicates that if the uncertainties and model simplifications would require the margin to be 5°C larger than that actually applied, then about 135 canisters, out of 6,000, would get peak temperatures in excess of the 100°C design limit. This is a very conservative upper bound estimate: the peak temperature distribution (Figure 5-7) applies for completely dry deposition holes, whereas in reality, at the time of the peak, the buffer will be at different stages of saturation with significant reductions of the temperature, cf. Figure 5-3.

Underestimating effects of uncertainties and model simplifications by as much as 5°C would thus impact on less than 135 canisters at Forsmark for which potentially the 100°C design limit would be exceeded by between 1°C and 5°C. For these canisters, temperatures in excess of 100°C would be found in small volumes in the canister/bottom top regions, cf. Figure 5-17. Note that the results include only the contribution from the local canister and do not show the absolute temperatures. A few centimetres away from the top, the temperatures are more than 5°C lower than the maximum at the top surface with peaks, consequently, below the threshold.

Table 5-3. Sensitivity to margin underestimates.

Margin underestimate	0	1	2	3	4	5
Canisters exceeding the design temperature	0	2	7	19	54	131

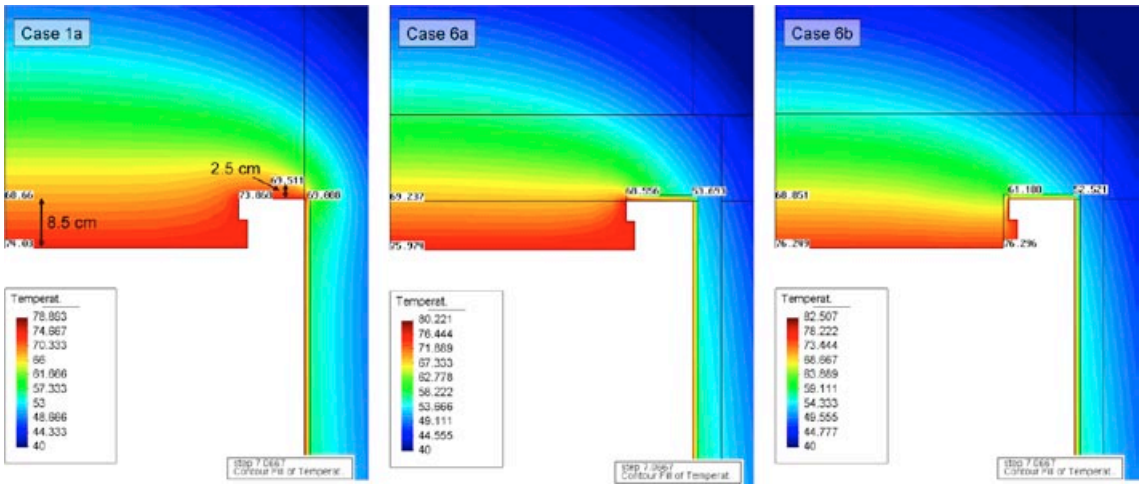

Figure 5-17. *Buffer temperatures at canister top for different assumptions of bentonite-copper contact in the flange region.*

5.9.2 Large scale thermal evolution

The calculation results presented specifically for the large scale thermal evolution are in general much less sensitive to spatial variability in heat transport properties. For points at some distance away from the canisters, the effective conductivity will be the average of conductivities in volumes that are large enough that the domain mean conductivity will be a valid approximation. The following conclusions are made (based on results obtained for layout D2, Forsmark):

- The temperature pulse reaches the ground surface after about 300 years (Figure 5-11).
- In the non-heated regions between the deposition areas, the maximum temperature increase is significantly lower (5–10°C rather than about 25°C) and occurs much later (after about 1,000 years rather than after 50 years) than in the deposition areas (cf. Figure 5-11 and Figure 5-12).

The *3DEC* model results presented here are identical to those generated in following sections to assess the large-scale thermomechanical evolution and its potential impact on hydraulic conditions. The models can also be used to assess, in a consistent way, the thermal stresses around transport tunnels, shafts, etc.

6 Assessment of large-scale THM evolution: temperate phase

6.1 General

As a result of the thermal load due to the decaying fuel (cf. Chapter 5), the rock mass will expand and subsequently contract, which will lead to changes in the stress field on all scales. These changes may in turn lead to changes in the hydrological conditions. By use of an analytical thermo-mechanical solution /Claesson and Probert 1996b/ (cf. Appendix A), the important features of the evolution of the thermally induced stresses around a generic square repository (1,000 m×1,000 m) can be seen, cf. Figure 6-1. In the following examples, mean value thermal, thermo-mechanical and mechanical properties in rock domain RFM029 and fracture domain FFM01 at Forsmark are used, cf. Table 4-5. The canister and tunnel spacings are set to 6 m and 40 m, respectively.

Figure 6-2 shows the thermally induced horizontal stress components (without considering *in situ* stresses) in vertical cross-sections 500 years after deposition of the canisters. Figure 6-3 shows the thermally induced vertical stress component 50 years after deposition in a vertical (left) and horizontal (right) cross-section. The following can be observed, cf. also e.g. /Probert and Claesson 1997b, Hökmark et al. 2006/:

- Within the deposition area there is increased compression in the horizontal and vertical directions at all times (blue colours).
- Outside the deposition area, there is loss of compression in the horizontal direction parallel with the edge of the repository (here σ_{yy}) and in the vertical direction (red colours).
- At some distance above and below the deposition area, there is loss of compression in both horizontal directions (red colours).

The observed differences in thermally induced stresses suggest that the implications for stress induced transmissivity changes will be different depending on location within the target area.

Inside the deposition areas the thermally induced stress increase is associated with rock expansion. This must be accounted for when defining boundary conditions for near-field models. By not allowing for large-scale deformations, the resulting near-field stresses will be overestimated. This was investigated in the SR-Can safety assessment /Fälth and Hökmark 2007/. /Fälth and Hökmark 2007/ demonstrated that by not allowing for the expansion of the near-field model boundaries, the

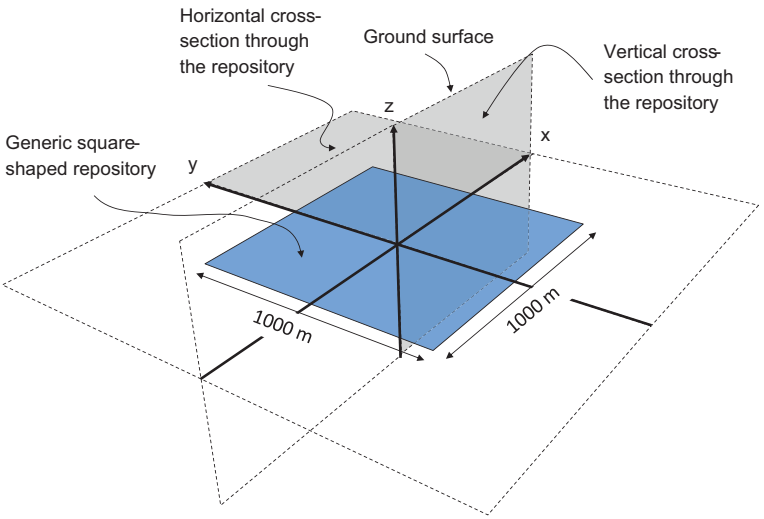

Figure 6-1. *Schematic view of repository layout and locations of plotting planes. Due to symmetry, the results are only shown in the grey-shaded areas.*

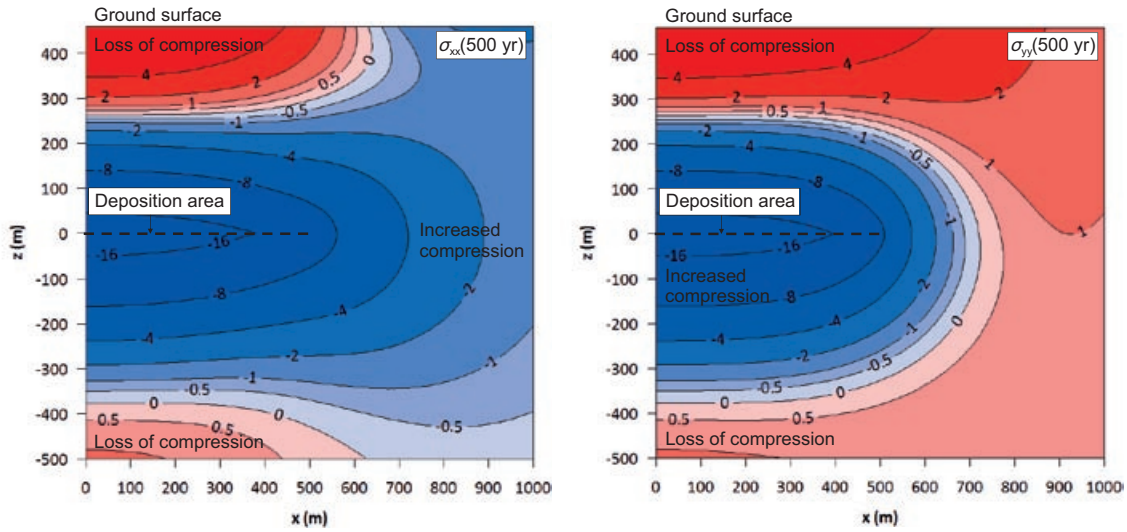

Figure 6-2. *Thermally induced horizontal stress additions (contours in MPa) parallel to the plane (σ_{xx}, left) and perpendicular to the plane (σ_{yy}, right) in a vertical cross-section passing through the centre of the repository after 500 years. Due to symmetry, only half of the region is shown, cf. Figure 6-1.*

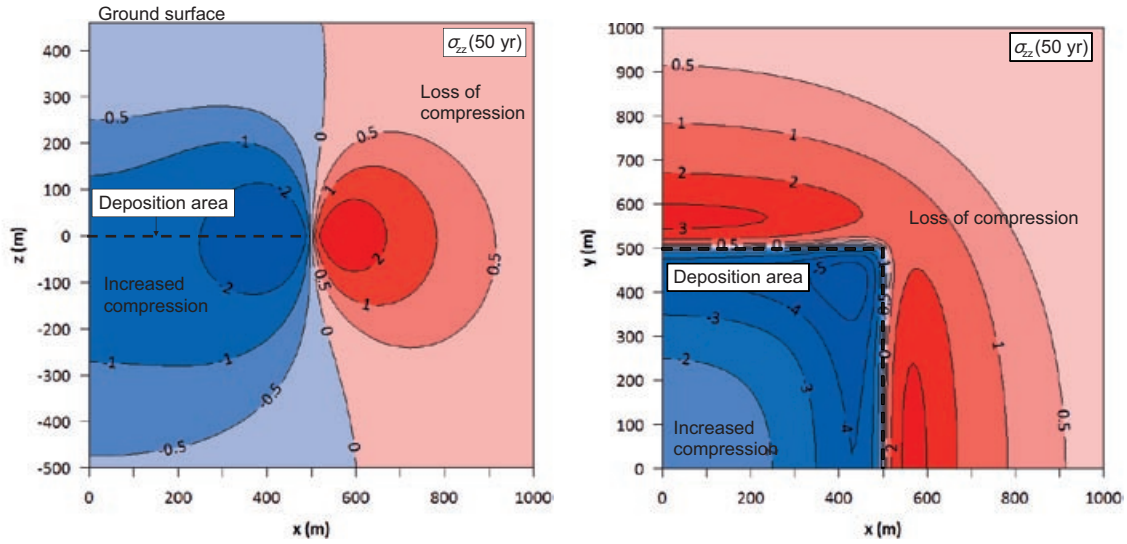

Figure 6-3. *Thermally induced vertical stress additions (contours in MPa), σ_{zz}, after 50 years in a vertical cross-section passing through the centre of the repository (left) and in a horizontal cross-section at repository level (right). Due to symmetry, only half of the region is shown in the left figure and a quarter in the right figure, cf. Figure 6-1.*

tangential stresses in the deposition hole walls were overestimated by about 7% at the time of stress maximum, cf. Figure 6-4. These results point to the need to derive suitable near-field boundary conditions for the temperate phase. In the present chapter, large-scale models are used to establish the amount of expansion and contraction of near-field models at different locations within the layout.

The large-scale thermo-mechanical evolution is important not only for defining boundary condition for near-field models, but also for assessment of the way the thermally induced stresses influence stresses in non-heated regions. The central area, for instance, includes numerous tunnels and caverns that potentially could be influenced by thermal stresses. Results from the large-scale models can easily be used to define boundary conditions for all types of arbitrarily located and oriented repository openings.

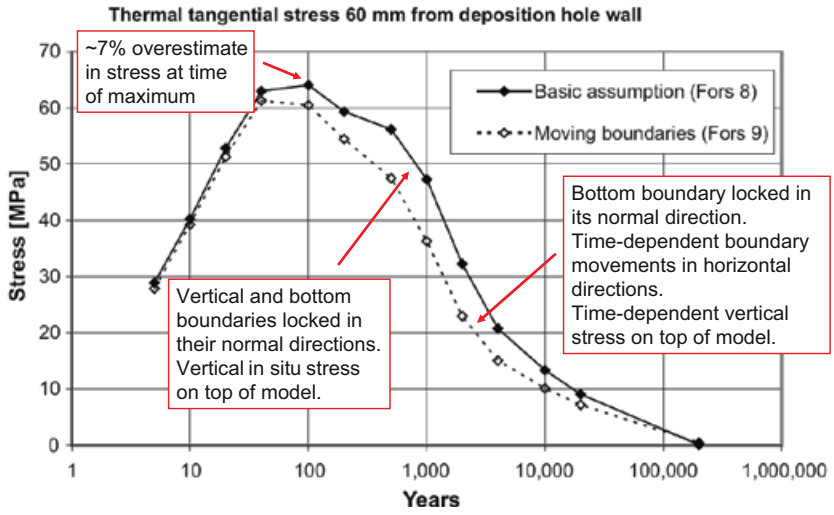

Figure 6-4. *Effects on thermally induced tangential stresses near the wall of a deposition hole for different assumptions regarding boundary conditions (note that compression is positive here). The stresses are overestimated by about 7% by not allowing for boundary movements. Modified from /Fälth and Hökmark 2007/.*

6.2 Data sensitivity and importance of layout details

Previous thermo-mechanical analyses of a KBS-3 repository were analysed using a generic repository consisting of rectangular deposition areas with simultaneous deposition of all canisters e.g. /Hökmark et al. 2006, Fälth and Hökmark 2007/. Examples of how differently sized deposition areas affect the thermal stresses are investigated in Appendix C.

In the following sections, the analytical thermo-mechanical solution /Claesson and Probert 1996b/ is used to demonstrate the impact on the thermally induced stresses due to different deposition sequences, variations in thermo-mechanical properties and sensitivity to tunnel spacing. Unless explicitly stated otherwise, mean value thermal, thermo-mechanical and mechanical rock mass properties in fracture domain FFM01 and rock domain RFM029 at the Forsmark site are used, cf. Table 4-5. The canister and tunnel spacings are set to 6 m and 40 m, respectively.

In situ stresses and the effects of the excavated openings are not considered here. Total stresses are obtained by adding the *in situ* stresses to the far-field average thermal stresses. Note that neither the actual temperature distribution around individual canisters nor the redistribution of stresses around excavated openings is captured by the analytical solution. Analyses of the evolution and distribution of stresses in the near-field require numerical tools as described in e.g. Chapter 9.

6.2.1 Deposition sequence

In the following example, it is assumed that the canisters will be deposited either simultaneously or at a rate of one canister every two or four days. Two generic deposition sequences have been chosen to demonstrate the impact of deposition order on thermally induced stresses, cf. Figure 6-5.

- Sequence 1: Deposition of each panel in turn (left to right, top to bottom).
- Sequence 2: Deposition of the inner parts of the middle panel first and moving outwards leaving the centre of the middle panel until last.

In the following example, all canisters are deposited at a rate of one canister every two days. As seen in Figure 6-6, distributing deposition over time has only a minor influence on the local stresses unless deposition in nearby tunnels took place a considerable time previously, as for Point C in Sequence II (cf. Figure 6-5, right).

Figure 6-7 shows the horizontal stresses at Point *C* in the time-scale of the first deposited sub-panel for each deposition rate (one canister every two days or one canister every four days) and for each deposition sequence. In the case of Sequence I, the thermal stress additions, at the time of deposition of the sub-panel including Point *C*, are practically zero (0–0.6 MPa). The influence on the stress additions at stress maximum is also negligible. Sequence II was deliberately chosen such that the stresses at Point *C* would be high. In this case, the stresses, at the time of deposition of the local sub-panel, have increased by about 8–10 MPa depending on deposition rate in the direction along tunnels and 6–9.5 MPa across tunnels. The stress additions at stress maximum show a moderate increase (1.5–2.5 MPa for the faster deposition rate and 2.2–3.8 MPa for the slower deposition rate) compared with simultaneous deposition.

Similarly to the analyses for the temperatures (Figure 5-9), the results presented here show that the deposition sequence approximation made in all models in this report, i.e. that all canisters are deposited simultaneously is valid, unless very specific sequences are used (for instance starting and finalizing the deposition in neighbouring tunnels or very nearby deposition areas). It also shows that the approximation made in here and in previous work (cf. e.g. /Hökmark et al. 2006/) that the stresses during the construction phase are not influenced by temperature effects is valid. Given a proposed deposition sequence, it can easily be checked (e.g. by use of the analytical solution) that these approximations hold.

6.2.2 Parameter variations

Figure 6-8 shows the effect on the average thermal stress addition at the centre of the repository (cf. e.g. Point C in Figure 6-5, left) due to variations in Young's modulus, Poisson's ratio, heat capacity and thermal expansion coefficient. The variations are expressed in terms of ±1 standard deviation of each parameter, except the thermal expansion coefficient where the range is given by the mean value of different rock types, cf. Table 4-5 and Table 4-7.

As seen in Figure 6-8, the range in thermally induced stresses due to variations in rock mass thermal, thermo-mechanical and mechanical properties is small. The thermally induced stresses are proportional to the value of Young's modulus and the thermal expansion coefficient. The variations in these two parameters result in a stress range of around ±3 MPa and ±1.5 MPa of the mean value, respectively. For the given variations in Poisson's ratio and heat capacity, the resulting thermally induced stresses are in the range ±0.5–1 MPa of the mean. It can therefore be concluded that, for the numerical large-scale modelling, it will be sufficient to consider mean value rock mass properties.

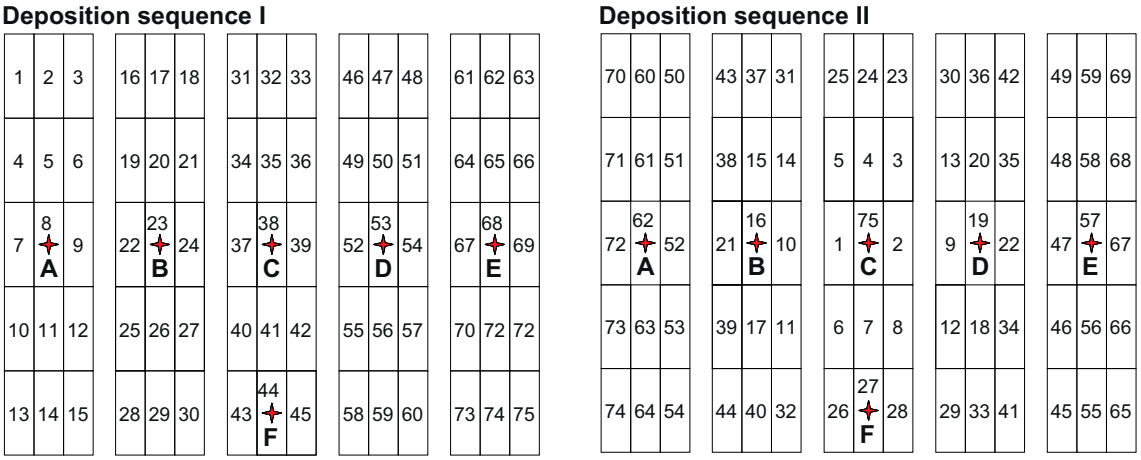

Figure 6-5. *Examples of deposition sequences: Sequence I (left) and Sequence II (right).*

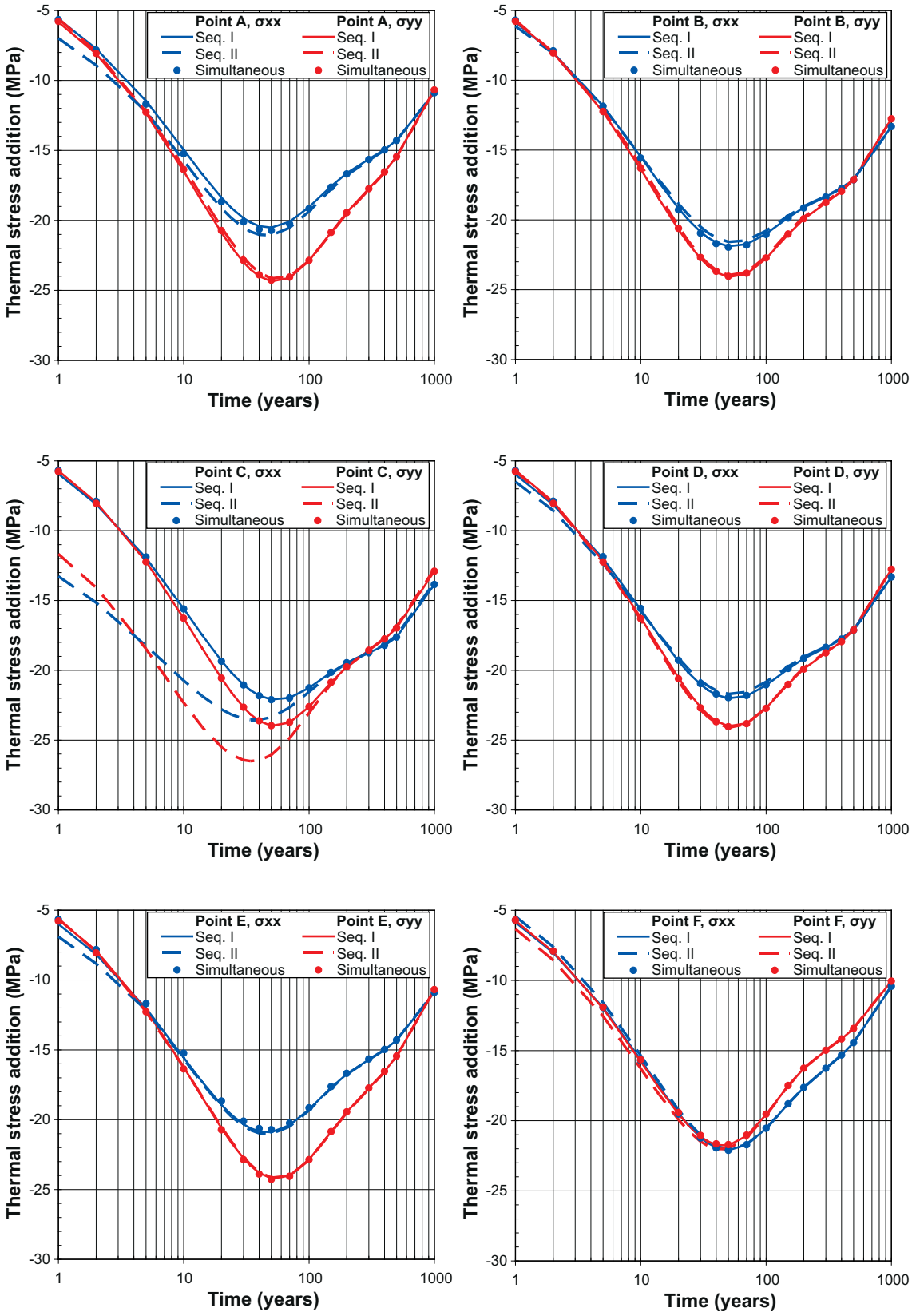

Figure 6-6. *Horizontal stresses at points A–F deposited either simultaneously or in sequence according to Figure 6-5. All stresses are shown in their local time scale.*

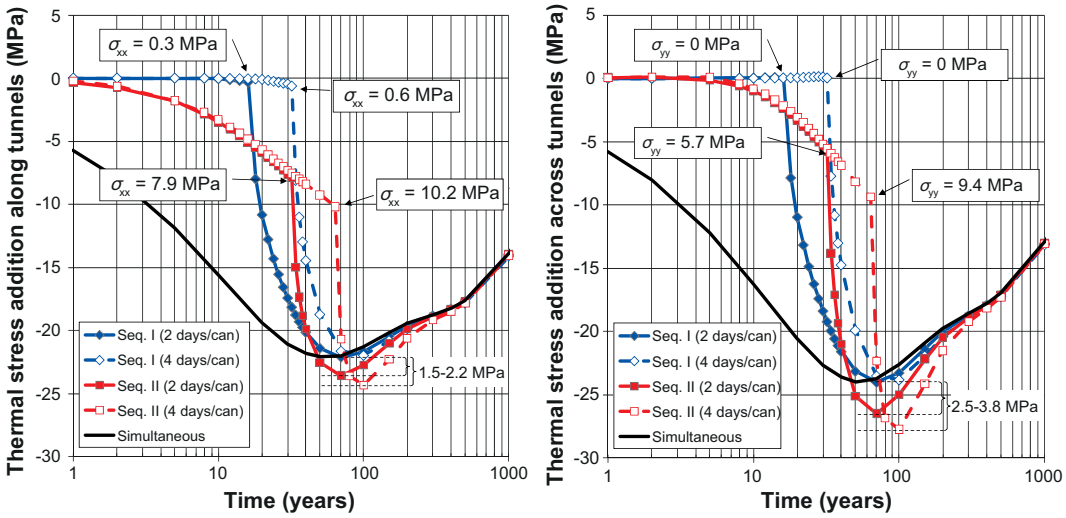

Figure 6-7. *Horizontal stresses along tunnels (left) and across tunnels (right) at Point C. All stresses are presented in the time-scale of the sub-panel deposited first.*

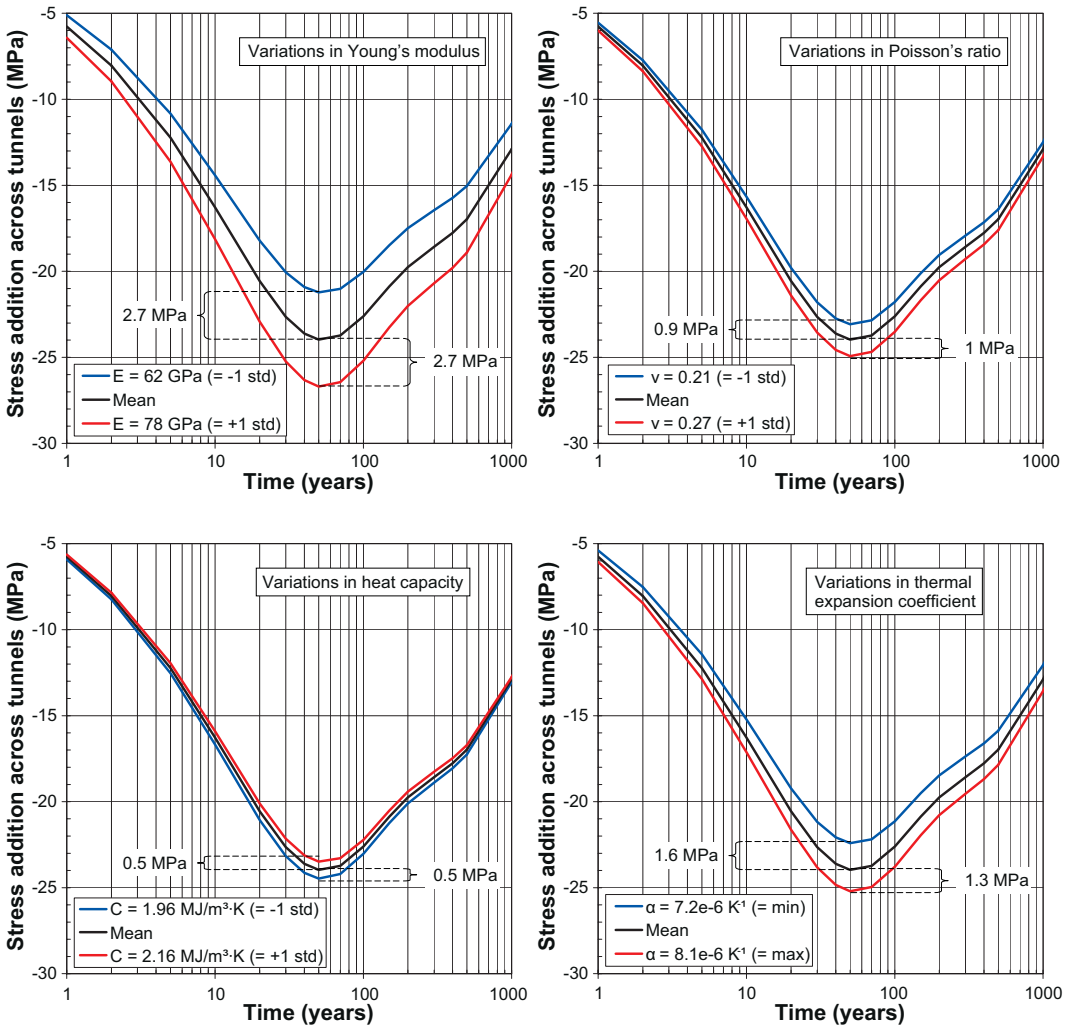

Figure 6-8. *Average thermal stress additions in the direction across tunnels at the centre of the repository (cf. Figure 6-5). The variations in Young's modulus, Poisson's ratio and heat capacity are expressed as ±1 standard deviation of the mean value whereas the span in the thermal expansion coefficient relates to the mean values of different rock types, cf. Table 4-5 and Table 4-7.*

6.2.3 Sensitivity to tunnel spacing

In Layout D2 no optimisation has been made, *i.e.* the tunnel spacing is 40 m and the canister spacing is determined by the thermal properties in each rock domain such that the peak buffer temperature does not exceed 100°C in any deposition hole /Hökmark et al. 2009/. However, an optimisation of the repository with respect to minimum use of space may be possible /Hökmark et al. 2009/. Figure 6-9 shows an example of the required canister and tunnel spacings for given values of the thermal conductivity. Note that, in this example, the uncertainty margin is set to 8°C whereas in Chapter 5 it is assumed to be around 5°C.

The canister spacing in rock domain RFM029 at Forsmark is 6 m /SKB 2009b/, which is also the minimum allowed canister spacing. However, in parts of the repository region the thermal conductivity may be significantly higher than the dimensioning thermal conductivity, in which case the only possibility for an optimisation would be to reduce the tunnel spacing. In general, a reduction in tunnel spacing will be accompanied by an increase in canister spacing. Even if the canister spacing must be increased beyond 6 m to meet the temperature criterion of 100°C, the total area per canister is likely to be reduced (cf. Figure 6-9), *i.e.* the average power density will be increased.

A number of issues will be affected by a higher power density.

- The risk of thermally induced spalling is increased or the spalling threshold may be exceeded earlier.
- The stress reductions seen in e.g. Figure 6-2 and Figure 6-3 are inversely proportional to the thermal load, i.e. the resulting increase in thermal load due to an optimisation of the layout would result in a more significant stress reduction near the ground surface and outside the deposition areas. This would in turn lead to an increase in transmissivity of fractures intersecting the volumes of rock with reduced stresses.

Figure 6-10 (top row) shows two examples of repository layouts with 6 m canister spacing and 40 m tunnel spacing (left) and 7 m canister spacing and 30 m tunnel spacing (right). The bottom row of the figure shows the resulting average thermally induced stresses evaluated at the centre of the repository region for each of the two layouts. At stress maximum (~70 years after deposition), the increase in thermal stress additions is of the order 3–4 MPa higher in the layout with 7 m canister spacing/30 m tunnel spacing than in the layout with reference canister spacing and tunnel spacing.

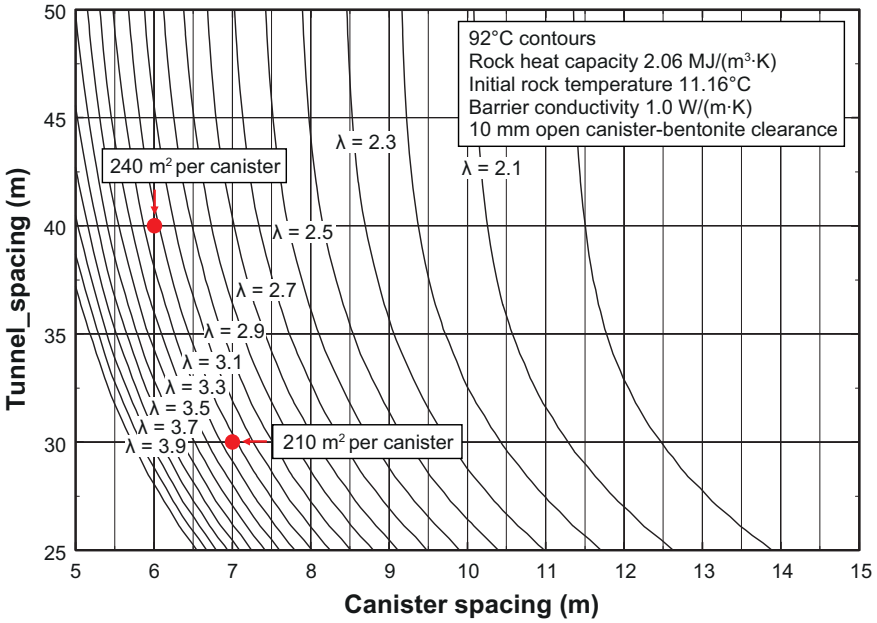

Figure 6-9. *Example of a tunnel/canister spacing chart for different values of the thermal conductivity (λ) in rock domain RFM029 at Forsmark assuming the uncertainty margin to be 8°C, modified from /Hökmark et al. 2009/. The dimensioning tunnel/canister spacing for rock domain RFM029 /SKB 2009b/ and the canister spacing (7 m) needed for a reduction in tunnel spacing to 30 m are marked with red circles.*

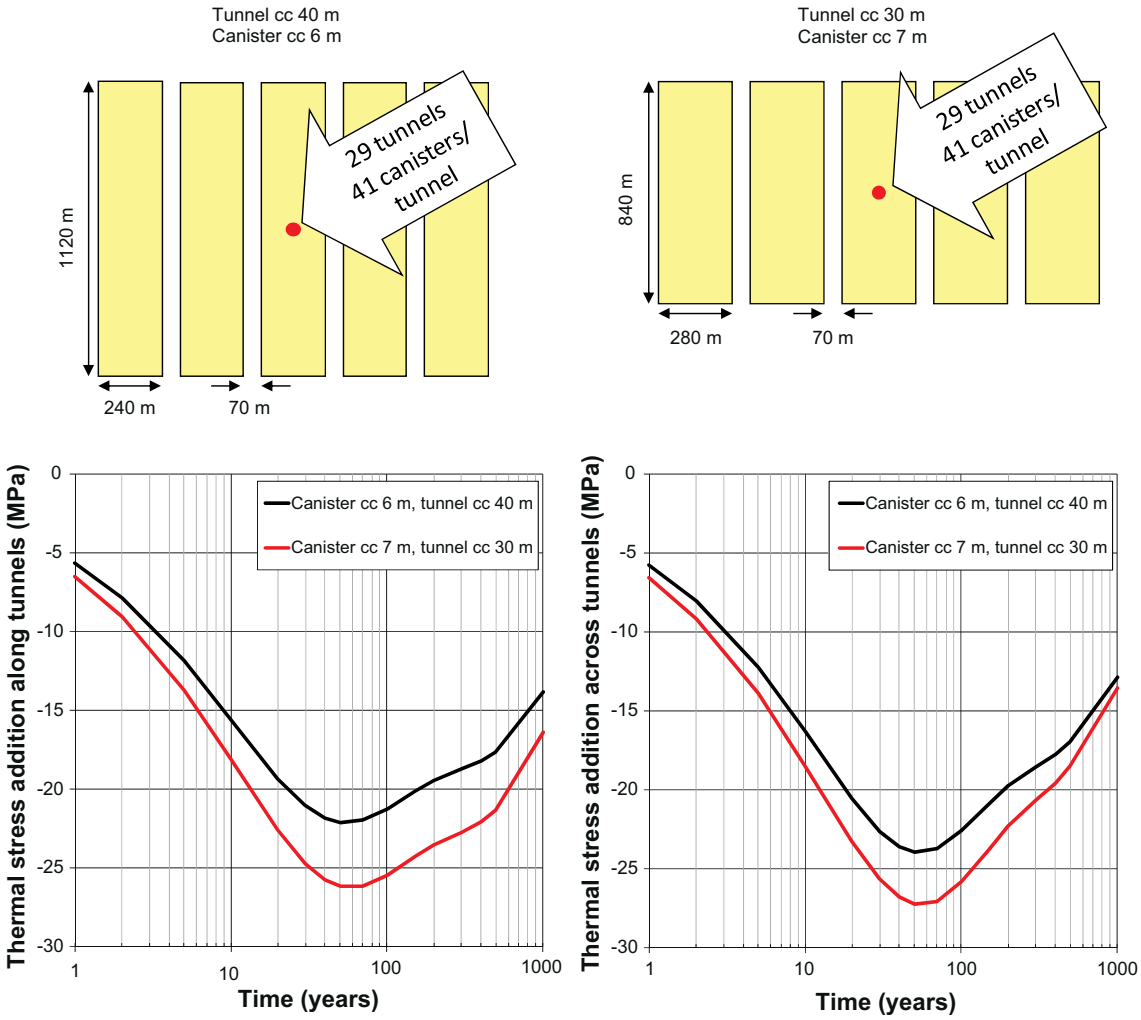

Figure 6-10. *Top left: Schematic repository layout with reference canister (centre-to-centre, cc) spacing (6 m) and tunnel spacing (40 m) in rock domain RFM029 at Forsmark. Top right: Repository layout with 7 m canister spacing and 30 m tunnel spacing. Bottom row: Resulting average thermally induced stresses in the along-tunnel direction (left) and in the across-tunnel direction (right).*

6.3 Description of modelling approach

6.3.1 Objectives

The large-scale *3DEC* models are used to investigate/determine the following:

- Boundary conditions for near-field models.
- Stress evolution in the rock between the repository and the ground surface.
- Heave of the ground surface.
- Stress-induced transmissivity variations at different locations within the repository region.
- The potential for shearing and a qualitative assessment of the impact on transmissivity.

6.3.2 Estimates of stress induced transmissivity changes

Similarly to the study by /Hökmark et al. 2006/ for the SR-Can safety assessment, no coupled THM analyses are performed:

- Thermally induced stresses are obtained by averaging the stresses from the large-scale models over an area of about 100×100 m symmetrically positioned around each scanline in depth-intervals of 50 m. These are then added to the *in situ* stresses.

- Variations in relative transmissivity are estimated from the numerically obtained stresses by use of the two stress-transmissivity models (A and B) presented in Figure 4-9. Model A can be considered a "worst case" option based on lower bound fracture normal stiffness estimates and is therefore very sensitive to normal stress variations. Model B is based on average fracture normal stiffness estimates and is less sensitive to variations in normal stress. However, both models are more sensitive to normal stress variations than the most conservative *in situ* correlation reported for Forsmark by /Follin et al. 2008/.

6.3.3 Shearing

Slip estimates are obtained by use of an analytical solution for the shear displacement, u_s, at the centre of a circular fracture with radius a totally embedded in an elastic medium /Eshelby 1957/, cf. Equation 6-1. Equation 6-2 gives the shear displacement at an arbitrary position (x, y) from the fracture's centre. Figure 6-11 (left) shows an example of the normalised shear displacement along a fracture of radius a. It should be noted that these expressions give only an approximation as in reality there is a variation in stress along the fracture. Only qualitative assessments of the impact of shearing on fracture transmissivities will be made, cf. Chapter 3.

$$u_s = \frac{24}{7\pi \cdot G}\tau_{drop} \cdot a \qquad \text{Eq. 6-1}$$

$$u_s = \frac{24}{7\pi \cdot G}\tau_{drop} \cdot \left(a^2 - \left(x^2 + y^2\right)\right)^{1/2} \qquad \text{Eq. 6-2}$$

Here, G is the shear modulus of the rock mass. The stress drop, τ_{drop}, is defined as the difference between the shear stress acting on the fracture plane and the fracture's strength (Equation 6-3). A factor of safety (FoS, cf. Equation 6-4) is defined as the ratio between shear strength and the shear stress.

$$\tau_{drop} = \tau - (c + \sigma_n \tan(\varphi)) \qquad \text{Eq. 6-3}$$

$$FoS = \frac{c + \sigma_n \tan(\varphi)}{\tau} \qquad \text{Eq. 6-4}$$

For a given state of stress, there exists a critical plane, θ, where the shear strength is first reached /e.g. Brady and Brown 1993/, cf. Figure 6-11 (right). This can be expressed as

$$\theta = (90 - \varphi)/2, \qquad \text{Eq. 6-5}$$

where φ is the friction angle. For a stress-state with horizontal-vertical principal stresses, the critical plane will be sub-vertical if the minimum stress is horizontal (strike slip stress regime, e.g. Laxemar /Hakami et al. 2008/, see Appendix I) and gently dipping if the minimum stress is vertical (reverse stress regime e.g. Forsmark /Glamheden et al. 2007a/).

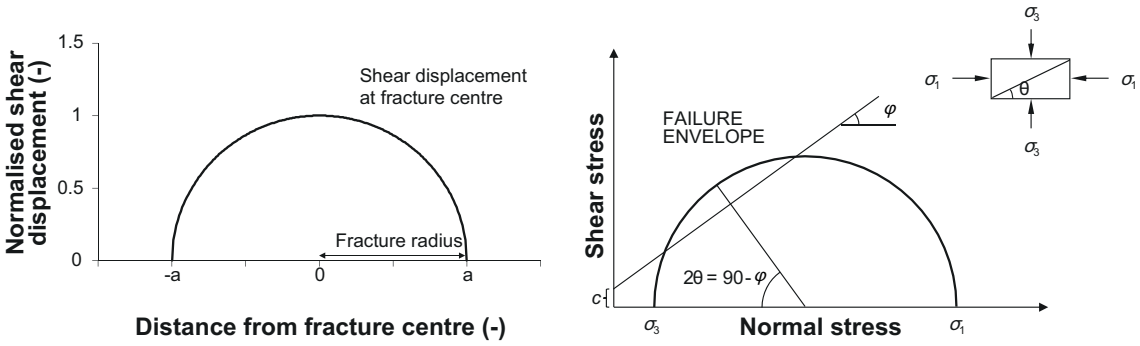

Figure 6-11. *Left: Normalised shear displacement as a function of distance from the centre of a fracture with radius a. Right: Orientation of the critical plane, θ.*

6.4 Overview of 3DEC models

Layout D2 for the Forsmark site contains approximately 6,900 canister positions with an expected loss of 13%. As no information is given regarding the distribution of the loss of canister positions across the repository region, it is assumed to be uniform. In order to achieve the average thermal load on a large scale, every 8th canister is removed uniformly across the repository region. The locations of heat sources in the large-scale model are presented in Figure 6-12 together with the locations chosen for near-field modelling in Chapters 8 and 9.

The modelled rock mass is represented by a linear elastic rectangular block with isotropic and homogeneous properties, cf. Section 4.6. Its dimensions are 8 km×7.4 km×~3 km. An outline of the large-scale model is shown in Figure 6-13. The small differences in mean value thermal and thermo-mechanical properties in rock domains RFM029 and RFM045 and mechanical properties in fracture domains FFM01 and FFM06 do not warrant a differentiation in material properties between the domains. Therefore, mean values of the thermo-mechanical properties in rock domain RFM029 and fracture domain FFM01 are used in the entire modelled domain, cf. Table 4-5. Where total stresses are required, the *in situ* stresses are added to the thermally induced stresses in a post-processing step. The *in situ* stresses and the initial temperature do not influence the calculations and are set to zero.

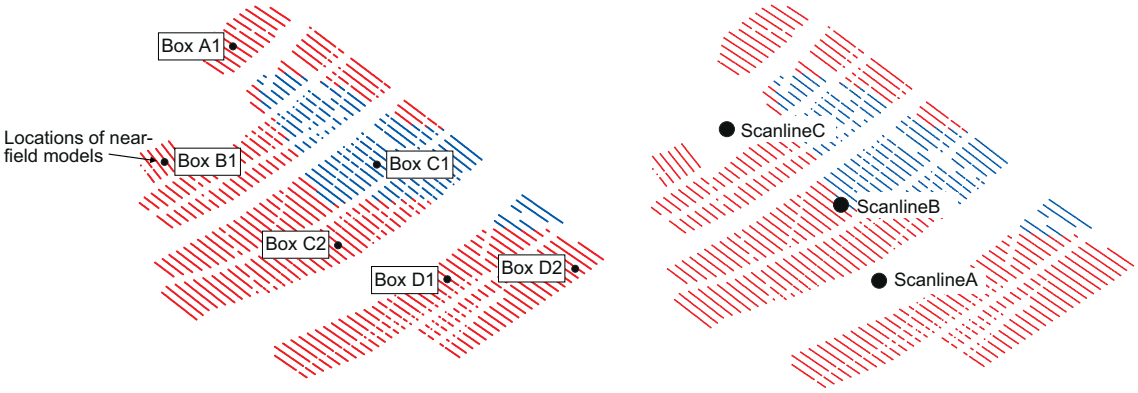

Figure 6-12. *Forsmark Layout D2 – version with 13% loss of canister positions. Red colour represents parts of the repository region with 6 m canister spacing and blue colour represents parts of the repository region with 6.8 m canister spacing. Left: Locations of near-field models, cf. Chapters 8 and 9. Right: Locations of vertical Scanlines A, B and C within the repository region.*

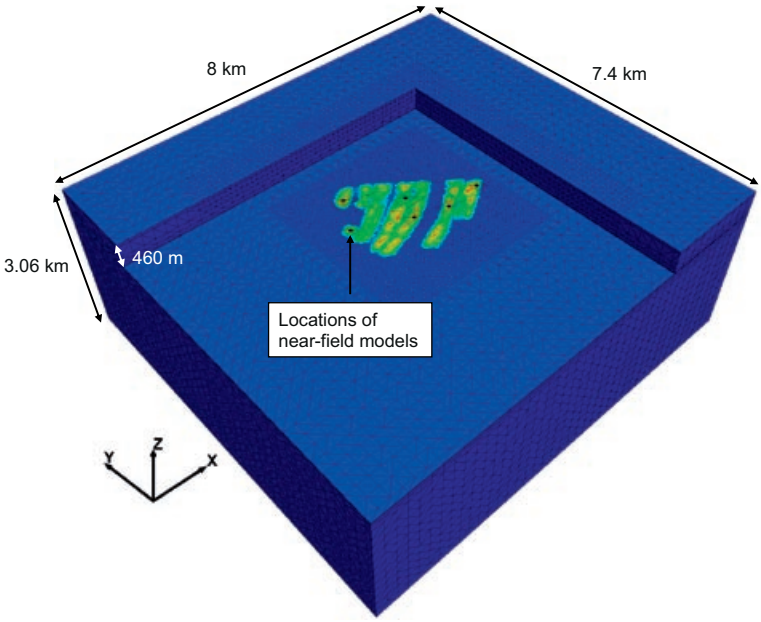

Figure 6-13. *Outline of Forsmark large-scale 3DEC model. Note that parts of the model are hidden from view.*

6.5 Boundary conditions for near-field models

Boundary conditions for the subsequent near-field modelling in Chapters 8 and 9 are obtained from the displacements on pre-defined cut-planes representing the near-field model boundaries and are evaluated as the relative expansion/contraction to the centre of the near-field model as a function of time. Effects on near-field boundary conditions due to steeply dipping deformation zones are analysed in Appendix B. Boundary conditions are obtained for two types and sizes of near-field models containing:

- One tunnel segment with seven canisters (spalling analyses). Model dimensions are 40 m (across tunnels) and 50 m (vertically);
- Five tunnel segments each with 33 potential canister positions (shearing, normal stress variations and transmissivity changes of fractures). Model dimensions are 200 m (across tunnels) and 200 m (vertically).

The dimensions of the near-field models in the along-tunnel-direction are determined by the local canister spacing.

Boundary conditions for the small and medium-sized near-field models are presented in Figure 6-14 and Figure 6-15, respectively. Near-field analyses are conducted in Chapters 8 (medium-scale) and 9 (small scale).

6.6 Stress evolution in rock between repository and ground surface

Figure 6-16 shows stresses as functions of depth along three vertical scan-lines: One between deposition areas (Scanline A), one through central parts of the repository region (Scanline B) and one through the central area (Scanline C). During the thermal phase the horizontal stresses lose compression by up to 5 MPa in the upper approximately 150 m of the rock. The loss of compression in the direction of the minor horizontal *in situ* stress is the most prominent. At repository level the loss of compression of the vertical stress on Scanlines A and C amounts to about 3.6 MPa and 3.1 MPa, respectively.

6.7 Heave of ground surface

Figure 6-17 (lower) shows the vertical displacement at the ground surface averaged over a 400 m×400 m area as indicated in the upper part of the figure. The maximum heave is about 75 mm after 1,000 years.

6.8 Effects on fractures and fracture zones

6.8.1 Transmissivity changes

The transmissivity effects on large fractures are presented as functions of depth on planes perpendicular to the present-day major horizontal *in situ* stress (σ_H), minor horizontal *in situ* stress (σ_h) and the vertical *in situ* stress (σ_v) at positions labelled A, B and C. Scanline A intersects the repository region between two deposition areas, Scanline B through central parts of a deposition area and Scanline C intersects the repository region in the central area, cf. Figure 6-12 (right).

In the present sections, examples of changes in effective normal stress and transmissivity during the thermal phase along Scanlines A and B on vertical fractures perpendicular to the major and minor horizontal *in situ* stress and on horizontal fractures are presented, cf. Figure 6-18, Figure 6-19, Figure 6-21 and Figure 6-22. A complete set of results is presented in Appendix E.

Along Scanline A, the following can be observed.

- **Vertical fractures striking perpendicular to the present-day major horizontal *in situ* stress (σ_H, i.e. striking 55° with respect to North), cf. Appendix E:** The changes in effective normal stress result in only negligible changes in relative transmissivity.
- **Vertical fractures striking perpendicular to the present-day minor horizontal *in situ* stress (σ_h, i.e. striking 145° with respect to North), cf. Figure 6-18:** The reductions in effective normal stress in the upper 100 m of rock result in an increase in relative transmissivity by at most a factor 2 (model A) and 1.3 (model B), respectively. Below a depth of 200 m there are only negligible changes in relative transmissivity for both stress-transmissivity models.
- **Horizontal fractures, cf. Figure 6-19:** At repository depth and about 150 m above and below that level the vertical stress is reduced, resulting in an increase in relative transmissivity by a factor around 2 (model A) and a factor around 1.5 (model B).

Along Scanline B, the following can be observed.

- **Vertical fractures striking perpendicular to the present-day major horizontal *in situ* stress (σ_H, i.e. striking 55° with respect to North), cf. Figure 6-20:** Close to the ground surface the reduction in effective normal stress may result in an increase in relative transmissivity by up to a factor 1.5 (model A). Below a depth of around 150 m, the changes in effective normal stress result in only negligible variations in relative transmissivity. For model B, the changes in relative transmissivity are negligible at all depths.
- **Vertical fractures striking perpendicular to the present-day minor horizontal *in situ* stress (σ_h, i.e. striking 145° with respect to North), cf. Figure 6-21:** The reductions in effective normal stress in the upper 100 m of rock result in an increase in relative transmissivity by at most a factor 2.5 (model A) and 1.5 (model B), respectively. Below a depth of 200 m there are only negligible changes in relative transmissivity for both stress-transmissivity models.
- **Horizontal fractures, cf. Figure 6-22:** Below a depth of around 50 m, the effective vertical stress increases resulting in a reduction of the relative transmissivity to, at minimum, about 0.6 (model A). For model B the changes are negligible. Note that the reduction in vertical stress beneath repository level is likely to be an interpolation error.

Along Scanline C, the following can be observed.

- **Vertical fractures striking perpendicular to the present-day major horizontal *in situ* stress (σ_H, i.e. striking 55° with respect to North), cf. Appendix E:** The changes in effective normal stress result in only negligible changes in relative transmissivity.
- **Vertical fractures striking perpendicular to the present-day minor horizontal *in situ* stress (σ_h, i.e. striking 145° with respect to North), cf. Appendix E:** The reductions in effective normal stress in the upper 100 m of rock result in an increase in relative transmissivity by at most a factor 1.5–1.6 (model A) and 1.2 (model B), respectively. Below a depth of about 150 m there are only negligible changes in relative transmissivity for both stress-transmissivity models.
- **Horizontal fractures, cf. Appendix E:** At repository depth and about 150 m above and below that level the vertical stress is reduced, resulting in an increase in relative transmissivity by up to a factor 2 (model A) and 1.3 (model B), respectively.

Figure 6-23 shows the thermally induced normal stress addition on a plane with the same orientation and approximate location in relation to the repository region as the fracture zone ZFMA2. The fracture normal stress is reduced by around 2 MPa near the ground surface and increased by 2–2.5 MPa around 200 m below the ground surface. These results are in good agreement with the ones obtained in the comparison between *3DEC* and the analytical solution provided in Appendix A. (The analysis in the appendix also shows that the corresponding shear stress addition is of the same order of magnitude, meaning that there would be very minor, if any, disturbances of the stability of this fracture zone during the heated period.)

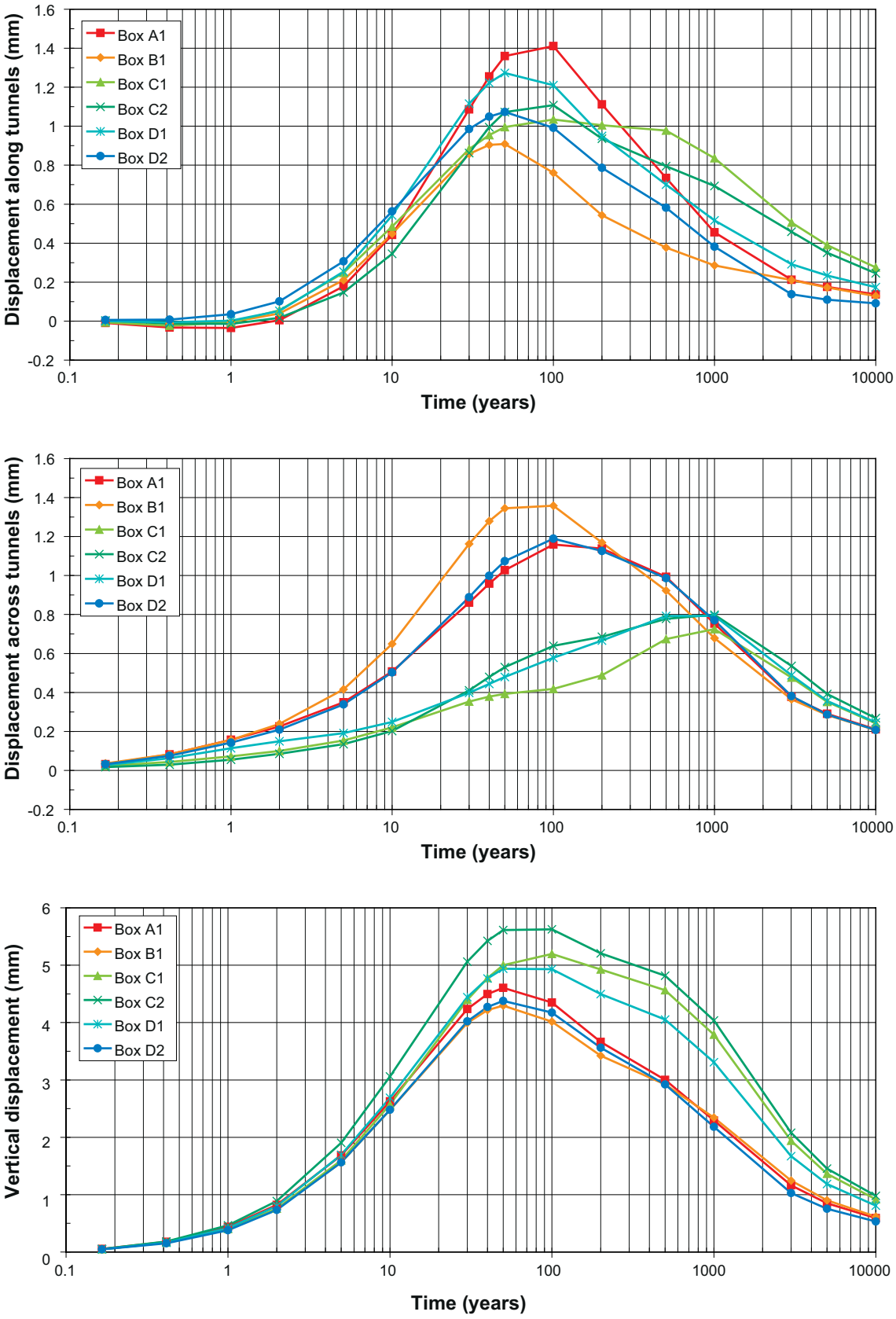

Figure 6-14. *Boundary conditions for small near-field models at Forsmark: Top: Horizontal displacement in the direction along tunnels. Middle: Horizontal displacement in the direction across tunnels. Lower: Vertical displacement.*

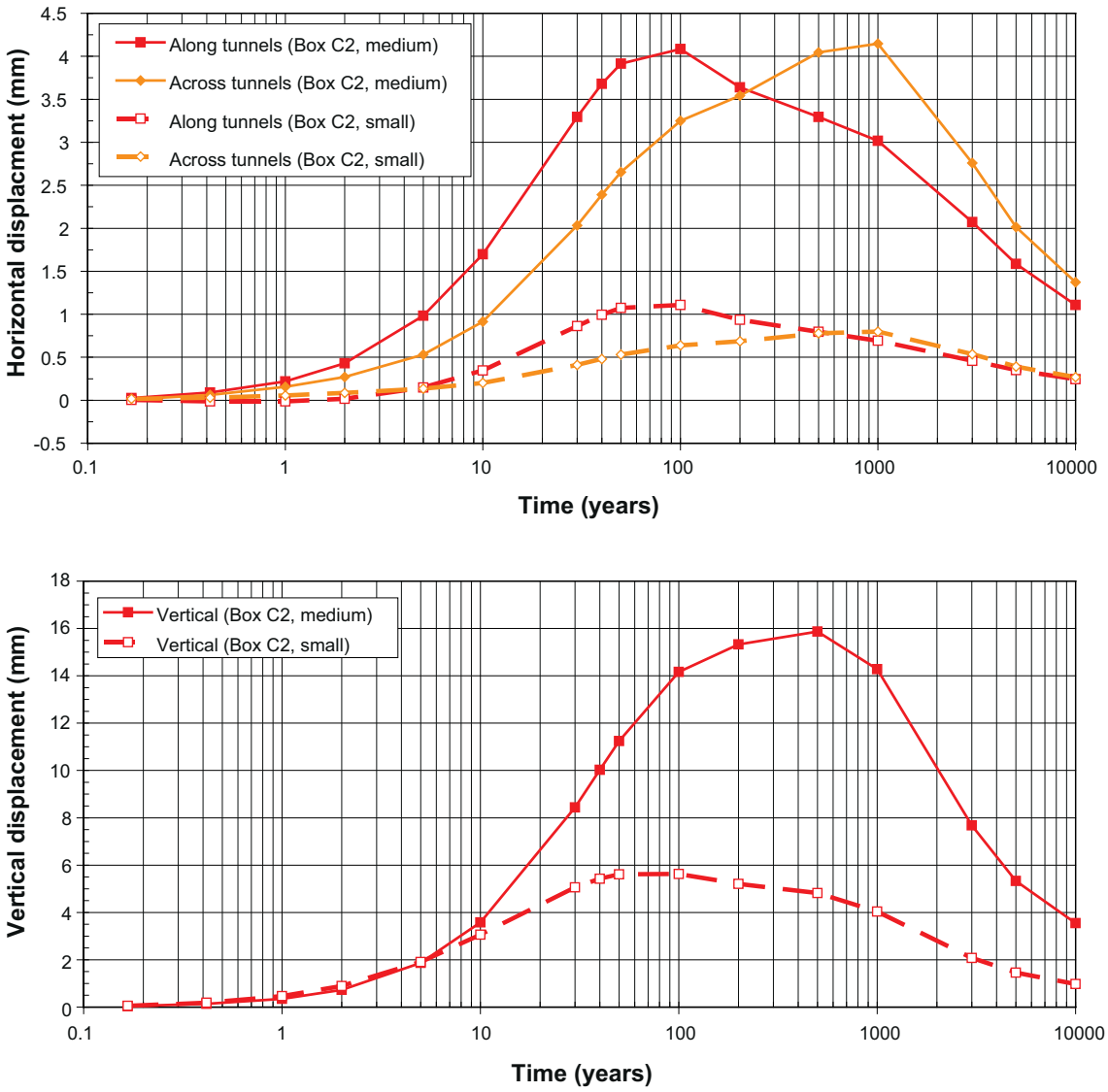

Figure 6-15. *Boundary conditions for near-field box C2 at Forsmark (small and medium-sized): Horizontal displacements (top) and vertical displacements (bottom).*

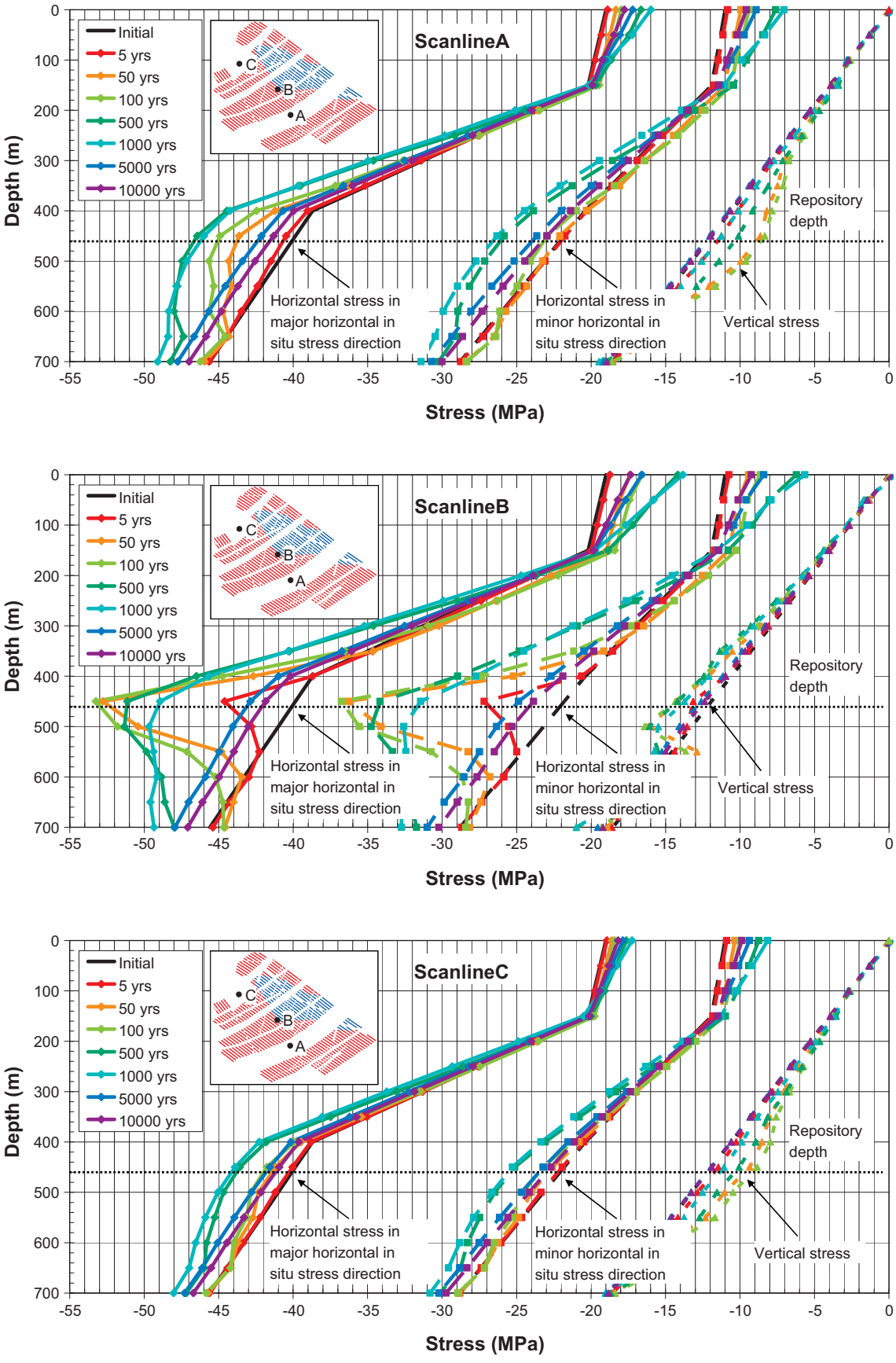

Figure 6-16. *Stresses along vertical scanlines through the repository region.*

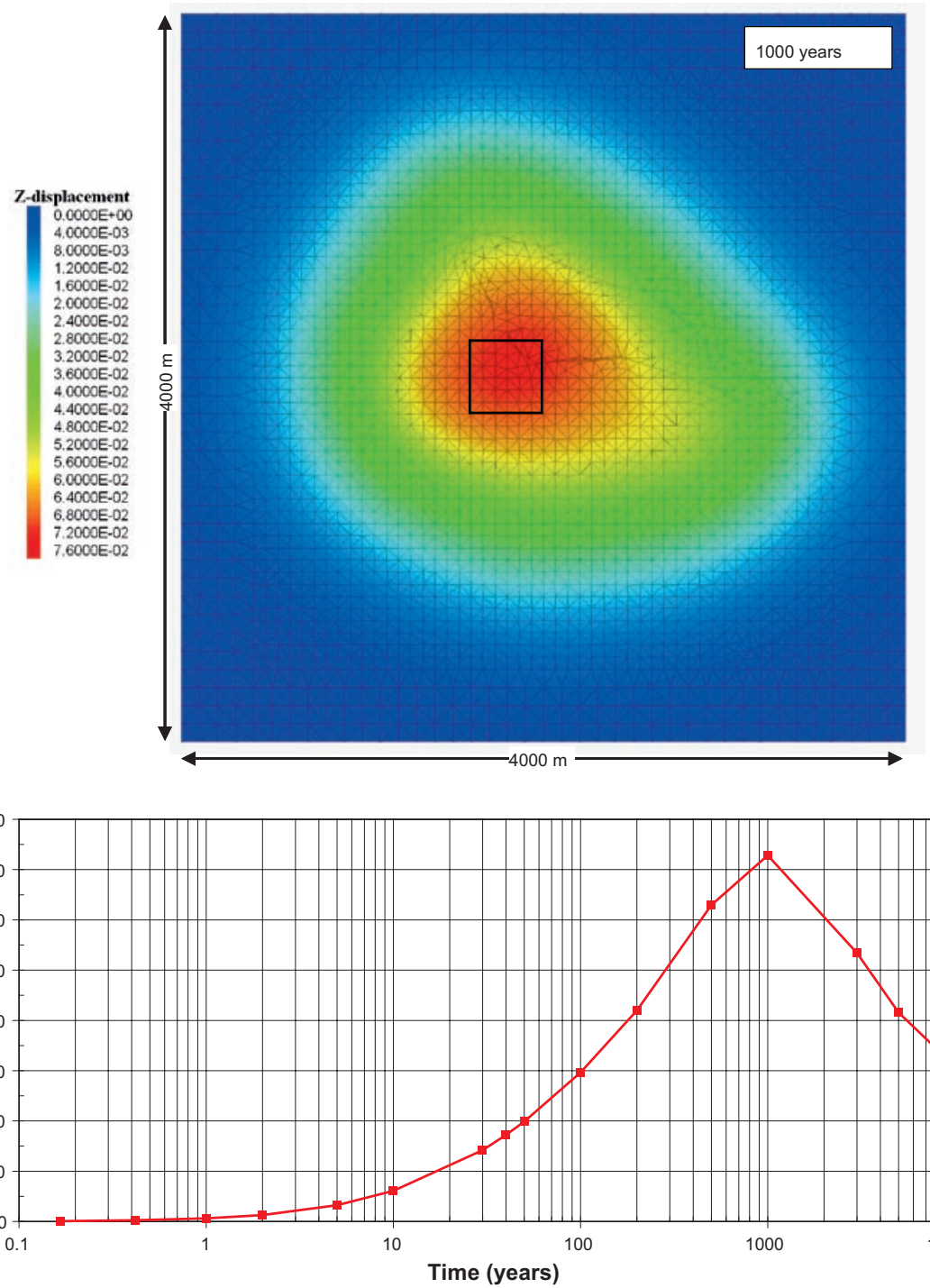

Figure 6-17. *Top: Heave of the ground surface after 1,000 years (legend in metres). Bottom: Temporal development of the vertical displacement at the ground surface averaged over the area marked in the upper figure.*

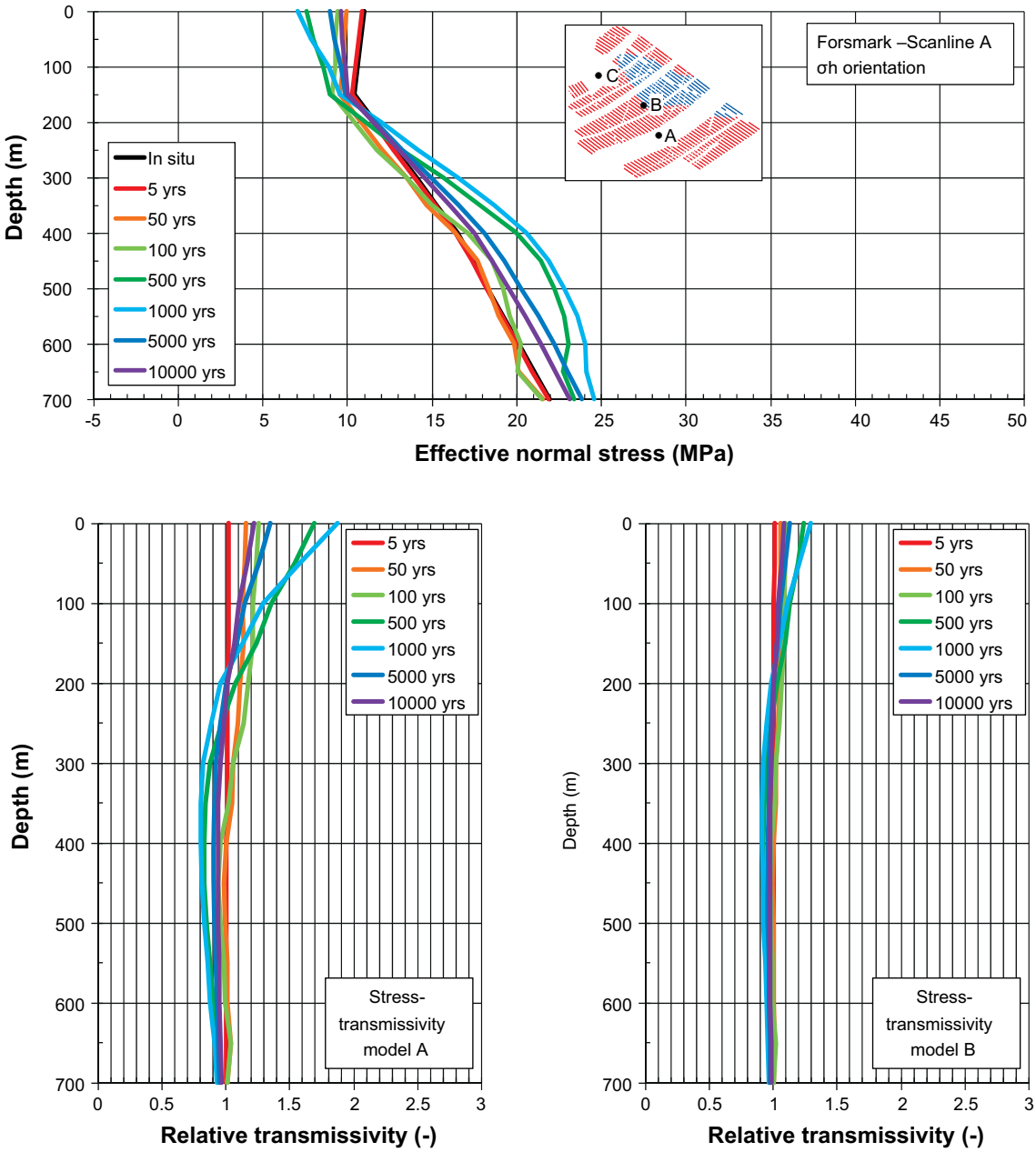

Figure 6-18. *Top: Effective stress as a function of depth along Scanline A in the direction of the present-day σh. Bottom: Relative transmissivity of vertical fractures striking perpendicular to the present-day σh.*

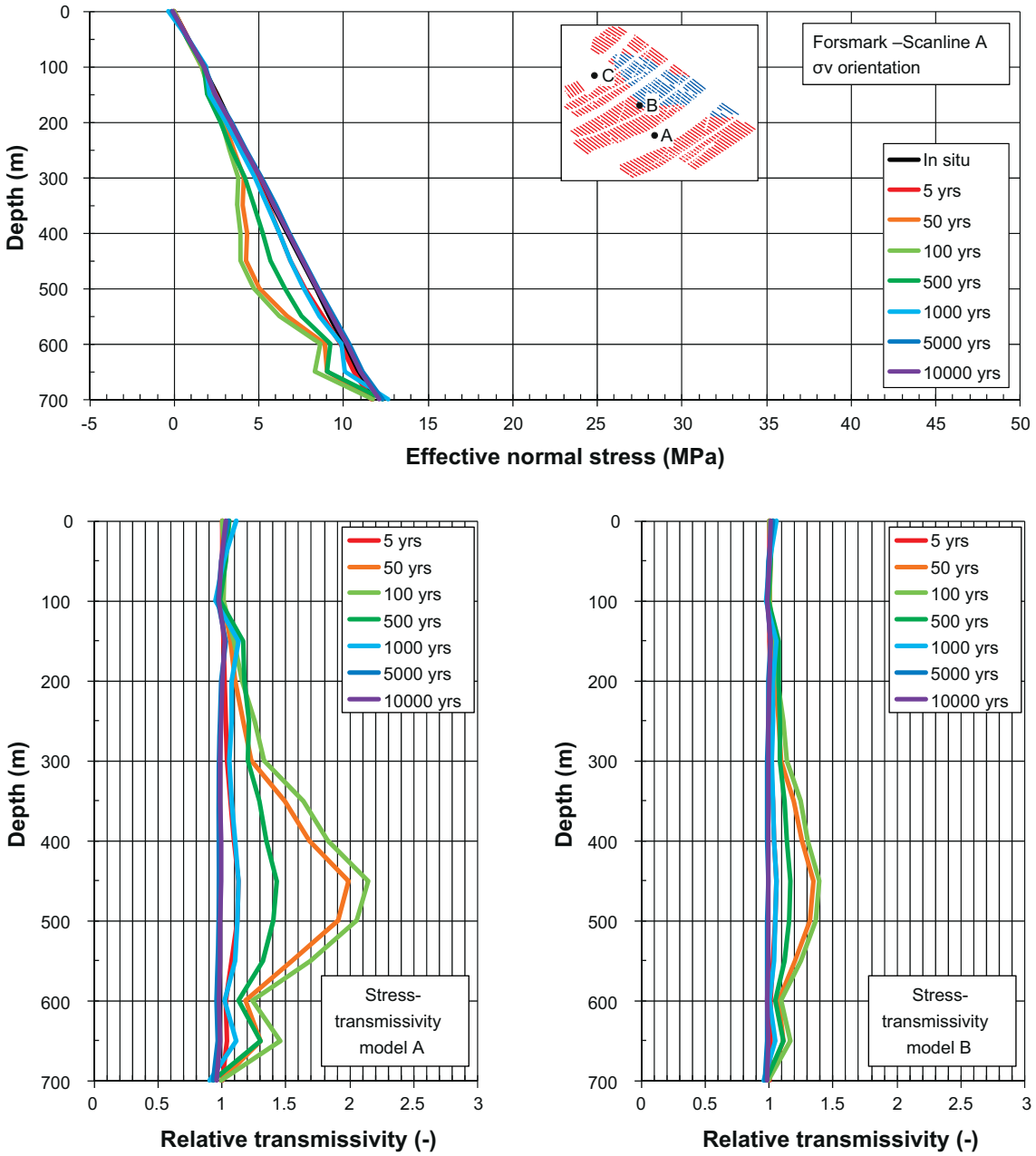

Figure 6-19. *Top: Effective stress as a function of depth along Scanline A in the direction of σv. Bottom: Relative transmissivity of horizontal fractures.*

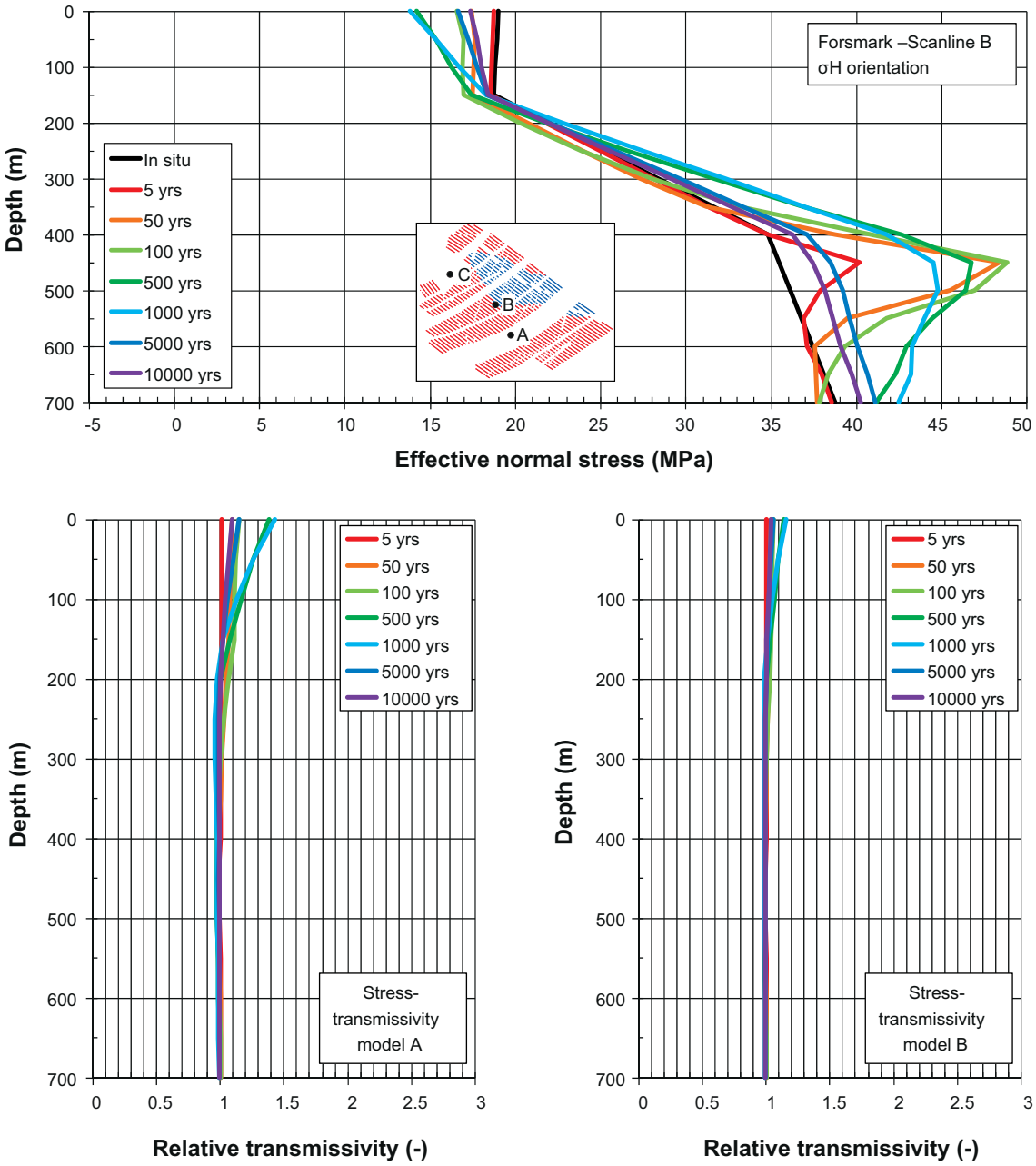

Figure 6-20. *Top: Effective stress as a function of depth along Scanline B in the direction of the present-day σH. Bottom: Relative transmissivity of vertical fractures striking perpendicular to the present-day σH.*

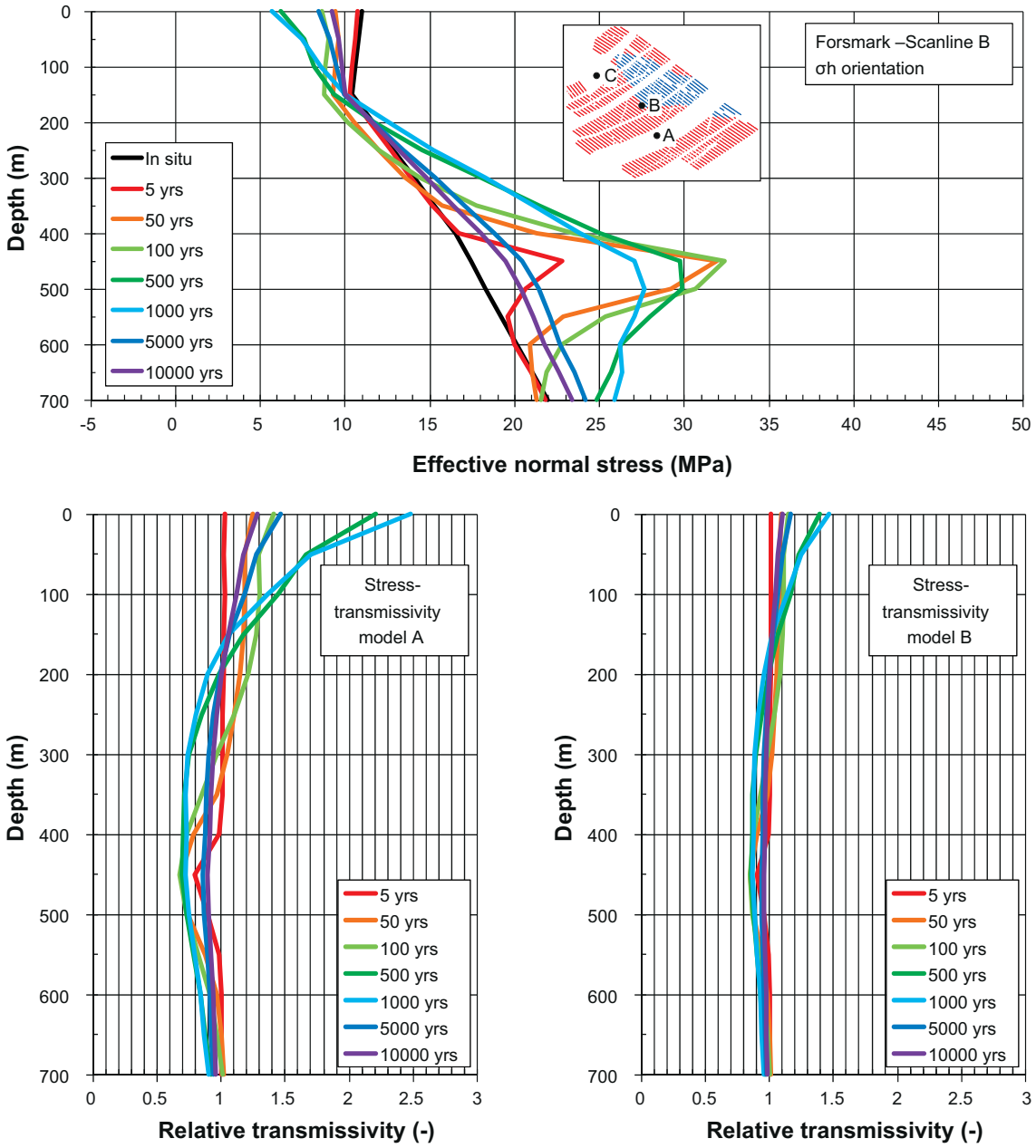

Figure 6-21. *Top: Effective stress as a function of depth along Scanline B in the direction of the present-day σh. Bottom: Relative transmissivity of vertical fractures striking perpendicular to the present-day σh.*

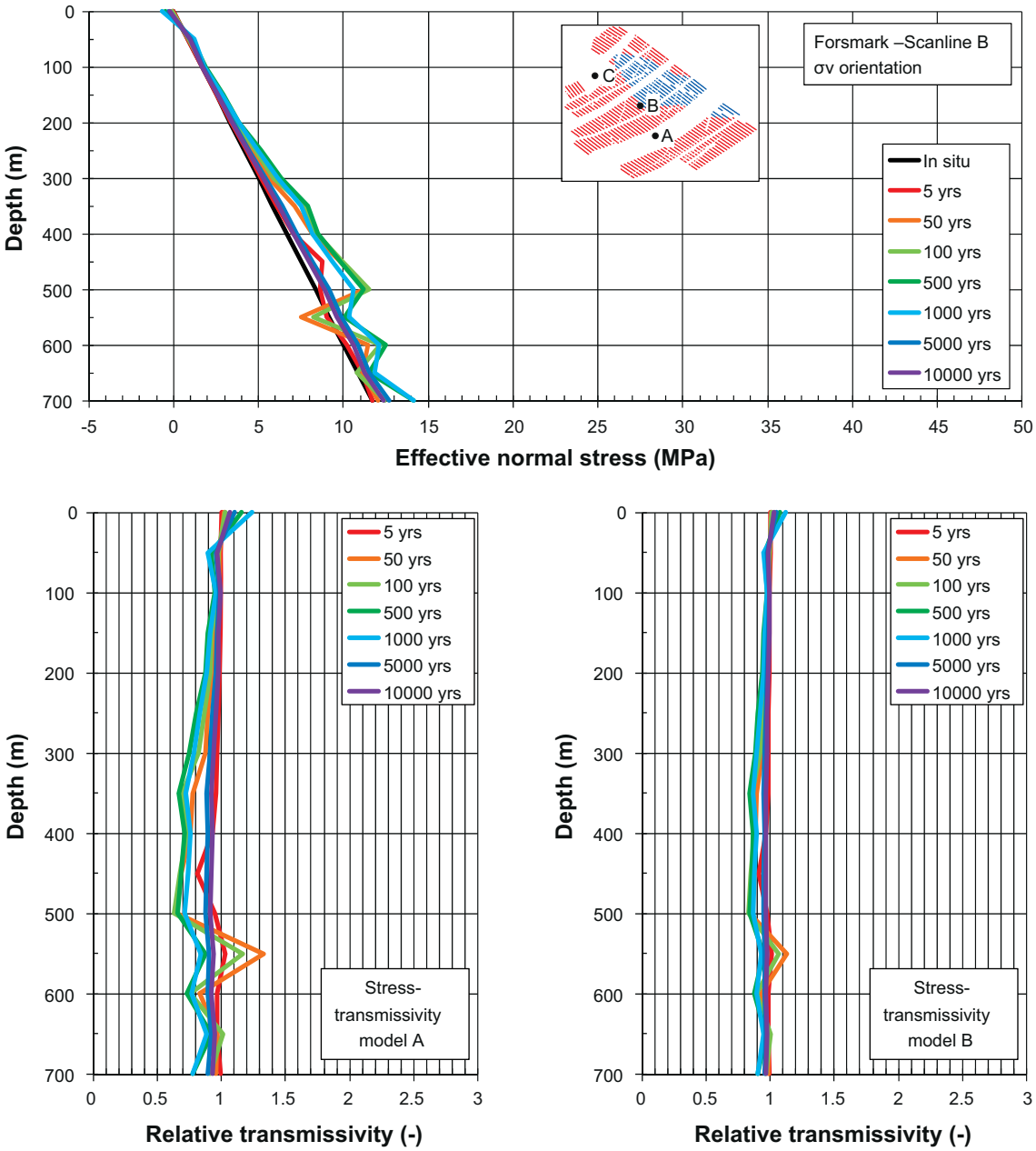

Figure 6-22. *Top: Effective stress as a function of depth along Scanline B in the direction of σv. Bottom: Relative transmissivity of horizontal fractures.*

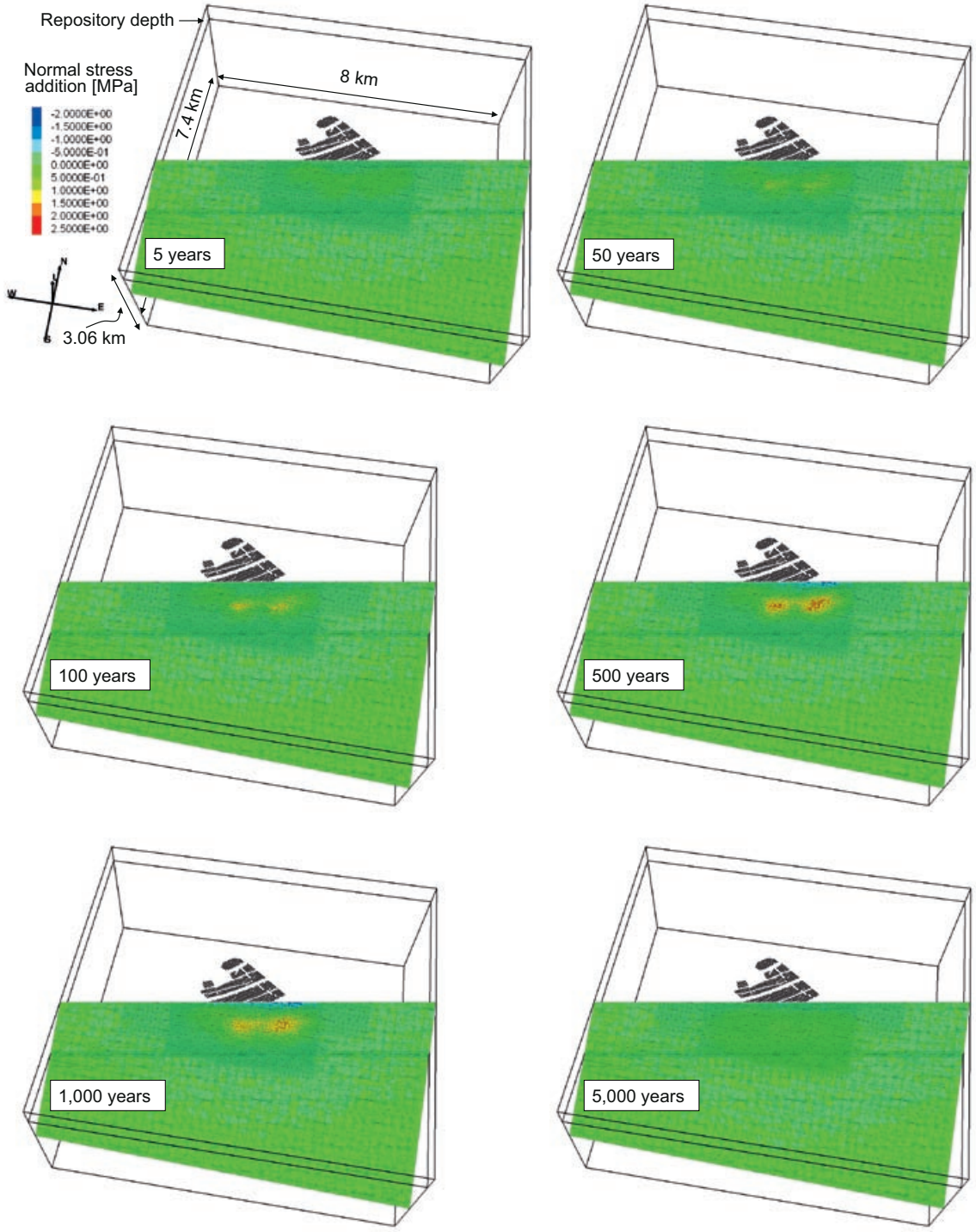

Figure 6-23. *Thermally induced normal stress addition at given points in time after deposition of the canisters, on a plane with the same orientation and approximate location in relation to the repository region as the fracture zone ZFMA2.*

6.8.2 Shearing

The thermally induced shear stresses are small compared with the total stress components (sum of thermal and *in situ* stress) in the directions of the *in situ* stresses. It is therefore assumed here that the principal stresses during the thermal phase have the same orientation as the *in situ* principal stresses.

Figure 6-25 and Figure 6-26 show the effective normal stress and factor of safety (cf. Equation 6-4) after 100 years at 450 m depth on Scanlines A and B, respectively. For comparison, the effective *in situ* normal stress and corresponding factor of safety at 450 m depth are presented in Figure 6-24.

The *in situ* effective normal stress associated with critically oriented fractures (*i.e.* dipping 27.1° along the major horizontal *in situ* stress) is about 13 MPa.

Fractures passing through non-heated parts of the repository region (Scanline A – Figure 6-25) are more unstable than those passing through the heated parts of the repository region (Scanline B – Figure 6-26).

On Scanline A (Figure 6-25, right), fractures dipping more than around 10–20° and less than around 35–50° are unstable irrespective of strike. The effective normal stress associated with the most unstable fracture orientations is about 11–12 MPa. On Scanline B (Figure 6-26, right) most fracture orientations become more stable as the rock is heated. Unstable fractures are dipping about 15–40° and striking 5–105° (or 185–285°) with respect to North, i.e. strike orientations approximately perpendicular to the major horizontal *in situ* stress. The effective normal stress associated with the most unstable fracture orientations is about 18 MPa.

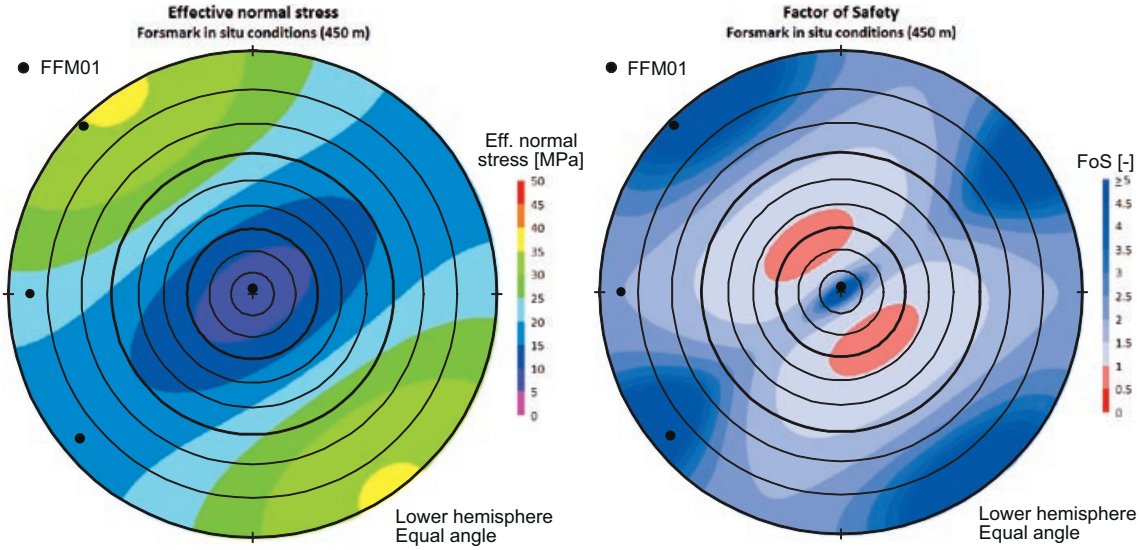

Figure 6-24. *Effective normal stress (left) and factor of safety (right) at 450 m for in situ conditions. Fracture pole orientations (global set) in fracture domain FFM01 (black circles) are compiled from Table 7-1 in /Fox et al. 2007/. Blue colours represent stability.*

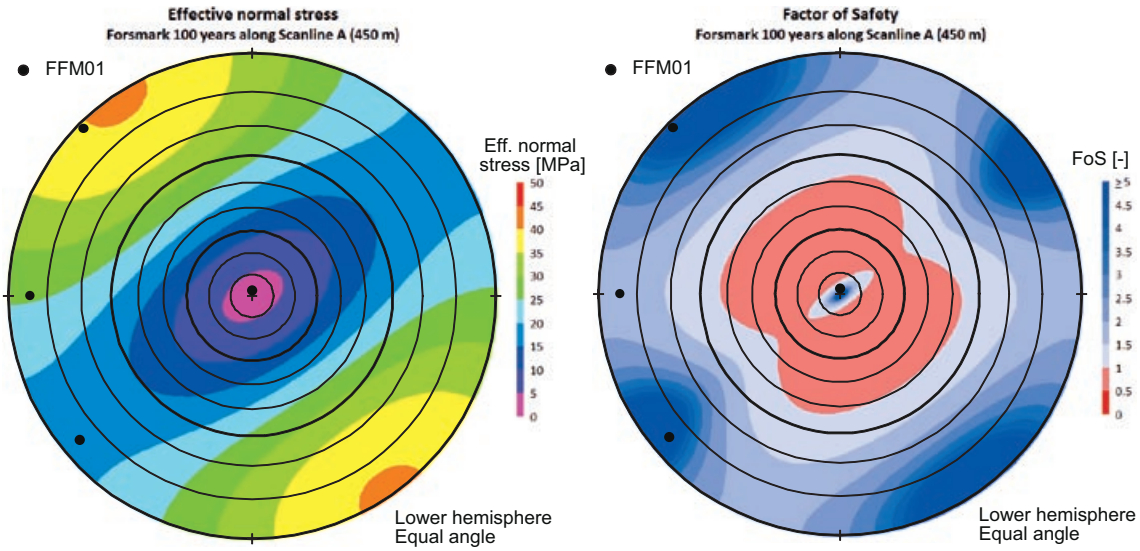

Figure 6-25. *Effective normal stress (left) and factor of safety (right) at 450 m depth along Scanline A after 100 years. Fracture pole orientations (global set) in fracture domain FFM01 (black circles) are compiled from Table 7-1 in /Fox et al. 2007/. Blue colours represent stability.*

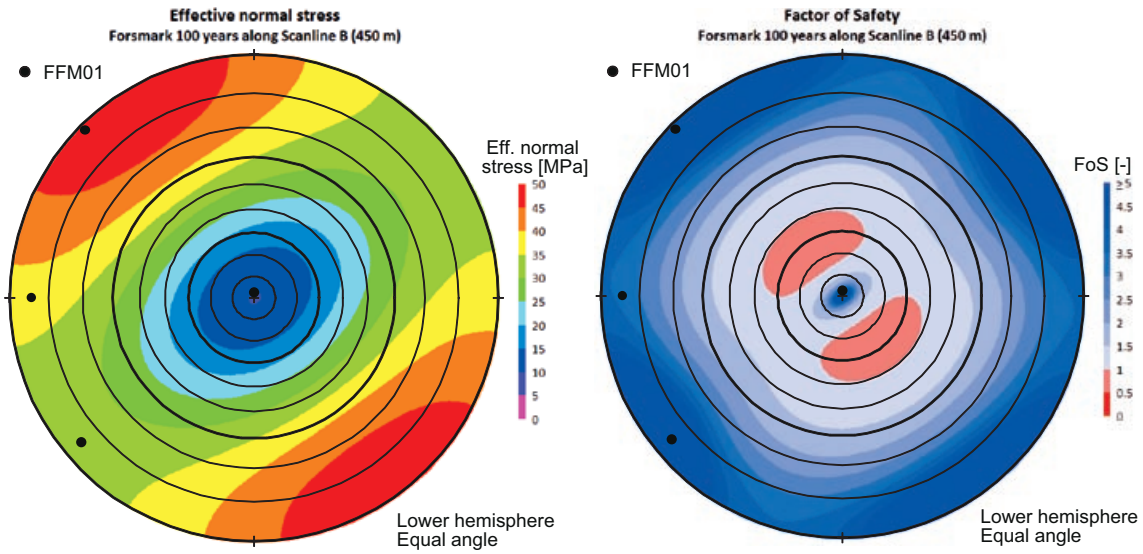

Figure 6-26. *Effective normal stress (left) and factor of safety (right) at 450 m depth along Scanline B after 100 years. Fracture pole orientations (global set) in fracture domain FFM01 (black circles) are compiled from Table 7-1 in /Fox et al. 2007/. Blue colours represent stability.*

The potential for and estimates of slip magnitudes are investigated at the following depths (see below) on Scanlines A (between deposition areas) and B (through a deposition area). A complete set of results is presented in Appendix E.

Scanline A

- 250 m. Point between the ground surface and repository level.
- 450 m. Increase in the major horizontal stress and reduction in the vertical stress.
- 600 m. Point beneath the repository

Scanline B

- 450 m. Increase in the major horizontal stress. Note that the deposition areas are located at depths between 450 m and 470 m. The influence of tunnels is examined in Chapter 8.

Estimates of slip magnitudes on optimally oriented fractures (dipping 27.1°) in the σ_H–σ_v-plane at different depths on Scanline A and Scanline B are presented in Figure 6-27 and Figure 6-28, respectively. This is the fracture orientation with the largest possible instability, given the Mohr-Coulomb fracture strength and the stress state, cf. Figure 4-6.

- Scanline A (between deposition areas): For a fracture with 150 m radius at 450 m depth, the maximum slip at the fracture centre is less than 27 mm, cf. Figure 6-27 (middle). Note that the stress acting on the fracture varies with depth, whereas in the analytical expression (Equation 6-1) the stress does not vary spatially. Therefore, the actual slip will be less. The slip on a similarly oriented fracture with the same radius would be around 6–7 mm at 250 m and 600 m depth, cf. Figure 6-27 (top and bottom).
- Scanline B (through a deposition area): For a fracture with 150 m radius at 450 m depth, the maximum slip would be around 6–7 mm according to the analytical expression, cf. Figure 6-28. Note that the actual slip will be less.

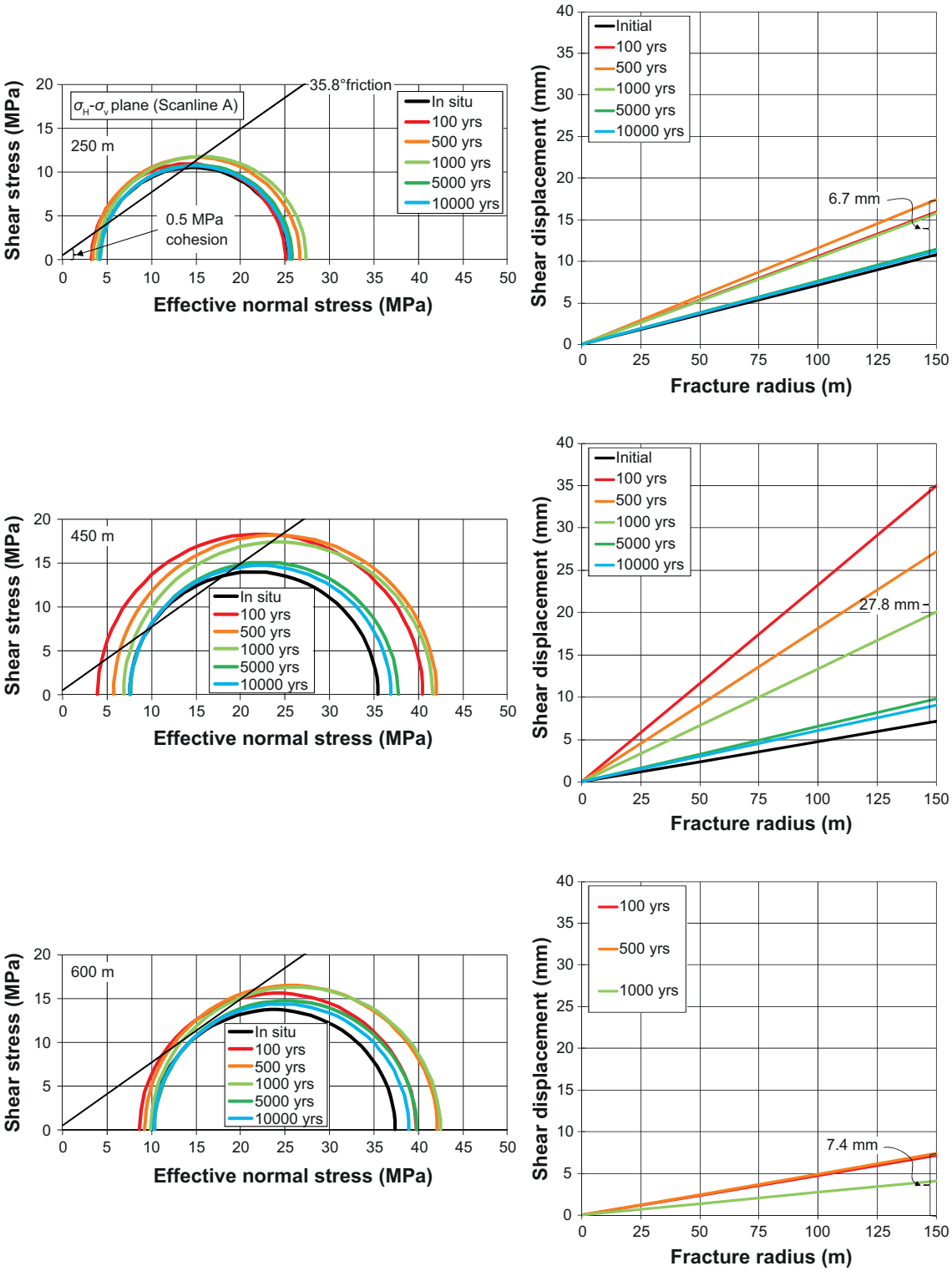

Figure 6-27. *Left column: Mohr circle representations of the stress state at given depths along Scanline A in the σH–σv-plane. Right column: Corresponding estimates of the maximum slip at the centre of a fracture dipping 27.1° from the horizontal plane.*

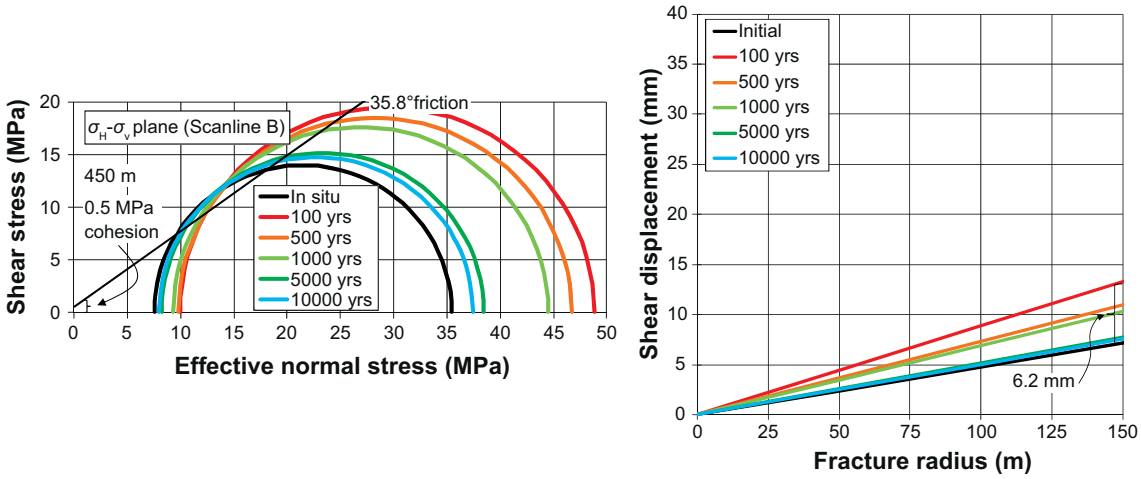

Figure 6-28. *Left column: Mohr circle representations of the stress state at given depths along Scanline B in the σH–σv-plane. Right column: Corresponding estimates of the maximum slip at the centre of a fracture dipping 27.1° from the horizontal plane.*

6.9 Summary

The results of this chapter are relevant for the large-scale thermo-hydro-mechanical evolution of the host rock at Forsmark during the heated period of the temperate phase. The large-scale calculations give deformations and stress changes. To assess the stability and the potential transmissivity effects on differently oriented fractures, the calculated stress increases were added to the *in situ* stresses specified in the **Data report**.

6.9.1 Stresses

Depending on position in relation to the heated deposition areas, the following general observations regarding the thermally induced stresses can be made.

- The horizontal stresses increase below a depth of 150–200 m (thermally induced increased compression).
- At shallow depths, there is a reduction in the horizontal stresses (thermally induced reduced compression). The most significant stress reductions are found directly above the heated deposition areas.
- The vertical stress increases along scanlines passing through the heated deposition areas.
- Outside and between deposition areas, particularly around repository depth, there is a reduction in vertical stress.

6.9.2 Displacements

The large scale analysis show the scope of the rock strain evolution within the heated areas. The maximum horizontal expansion is reached some 100 years after deposition and corresponds to strains between 0.005 and 0.008% along tunnels as well as across tunnels (cf. boundary displacements of boxes with 40 m side-lengths shown in Figure 6-14). The vertical strain is significantly higher, about 3 times, depending on the proximity to the free ground surface. After about 1,000 years, the rock has almost contracted back to the initial volume. The variation in strain is due to differences in the positions of the boxes being monitored, e.g. if they are located in central or peripheral parts of the heated repository. The expansion-contraction evolution of the different boxes calculated here is used to specify boundary conditions for the medium-scale and small-scale models analyzed in Chapter 8 and Chapter 9, respectively.

The heave of the ground surface is at maximum (about 70 mm) after about 1,000 years and returns back very slowly: after 10,000 years, the heave is still about 30 mm.

6.9.3 Fracture stability

The following can be concluded regarding the potential for fracture instability.

- The largest potential instability is found for fracture areas intersecting non-heated regions, cf. e.g. Figure 6-25. The instability is at maximum at the repository horizon, where fractures dipping less than around 40–50° irrespective of strike (except near-horizontal ones) are unstable, cf. Figure 6-25 (right). Estimating the maximum shear displacements (at the fracture centre) of an optimally oriented fracture from the analytical results shown in Figure 6-27, a 300 m diameter fracture with the most unfavourable orientation might slip at maximum by about 27 mm.
- Fractures intersecting the heated deposition areas are significantly more stable, cf. Figure 6-26 (right). A 300 m diameter fracture would slip around 6 mm, cf. Figure 6-28.

These results are obtained by use of analytical solutions using the numerically obtained stress results, assuming the fracture strength determined in laboratory-scale experiments to be valid for large fractures. The implications of this assumption are discussed in Chapter 10. The shear displacement results are given for 300 m diameter fractures, but can, at least in principle, be scaled to arbitrarily-sized fractures. The impact of the shear displacements on fracture transmissivities are discussed in the following section.

6.9.4 Transmissivity changes

Normal stress variations

A summary of the effective normal stress impact on the relative transmissivity during the temperate phase is provided by the following.

- **Vertical fractures striking perpendicular to the present-day *in situ* σ_H, i.e. striking 55° with respect to North:**
  - Insignificant transmissivity changes at all depths for fractures between or outside the deposition areas, regardless of stress-transmissivity model.
  - Transmissivity increase, at shallow depths, by at most a factor 1.5 for fractures above the heated deposition areas.
- **Vertical fractures striking perpendicular to the present-day *in situ* σ_h, i.e. striking 145° with respect to North:**
  - Unchanged or reduced transmissivities at all depths below 200 m.
  - Transmissivity increase, at shallow depths, by at most a factor 2.5 for fractures above the heated deposition areas. For fractures between or outside the deposition areas the effects are smaller.
- **Horizontal fractures:**
  - Transmissivity increase by a factor around 2 for parts of fracture that pass through, or within ±150 m, of non-heated regions of the repository horizon.
- **Gently dipping deformation zone ZFMA2:**
  - The normal stress contours shown in Figure 6-23 indicate that the transmissivity of this gently dipping zone will be reduced everywhere except for the near-surface parts.

All of the transmissivity estimates made above were obtained assuming the most sensitive stress-transmissivity model considered here: “Model A”, cf. Figure 4-9. “Model B”, which is based on mean values of the measured fracture normal stiffnesses, is more likely to be representative of the general response of the fracture system to stress changes. Since variations in normal stiffness and in sensitivity to stress changes are typically large within any fracture population /Fransson 2009/, there will probably be individual fractures, or parts of fractures, that would be even more sensitive to stress changes. For the purpose of this report, i.e. to provide conservative estimates of the change in relative transmissivity that is relevant to a majority of the fractures, the “Model A” results are judged to be adequate.

Shearing

The following can be concluded regarding transmissivity effects due to shearing.

- The largest potential instability is found for fracture areas intersecting non-heated regions, cf. e.g. Figure 6-25. These regions are, however, very small in comparison to the footprint of the repository. Because of the accompanying reduction of the normal stress (1–2 MPa compared with *in situ* conditions), the transmissivity is likely to increase. The effective normal stress is however still over about 5 MPa, i.e. larger than the normal stresses applied in the laboratory-scale shear box flow tests described by /Olsson 1998/ Therefore, the expected transmissivity increase is likely to be small.
- Fractures intersecting the heated deposition areas are significantly more stable, cf. Figure 6-26 (right). The slip movements are accompanied by a normal stress increase (around 5 MPa compared with *in situ* conditions), which means that the transmissivity might decrease rather than increase.
- Above and below the repository horizon, there are only marginal impacts on fracture stability.

7 Assessment of large-scale THM evolution: glacial phase

7.1 Introduction

The present study builds on the work by /Hökmark et al. 2006/ for the SR-Can safety assessment. In SR-Can, the representation of the glacial load was based on preliminary ice/crust/mantle calculations in 2D. Since then, the technique for performing this type of analyses has been developed significantly, and now includes 3D representations of the crust/mantle-system and variations of the lithosphere stiffness /Lund et al. 2009/, cf. Sections 2.6 and 4.8. An additional factor, not considered by /Lund et al. 2009/, is that the temperature reduction of the rock mass during permafrost will reduce the horizontal stresses.

The magnitude of the glacially induced pore pressure is of great importance for stress induced transmissivity changes (e.g. Figure 4-9) (or hydraulic jacking /Lönnqvist and Hökmark 2010/) and stability of fractures (e.g. Figure 7-1). /Hökmark et al. 2006/ made two assumptions regarding the excess pore pressure during glacial maxima and as the ice margin was passing. The excess pore pressure was either assumed to be zero during the entire glacial cycle or schematically assumed to be 90% of the maximum mechanical load during glacial maxima and 25% of the maximum mechanical load as the ice margin was passing. The schematic percentages assumed by /Hökmark et al. 2006/ may not be conservative enough during glacial maxima and overly conservative during the retreat phase. It is often assumed that the hydrostatic pressure at the boundary between ice and rock is about 90% of the thickness of the ice /e.g. Grasby and Chen 2005, Moeller et al. 2007, Bense and Person 2008/, i.e. about 98% of the mechanical load. For high values of the hydraulic diffusivity or long durations of ice cover, it can be shown that the excess pore pressure is approximately equal to the boundary pressure /e.g. Lönnqvist and Hökmark 2010/. Furthermore, for the ice load assumed here (cf. Figure 4-12), assuming 25% of the maximum ice load as the ice margin is passing would result in a residual pore pressure sufficiently high to initiate hydraulic jacking of horizontal fractures at depths of nearly 400 m. /Lönnqvist and Hökmark 2010/ showed that the maximum jacking depth during the retreat phase was around 100 m, cf. also Section 7.6.

The discussion above points to the need for a revised pore pressure model during the glacial cycle. Results regarding pore pressure from the study on hydraulic jacking /Lönnqvist and Hökmark 2010/ and specific analyses conducted for the purpose of this report are provided in Appendix D.

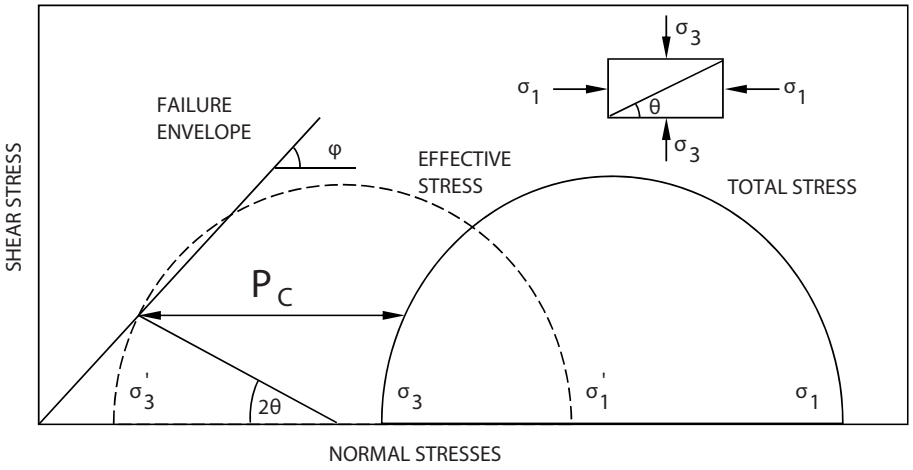

Figure 7-1. *Influence of fluid pressure P_C on conditions for shear failure on the plane θ.*

The main objectives are as follows.

- Estimate effective stresses and accompanying transmissivity impacts at different depths during the glacial cycle.
- Estimate the potential for shearing at different depths and magnitude of the shear displacement of optimally oriented fractures.
- Assess the potential for hydraulic jacking at different depths during different phases of the glacial cycle /Lönnqvist and Hökmark 2010/.

To accomplish this, the following additional objectives are required:

- Estimate the glacially induced pore pressure at different depths during the glacial cycle, cf. Appendix D.
- Estimate the thermo-mechanical effects at different depths due to the temperature reduction during permafrost conditions.

7.2 Description of modelling approach

Similarly to the study by /Hökmark et al. 2006/ for the SR-Can safety assessment, no coupled THM or HM analyses are performed. The approach is described in the following subsections.

7.2.1 Estimates of stress induced transmissivity changes

In the same way as in the large-scale modelling for the temperate phase (Chapter 6), fractures are not modelled explicitly. Instead, stress-induced transmissivity changes are evaluated on hypothetical fracture planes with orientations perpendicular to the present-day *in situ* stress components, *i.e.* vertical or horizontal planes.

Two stress-transmissivity models (A and B) are selected to estimate changes in relative transmissivity due to normal stress variations, cf. Figure 4-9. Model A can be considered a "worst case" option based on lower bound fracture normal stiffness estimates and is therefore particularly sensitive to normal stress variations. Model B is based on average fracture normal stiffness estimates and is less sensitive to variations in normal stress. Both models are, however, more sensitive to normal stress variations than the most conservative *in situ* correlation reported for Forsmark by /Follin et al. 2008/.

7.2.2 Hydraulic shearing

Similarly to the temperate phase, slip estimates are here assessed on optimally oriented fractures by use of the analytical solution, described in subsection 6.3.3, for the shear displacement at the centre of a circular fracture, cf. Equation 6-1. It should be reiterated that this expression gives only an approximation as in reality there is a variation in stress along the fracture.

During the temperate phase, the potential for slip is related to variations in thermally induced stresses without changes in pore pressure. However, during the glacial phase variations in both stresses and pore pressures have to be considered. Using the linear Mohr-Coulomb shear strength criterion, Equation 6-3, the critical fluid pressure, P_C, required to induce failure (see Figure 7-1) can be expressed as

$$P_C = \sigma_n - \frac{\tau - c}{\tan(\varphi)}, \qquad \text{Eq. 7-1}$$

where σ_n is the normal stress, τ is the shear stress, φ is the total friction angle and c is cohesion. An example of the influence of pore pressure on shear displacements of differently oriented fractures at repository depth in Forsmark is shown in Figure 7-2. Given that the hydrostatic pore pressure is about 4.5 MPa, optimally oriented fractures are would already be in a state of frictional failure, whereas less critically oriented fractures would not slip until the pore pressure is increased by a few MPa. In the following sections, only shear displacement in addition to those that have occurred in the past are evaluated.

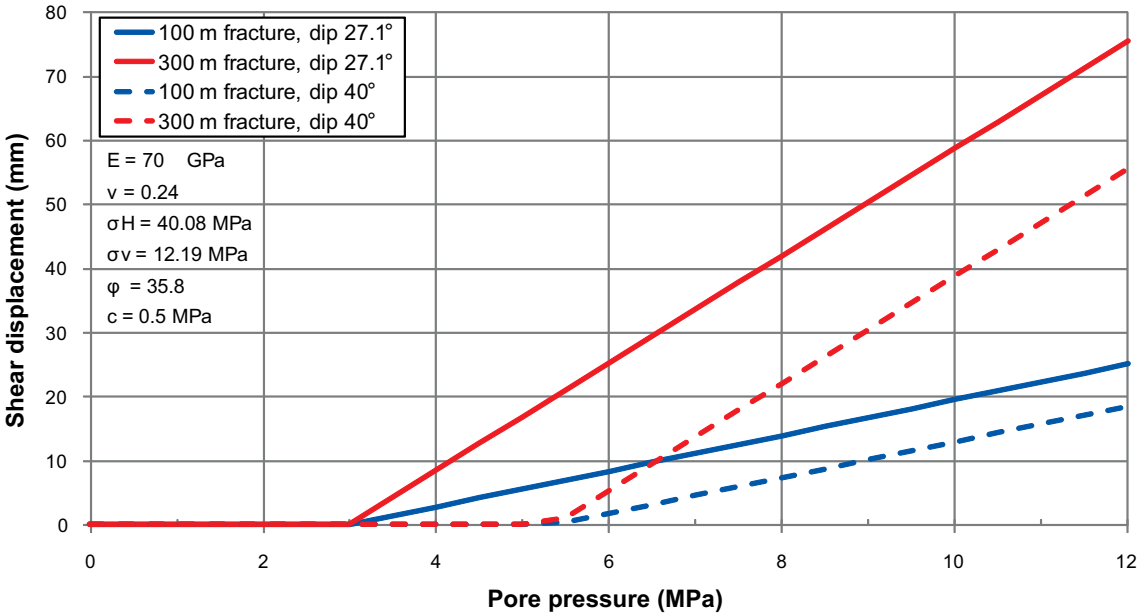

Figure 7-2. *Example of the influence of pore pressure on shear displacements of a fracture dipping 27.1° along the major principal stress.*

7.3 Glacially induced stresses and pore pressure

7.3.1 Temporal evolution of glacial stresses

Figure 7-3 (left) shows the temporal evolution of the glacially induced stresses at 500 m depth at Forsmark in the directions of the present-day *in situ* stresses. As there are only marginal variations in the glacially induced stresses in the upper 1.5 km of the rock (cf. Section 6.4 in the **Data report**), the glacial stresses obtained at 500 m are used at all depths and added to the *in situ* stresses, cf. Figure 7-3 (right).

Five points in time during the glacial cycle, cf. Figure 7-3 (left), are selected for further investigation. These correspond to present-day conditions (*in situ*), the first glacial maximum (12 ka), the ice margin retreating over the site (15 ka), stress reductions due to the forebulge (39 ka), the second glacial maximum (54.5 ka) and the ice margin retreating over the site (58 ka).

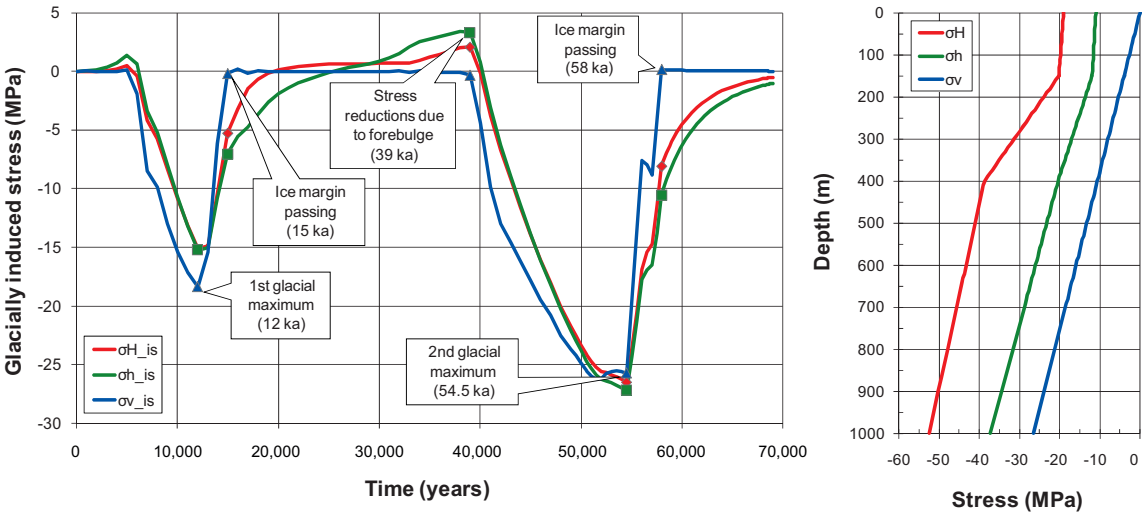

Figure 7-3. *Left: Glacially induced stress components in the orientations of the present-day in situ stresses (cf. Figure 4-12, Figure 4-13 and Section 6.4 in the **Data report**). Plot symbols mark the points in time used in the modelling work. Right: Present-day in situ stresses (Table 4-1) as functions of depth.*

7.3.2 Glacially induced pore pressure

Based on the modelling results provided in Appendix D, the following glacially induced pore pressure model at the different points in time indicated in Figure 7-3 is proposed for the Forsmark site, cf. Figure 7-4.

1. The excess pore pressure is 98% of the glacially induced vertical load (Figure 4-13) at all times and at all depths. This approach will result in a conservative estimate of the pore pressure during times of ice cover, but underestimate the pore pressure as the ice front is retreating or in combination with proglacial permafrost, cf. e.g. Figure D-2.
2. An alternative pore pressure model (denoted (alt.) in Figure 7-4), which takes additional residual or permafrost-induced excess pore pressures into account:
   - As the ice sheet covers the site, i.e. at 12 ka and 54.5 ka, the excess pore pressure is 98% of the glacially induced vertical load at all depths, i.e. the same as described above.
   - The residual pore pressure is $(2/3)\cdot z/450$ MPa ($z \leq 450$ m) and $(2/3)\cdot(3\cdot z/275–43/11)$ MPa ($z > 450$ m) during the first episode of frontal retreat (15 ka).
   - The excess pore pressure during the advancement of the ice front in combination with proglacial permafrost is 3.3 MPa at all depths (39 ka).
   - The residual pore pressure is $z/450$ MPa ($z \leq 450$ m) and $3\cdot z/275–43/11$ MPa ($z > 450$ m) during the second episode of frontal retreat (58 ka).

7.3.3 Thermo-mechanical effects during permafrost conditions

Similarly to the temperate phase (cf. Chapter 6), the temperature changes introduced during permafrost conditions (cf. Figure 4-14) will alter the stresses in the rock mass. Figure 7-5 (left) shows the temperature reduction (compared with present-day conditions) at the time of greatest temperature reduction /Hartikainen et al. 2010/. The modelled rock mass is represented in *3DEC* by a linear elastic rectangular block with dimensions 5 km×5 km×5 km. An outline of the model is shown in Figure 7-5 (right).

In the model, mean values of the thermo-mechanical properties in rock domain RFM029 and fracture domain FFM01 are used throughout the modelled domain, cf. Table 4-5. However, as opposed to the temperate phase described in Chapter 6, the temperature reduction during permafrost conditions affects much larger volumes of the rock mass meaning that thermo-mechanical properties on a

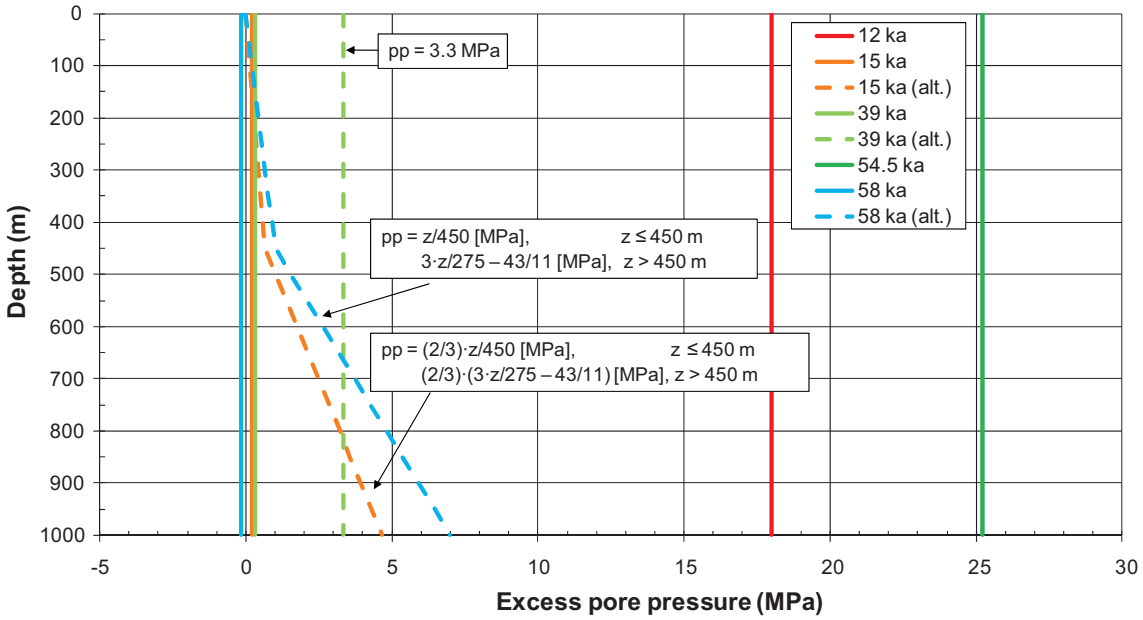

Figure 7-4. *Glacially induced pore pressure model for Forsmark, cf. Appendix D.*

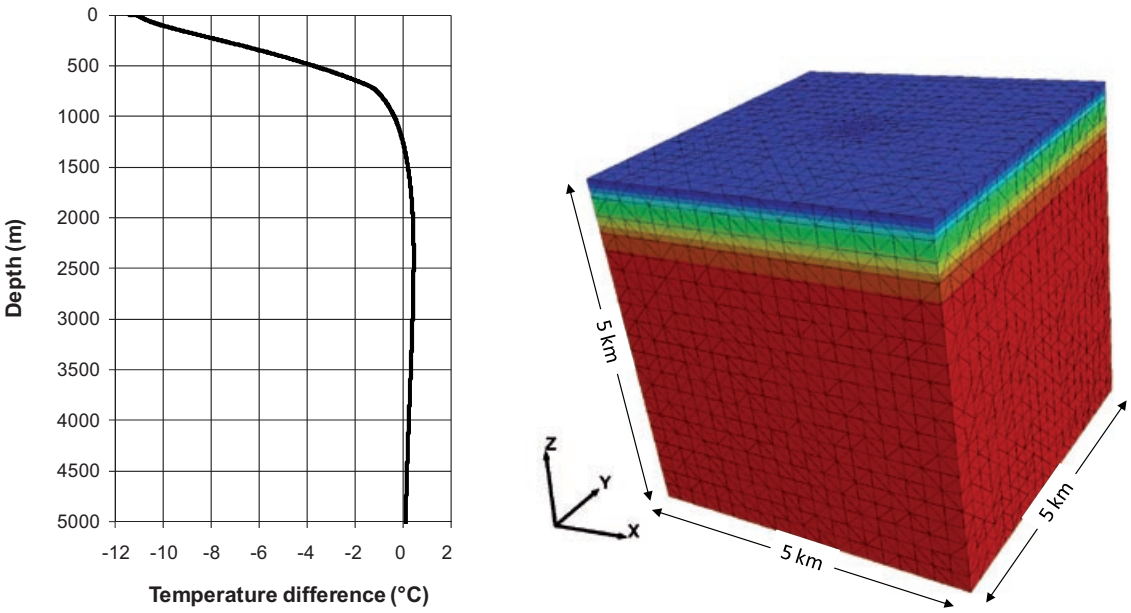

Figure 7-5. *Left: Temperature reduction as a function of depth, cf. Figure 4-14. Right: Permafrost model outline.*

larger scale have to be considered, i.e. accounting for surrounding rock with lower stiffness and the presence of deformation zones, which will effectively reduce the deformation modulus of the rock mass. Based on the work by /Mas Ivars and Hakami 2005, Hakami 2006, Glamheden et al. 2007b/, which give values of the rock mass deformation modulus in the range 40–45 GPa, the results from the present modelling work are scaled to an effective deformation modulus of 40 GPa. Figure 7-6 shows the resulting stress reduction as a function of depth.

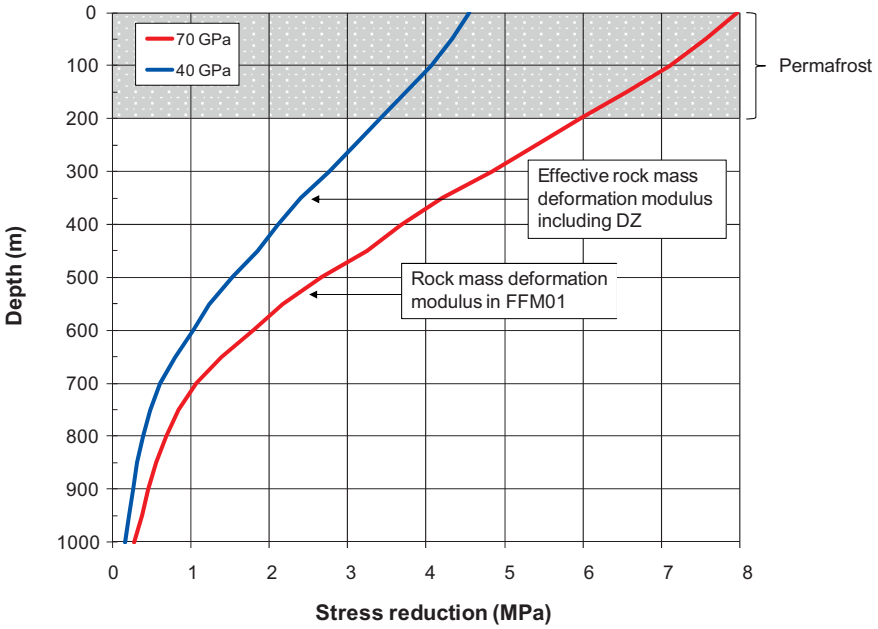

Figure 7-6. *Stress reduction during permafrost conditions. The red line is the calculation result. The blue line, which is used in the subsequent analyses, shows the results scaled to relevant large-scale elastic properties.*

7.4 Transmissivity changes

The results are sensitive to assumptions regarding the magnitude of glacially induced pore pressures. Two cases are considered (cf. Figure 7-4): 1) the excess pore pressure is 98% of the glacially induced mechanical load at all times (i.e. approximately zero as the ice margin passes over the site at 15 and 58 kyr) and 2) assuming transient changes in pore pressure as the ice margin is passing over the site (15 and 58 kyr) and in combination with proglacial permafrost (39 kyr). In addition to variations in pore pressure, thermo-mechanical effects due to permafrost (Figure 7-6, blue curve) are also considered. The following is found.

- **Vertical fractures striking perpendicular to the present-day major horizontal *in situ* stress (σ_H), i.e. striking 55° with respect to North.**
  - *Pore pressure assumptions, cf. Figure 7-7.* The effective normal stress is reduced compared with *in situ* stress levels during the first glacial maximum (12 ka) and during the forebulge (39 ka). As the ice margin is passing over the site (15 and 58 ka) and during the second glacial maximum (54.5 ka), the effective normal stress increases. These changes in effective normal stresses result in only negligible variations in relative transmissivity.
  - *Thermo-mechanical effects, cf. Figure 7-8:* The additional effective stress reduction during permafrost conditions result in only negligible variations in relative transmissivity below a depth of around 300 m.
- **Vertical fractures striking perpendicular to the present-day minor horizontal *in situ* stress (σ_h), i.e. striking 145° with respect to North**.
  - *Pore pressure assumptions, cf. Figure 7-9.* The effective normal stress is reduced during the first glacial maximum (12 ka) and during the forebulge (39 ka) and increased as the ice margin passes (15 and 58 ka) and during the second glacial maximum (54.5 ka). The maximum increase in relative transmissivity occurs during the forebulge (39 ka) when the relative transmissivity is increased by a factor around 2 (model A) and by a factor around 1.3 (model B) in the upper 150 m. At repository depth and below, the increase in relative transmissivity is a factor around 1.3 or less. As the ice passes (15 and 58 ka), the normal stresses are sufficiently high that an increase in residual pore pressure does not affect the relative transmissivity values in any significant way. During the forebulge in combination with proglacial permafrost (39 ka), the increase in pore pressure results in an increase in relative transmissivity by a factor of 2–3 (model A) and 1.3–1.6 (model B) in the upper 400 m of the rock. At repository level (460 m), the relative transmissivity is increased by at most a factor 1.8 (model A).
  - *Thermo-mechanical effects, cf. Figure 7-10:* The additional effective stress reduction during permafrost conditions, result in an increase in relative transmissivity by a factor 3–7.5 (model A) and 1.5–2.5 (model B). At repository level, the relative transmissivity is increase by a factor around 2.5 (model A) and 1.5 (model B).
- **Horizontal fractures, cf. Figure 7-11:** The effective vertical stress is unaffected or marginally increased at all times and at all depths when residual/transient pore pressures are not considered, resulting in only negligible variations in the relative transmissivity. As the ice front is retreating (15 and 58 ka), the maximum increase in relative transmissivity is in the range 1.5–2.1 (model A). For model B the maximum increase is less than a factor 1.4 at all depths. In combination with proglacial permafrost (39 ka), the maximum increase in relative transmissivity is a factor 2.3 directly below the permafrost and decreases with depth (model A). For model B the maximum increase is less than a factor 1.5 at all depths.

The largest variations in relative transmissivity appear to coincide with the time of the forebulge in combination with proglacial permafrost (39 ka) and are found near the ground surface where the *in situ* stresses are low, cf. Figure 7-9 and Figure 7-11.

The relative transmissivity of all fracture orientations are evaluated at two depths: 250 m and repository depth (460 m), cf. Figure 7-12 and Figure 7-13, respectively. After 39 ka (with permafrost conditions), the relative transmissivity increases for all fracture orientations – although only marginally for steeply dipping fractures oriented approximately perpendicular to the major horizontal *in situ* stress. The largest increase in relative transmissivity at 250 m depth is a factor around 3–3.5 and at 460 m depth a factor around 2–2.5. If thermo-mechanical effects due to the permafrost are also included, the largest increase in relative transmissivity at 250 m is a factor 6.5–7 for steeply dipping fractures oriented approximately perpendicular to the minor horizontal *in situ* stress. The corresponding result for 460 m depth is a maximum increase in relative transmissivity by a factor 2.5–3.

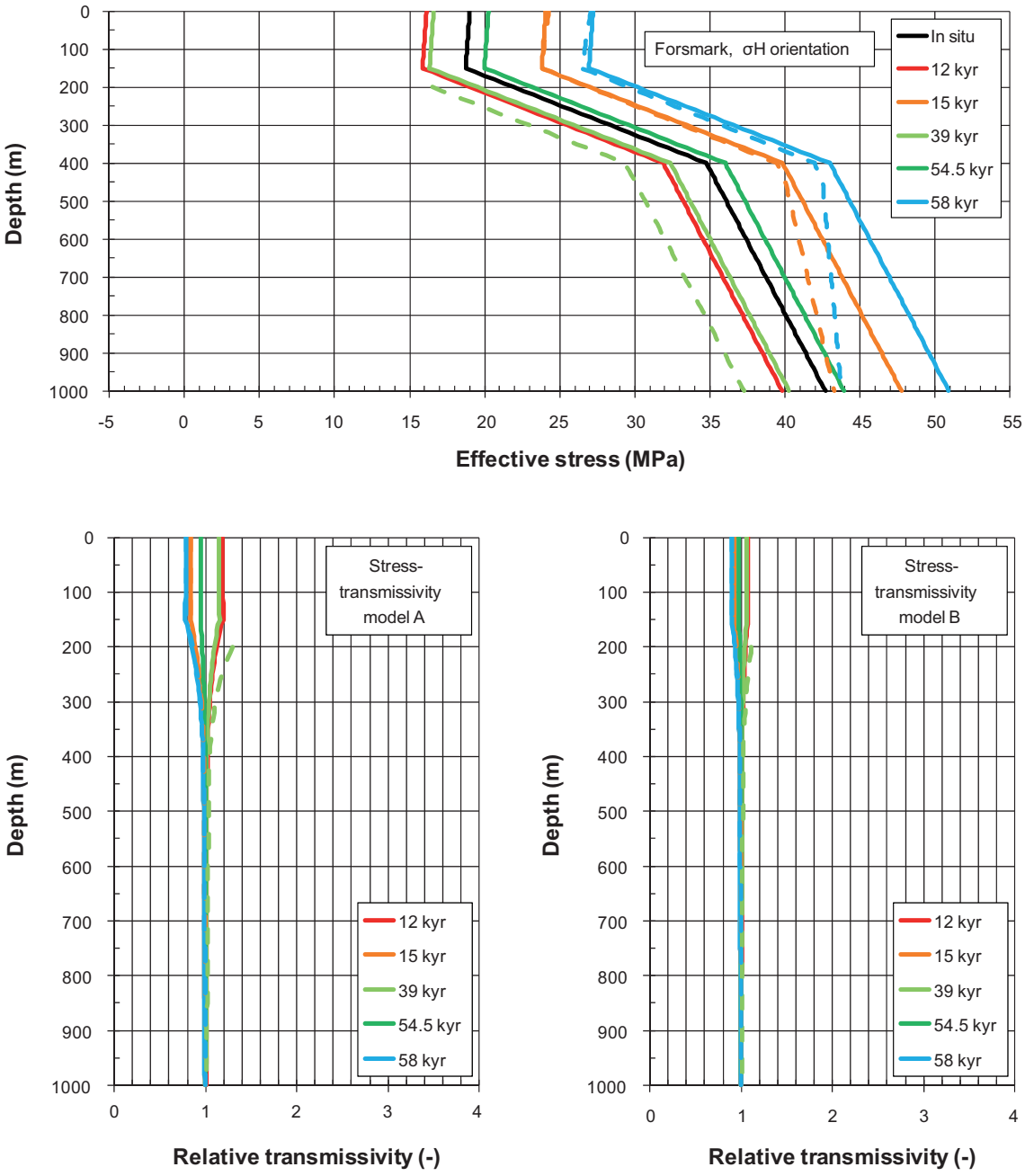

Figure 7-7. *Top: Effective stress as a function of depth in the direction of the present-day σH. Bottom: Relative transmissivity of vertical fractures striking perpendicular to the present-day σH. Effects due to residual pore pressures are marked with dashed lines.*

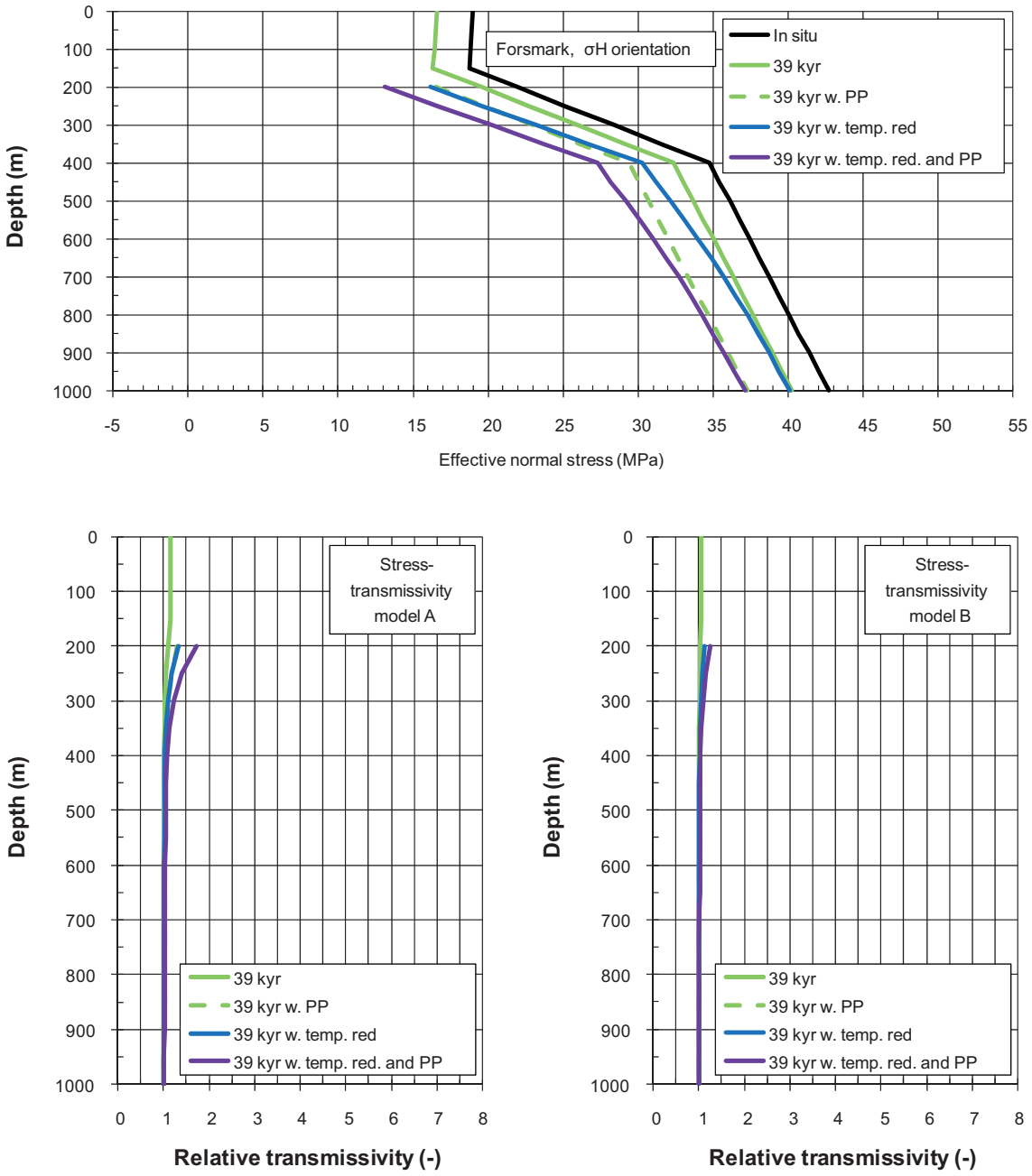

Figure 7-8. *Top: Effective stress as functions of depth in the direction of the present-day σH during the forebulge without permafrost (39 kyr) and with permafrost conditions here represented by increased pore pressure (green dashed line), temperature reduction only (blue line, cf. Figure 7-6) and temperature reduction in combination with increased pore pressure (purple line). Note that the black and green curves are the same as in the previous figure. Bottom: Relative transmissivity of vertical fractures striking perpendicular to the present-day σH.*

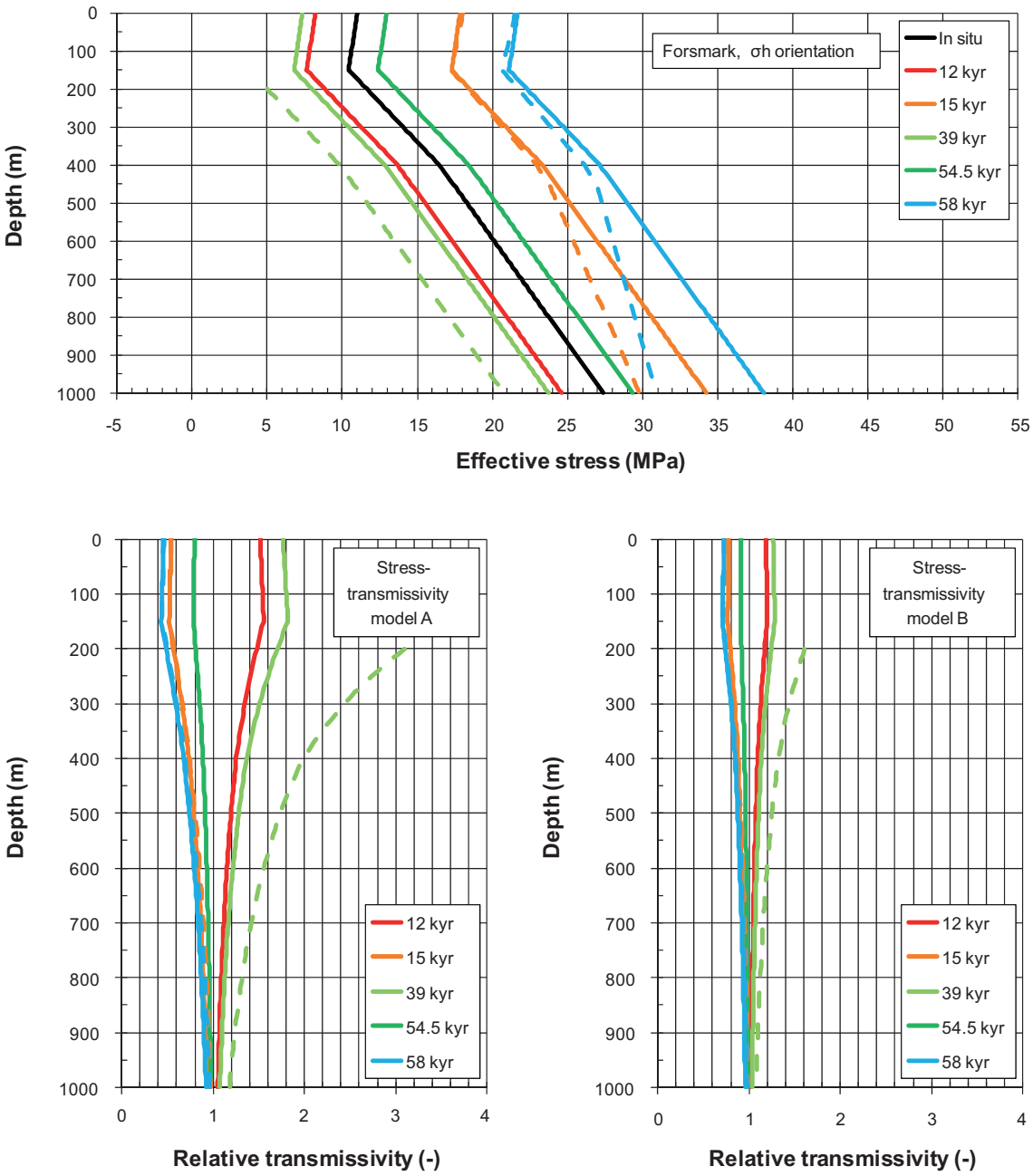

Figure 7-9. *Top: Effective stress as a function of depth in the direction of the present-day σh. Bottom: Relative transmissivity of vertical fractures striking perpendicular to the present-day σh. Effects due to residual pore pressures are marked with dashed lines.*

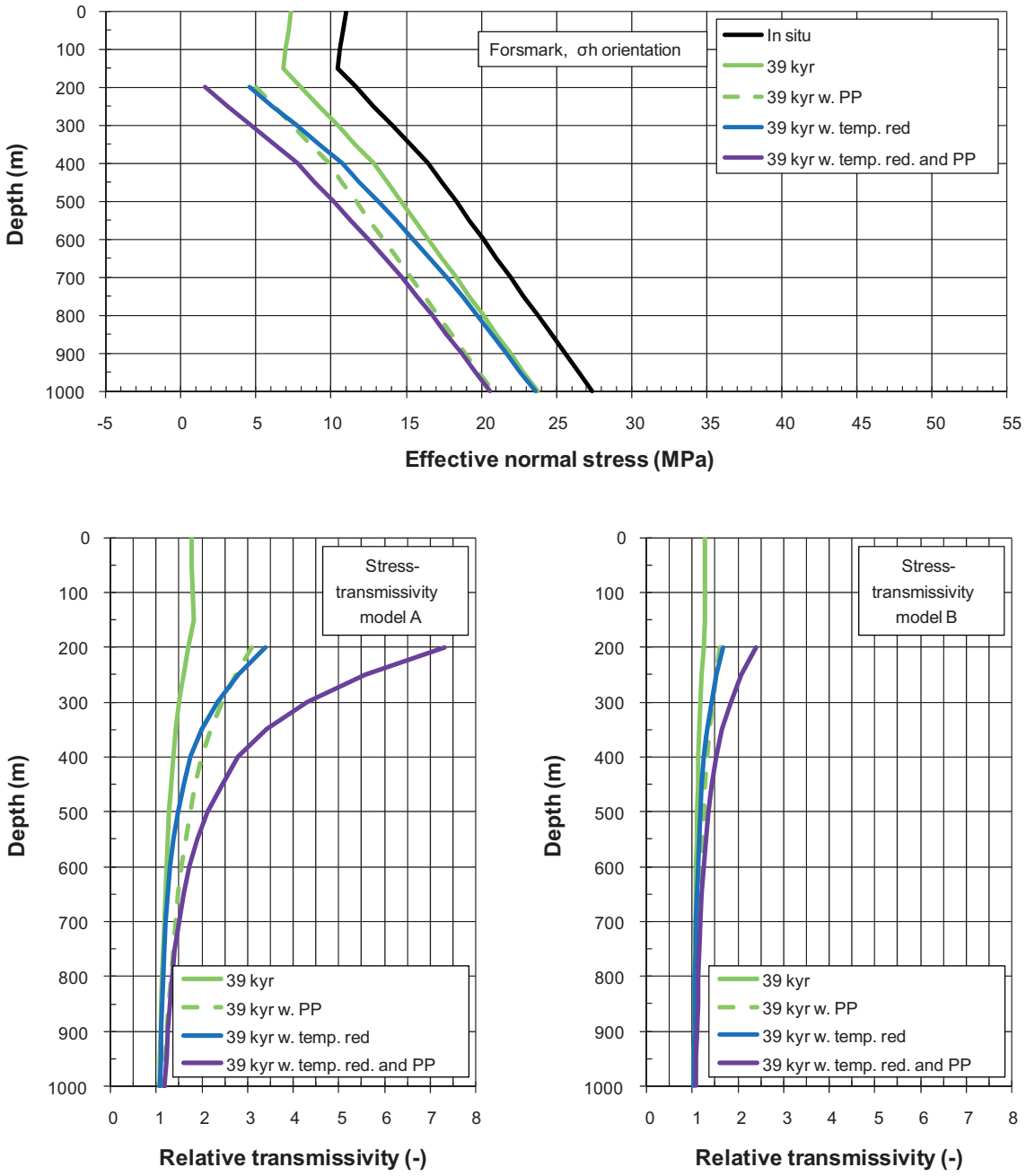

Figure 7-10. *Top: Effective stress as functions of depth in the direction of the present-day σh during the forebulge without permafrost (39 kyr) and with permafrost conditions here represented by increased pore pressure (green dashed line), temperature reduction only (blue line, cf. Figure 7-6) and temperature reduction in combination with increased pore pressure (purple line). Note that the black and green curves are the same as in the previous figure. Bottom: Relative transmissivity of vertical fractures striking perpendicular to the present-day σh.*

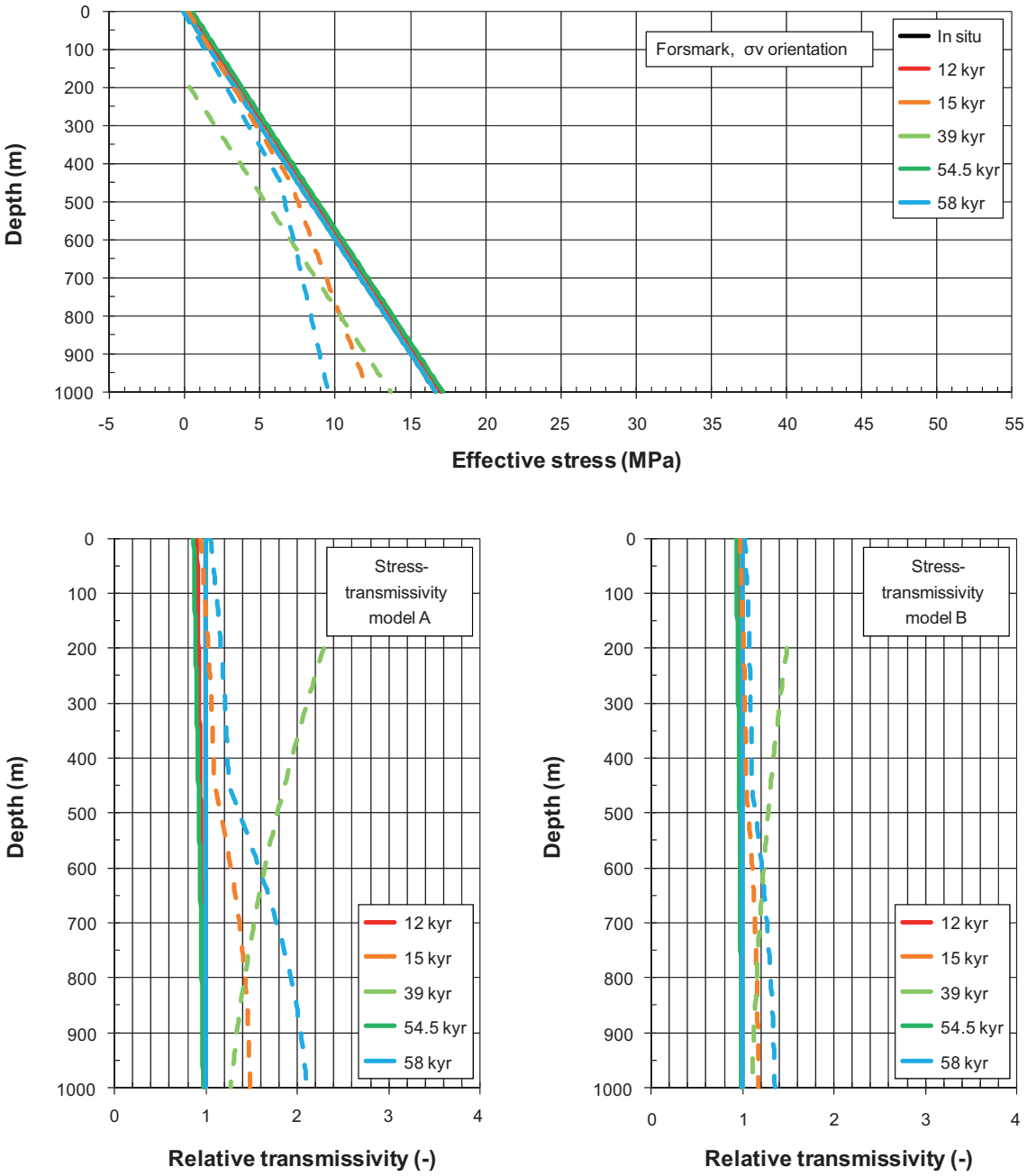

Figure 7-11. *Top: Effective stress as a function of depth in the direction of σv. Bottom: Relative transmissivity of horizontal fractures. Effects due to residual pore pressures are marked with dashed lines.*

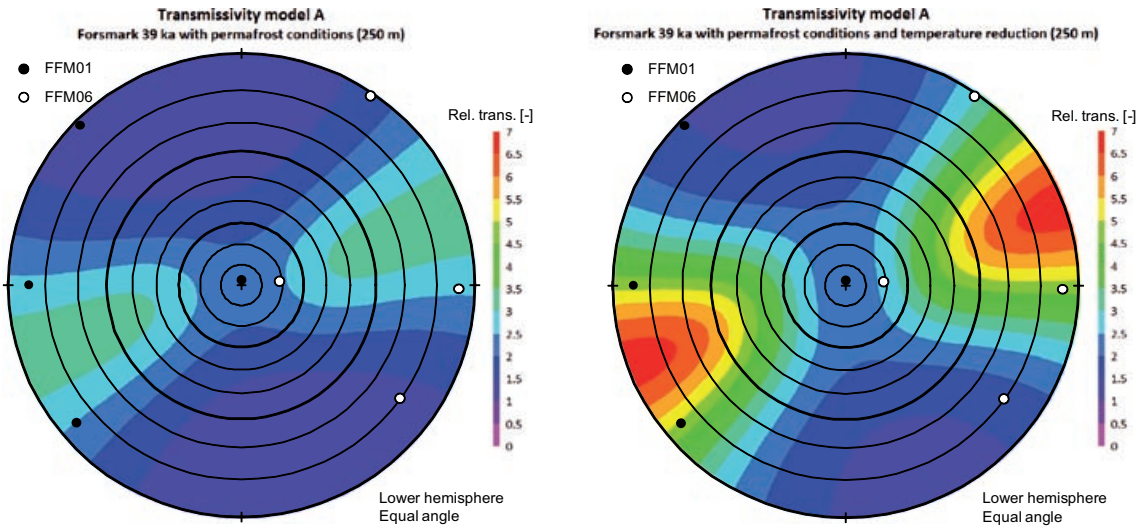

Figure 7-12. *Relative transmissivity at 250 m depth after 39 ka with permafrost conditions (left) and 39 ka with permafrost conditions and temperature reduction (right). Fracture pole orientations (global set) in fracture domains FFM01 (black circles) and FFM06 (white circles) are compiled from Table 7-1 in /Fox et al. 2007/.*

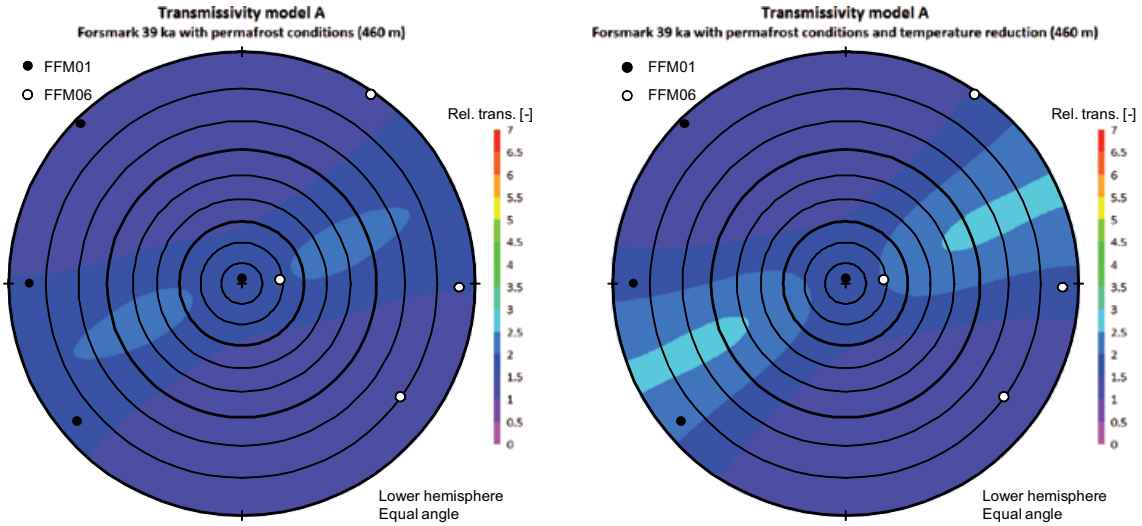

Figure 7-13. *Relative transmissivity at 460 m depth after 39 ka with permafrost conditions (left) and 39 ka with permafrost conditions and temperature reduction (right). Fracture pole orientations (global set) in fracture domains FFM01 (black circles) and FFM06 (white circles) are compiled from Table 7-1 in /Fox et al. 2007/.*

7.5 Shearing under hydro-mechanical load

Estimates of the maximum shear displacement are made on fractures striking perpendicular to the major horizontal *in situ* stress and dipping 27.1°. This is the fracture orientation with the largest possible instability, given the Mohr-Coulomb fracture strength and the stress state, cf. Figure 4-6. Similarly to the analyses conducted for the temperate phase in Chapter 6, the small differences in the mean value elastic properties of the rock mass in fracture domains FFM01 and FFM06 do not warrant a differentiation in material properties between the domains. Here, the elastic properties of the rock mass in Fracture domain FFM01 are used, cf. Table 4-5.

Figure 7-14 shows the temporal evolution of the total principal stresses and the orientation of the major principal stress at repository depth (460 m) during the glacial phase at Forsmark. The orientation of the major horizontal principal stress is in the range 138–153° with respect to North.

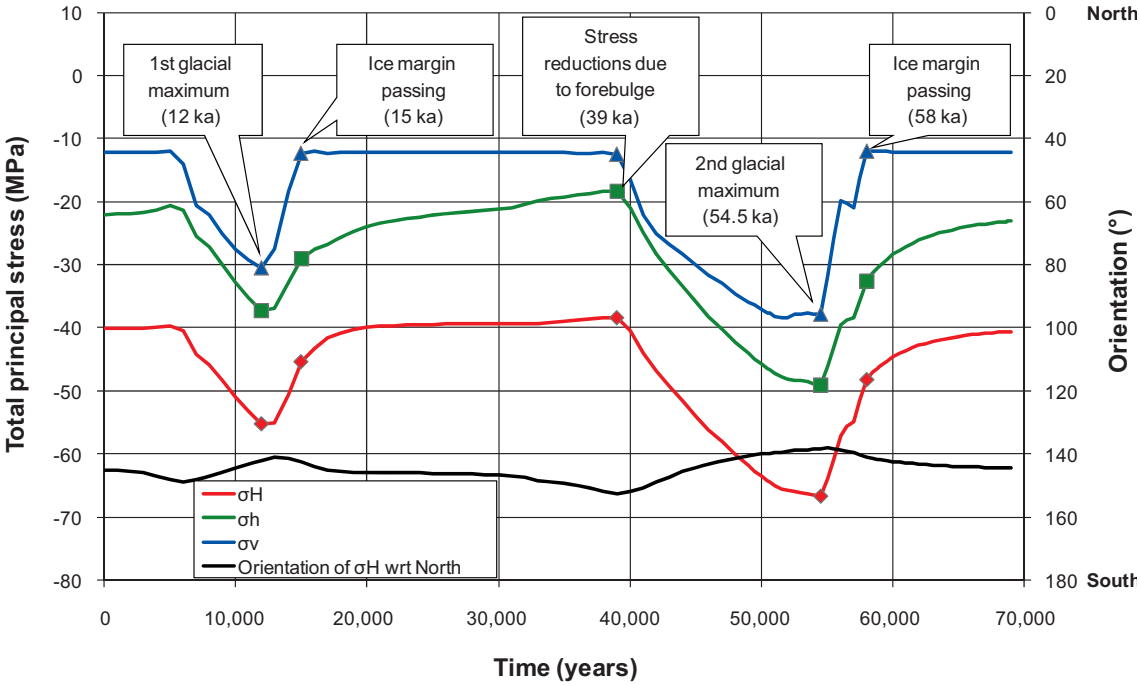

Figure 7-14. *Total principal stresses at repository depth (460 m) during the glacial phase at Forsmark and the orientation of the major horizontal stress with respect to North, cf. Sections 4.4 and 4.8.*

Figure 7-15 shows Mohr-circle representations of the state of stress, at repository level, at the times marked with plot symbols in Figure 7-14: Present-day conditions (*in situ*), first glacial maximum (12 ka), ice margin passing (15 ka), stress reductions due to forebulge (39 ka), second glacial maximum (54.5 ka) and ice margin passing (58 ka). Additional results that include thermo-mechanical effects due to the temperature reduction during permafrost conditions are presented in Figure 7-16. As seen in the two figures, the points in time associated with the largest potential fracture instabilities are the two glacial retreats (15 and 58 ka) and the forebulge in combination with proglacial permafrost (39 ka). Note that the orientation of the major horizontal principal stress (σ_H) varies with time, cf. Figure 7-14.

Figure 7-17 (left column) shows the effective normal stress at repository depth (460 m) during the forebulge (39 ka) in combination with proglacial permafrost (here represented by an increase in pore pressure by about 3.3 MPa, top) and considering thermo-mechanical effects (bottom). Note that at 39 ka (without considering permafrost conditions), all orientations are either stable or more stable than under *in situ* conditions. The right column of the figure shows the corresponding shear displacement at the centre of a circular fracture with a radius of 100 m. The maximum shear displacement is less than 9 mm for all fracture orientations. The corresponding effective normal stress associated with the largest shear displacement is between 9 and 10 MPa.

Figure 7-18 (left column) shows the effective normal stress at repository depth (460 m) during the second retreat of the ice sheet (58 ka) without considering residual pore pressure (top) and with residual pore pressure (bottom). The right column of the figure shows the corresponding shear displacement at the centre of a circular fracture with a radius of 100 m. Without considering the effects of residual pore pressures, the maximum shear displacement is less than 9 mm for all fracture orientations. The corresponding effective normal stress associated with the largest shear displacement is around 12–14 MPa. When residual pore pressures are considered, here about 1.1 MPa, the maximum shear displacement is around 12 mm and the corresponding effective normal stress is around 12 MPa.

Figure 7-19 shows an estimate of the maximum slip at the centre of a fracture dipping 27.1° in the σ_H–σ_v-plane at 250 m (left) and repository depth (right). If residual pore pressures are not considered, the largest shear displacements occur when the ice margin passes the site (15 and 58 kyr). For a fracture with radius 100 m, the induced maximum slip is about 5–5.5 mm during the first retreat and 8 mm during the second retreat at both depths. At all other points in time, the total slip magnitude is less than the slip due to the *in situ* stress state.

When increased pore pressure levels as the ice margin passes and during permafrost conditions are considered (marked with dashed lines in the figure), the maximum induced slip on a fracture with radius 100 m at the end of the glaciation (58 kyr) is 10 mm (250 m depth) and 12 mm (repository depth). The maximum induced slip during permafrost conditions is about 6.5 mm at both depths.

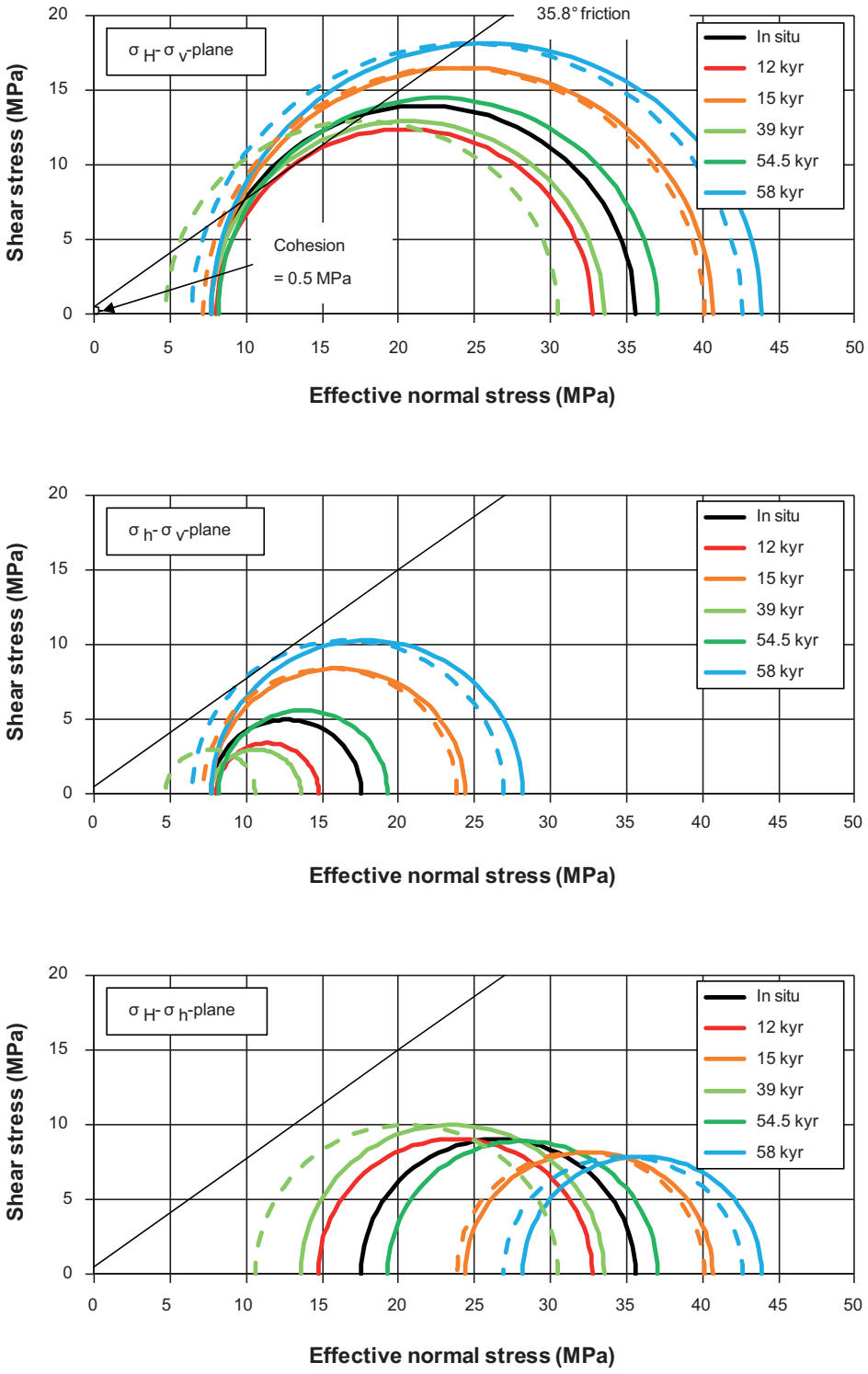

Figure 7-15. *Mohr circle representations of stresses at repository depth at Forsmark at present day conditions (in situ), first glacial maximum (12 kyr), ice margin passing (15 kyr), stress reductions due to forebulge (39 kyr), second glacial maximum (54.5 kyr) and edge passing at the end of the glacial cycle (58 kyr). Effects due to residual pore pressures are marked with dashed lines, i.e. the circles are moved to the left by the pore pressure value.*

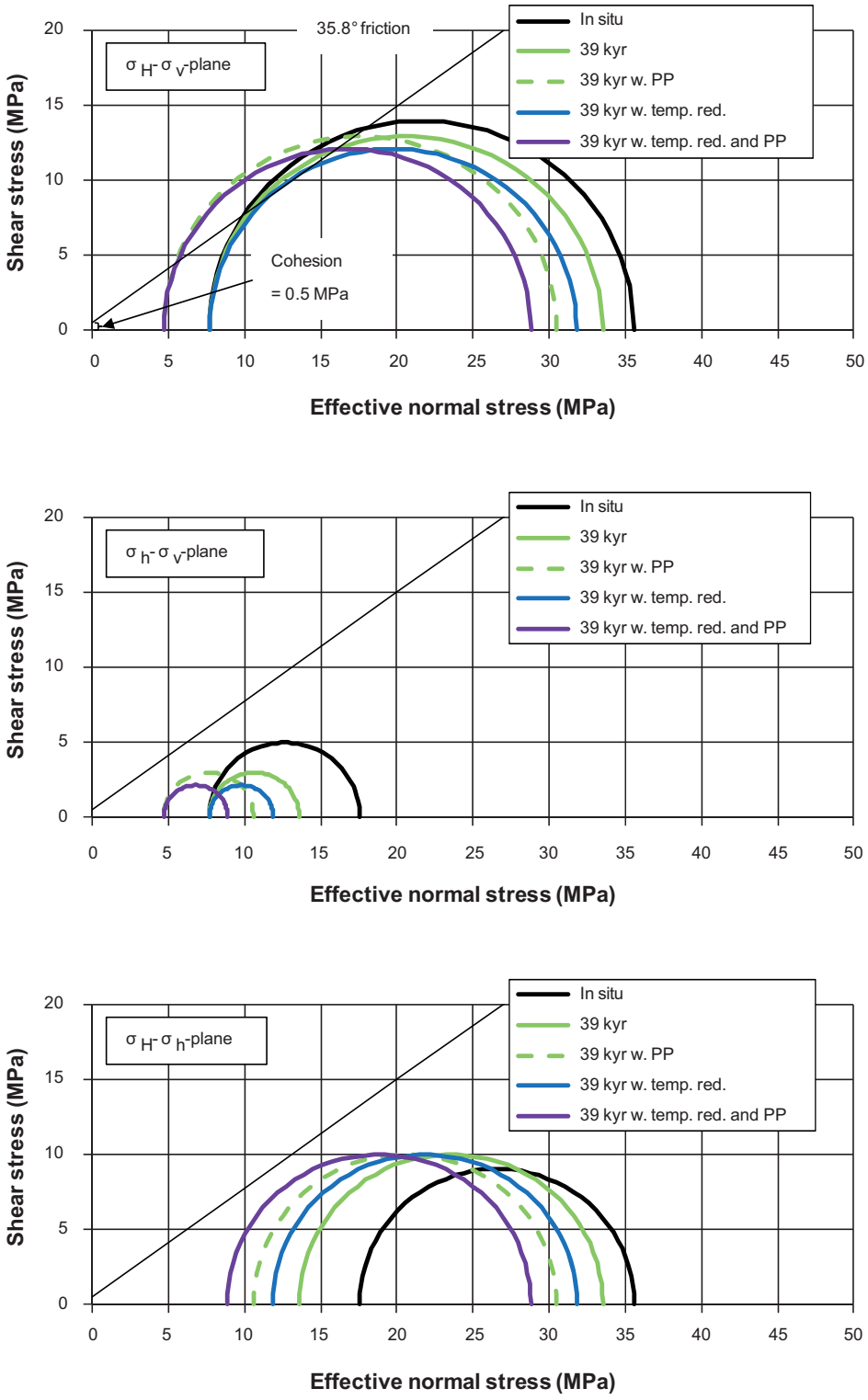

Figure 7-16. *Mohr circle representation of stresses at repository depth at Forsmark at present-day conditions (in situ) and during the forebulge (39 kyr) with and without permafrost induced pore pressure and temperature reduction.*

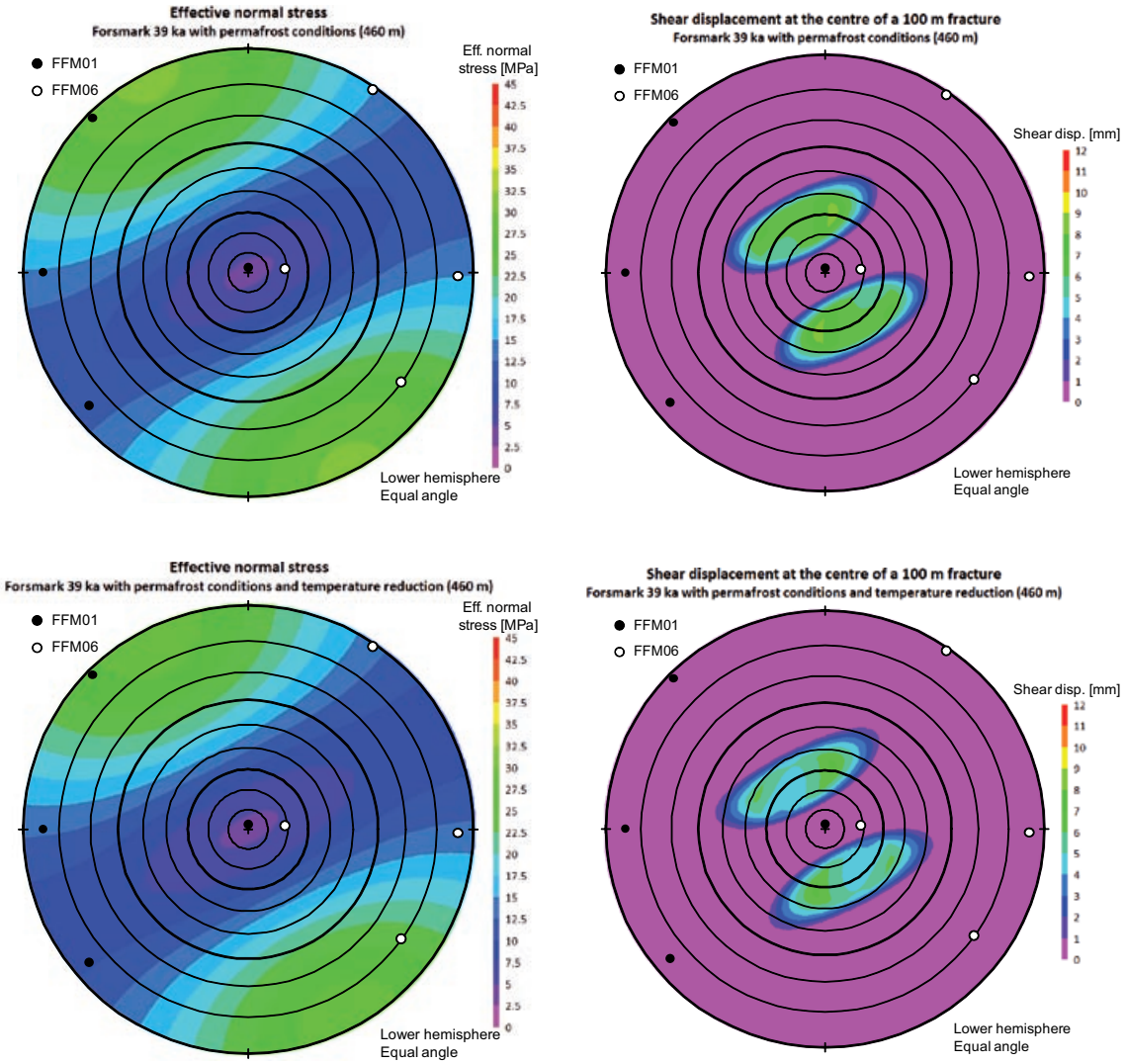

Figure 7-17. *Left: Effective normal stress at repository depth (460 m) after 39 ka with permafrost conditions. Right: Corresponding shear displacement at the centre of a fracture with radius 100 m. Note that the shear displacement presented here is in excess of that due to the in situ stress state. Fracture pole orientations (global set) in fracture domains FFM01 (black circles) and FFM06 (white circles) are compiled from Table 7-1 in /Fox et al. 2007/.*

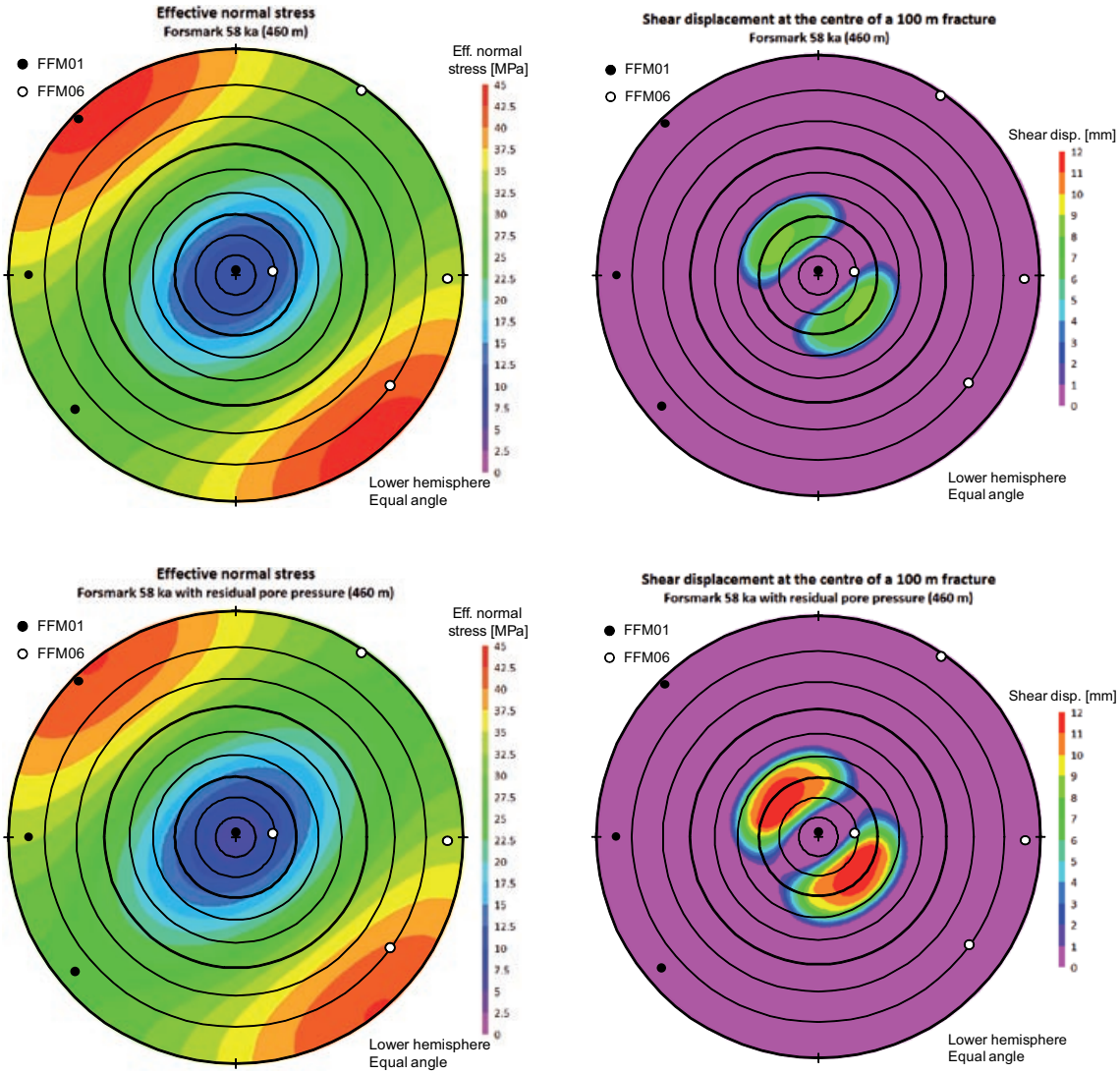

Figure 7-18. *Left column: Effective normal stress at repository depth (460 m) after 58 ka (top) and 58 ka with residual pore pressure (bottom). Right column: Corresponding shear displacement at the centre of a fracture with radius 100 m. Note that the shear displacement presented here is in excess of that due to the in situ stress state. Fracture pole orientations (global set) in fracture domains FFM01 (black circles) and FFM06 (white circles) are compiled from Table 7-1 in /Fox et al. 2007/.*

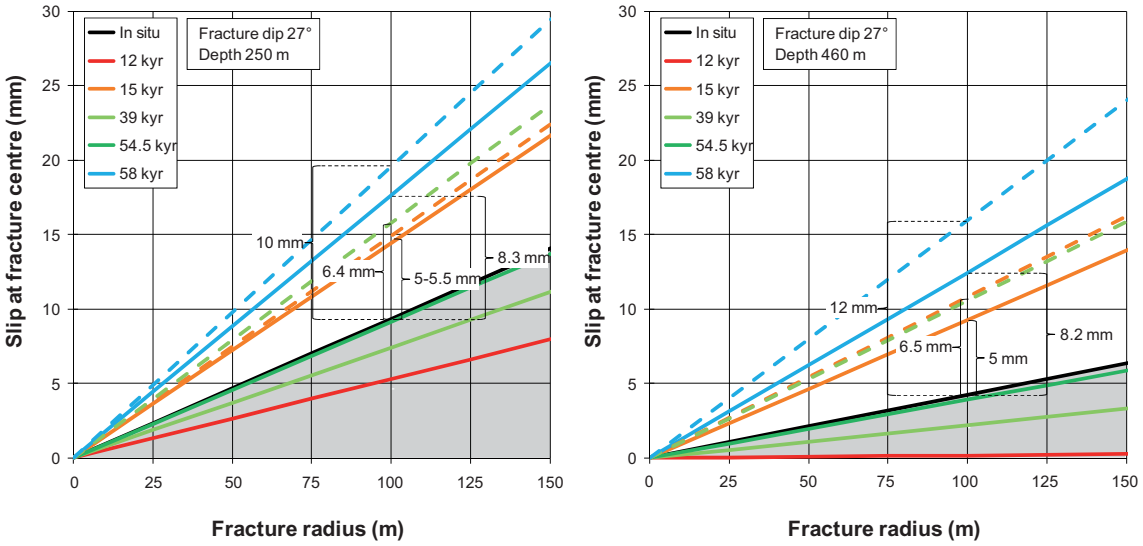

Figure 7-19. *Slip magnitude estimates at 250 m (left) and repository depth (right) assuming the excess pore pressure to be 98% of the glacially induced vertical load or residual and permafrost induced excess pore pressures (dashed lines). Curves drawn in the grey shaded area represent instants of time when the stability is higher than under in situ conditions.*

7.6 Hydraulic jacking

7.6.1 General

Hydraulic jacking is a phenomenon that occurs when the pore pressure in a fracture exceeds both the normal stress acting on the fracture and the fracture's tensile strength. This can lead to changes in apertures and corresponding transmissivities, which are difficult to assess. Hydraulic jacking is most likely initiated during a glacial period when high pore pressures must be assumed to build up in the rock in front of an advancing ice sheet in combination with proglacial permafrost and below the ice sheet. As the ice sheet retreats at the end of the glacial phase, the pore pressure may remain high for a long time after the ice is gone.

Hydraulic jacking is first initiated in fractures orientated perpendicular to the least principal stress. The present understanding is that the horizontal stress components due to the ice load are of the same magnitude or greater than the corresponding vertical stress component and that they exist outside the ice /Lund et al. 2009/. In a reverse stress field ($\sigma_H > \sigma_h > \sigma_v$), which is the case at Forsmark /Glamheden et al. 2007a/, this implies that hydraulic jacking is mainly of concern for sub-horizontal fractures. In the following sections, the potential for hydraulic jacking of horizontal fractures and the associated maximum jacking depth is investigated based on results from a study by /Lönnqvist and Hökmark 2010/. However, in a strike-slip type stress regime ($\sigma_H > \sigma_v > \sigma_h$), e.g. Laxemar /Hakami et al. 2008/, hydraulic jacking may be of greater concern for steeply dipping fractures. Hydraulic jacking of steeply dipping fractures is not treated further here. Figure 7-20 shows the principles of hydraulic jacking during the retreat of the ice sheet.

As the jacking process progresses, the fracture surfaces separate and the apertures may become very large /SKB 2006b/. Near the ground surface, the rock above sub-horizontal fractures can be lifted, but otherwise the apertures are controlled by the deformation properties of the surrounding rock /Hökmark et al. 2006/. It is likely that the jacking process will continue as long as there are tensile conditions in the fracture /SKB 2006b/, but it is also believed to be a reversible process /Hökmark et al. 2006/ as long as there is no shear component or the fracture is filled with solid materials. Possible indications of hydraulic jacking events, in the form of sediment-filled fractures, have been found at several Swedish sites. An example is Forsmark (cf. Figure 7-21) where such fractures have been found to depths of a few tens of metres /Hökmark et al. 2006/.

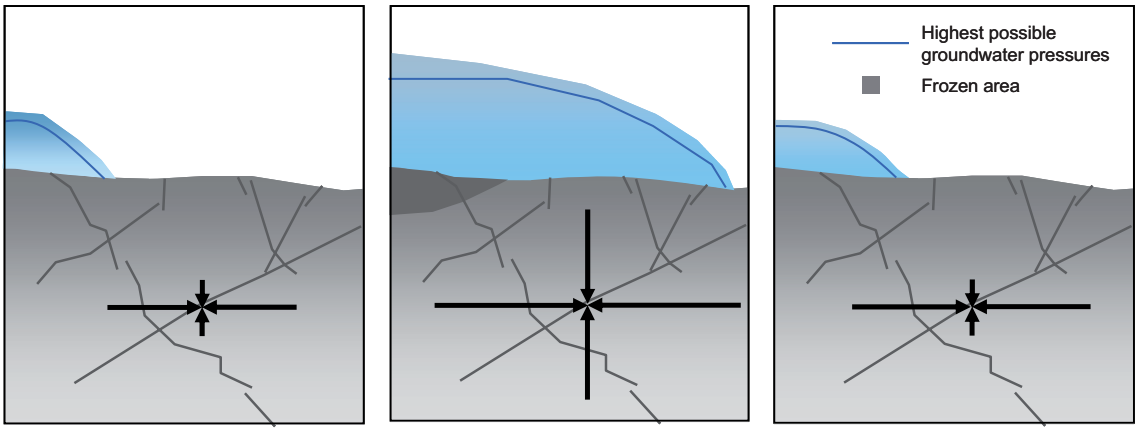

Figure 7-20. *Principles of hydraulic jacking during the retreat of the ice sheet, after /Boulton et al. 2001/. Left: Before the ice sheet reaches the site, the horizontal stresses dominate; in a strike-slip stress regime, e.g. Laxemar /Hakami et al. 2008/, only one horizontal stress component is greater than the vertical stress component. Middle: As the ice sheet covers the site, the stresses and pore pressure increase. Right: When the ice has retreated the vertical stress additions due to the ice load decrease faster than the excess pore pressure and horizontal excess stress components, which may cause sub-horizontal fractures to open.*

Figure 7-21. *Example of a horizontal sediment-filled fracture at Forsmark, which was exposed during the construction of the nuclear power plant in the 1970s. From /Leijon 2005/.*

In theory, hydraulic jacking may also be initiated at substantially larger depths /Lindblom 1997, Talbot 1999, Hökmark et al. 2006, Lönnqvist and Hökmark 2010/. /Lönnqvist and Hökmark 2010/ identified four cases (Figure 7-22) for which high pressures can be transferred to the ice margin and beyond where the lack of vertical stress additions due to the ice could potentially initiate hydraulic jacking of horizontal fractures at large depths:

1. The steady state pressure distribution due to a stationary ice, which can be considered an upper bound estimate of an advancing ice without permafrost in a continuum representation of the rock.
2. A few highly transmissive fractures in otherwise low permeable rock may transfer high pressures from far under the ice to the ice front and beyond.
3. The time period leading up to a glaciation is characterized by cold climate during which permafrost in many cases may develop in front of the advancing ice sheet /SKB 2006a/. Permafrost is defined as ground that remains at or below 0°C for at least two consecutive years /Gascoyne 2000/ and can be considered to be a more or less impermeable layer /e.g. Vidstrand 2003/. During permafrost conditions, the reduced permeability in the upper part of the rock will restrict drainage to the ground surface and promote pressure build-up in regions of low vertical stress outside the ice-front.

4. Depending on the permeability of the rock and the frontal retreat rate of the ice, the high pore pressures that have been building up during the advance of the ice sheet and during a following long or short period of quasi-stationary conditions might remain high for a long time after the ice is gone.

In the following, results and examples from /Lönnqvist and Hökmark 2010/ based on data from the proposed repository site at Forsmark, cf. Section 4.7, are used to establish estimates of the maximum jacking depth during a glacial cycle.

7.6.2 Modelling approach

In the study by /Lönnqvist and Hökmark 2010/, jacking depth is defined as the maximum depth at which the effective vertical stress is zero, assuming that the tensile strength is zero. The excess pore pressure is calculated using a 2D continuum approach in which the hydrological conditions can be approximated by a bulk hydraulic diffusivity /Itasca 2005/, cf. Section 4.7.

The following is assumed throughout the study /Lönnqvist and Hökmark 2010/:

- The ice sheet is represented by a generic ice profile /Paterson 1994/ with a maximum height of 3,000 m, cf. Figure 7-23.
- The mechanical load at the ground surface is given by the weight of the ice. The hydrostatic pressure at the ice/bed interface is approximately 98% of the mechanical ice load at all times.
- The total vertical stress is equal to the weight of the overburden at all depths.
- The ice front is moving at a constant speed although periods of quasi-stationary conditions can be considered.
  - Its advance rate is 40 m/year, which is a typical value in the reconstruction of the Weichselian ice sheet /SKB 2006a/. As an upper bound estimate, analyses where the pore pressure distribution has reached steady state conditions before retreat are also performed.
  - Its retreat rate is in the range 200–500 m/year /SKB 2006b, Talbot 1999/.
- The one-dimensional loading efficiency /Neuzil 2003/ is not considered. 1D calculations /Lönnqvist and Hökmark 2010/ show that excluding the loading efficiency, the pore pressure is underestimated during the advance of the ice sheet and overestimated during the retreat. However, given the schematic 2D representations of the ice sheet profile and rock mass, these effects are not considered to be significant.

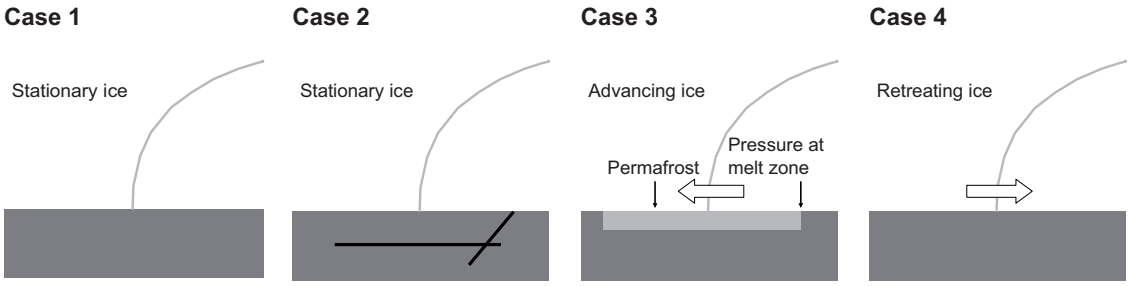

Figure 7-22. *Four cases for which high pressures could be transferred to the ice front where the lack of vertical stress additions due to the ice could potentially initiate hydraulic jacking at large depths.*

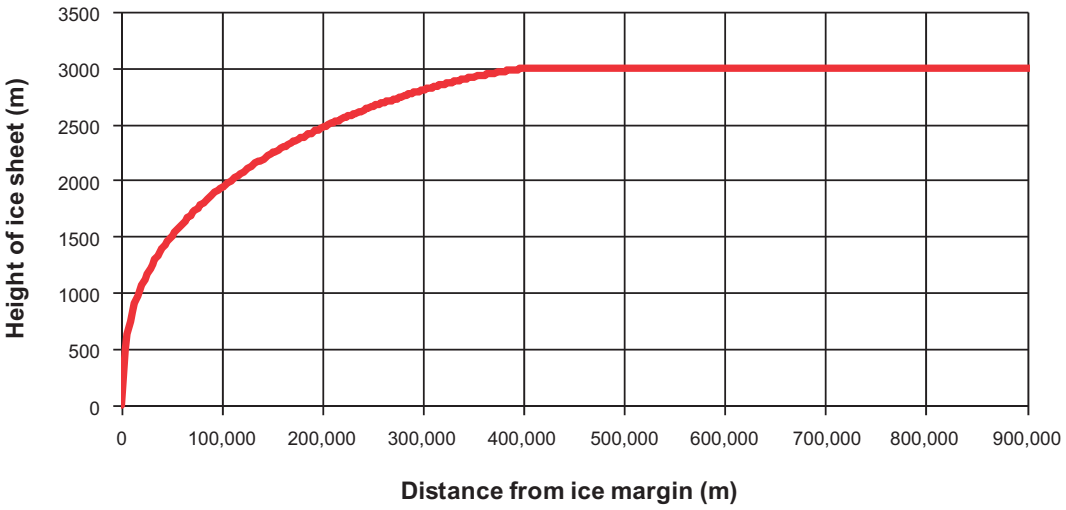

Figure 7-23. *Ice sheet profile used in the hydraulic jacking study /Lönnqvist and Hökmark 2010/.*

7.6.3 Advancing and stationary ices

Stationary ices

The steady state pressure distribution due to a stationary ice (Case 1, cf. Figure 7-22), which can be considered an upper bound estimate of an advancing ice without permafrost in a continuum representation of the rock (cf. point 3, below) is not sufficient to initiate hydraulic jacking at depths greater than about 30 m /Lönnqvist and Hökmark 2010/.

Analytical estimates of Case 2 indicate that in order to cause hydraulic jacking at 400 m depth a horizontal fracture at least 7.6 km long in otherwise impermeable rock is needed, which points to the fact that very specific conditions regarding fracture length and connectivity are required to initiate hydraulic jacking at large depths. This is supported by results from a numerical study based on data from the Whiteshell Research Area in Canada in which there was no indication that hydraulic jacking would take place at any depth during a glacial cycle /Chan et al. 2005/.

Advancing ice sheet with permafrost conditions

Preceding the glacial advance the proposed repository sites at Forsmark and Laxemar are located above sea-level with permafrost conditions as the ice front advances towards and over them /SKB 2006b/. As described above, permafrost acts as a more or less impermeable layer, which restricts drainage to the ground surface and promotes pressure build-up in regions of low vertical stress outside the ice-front /Lönnqvist and Hökmark 2010/.

/Lönnqvist and Hökmark 2010/ identified a number of issues, which may influence the maximum jacking depth during permafrost conditions, cf. Figure 7-24:

- Permafrost depth;
- Permeability of the rock below the permafrost;
- Distance from repository site to the ice front at the time when the permafrost layer is first breached (melted) at some position behind the advancing front.
- Melting rate of the permafrost.
- Seasonal boundary pressure variations at the permafrost melt zone.
- Taliks (unfrozen parts) within the permafrost body.

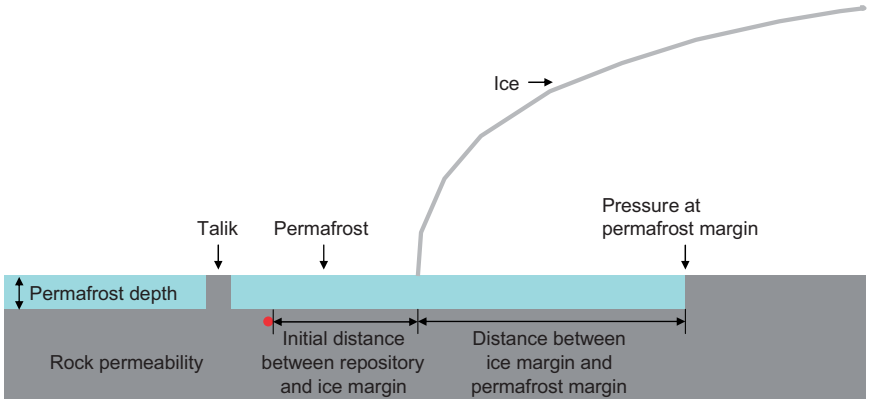

Figure 7-24. *Factors that can influence the maximum jacking depth during permafrost conditions. From /Lönnqvist and Hökmark 2010/.*

In the reference scenario of the SR-Can safety assessment /SKB 2006b/, the maximum permafrost thickness is about 250 m at Forsmark and 160 m at Laxemar. However, for the most severe surface conditions, the permafrost may gain a thickness of about 400 m at Forsmark /SKB 2006b/. In the modelling work by /Lönnqvist and Hökmark 2010/, the permafrost depth is set to 200 m.

/Lönnqvist and Hökmark 2010/ modelled the evolution of the excess pore pressure in the rock mass during permafrost conditions by use of the thermal logic in the numerical finite element code Code_Bright /CIMNE 2004/. The rock mass was represented by a rectangular block subdivided into three layers (Figure 7-25) with hydraulic properties based on site data from Forsmark, cf. Section 4.7:

- The permafrost layer (0–200 m) is represented by a rectangular region of uniform thickness, which is impermeable ($\kappa = 1.0 \cdot 10^{-14}$ m^2/s);
- A layer with high-diffusivity rock (200–400 m) set to either $1 \cdot 10^{-1}$ m^2/s (denoted ‘high’) or $1 \cdot 10^{-2}$ m^2/s (denoted ‘low’);
- Rock below 400 m with diffusivity $1 \cdot 10^{-4}$ m^2/s.

The advancement of the ice front can be assumed to last approximately 10,000 years, cf. Figure 2-2 (left). As a typical figure of the speed by which the ice front is advancing is 40 m/year /SKB 2006a/, the furthest distance the repository can be located at, in order to be located directly beneath the ice margin at some point during the advancement of the ice front, is 400 km /Lönnqvist and Hökmark 2010/.

The permafrost starts melting when the ice front passes over it. As the permafrost is assumed to melt linearly, the distance between the permafrost melt zone and the ice front remains constant. The maximum jacking depth for three different permafrost melting rates was investigated /Lönnqvist and Hökmark 2010/:

- Case A (main scenario in the SR-Can safety assessment, cf. the **Climate report**): 125 m during the first 4,300 years (0.03 m/a), the remaining 75 m in 30 years (2.5 m/a), which corresponds to a distance of 173.2 km between the permafrost melt zone and the ice front.
- Case B: 200 m in 200 years (1 m/a), which corresponds to a distance of 8 km between the permafrost melt zone and the ice front.
- Case C: 200 m in 7,900 years (0.025 m/a), which corresponds to a distance of 316 km between the permafrost melt zone and the ice front.

Of the three suggested melting rates, Case B was the only one, which could raise the pore pressure sufficiently at the ice front to initiate hydraulic jacking beneath the permafrost, cf. Figure 7-26. For the most conservative case (indicated with a red solid line in Figure 7-26), the maximum jacking depth is about 350 m /Lönnqvist and Hökmark 2010/.

/Lönnqvist and Hökmark 2010/ represent seasonal variations in the boundary pressure with a sinusoidal function where the pressure during the winter season is set to zero, the previously assumed annual average (98% of the mechanical load) during the summer season and a short pressure peak

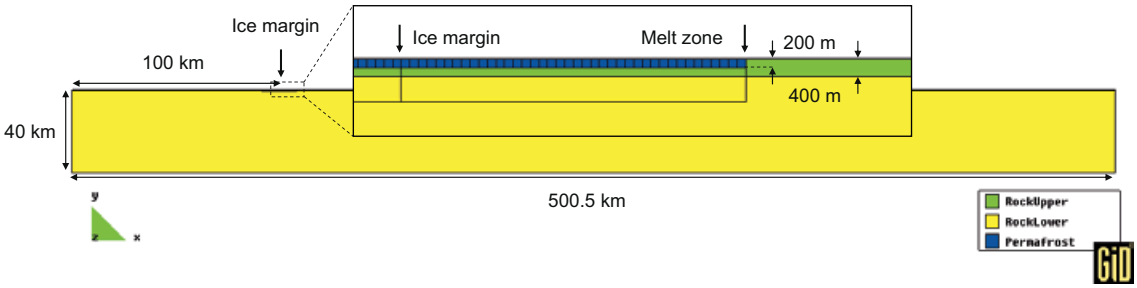

Figure 7-25. *Schematic view of Code_Bright model.*

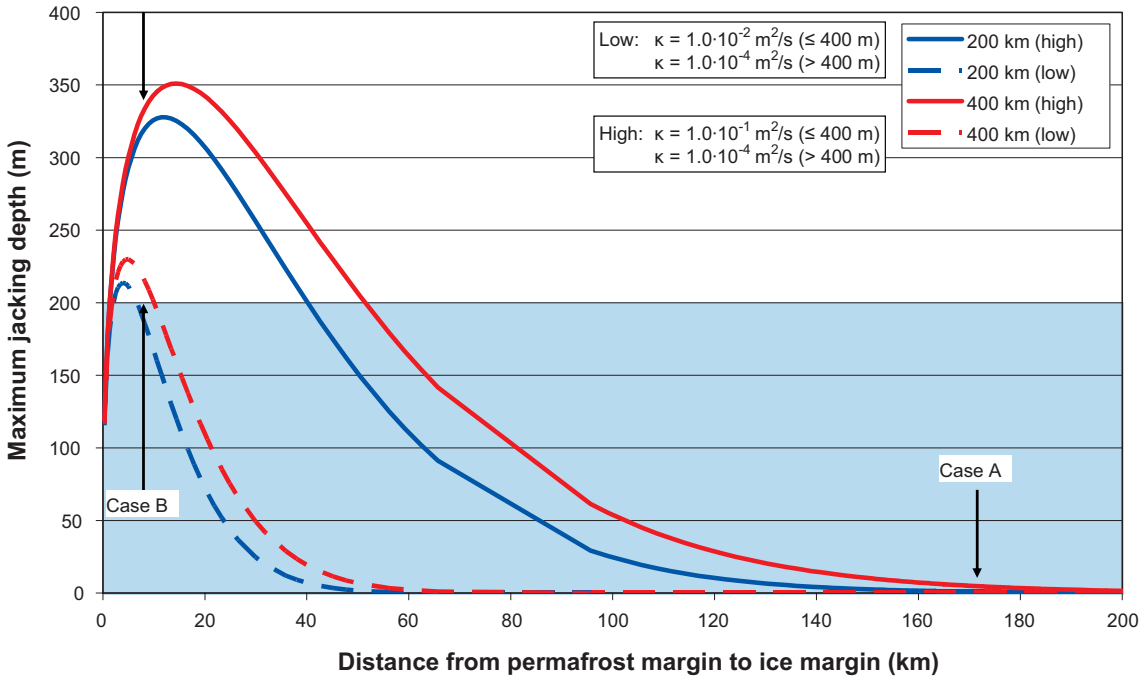

Figure 7-26. *Maximum jacking depth beneath the ice margin as functions of distance from the ice margin to the permafrost margin for a number of initial distances from the repository to the ice margin. The permafrost depth is 200 m (marked in blue); hydraulic jacking cannot occur at more shallow depths than 200 m. Note that the distance between the melt zone and ice front in Case C is over 300 km and not shown in the figure. Modified from /Lönnqvist and Hökmark 2010/.*

between the seasons representing a spring flood. By allowing for seasonal variations the annual average boundary pressure is reduced by about 40–50%, which corresponds to a reduction in the maximum jacking depth by the same amount /Lönnqvist and Hökmark 2010/. Consequently, the most conservative estimate of the maximum jacking depth presented in Figure 7-26 (350 m) would be reduced to about 175–210 m, *i.e.* only marginally below the permafrost. /Lönnqvist and Hökmark 2010/ found that the pore pressure beneath the permafrost is completely determined by the pressure at the melting zone and the diffusivity of the rock, which implies that the permafrost thickness will not influence the maximum jacking depth.

A further factor, which may contribute to a reduction in the maximum jacking depth, is the presence of open taliks near the repository region. /Lönnqvist and Hökmark 2010/ found that taliks are more influential when the hydraulic diffusivity is high, *i.e.* would reduce the excess pore pressure more efficiently. However, /Lönnqvist and Hökmark 2010/ note that in order to quantify their influence site-specific conditions have to be considered, *e.g.* their number, sizes and locations in relation to the repository.

7.6.4 Retreating ice sheet

The retreat phase of the glaciation without permafrost conditions is studied by use of specifically derived analytical expressions for pore water dissipation in a semi-infinite rectangular region with uniform hydraulic diffusivity /Carslaw and Jaeger 1959, Lönnqvist and Hökmark 2010/.

During the last deglaciation of the Weichselian ice cycle, the frontal retreat rates were about 200 and 300 m/year at present day Laxemar and Forsmark, respectively /SKB 2006b/. A much faster frontal retreat rate (500 m/year) suggested by /Talbot 1999/ is analysed as an upper bound limit in addition to the retreat rates given for Forsmark and Laxemar /Lönnqvist and Hökmark 2010/.

The bulk hydraulic conductivity of the rock at the proposed repository site at Forsmark is in the range $1.0 \cdot 10^{-9}$–$1.0 \cdot 10^{-8}$ m/s /Follin et al. 2007/, cf. Section 4.7. In Figure 7-27, the effects of a slow build-up of pore pressures during the advancement of the ice sheet are approximated by assuming that the initial pore pressure distribution has reached steady state before its subsequent retreat. This results in a maximum jacking depth that is less than 100 m even for the fastest retreat speed. For the retreat speed relevant for Forsmark (300 m/year) the maximum jacking depth is around 50 m.

For low diffusivity rock the assumption that the pore pressures will have reached steady state conditions during the advance of the ice sheet will greatly overpredict the maximum jacking depth, cf. Figure 7-28. However, if the hydraulic conductivity is higher than about $1.0 \cdot 10^{-10}$ m/s, the difference between retreating from steady state conditions or after having advanced at 40 m/year for 10,000 years (with or without allowing for subsequent quasi-stationary periods) is marginal. For the range in hydraulic conductivity relevant for Forsmark ($1.0 \cdot 10^{-9}$–$1.0 \cdot 10^{-8}$ m/s), the maximum jacking depth is around 50 m regardless of whether the pore pressure distribution has reached steady state conditions or not.

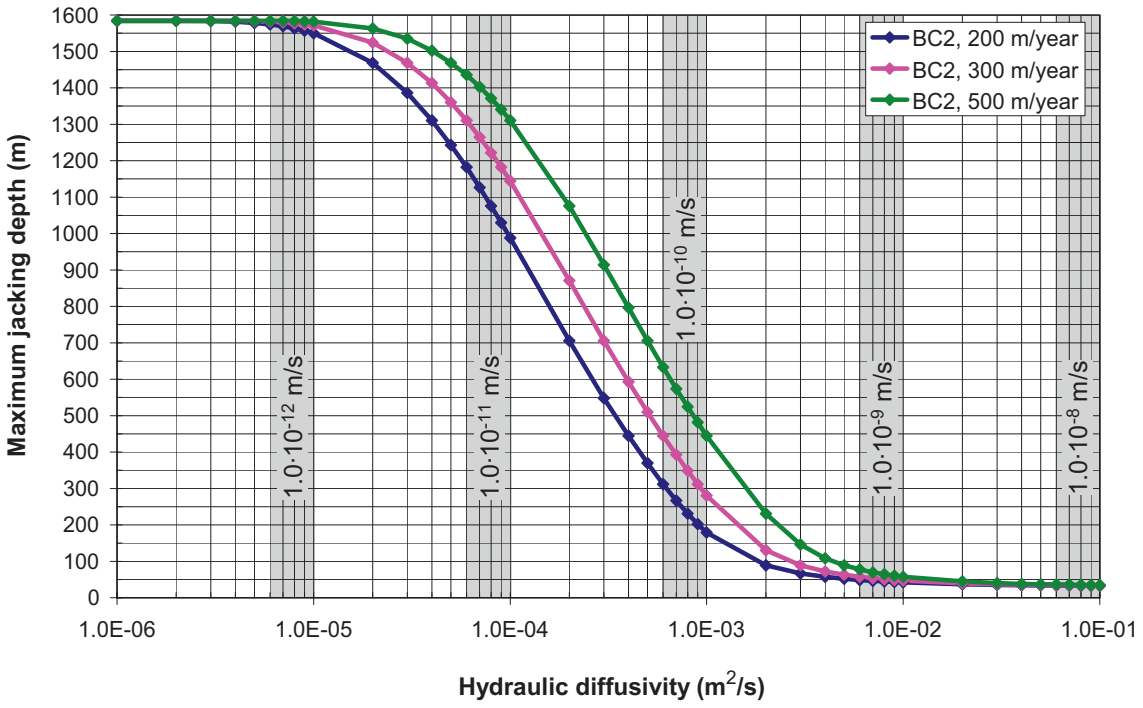

Figure 7-27. *Maximum jacking depth during retreat from steady state conditions as functions of hydraulic diffusivity for three assumptions regarding the retreat speed of the ice sheet (200, 300 and 500 m/year). BC2 is a model code. Grey shaded areas correspond to values of the hydraulic conductivity for a given range of hydraulic diffusivity values. Modified from /Lönnqvist and Hökmark 2010/.*

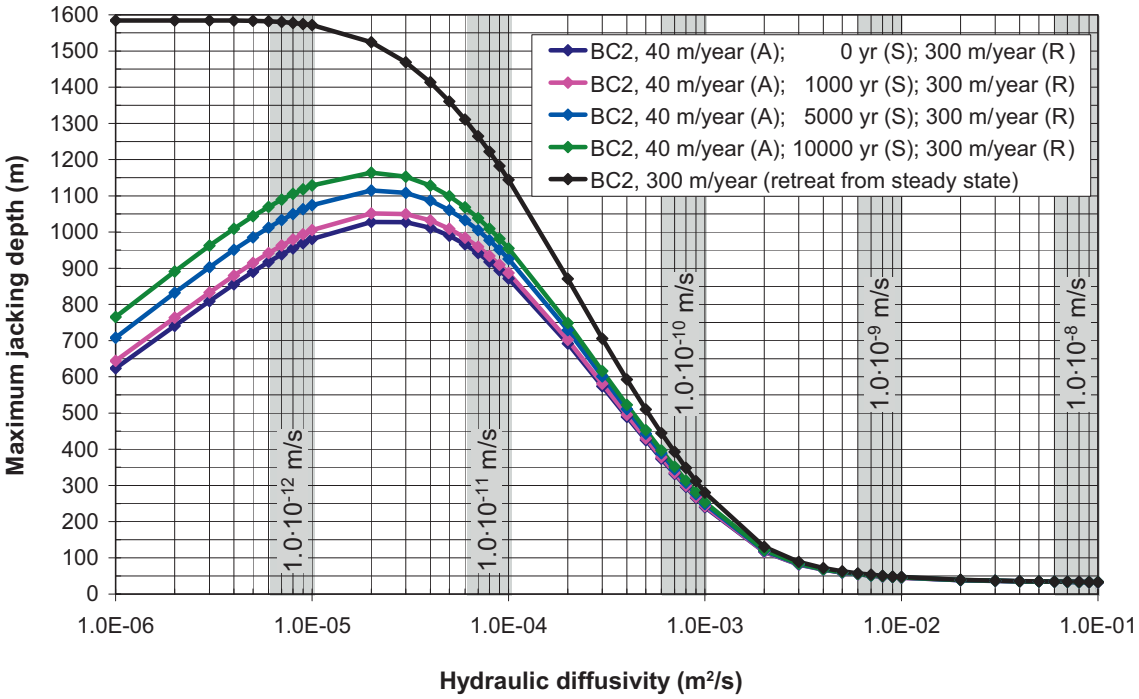

Figure 7-28. *Maximum jacking depth during retreat as functions of hydraulic diffusivity. The ice sheet is advancing at 40 m/year (A), quasi stationary for 0–10 ka (S) and retreating at 300 m/year (R). BC2 is a model code. Grey shaded areas correspond to values of the hydraulic conductivity for a given range of hydraulic diffusivity values. From /Lönnqvist and Hökmark 2010/.*

7.7 Summary

The results of this chapter are relevant for the large-scale thermo-hydro-mechanical evolution of the host rock at Forsmark during a glacial cycle. Glacially induced stresses calculated by /Lund et al. 2009/ are added to the *in situ* stresses to find the evolution of the total stresses that totally control the response of the fracture system. Five stress models corresponding to different points of time in the glacial cycle are picked for the assessment (cf. Figure 7-3). Note that the time-scale provided is a relative one, i.e. with time zero indicating the first noticeable mechanical effects of the approaching ice sheet.

1. The time of the first glacial maximum (12 kyr).
2. The time of the passing of the ice margin during the retreat of the ice (15 kyr).
3. The time of forebulge stresses at the time preceding the second period of ice-load (39 kyr).
4. The time of the second glacial maximum (54.5 kyr).
5. The time of the passing of the ice margin during the retreat of the ice (58 kyr).

There are two versions of the forebulge stress model: without and with account of the reduction of the horizontal stresses that would follow from the lowered rock temperatures in case of proglacial permafrost conditions. The thermally induced stress reduction is obtained from a large scale *3DEC* model and added to the forebulge stress model. The different stress models are combined with two sets of assumptions regarding the excess pore pressure:

1. The excess pore pressure is 98% of the glacially induced mechanical load at all times and at all depths (i.e. approximately zero as the ice margin passes over the site at 15 and 58 kyr).
2. Transient changes in pore pressure are assumed as the ice margin is passing over the site (15 and 58 kyr) and in combination with proglacial permafrost (39 kyr).

This gives altogether 10 cases to analyze with respect to stability and transmissivity changes, cf. Table 7-1.

Table 7-1. Summary of cases studied.

	Stress	Pore pressure assumption	Excess pore pressure at repository depth
1	In situ + glacially induced	1)	18 MPa (98% of ice load)
2	In situ + glacially induced	1)	0 MPa (98% of ice load)
		2)	0.7 MPa (residual overpressure, cf. Appendix D)
3	In situ + glacially induced	1)	0 MPa (98% of ice load)
		2)	3.3 MPa (permafrost pore pressure)
	In situ + glacially induced + thermally -induced stress reduction (permafrost)	1)	0 MPa (98% of ice load)
		2)	3.3 MPa (permafrost pore pressure)
4	In situ + glacially induced	1)	25 MPa (98% of ice load)
5	In situ + glacially induced	1)	0 MPa (98% of ice load)
		2)	1 MPa (residual overpressure, cf. Appendix D)

7.7.1 Fracture stability

The following can be concluded regarding the potential for fracture instability.

- The largest shear displacements occur in connection with the second episode of ice frontal retreat. An optimally oriented fracture with a 100 m radius might slip at most about 12 mm assuming the highest possible residual pore pressure considered here (i.e. about 1.1 MPa at repository depth), cf. Figure 7-19 (right). Smaller fractures slip correspondingly less.
- The pore pressure assumption is crucial. Without any residual excess pore pressure, the maximum slip on a correspondingly oriented fracture with a 100 m radius is less than 9 mm.
- There is a limited range in fracture orientations that would result in large shear displacements, cf. Figure 7-18 (bottom right). However, very few sub-horizontal fracture sets in fracture domains FFM01 and FFM06 appear to be within this range.

7.7.2 Transmissivity changes

Normal stress variations

The results are sensitive to assumptions regarding the magnitude of glacially induced pore pressures. A summary of the effective normal stress impact on relative transmissivity (model A) during the glacial phase is provided below for two assumptions regarding the excess pore pressure (cf. Figure 7-4) and thermo-mechanical effects due to temperature reductions during permafrost conditions (cf. Figure 7-6):

- **Vertical fractures striking perpendicular to the major horizontal *in situ* stress (σ_H), i.e. striking 55° with respect to North:**
  - *Pore pressure assumption 1.* Insignificant transmissivity changes at all times and at all depths.
  - *Pore pressure assumption 2.* Insignificant transmissivity changes at all times and at all depths.
  - *Thermo-mechanical effects in combination with proglacial permafrost.* Transmissivity increase, at shallow depths, by less than a factor 2. Insignificant transmissivity changes at depths below 300 m.
- **Vertical fractures striking perpendicular to the minor horizontal *in situ* stress (σ_h), i.e. striking 145° with respect to North:**
  - *Pore pressure assumption 1.* Transmissivity increase, at shallow depths, by less than a factor 2. At repository depth the maximum increase is a factor 1.4.
  - *Pore pressure assumption 2.* Transmissivity increase, directly below the permafrost, by at most a factor 3. At repository depth the maximum increase is a factor 1.8.
  - *Thermo-mechanical effects in combination with proglacial permafrost.* Transmissivity increase, directly below the permafrost, by a factor around 7.5. At repository depth the maximum increase is a factor 2.5.

- **Horizontal fractures:**
  - *Pore pressure assumption 1.* Insignificant transmissivity changes at all times and at all depths.
  - *Pore pressure assumption 2.* Transmissivity increase, directly below the permafrost, by a factor around 2.4. Maximum transmissivity increase below a depth of 400 m is factor around 2.
  - *Thermo-mechanical effects in combination with proglacial permafrost.* Not applicable.

The largest impact on fracture transmissivity at shallow depth and at repository depth is for permafrost conditions. For this case, changes of arbitrarily oriented fractures can be estimated using the contoured pole plots (cf. Figure 7-12 and Figure 7-13).

Shearing

The following can be concluded regarding transmissivity effects due to shearing.

- The largest shear displacements occur in connection with the second episode of ice frontal retreat assuming the highest possible residual pore pressure considered here (i.e. about 1.1 MPa at repository depth). The effective normal stresses are reduced but are still above approximately 10–20 MPa for the most unstable fractures (Figure 7-18, bottom), i.e. well above the highest normal stresses applied in the lab scale transmissivity tests performed by /Olsson 1998/. Therefore the additional increase in transmissivity caused by shearing is likely to be modest. If the residual pore pressure is less than assumed here, the effective stress will be higher and consequently the increase in transmissivity will be less.
- For fractures dipping more than 45°, the normalised shear displacement is less than 2 mm regardless of strike. Fracture with radii larger than 100 m will move correspondingly more. The effective normal stress is significantly increased, which will mean that the resulting transmissivity is likely to be reduced rather than increased regardless of the magnitude of the displacement.

7.7.3 Hydraulic jacking

The following conclusions can be made regarding the potential for hydraulic jacking of horizontal fractures during different phases of the glacial cycle /Lönnqvist and Hökmark 2010/:

- **Advancing ice front**
  - *without permafrost.* Hydraulic jacking is unlikely to be initiated at greater depths than about 30 m.
  - *in combination with proglacial permafrost.* For the most conservative case, the maximum jacking depth is 350 m. By allowing for seasonal variations in the boundary pressure, the maximum jacking depth may be reduced by 40–50%, *i.e.* to about 200 m. Note that the maximum jacking depth is very sensitive to assumptions regarding the hydraulic diffusivity of the rock mass.
- **Retreating ice front.** If the effects of a slow build-up of pore pressures during the advancement of the ice sheet are approximated by assuming that the pore pressure distribution has reached steady state before its subsequent retreat, the jacking depth is around 50 m for the retreat speed relevant for Forsmark (300 m/year). The maximum jacking depth is unlikely to be more than 100 m.

Note that the jacking potential is greater at shallow depths. If hydraulic jacking occurs at all, it is therefore likely to be initiated near the ground surface. The jacking process, i.e. the increased transmissivity of shallow fractures, will contribute to reduce the pore pressure beneath the affected rock layer and will thus prevent hydraulic jacking from occurring further down into the rock. This is, however, not considered in the estimates of the maximum jacking depths provided above, which consequently can be considered as conservative estimates.

8 Assessment of medium-scale THM evolution – Transmissivity changes and shearing of near-field fractures

8.1 Introduction

As part of the safety assessment SR-Can, /Hökmark et al. 2006/ and /Fälth and Hökmark 2007/ investigated stress-induced transmissivity changes and shearing of near-field fractures during the construction and operational phase and during the initial temperate phase at the Forsmark, Laxemar and Simpevarp repository sites. For the Forsmark site the effects of a glaciation were also investigated. In their calculations, the representation of the glacial load was based on preliminary ice/crust/mantle 2D calculations but increased pore pressures due to the ice sheet were not considered. /Hökmark et al. 2006/ found that the combined effects of normal stress variations and shearing may results in transmissivity increases of up to two orders of magnitude localised to regions around the tunnel openings (see below). The aim of the present study is to confirm the results obtained by /Hökmark et al. 2006, Fälth and Hökmark 2007/ with the additional purpose of considering 1) larger fractures (radius 50 m) and 2) a more relevant representation of stresses and pore pressures during a glacial cycle, cf. also Chapter 7.

8.1.1 Results from SR-Can

The near-field models considered by /Hökmark et al. 2006, Fälth and Hökmark 2007/ incorporated a small number of well defined schematic fractures with sizes of a few tens of metres without any real link to fracture orientations observed at the sites. These fracture orientations are shown in Figure 8-1. Similarly to the present study, transmissivity effects due to changes in normal stress were assessed using Equations 4-1 and 4-2 and qualitative assessments were made regarding transmissivity effects due to shearing.

Examples of results from the study by /Hökmark et al. 2006/ are shown in Figure 8-2 for a fracture dipping 20° along the deposition tunnel (fracture #4). The upper left part of the figure shows the temporal evolution of the relative transmissivity associated with changes in normal stress at selected points on the fracture. The variations in relative transmissivity range between 95% (at minimum) and 117% (at maximum). The maximum observed shear displacement, at the same points, is in the range 4–5 mm, cf. Figure 8-2 (lower left). /Hökmark et al. 2006/ estimated, by comparing the modelling results to laboratory-scale transmissivity tests (Figure 3-9) performed by /Olsson 1998/, that locally the relative transmissivity could increase by two orders of magnitude. However, /Hökmark et al. 2006/ noted that the shear displacements were much smaller on most parts of the fracture plane and the normal stress acting on the fracture was greater than 10 MPa, *i.e.* well above the highest normal stresses applied the laboratory tests by /Olsson 1998/. This suggests that the increase in relative transmissivity would be less than two orders of magnitude.

/Hökmark et al. 2006/ estimated that within a distance of 2 m from the tunnel openings, the relative transmissivity may increase by up to two orders of magnitude. Elsewhere, no changes were predicted. These transmissivity changes apply for the construction and operational phase and for the initial temperate phase. /Hökmark et al. 2006/ suggested that they are also applicable for the glacial phase, although this has to be verified for the proposed reference glacial cycle. A summary of the main findings are provided in Figure 8-3.

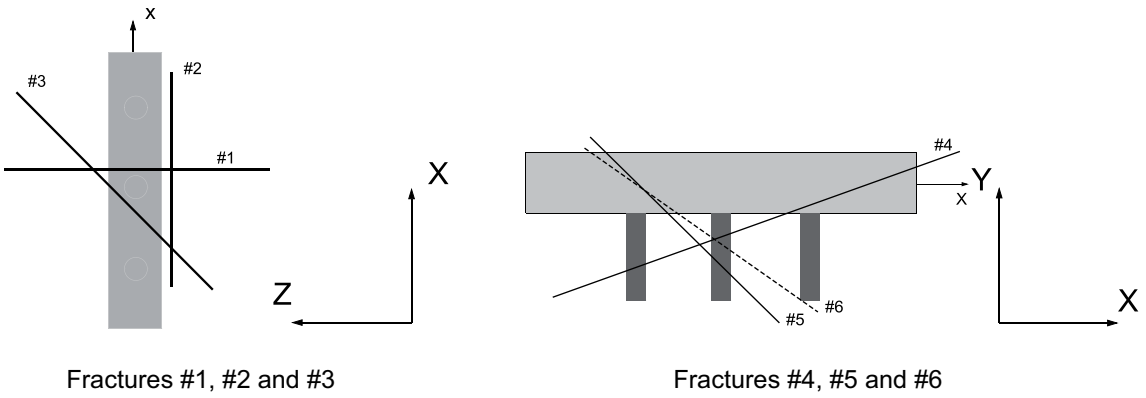

Figure 8-1. *Fracture orientations used in THM modelling for SR-Can (note that y is vertical), from /Hökmark et al. 2006/. Fractures #1–3 are vertical and intersect the tunnel as indicated in the left figure. Fractures #4–6 (right figure) are gently dipping. Fractures #4 and #5 strike normal to the tunnel and dip 20° and 45°, respectively. Fracture #6 strikes 45° relative to the tunnel and dips 45°.*

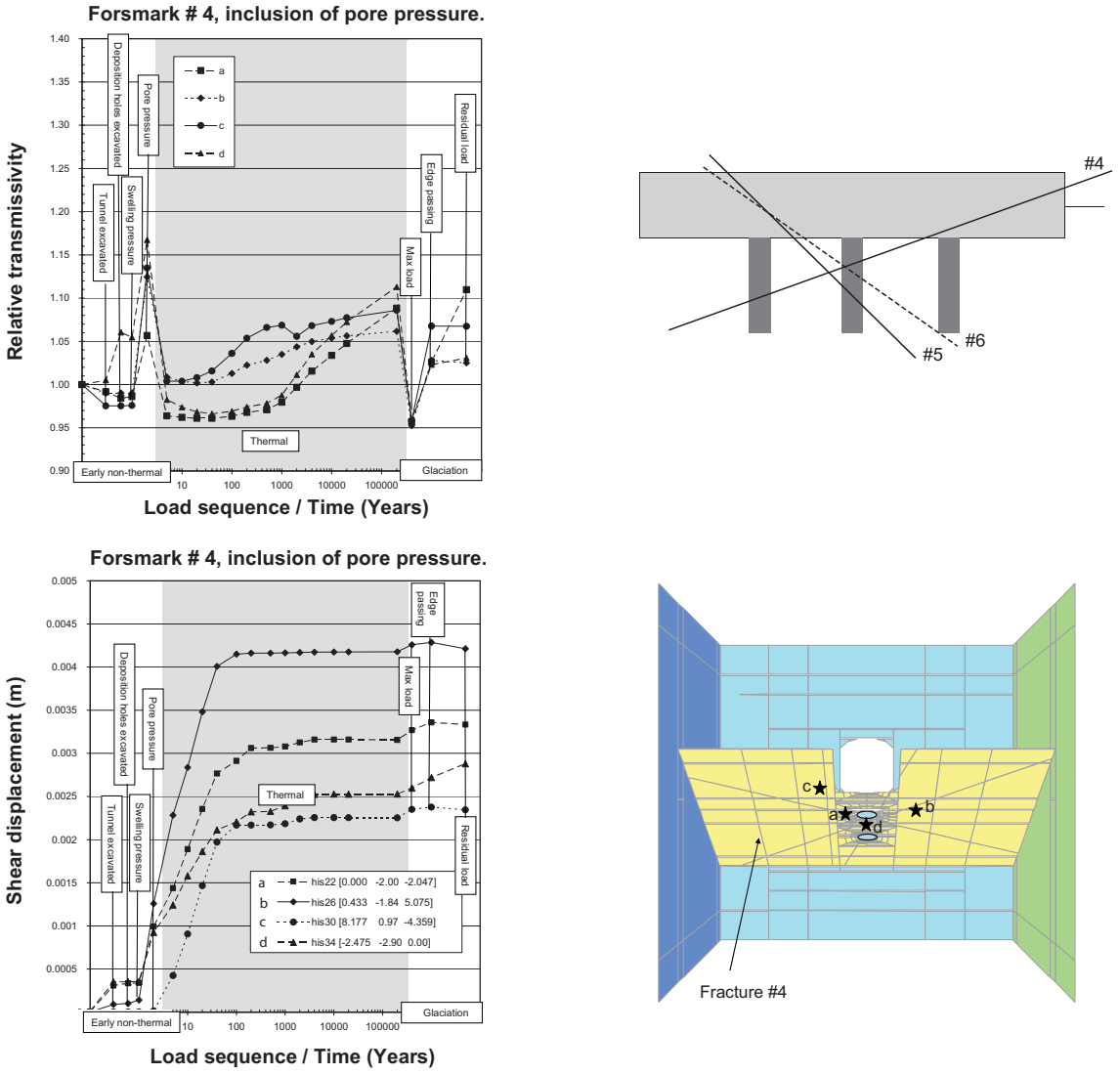

Figure 8-2. *Temporal development the relative transmissivity associated with variations in normal stress (upper left) and of the shear displacement (lower left) on fracture #4, from /Hökmark et al. 2006/.*

Fractures	Nr		Dip range	Strike range
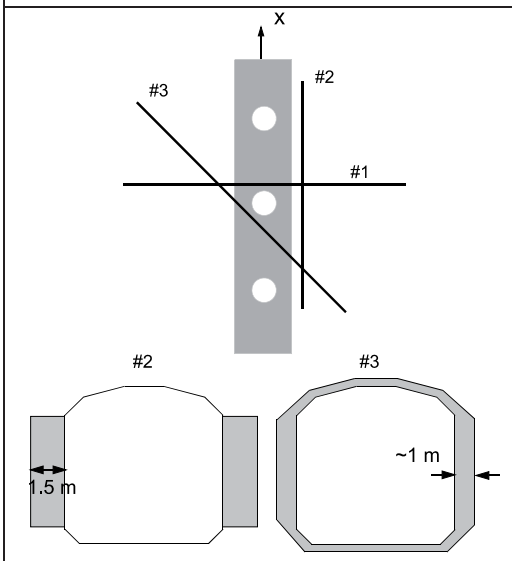	#1	No change in transmissivity	65-90	0±22.5, 180±22.5
	#2	Two orders of magnitude increase at the height section opposing the tunnel, no change elsewhere.	65-90	90±22.5, 270±22.5
	#3	Two orders of magnitude increase at up to 1 m distance from the tunnel periphery	65-90	45±22.5, 270±22.5
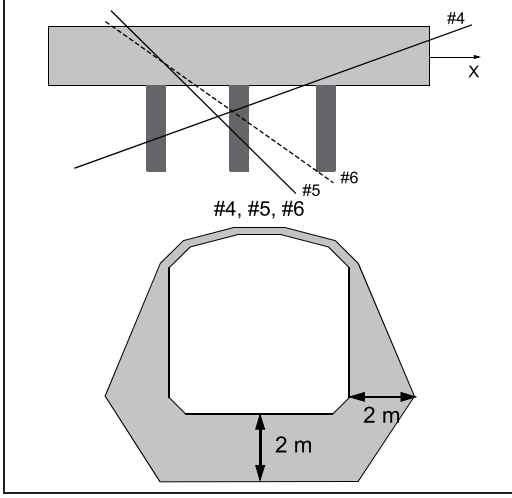	#4	Two orders of magnitude increase in region shown in left figure, no change elsewhere.	0 - 65	-
	#5	Two orders of magnitude increase in region shown in left figure, no change elsewhere	0 - 65	-
	#6	Two orders of magnitude increase in region shown in left figure, no change elsewhere	0 - 65	-

Figure 8-3. *Summary of transmissivity results from the near-field thermo-mechanical modelling for the safety assessment SR-Can, modified from /Hökmark et al. 2006/. Note that these estimates include transmissivity effects due to shearing. The grey shaded areas around the tunnel represent regions with increased transmissivity as given in the right column.*

8.2 Description of 3DEC models

8.2.1 Repository layout and model location

The medium-sized near-field models with fractures are located in fracture domain FFM01/rock domain RFM029 at Forsmark at the position marked Box C2 in Figure 8-4.

8.2.2 Model geometry and fracture orientations

An outline of the medium-sized near-field models is shown alongside a cross-sectional view of the deposition tunnel geometries in Figure 8-5. The medium-sized near-field models are 198 m (along tunnels), 200 m (across tunnels) and 200 m (vertically) and incorporate five tunnel segments of which the central tunnel is based on SKB's reference near-field design given in the **Underground openings construction report**. The other four tunnel segments are represented by circular cylinders

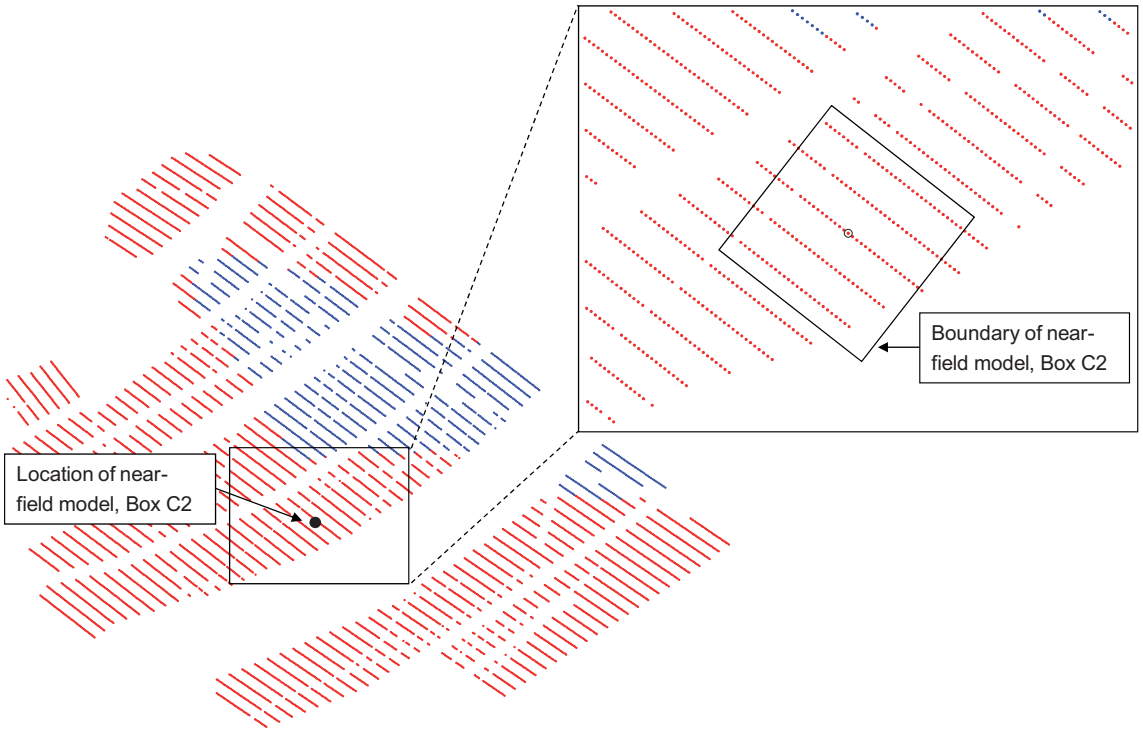

Figure 8-4. *Forsmark Layout D2 (version with 13% loss of canister positions) and location chosen for the medium-scale near-field field modelling (Box C2). Red colour represents 6 m canister spacing (coincides with rock domain RFM029 and fracture domain FFM01) and blue colour represents 6.8 m canister spacing (coincides with rock domain RFM045 and fracture domain FFM06).*

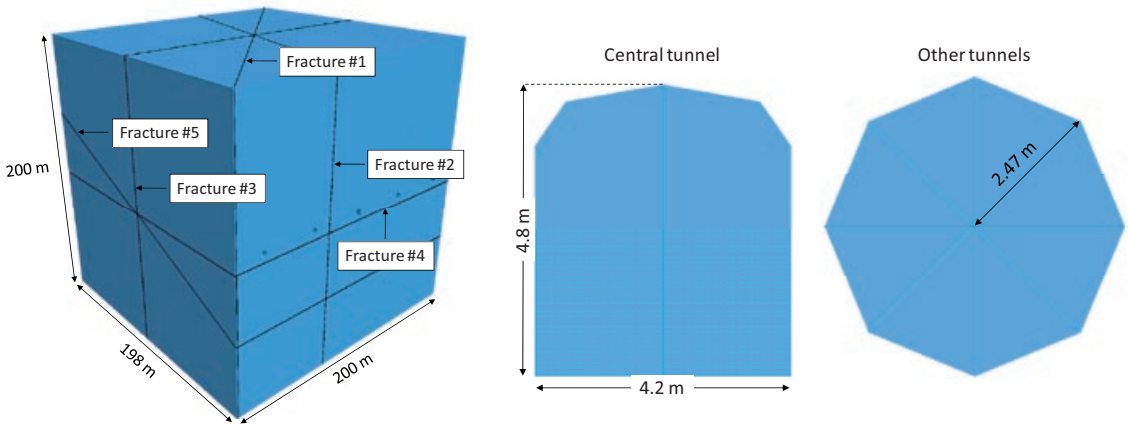

Figure 8-5. *Left: Outline of the medium-sized near-field models. Middle and right: Design of deposition tunnels.*

with the same cross-sectional area as the central tunnel (i.e. 19.2 m^2 /Lindman et al. 2007/). Note that deposition holes are not included here. The influence of the deposition holes on near-field fractures is an issue on a very small scale. Details in the induced loads and *in situ* stresses have changed since SR-Can. These changes have, however, smaller effects than the locations and orientations of the arbitrarily chosen fractures considered for the near-field modelling. The proximity to the repository openings and the geometry of the fracture system, *i.e.* the style of intersection with tunnels and deposition holes, are more important than the background stresses. Therefore, the issue of details in the near-field geometry, e.g. the impact of the deposition holes, is judged to be adequately covered in the SR-Can THM-analyses /Hökmark et al. 2006/, see subsection 8.1.1 for results examples.

The fracture system in the present modelling work is stylized with five explicitly modelled fractures with orientations based on site data /Fox et al. 2007/, cf. Figure 4-7. In the modelling work, all fractures are represented by circular, planar features with a radius of 50 m. There are two different models with fractures.

- **Model 1a** (Figure 8-6, upper) contains three vertical fractures (fractures no. 1–3) and one horizontal fracture (fracture no. 4). The centre points of the vertical fractures are located at the centre of the model, whereas the centre point of the horizontal fracture is located 3 m below the tunnel floor.
- **Model 2a** (Figure 8-6, lower) contains one fracture (fracture no. 5) specifically orientated such that the potential for shear failure is large. The centre point of the fracture is located 3 m below the tunnel floor.

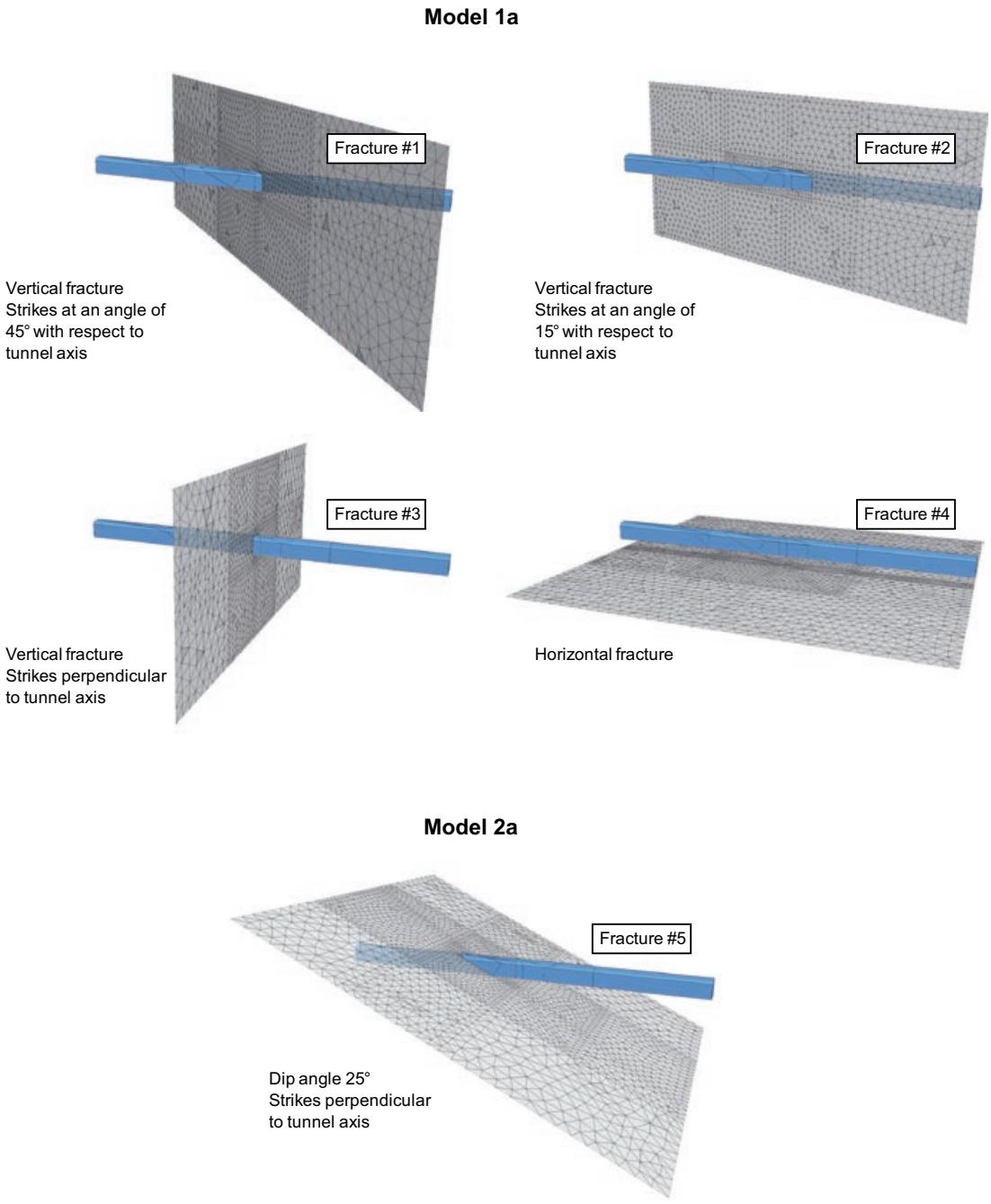

Figure 8-6. *Orientations of fractures in medium-sized near-field models for Forsmark.*

8.2.3 Input data

The properties of the fractures and rock mass are presented in Table 4-3 and Table 4-5 (fracture domain FFM01/ rock domain RFM029), respectively. Note that all modelled fractures extend to the model boundaries. Portions of each fracture located outside the 50 m radius are given fictitious properties with high strength in order to simulate elastic conditions, cf. Appendix F.

The reference *in situ* stress magnitudes and orientation (with respect to North) are used, cf. Table 4-2 (top row). At the location labelled Box C2, the tunnel axes deviate by 17° from the major horizontal *in situ* stress.

8.2.4 Calculation sequence

The models are analysed with regard to normal stress variations with accompanying transmissivity impact and shearing during the four repository phases:

- the operational phase (hydro-mechanical impact), *i.e.* excavation of deposition tunnels,
- the temperate phase (thermo-hydro-mechanical impact),
- the glacial phase (hydro-mechanical impact) and
- permafrost conditions (hydro-mechanical impact), cf. Appendix G.

Construction and operational phase

No thermal effects due to already placed fuel in other parts of the repository region are considered in any of the near-field models during the construction of the repository, *i.e.* the transition from *in situ* conditions to excavated state is assumed to take place in undisturbed rock. For the deposition sequence projected for the Forsmark site /Hansson et al. 2009/, this is a valid approach, cf. Chapter 6.

During *in situ* conditions and the subsequent excavation phase, the top and bottom of the models are locked in the vertical direction and all six boundaries are locked in the horizontal directions. The pore pressure is assumed to be that normally prevailing at repository depth (460 m), *i.e.* $\rho \cdot g \cdot z = 4.5$ MPa, and the pressure inside the tunnels is zero.

Temperate phase

The canisters are positioned according to Layout D2, cf. Figure 8-4, without considering any loss of canister positions, *i.e.* all available canister positions are assumed to be filled. At the location of the near-field model Box C2, the canister spacing is 6 m.

Similarly to the temperature calculations in Chapter 5, all canisters have an initial power of 1,700 W with power decay according to SKB's reference fuel /Hökmark et al. 2009/, cf. Figure 5-1 (left) and are deposited simultaneously. Furthermore, temperature effects due to mirror sources are not considered. This effect is minor and judged not to influence the results presented in the following sections, cf. Appendix F.

Figure 8-7 shows an example of the temperature distribution in a horizontal plane at canister mid-height after 100 years. The asymmetry of the temperature distribution is caused by the layout (cf. Figure 8-4), *i.e.* the positioning of the near-field model with respect to the deposition area and the lack of canister positions in the lower right corner and outside the upper left of the figure.

Displacement-type boundary conditions for the thermal phase are obtained from the large-scale models in Chapter 6 using mean values of the thermal, thermo-mechanical and mechanical properties in fracture domain FFM01, cf. Figure 6-15 (solid lines). After 100,000 years, the temperature at repository level is assumed to have returned to *in situ* conditions and the boundary displacements are assumed to be zero. As the *in situ* stresses are not perfectly aligned with the axes of the models roller boundaries are not appropriate. Therefore, a routine using the built-in programming language *FISH* /Itasca 2007/ has been developed that controls the horizontal displacement of each gridpoint on the vertical boundaries such that the thermal expansion and contraction of the box being modelled agree

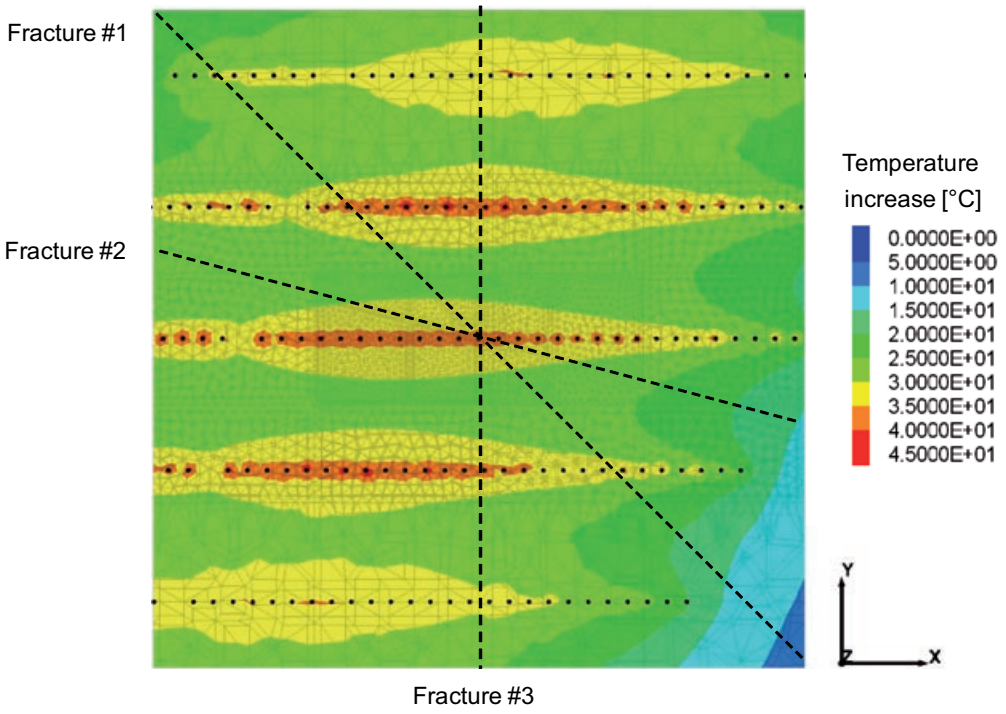

Figure 8-7. *Example of temperature distribution on a horizontal plane at canister mid-height after 100 years. Intersections of the three steeply dipping fractures with the plane are marked with dashed lines. Canister positions are marked with black circles (note that canisters located outside the model boundaries are hidden from view), cf. also Figure 8-4.*

with the results of the large-scale models. The scheme for controlling the boundary gridpoints does not move the model origin. It preserves the right angles at the model corners and the planar shape of the boundaries.

The pore pressure during the temperate phase is assumed to be the same as during the constructional and operational phase, *i.e.* 4.5 MPa, and the pressure inside the tunnels is zero.

Glacial phase

After the temperate phase, the boundary conditions are changed to roller boundaries and the models are cycled to equilibrium. Note that no residual thermal effects from the decaying nuclear fuel or other temperature variations (*e.g.* permafrost) are considered during the glacial phase. The additional horizontal stress reduction due to the presence of permafrost can be shown to have only a marginal effect on stress induced transmissivities and shear displacements, cf. Appendix G. Thereafter, the tunnel pressure is increased to 1 MPa and the model is again cycled to equilibrium in preparation for the glacial phase.

Stress boundary conditions for the glacial phase are provided in Figure 4-13. Here, the principal stress components are assumed to be aligned with the model axes at all times, i.e. σ_H is aligned with the tunnel axis. Although this is strictly not the case, the errors associated with this approximation are judged to be small, cf. Appendix F.

Two assumptions are made regarding the magnitude of the excess pore pressure, cf. Figure 7-4:

1. It is assumed to be about 98% of the glacially induced vertical load at all times.
2. It is assumed to be about 98% of the glacially induced vertical load as the ice covers the site (at 12 ka and 54.5 ka), 0.74 MPa as the edge is passing at 15 ka, about 3.3 MPa in combination with proglacial permafrost (39 ka) and 1.11 MPa as the edge is passing at 58 ka.

8.3 Stress-induced transmissivity changes

Figure 8-8 shows the stress-transmissivity models described in Section 4.7 normalised to the *in situ* effective normal stress of each fracture in the near-field models. On the steeply dipping fractures (fractures no. 1, 2 and 3) an increase in relative transmissivity by one order of magnitude would require a reduction in effective normal stress to below about 2–4 MPa (model A). For the gently dipping fracture no. 5, a corresponding increase in relative transmissivity would require a reduction in effective normal stress to below about 1 MPa. The maximum increase in relative transmissivity on fracture no. 4 is a factor approximately 6.5 for zero normal stress. Stress-transmissivity model B does not result in increases in relative transmissivity above a factor 4.5.

Fracture 1, which is the second highest in compression initially, has an *in situ* effective normal stress of about 21.5 MPa. At the monitored points shown in Figure 8-9, the largest reductions in effective normal stress occur during the two glacial maxima (12 ka and 54.5 ka). At points where the effective normal stress is (close to) zero, the relative transmissivity increases by a factor 23 (transmissivity model A) or by a factor 4 (transmissivity model B). Figure 8-10 (left column) shows a projection of the effective normal stress onto the vertical plane perpendicular to the deposition tunnel after excavation, 100 years of heating, during the first glacial maximum (12 ka) and during the forebulge in combination with high pore pressures due to permafrost (39 ka). In the right column of the figure estimates of the relative transmissivity are given using the stress-transmissivity relation (A) shown in Figure 8-8.

Fracture no. 2 deviates from the deposition tunnel axis by 15° and has the initially smallest effective normal stress (17.6 MPa) of the steeply dipping fractures considered here. At the monitored points shown in Figure 8-11, the largest reductions in effective normal stress occur during the two glacial maxima (12 ka and 54.5 ka). At points where the effective normal stress is (close to) zero, the relative transmissivity increases by a factor 20 (transmissivity model A) or by a factor 4 (transmissivity model B). Figure 8-12 (left column) shows a projection of the effective normal stress onto the vertical plane perpendicular to the deposition tunnel after excavation, 100 years of heating, during the first glacial maximum (12 ka) and during the forebulge in combination with high pore pressures due to permafrost (39 ka). In the right column of the figure estimates of the relative transmissivity are given using the stress-transmissivity relation (A) shown in Figure 8-8.

Fracture no. 3 strikes perpendicular to the deposition tunnel and has the highest effective normal stress (34 MPa) of the steeply dipping fractures considered here. Although there are stress reductions at points near the tunnel walls (point D), the fracture is in sufficiently high compressions that the resulting variations in relative transmissivity are only marginal. Figure 8-14 (left column) shows a projection of the effective normal stress onto the vertical plane perpendicular to the deposition tunnel after excavation, 100 years of heating, during the first glacial maximum (12 ka) and during the forebulge in combination with high pore pressures due to permafrost (39 ka). In the right column of the figure estimates of the relative transmissivity are given using the stress-transmissivity relation (A) shown in Figure 8-8.

Fracture no. 4 is horizontal with an initial effective normal stress of about 7.7 MPa. The maximum observed increase in relative transmissivity is a factor 6–7 (model A) or 2–3 (model B) and occurs during the two glacial maxima. The top row of Figure 8-16 shows the effective normal stress after excavation, 100 years of heating, during the first glacial maximum (12 ka) and during the forebulge in combination with high pore pressures due to permafrost (39 ka). In the bottom row of the figure estimates of the relative transmissivity are given using the stress-transmissivity relation (A) shown in Figure 8-8.

Fracture no. 5 dips 25° along the deposition tunnel and has an *in situ* effective normal stress of about 12.4 MPa. Figure 8-17 shows the temporal evolution of the effective normal stress and corresponding relative transmissivity at selected points on the fracture. At points located close to the tunnel roof or floor, there is a reduction in effective stress after excavation. During the two glacial maxima the effective stress at these points approaches zero, which corresponds to an increase in relative transmissivity by a factor 13 (transmissivity model A) or 3 (transmissivity model B). For points located approximately 10 m from the tunnel opening (points E and G) the maximum increase in relative transmissivity is a factor less than 2 (transmissivity model A). Figure 8-18 (left column) shows a projection of the effective normal stress onto the vertical plane perpendicular to the deposition tunnel after excavation, 100 years of heating, during the first glacial maximum (12 ka) and during the forebulge in combination with high pore pressures due to permafrost (39 ka). In the right column of the figure estimates of the relative transmissivity are given using the stress-transmissivity relation (A) shown in Figure 8-8.

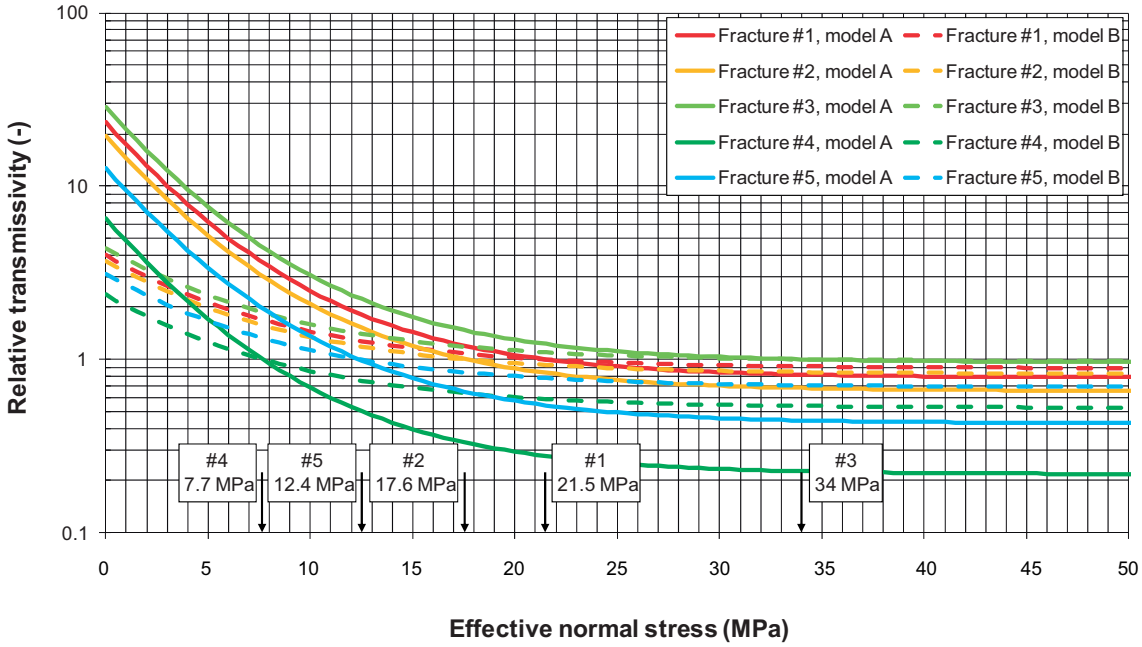

Figure 8-8. *Transmissivity models A and B (cf. Figure 4-9) normalised to the present-day in situ effective stress of each fracture in the near-field models.*

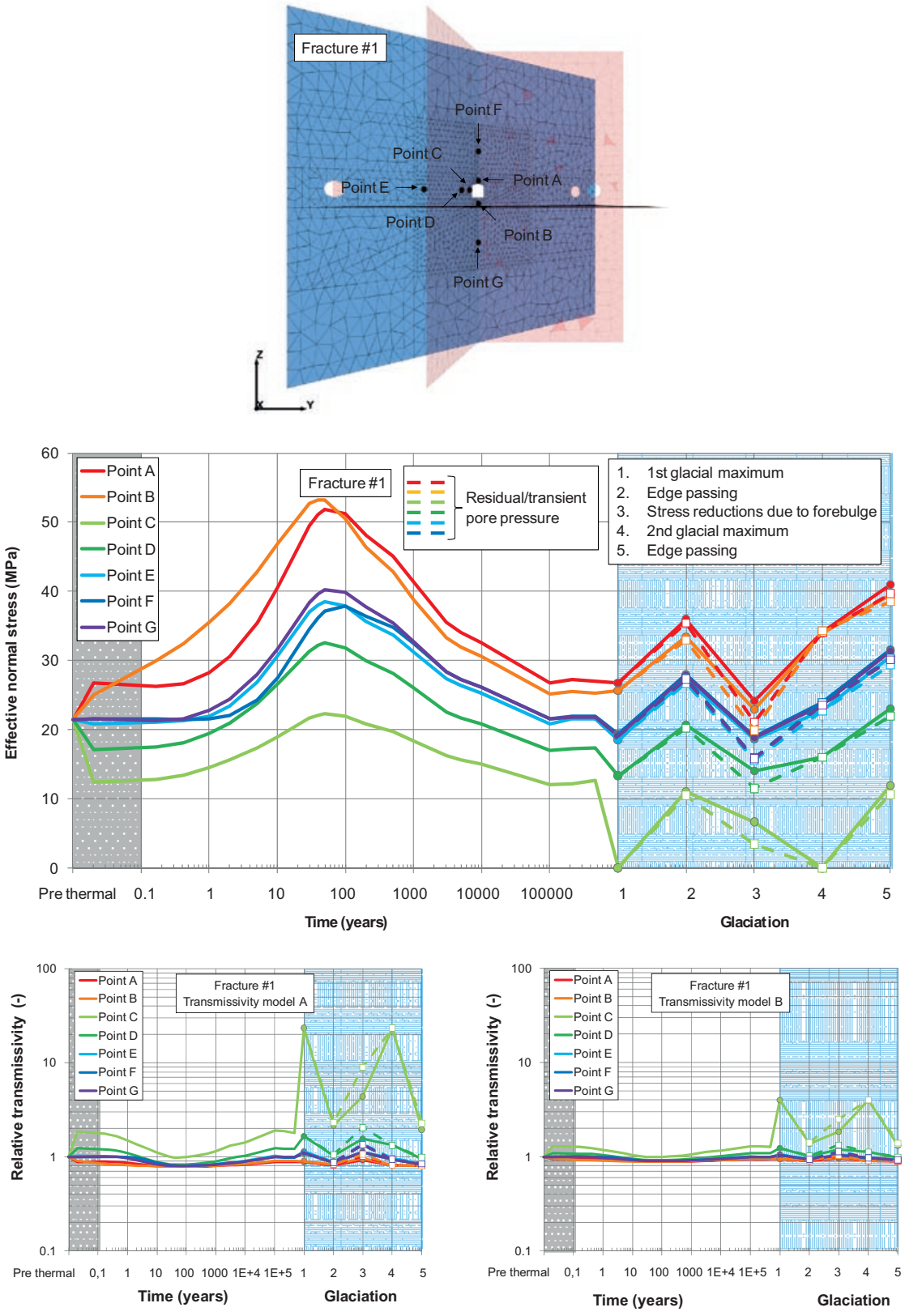

Figure 8-9. *Locations of history points on Fracture #1 (top). Temporal evolution of the normal stress at selected points (middle). Temporal evolution of the relative transmissivity based on the stress-transmissivity models in Figure 8-8 (bottom row). Grey and blue areas represent pre thermal time and glaciation, respectively.*

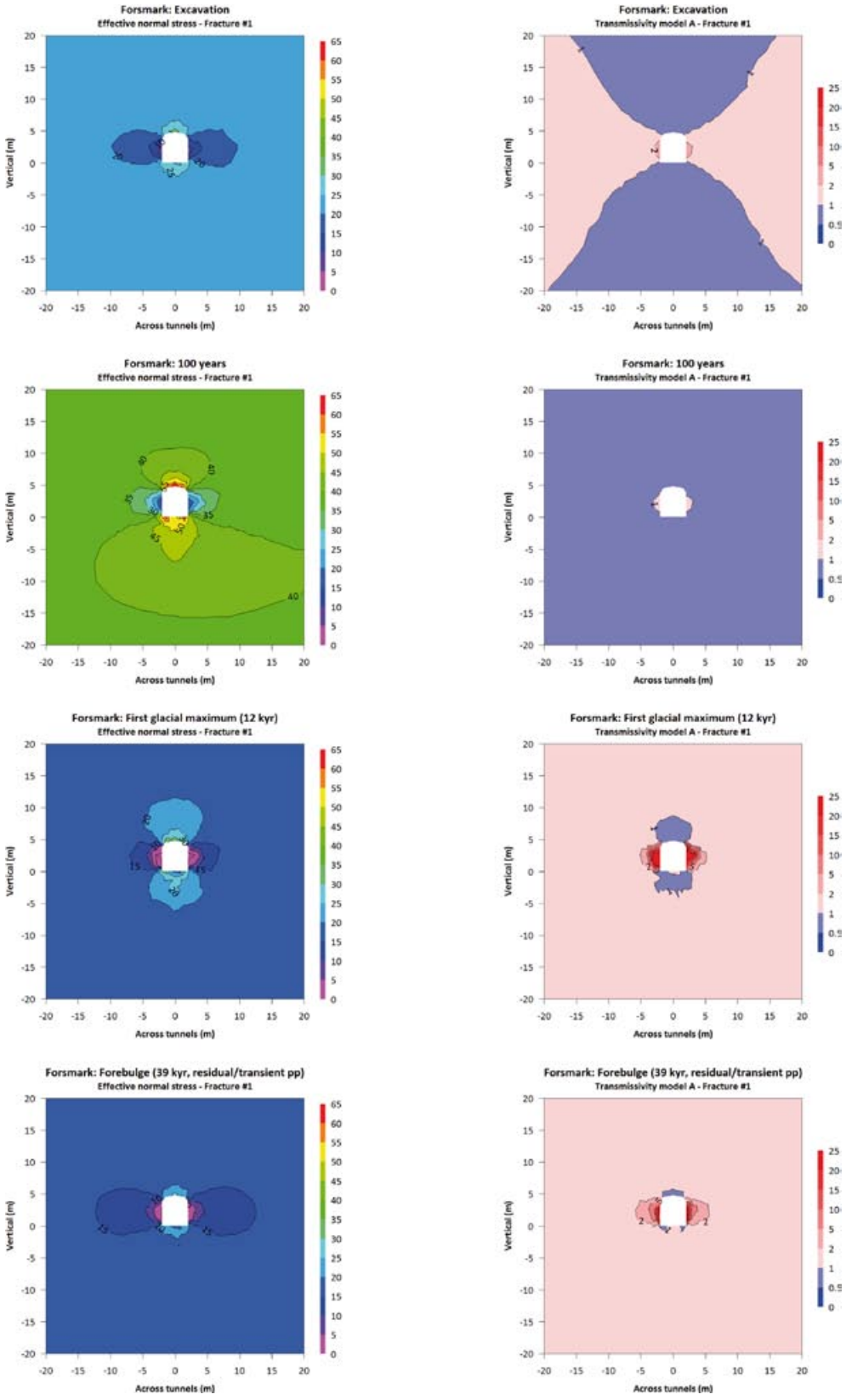

Figure 8-10. *Projection of the effective normal stress (left column) and corresponding relative transmissivity (right column) on fracture #1 onto the vertical plane perpendicular to the deposition tunnel at selected points in time. The asymmetry during the temperate phase (second row) is caused by the thermal load, cf. Figure 8-7.*

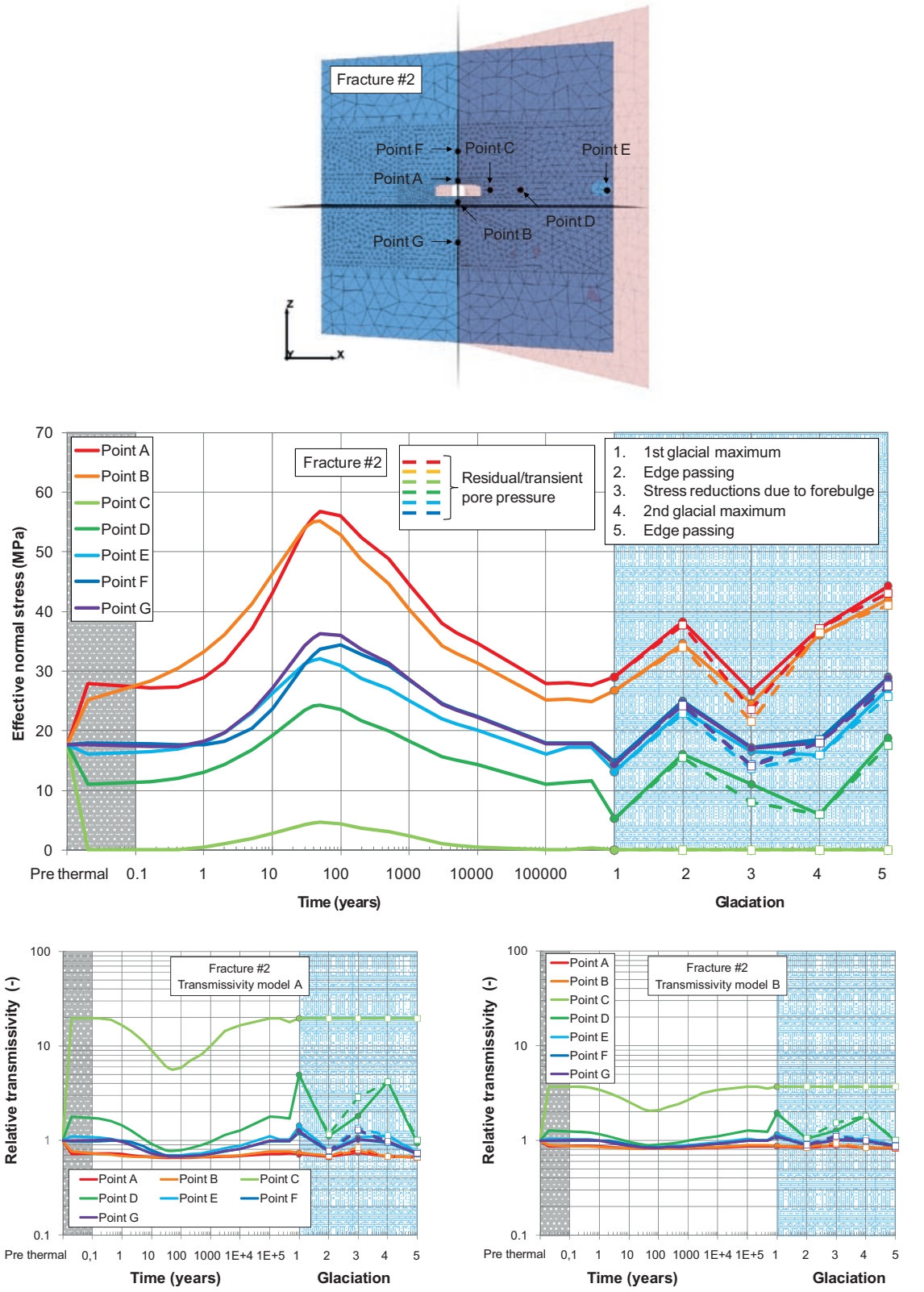

Figure 8-11. *Locations of history points on Fracture #2 (top). Temporal evolution of the normal stress at selected points (middle). Temporal evolution of the relative transmissivity based on the stress-transmissivity models in Figure 8-8 (bottom row). Grey and blue areas represent pre thermal time and glaciation, respectively.*

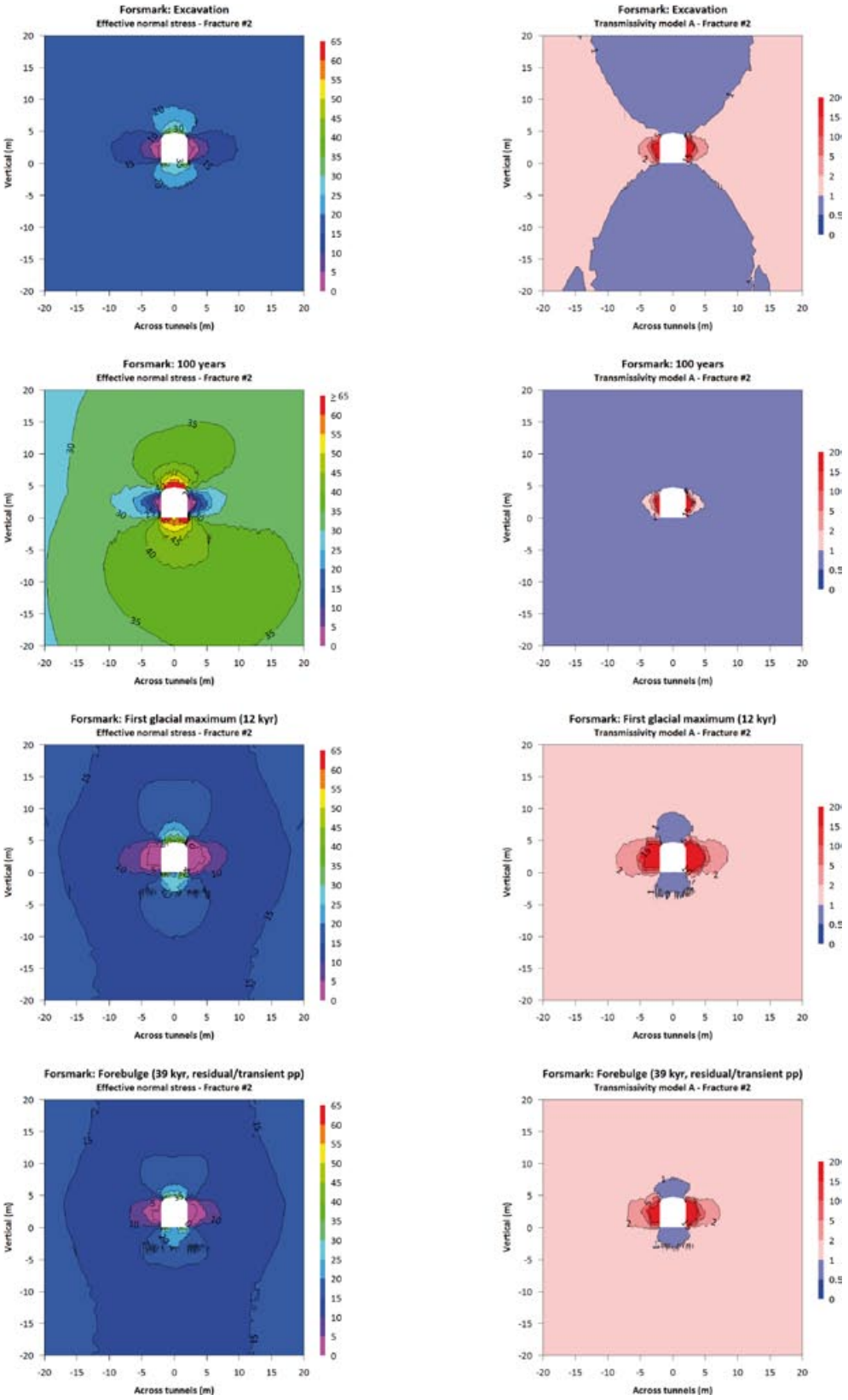

Figure 8-12. *Projection of the effective normal stress (left column) and corresponding relative transmissivity (right column) on fracture #2 onto the vertical plane perpendicular to the deposition tunnel at selected points in time. The asymmetry during the temperate phase (second row) is caused by the thermal load, cf. Figure 8-7.*

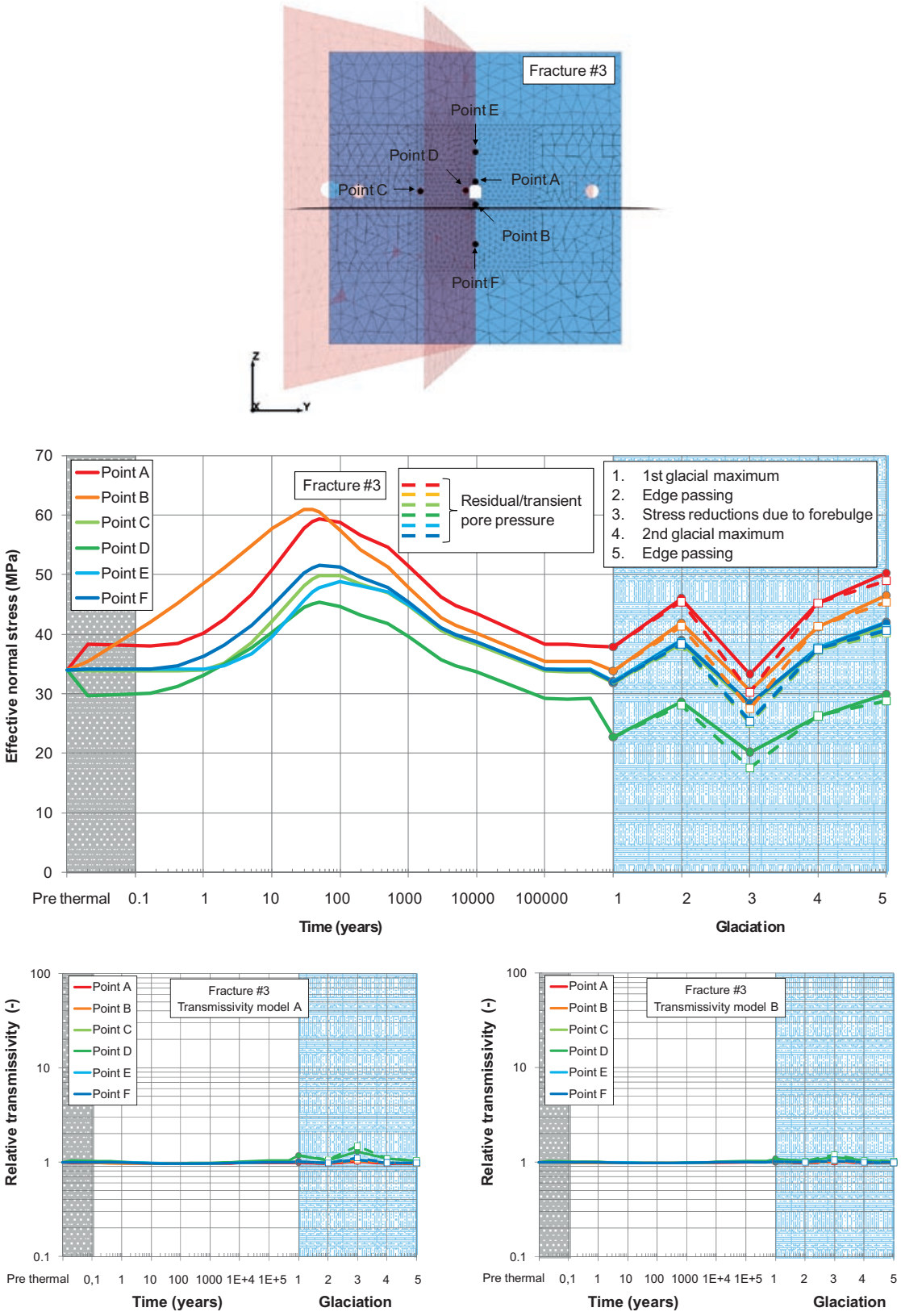

Figure 8-13. *Locations of history points on Fracture #3 (top). Temporal evolution of the normal stress at selected points (middle). Temporal evolution of the relative transmissivity based on the stress-transmissivity models in Figure 8-8 (bottom row). Grey and blue areas represent pre thermal time and glaciation, respectively.*

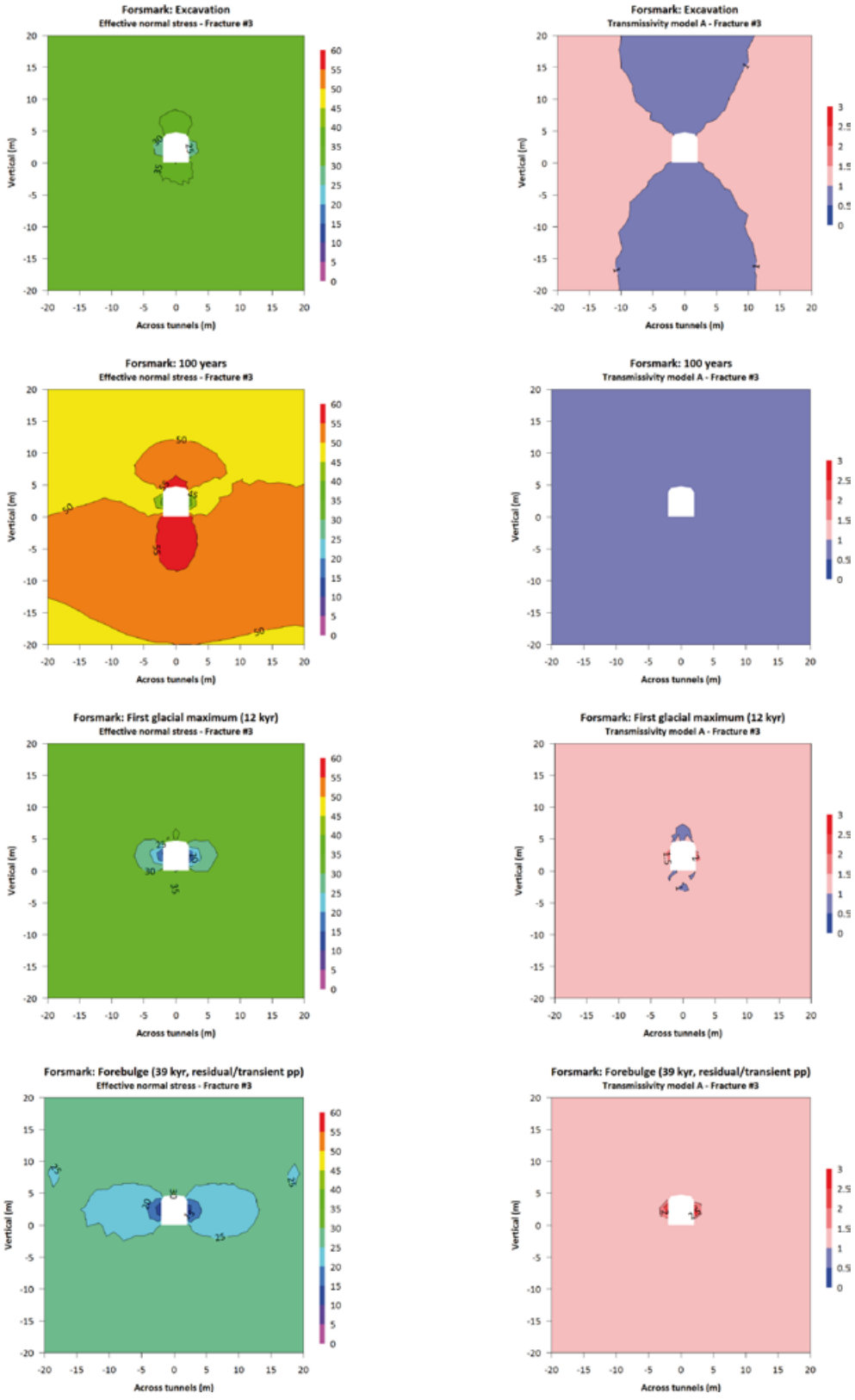

Figure 8-14. *Projection of the effective normal stress (left column) and corresponding relative transmissivity (right column) on fracture #3 onto the vertical plane perpendicular to the deposition tunnel at selected points in time. The asymmetry during the temperate phase (second row) is caused by the thermal load, cf. Figure 8-7.*

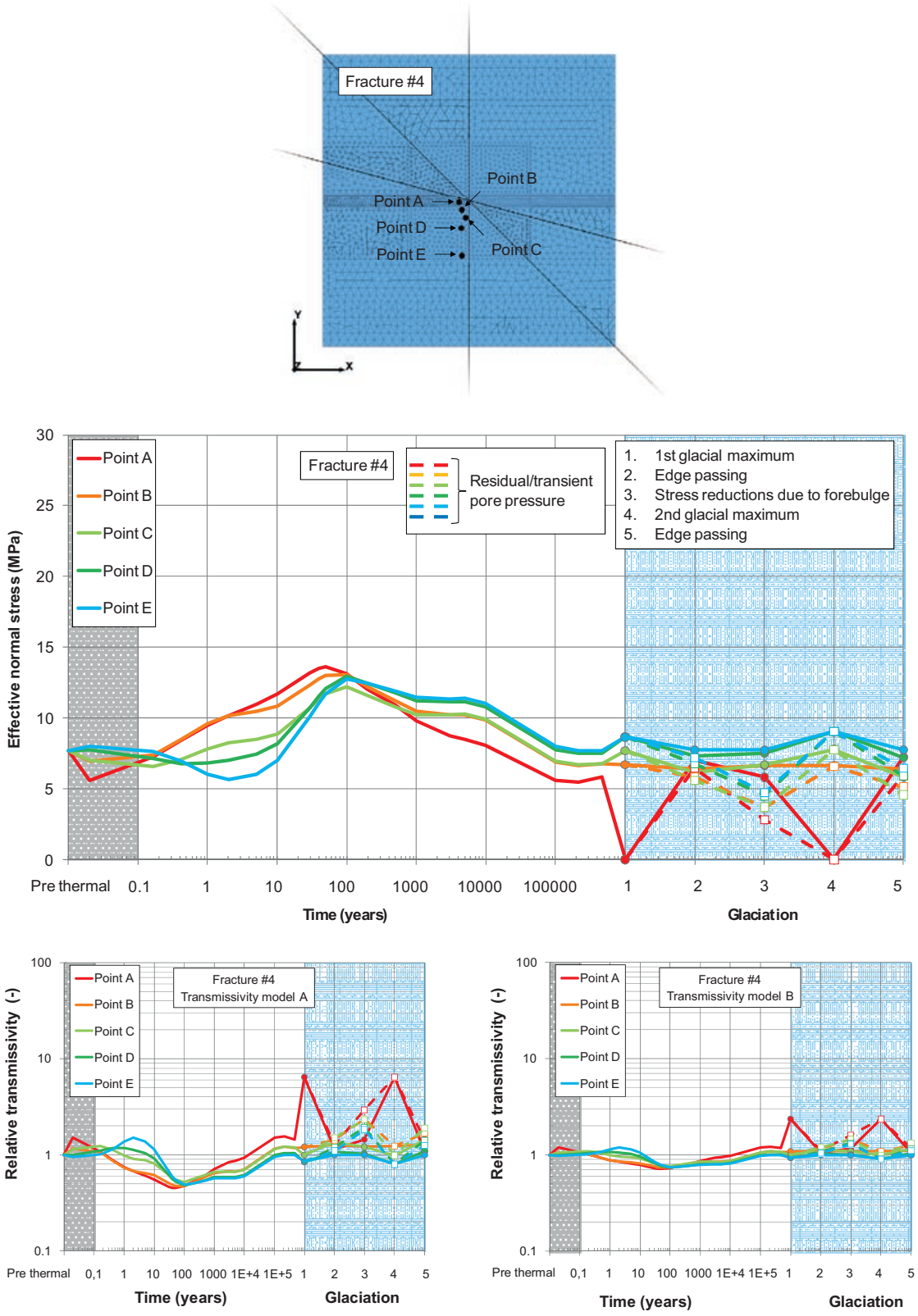

Figure 8-15. *Locations of history points on Fracture #4 (top). Middle: Temporal evolution of the normal stress at selected points (middle). Temporal evolution of the relative transmissivity based on the stress-transmissivity models in Figure 8-8 (bottom row). Grey and blue areas represent pre thermal time and glaciation, respectively.*

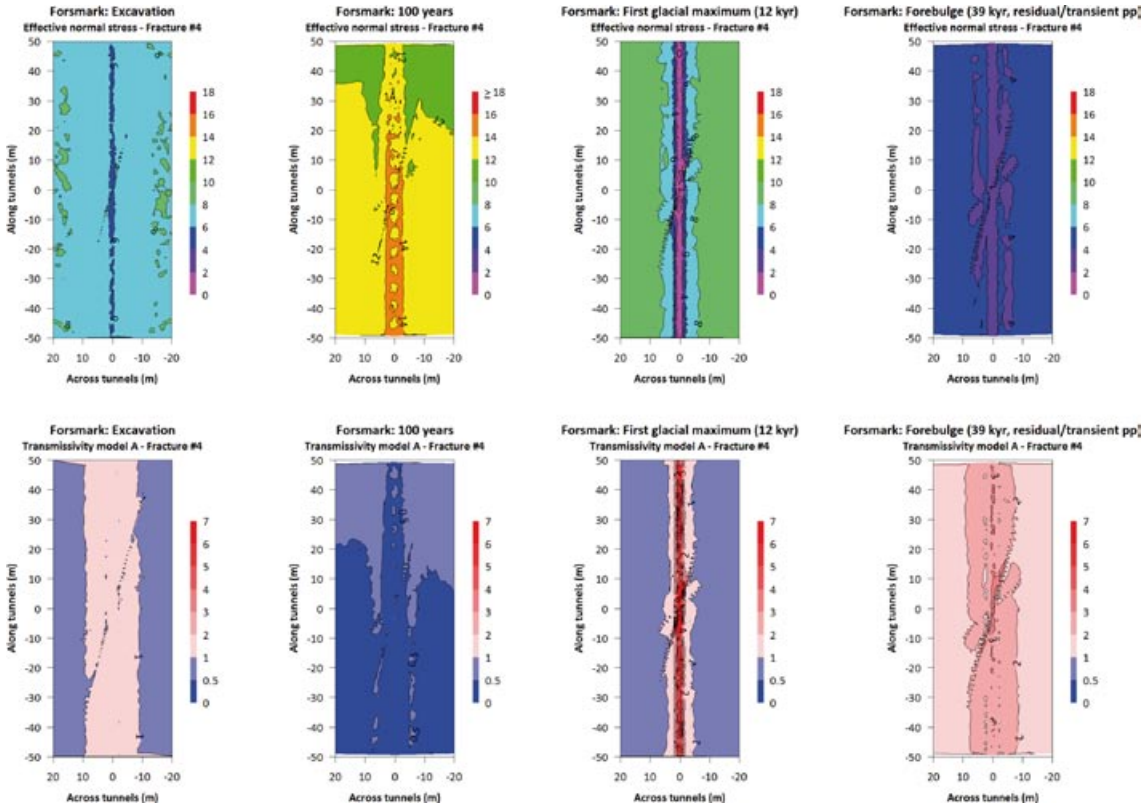

Figure 8-16. *Effective normal stress (top row) and corresponding relative transmissivity on fracture #4 at selected points in time. The asymmetry during the temperate phase (second column) is caused by the thermal load, cf. Figure 8-7.*

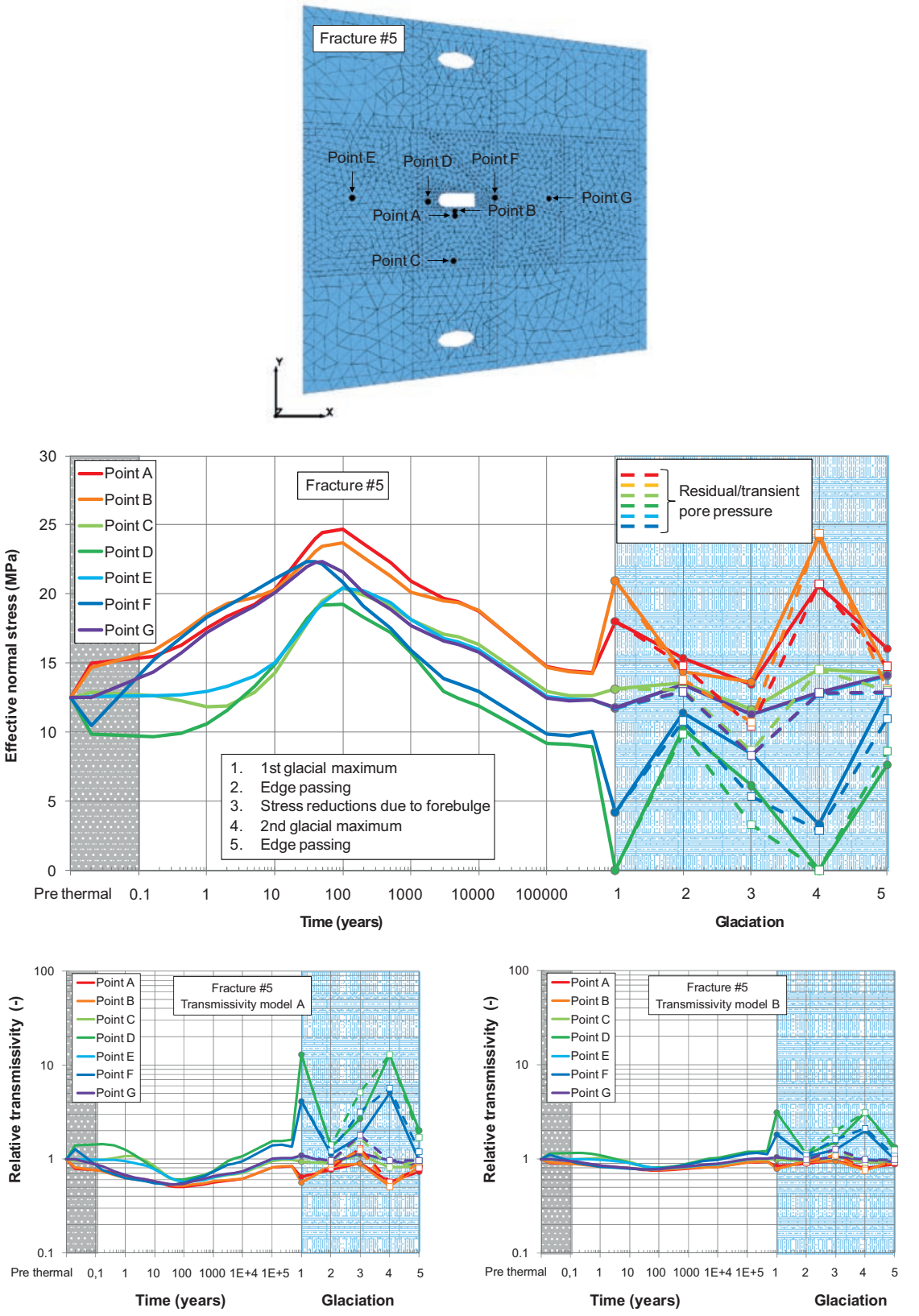

Figure 8-17. *Locations of history points on Fracture #5 (top). Temporal evolution of the normal stress at selected points (middle). Temporal evolution of the relative transmissivity based on the stress-transmissivity models in Figure 8-8 (bottom row). Grey and blue areas represent pre thermal time and glaciation, respectively.*

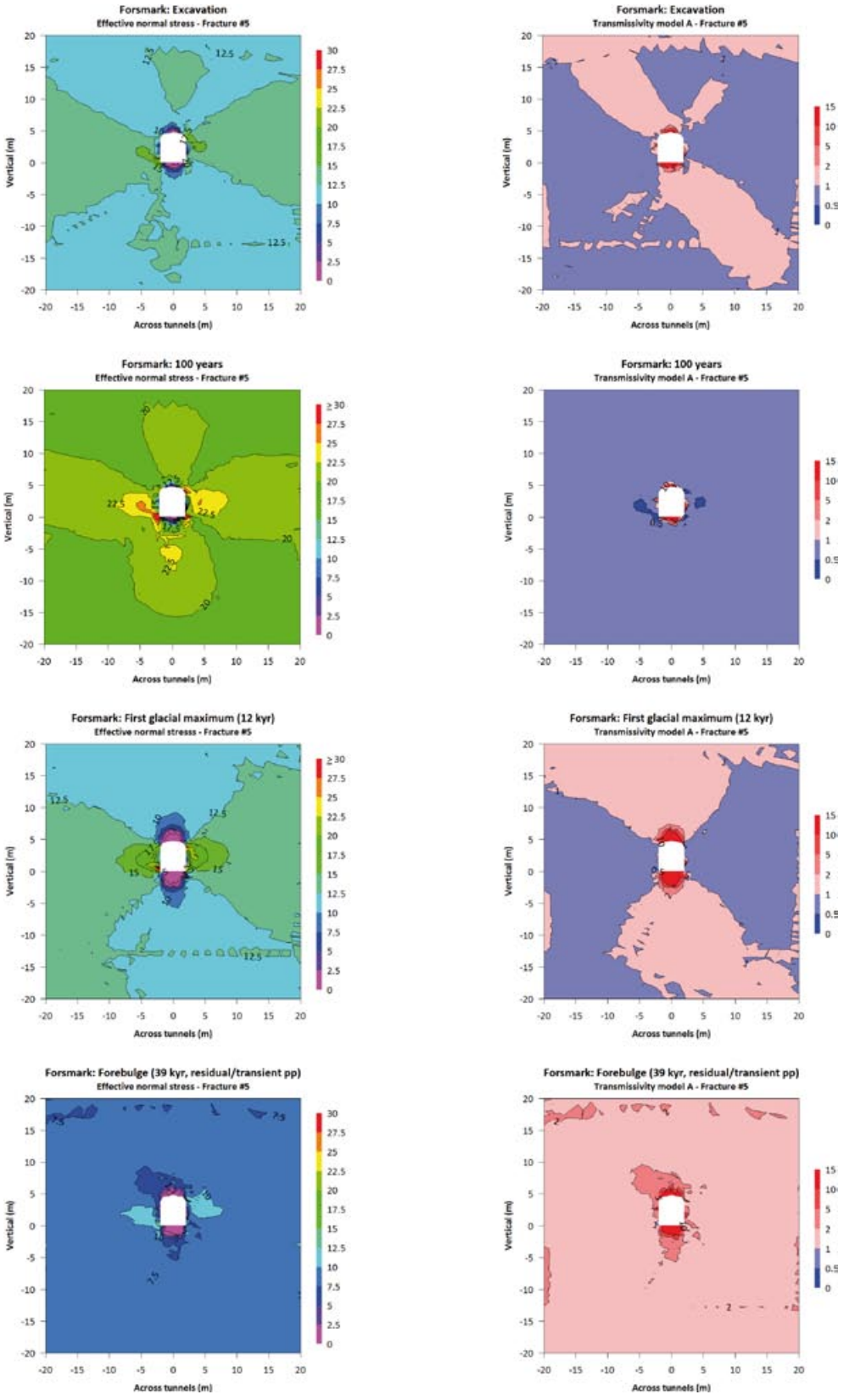

Figure 8-18. *Projection of the effective normal stress (left column) and corresponding relative transmissivity (right column) on fracture #5 onto the vertical plane perpendicular to the deposition tunnel at selected points in time.*

8.4 Shearing

The shear displacement on the vertical fractures is confined to a limited area close to the tunnel and is not sensitive to the pore pressure model during the glaciations, cf. Figure 8-19 and Figure 8-20. The maximum shear displacement on the vertical fractures #1 and #2 occur during the second glacial maximum and are of the order of 3.5–4 mm and 5–5.5 mm, respectively. The maximum shear displacement on fracture #3 is less than 0.1 mm at all times.

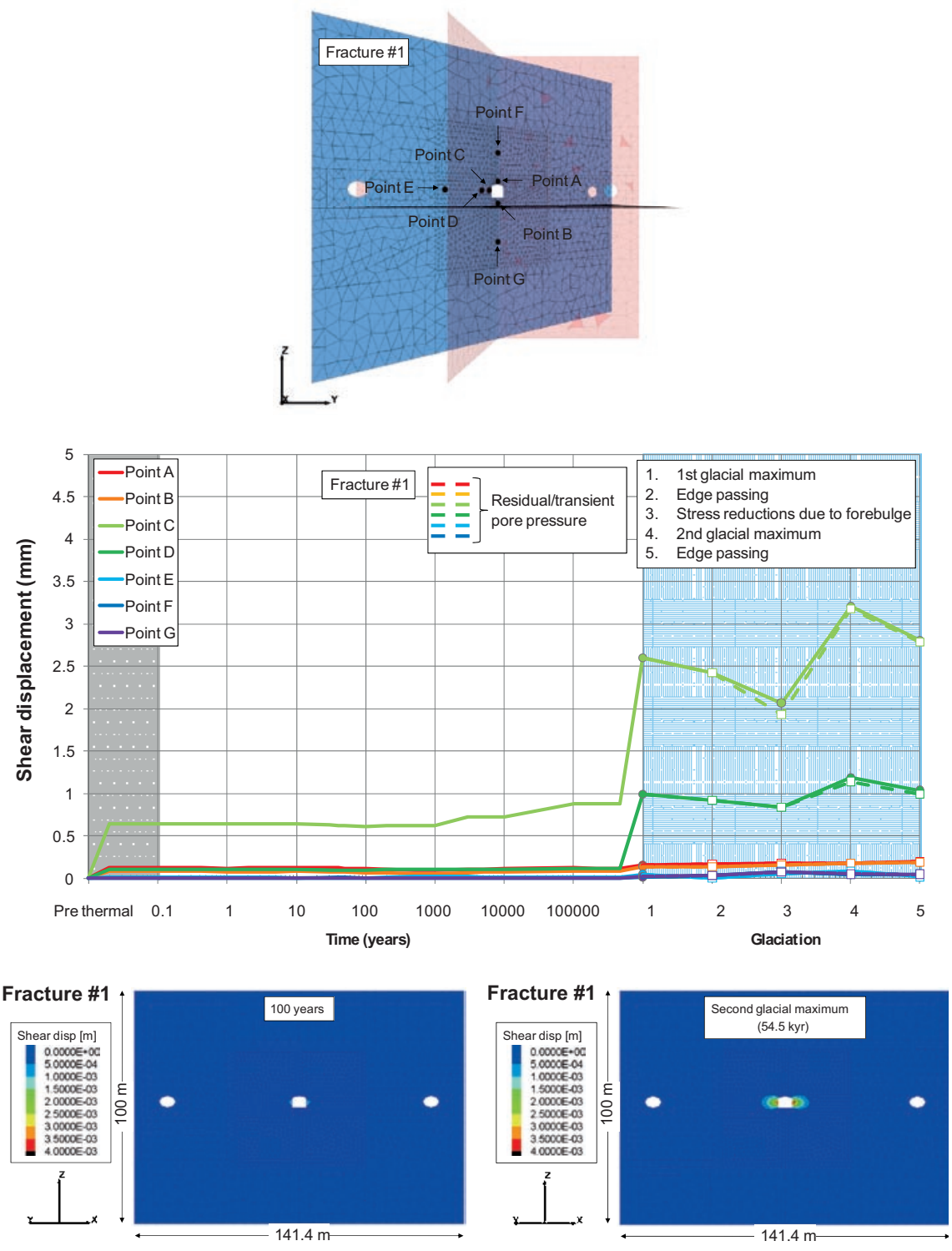

Figure 8-19. *Locations of history points on fracture #1 (top). Temporal evolution of the shear displacement at selected points (middle). Grey and blue areas represent pre thermal time and glaciation, respectively. Lower: Shear displacement after 100 years of heating (left) and during the second glacial maximum at 54.5 ka (right).*

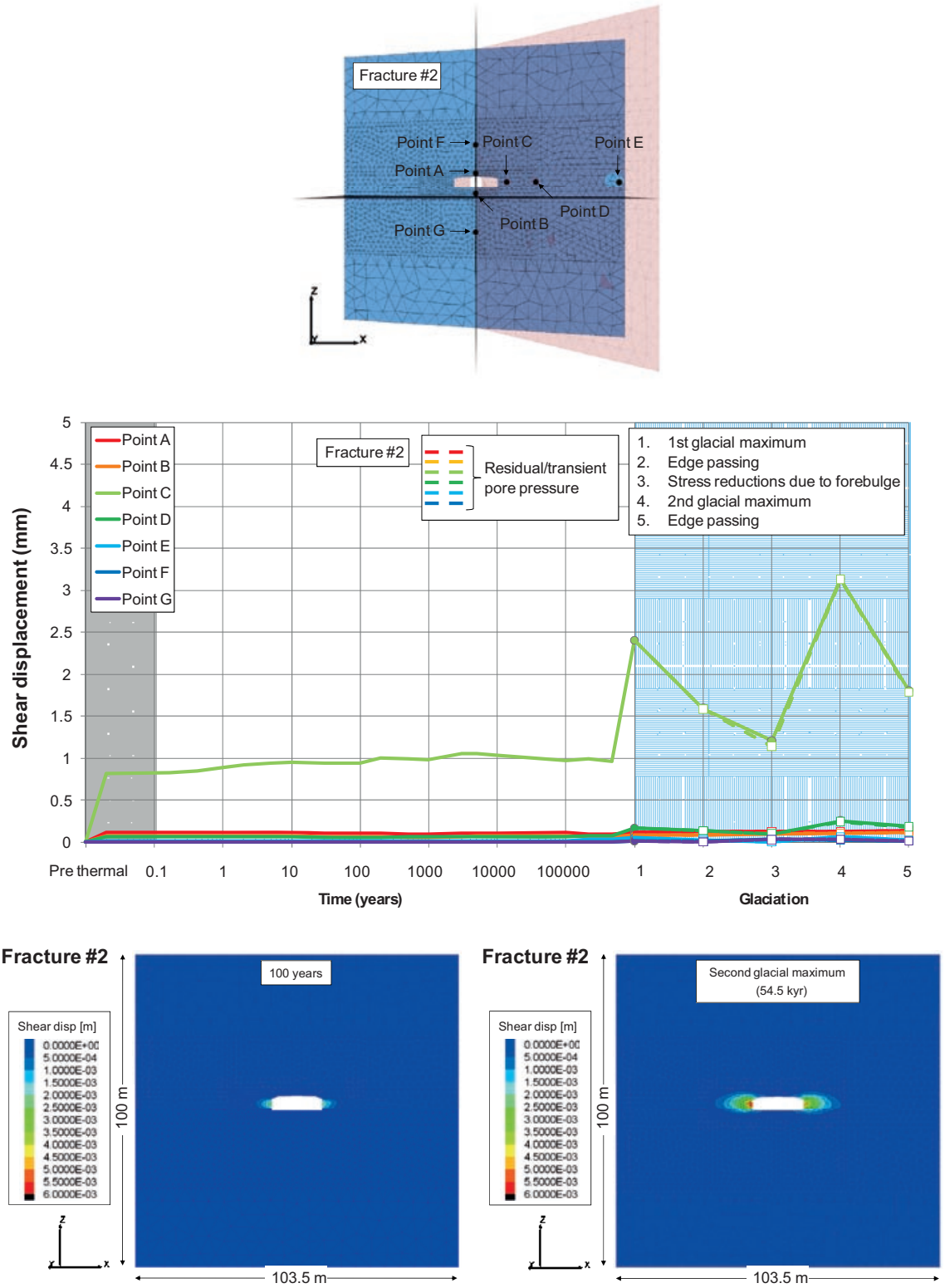

Figure 8-20. *Locations of history points on fracture #2 (top). Temporal evolution of the shear displacement at selected points (middle). Grey and blue areas represent pre thermal time and glaciation, respectively. Lower: Shear displacement after 100 years of heating (left) and during the second glacial maximum at 54.5 ka (right).*

The maximum shear displacement on the horizontal fracture #4 is less than 0.1 mm at the monitored points during the temperate phase, cf. Figure 8-21. During the glacial phase the maximum shear displacement increases to about 0.5–0.6 mm along the tunnel, cf. Figure 8-21 (lower)

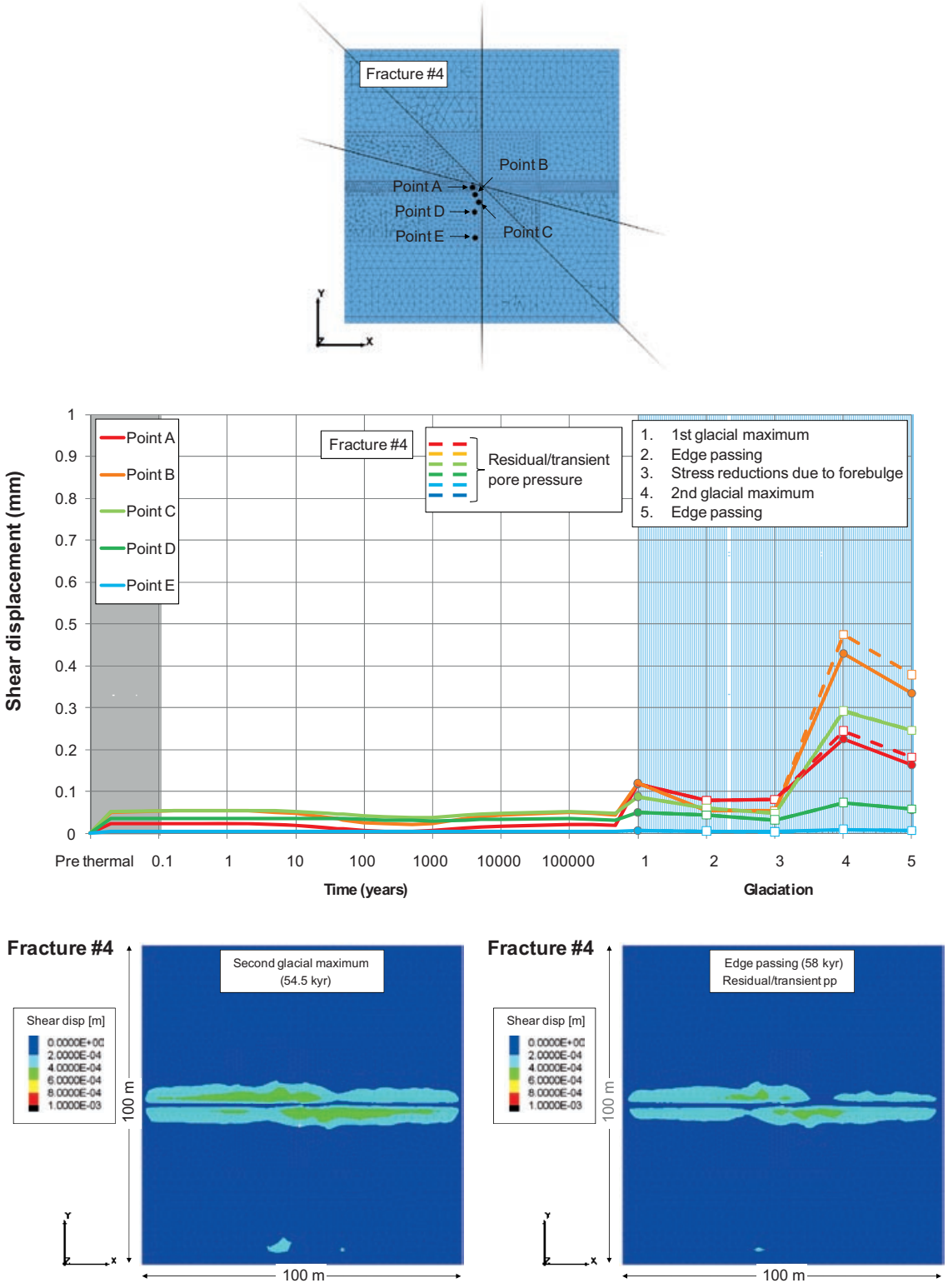

Figure 8-21. *Locations of history points on fracture #4 (top). Temporal evolution of the shear displacement at selected points (middle). Grey and blue areas represent pre thermal time and glaciation, respectively. Lower: Shear displacement during the second glacial maximum at 54.5 ka (left) and at the end of glaciation with residual pore pressure (right).*

At the monitored points on fracture #5 (Figure 8-22, middle), the maximum shear displacement at the end of the glaciation is about 7 mm when residual pore pressure is considered. Otherwise it is about 6.7 mm. The maximum shear displacement around the central tunnel is about 8–9 mm (when residual pore pressure is considered) and 7–8 mm otherwise, cf. Figure 8-22 (lower).

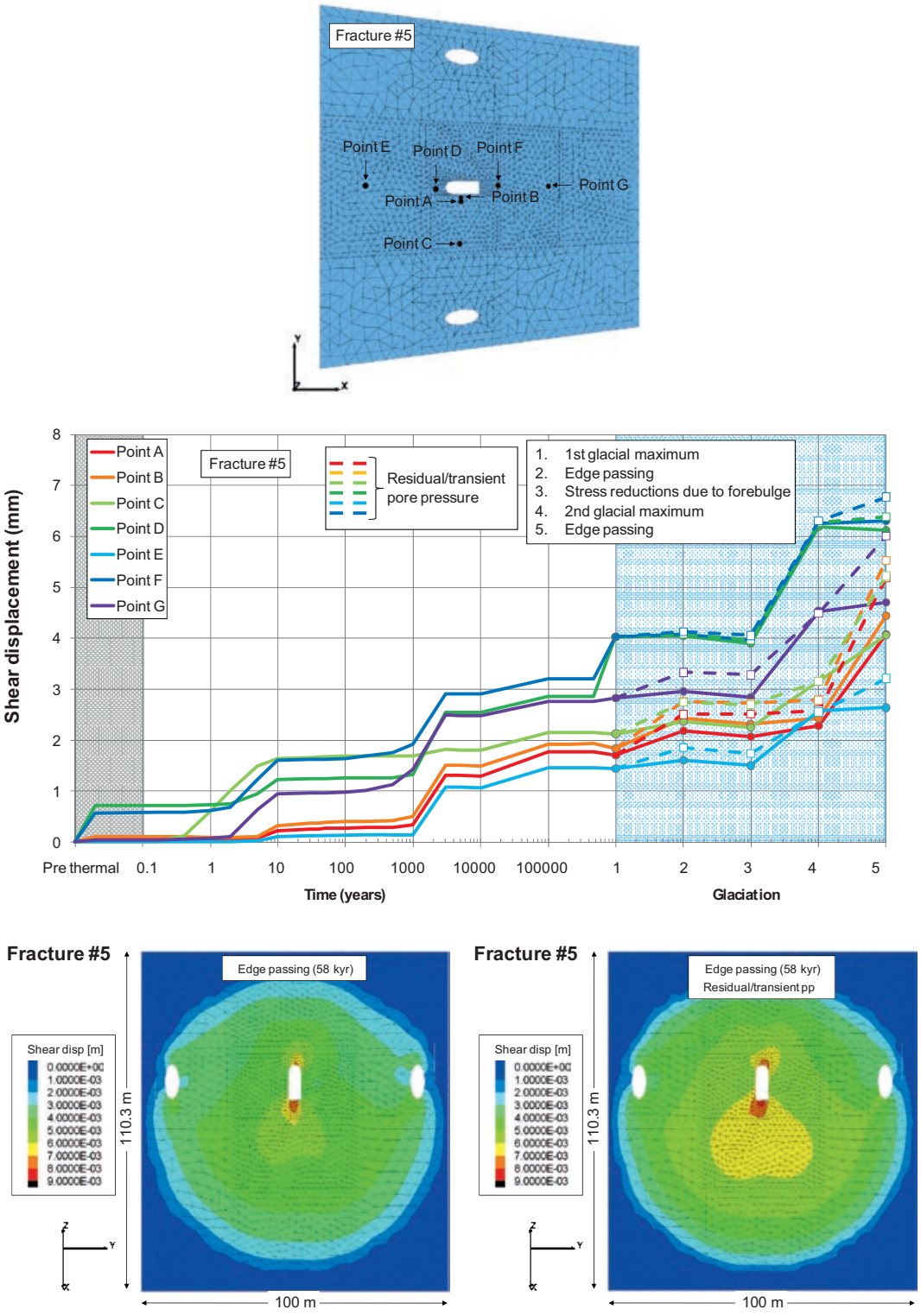

Figure 8-22. *Locations of history points on fracture #5 (top). Temporal evolution of the shear displacement at selected points (middle). Grey and blue areas represent pre thermal time and glaciation, respectively. Lower: Shear displacement at the end of glaciation without residual pore pressure (left) and with residual pore pressure (right).*

8.5 Summary

8.5.1 Excavation and operational phase

The range of the disturbance generated by the excavation is small enough that the results summarized in subsection 8.1.1 cover this phase. The results are independent of the size of the fractures that intersect the near-field.

8.5.2 Temperate phase

During the heated period of the temperate phase, the compression increases for almost all fractures, possibly with exception for portions that are directly affected by the proximity to the repository openings. This issue is adequately covered by the SR-Can analyses summarized in subsection 8.1.1. For horizontal fractures there is a modest loss of compression between tunnels in the early stages of the heated period. It can therefore be concluded that transmissivity changes caused by normal stress variations during the heated period do not require any detailing other than that provided in subsection 8.1.1 for the near-field. At some distance from the repository openings, the transmissivity changes agree well with corresponding results presented for the large scale, cf. Chapter 6.

Fracture shear displacements on the larger fractures considered here are only locally affected by proximity to the repository openings, i.e. in the same way as the smaller fractures considered in SR-Can analyses. At some distance from the openings, the size of the fracture determines the magnitude of the shear displacements. Note that the result obtained here for the worst oriented fracture (Fracture #5) agrees well with the results obtained for similarly oriented fractures intersecting the heated areas in the large-scale models (cf. Figure 6-28).

8.5.3 Glacial phase

During the glacial phase, the magnitude of the glacially induced pore pressure is decisive of the potential for increased fracture instability or increased transmissivity. With the exception of the time-period leading up to a glaciation during which the crustal flexure tends to reduce the horizontal stresses, cf. e.g. Figure 7-3 (left), the compression of the rock increases.

Fracture stability

For steeply dipping fractures, the choice of pore pressure model (either 98% of the local vertical load or with additional residual or permafrost induced excess pore pressures) does not have any significant impact on the potential for shearing, cf. Figure 8-19 and Figure 8-20. Instead, the proximity to the tunnel openings determines the magnitude of the shear displacement.

- Shear displacements of the order of 3.5–4 mm were found close to the tunnel opening on the fracture striking the deposition tunnel at an angle of 45° (fracture #1). At a perpendicular distance of around 4 m from the tunnel opening the shear displacement is less than 1 mm.
- Shear displacements of the order of 5–5.5 mm were found close to the tunnel opening on the fracture striking the deposition tunnel at an angle of 15° (fracture #2). At a perpendicular distance of around 2.5 m from the tunnel opening the shear displacement was less than 1 mm.
- No or only insignificant slip movements were observed on the vertical fracture striking perpendicular to the deposition tunnel (fracture #3).

For horizontal fractures, none of the load scenarios will induce anything but marginal shear stresses. On the horizontal fracture (#4), the maximum shear displacement was in the range 0.5–0.6 mm.

For gently dipping fractures, the stability margin is smaller and the choice of pore pressure model is of greater importance, cf. Figure 8-22.

- The orientation of fracture #5 (dipping 25° along the deposition tunnel) was specifically chosen such that the potential instability would be large. Depending on whether residual pore pressure was considered during episodes of glacial retreat or not, the largest observed shear displacement was around 7–8 mm (no residual pore pressure) or 8–9 mm (1.1 MPa residual pore pressure). Similarly to the results obtained for the temperate phase, the glacially induced shear displacements agree well with the corresponding estimates made for similarly oriented fractures in Chapter 7 (cf. Figure 7-19, right).

- As opposed to the other fractures considered, the proximity to the tunnel is not decisive of the slip magnitude. Since the fracture is potentially unstable at all distances from the tunnel, the magnitude of the slip is determined by the fracture's size – here 50 m radius.

Transmissivity changes

Normal stress variations

The relative transmissivity results presented in the contour plots for the different fractures confirm in principle the result from SR-Can (Figure 8-3). Note, however, that the SR-Can results also include possible transmissivity effects of shear displacements.

- The changes in transmissivity are concentrated to a limited region around the tunnel. The size of the fracture is unimportant. If the fracture is almost parallel to the tunnel periphery, then the high-transmissivity part of the fracture may be large, i.e. extend along large distances of the tunnel. In this case, the size of the fracture will become important.
- At distances larger than approximately 2 m from the tunnel, there are only marginal changes in relative transmissivity.
- The two-order-magnitude increase suggested in the SR-Can estimates appear to be exaggerated. However, it should be noted that the stress-transmissivity relations become very uncertain as the effective normal stress approaches zero, e.g. when rock blocks are close to detach from the tunnel wall. Very close to the periphery of the tunnel, the normal stress could be low enough that, theoretically, the transmissivity increase could be even larger for fractures that are almost parallel to the tunnel axis. The details of the response of such fractures are likely to be influenced by the general properties of the EDZ and the irregular geometry of the rock wall/floor, see Section 6.5 of the **Data report**. In addition, effects due to shearing are not included in the transmissivity contour plots. Therefore, for representative fractures sub-parallel to the tunnel axis and located within the regions indicated in Figure 8-3, the two-order-of- magnitude estimate is judged to be relevant.

Shearing

As opposed to the SR-Can study, the fractures included here are significantly larger. Shear displacements that are not directly a result of the proximity to the openings, i.e. on gently dipping fractures, will depend on the size of the fracture. Also note that all shear displacements presented in the plots are total ones, i.e. accumulated over time.

- Even if the shear displacements are large for large (gently dipping) fractures, the effective normal stress is small only in a limited area around the tunnel opening. During periods of large shear displacements, the effective normal stress is higher than about 7.5 MPa at distances larger than about 5 m from the tunnel. This is well above the highest normal stresses applied in the lab-scale transmissivity tests performed by /Olsson 1998/. Therefore the additional increase in transmissivity caused by shearing is likely to be modest.

8.5.4 Concluding remarks

In summary, also when the additional transmissivity effects due to shearing are taken into account, the estimates made in SR-Can, i.e. an increase in relative transmissivity by about two orders or magnitude within a distance of 1–2 m from the tunnel openings and no change elsewhere (Figure 8-3), are still valid even though the fractures considered here are larger.

9 Assessment of spalling potential in the near-field

9.1 General

As part of the SR-Can safety assessment, /Hökmark et al. 2006/ and /Fälth and Hökmark 2007/ investigated the potential for stress induced spalling in the walls of deposition holes during the construction and operational phase and during the initial temperate phase at the Forsmark, Laxemar and Simpevarp repository sites.

In order to determine the effects of slipping fractures on the stresses around deposition holes, /Hökmark et al. 2006/ compared results from a linear elastic model with corresponding results from models with fractures. For the Forsmark site, /Hökmark et al. 2006/ found that slipping fractures reduced the maximum stress at deposition hole mid-height by up to 15% depending on friction. At positions 1 m below the tunnel floor there were stress reductions in the range 10–15% as well as increases in stress by up to 50%. However, /Hökmark et al. 2006/ concluded that structurally controlled stress concentrations should not be considered relevant for spalling risk estimates, which means that linear elastic models are relevant approximations.

Based on the findings by /Hökmark et al. 2006/, the results in the present study are obtained using linear elastic models. The potential for spalling, in the walls of deposition holes and in the deposition tunnel roof, is investigated during three of the repository phases considered here, cf. Section 2.2:

- the construction and operational phase (mechanical impact), *i.e.* excavation of tunnels and deposition holes,
- the temperate phase (thermo-mechanical impact),
- the glacial phase (mechanical impact).

9.2 Description of 3DEC models

9.2.1 Repository layout and model locations

The layout at Forsmark site (Layout D2, version with 13% loss of canister positions) is presented in Figure 9-1. The canisters are positioned 6 m (RFM029 and FFM01) or 6.8 m (RFM045 and FFM06) apart in parallel tunnels with a spacing of 40 m.

Six locations (cf. Figure 9-1) within the repository region have been selected for near-field thermo-mechanical modelling. Five models (labelled Box A1, B1, C2, D1 and D2) are located within fracture domain FFM01 and rock domain RFM029. These are analysed with respect to variations in tunnel orientation and overall position within repository region. One model (labelled Box C1) is located within fracture domain FFM06 and rock domain RFM045. In the following sections examples using models Box A1 (where the orientation of the major horizontal *in situ* stress deviates the most from the deposition tunnel axis) and B1 (where the major horizontal *in situ* stress is approximately aligned with the deposition tunnel) are presented. Details regarding the remaining near-field models are presented in Appendix H.

9.2.2 Model geometry

The design of tunnels and deposition holes is based on SKB's reference near-field design given in the **Underground openings construction report**, cf. Figure 9-2 (left). The deposition holes are designed with a cut-off wedge at the top for easier emplacement of the canisters.

The near-field models are linear elastic, excluding any fractures that may exist in the region, and incorporating a tunnel segment with seven canisters, three of which have explicitly modelled deposition holes. Each near-field model is 40 m (across tunnels) and 50 m (vertically). The dimension in the along-tunnel-direction is determined by the canister spacing, which varies between rock domains. A part of a tunnel segment is shown alongside cross-sectional views of the deposition holes in Figure 9-2 (right).

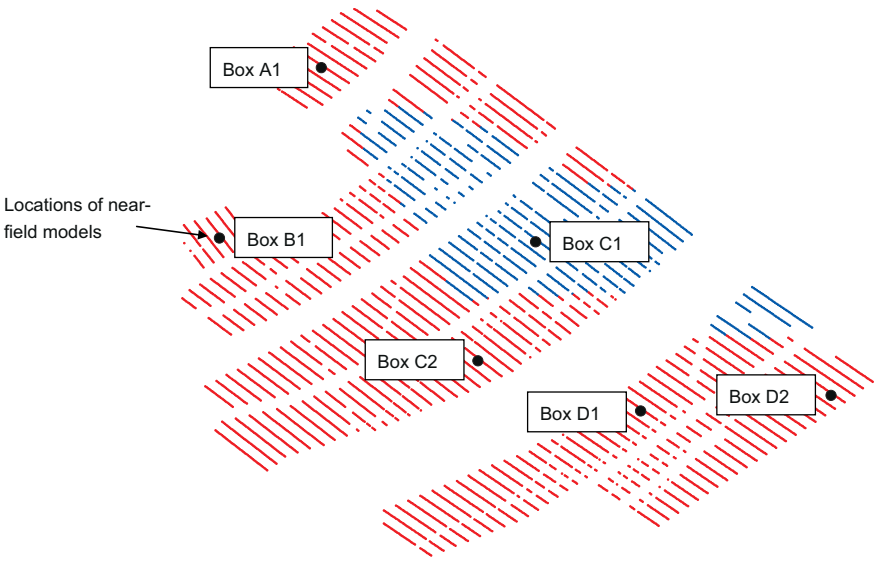

Figure 9-1. *Forsmark Layout D2 (version with 13% loss of canister positions) and locations of near-field models, cf. Section 4.3. Red colour represents 6 m canister spacing (coincides with rock domain RFM029 and fracture domain FFM01) and blue colour represents 6.8 m canister spacing (coincides with rock domain RFM045 and fracture domain FFM06).*

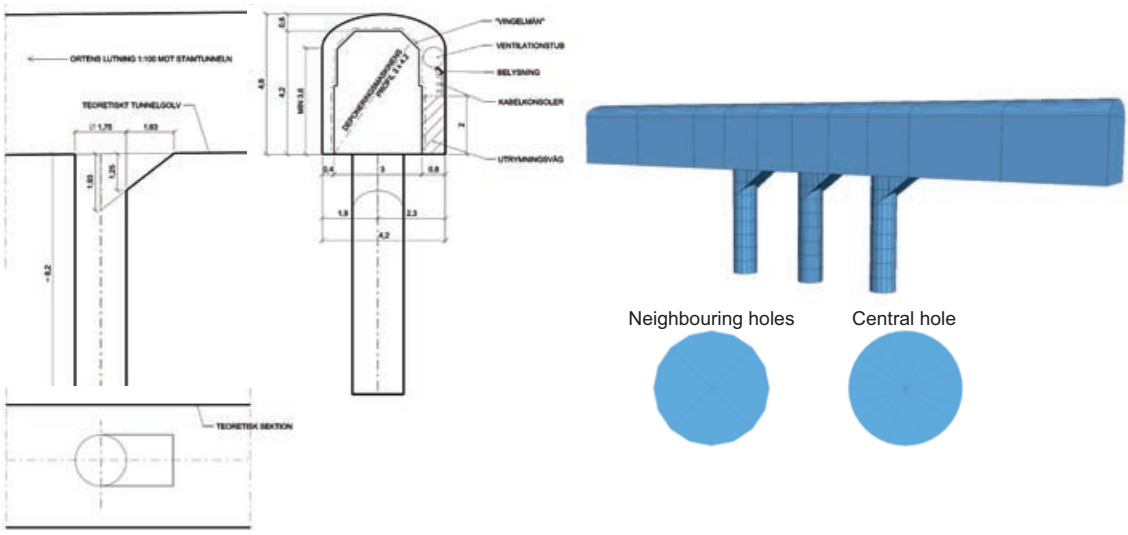

Figure 9-2. *Left: SKB's current reference design of deposition tunnels and holes. From /SKB 2007/. Right: Design of central tunnel in near-field models. The central deposition hole is represented by 40 tangential sections and the neighbouring holes by 16 tangential sections.*

9.2.3 Input data

The thermal, mechanical and thermo-mechanical properties of the rock mass and *in situ* stresses used in the modelling work are presented in Table 4-5 (fracture domain FFM01/rock domain RFM029) and Table 4-2, respectively. The major horizontal *in situ* stress deviates by about 20° from the tunnel axis in most parts of the repository region (22° at the location marked Box A1) with the exception of the small sub-panel containing Box B1 where the stress is approximately aligned with the deposition tunnels (deviation 3°).

Each model is analysed with both mean (models labelled '1a') and dimensioning values (models labelled '1b') of the thermal properties, cf. Table 4-5 (rock domain RFM029). Models with mean thermal properties will be relevant for a large majority of the canisters, whereas models with dimensioning thermal properties will be relevant for the hottest canisters (cf. Chapter 5).

In order to investigate the influence of uncertainties, a further set of models where uncertainties associated with Young's modulus in fracture domain FFM01 (expressed as +1 std, cf. Table 4-7) and *in situ* stress magnitudes (Table 4-2) are accounted for are also analysed. The most unfavourable orientation of the major horizontal *in situ* stress with respect to the tunnel axis for each of the four alternative stress states (I, III, IV and V) is 37° in Box A1.

The total stresses at repository depth during the glacial phase are obtained from Figure 4-13. The mechanical impact during the glacial phase is only evaluated in Box A1, in which the deposition tunnel is oriented 123° with respect to North.

It is assumed that the spalling strength is in the range 52–62% of the uniaxial compressive strength (UCS) of intact rock, *i.e.* approximately 117–140 MPa in fracture domain FFM01, cf. Table 4-6.

9.2.4 Calculation sequence

Construction and operational phase

No thermal effects due to already placed fuel in other parts of the repository region are considered in any of the near-field models during the construction of the repository, *i.e.* the transition from *in situ* conditions to excavated state is assumed to take place in undisturbed rock, cf. subsection 6.2.1.

During *in situ* conditions and the subsequent excavation phase, the top and bottom of the models are locked in the vertical direction and all six boundaries are locked in the horizontal directions.

Temperate phase

The canisters are positioned according to Layout D2 (Figure 9-1) without considering any loss of canister positions, *i.e.* as opposed to the large-scale models (cf. Chapter 6), all available canister positions are assumed to be filled. Similarly to the temperature calculations in Chapter 5, all canisters have an initial power of 1,700 W with power decay according to SKB's reference fuel /Hökmark et al. 2009/, cf. Figure 5-1 (left) and are deposited simultaneously. Furthermore, temperature effects due to mirror sources are not considered. However, this effect is minor and judged not to influence the results presented in the following sections, cf. Appendix F.

Displacement-type boundary conditions for the thermal phase are obtained from the large-scale models in Chapter 6 using mean values of the thermo-mechanical properties, cf. Figure 6-14. These boundary conditions are judged to be relevant also for models with the dimensioning value of the heat conductivity. As the *in situ* stresses are not perfectly aligned with the axes of the models roller boundaries are not appropriate. Therefore, a routine using the built-in programming language *FISH* /Itasca 2007/ has been developed that controls the horizontal displacement of each gridpoint on the vertical boundaries such that the thermal expansion and contraction of the box being modelled agree with the results of the large-scale models. The scheme for controlling the boundary gridpoints does not move the model origin. It preserves the right angles at the model corners and the planar shape of the boundaries.

The thermally induced deformations of the rock mass in a semi-infinite homogeneous material are independent of the deformation modulus /e.g. Claesson and Probert 1996b/, which means that the boundary conditions presented in Figure 6-14 are relevant regardless of the value of the deformation modulus of the rock mass. In the following sections, the results presented for other values of the deformation modulus than the mean value in each rock domain are obtained by scaling the thermally induced stresses with the deformation modulus, cf. Appendix B.

Glacial phase

No residual thermal effects from the decaying nuclear fuel or other temperature variations (*e.g.* permafrost) are considered during the glacial phase. As the small near-field models are linear elastic, the glacial stresses are added to the *in situ* stresses at repository level and entered into the code in the same way as *in situ* stresses.

The same type of boundary conditions as during the construction and operation phase is used, *i.e.* the top and bottom of the model are locked in the vertical direction and all six boundaries are locked in the horizontal directions.

9.2.5 Evaluation of results

All results presented here are obtained using linear elastic models and the spalling strength is assumed to be in the range 52–62% of the uniaxial compressive strength (UCS) of intact rock, *i.e.* approximately 117–140 MPa in fracture domain FFM01 and 194–231 MPa in fracture domain FFM06, cf. Table 4-6. Note that the spalling strength is used just to evaluate the results; it is not be an input parameter to the linear elastic models.

The results can only be used to predict whether the nominal spalling strength will be exceeded or not and in which parts of the deposition holes or tunnel walls it may occur. In reality the strength will be reached rather than exceeded. Once the strength is reached and the failure is in progress, the linear elastic models are not strictly valid. Nevertheless we use the term "exceed" in the following, bearing in mind that the models cannot be used to predict the actual width and shape of the spalled zone or how the failure will develop over time.

The approach of using linear elastic models is justified by the experience from the APSE and CAPS experiments which is that linear elastic models are useful for predicting how deep below the tunnel floor spalling will occur in highly stressed KBS-3 type cylindrical holes /Andersson 2007, Glamheden et al. 2010/

9.3 Results

Results presented are obtained from models of Boxes A1 and B1 with the most likely stress model and the most likely stress orientation (cf. Figure 4-4). For the two models this means that the horizontal *in situ* stresses are oriented as shown in Figure 9-3 in relation to the tunnel axis.

Results are presented for the two assumptions considered for thermal properties: mean values (relevant for a large majority of the canisters) and dimensioning values (relevant for the hottest canisters, cf. Chapter 5).

Results based on a number of high-stress alternatives are presented in the uncertainty section (Section 9.4).

9.3.1 Stresses in walls of deposition holes

Figure 9-4 shows the principal stresses around a deposition hole (coloured after the major principal stress) in a horizontal cross-section at canister mid-height (top row) and in a vertical cross-section through the deposition hole axis after excavation (left) and after 50 years of heating for the mean value of the thermal conductivity (middle) and the dimensioning value of the thermal conductivity (right).

Figure 9-5 and Figure 9-6 show the major principal along the deposition hole perimeter at different depths below the tunnel floor in near-field models Box A1 and B1, respectively. The upper part of each figure shows the stresses after excavation of the deposition holes. The lower parts show the corresponding stresses after 50 years of heating for mean value properties (left) and dimensioning thermal properties (right).

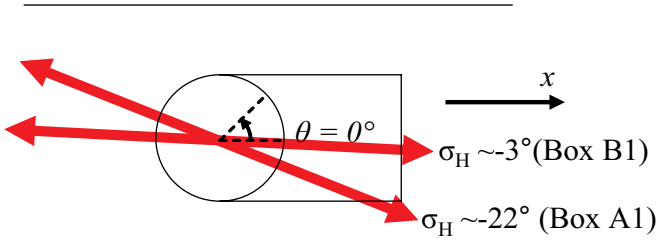

Figure 9-3. *Orientation of the major horizontal in situ stress with respect to the tunnel and definition of azimuthal angle.*

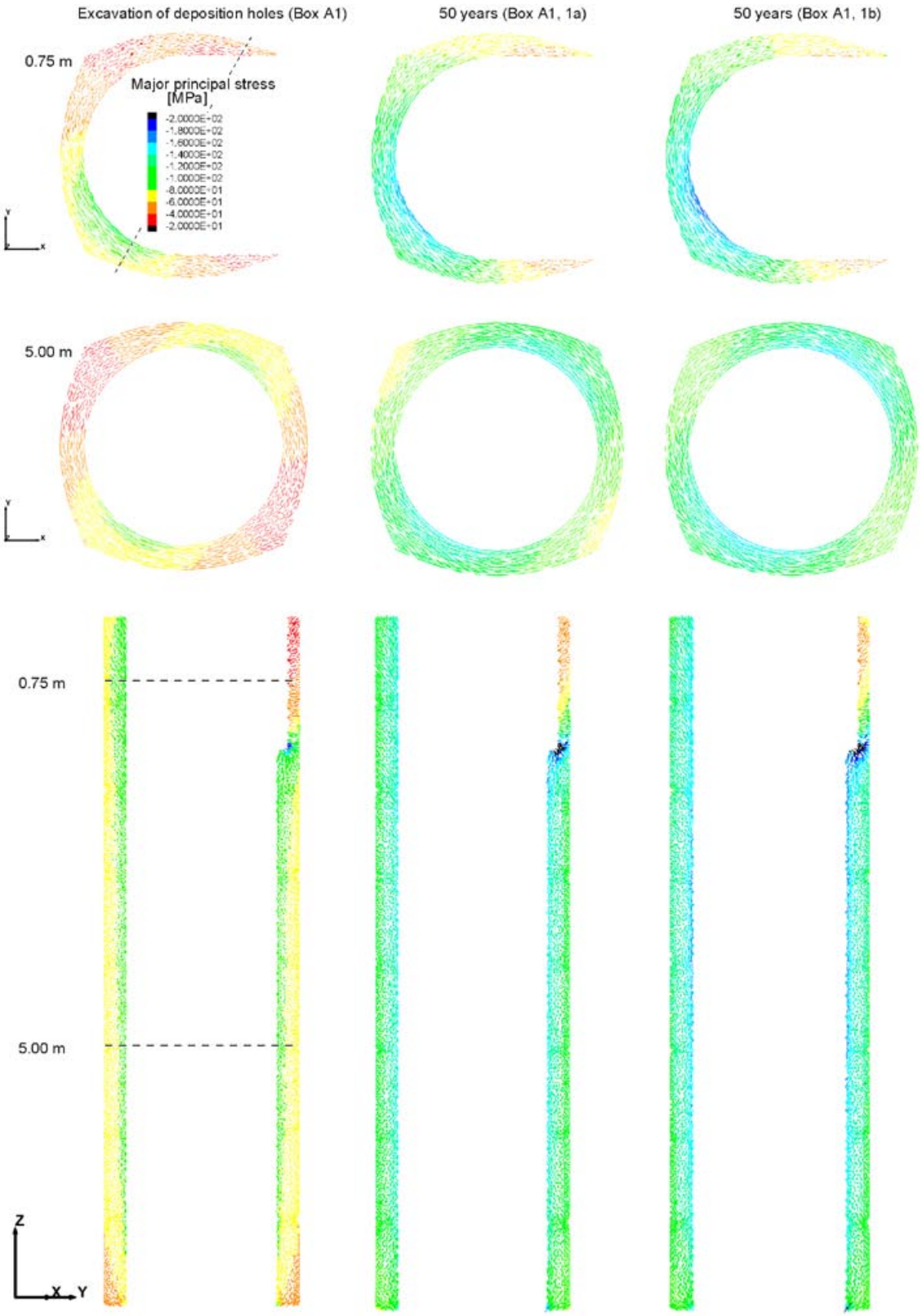

Figure 9-4. *Upper and middle rows: Examples of the stress distribution around the central deposition hole in Box A1 in two horizontal cross-sections 0.75 and 5 m below the tunnel floor, respectively. Bottom row: Corresponding results in the vertical cross-section marked with a dashed line in the uppermost left figure.*

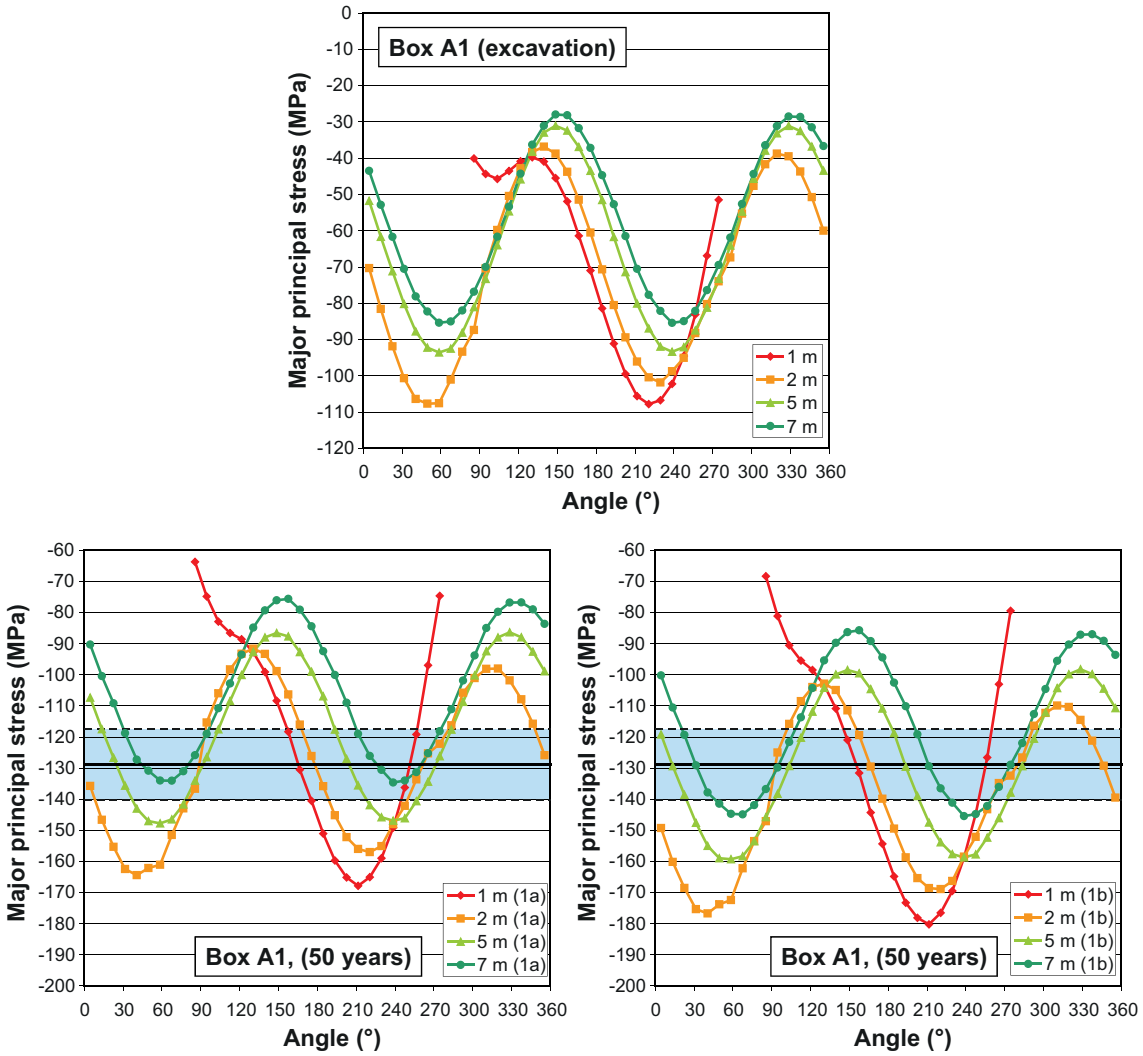

Figure 9-5. *Tangential stress at different depths after excavation (top) and after 50 years of heating (bottom left and right) in Box A1 located in FFM01. Blue colour represents spalling strength (52–62% of UCS in FFM01).*

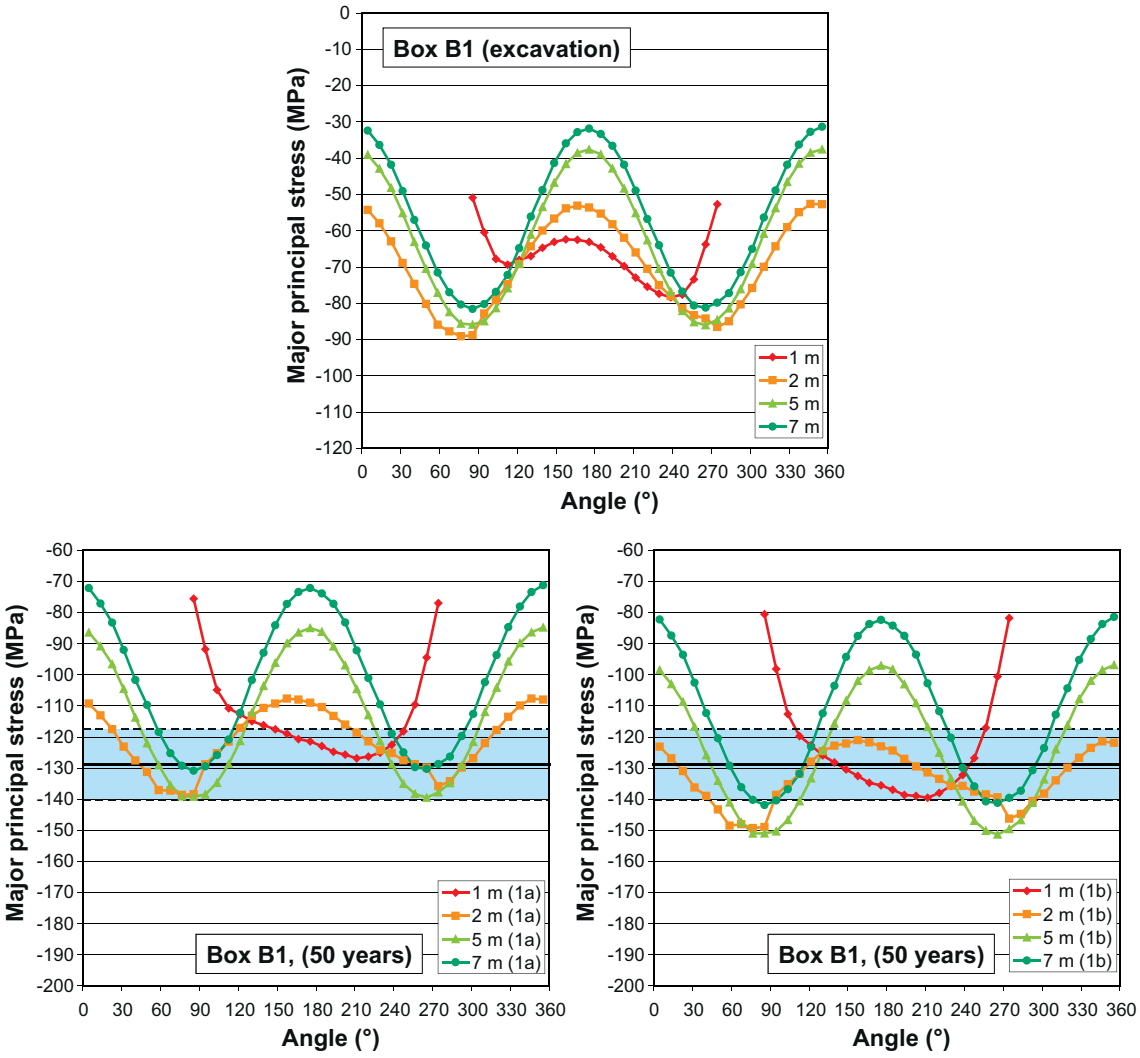

Figure 9-6. *Tangential stress at different depths after excavation (top) and after 50 years of heating (bottom left and right) in Box B1 located in FFM01. Blue colour represents spalling strength (52–62% of UCS in FFM01).*

In the near-field models where the major *in situ* stress deviates from the tunnel axis by ~20° the highest stresses are found in the upper parts of the deposition hole, whereas in the case where the major stress is approximately parallel to the tunnel axis the maximum stress is found approximately at canister mid-height (5 m), cf. Figure 9-5 and Figure 9-6. This is because the stress concentration below the tunnel floor is significantly higher in case the tunnel is aligned off the major horizontal stress. Although the spalling strength (here assumed to be in the range 52–62% of the UCS) is not exceeded anywhere after excavation of the deposition holes, the stresses in the upper 2 m of the deposition holes in the boxes with the most unfavourable tunnel orientation are within 10–15 MPa of the lower limit of the spalling strength.

Figure 9-7 shows the temporal evolution of the major principal stress at canister mid-height (5 m) in each near-field model in fracture domain FFM01/rock domain RFM029. During the temperate phase and assuming mean value thermal properties, the lower limit of the spalling strength is reached within 6 months of deposition of the canisters, cf. Figure 9-7 (left). If, instead, the thermal properties are of the order of the dimensioning value, the lower limit of the spalling strength will be exceeded earlier, cf. Figure 9-7 (right). The upper limit of the spalling strength is also likely to be exceeded, although only marginally in Box B1 when mean value thermal properties are assumed.

As seen in the Figure 9-5, Figure 9-6 and Figure 9 7, the highest stresses are found in Box A1. Figure 9-8 shows the maximum tangential stress in Box A1 after excavation and after 50 years along the deposition hole wall. The stress perturbation at depths between –1.5 m and –2 m is caused by the wedge, cf. also Figure 9-2.

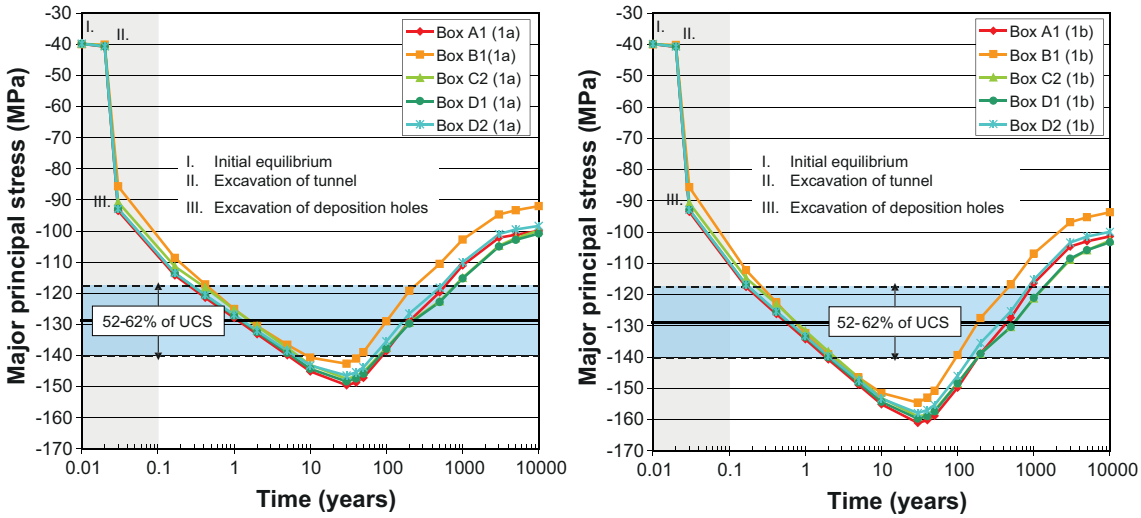

Figure 9-7. *Temporal development of thermally induced stresses at canister mid-height (5 m) on deposition hole walls in boxes in FFM01. Left: Mean heat transport properties. Right: Dimensioning value of heat transport properties.*

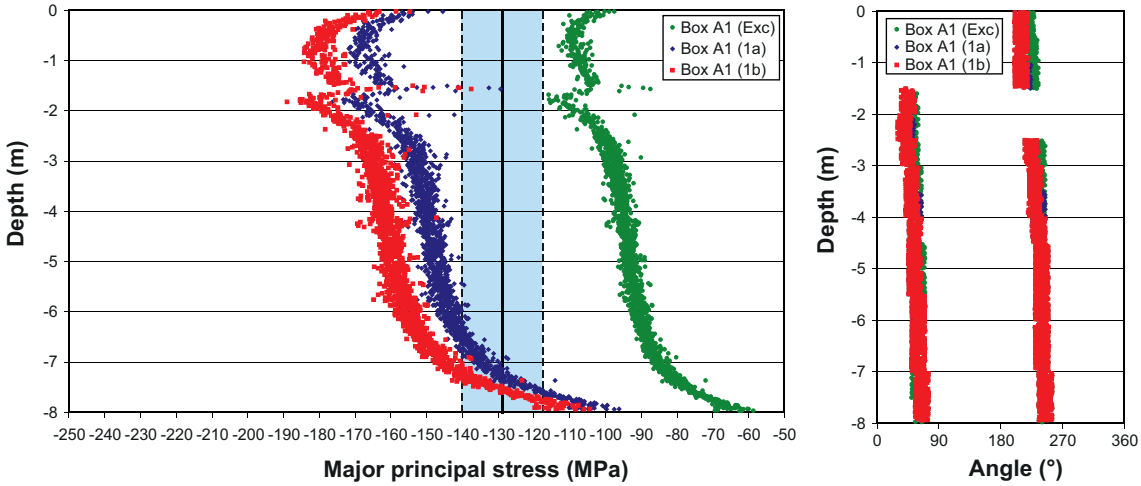

Figure 9-8. *Left: Maximum tangential stress in Box A1 after excavation and 50 years (1a and 1b) along deposition hole wall. Right: Location of maximum stress on deposition hole perimeter. Blue area represents spalling strength in fracture domain FFM01 (52–62% of UCS).*

9.3.2 Stresses in deposition tunnel walls and roof

The major principal stress in the centre of the tunnel roof is presented in Figure 9-9 (fracture domain FFM01/rock domain RFM029). As opposed to the stresses in the deposition hole walls (cf. previous section), the stresses in the centre of the tunnel roof will not exceed the spalling strength during the temperate phase.

At the end of the temperate phase, the temperatures are assumed to have returned to post-excavation levels, i.e. no residual thermal effects are considered during the glacial cycle. Figure 9-10 shows the major principal stress in the centre of the roof at selected points in time during the glacial cycle. During the second glacial maximum (54.5 ka) the major principal stress reach a maximum of about 95 MPa, *i.e.* well below the spalling threshold.

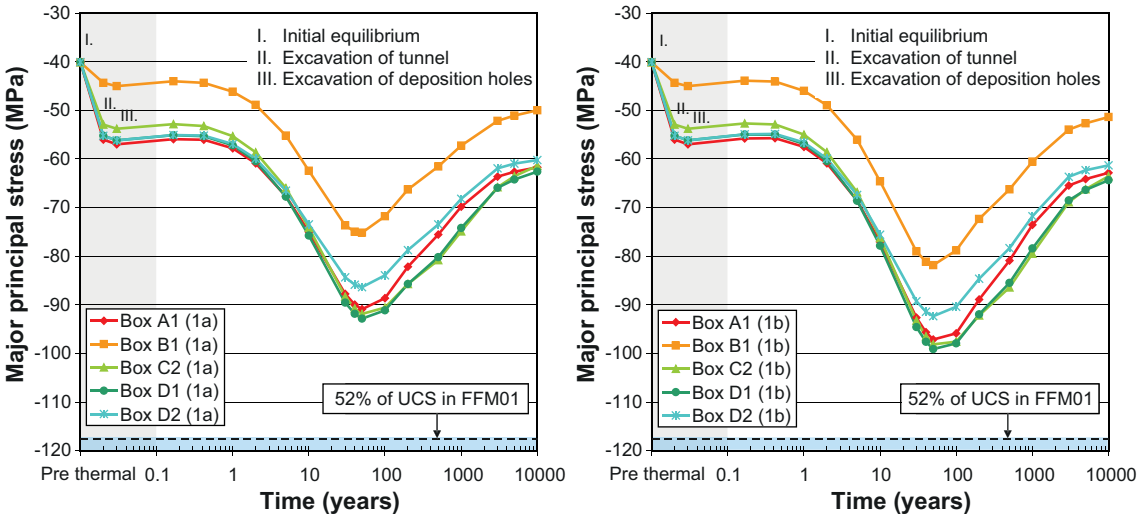

Figure 9-9. *Temporal development of thermally induced stresses in the centre of tunnel roof in boxes in FFM01. Left: Mean heat transport properties. Right: Dimensioning value of thermal properties.*

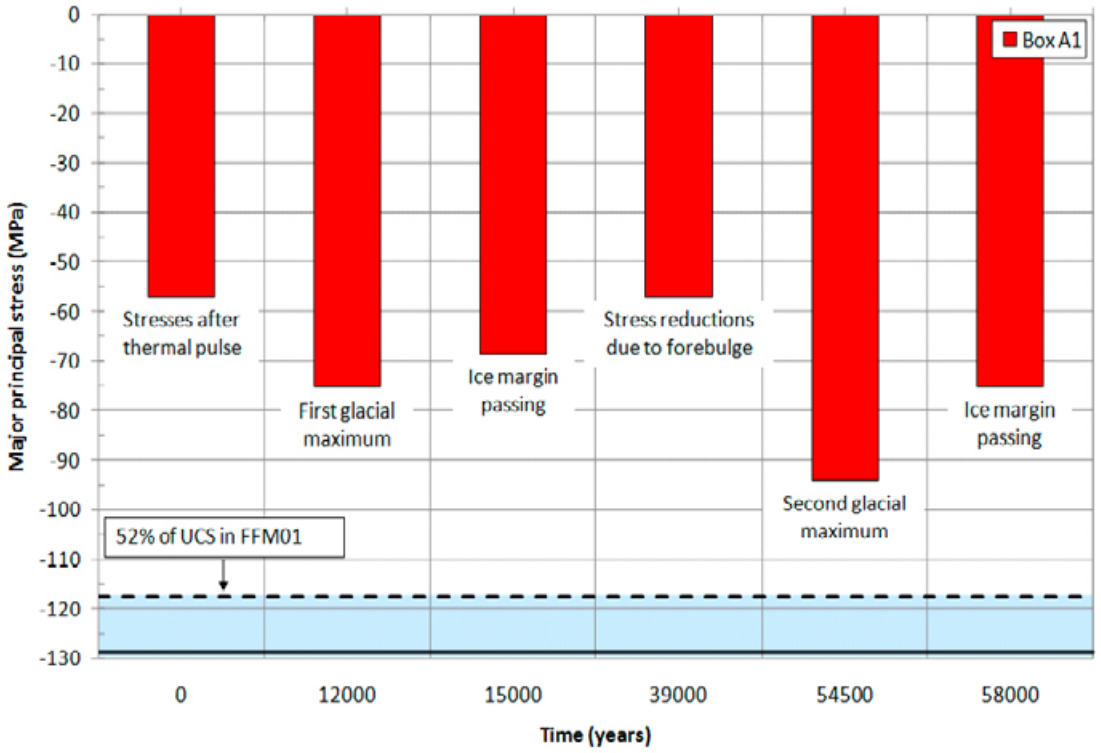

Figure 9-10. *Stresses in the centre of the roof in Box A1 during the glacial phase.*

Figure 9-11 shows a comparison of the major principal stress in a vertical cross section perpendicular to the tunnel at stress maximum during the temperate phase and glacial phase. During both the temperate and glacial phases, there are stress concentrations in the corners of the tunnel roof. The magnitudes of these are around 105 MPa (1a), 115 MPa (1b) and 130 MPa (54.5 ka).

In the stress model given by /SKB 2005/ and used in SKI's review of SR-Can /Rutqvist and Tsang 2008/, the ratio between σ_{yy} (stress across tunnel) and σ_{zz} (vertical stress) is close to 3. Therefore, there is potential for tensile stresses to develop already after excavation. In the most recent stress model for the Forsmark site /Glamheden et al. 2007a/ the ratio between σ_{yy} and σ_{zz} is around 2, which implies that tensile stresses are unlikely to develop after excavation, cf. Appendix H.

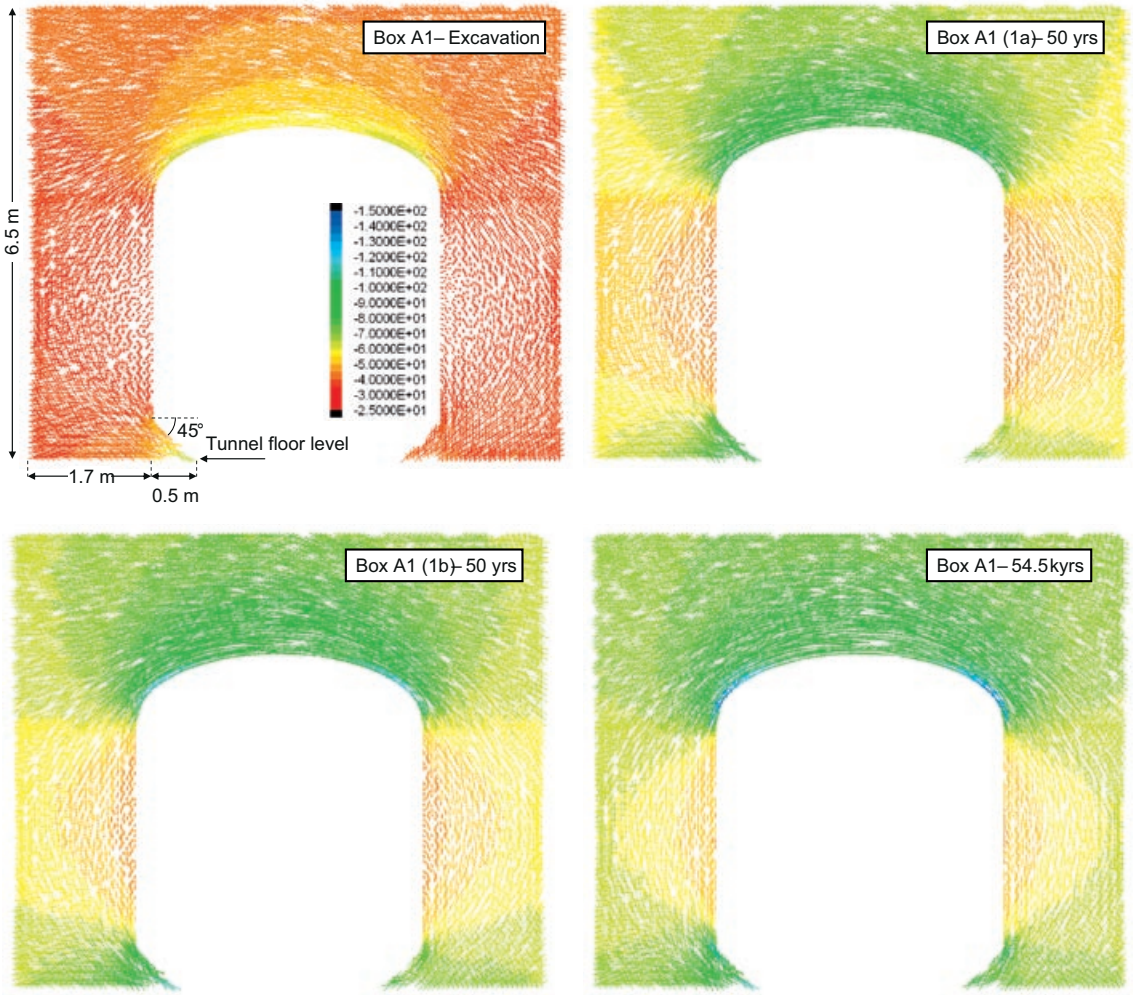

Figure 9-11. *Major principal stress (legend in MPa) in a vertical cross section through the centre of the deposition tunnel in Box A1. Top row: Major principal stress after excavation (left) and at thermal stress maximum (50 years) in model 1a (right). Bottom row: Major principal stress at thermal stress maximum (50 years) in model 1b (left) at glacial stress maximum (54.5 kyr) (right).*

9.4 Uncertainties

The results presented here are based on the *in situ* stress assumptions shown in Figure 9-12 and for the two assumptions considered for thermal properties: mean values (relevant for a large majority of the canisters) and dimensioning values (relevant for the hottest canisters, cf. Chapter 5).

9.4.1 Stresses in deposition hole walls

The tangential stress after excavation in Box A1 is presented in Figure 9-13. As the *in situ* stress tensor is rotated to its most unfavourable orientation with respect to the tunnel whilst keeping the mean value stress magnitudes (I), the spalling strength is exceeded in the upper 2 m of the deposition hole in Box A1. For the upper limit of stress magnitudes and most unfavourable orientation (III), the spalling strength is likely to be exceeded down to canister mid-height. For the spalling strength to be exceeded along most of the deposition hole wall after excavation of the deposition holes, the stress magnitudes need to be of the order of the 'Proposed Maximum Stress Model', cf. Table 4-2.

Figure 9-14 shows the maximum tangential stress in Box A1 after excavation and after 50 years along the deposition hole wall. The *in situ* stresses used for these calculations were Stress case III, *i.e.* upper limit stress magnitudes and most unfavourable orientation (37° with respect to tunnel orientation), cf. Table 4-2. Similarly to Figure 9-8, the stress perturbation at depths between –1.5 m and –2 m is caused by the wedge.

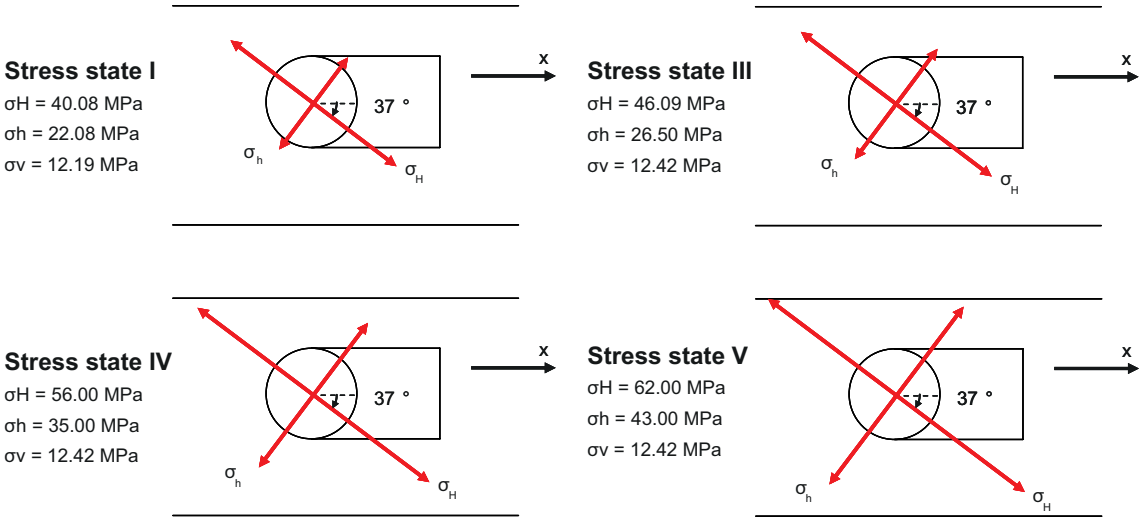

Figure 9-12. *Summary of alternative stress states I, III, IV and V, cf. Table 4-2.*

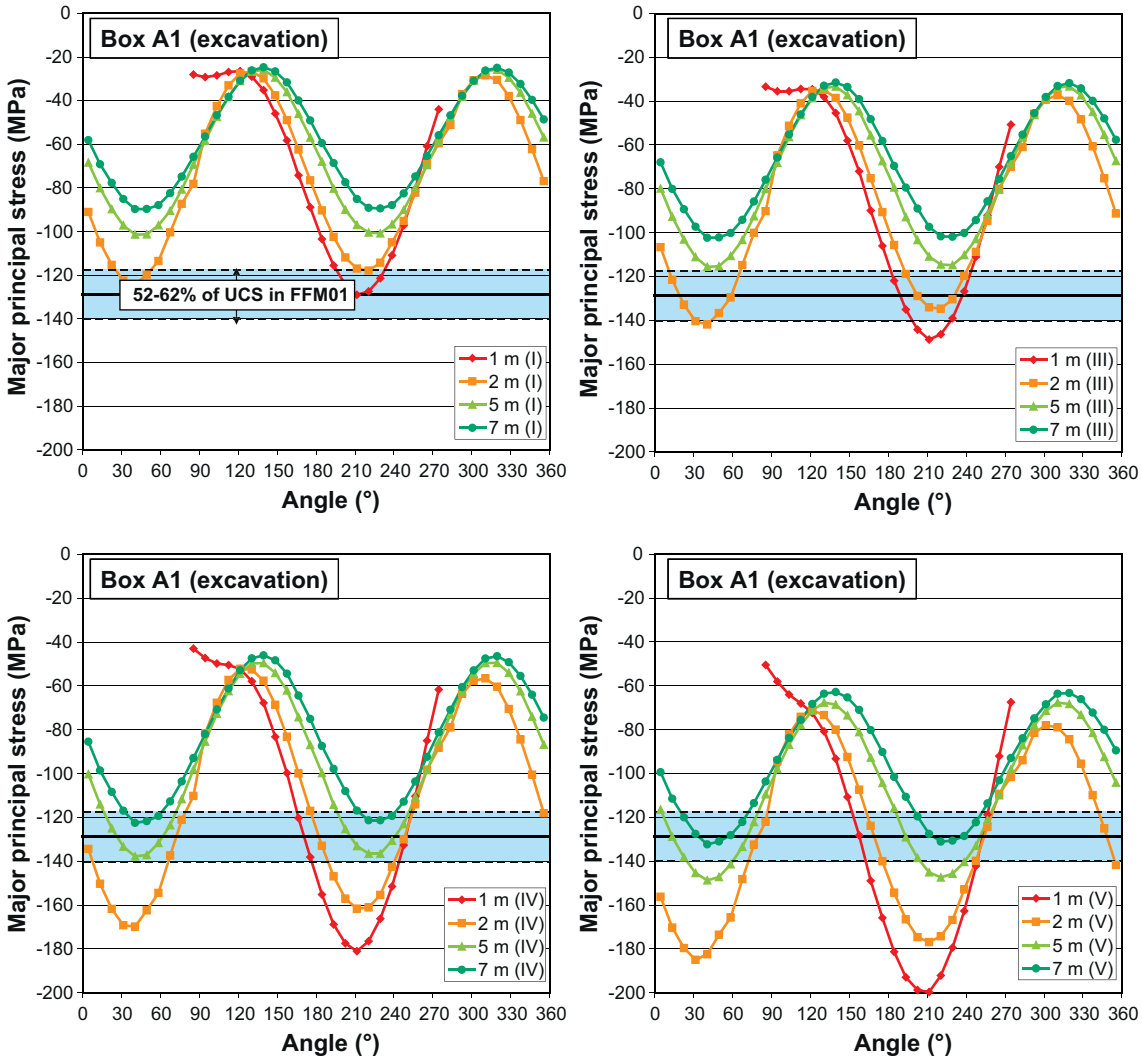

Figure 9-13. *Tangential stress at different depths below the tunnel floor after excavation for different in situ stress assumptions (cf. Table 4-2) in Box A1 located in FFM01.*

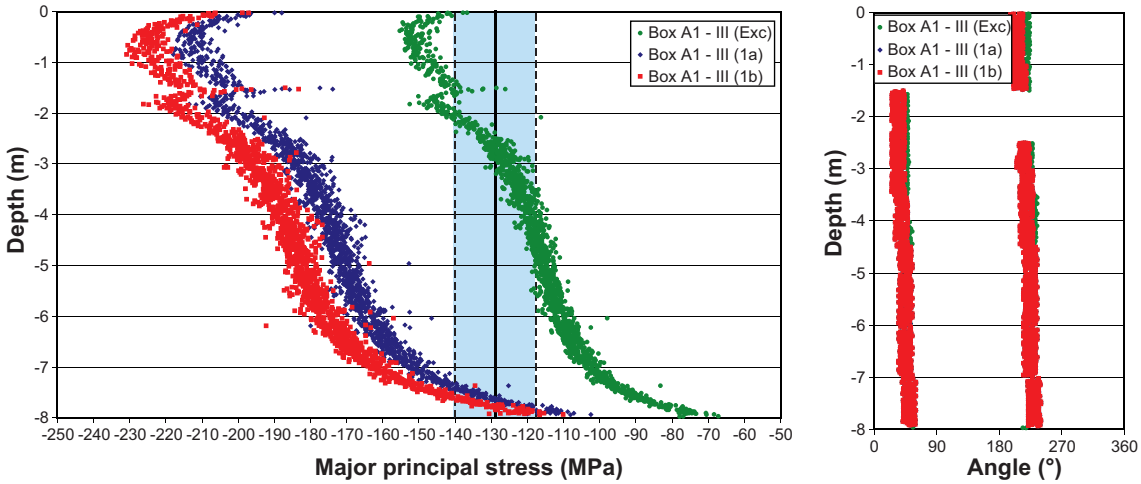

Figure 9-14. *Left: Maximum tangential stress in Box A1 (stress case III, cf. Table 4-2) after excavation and 50 years (1a and 1b) along deposition hole wall. Right: Location of maximum stress on deposition hole perimeter. Blue area represents spalling strength in fracture domain FFM01 (52–62% of UCS).*

9.4.2 Stresses in deposition tunnel roof

Figure 9-15 shows the thermally induced stresses in the roof of the deposition tunnel in Box A1 for the mean value and orientation of the *in situ* stress compared with the four more unfavourable stress assumptions (I, III, IV and V), cf. Table 4-2. As seen in the figures, stress magnitudes and orientations as in the upper limit of the stress model are needed for the thermally induced stresses to exceed 52% of the UCS in FFM01.

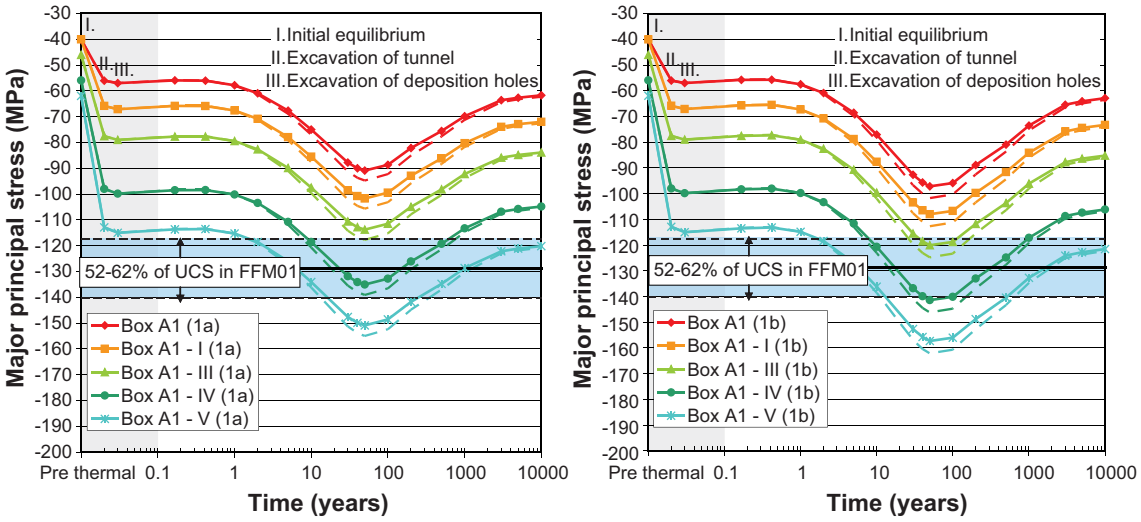

Figure 9-15. *Temporal development of thermally induced stresses in tunnel roof in Box A1 in FFM01. Left: Mean heat transport properties. Right: Dimensioning value of heat transport properties. Plot symbols represent mean mechanical properties (E = 70 GPa), whereas dashed lines represent Young's modulus plus 1 standard deviation (E = 78 GPa).*

9.5 Summary

All results presented here are obtained using linear elastic models and the spalling strength is assumed to be in the range 52–62% of the uniaxial compressive strength (UCS) of intact rock, *i.e.* approximately 117–140 MPa in fracture domain FFM01 and 194–231 MPa in fracture domain FFM06, cf. Table 4-6.

If the high spalling strength assumed for fracture domain FFM06 is relevant for typical rock in that domain, the spalling strength will not be exceeded in fracture domain FFM06 during excavation or the subsequent temperate phase when mean thermal, mechanical and thermo-mechanical properties, *in situ* stresses and their orientations are considered. All observations below relate to the spalling potential in FFM01.

The results can only be used to predict whether the nominal spalling strength will be exceeded or not and in which parts of the deposition holes or tunnel walls it may occur. The models cannot be used to predict the actual size and shape of the spalled zone or how the failure will develop over time.

9.5.1 Spalling potential in deposition hole walls

Construction and operational phase

The following conclusions are drawn:

- For the models with mean values of the mechanical properties, *in situ* stress magnitudes and orientations, the spalling strength is not exceeded at any depth in the walls of the deposition holes.
- For the most unfavourable stress orientation (37° with respect to tunnel orientation) but mean value stress magnitudes (σ_H = 40.08 MPa, σ_h = 22.08 MPa and σ_v = 12.19 MPa), the spalling strength may be exceeded in the upper 2 m of the deposition hole.

Temperate phase

For the models with mean values of the mechanical properties, *in situ* stress magnitudes and orientations, the following conclusions can be drawn:

- The spalling strength is exceeded at canister mid-height (5 m) in all models within a few months to 10 years (mean thermal conductivity) and 2 months to 2 years (dimensioning thermal conductivity).
- In the model with the highest stresses (Box A1), the spalling strength is exceeded after 50 years from the tunnel floor down to a depth of about 6.5–7.5 m (mean thermal conductivity) and 7.2–7.8 m (dimensioning thermal conductivity), respectively.

When uncertainties in mechanical properties, *in situ* stresses and their orientations are taken into account, the following conclusions can be drawn:

- The spalling strength is likely to be exceeded at canister mid-height during the temperate phase even when the lower limit of the stress magnitudes (σ_H = 34.07 MPa, σ_h = 17.66 MPa and σ_v = 11.96 MPa) and most favourable tunnel orientations (0°) are considered.
- For the most unfavourable stress orientation (37°) and upper limit of stress magnitudes (σ_H = 46.09 MPa, σ_h = 26.5 MPa and σ_v = 12.42 MPa), the spalling strength is exceeded from the tunnel floor down to a depth of around 7.3–7.9 m (mean value of the thermal conductivity) and 7.6–7.9 m (dimensioning value of the thermal conductivity), respectively.
- For the spalling strength to be exceeded in the centre of the tunnel roof, the stresses need to be elevated compared with the mean (σ_H = 46.09 MPa, σ_h = 26.5 MPa and σ_v = 12.42 MPa) and unfavourably oriented.

Case overview

Given the mean values of the intact rock elastic and thermo-elastic properties established for rock domain RFM029 in Forsmark, cf. Chapter 4, the maximum tangential stress during the construction/operational and temperate phases are determined by the assumed *in situ* stress and the local temperature increase. For the overview made in this section, the *in situ* stress cases below are included:

- 0: Most likely stress magnitudes (σ_H = 40.08 MPa, σ_h = 22.08 MPa and σ_v = 12.19 MPa) and most likely orientation with respect to tunnel orientation (22° in Box A1 and 3° in Box B1).
- I: Most likely stress magnitudes and most unfavourable orientation (about 33–37°) of the major horizontal *in situ* stress with respect to the tunnel orientation.
- II: Lower limit stress magnitudes (σ_H = 34.07 MPa, σ_h = 17.66 MPa and σ_v = 11.96 MPa) and most favourable orientation (about 0–3°) of the major horizontal *in situ* stress with respect to the tunnel orientation.
- III: Upper limit stress magnitudes (σ_H = 46.09 MPa, σ_h = 26.5 MPa and σ_v = 12.42 MPa) and most unfavourable orientation (about 33–37°) of the major horizontal *in situ* stress with respect to the tunnel orientation.

For the thermal properties two cases are considered:

- Mean domain thermal conductivity.
- Dimensioning domain thermal conductivity, i.e. the lowest conductivity that effectively could control the local rock temperature at the time of the temperature peak (cf. Chapter 5).

Considering that the tunnels in Box A1 and Box B1 are differently oriented, this gives the ten combinations shown in Table 9-1.

Table 9-2 shows the depth sections in which the nominal spalling strength was exceeded. Variations around the mean UCS (226 MPa) and the mean spalling strength estimate (57% of the UCS) are not considered. Therefore, the table indicates the relative importance of the different factors that control the stress evolution at different depths, but cannot be used to quantify how the actual spalling potential will vary between holes and along the axes of the holes. Note also that some cases that would give less spalling are not included. A considerable fraction of the deposition will, for instance, have effective conductivities that are higher than the mean, which will give lower temperatures and lower stresses.

Table 9-2 confirms that the spalling strength will be exceeded during construction only for the worst case assumptions made here, and hardly ever below deposition hole mid-height. Similarly, for the spalling strength to be exceeded below the 7 metre level during the first 5 years after deposition, worst case assumptions must be made.

Eventually, after more than 5 years, the strength will be exceeded below the 7-metre-level for all but the most favourable cases. The nominal strength is, however, not exceeded down to very bottom of the hole for any of the cases. Unless the lower bound strength (52% of the UCS) applies, there will always be a 0.1–0.2 m section of intact rock wall in the bottom. Figure 9-14 illustrates the way the tangential stresses decrease toward the bottom.

Again, exceeding the spalling potential does not necessarily mean that spalling actually will take place or that the spalled zone, if it develops at all, will be continuous from the tunnel floor to the maximum depth. At present there is, however, not sufficient evidence that a supporting pressure, large enough to suppress the spalling, will have time to develop in the pellets-filled gap between the bentonite blocks and the rock wall. Therefore, spalled zones should be assumed to extend according to Table 9-2, to have shape and dimensions according to the findings of the full-scale APSE test (cf. Section 3.3) and to have permeabilities as proposed by /Neretnieks and Andersson 2009/.

The influence on boundary conditions due to steeply dipping deformation zones is not considered here. The effects of these, for the Forsmark site, would be a reduction in the major principal stress at canister mid-height by about 2–3 MPa, cf. Appendix B.

Table 9-1. Summary of stress and conductivity assumptions.

Thermal conductivity	0 Most likely stress magnitudes, most likely stress orientation	I Most likely stress magnitudes, most unfavourable stress orientation	II Lower limit stress magnitudes, most favourable stress orientation	III Upper limit stress magnitudes, most unfavourable stress orientation
Mean	C (Box B1) D (Box A1)	F	A	H
Dimensioning	E (Box B1) G (Box A1)	I	B	J

Table 9-2. Nominal spalling strength (about 130 MPa) is exceeded within indicated depth intervals and time intervals.

Depth (m)	Excavation	0–1 years
0–1	F H I J	D F G H I J
1–2	H J	D E F G H I J
2–3	H J	D E F G H I J
3–4		D E F G H I J
4–5		E F G H I J
5–6		E F G H I J
6–7		H I J
7–8		J

Depth (m)	1–5 years	5–50 years
0–1	D E F G H I J	B D E F G H I J
1–2	B C D E F G H I J	A B C D E F G H I J
2–3	B C D E F G H I J	A B C D E F G H I J
3–4	B C D E F G H I J	A B C D E F G H I J
4–5	B C D E F G H I J	A B C D E F G H I J
5–6	B C D E F G H I J	B C D E F G H I J
6–7	C D E F G H I J	B C D E F G H I J
7–8	H I J	D E F G H I J

Glacial phase

For the glacial phase, tangential stresses in the walls of the deposition holes are not of major importance. The maximum effective background stresses during the different glacial phases are of similar magnitudes as those occurring during the time of the thermal load. Additionally, as shown in SR-Can, during the glacial cycle there will be a significant swelling pressure in all deposition holes apart from those where the buffer is lost due to colloid formation and erosion. Therefore, if spalling did not take place during the temperate phase it will not happen during the glacial cycle. Furthermore, if the buffer is lost, the impact of spalling is insignificant to safety. This justifies not addressing the question of spalling in the walls of the deposition holes during the glacial cycle.

9.5.2 Spalling potential in deposition tunnel roof

Construction and operational phase

The spalling strength is not exceeded in the deposition tunnel roof.

Temperate phase

The spalling strength is not exceeded in the centre of the deposition tunnel roof. However, at the tunnel corners the maximum stress (assuming dimensioning thermal conductivity) is within a few MPa of the lower spalling strength estimate.

Glacial phase

The major principal stress, in the centre of the deposition tunnel roof, reaches its maximum value of around 95 MPa during the second glacial maximum (54.5 ka). This is about 20 MPa below the lower limit (52%) of the spalling threshold. However, in the roof corners, the stresses are significantly higher – at the time of the second glacial maximum (54.5 ka) around 130 MPa, cf. Figure 9-11.

10 Conclusions and discussion

10.1 General

Three main issues are addressed in the previous chapters:

1. The thermal evolution of the repository on the scale of the individual canisters and deposition holes in particular and on all scales in general.
2. The possibility of stress-induced failure, spalling, in the walls of deposition tunnels and deposition holes.
3. Transmissivity changes of existing fractures.

The potential formation and evolution of an Excavation Damaged Zone (EDZ) is an additional, potentially important, issue of relevance to the THM evolution. The EDZ and its importance to the THM evolution and the safety assessment are handled in Section 6.5 of the **Data Report**. Other processes that could disturb the hydraulic conditions (propagation and coalescence of water-bearing fractures are not considered, cf. discussion in Chapter 3).

Note that the following conclusions relate to the Forsmark site. Results relevant for Laxemar are given in Appendix I.

10.2 Thermal evolution

One specific objective considered here is to demonstrate that Layout D2 for Forsmark will satisfy the buffer temperature criterion (the peak buffer temperature must not exceed 100°C in any deposition hole at any time). This is a problem on the scale of a few tunnels and with a time-scale of up to about 20 years. The calculations conducted to establish the Layout D2 canister spacing with full account of the spatial variability of rock heat transport properties in the different rock domains are presented in the Site Engineering Report for Forsmark /SKB 2009b/. In this report additional perspectives on the temperature margin applied in the layout work are considered. The following is concluded:

- Even assuming all canisters to be deposited in completely dry deposition holes, i.e. having insulating canister-bentonite air-gaps and unsaturated, low conductive buffers, the number of deposition holes where the buffer would get peak temperatures close to the threshold is very small. Out of 6,000 deposition holes, 5,994 would have a margin of 7°C or more, about 98% of the deposition holes would have a margin of 10°C or more (cf. Figure 5-7). In reality, because about 1,000 deposition holes are located close tunnel ends will get significantly reduced peak temperatures /Hökmark et al. 2009/, the fraction of deposition holes where the buffer temperature is very far from its maximum allowed value is even larger.
- For the buffer in deposition holes with some access to water, the peak temperatures will be lower. This means that the distribution shown in Figure 5-7 is valid only for a fraction of the deposition holes, whereas remaining deposition holes get lower, or much lower, peak temperatures, cf. Figure 5-15.
- If the margin applied in the layout work (less than 5°C) would turn out to be too small because of conditions not considered in the dimensioning calculation model (for instance uncertainties in the canister power, mistakes made during emplacement, etc.), temperatures in excess of the design limit will only be found for very few canisters (cf. Figure 5-8). The excess temperature would be found only in small volumes just above the canister top. A few cm away from the top, the temperatures would be well below the threshold (cf. Figure 5-17).

The large-scale and long-term thermal evolution controls the temperature in all repository components: plugs, shafts, top seals etc. and must be well documented and described even if these temperatures are of little direct importance for the safety assessment. The most important aspect of the large-scale and long-term thermal evolution is the impact on the mechanical evolution. The large scale thermal evolution described in Chapter 5 is identical to the thermal evolution in the thermo-mechanical models used

to assess stress concentrations and transmissivity changes during the temperate phase. The large scale evolution is also important to the question of the deposition sequence. The following is concluded:

- The approximation of simultaneous deposition all canisters that is made in the Site Engineering Report to establish the canister spacing in the different rock domains is valid if the deposition is made in a panel by panel fashion as proposed for Layout D2 (cf. Figure 5-11). Deposition sequences with long time intervals between neighbouring tunnels may violate the validity of this approximation. The tools described here can easily be applied to examine if a given sequence should be approved or rejected from the peak temperature point of view.

10.3 Spalling

All estimates of the spalling potential made in this report are based on results from linear elastic models, i.e. without consideration of any structurally controlled failures. For sparsely fractured rock, this is judged to be a valid approximation. The experience from corresponding spalling analyses performed for the SR-Can assessment /Fälth and Hökmark 2007/ is that slipping low strength-fractures that intersect the deposition hole tend to increase the tangential stresses between the intersection and the floor, and to reduce them below the intersection. Sporadic local, structurally controlled failures should, however, not be considered important for the overall assessment of the spalling potential, meaning that the linear elastic models analysed here are judged to be adequate.

The results presented here can only be used to predict whether the nominal spalling strength will be exceeded or not and in which parts of the deposition holes or tunnel walls it may occur. The models cannot be used to predict the actual size and shape of the spalled zone or how the failure will develop over time. The spalling strength is assumed to be 57% ±5% of the uniaxial compressive strength for unsupported openings. The discussion in Chapter 3 shows that this is likely to be a conservative estimate, at least for the heating stage. The following general observations are made:

- The results of the analysis made in Section 6.2 show that the assumption made here and in previous work (cf. e.g. /Hökmark et al. 2006/) that the stresses during the construction phase and, consequently, the spalling potential are not influenced by temperature effects is valid as long as construction and deposition, respectively, is not started and finalized simultaneously in neighbouring tunnels or very nearby deposition areas.
- The location within the repository region as well as the local effective heat conductivity will impact on the tangential stresses during the temperate phase. Deposition holes in rock with a local effective conductivity equal to the domain mean will get lower temperatures and lower stresses than holes in rock with the lowest possible effective (dimensioning) conductivity. Similarly to the analyses of the temperature evolution (Chapter 5), the deposition sequence approximation made in all analyses of the near-field stress evolution, i.e. that all canisters are deposited simultaneously, is valid unless very specific sequences are used (Section 6.2). Starting and finalizing the deposition in neighbouring tunnels or very nearby deposition areas with tens of years in between, for instance, would probably mean considerable stress disturbances. The type of analysis described in Section 6.2 can easily be used to check whether a proposed variation in the deposition order would give any such effects.
- A general conclusion of the analyses of the spalling potential is that spalling in deposition holes during the construction and operational phase will occur only by way of exception whereas the nominal spalling strength will be exceeded for a large majority of the deposition holes at some point of time during the heated phase. This is very much a confirmation of the conclusions drawn for the SR-Can assessment. A summary of the findings of the numerical modelling, detailing the projected evolution of the tangential stress at different depths below the tunnel floor for different stress and temperature assumptions is found in Section 9.5 (Table 9-2). These results relate to the conditions in fracture domain FFM01 at Forsmark. For fracture domain FFM06, the projected stress evolution is almost identical to that in FFM01, whereas the spalling strength is about 50 MPa higher, meaning that spalling risk is likely to be much less.
- For the glacial phase, tangential stresses in the walls of the deposition holes are not of major importance. The maximum effective background stresses during the different glacial phases are of similar magnitudes as those occurring during the time of the thermal load. Additionally, as shown in SR-Can, during the glacial cycle there will be a significant swelling pressure in all

deposition holes apart from those where the buffer is lost due to colloid formation and erosion. Therefore, if spalling did not take place during the temperate phase it will not happen during the glacial cycle. Furthermore, if the buffer is lost, the impact of spalling is insignificant to safety. This justifies not addressing the question of spalling in the walls of the deposition holes during the glacial cycle.

- There will not be any spalling in the centre of the roof of deposition tunnels during the construction and operational phase. During the heated phase, and possibly during the glacial cycle, this may occur by way of exception (cf. subsection 9.4.2), e.g. if the major horizontal stress should be maximally aligned off the tunnel axis or take on the maximum value within the uncertainty range given in the site report.

As stated above, the modelling reported here does not give any results relating to the shape and size of the spalled zone. For the safety assessment, size and shape estimates will have to be based on field test observations made in the full-scale APSE test. Here the maximum depth of failure was about 0.13 m, whereas the average was about 0.07 m, say 0.1 m to be on the safe side. The width of the spalled zone was about 0.5 m at the average, cf. discussion in subsection 3.3.1.

The modelling does not give any indications of the properties of the spalled zone. For the SR-Site assessment the permeability model suggested by /Neretnieks and Andersson 2009/, based on size and shape analyses of rock fragments formed in the unsupported spalled zone of the APSE experiment. Field observations reported from the CAPS experiment suggest, however, that the support pressure provided by the pellets filling out the annular space between the rock wall and bentonite blocks are likely to limit the growth and extension of the spalled zone very efficiently, also if that pressure will not be sufficient to inhibit crack formation. Injection tests performed within the CAPS experiment in a supported spalled zone indicated that the permeability was not significantly increased /Glamheden et al. 2010/.

The possibility of spalling in other repository openings than deposition tunnels and deposition holes is not considered an issue for the long term safety and is not considered in this report.

10.4 Transmissivity changes

Transmissivity estimates made in this report are based on calculated variations of fracture normal stresses and calculated fracture shear displacements.

10.4.1 Variations in normal stress

Except for portions of fractures that intersect the repository openings or run parallel with the openings, the analyses conducted here on different scales indicate that changes in fracture transmissivities caused by normal stress variations are modest. This applies for the entire evolution of the repository. The potential for large increases can only be significant at times when the compressive stresses decrease or when fractures are opened by large excess pore pressures. This may potentially be the case for:

- Subhorizontal fractures at repository depth during the heated period of the temperate phase. If the fractures are located in non-heated regions, i.e. between or outside the panels the transmissivity increase may amount to a factor of 2 at maximum due to loss of vertical compression (cf. Figure 6-19). Within the heated regions fracture transmissivities are reduced.
- Subvertical fractures at shallow depths during the heated period of the temperate phase. Fracture transmissivities may increase by a factor of 2 at maximum due to loss of horizontal compression near the ground surface above the heated repository (cf. Figure 6-21). Deeper down, the transmissivities are reduced.
- Subhorizontal fractures under an impermeable permafrost layer. For worst case permafrost pore pressure assumptions, transmissivities may increase by a factor of about 2 at repository depth and a little more just below the permafrost layer (cf. Figure 7-11).

- Subvertical fractures at shallow depths during periods of glacial forebulge stress conditions. The effects of the forebulge stress disturbance (minor loss of horizontal compression) are modest: fracture transmissivities increase by a factor of 2 at maximum (cf. Figure 7-9). In combination with worst-case permafrost pore pressure assumptions, the relative increase may be a factor of 3 (Figure 7-9). If additionally the temperature reduction associated with permafrost conditions are taken into account, the transmissivity increase may be a factor of 7 just below the permafrost layer and about 3 at repository depth (cf. Figure 7-10). This increase is the largest one found among the many cases considered here and is relevant only for fractures with the most unfavourable strike and under the assumption that the most sensitive stress-transmissivity model applies (cf. Figure 4-9).
- Subhorizontal fractures under the ice-margin during times of ice retreat. In case residual excess pore pressures exist, fracture transmissivities may increase by a factor of about 1.5 at repository and a factor of 2 at larger depths (cf. Figure 7-11).

During periods of ice load, the compressive stresses increase on all fractures. The increase in compression is at least approximately, sufficient to balance the effects of excess pore pressures, meaning that possible transmissivity increases are insignificant.

10.4.2 Shear displacements

For fracture shear displacements there is no generally applicable model for direct calculation of the transmissivity effects. Additionally, there are no records of any field scale experiments /Fransson 2009/. The modelling presented here gives the amount of shear displacement on differently-oriented fractures and the effective normal stress conditions that prevailed during the movement. Following the discussion in subsection 3.4.2, shear displacements that take place under normal stresses larger than about 5 MPa can be assumed to have only insignificant effects on the fracture transmissivities. For the stress evolution considered here, significant shear displacements only occur at times of increased stress anisotropy (reduced stability) on fractures dipping along the major horizontal stress. Large displacements are found when the anisotropy is largest:

- During the heated period of the temperate phase on fracture located between or outside the heated panels. Displacements may be about 27 mm for 300 m diameter optimally-oriented fractures and correspondingly less for smaller fractures (cf. Section 6.9). The effective normal stresses are however above 5 MPa, meaning that transmissivity effects can be judged to be minor.
- Under the ice-margin during times of ice retreat. In case residual excess pore pressures exist, displacements may be about 18 mm for 300 m diameter optimally-oriented fractures and correspondingly less for smaller fractures. The effective normal stresses are reduced because of the residual excess pore pressure, but are still above 10–20 MPa, meaning that transmissivity effects can be judged to be minor.

It should be noted that fractures of 300 m diameter are rare. 50 m diameter fractures would slip by less than about 5 mm at maximum. Additionally, the largest shear displacements are found at the central part of the fractures. Assuming the idealized slip distribution given by Equation 6-2, about 50% of the fracture area would slip by 70% or less of the maximum.

10.5 Hydraulic jacking

The following conclusions are made regarding the potential for hydraulic jacking of horizontal fractures during different phases of the glacial cycle /Lönnqvist and Hökmark 2010/:

- The steady state pressure distribution due to a stationary ice, which can be considered an upper bound estimate of an advancing ice without permafrost in a continuum representation of the rock, is not sufficient to initiate hydraulic jacking to greater depths than about 30 m.

- The pore pressure distribution due to an advancing ice sheet in combination with proglacial permafrost.
  - The pore pressure beneath the permafrost is completely determined by the pressure at the melting zone, the diffusivity of the rock and the time-frame of the advancement, which implies that an increased permafrost thickness will not influence the maximum jacking depth. The maximum jacking depth in high-diffusivity rock is larger than in rock with low diffusivity.
  - For the assumptions made in the present modelling work, melting rates of more than about 0.1 m/year (applies for 200 m thick permafrost) would be required to raise the pore pressure sufficiently below the permafrost to initiate hydraulic jacking. The corresponding minimum melting rate for 400 m thick permafrost is about 0.3 m/year.
  - By allowing for seasonal variations (instead of assuming an annual average of 98% of the excess mechanical load) in the boundary pressure, the maximum jacking depth may be reduced by about 40–50%.
  - The presence of open taliks (unfrozen parts) near the repository region may contribute to a reduction in the maximum jacking depth. Taliks are more influential when the hydraulic diffusivity is high, *i.e.* would reduce the excess pore pressure more efficiently. However, in order to quantify their influence site-specific conditions have to be considered, *e.g.* their number, sizes and locations in relation to the repository.
- If the effects of a slow build-up of pore pressures during the advancement of the ice sheet are approximated by assuming that the initial pore pressure distribution has reached steady state before its subsequent retreat without permafrost conditions, the maximum jacking depth is around 50 m for the retreat speed relevant for Forsmark (300 m/year).

Hydraulic jacking is likely to be initiated at shallow depths. The subsequent reduction in pressure will thus prevent hydraulic jacking from occurring further down into the rock. Therefore, the maximum jacking depths presented in /Lönnqvist and Hökmark 2010/ can be considered as conservative estimates.

Table 10-1. Maximum jacking depths during different parts of the glacial cycle, compiled from /Lönnqvist and Hökmark 2010/.

Time during glacial phase	Maximum jacking depth (m)
Advancing ice in combination with proglacial permafrost	200
Retreating ice without permafrost	100

10.6 Remarks on the relevance of the results

All rock mechanics modelling results presented here are based on idealized descriptions of the rock mass and, in particular, of the fractures:

Parameter values of fracture properties are based on results of laboratory scale tests and then applied here to fractures of very different sizes, assuming these fractures to be perfectly planar. For perfectly planar fractures with uniform properties subjected to uniform loads, shear displacements scale with the size of the fracture, as pointed out at several places in this report (cf. e.g. subsection 6.3.3). While this approach allows for a convenient handling of the calculation results, and possibly is relevant in many cases, it is likely to give overly conservative estimates of shear displacements on large fractures. For some large fractures, effects of large-scale undulations and in-plane asperities would prevent large shear displacements. Therefore, the largest shear displacements found in the analyses are probably overestimates. For the purpose of this study, this will not be very important: the largest shear displacements were found to take place under normal stresses that are judged to be sufficient to suppress dilation and transmissivity increases.

The same mechanical properties and the same type of stress-transmissivity relation were applied to all fractures, irrespective of whether the fracture would be a deformation zone rather than an actual single fracture. The implications of this are not obvious; the deformation zones at Forsmark are stiff /Glamheden et al. 2007a/ and may possibly be almost as sensitive to stress changes as single fractures, meaning that the relative transmissivities calculated here may be approximately relevant also for typical Forsmark deformation zones.

For fractures in very low compression, the stress-transmissivity relation becomes uncertain; when the normal stress approaches zero, the transmissivity becomes indefinite. For fractures in a compression of a few MPa, the stress-transmissivity relation is probably relevant, at least on the average, as an upper bound estimate of the sensitivity to stress changes.

For deformation zones, the individual water-bearing fractures that determine the gross flow properties are not necessarily aligned with the plane of deformation zone. This means that the transmissivity response of the individual fractures will not necessarily be determined by the stress acting on the plane of the deformation zone as assumed here. However, given the complex hydro-mechanical interaction of multiple intersecting fractures within the deformation zone, this is judged to be the most relevant approximation for the average deformation zone.

11 References

SKB's (Svensk Kärnbränslehantering AB) publications can be found at www.skb.se/publications.

Ageskog L, Jansson P, 1999. Heat propagation in and around the deep repository. Thermal calculations applied to three hypothetical sites: Aberg, Beberg and Ceberg. SKB TR-99-02, Svensk Kärnbränslehantering AB.

Andersson C, Eng A, 2005. Äspö Pillar Stability Experiment. Final experiment design, monitoring results and observations. SKB R-05-02, Svensk Kärnbränslehantering AB.

Andersson J C, 2007. Äspö Hard Rock Laboratory. Äspö Pillar Stability Experiment, Final report. Rock mass response to coupled mechanical thermal loading. SKB TR-07-01, Svensk Kärnbränslehantering AB.

Back P-E, Wrafter J, Sundberg J, Rosén L, 2007. Thermal properties. Site descriptive modelling Forsmark – stage 2.2. SKB R-07-47, Svensk Kärnbränslehantering AB.

Bandis S, 1980. Experimental studies of scale effects on shear strength and deformation of rock joints. Ph.D. Thesis, Department of Earth Sciences, University of Leeds, UK.

Bandis S, Lumsden A, Barton N, 1983. Fundamentals of rock joint deformation. International Journal of Rock Mechanics and Mining Sciences & Geomechanics Abstracts, Vol. 20, Issue 6, pp 249–268.

Barton N, Choubey V, 1977. The shear strength of rock joints in theory and practice. Rock Mechanics and Rock Engineering, Vol. 10, Nos. 1–2, pp 1–54.

Barton N, 1982. Modelling rock joint behaviour from *in situ* block tests: Implications for nuclear waste repository design. Technical Report ONWI-308, Office of Nuclear Waste Isolation, Columbus, Ohio.

Barton N, Bandis S, Bakhtar K, 1985. Strength, deformation and conductivity coupling of rock joints. International Journal of Rock Mechanics and Mining Sciences & Geomechanics Abstracts, Vol. 22, Issue 3, pp 121–140.

Bense V F, Person M A, 2008. Transient hydrodynamics within intercratonic sedimentary basins during glacial cycles. Journal of geophysical research, Volume 113, F04005, doi:04010.01029/02007JF000969.

Boulton G S, Kautsky U, Morén L, Wallroth T, 2001. Impact of long-term climate change on a deep geological repository for spent nuclear fuel. SKB TR-99-05, Svensk Kärnbränslehantering AB.

Brady B H G, Brown E T, 1993. Rock mechanics for underground mining. Chapman & Hall, London, UK.

Brantberger M, Zetterqvist A, Arnbjerg-Nielsen T, Olsson T, Outters N, Syrjänen P, 2006. Final repository for spent nuclear fuel. Underground design Forsmark, Layout D1. SKB R-06-34, Svensk Kärnbränslehantering AB.

Carslaw H S, Jaeger J C, 1959. Conduction of Heat in Solids, 2nd ed. Oxford University Press, UK.

Chan T, Christiansson R, Boulton G S, Eriksson L O, Hartikainen J, Jensen M R, Mas Ivars D, Stanchell F W, Vistrand P, Wallroth T, 2005. DECOVALEX III/BENCHPAR PROJECTS. The Thermal-Hydro-Mechanical Responses to a Glacial Cycle and their Potential Implications for Deep Geological Disposal of Nuclear Fuel Waste in Fractured Crystalline Rock Mass. SKI 2005:28, Strålsäkerhetsmyndigheten (Swedish Radiation Safety Authority), Stockholm, Sweden.

Cho N, Martin C D, Christiansson R, 2002. Suppressing fracture growth around underground openings. In Proc. 5th North American Rock Mechanics Symposium and 17th Tunnelling Association of Canada Conference NARMS/TAC 2002, Toronto.

CIMNE, 2004. Code_Bright. Version 2.2 users guide. Departemento de Ingeniera del Terreno, Cartográfica y Geofisica Universidad Politècnica de Catalũna, Spain. (CIMNE=International Center for Numerical methods in Engineering.)

Claesson J, Probert T, 1996a. Temperature field due to time-dependent heat sources in a large rectangular grid. Derivation of an analytical solution. SKB TR-96-12, Svensk Kärnbränslehantering AB.

Claesson J, Probert T, 1996b. Thermoelastic stress due to a rectangular heat source in a semi-infinite medium. Derivation of an analytical solution. SKB TR-96-13, Svensk Kärnbränslehantering AB.

Damjanac B, Fairhurst C, 2010. Evidence for a Long-Term Strength Threshold in Crystalline Rock. Rock Mechanics and Rock Engineering, doi: 10.1007/s00603-00010-00090-00609.

Dershowitz W, Wallman O, Kindred S, 1991. Discrete Fracture Modelling for the Stripa Site Characterization and Validation Drift Inflow Predictions. Stripa Project Technical Report 91-16, Svensk Kärnbränslehantering AB.

Diederichs M, 2007. The 2003 Canadian Geotechnical Colloquium: Mechanistic interpretation and practical application of damage and spalling criteria for deep tunnelling. Canadian Geotechnical Journal, Vol. 44, No. 9, pp 1082–1116.

Esaki T, Du S, Mitani Y, Ikusad K, Jing L, 1999. Development of a shear-flow test apparatus and determination of coupled properties for a single rock joint. International Journal of Rock Mechanics and Mining Sciences, Vol. 36, pp 641–650.

Eshelby J D, 1957. The Determination of the Elastic Field of an Ellipsoidal Inclusion, and Related Problems. Proceedings of the Royal Society of London. Series A, Mathematical and Physical Sciences, Vol. 241, No. 1226, pp 376–396.

Follin S, Levén J, Hartley L, Jackson P, Yoyce S, Roberts D, Swift B, 2007. Hydrogeological characterisation and modelling of deformation zones and fracture domains, Forsmark modelling stage 2.2. SKB R-07-48, Svensk Kärnbränslehantering AB.

Follin S, Hartley L, Jackson P, Roberts D, Marsic N, 2008. Hydrogeological conceptual model development and numerical modelling using CONNECTFLOW, Forsmark modelling stage 2.3. SKB R-08-23, Svensk Kärnbränslehantering AB.

Fox A, La Pointe P, Hermanson J, Öhman J, 2007. Statistical geological discrete fracture network model. Forsmark modelling stage 2.2. SKB R-07-46, Svensk Kärnbränslehantering AB.

Fransson Å, 2009. Literature survey: Relations between stress change, deformation and transmissivity for fractures and deformation zones based on *in situ* investigatons. SKB R-09-13, Svensk Kärnbränslehantering AB.

Fälth B, Hökmark H, 2007. Mechanical and thermo-mechanical discrete fracture near-field analyses based on preliminary data from the Forsmark, Simpevarp and Laxemar sites. SKB R-06-89, Svensk Kärnbränslehantering AB.

Fälth B, Hökmark H, Munier R, 2010. Effects of large earthquakes on a KBS-3 repository. Evaluation of modelling results and their implications for layout and design. SKB TR-08-11, Svensk Kärnbränslehantering AB.

Gascoyne M, 2000. A review of published literature on the effects of permafrost on the hydrogeochemistry of bedrock. SKB R-01-56, Svensk Kärnbränslehantering AB.

Glamheden R, Fredriksson A, Röshoff K, Karlsson J, Hakami H, Christiansson R, 2007a. Rock Mechanics Forsmark. Site descriptive modelling Forsmark stage 2.2. SKB R-07-31, Svensk Kärnbränslehantering AB.

Glamheden R, Maersk Hansen L, Fredriksson A, Bergkvist L, Markström I, Elfström M, 2007b. Mechanical modelling of the Singö deformation zone. Site descriptive modelling Forsmark stage 2.1. SKB R-07-06, Svensk Kärnbränslehantering AB.

Glamheden R, Fälth B, Jacobsson L, Harrström J, Berglund J, Bergkvist L, 2010. Äspö Hard Rock Laboratory. Counterforce Applied to Prevent Spalling. SKB TR-10-37, Svensk Kärnbränslehantering AB.

Goodman R, 1976. Methods of geological engineering in discontinuous rock. West, New York,

Grasby S, Chen Z, 2005. Subglacial recharge into the Western Canadian Sedimentary Basin – Impact of Pleistocene glaciation on basin hydrodynamics. Bulletin of the Geological Society of America, Volume 117, pp 500–514, doi:510.1130/B25571.25571.

Hakami E, 1995. Aperture distribution of rock fractures. Ph.D. Thesis, Department of Civil and Environmental Engineering Royal Institute of Technology, Stockholm, Sweden.

Hakami H, 2006. Numerical studies on spatial variation of the *in situ* stress field at Forsmark – a further step. Site descriptive modelling Forsmark – stage 2.1. SKB R-06-124, Svensk Kärnbränslehantering AB.

Hakami E, Fredriksson A, Lanaro F, Wrafter J, 2008. Rock mechanics Laxemar. Site descriptive modelling. SDM-Site Laxemar. SKB R-08-57, Svensk Kärnbränslehantering AB.

Hansson B, Magnusson J, Söderlund P, 2009. Underground design Forsmark, Layout D2. Layout and construction plan. SKB R-08-113, Svensk Kärnbränslehantering AB.

Hartikainen J, Kouhia R, Wallroth T, 2010. Permafrost simulations at Forsmark using a numerical 2D thermo-hydro-chemical model. SKB TR-09-17, Svensk Kärnbränslehantering AB.

Hökmark H, 1990. Distinct element method modelling of fracture behaviour in near field rock. Stripa Project Technical Report 91-01, Svensk Kärnbränslehantering AB.

Hökmark H, Fälth B, 2003. Thermal dimensioning of the deep repository. Influence of canister spacing, canister power, rock thermal properties and nearfield design on the maximum canister surface temperature. SKB TR-03-09, Svensk Kärnbränslehantering AB.

Hökmark H, Claesson J, 2005. Use of an analytical method for calculating temperatures in repository host rock. Engineering Geology, Vol. 81, Issue 3, pp 353–364.

Hökmark H, Fälth B, Wallroth T, 2006. T-H-M couplings in rock. Overview of results of importance to the SR-Can safety assessment. SKB R-06-88, Svensk Kärnbränslehantering AB.

Hökmark H, Lönnqvist M, Kristensson O, Sundberg J, Hellström G, 2009. Strategy for thermal dimensioning of the final repository for spent nuclear fuel. SKB R-09-04, Svensk Kärnbränslehantering AB.

Ikonen K, 2003. Thermal analyses of nuclear fuel repository. Posiva report 2003-04, Posiva Oy, Olkiluoto, Finland.

Itasca, 2005. *FLAC* – Fast Lagrangian Analysis of Continua, User's guide. Itasca Consulting Group Inc. Minneapolis, Minnesota, USA.

Itasca, 2007. *3DEC* – 3-Dimensional Distinct Element Code, User's Guide. Itasca Consulting Group Inc. Minneapolis, Minnesota, USA.

Koyama T, 2007. Stress, Flow and Particle Transport in Rock Fractures. Ph.D. Thesis, Division of Engineering Geology and Geophysics, Department of Land and Water Resources Engineering, Royal Institute of Technology (KTH), Sweden.

Kristensson O, Hökmark H, 2007. Prototype Repository. Thermal 3D modelling of Äspö Prototype Repository. SKB IPR-07-01, Svensk Kärnbränslehantering AB.

Leijon B, 2005. Investigations of superficial fracturing and block displacements at drill site 5. Forsmark site investigation. SKB P-05-199, Svensk Kärnbränslehantering AB.

Lindblom U, 1997. Hydromechanical instability of a crystalline rock mass below a glaciation front. SKB U-97-13, Svensk Kärnbränslehantering AB.

Lindman S-O, Lönnblad C, Palmer S, 2007. Projektering slutförvar. Referensutformning för slutförvarsanläggningen. SKB PIR-07-22, Svensk Kärnbränslehantering AB.

Liu H-H, Rutqvist J, Zhou Q, Bodvarsson G S, 2003. Upscaling of normal stress-permeability relationships for fracture networks obeying fractional Levy motion. In GeoProc 2003 International Conference on Coupled T-H-M-C processes in Geo-systems: Fundamentals, Modelling, Experiments & Applications, Royal Institute of Technology. Dept. of Water Resources Engineering, Stockholm, Sweden.

Lund B, Schmidt P, Hieronymus C, 2009. Stress evolution and fault stability during the Weichselian glacial cycle. SKB TR-09-15, Svensk Kärnbränslehantering AB.

Löfman J, 2005. Simulation of hydraulic disturbances caused by the decay heat of the repository in Olkiluoto. Posiva 2005-07, Posiva Oy, Olkiluoto, Finland.

Lönnqvist M, Hökmark H, 2010. Assessment of Potential for Glacially Induced Hydraulic Jacking at Different Depths. SKB R-09-35, Svensk Kärnbränslehantering AB.

Lönnqvist M, Kristensson O, Fälth B, 2010. Assessment of a KBS-3 nuclear waste repository as a plane of weakness. SKB R-10-36, Svensk Kärnbränslehantering AB.

Martin C D, Davison C C, Kozak E T, 1990. Characterizing normal stiffness and hydraulic conductivity of a major shear zone in granite. In Rock Joints (Ed. Barton and Stephansson), Balkema, Rotterdam, The Netherlands.

Martin C D, 2005. Preliminary assessment of potential underground stability (wedge and spalling) at Forsmark, Simpevarp and Laxemar sites. SKB R-05-71, Svensk Kärnbränslehantering AB.

Martin C D, 2007. Quantifying *in situ* stress magnitudes and orientations for Forsmark. Forsmark stage 2.2. SKB R-07-26, Svensk Kärnbränslehantering AB.

Martino J, Read R, 1995. Mine-By Experiment Phase III – Heated Failure Tests. Technical Progress Report and Summary of Stage 3. AECL, Whiteshell Laboratories, Pinnawa, Manitoba, Canada.

Mas Ivars D, Hakami H, 2005. Effect of a sub-horizontal fracture zone and rock mass heterogeneity on the stress field in Forsmark area – a numerical study using 3DEC. Preliminary site description Forsmark area – version 1.2. SKB R-05-59, Svensk Kärnbränslehantering AB.

Moeller C A, Mickelson D M, Anderson M P, Winguth C, 2007. Groundwater flow beneath Late Weichselian glacier ice in Nordfjord, Norway. Journal of glaciology, Volume 53, No. 180, pp 84–90.

Munier R, 2010. Full perimeter intersection criteria. Definitions and implementations in SR-Site. SKB TR-10-21, Svensk Kärnbränslehantering AB.

Neretnieks I, Andersson J C, 2009. Characterisation of spalling fragments to obtain data for flow and transport in damaged zones. Paper presented at "Sinorock 2009" Congress 19–22 May, Hongkong.

Neuzil C E, 2003. Hydromechanical coupling in geologic processes. Hydrogeology Journal, Vol. 11, No. 1, pp 41–83.

Olofsson I, Simeonov A, Stephens M, Follin S, Nilsson A-C, Röshoff K, Lindberg U, Lanaro F, Fredriksson A, Persson L, 2007. Site descriptive modelling Forsmark, stage 2.2. A fracture domain concept as a basis for the statistical modelling of fractures and minor deformation zones, and inter-disciplinary coordination. SKB R-07-15, Svensk Kärnbränslehantering AB.

Olsson R, 1998. Mechanical and hydromechanical behaviour of hard rock joints. A laboratory study. Ph.D. Thesis, Department of Geotechnical Engineering, Chalmers University of Technology, Sweden.

Paterson W S B, 1994. The physics of glaciers. Elsevier Science Ltd. Oxford, UK,

Probert T, Claesson J, 1997a. Temperature field due to time-dependent heat sources in a large rectangular grid. Application for the KBS-3 repository. SKB TR-97-27, Svensk Kärnbränslehantering AB.

Probert T, Claesson J, 1997b. Thermoelastic stress due to a rectangular heat source in a semi-infinite medium. Application for the KBS-3 repository. SKB TR-97-26, Svensk Kärnbränslehantering AB.

Raven K G, Gale J E, 1985. Water flow in natural rock fractures as a function of stress and sample size. International Journal of Rock Mechanics and Mining Sciences & Geomechanics Abstracts, Vol. 22, Issue 4, pp 251–261.

Rhén I, Forsmark T, Hartley L, Jackson P, Roberts D, Swan D, Gylling B, 2008. Hydrogeological conceptualisation and parameterisation. Site descriptive modelling. SDM-Site Laxemar. SKB R-08-78, Svensk Kärnbränslehantering AB.

Rutqvist J, Tsang C-F, 2008. Review of SKB's Work on Coupled THM Processes Within SR-Can. External review contribution in support of SKI's and SSI's review of SR-Can. SKI Report 2008:08, Strålsäkerhetsmyndigheten (Swedish Radiation Safety Authority), Stockholm, Sweden.

Shen B, Stephansson O, 1996. SITE-94. Modelling of Rock Fracture Propagation for Nuclear Waste Disposal. SKI Report 96-18, Strålsäkerhetsmyndigheten (Swedish Radiation Safety Authority), Stockholm, Sweden.

SKB, 2005. Preliminary site description. Forsmark area – version 1.2. SKB R-05-18, Svensk Kärnbränslehantering AB.

SKB, 2006a. Climate and climate-related issues for the safety assessment SR-Can. SKB TR-06-23, Svensk Kärnbränslehantering AB.

SKB, 2006b. Long-term safety for KBS-3 repositories at Forsmark and Laxemar – a first evaluation. Main report of the SR-Can project. SKB TR-06-09, Svensk Kärnbränslehantering AB.

SKB, 2006c. Site descriptive modelling Forsmark stage 2.1. Feedback for completion of the site investigation including input from safety assessment and repository engineering. SKB R-06-38, Svensk Kärnbränslehantering AB.

SKB, 2007. Final repository facility. Underground design premises/D2. SKB R-07-33, Svensk Kärnbränslehantering AB.

SKB, 2008. Site description of Forsmark at completion of the site investigation phase. SDM-Site Forsmark. SKB TR-08-05, Svensk Kärnbränslehantering AB.

SKB, 2009a. Design premises for a KBS-3V repository based on results from the safety assessment SR-Can and some subsequent analyses. SKB TR-09-22, Svensk Kärnbränslehantering AB.

SKB, 2009b. Site engineering report Forsmark. Guidelines for underground design Step D2. SKB R-08-83, Svensk Kärnbränslehantering AB.

SKB, 2009c. Underground design Forsmark Layout D2. SKB R-08-116, Svensk Kärnbränslehantering AB.

SKB, 2009d. Underground design Laxemar. Layout D2. SKB R-09-16, Svensk Kärnbränslehantering AB.

SKB, 2010a. Climate and climate related issues for the safety assessment SR-Site. SKB TR-10-49, Svensk Kärnbränslehantering AB.

SKB, 2010b. Comparative analysis of safety related site characteristics. SKB TR-10-54, Svensk Kärnbränslehantering AB.

SKB, 2010c. Data report for the safety assessment SR-Site. SKB TR-10-52, Svensk Kärnbränslehantering AB.

SKB, 2010d. Design, construction and initial state of the underground openings for operational and long-term safety. SKB TR-10-18, Svensk Kärnbränslehantering AB.

SKB, 2010e. Geosphere process report for the safety assessment SR-Site. SKB TR-10-48, Svensk Kärnbränslehantering AB.

SKB, 2010f. Model summary report for the safety assessment SR-Site. SKB TR-10-51, Svensk Kärnbränslehantering AB.

SKB, 2010g. Site Engineering Report Design Step D2. Guidelines For Underground Design. Laxemar Site. SKB R-08-88, Svensk Kärnbränslehantering AB.

SKB, 2010h. Spent nuclear fuel for disposal in the KBS-3 repository. SKB TR-10-13, Svensk Kärnbränslehantering AB.

Stephens M B, Fox A, La Pointe P, Simeonov A, Isaksson H, Hermanson J, Öhman J, 2007. Geology Forsmark. Site descriptive modelling Forsmark stage 2.2. SKB R-07-45, Svensk Kärnbränslehantering AB.

Sundberg J, Wrafter J, Back P-E, Rosén L, 2008a. Thermal properties Laxemar. Site descriptive modelling SDM-Site Laxemar. SKB R-08-61, Svensk Kärnbränslehantering AB.

Sundberg J, Wrafter J, Ländell M, Back P-E, Rosén L, 2008b. Thermal properties Forsmark. Modelling stage 2.3. Complementary analysis and verification of the thermal bedrock model, stage 2.2. SKB R-08-65, Svensk Kärnbränslehantering AB.

Talbot C J, 1999. Ice ages and nuclear waste isolation. Engineering Geology, Vol. 52, Issues 3–4, pp 177–192.

Thunvik R, Braester C, 1980. Hydrothermal conditions around a radioactive waste repository. Part 1: A mathematical model for the flow of groundwater and heat in fractured rock. Part 2: Numerical solutions. SKBF/KBS TR 80-19, Svensk Kärnbränslehantering AB.

Vidstrand P, 2003. Surface and subsurface conditions in permafrost areas – a literature review. SKB TR-03-06, Svensk Kärnbränslehantering AB.

Vidstrand P, Follin S, Zugec N, 2010. Groundwater flow modelling of the permafrost and glacial periods – SR-Site Forsmark. SKB R-09-21, Svensk Kärnbränslehantering AB.

Vik G, Barton N, 1988. Stage I Joint Characterization and Stage II Preliminary Prediction using Small Core Samples. Stripa Project Technical Report 88-08, Svensk Kärnbränslehantering AB.

Wu P, 2009. State-of-the-Science Review of the Stress Field during a Glacial Cycle and Glacially Induced Faulting. NWMO TR-2009-09, Nuclear Waste Management Organization.

Åkesson M, Börgesson L, Kristensson O, 2010a. SR-Site Data Report. THM modelling of buffer, backfill and other system components. SKB TR-10-44, Svensk Kärnbränslehantering AB.

Åkesson M, Kristensson O, Börgesson L, Dueck A, Hernelind J, 2010b. THM modelling of buffer, backfill and other system components. Critical processes and scenarios. SKB TR-10-11, Svensk Kärnbränslehantering AB.

Unpublished documents

SKBdoc id, version	Title	Issuer, year
1198314, 1.0	Källstyrkor för bränsleelement under driftskede för Clink, slutförvars-anläggning och slutförvar	Alara Engineering, 2010

Appendix A

Tools

A1 3DEC

3DEC (3 Dimensional Distinct Element Code) is a numerical code based on the distinct element method /Itasca 2007/. It is used here to model the response of the rock mass due to thermal loading. The rock mass is represented by deformable blocks, which are divided into a mesh of finite difference elements.

The temperatures and temperature increments at each gridpoint are calculated at every time step using a built-in analytical solution based on regular grids of point sources. Contrary to the analytical solution described in the following section, the *3DEC* thermal logic accounts for the exact position of the individual heat sources. Depending on the required level of detail, point sources within a selected part of the source grid can be substituted by vertical line sources, or combinations of line sources, to better reflect the temperature distribution around the spent fuel canisters (cf. /Fälth and Hökmark 2007, Hökmark et al. 2009/.)

For large and/or finely zoned models with many gridpoints, the temperature calculations are very time consuming. Therefore, a temperature handling scheme, devised by /Fälth and Hökmark 2007/, is used to export the temperatures to a file that can be read back into other models with identical source grids (see Figure A-1), thus reducing the total calculation time considerably. Thermally induced stresses are subsequently calculated from the temperature increments at each time step.

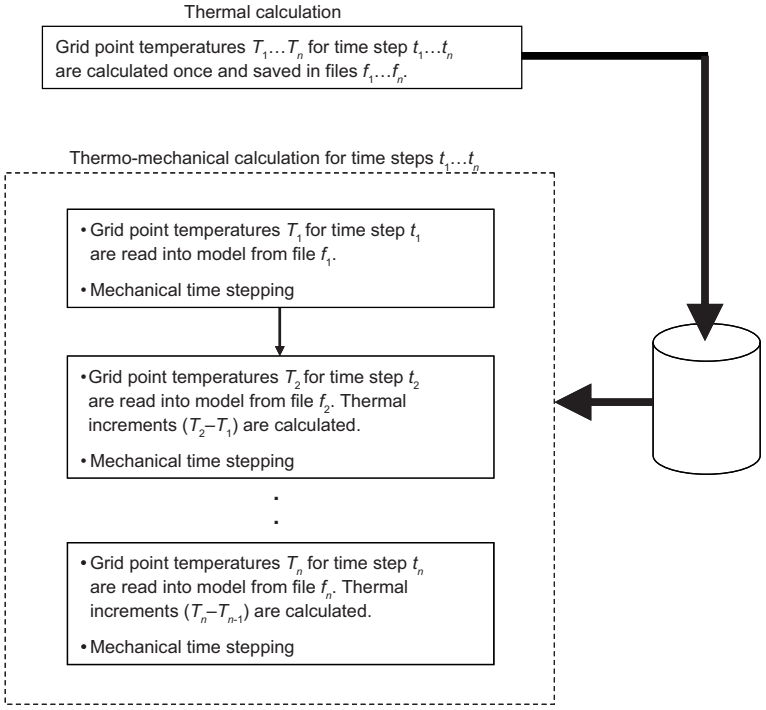

Figure A-1. *Schematic view of temperature handling scheme. From /Fälth and Hökmark 2007/.*

A2 Thermo-mechanical analytical solution

A2.1 General

The thermo-mechanical analytical solution by /Claesson and Probert 1996b/ is derived from Navier's equation (Equation A-1) for the displacement field, $\boldsymbol{u} = (u_x, u_y, u_z)$ in homogenous and linear elastic rock.

$$\nabla^2 \boldsymbol{u} + \frac{1}{1-2\nu}\nabla e = \frac{2\alpha(1+\nu)}{1-2\nu}\nabla T,\ e = \nabla \cdot \boldsymbol{u} \qquad \text{Eq. A-1}$$

Here, ν (–) is Poisson's ratio, α (1/K) is the coefficient of linear thermal expansion and T (K or °C) is the temperature. The temperature distribution is given by rectangular heat sources /Claesson and Probert 1996a/. These provide the average repository-scale temperatures without account of the actual temperature distribution around individual canisters. The heated panels can be positioned anywhere within the repository host rock and be introduced sequentially in time. The contribution from a repository consisting of several heated panels is obtained by a superposition of the solution for one heated panel, cf. Figure A-2.

The six strain (and stress) components are derived from the three displacement components (u_x is the displacement in the x-direction etc.), by use of the following expressions. The complete set of equations is listed in Section A.2.5.

$$\varepsilon_{xx} = \frac{\partial u_x}{\partial x},\quad \varepsilon_{xy} = \frac{1}{2}\left(\frac{\partial u_x}{\partial y} + \frac{\partial u_y}{\partial x}\right) \qquad \text{Eq. A-2}$$

$$\sigma_{xx} = 2\mu\left(\varepsilon_{xx} + \frac{\nu}{1-2\nu}e - \frac{1+\nu}{1-2\nu}\alpha T\right),\ \sigma_{xy} = 2\mu\varepsilon_{xy},\quad \mu = \frac{E}{2(1+\nu)} \qquad \text{Eq. A-3}$$

The analytical thermo-mechanical solution gives a good representation of the average repository-scale response of a heated rock mass /Probert and Claesson 1997b, Hökmark et al. 2006/, cf. Section A.2.2, and can be used to quickly demonstrate the effects of various layout assumptions and parameter variations. It should, however, be noted that the solution is derived for uniform and homogeneously distributed properties and does not account for any spatial distribution of properties nor for fractures or cavities in the rock and does not capture the thermo-mechanical evolution in the near vicinity of a canister. To find the stress distribution in the near-field of a canister, numerical tools must be employed, cf. Chapter 9 of the main text.

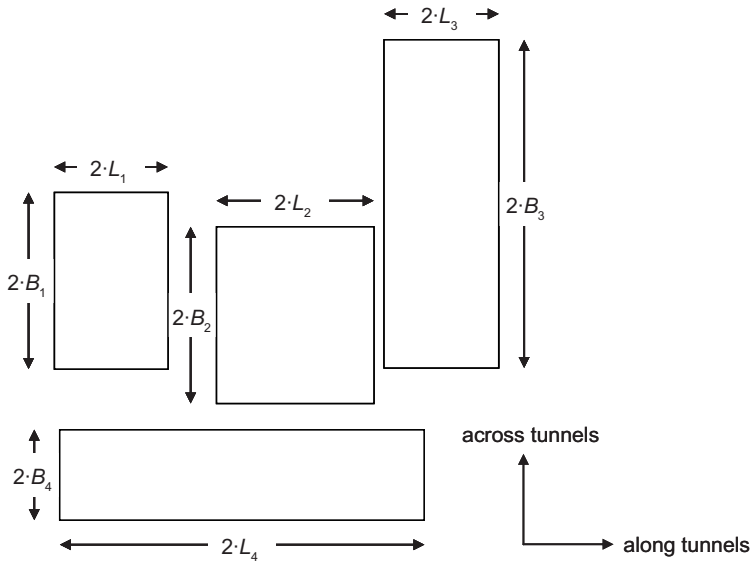

Figure A-2. *Examples of rectangular heated panels of different sizes.*

The equations are valid at the ground surface for the first approximately 250 years after deposition /Claesson and Probert 1996b/. As time progresses, the error introduced at the ground surface propagates downwards and the solution is valid at repository level for approximately the first 1,000 years after deposition. The solution is not valid after long times (10,000 years).

The analytical solution has been implemented in the commercially available spreadsheet program MathCad.

A2.2 Comparison between analytical solution and 3DEC models

By use of a schematic representation of a KBS-3 repository at Forsmark based on Layout D1 /Brantberger et al. 2006/, cf. Figure A-3 (left), the large-scale thermo-mechanical evolution was investigated using the numerical code *3DEC* (version 3.0) and the analytical solution. Material properties used in the models are presented in Table A-1.

Figure A-3 (right) shows numerically and analytically obtained thermally induced normal and shear stresses on the deformation zone ZFMA2 (cf. left part of figure) 500 years after deposition of the nuclear waste. As demonstrated in the figure, there is a very good agreement between the analytical solution and *3DEC*.

Table A-1. Material properties /SKB 2005, SKB 2006c/.

Model parameter	Value	Unit
Heat conductivity	3.55	W/(m·K)
Heat capacity	2.18	MJ/(m³·K)
Linear expansion coefficient	$7.7 \cdot 10^{-6}$	1/K
Young's modulus	67	GPa
Poisson's ratio	0.23	–

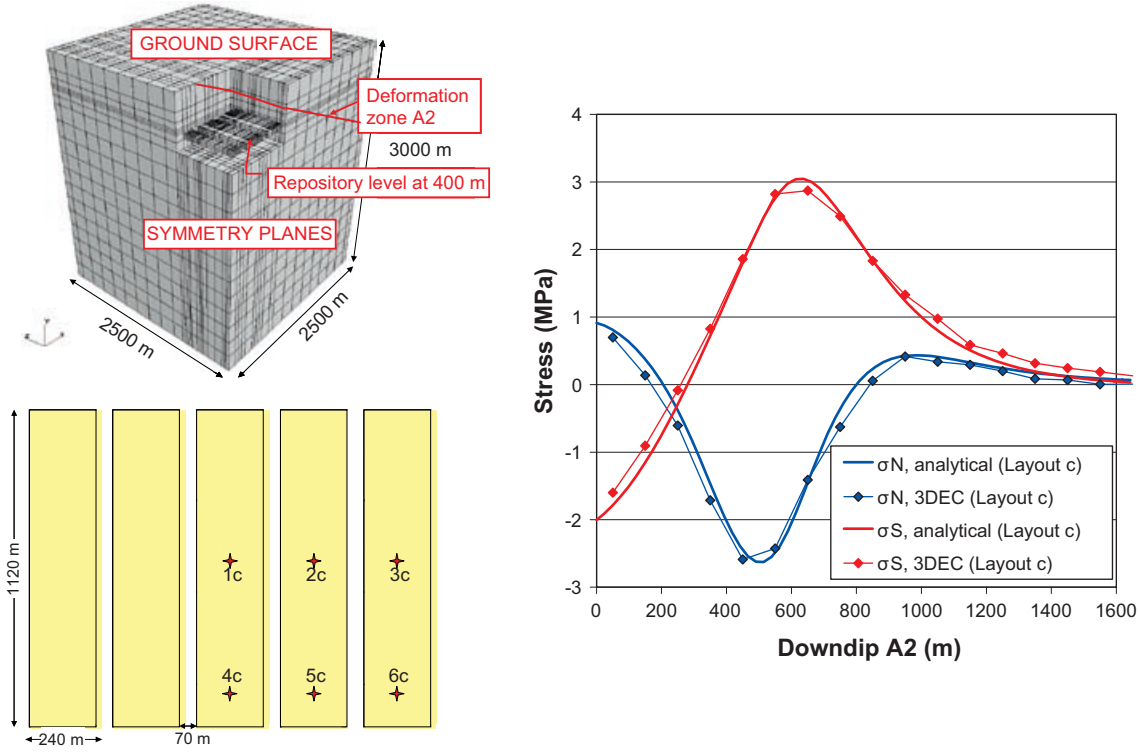

Figure A-3. *View of 3DEC model and schematic repository layout (left). Changes in shear and normal stress on deformation zone A2 500 years after deposition of the canisters (right).*

A2.3 Input variables and constants

The rock's thermo-mechanical properties are used as input to the equations, cf. Table A-2.

Table A-2. Thermo-mechanical properties used as input to the analytical solution.

Property	Unit	Symbol
Young's modulus	Pa	E
Poisson's ratio	–	v
Density	kg/m^3	ρ
Specific heat	J/(kg·K)	c
Thermal conductivity	W/(m·K)	λ
Thermal diffusivity	m^2/s	a
Coefficient of linear thermal expansion	1/K	α

The thermal diffusivity, a, of the rock is defined as $a = \dfrac{\lambda}{\rho \cdot c}$.

The displacement, strain and stress components involve two constants, u_0 and p_0, defined below.

$$u_0 = \frac{1+\nu}{1-\nu} e_0 \frac{\alpha}{\pi \cdot \rho \cdot c},$$

$$p_0 = \frac{E}{1+\nu} u_0$$

The constant e_0 is the instantaneous heat release per unit are at $t = 0$. As the analytical solution is derived on the basis that the heat release is continuous, this constant is arbitrarily chosen to be 1 ($e_0 = 1$).

A2.4 Heat load

Temperature field

The temperature field from an instantaneous quadrantal heat source in an infinite medium is given by the following expression /Claesson and Probert 1996a/.

$$T_{qi}(x,y,z,t) = \frac{e_0}{\rho \cdot c} \operatorname{erf}\left(\frac{x}{\sqrt{4 \cdot a \cdot t}}\right) \operatorname{erf}\left(\frac{y}{\sqrt{4 \cdot a \cdot t}}\right) \frac{1}{\sqrt{4 \cdot \pi \cdot a \cdot t}} \exp\left(-\frac{z^2}{4 \cdot a \cdot t}\right)$$

The solution for any time-dependent heat source, $q(t)$, at time t is found by multiplying the above expression (index qs) at time $t - \tau$ by $q(\tau)/e_0$ and integrating over the interval $0 < \tau < t$. The total solution for a rectangular heat source is found by superposition of four quadrantal solutions, where x is replaced by $x \pm L$ and y by $y \pm B$ /Claesson and Probert 1996b/.

Each heated panel has dimensions $2L$ (along tunnels) and $2B$ (across tunnels). In the case of a repository consisting of several heated panels, each panel need not have the same size or power density and can be located anywhere within the repository host rock. L and B are defined as follows:

$L = \dfrac{n_x \cdot p_x}{2}$, where n_x is the number of canisters in each tunnel and p_x is the canister spacing.

$B = \dfrac{n_y \cdot p_y}{2}$, where n_y is the number of tunnels in the rectangular panel and p_y is the tunnel spacing.

Power and decay function

As in Chapter 5, the decay function of SKB's reference fuel /Hökmark et al. 2009/ is used as input to the analytical solution and the initial power of each canister is assumed to be 1,700 W. The power function is given by the following expression:

$$q_i(t) = \frac{P(0)}{p_x \cdot p_y} a_i \exp(-t / t_i),$$

where p_x and p_y are canister and tunnel spacing, respectively and the initial power is $P(0)$. The exponential coefficients, a_i and t_i, are presented in Table 5-1.

A2.5 Structure of solution and list of equations

Each displacement, strain and stress component consists of a time-dependent (index *qi*) and a time-independent (index *mb*) part /Claesson and Probert 1996b/.

The time-dependent part is the solution for an instantaneous quadrantal heat source in an infinite medium. The time-independent part is a corresponding solution that accounts for a mirror heat source at $z = 2H$ ($z = 0$ is repository level and $z = H$ is the ground surface) as well as the mechanical boundary conditions at the ground surface. The two solutions are combined to form the solutions for an instantaneous quadrantal heat source in a semi-infinite medium (index *qs*).

The solution for any time-dependent heat source, $q(t)$, at time t is found by multiplying the above expression (index *qs*) at time $t - \tau$ by $q(\tau)/e_0$ $0 < \tau < t$. The total solution for a rectangular heat source is found by superposition of four quadrantal solutions, where x is replaced by $x \pm L$ and y by $y \pm B$.

The equations for each of the displacement, strain and stress components are presented under the headings 'Displacement components', 'Strain components' and 'Stress components'.

Space variables and auxiliary functions

The solution is derived in a right-handed Cartesian coordinate system, where x and y are the space variables in the two horizontal directions and z in the vertical direction. r and r_m are the distances from the origin ($z = 0$ is repository level) and from the mirror sources at $z = 2H$ to an arbitrary point (x, y, z), respectively.

$$r = r(x, y, z) = \sqrt{x^2 + y^2 + z^2}$$

$$r_m = r_m(x, y, z) = \sqrt{x^2 + y^2 + (2H - z)^2}$$

The following expressions appear in many of the components and are used to simplify the equations; they have no direct physical meaning. The parameter p is a space variable, which can be either x or y.

$$C(p, r, t) = \frac{1}{r} \cdot \frac{p}{r^2 - p^2} \left(\operatorname{erf}\left(\frac{r}{\sqrt{4 \cdot a \cdot t}} \right) - r \cdot \exp\left(-\frac{r^2 - p^2}{4 \cdot a \cdot t} \right) \cdot \frac{\operatorname{erf}\left(\frac{p}{\sqrt{4 \cdot a \cdot t}} \right)}{p} \right)$$

$$D(p, r_m) = r_m^2 - p^2$$

$$B(p, z, r_m, H) = 2(H - z)(2H - z)\left(\frac{1}{r_m^2} + \frac{2}{D(p, r_m)} \right)$$

$$G(p, z, r_m, H, \xi) = \frac{1}{r_m} \cdot \frac{p}{D(p, r_m)} \left(\xi - B(p, z, r_m, H) \right)$$

Displacement field

Time-dependent displacement components

$$u_{qi}(x,y,z,t) = -u_0 \int_0^{1/\sqrt{4at}} \frac{\operatorname{erf}(y \cdot s)}{s} \exp\left(-(r^2 - y^2) \cdot s^2\right) ds$$

$$v_{qi}(x,y,z,t) = u_{qi}(y,x,z,t)$$

$$w_{qi}(x,y,z,t) = u_0 \sqrt{\pi} \cdot z \int_0^{1/\sqrt{4at}} \operatorname{erf}(x \cdot s) \operatorname{erf}(y \cdot s) \exp\left(-z^2 \cdot s^2\right) ds$$

Time-independent displacement components

$$u_{mb}(x,y,z) = u_0 \left(-\left(\frac{3}{2} - 2\nu\right) \ln\left(\frac{r_m + y}{r_m - y}\right) + \frac{2(H-z)}{r_m} \cdot \frac{y(2H-z)}{{r_m}^2 + x^2} \right)$$

$$v_{mb}(x,y,z) = u_{mb}(y,x,z)$$

$$w_{mb}(x,y,z) = u_0 \left((3-4\nu) \arctan\left(\frac{x \cdot y}{(2H-z) r_m}\right) + \frac{2(H-z)}{r_m} \left(\frac{x \cdot y}{{r_m}^2 - x^2} + \frac{x \cdot y}{{r_m}^2 - y^2} \right) \right)$$

Quadrantal solution

$u_{qs}(x, y, z, t) = u_{qi}(x, y, z, t) + u_{mb}(x, y, z)$

$v_{qs}(x, y, z, t) = v_{qi}(x, y, z, t) + v_{mb}(x, y, z)$

$w_{qs}(x, y, z, t) = w_{qi}(x, y, z, t) + w_{mb}(x, y, z)$

Displacement components

$$u(x,y,z,t) = \sum_{j=0}^{J-1} \sum_{n_x=0}^{1} \sum_{n_y=0}^{1} \frac{(2n_x - 1)(2n_y - 1)}{4} \cdot \left(\int_0^t \frac{q_j(\tau)}{e_0} u_{qs}(x + (2n_x - 1)L, y + (2n_y - 1)B, z, t - \tau) d\tau \right) \quad \text{Eq. A-4}$$

$$v(x,y,z,t) = \sum_{j=0}^{J-1} \sum_{n_x=0}^{1} \sum_{n_y=0}^{1} \frac{(2n_x - 1)(2n_y - 1)}{4} \cdot \left(\int_0^t \frac{q_j(\tau)}{e_0} v_{qs}(x + (2n_x - 1)L, y + (2n_y - 1)B, z, t - \tau) d\tau \right) \quad \text{Eq. A-5}$$

$$w(x,y,z,t) = \sum_{j=0}^{J-1} \sum_{n_x=0}^{1} \sum_{n_y=0}^{1} \frac{(2n_x - 1)(2n_y - 1)}{4} \cdot \left(\int_0^t \frac{q_j(\tau)}{e_0} w_{qs}(x + (2n_x - 1)L, y + (2n_y - 1)B, z, t - \tau) d\tau \right) \quad \text{Eq. A-6}$$

Strain field

Time-dependent strain components

$\varepsilon xx_{qi}(x, y, z, t) = u_0 \cdot x \cdot C(y, r, t)$

$\varepsilon yy_{qi}(x, y, z, t) = u_0 \cdot y \cdot C(x, r, t)$

$$\varepsilon zz_{qi}(x,y,z,t) = \frac{1+\nu}{1-\nu}\cdot\alpha\cdot T_{qi}(x,y,z,t) - u_0\left(x\cdot C(y,r,t) + y\cdot C(x,r,t)\right)$$

$$\varepsilon xy_{qi}(x,y,z,t) = -\frac{u_0}{r}\cdot \operatorname{erf}\left(\frac{r}{\sqrt{4\cdot a\cdot t}}\right)$$

$\varepsilon xz_{qi}(x, y, z, t) = u_0 \cdot z \cdot C(y, r, t)$

$\varepsilon yz_{qi}(x, y, z, t) = u_0 \cdot z \cdot C(x, r, t)$

Time-independent strain components

$\varepsilon xx_{mb}(x, y, z) = u_0 \cdot x \cdot G(y, z, r_m, H, 3–4\nu)$

$\varepsilon yy_{mb}(x, y, z) = u_0 \cdot y \cdot G(x, z, r_m, H, 3–4\nu)$

$\varepsilon zz_{mb}(x, y, z) = –u_0\left(x \cdot G(y, z, r_m, H, 4\nu–1) + y \cdot G(x, z, r_m, H, 4\nu–1)\right)$

$$\varepsilon xy_{mb}(x,y,z) = \frac{u_0}{r_m}\left(\frac{2(H-z)(2H-z)}{{r_m}^2} - 3 + 4\nu\right)$$

$$\varepsilon xz_{mb}(x,y,z) = -u_0\left(\frac{1}{r_m}\cdot\frac{y(4H-3z)}{D(y,r_m)} + (2H-z)\cdot G(y,z,r_m,H,0)\right)$$

$\varepsilon yz_{mb}(x, y, z) = \varepsilon xz_{mb}(y, x, z)$

Quadrantal solution

$\varepsilon xx_{qs}(x, y, z, t) = \varepsilon xx_{qi}(x, y, z, t) + \varepsilon xx_{mb}(x, y, z)$

$\varepsilon yy_{qs}(x, y, z, t) = \varepsilon yy_{qi}(x, y, z, t) + \varepsilon yy_{mb}(x, y, z)$

$\varepsilon zz_{qs}(x, y, z, t) = \varepsilon zz_{qi}(x, y, z, t) + \varepsilon zz_{mb}(x, y, z)$

$\varepsilon xy_{qs}(x, y, z, t) = \varepsilon xy_{qi}(x, y, z, t) + \varepsilon xy_{mb}(x, y, z)$

$\varepsilon xz_{qs}(x, y, z, t) = \varepsilon xz_{qi}(x, y, z, t) + \varepsilon xz_{mb}(x, y, z)$

$\varepsilon yz_{qs}(x, y, z, t) = \varepsilon yz_{qi}(x, y, z, t) + \varepsilon yz_{mb}(x, y, z)$

Strain components

$$\varepsilon xx(x,y,z,t) = \sum_{j=0}^{J-1}\sum_{n_x=0}^{1}\sum_{n_y=0}^{1}\frac{(2n_x-1)(2n_y-1)}{4}\cdot\left(\int_0^t \frac{q_j(\tau)}{e_0}\varepsilon xx_{qs}(x+(2n_x-1)L, y+(2n_y-1)B, z, t-\tau)d\tau\right) \quad \text{Eq. A-7}$$

$$\varepsilon yy(x,y,z,t) = \sum_{j=0}^{J-1}\sum_{n_x=0}^{1}\sum_{n_y=0}^{1}\frac{(2n_x-1)(2n_y-1)}{4}\cdot\left(\int_0^t \frac{q_j(\tau)}{e_0}\varepsilon yy_{qs}(x+(2n_x-1)L, y+(2n_y-1)B, z, t-\tau)d\tau\right) \quad \text{Eq. A-8}$$

$$\varepsilon zz(x,y,z,t) = \sum_{j=0}^{J-1}\sum_{n_x=0}^{1}\sum_{n_y=0}^{1}\frac{(2n_x-1)(2n_y-1)}{4}\cdot\left(\int_0^t \frac{q_j(\tau)}{e_0}\varepsilon zz_{qs}(x+(2n_x-1)L, y+(2n_y-1)B, z, t-\tau)d\tau\right) \quad \text{Eq. A-9}$$

$$\varepsilon xy(x,y,z,t) = \sum_{j=0}^{J-1}\sum_{n_x=0}^{1}\sum_{n_y=0}^{1}\frac{(2n_x-1)(2n_y-1)}{4}\cdot\left(\int_0^t \frac{q_j(\tau)}{e_0}\varepsilon xy_{qs}(x+(2n_x-1)L, y+(2n_y-1)B, z, t-\tau)d\tau\right) \quad \text{Eq. A-10}$$

$$\varepsilon xz(x,y,z,t) = \sum_{j=0}^{J-1}\sum_{n_x=0}^{1}\sum_{n_y=0}^{1}\frac{(2n_x-1)(2n_y-1)}{4}\cdot\left(\int_0^t \frac{q_j(\tau)}{e_0}\varepsilon xz_{qs}(x+(2n_x-1)L, y+(2n_y-1)B, z, t-\tau)d\tau\right) \quad \text{Eq. A-11}$$

$$\varepsilon yz(x,y,z,t) = \sum_{j=0}^{J-1}\sum_{n_x=0}^{1}\sum_{n_y=0}^{1}\frac{(2n_x-1)(2n_y-1)}{4}\cdot\left(\int_0^t \frac{q_j(\tau)}{e_0}\varepsilon yz_{qs}(x+(2n_x-1)L, y+(2n_y-1)B, z, t-\tau)d\tau\right) \quad \text{Eq. A-12}$$

Stress field

Time-dependent stress components

$$\sigma xx_{qi}(x,y,z,t) = \frac{p_0}{u_0}\varepsilon xx_{qi}(x,y,z,t) - \frac{E\cdot\alpha}{1-\nu}T_{qi}(x,y,z,t)$$

$$\sigma yy_{qi}(x,y,z,t) = \frac{p_0}{u_0}\varepsilon yy_{qi}(x,y,z,t) - \frac{E\cdot\alpha}{1-\nu}T_{qi}(x,y,z,t)$$

$$\sigma zz_{qi}(x,y,z,t) = \frac{p_0}{u_0}\left(\varepsilon zz_{qi}(x,y,z,t) - \frac{1+\nu}{1-\nu}\cdot\alpha\cdot T_{qi}(x,y,z,t)\right)$$

$$\sigma xy_{qi}(x,y,z,t) = \frac{p_0}{u_0}\varepsilon xy_{qi}(x,y,z,t)$$

$$\sigma xz_{qi}(x,y,z,t) = \frac{p_0}{u_0}\varepsilon xz_{qi}(x,y,z,t)$$

$$\sigma yz_{qi}(x,y,z,t) = \frac{p_0}{u_0}\varepsilon yz_{qi}(x,y,z,t)$$

Time-independent stress components

$$\sigma xx_{mb}(x,y,z) = p_0\left(x\cdot G(y,z,r_m,H,3) + 4\nu\frac{1}{r_m}\cdot\frac{x\cdot y}{D(x,r_m)}\right)$$

$$\sigma yy_{mb}(x,y,z) = p_0\left(y\cdot G(x,z,r_m,H,3) + 4\nu\frac{1}{r_m}\cdot\frac{x\cdot y}{D(y,r_m)}\right)$$

$$\sigma zz_{mb}(x,y,z) = -p_0\left(x\cdot G(y,z,r_m,H,-1) + y\cdot G(x,z,r_m,H,-1)\right)$$

$$\sigma xy_{mb}(x,y,z) = \frac{p_0}{u_0}\varepsilon xy_{mb}(x,y,z)$$

$$\sigma xz_{mb}(x,y,z) = \frac{p_0}{u_0}\varepsilon xz_{mb}(x,y,z)$$

$$\sigma yz_{mb}(x,y,z) = \frac{p_0}{u_0}\varepsilon yz_{mb}(x,y,z)$$

Quadrantal solution

$\sigma xx_{qs}\ (x, y, z, t) = \sigma xx_{qi}\ (x, y, z, t) + \sigma xx_{mb}\ (x, y, z)$

$\sigma yy_{qs}\ (x, y, z, t) = \sigma yy_{qi}\ (x, y, z, t) + \sigma yy_{mb}\ (x, y, z)$

$\sigma zz_{qs}\ (x, y, z, t) = \sigma zz_{qi}\ (x, y, z, t) + \sigma zz_{mb}\ (x, y, z)$

$\sigma xy_{qs}\ (x, y, z, t) = \sigma xy_{qi}\ (x, y, z, t) + \sigma xy_{mb}\ (x, y, z)$

$\sigma xz_{qs}\ (x, y, z, t) = \sigma xz_{qi}\ (x, y, z, t) + \sigma xz_{mb}\ (x, y, z)$

$\sigma yz_{qs}\ (x, y, z, t) = \sigma yz_{qi}\ (x, y, z, t) + \sigma yz_{mb}\ (x, y, z)$

Stress components

$$\sigma xx(x,y,z,t) = \sum_{j=0}^{J-1}\sum_{n_x=0}^{1}\sum_{n_y=0}^{1}\frac{(2n_x-1)(2n_y-1)}{4}\cdot\left(\int_0^t \frac{q_j(\tau)}{e_0}\sigma xx_{qs}(x+(2n_x-1)L, y+(2n_y-1)B, z, t-\tau)d\tau\right) \quad \text{Eq. A-13}$$

$$\sigma yy(x,y,z,t) = \sum_{j=0}^{J-1}\sum_{n_x=0}^{1}\sum_{n_y=0}^{1}\frac{(2n_x-1)(2n_y-1)}{4}\cdot\left(\int_0^t \frac{q_j(\tau)}{e_0}\sigma yy_{qs}(x+(2n_x-1)L, y+(2n_y-1)B, z, t-\tau)d\tau\right) \quad \text{Eq. A-14}$$

$$\sigma zz(x,y,z,t) = \sum_{j=0}^{J-1}\sum_{n_x=0}^{1}\sum_{n_y=0}^{1}\frac{(2n_x-1)(2n_y-1)}{4}\cdot\left(\int_0^t \frac{q_j(\tau)}{e_0}\sigma zz_{qs}(x+(2n_x-1)L, y+(2n_y-1)B, z, t-\tau)d\tau\right) \quad \text{Eq. A-15}$$

$$\sigma xy(x,y,z,t) = \sum_{j=0}^{J-1}\sum_{n_x=0}^{1}\sum_{n_y=0}^{1}\frac{(2n_x-1)(2n_y-1)}{4}\cdot\left(\int_0^t \frac{q_j(\tau)}{e_0}\sigma xy_{qs}(x+(2n_x-1)L, y+(2n_y-1)B, z, t-\tau)d\tau\right) \quad \text{Eq. A-16}$$

$$\sigma xz(x,y,z,t) = \sum_{j=0}^{J-1}\sum_{n_x=0}^{1}\sum_{n_y=0}^{1}\frac{(2n_x-1)(2n_y-1)}{4}\cdot\left(\int_0^t \frac{q_j(\tau)}{e_0}\sigma xz_{qs}(x+(2n_x-1)L, y+(2n_y-1)B, z, t-\tau)d\tau\right) \quad \text{Eq. A-17}$$

$$\sigma yz(x,y,z,t) = \sum_{j=0}^{J-1}\sum_{n_x=0}^{1}\sum_{n_y=0}^{1}\frac{(2n_x-1)(2n_y-1)}{4}\cdot\left(\int_0^t \frac{q_j(\tau)}{e_0}\sigma yz_{qs}(x+(2n_x-1)L, y+(2n_y-1)B, z, t-\tau)d\tau\right) \quad \text{Eq. A-18}$$

Appendix B

Effects of steeply dipping deformation zones and variations in Young's modulus

B1 General

In the near-field there will be significantly increased tangential stresses around the repository openings, in particular around the deposition holes (cf. Chapter 9 and /Fälth and Hökmark 2007/). Some distance away from the openings the stress changes will be unaffected by the boundaries and take on much smaller average values.

The proposed repository location at Forsmark is intersected by a number of large and steeply dipping fracture zones /SKB 2006c/. Figure B-1 (left) shows a map of the known fracture zones in the region at repository level (400 m depth).

The effects of steeply dipping deformation zones on rock mass deformations and tangential stresses in deposition hole walls are investigated by use of the numerical code *3DEC* (version 3.0). Here, a generic repository layout based on Layout D1 for the Forsmark site /Brantberger et al. 2006/, cf. Figure B-1, is used. Canister spacing and tunnel spacing are set to 6 m and 40 m, respectively.

B2 Description of numerical models

B2.1 Rock mass properties

The thermo-mechanical properties for the rock mass are obtained from versions 1.2 and 2.2 of the Site Descriptive Model (SDM) /SKB 2005, SKB 2006c/, cf. Table B-1.

Table B-1. Rock mass properties /SKB 2005, SKB 2006c/.

Model parameters	Unit	Value
Density (ρ)	kg/m^3	2,700
Heat conductivity (λ)	W/(m·K)	3.55
Heat capacity (C)	MJ/(m^3·K)	2.18
Heat diffusivity (a = λ/C)	m^2/s	$1.63 \cdot 10^{-6}$
Linear expansion coefficient (α)	K^{-1}	$7.7 \cdot 10^{-6}$
Young's modulus (E)	GPa	67
Poisson's ratio (ν)	–	0.23

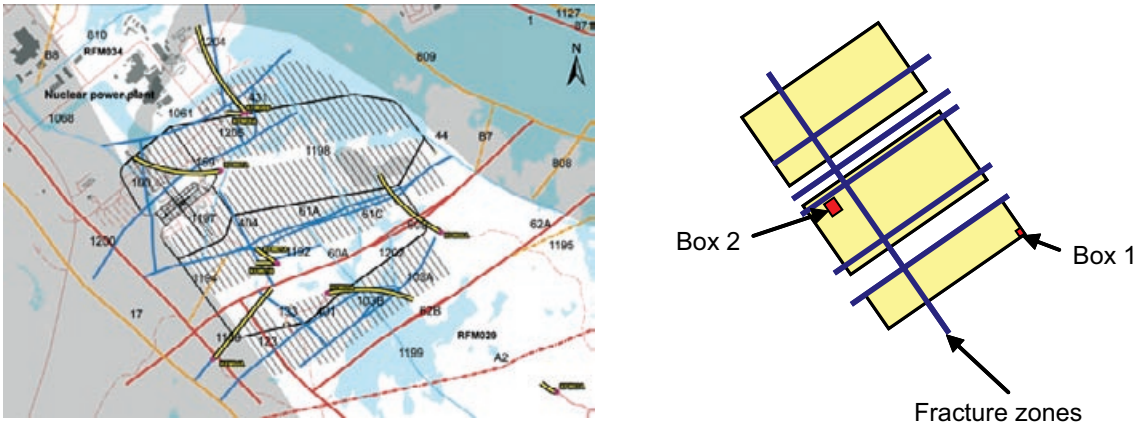

Figure B-1. *Left: Deformation zones and preliminary repository layout (D1) at Forsmark /SKB 2006c/. Right: Approximation of layout and deformation zones for numerical modelling work. Note that the approximate layout is quarter-symmetric around Box 1.*

The *in situ* stresses at repository level (400 m depth) are obtained from an early draft of /Martin 2007/, cf. Table B-2. The deposition tunnels are assumed to be perfectly aligned with the major horizontal *in situ* stress at all positions within the repository region.

Table B-2. In situ stresses at 400 m depth.

σH	σh	σv
–38.6 MPa	–22.7 MPa	–10.6 MPa

B2.2 Deformation zone properties

The joint normal stiffness (*JKN*) is calculated from the deformation properties of the deformation zone and the surrounding rock mass by use of Equation B-1, where E is the effective deformation modulus of the fracture zone and w is its width. In the present modelling work, the mechanical properties of the deformation zones have been chosen to be those of typical fracture zones in the Forsmark area /Glamheden et al. 2007a/ and in the Laxemar area /Hakami et al. 2008/.

$$JKN = \frac{E}{w}$$
$$\frac{1}{E} = \frac{1}{E_{zone}} - \frac{1}{E_{rock}} \qquad \text{Eq. B-1}$$

/Glamheden et al. 2007a/ gives estimates of the normal stiffness of vertical and steeply dipping fracture zones at Forsmark in the range 80–90 GPa/m. However, the deformation modulus of all deformation zones is in the range 46–77 GPa /Glamheden et al. 2007a/. Applying Equation B-1 to the lower limit of the range and assuming that the deformation zone has a width of 25 m results in a joint normal stiffness of 6 GPa/m. The normal stiffness of steeply dipping deformation zones at Laxemar varies between around 0.2 and 3 GPa/m /Hakami et al. 2008/.

In the present modelling work two sets of fracture properties are used, cf. Table B-3:

- JKN = 1.5 GPa/m and JKS = 0.3 GPa/m;
- JKN = 6.0 GPa/m and JKS = 3.0 GPa/m.

The cohesion and tensile strength are set to 500 MPa for all fractures.

B2.3 Initial and boundary conditions

Large-scale models

As *in situ* stresses and the rock's initial temperature do not influence the analyses performed here, they are consequently set to zero.

All boundaries, with the exception of the top representing the ground surface, are locked in their normal directions (roller boundaries).

Near-field models

Similarly to the large-scale models, the *in situ* temperature is set to zero. The major horizontal *in situ* stress is assumed to be perfectly aligned with the deposition tunnels at all positions within the repository region.

The near-field models (cf. Section B.4) do not have any explicitly modelled fractures. Instead, the additional deformations due to the fracture zones are handled by use of displacement type boundary conditions from the large-scale models. These are obtained from displacements on pre-defined cut-planes in the large-scale models representing the near-field model boundaries, cf. Figure B-2 (right).

B2.4 Description of models

Three models (labelled B, C and D) have active fractures and portions of softer rock outside the deposition areas, cf. Table B-3. In addition to these models, a linear elastic model (A) is analysed for comparison. Linear elastic near-field models are analyzed using boundary conditions from large-scale models A, B and C.

Table B-3. Large-scale model map and fracture properties.

Model code	Fracture properties	Description
A	–	Linear elastic (no fractures)
B	JKN = 1.5 GPa/m JKS = 0.3 GPa/m	All joints active from ground surface to bottom of model.
C	JKN = 6.0 GPa/m JKS = 3.0 GPa/m	All joints active from ground surface to bottom of model.
D	JKN = 6.0 GPa/m JKS = 3.0 GPa/m	Same as C, but with E = 30 GPa between z = 800 m and z = 1,400 m, cf. Figure B-2 (left).

B3 Effects on near-field boundary deformations

In the large-scale models, the system of excavated tunnels and deposition holes is not explicitly modelled. Instead, the heat sources are positioned, according to the specified layout, in the rock mass at 400 m depth. In the present modelling work, the canister spacing is 6 m and the tunnel spacing is 40 m. Due to the symmetry of the repository layout, only a quarter needs to be modelled, cf. Figure B-2.

The steeply dipping fracture zones are represented by six vertical, planar features positioned in the repository region as shown in Figure B-2 (right) and cutting through the entire modelled rock mass. Their mechanical properties are presented in Table B-3.

B3.1 Effects due to variations in Young's modulus

The thermally induced deformations of the rock mass in a semi-infinite homogeneous material are independent of the deformation modulus /e.g. Claesson and Probert 1996b/. Figure B-3 shows the resulting relative expansions/contractions at the boundaries of the near-field models marked Box 1 and 2 in Figure B-2 (right) for two values of Young's modulus (67 GPa and 60 GPa). With the exception of early times (when there is a small discrepancy between the results), there is a very good agreement between the results.

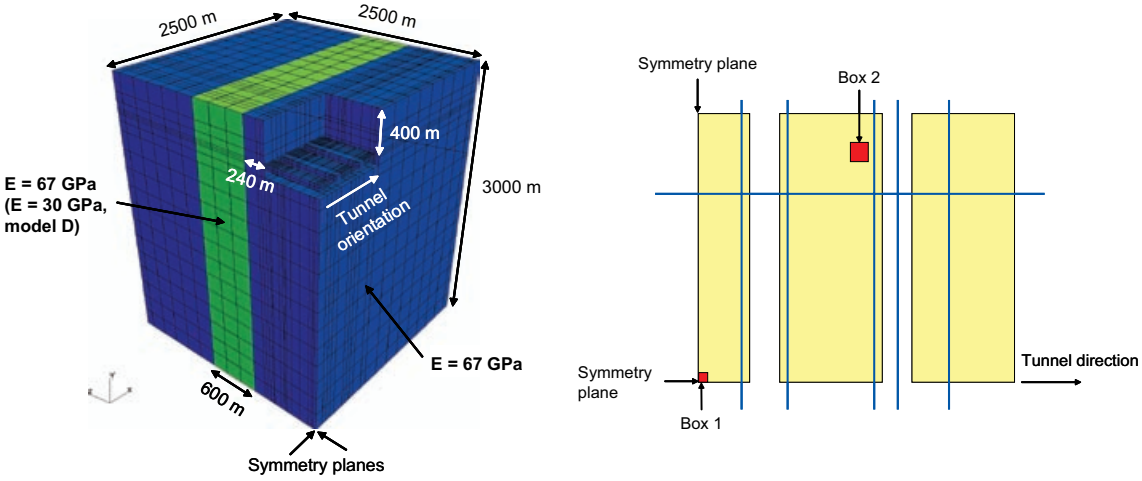

Figure B-2. Left: Outlines of large-scale 3DEC model. Right: Repository layout with deformation zones outlined in blue. Box 1 and 2 denote locations of near-field models.

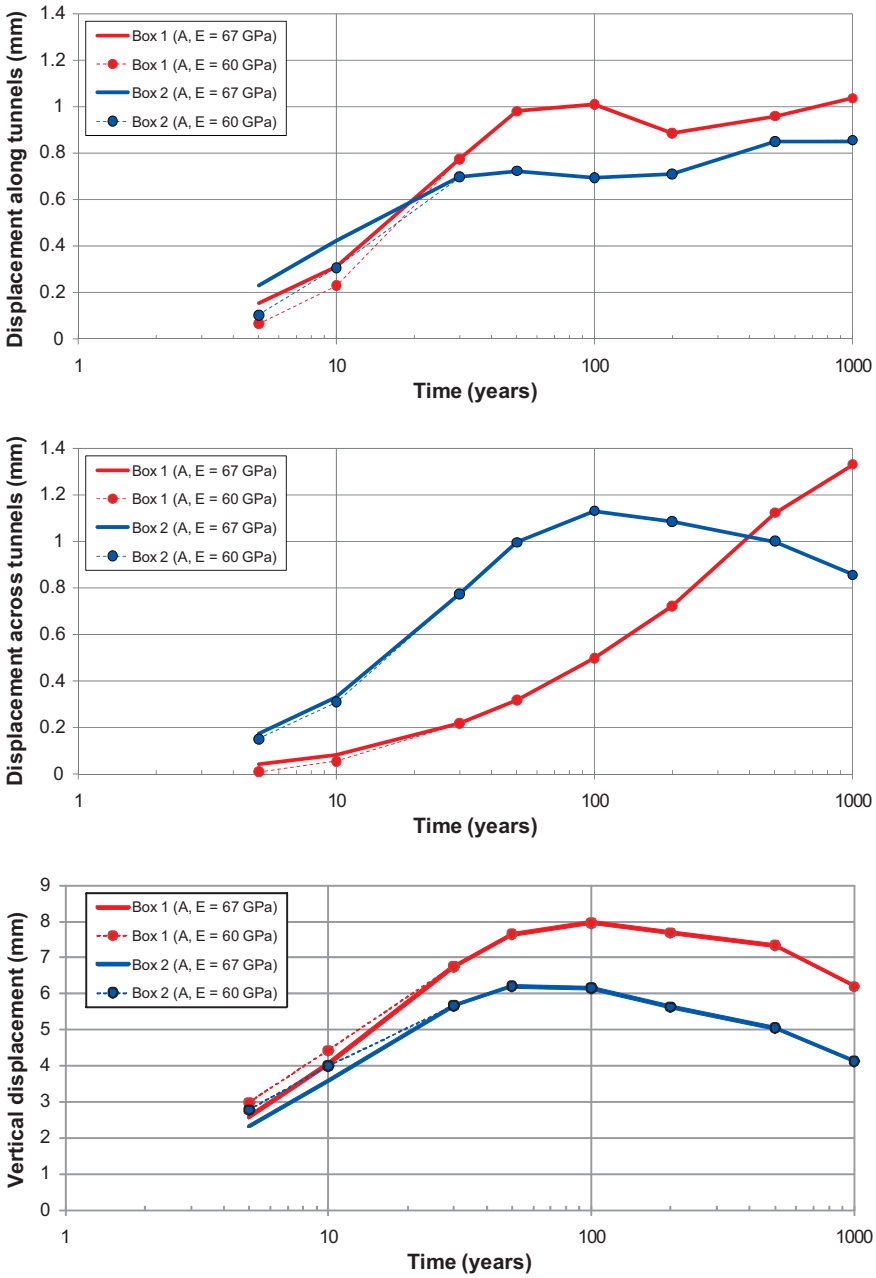

Figure B-3. *Near-field boundary conditions. Top: Relative displacement along tunnels. Middle: Relative displacement across tunnels. Lower: Relative displacement in the vertical direction.*

B3.2 Effects due to deformation zones

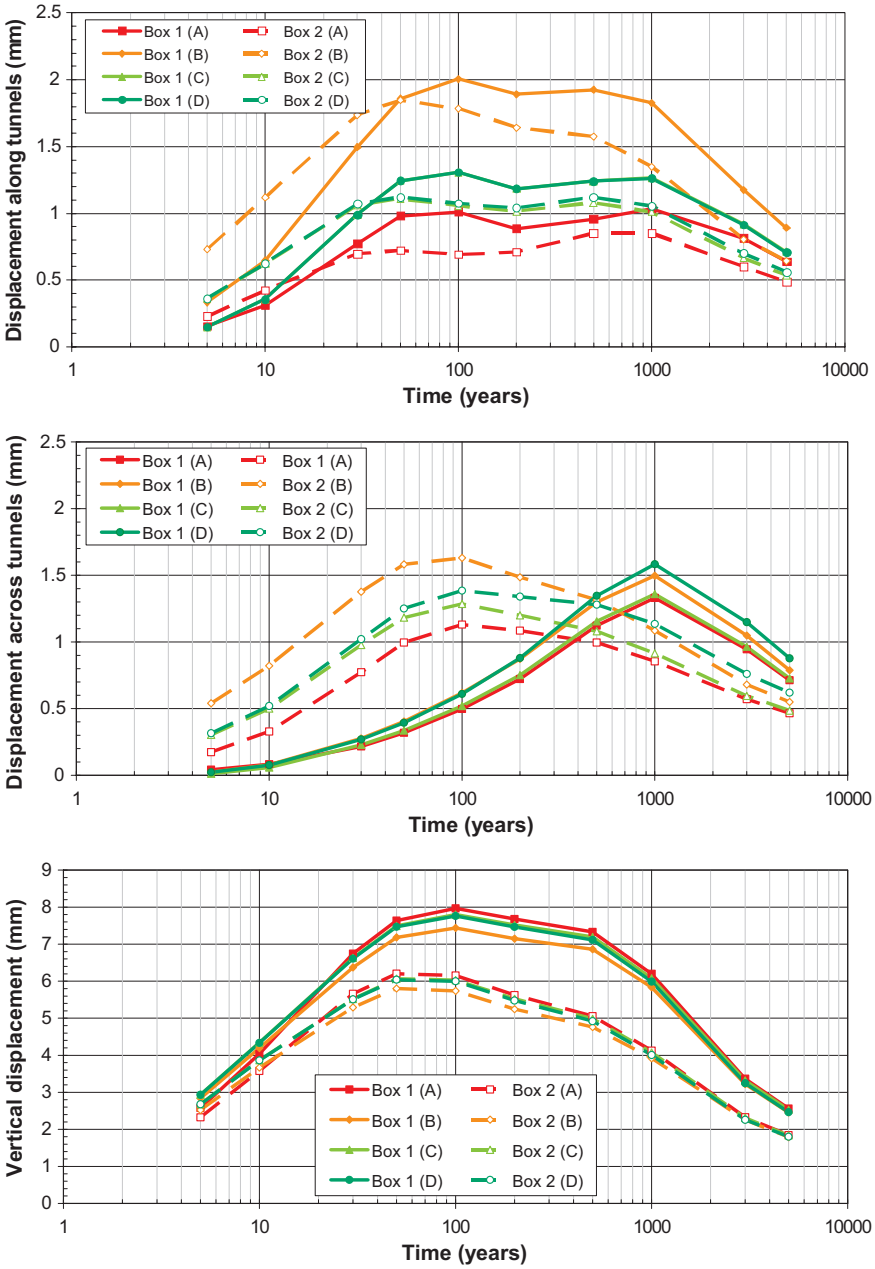

Figure B-4. *Near-field boundary conditions. Top: Relative displacement along tunnels. Middle: Relative displacement across tunnels. Lower: Relative displacement in the vertical direction.*

B4 Effects on stresses in the near-field

Each near-field model corresponds to one of the two boxes in the large-scale models (cf. Figure B-2, right) and consists of one tunnel segment with seven canisters, where three deposition holes are explicitly modelled. The near-field design is based on Layout D1 /Brantberger et al. 2006/ with cylindrical deposition holes. The dimensions of the near-field models are 42 m along tunnels, 40 m across tunnels and 50 m high (cf. Figure B-5, left).

Figure B-6 shows the resulting tangential stresses in the deposition hole walls using boundary conditions from models A, B and C in Figure B-4. At canister mid-height (5 m below the tunnel floor), the stress reduction due to the presence of steeply dipping deformation zones is about 6–8 MPa (model B) and 2–3 MPa (model C). At 1 m below the tunnel floor the stress reduction is about 1.5–10 MPa (model B) and 0.5–3 MPa (model C).

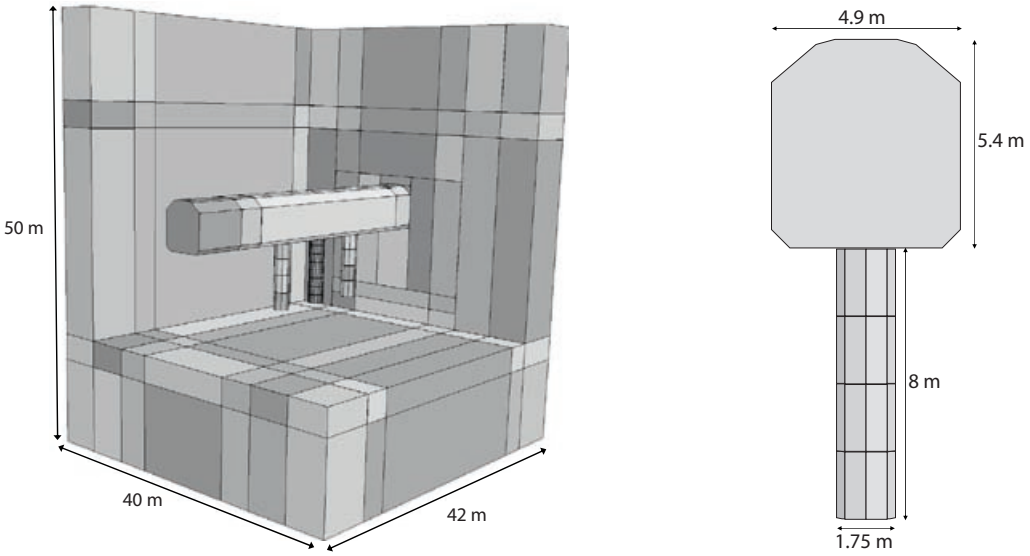

Figure B-5. *Left: Outline of near-field 3DEC models. Right: Tunnel and deposition hole dimensions based on Layout D1 /Brantberger et al. 2006/.*

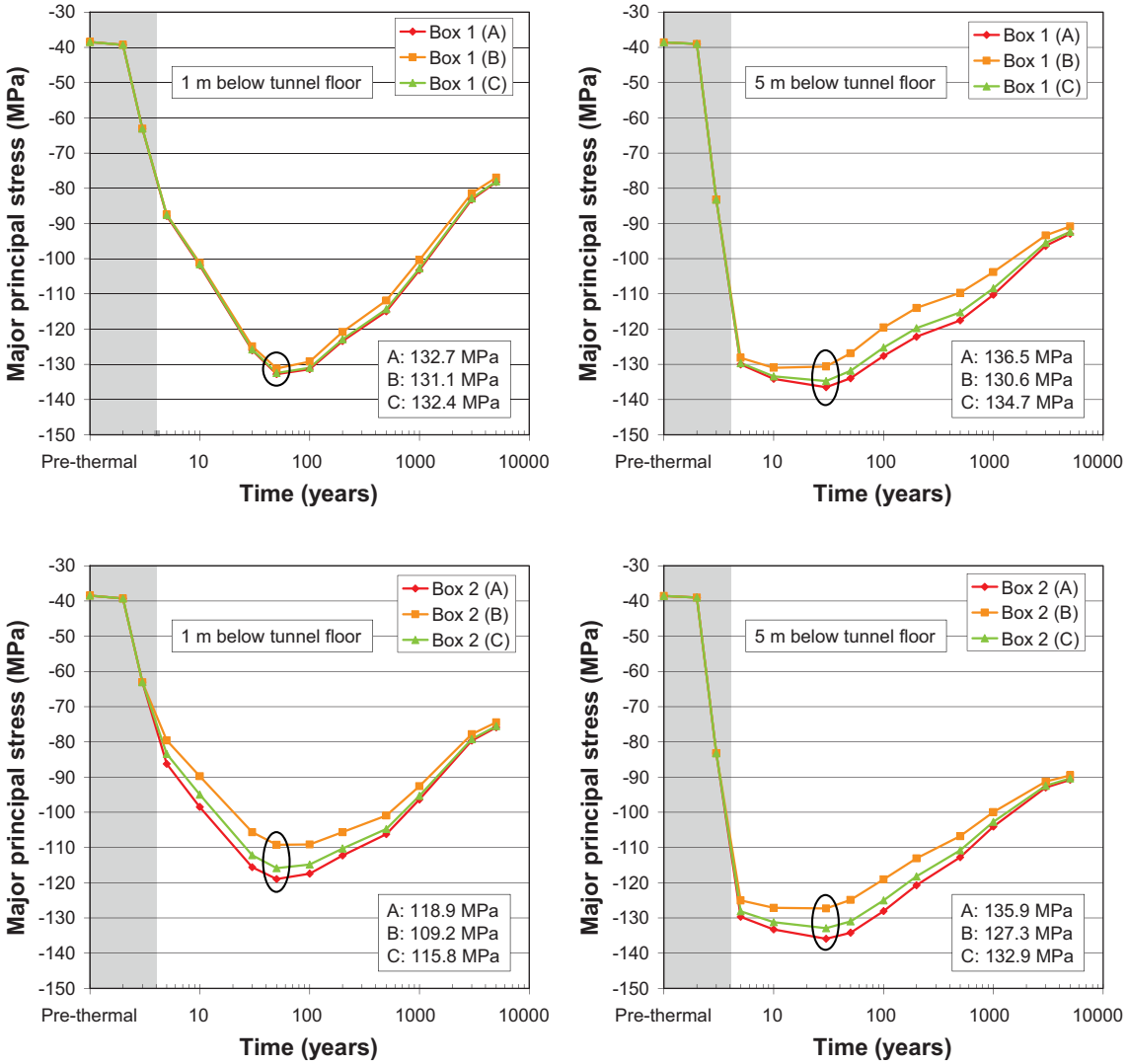

Figure B-6. *Thermally induced tangential stresses on the bore hole wall. Left column: At positions 1 m below the tunnel floor. Right column: At canister mid-height (5 m below the tunnel floor).*

Appendix C

Importance of size of deposition areas

Previous thermo-mechanical analyses of a KBS-3 repository have been analysed using a generic repository consisting of rectangular deposition areas with simultaneous deposition of all canisters e.g. /Fälth and Hökmark 2007, Hökmark et al. 2006/. In the following, the analytical thermo-mechanical solution will be used to demonstrate the impact on stresses due to various layout assumptions and deposition sequences using mean value rock mass properties from the Forsmark site (FFM01/RFM029), cf. Table 4-5. The power density is set to 7 W/m^2 (corresponding to a canister spacing of 6 m and tunnel spacing of 40 m).

Examples of the temporal development of the average thermal stresses at the centre of differently sized generic deposition areas are presented in Figure C-1. The *in situ* stresses and the effects of the excavated openings are not considered here.

The panels' sizes and layout have different impacts on the stresses along tunnels and those across tunnels. In the case of square-shaped repositories, the stresses along and across tunnels are equal. In the direction along tunnels, the largest square-shaped repository (2) has higher stresses at its centre than the one panel repository (3), due to the fact that the additional heat in layout 3 increases the expansion along tunnels. In the direction across tunnels, the two square repositories (1 and 2) have the smallest stresses. Here, the single panel repository (3) experiences the highest thermal stresses. In repository layouts 4 and 5, large expansions along tunnels are not possible to the same extent as in layout 3 and consequently the stresses increase compared with layout 3.

Another aspect that is clearly observed in the analyses is that the vertical thermal stress additions increase significantly with a reduction in repository size. However, if the repository design is such that it is reasonably large and symmetric in size, the vertical stress additions are small in comparison with the horizontal stress additions.

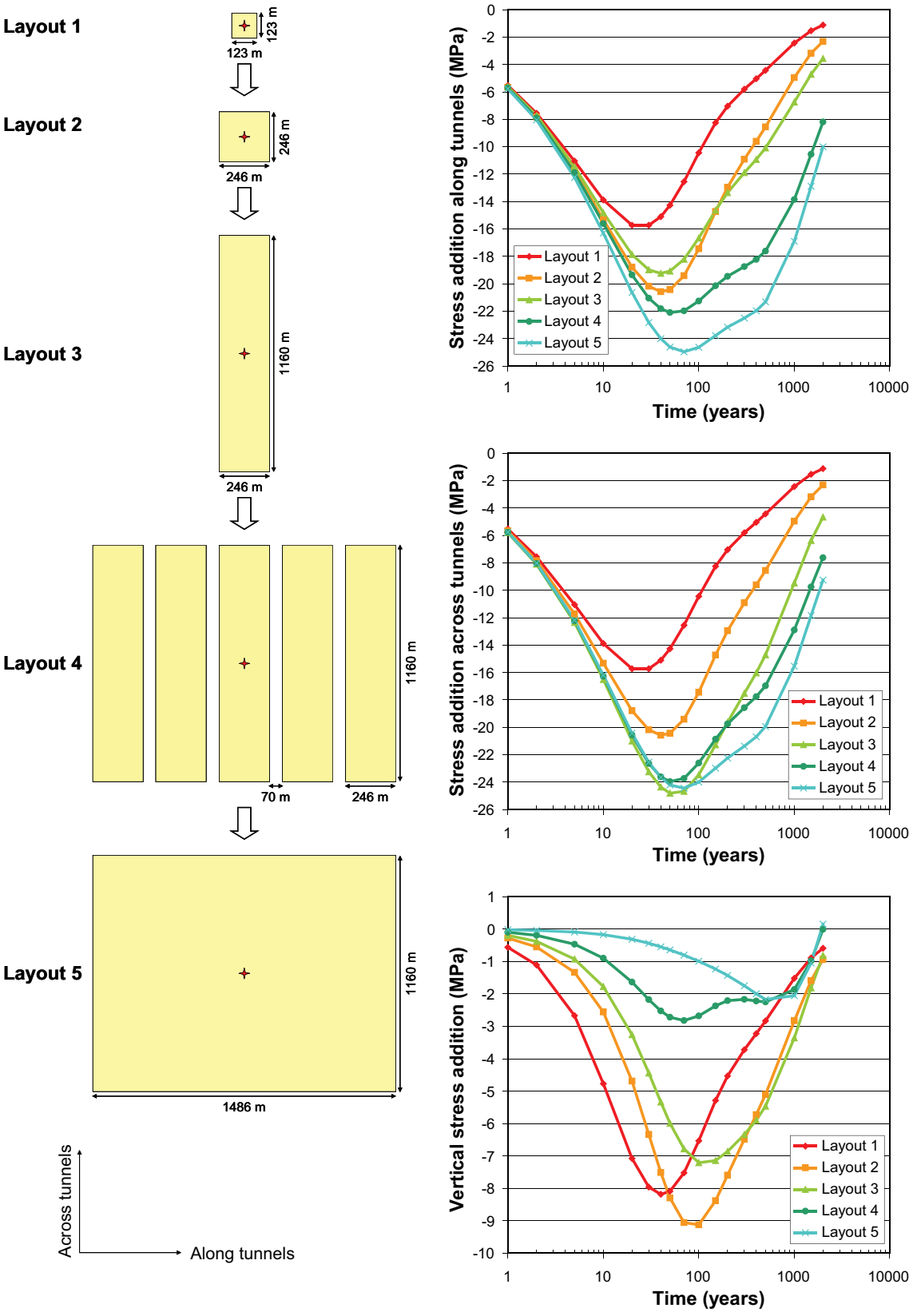

Figure C-1. *Left: Schematic repository layouts in different sizes. Right column: Stresses at the centre of each layout along tunnels (top), across tunnels (middle) and vertically (bottom).*

Appendix D

Glacially induced pore pressure

D1 Introduction

The magnitude of the glacially induced pore pressure is of great importance for stress induced transmissivity changes and stability of fractures. In /Hökmark et al. 2006/, two pore pressure cases at 500 m depth were studied: the pore pressure (in excess of hydrostatic pressure) was assumed to be 1) constant with time (i.e. zero) or 2) schematically assumed to be 90% of the maximum mechanical load (11 MPa) during glacial maxima and 25% of the maximum mechanical load (3.1 MPa) as the ice margin was passing over the site. Sensitivity analyses were performed by doubling the mechanical load and excess pore pressure. Elevated pore pressure levels in combination with proglacial permafrost were not considered.

It should be noted that the maximum ice sheet thickness considered by /Hökmark et al. 2006/ was about 1.4 km, whereas in the present study is nearly 3 km (cf. Figure 4-12), which would correspond to an excess pore pressure of 23 MPa during glacial maxima and 6.5 MPa as the ice margin is passing following the schematic percentages of the maximum load described above. The 90% of the maximum load assumed during glacial maxima may not be sufficiently conservative. It is often assumed that the hydrostatic pressure at the ice/bed interface is 90% of the (local) ice sheet thickness /e.g. Grasby and Chen 2005, Moeller et al. 2007, Bense and Person 2008/, i.e. approximately 98% of the mechanical ice load. Furthermore, assuming 25% of the maximum mechanical load as the ice margin is passing over the site, is likely to be overly conservative. /Lönnqvist and Hökmark 2010/ found that the maximum jacking depth, cf. Section 7.6, during the retreat of the ice margin is about 100 m. The excess pore pressure estimate (6.5 MPa) made above corresponds to a maximum jacking depth of nearly 400 m.

In the following sections, estimates of the excess pore pressure during different parts of the glacial cycle are made based on results from the study on hydraulic jacking /Lönnqvist and Hökmark 2010/ and modelling work specifically conducted for the present report. In particular, the excess pore pressure during the following points in time is of interest, cf. Figure 4-12 and Figure 4-13:

- during glacial maxima, *i.e.* 12 ka and 54.5 ka,
- as the ice margin is passing over the site, *i.e.* 15 ka and 58 ka,
- in combination with proglacial permafrost, *i.e.* 39 ka.

D2 Representation of ice sheet

Similarly to the study on hydraulic jacking by /Lönnqvist and Hökmark 2010/, the ice sheet is represented by a generic ice profile /Paterson 1994/ with a maximum thickness of 3 km, cf. Figure D-1. The hydrostatic pressure at the ice/bed interface is assumed to be 90% of the (local) ice sheet thickness, i.e. approximately 98% of the mechanical ice load, at all times.

The ice front is assumed to be moving at a constant speed. Typical frontal advance and retreat rates at present-day Forsmark /SKB 2006a, b/ in the reconstruction of the Weichselian ice sheet are 40 m/year and 300 m/year, respectively. As an upper bound estimate, the pore pressure distribution is assumed to have reached steady state conditions before retreat.

D3 Pore pressures during periods of ice cover

Figure D-2 shows examples of the excess pore pressure at 500 m depth during a glacial cycle for different values of the hydraulic diffusivity. The results are obtained using the analytical continuum approach described in /Lönnqvist and Hökmark 2010/ for a 3,000 m high ice (Figure D-1) and typical frontal advance rates (40 m/year) and retreat rates (300 m/year) at the Forsmark site /SKB 2006a, b/. As seen in Figure D-2, for high values of the hydraulic diffusivity or long durations of the ice cover, the excess pore pressure can be approximated by the boundary pressure. However, this approximation does not account for residual or permafrost induced excess pore pressures. As the ice retreats at the end of the glaciation, high residual pore pressure might remain for a long period of time after the ice is gone /e.g. Lönnqvist and Hökmark 2010/.

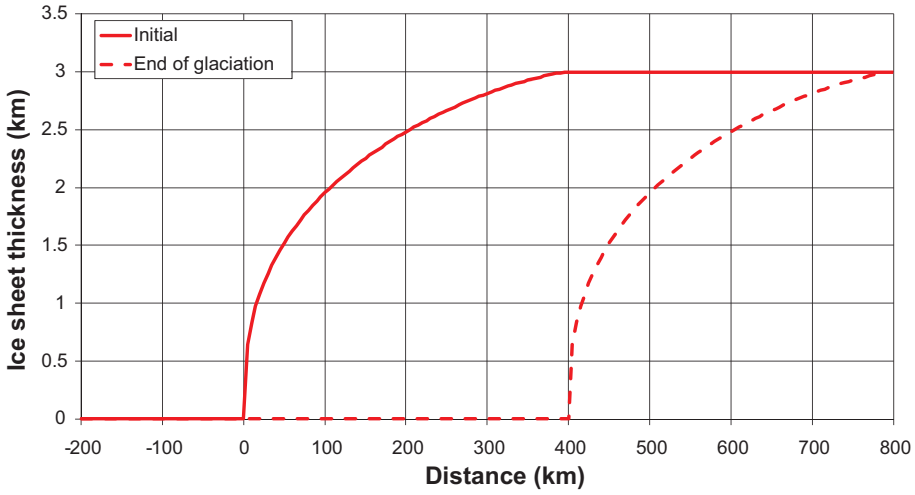

Figure D-1. *Generic ice sheet profile based on /Paterson 1994/.*

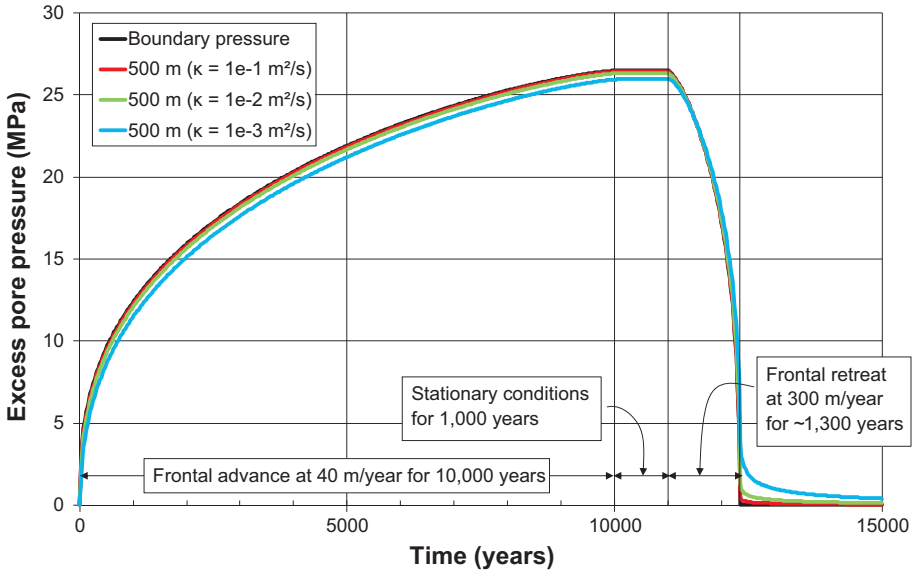

Figure D-2. *Example of excess pore pressure at 500 m depth for three assumptions regarding hydraulic diffusivity during a glacial cycle. The results are obtained using the analytical continuum approach described in /Lönnqvist and Hökmark 2010/ for a 3,000 m high ice and typical frontal advance and retreat rates at the Forsmark site /SKB 2006a, b/.*

D4 Retreating ice margin

As the ice retreats at the end of the glaciation, elevated residual pore pressures might remain for a long period of time after the ice is gone, cf. e.g. Figure D-2. Scoping calculations performed by /Lönnqvist and Hökmark 2010/ showed that in the case with depth variations in hydraulic diffusivity – as is the case at Forsmark (Figure 4-10, left) – the low diffusivity at large depths will prevent an upwards transfer of pore pressures and thus contribute to a more efficient drainage of the upper part of the system. However, the analytical solution /Lönnqvist and Hökmark 2010/ does not account for spatial variations in hydraulic diffusivity. Here, the excess pore pressure, at the end of the glacial cycle, is estimated in 2D by use of the thermal logic in the numerical finite element code Code_Bright /CIMNE 2004/.

D4.1 Modelling approach

For the purpose of this study, the excess pore pressure is assumed to have reached steady state conditions before retreat. Similarly to the analytical solution /Lönnqvist and Hökmark 2010/, the total excess pore pressure at a given point in the rock mass at the end of the glaciation is obtained by superposition of results from three different models as shown schematically in Figure D-3 (left). Cases 2 (stationary ice and initially zero pore pressure) and 3 (retreating ice front from initially zero pore pressure) are obtained from the Code_Bright models (see below). Case 1 (steady state pressure distribution), however, cannot be handled by use of a finite sized numerical model and is, for the purpose of this study, approximated to be equal to the boundary pressure at all depths, cf. Figure D-3 (right).

In the Code_Bright models, the rock mass is represented by a rectangular block subdivided into three layers (cf. Figure D-4, left), which can take on different hydraulic properties. Here, the hydraulic properties are based on site data from fracture domain FFM01 at Forsmark, cf. Figure 4-10 (left). Note that, these values are based on individual fractures and do not include effects of deformation zones. The distribution of permeabilities at 465 m depth /Vidstrand et al. 2010/, shown in Figure 4-10 (right), suggests that the hydraulic diffusivity in each depth-interval might be a factor of ten higher than those obtained from the left part of the figure.

The boundary conditions used in the modelling work, Figure D-4 (right), are step-function-approximations of the generic ice profile shown in Figure D-1. For the retreating ice front (Case 3 in Figure D-3, left), the retreat phase is sub-divided into nine time-intervals in which ice front is stationary at a position given by the centre-point in each time-interval. The first six time-intervals are 200 years followed by one 100-year-interval and one 30-year-interval. The final time-interval is approximately 3 years.

Figure D-5 shows comparisons between the analytical solution and Code_Bright models for homogeneous values of the hydraulic diffusivity. The pore pressure in all cases is evaluated at functions of depth at the position of the ice margin at the end of the glaciation shown in Figure D-4 (left), i.e. 400 km from the ice margin for the stationary ice (Case 2). Case 2 gives the best fit between numerical and analytical results, cf. Figure D-5 (left). Close to the ice margin the pressure gradient becomes very steep and difficult to approximate in a numerical model. Consequently, the fit between analytical and numerical results for Case 3 (Figure D-5, middle) is somewhat poorer. However, as seen in Figure D-5 (right), the total excess pore pressure in homogeneous rock can be approximated very well by the Code_Bright models.

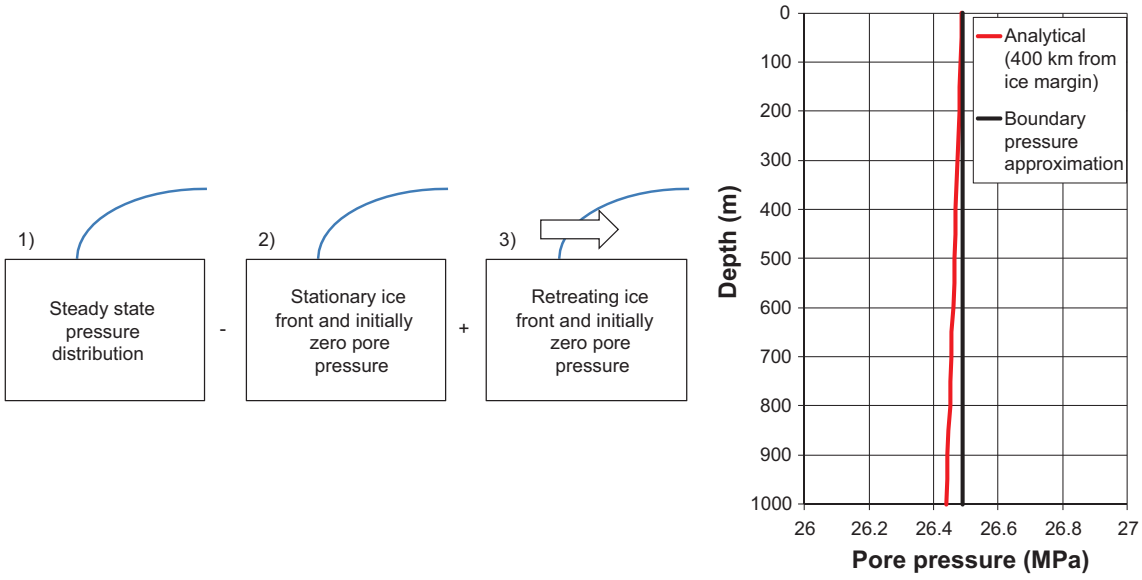

Figure D-3. *Left: Principle for finding the total excess pore pressure at the end of the glaciation. Right: Comparison between analytically obtained steady state pressure (red line) 400 km from the ice margin and boundary pressure approximation, modified from /Lönnqvist and Hökmark 2010/.*

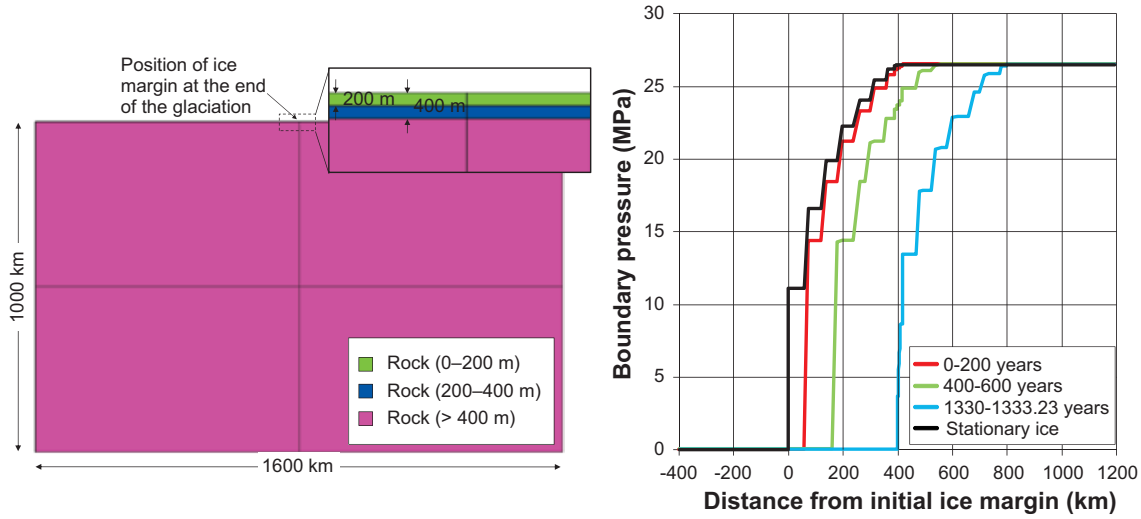

Figure D-4. *Left: Schematic view of Code_Bright model. Right: Examples of boundary conditions in different time intervals.*

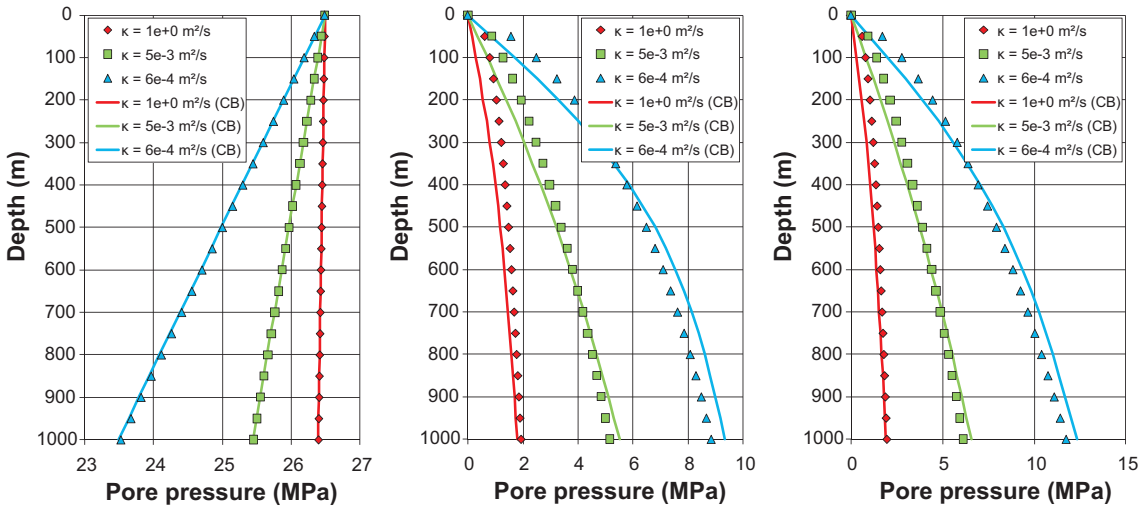

Figure D-5. *Comparison between results from the analytical solution (symbols) and Code_Bright (lines) at the end of the glacial cycle. All results are evaluated as functions of depth at the position of the ice margin at the end of the glaciation marked in Figure D-4 (left), i.e. 400 km from the ice margin for the stationary ice (Case 2). Left: Excess pore pressure due to a stationary ice front in rock where the initial pore pressure is zero (Case 2). Middle: Excess pore pressure due to a retreating ice front in rock where the initial pore pressure is zero (Case 3). Right: Total excess pore pressure as functions of depth beneath the ice front.*

D4.2 Results

Figure D-6 shows the excess pore pressure beneath the ice margin at the end of the glaciation as functions of depth for different assumptions regarding the hydraulic diffusivity. As seen in Figure D-5, the Code_Bright models underestimate the pore pressure slightly at shallow depths compared with the analytical solution. A proposed pore pressure model, for use in the subsequent modeling work, is marked with a black line. The maximum ice sheet thickness at Forsmark is about 2.9 km during the second glacial maximum and about 2 km during the first maximum (Figure 4-12), which suggests that the excess pore pressure during the first glacial maximum should be about two thirds of the excess pressure during the second glacial maximum.

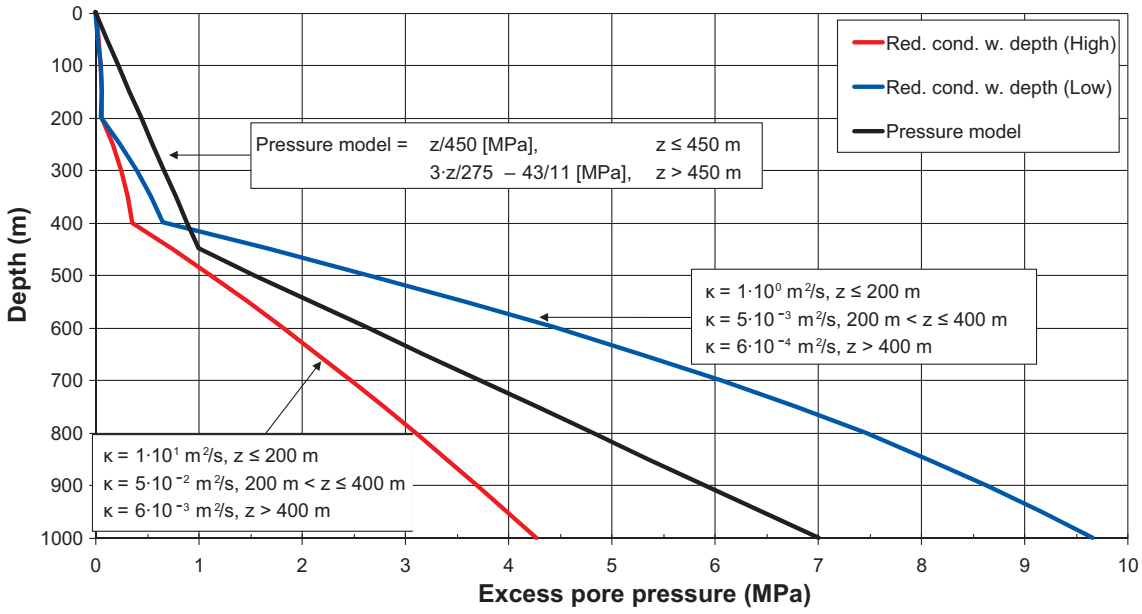

Figure D-6. *Excess pore pressure as functions of depth for 'Low' hydraulic diffusivity based on hydraulic conductivity estimates proposed for fracture domain FFM01 at Forsmark in Figure 4-10 (left) and 'High' hydraulic diffusivity based on the distribution of permeabilities at 465 m depth shown in Figure 4-10 (right). The proposed pore pressure model (black line) lies between the numerically obtained results for repository depth and below. The pore pressures above repository depth are chosen to account for the slight underestimate in results by the numerical model, cf. Figure D-5.*

D5 Permafrost conditions

D5.1 Modelling approach

/Lönnqvist and Hökmark 2010/ modelled the evolution of the excess pore pressure in the rock mass during permafrost conditions by use of the thermal logic in the numerical finite element code Code_Bright /CIMNE 2004/. The rock mass was represented by a rectangular block subdivided into three layers (Figure D-7) with hydraulic properties based on site data from Forsmark, cf. Section 4.8:

- The permafrost layer (0–200 m) is represented by a rectangular region of uniform thickness, which is impermeable ($\kappa = 1.0 \cdot 10^{-14}$ m²/s);
- A layer with high-diffusivity rock (200–400 m) set to either $1 \cdot 10^{-1}$ m²/s (denoted 'high') or $1 \cdot 10^{-2}$ m²/s (denoted 'low');
- Rock below 400 m with diffusivity $1 \cdot 10^{-4}$ m²/s.

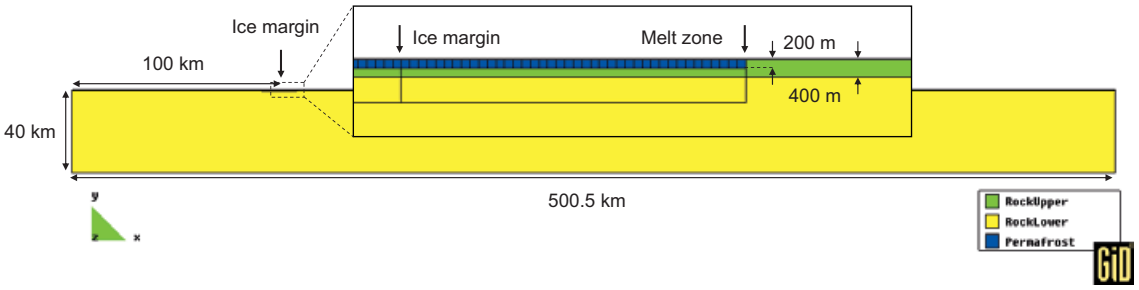

Figure D-7. *Schematic view of Code_Bright model, from /Lönnqvist and Hökmark 2010/.*

The advancement of the ice front was assumed to last approximately 10,000 years at a rate of 40 m/year /Lönnqvist and Hökmark 2010/. The permafrost starts melting when the ice front passes over it and is assumed to melt linearly, implying that the distance between permafrost melt zone and ice front remains constant /Lönnqvist and Hökmark 2010/. /Lönnqvist and Hökmark 2010/ investigated the maximum jacking depth for a number of permafrost melting rates. For the most conservative case, the estimated maximum jacking depth was about 350 m. In the following, examples from a slightly less conservative case that was modelled explicitly are shown. This case (Case B) had a melting rate of 1 m/a and resulted in a maximum jacking depth of around 330 m /Lönnqvist and Hökmark 2010/.

D5.2 Results

Figure D-8 shows the excess pore pressure for Case B as functions of depth during permafrost conditions for two assumptions regarding the hydraulic diffusivity of the rock mass. As seen in the figure, there is little variation in excess pore pressure with depth – less than 0.5 MPa in the upper 1 km of rock. Note, that these pressure estimate do not include effects due to seasonal variations, which in /Lönnqvist and Hökmark 2010/ were shown to reduce the pressure by 40–50%. Taking seasonal variations into account would reduce the maximum jacking depth from 330–350 m to about 165–210 m. The excess pore pressure needed to initiate hydraulic jacking at a given depth (z in metres) beneath the ice margin (i.e. assuming that the excess vertical stress is zero) is given by Equation D-1:

$$(\rho_{rock} - \rho_{water}) \cdot 10^{-6} \cdot g \cdot z = 1.7 \cdot 10^{-3} \cdot g \cdot z \text{ (MPa)} \qquad \text{Eq. D-1}$$

where ρ_{rock} is the density of rock (2,700 kg/m^3), ρ_{water} is the density of water (1,000 kg/m^3) and g is the acceleration due to gravity (9.81 m/s^2).

For the purpose of this study, the maximum jacking depth is assumed to be 200 m (cf. Section 7.6) during permafrost conditions, which corresponds to an excess pore pressure of about 3.3 MPa (Equation D-1) and that this pressure does not vary with depth (black line in Figure D-8).

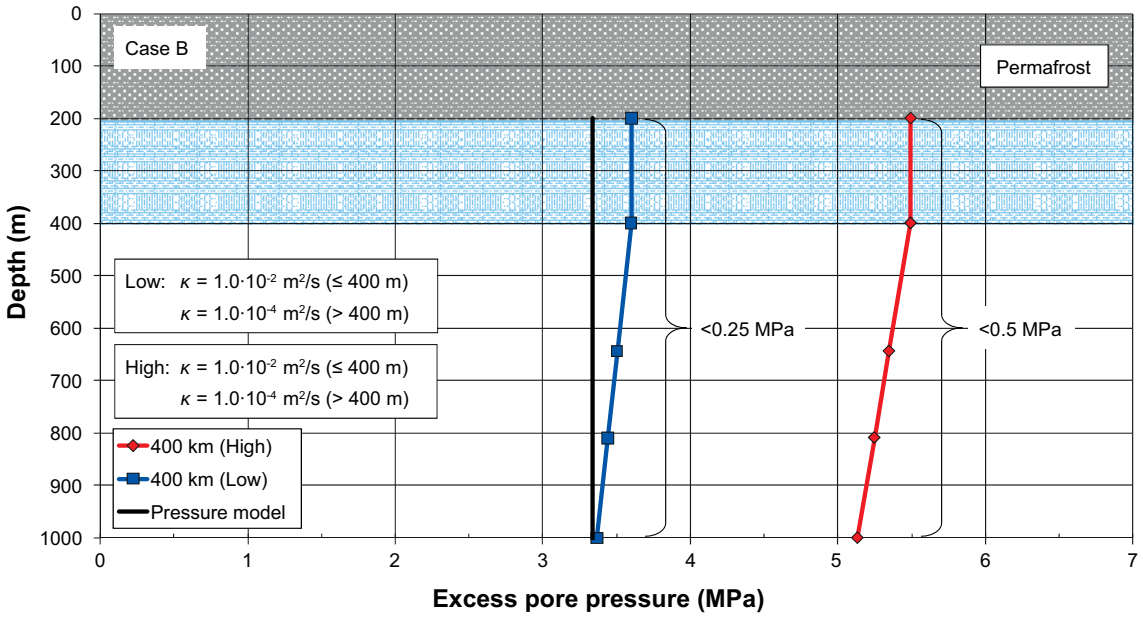

Figure D-8. *Excess pore pressure during permafrost conditions, results from Case B described in /Lönnqvist and Hökmark 2010/. The pressure model (black line) is based on an assumed maximum jacking depth of 200 m when seasonal variations in the boundary hydrostatic pressure are accounted for. This corresponds to an excess pore pressure of about 3.3 MPa, which is assumed not to vary with depth.*

D6 Summary

Based on the modelling results provided in the previous sections, the following glacially induced pore pressure model at the different points in time indicated in Figure D-9 is proposed for the Forsmark site:

1. The excess pore pressure is 98% of the glacially induced vertical load (Figure 4-13) at all times and at all depths. This approach will result in a conservative estimate of the pore pressure during times of ice cover, but underestimate the pore pressure as the ice front is retreating or in combination with proglacial permafrost, cf. e.g. Figure D-2.
2. An alternative pore pressure model (denoted (alt.) in Figure D-9), which takes additional residual or permafrost induced excess pore pressures into account:
   - As the ice sheet covers the site, i.e. at 12 ka and 54.5 ka, the excess pore pressure is 98% of the glacially induced vertical load at all depths, i.e. the same as described above.
   - The residual pore pressure is $(2/3)\cdot z/450$ MPa ($z \leq 450$ m) and $(2/3)\cdot(3\cdot z/275–43/11)$ MPa ($z > 450$ m) during the first episode of frontal retreat (15 ka).
   - The excess pore pressure during the advancement of the ice front in combination with proglacial permafrost is 3.3 MPa at all depths (39 ka).
   - The residual pore pressure is $z/450$ MPa ($z \leq 450$ m) and $3\cdot z/275–43/11$ MPa ($z > 450$ m) during the second episode of frontal retreat (58 ka).

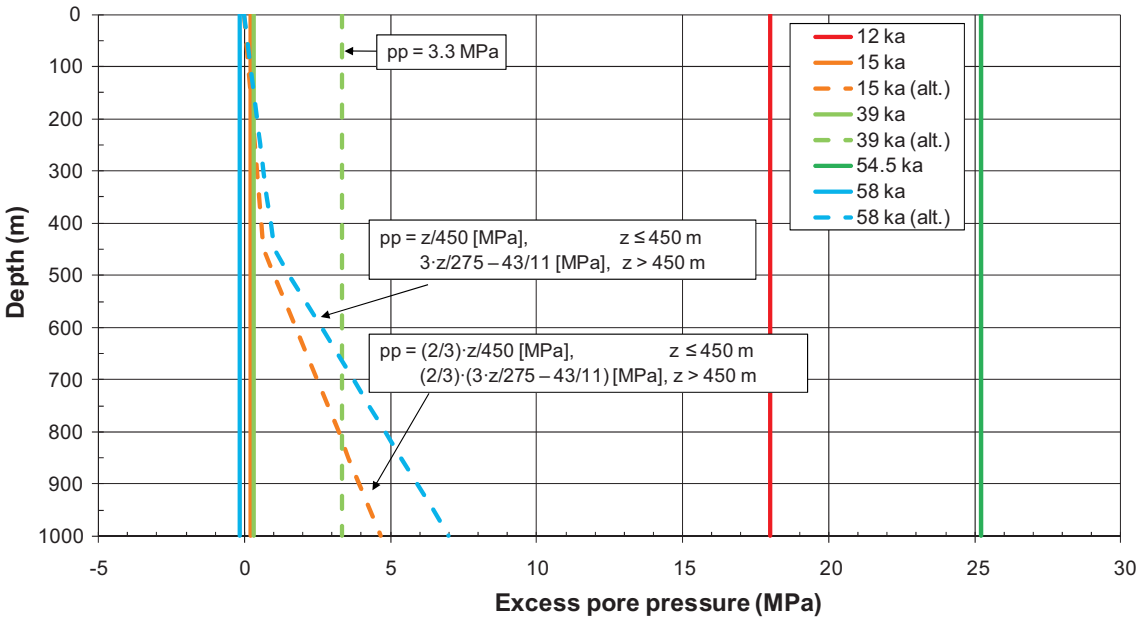

Figure D-9. *Glacially induced pore pressure model for Forsmark.*

Appendix E

Complementary analyses of the large-scale THM evolution during the temperate phase

E1 General

In the present section complementary results from the large-scale Forsmark modelling work of Chapter 6 are presented. Unless explicitly stated otherwise, the same parameter values and *in situ* stress models are used.

E2 Transmissivity changes

Transmissivity changes during the thermal phase along Scanlines A, B and C on fractures perpendicular to the major horizontal, minor horizontal and vertical *in situ* stresses are presented in Figure E-1 to Figure E-4.

Along Scanline A, the following can be observed

- **on vertical fractures striking perpendicular to the major horizontal *in situ* stress (σ_H, i.e. striking 55° with respect to North), cf. Figure E-1:** The changes in effective normal stress result in only negligible changes in relative transmissivity.

Along Scanline C, the following can be observed

- **on vertical fractures striking perpendicular to the major horizontal *in situ* stress (σ_H, i.e. striking 55° with respect to North), cf. Figure E-2:** The changes in effective normal stress result in only negligible changes in relative transmissivity.
- **on vertical fractures striking perpendicular to the minor horizontal *in situ* stress (σ_h, i.e. striking 145° with respect to North), cf. Figure E-3:** The reductions in effective normal stress in the upper 100 m of rock result in an increase in relative transmissivity by at most a factor 1.5–1.6 (model A) and 1.2 (model B), respectively. Below a depth of about 150 m there are only negligible changes in relative transmissivity for both stress-transmissivity models.
- **on horizontal fractures, cf. Figure E-4:** At repository depth and about 150 m above and below that level the vertical stress is reduced, resulting in an increase in relative transmissivity by up to a factor 2 (model A) and 1.3 (model B), respectively.

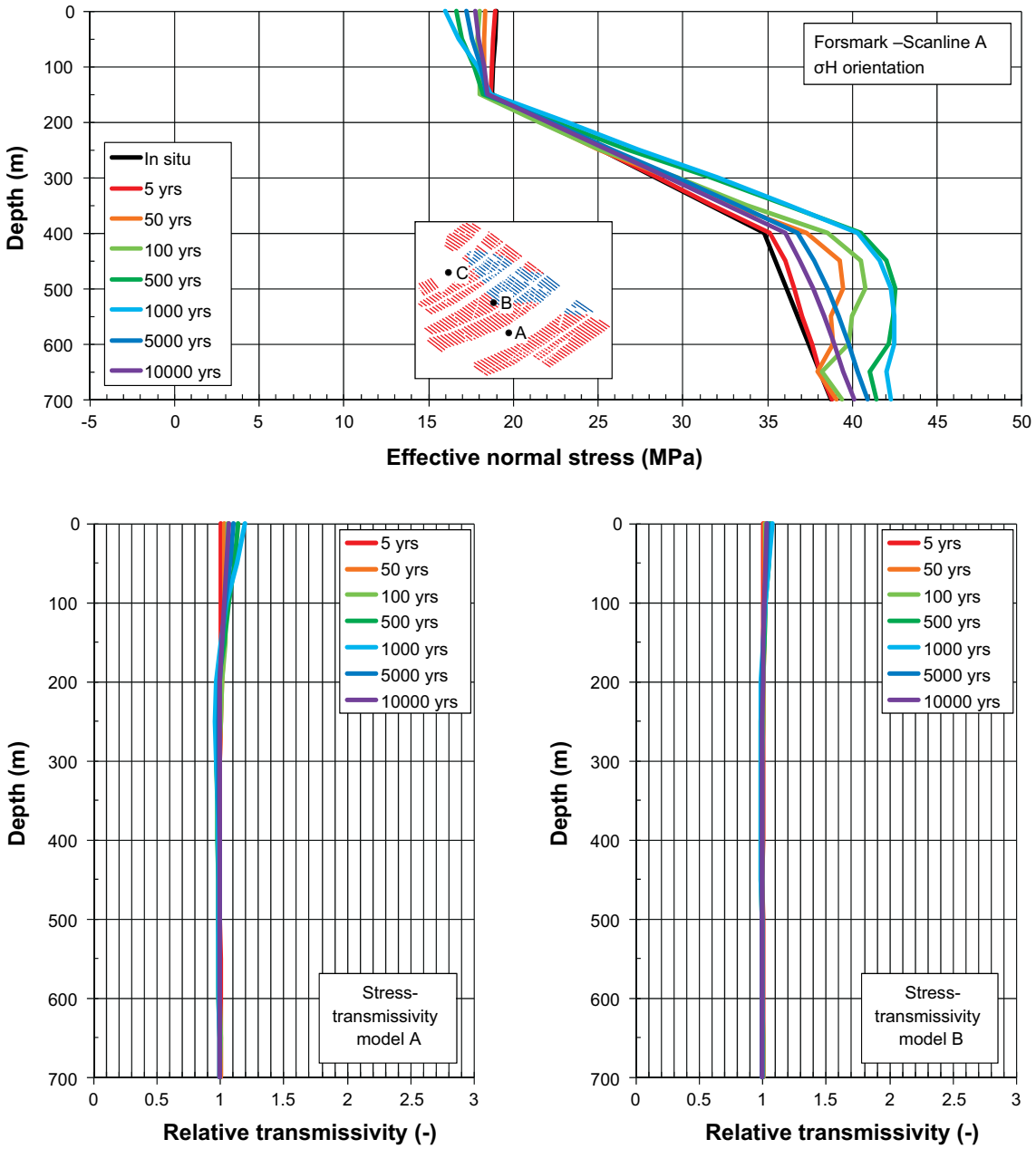

Figure E-1. *Top: Effective stress as a function of depth along Scanline A in the direction of the present-day σH. Bottom: Relative transmissivity of vertical fractures striking perpendicular to the present-day σH.*

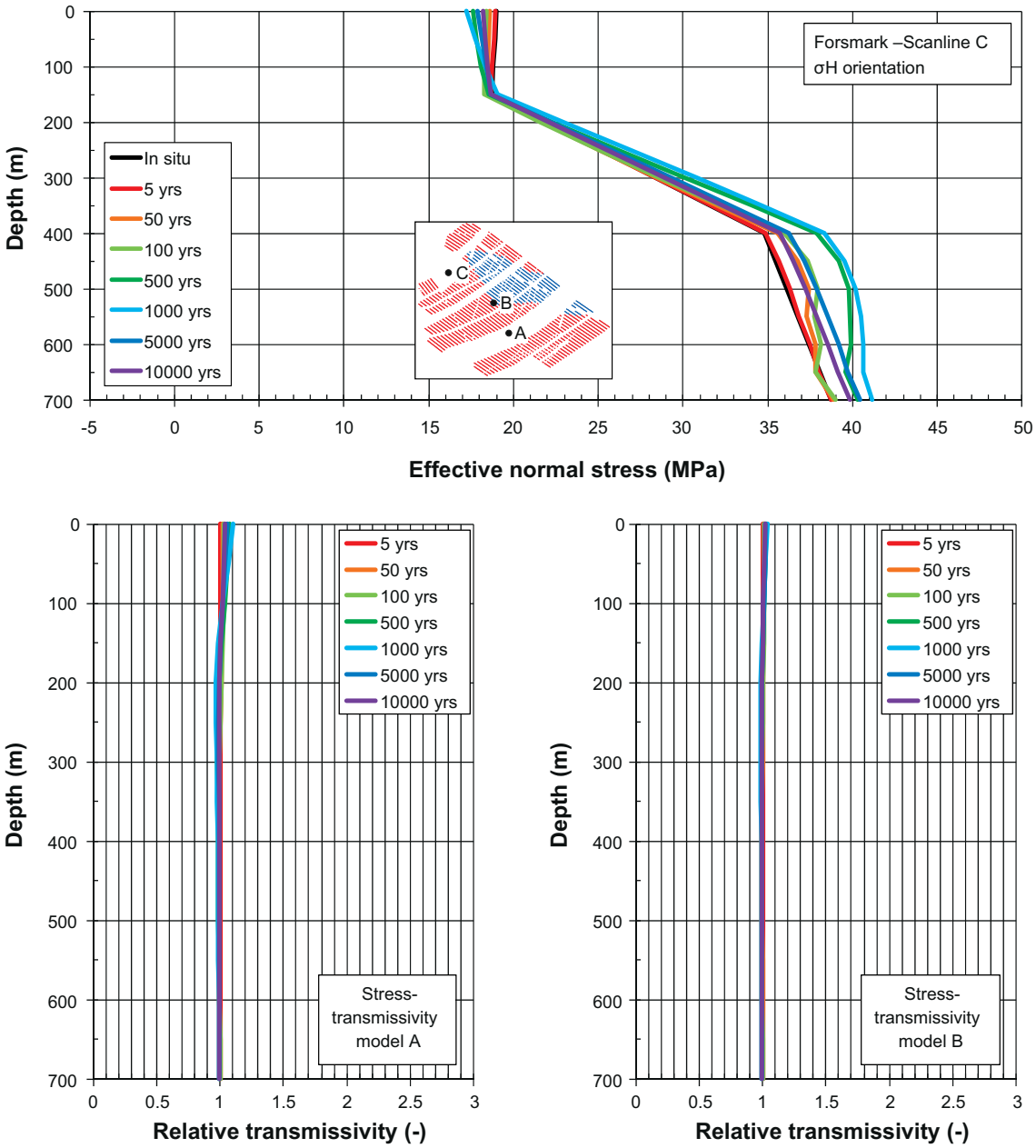

Figure E-2. *Top: Effective stress as a function of depth along Scanline C in the direction of the present-day σH. Bottom: Relative transmissivity of vertical fractures striking perpendicular to the present-day σH.*

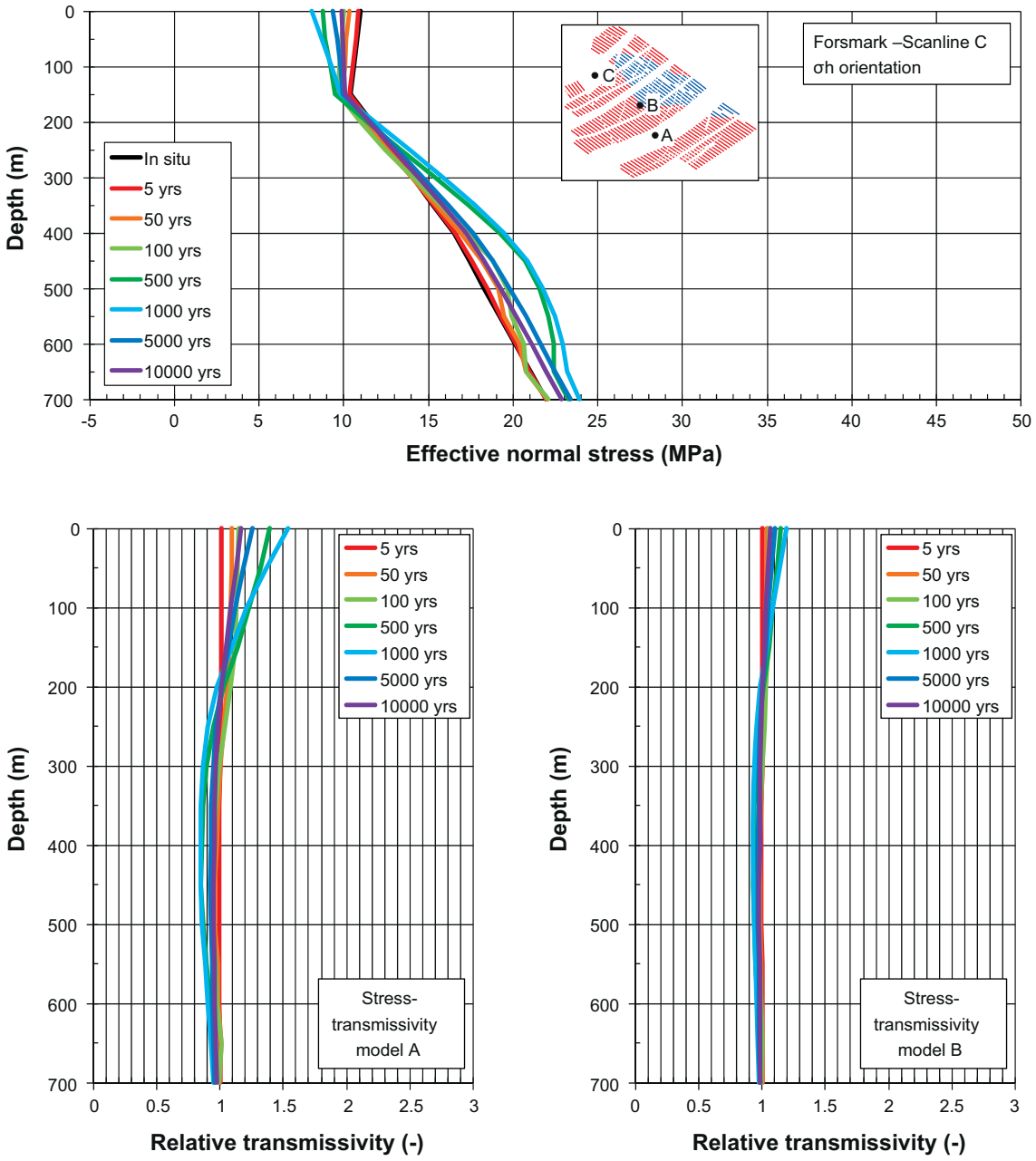

Figure E-3. *Effective stress as a function of depth along Scanline C in the direction of the present-day σh. Bottom: Relative transmissivity of vertical fractures striking perpendicular to the present-day σh.*

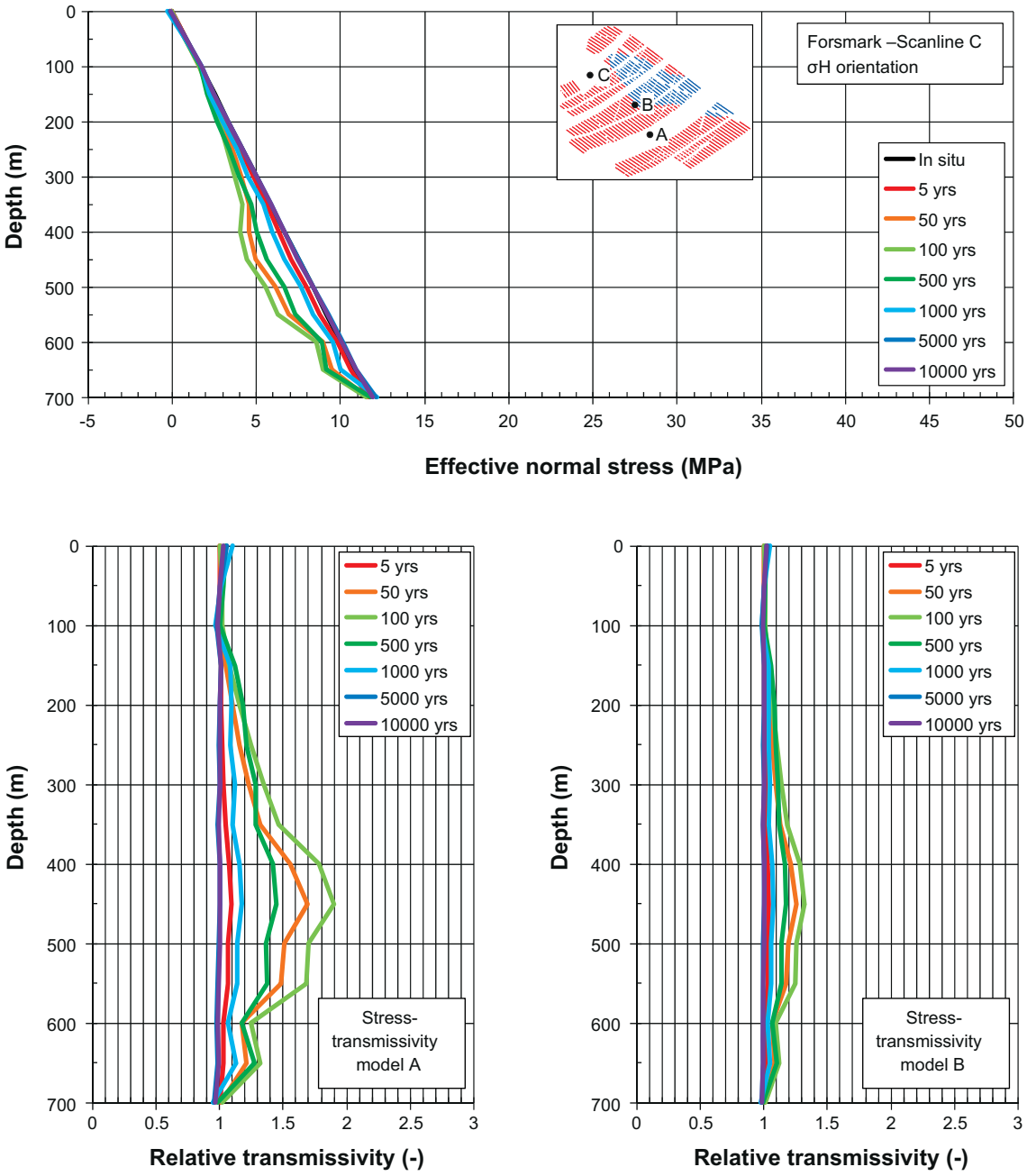

Figure E-4. *Top: Effective stress as a function of depth along Scanline C in the direction of σv. Bottom: Relative transmissivity of horizontal fractures.*

E3 Shearing

Estimates of slip magnitudes on fractures in the σ_H–σ_v-plane at different depths on Scanlines A, B and C are presented in Figure E-5 to Figure E-7. Results are presented for at the following depths:

Scanlines A and C

- 100 m. Reduction in the major horizontal stress (A and C)
- 250 m. Point between the ground surface and repository level (C only)
- 450 m. Increase in the major horizontal stress and reduction in the vertical stress (C only)
- 600 m. Point beneath the repository (C only)

Scanline B

- 100 m. Reduction in the major horizontal stress.
- 250 m. Point between the ground surface and repository level.
- 450 m. Increase in the major horizontal stress.
- 600 m. Point beneath the repository

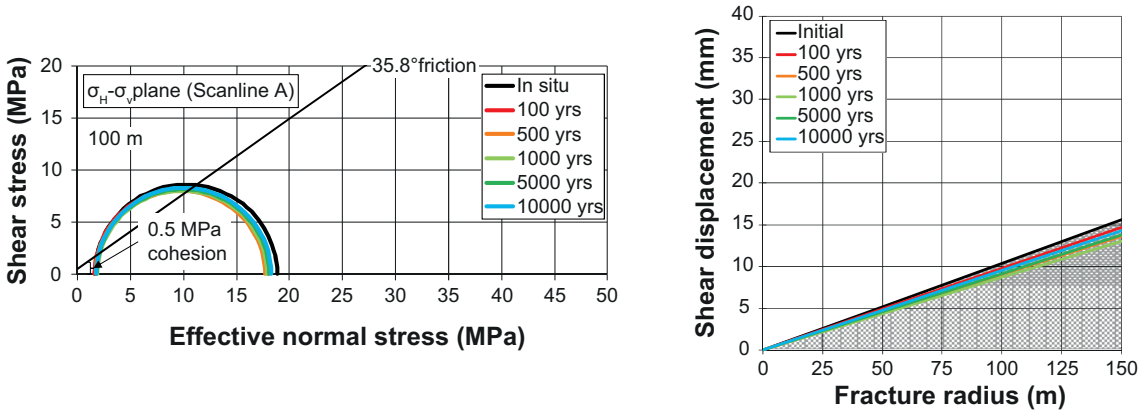

Figure E-5. *Left: Mohr circle representations of the stress state at given depths along Scanline A in the σH–σv-plane. Right: Corresponding estimates of the maximum slip at the centre of a fracture dipping 27.1°. Curves drawn in the grey shaded area represent instants of time when the stability is higher than under in situ conditions.*

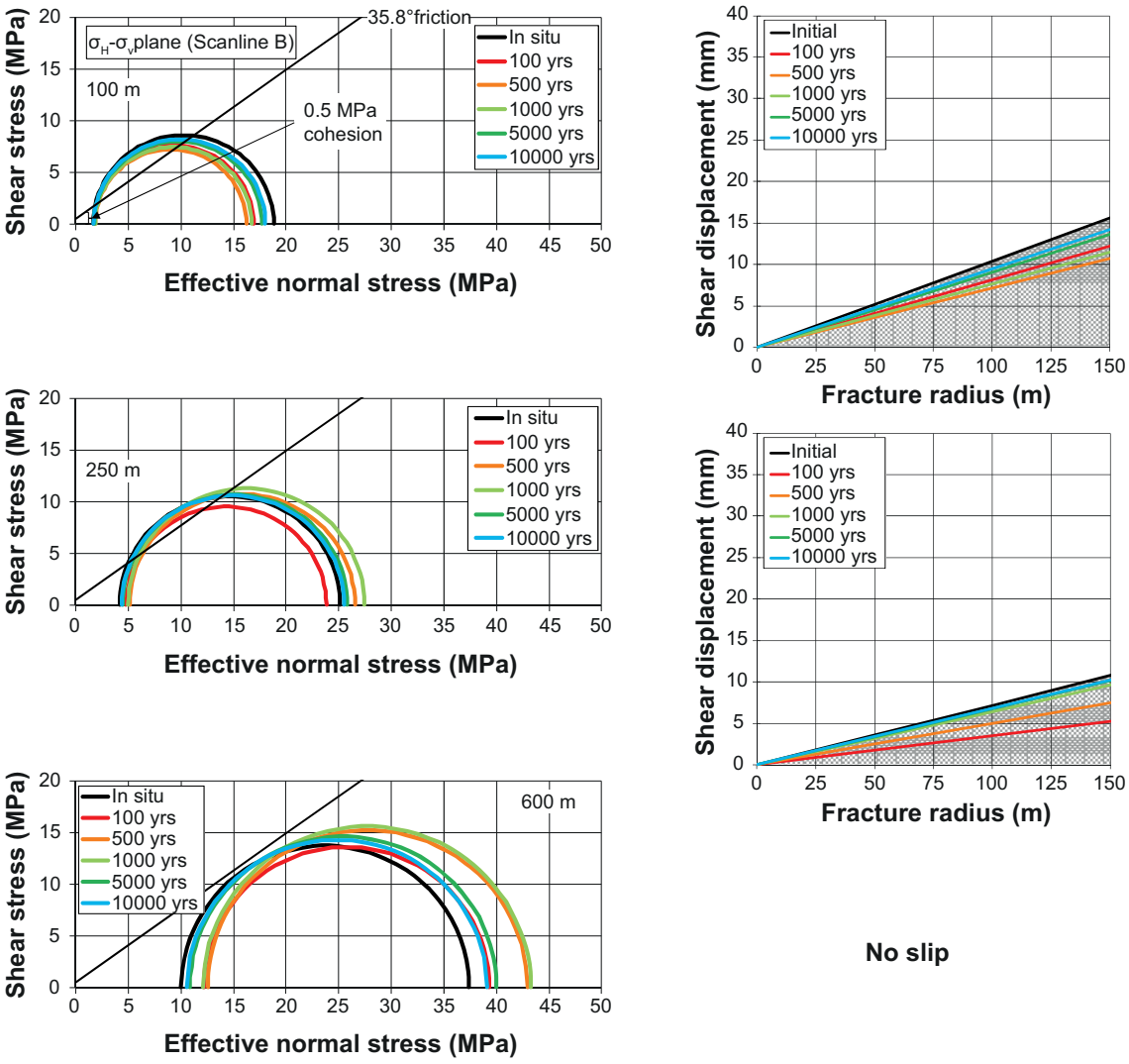

Figure E-6. *Left column: Mohr circle representations of the stress state at given depths along Scanline B in the σH–σv-plane. Right column: Corresponding estimates of the maximum slip at the centre of a fracture dipping 27.1°. Curves drawn in the grey shaded area represent instants of time when the stability is higher than under in situ conditions.*

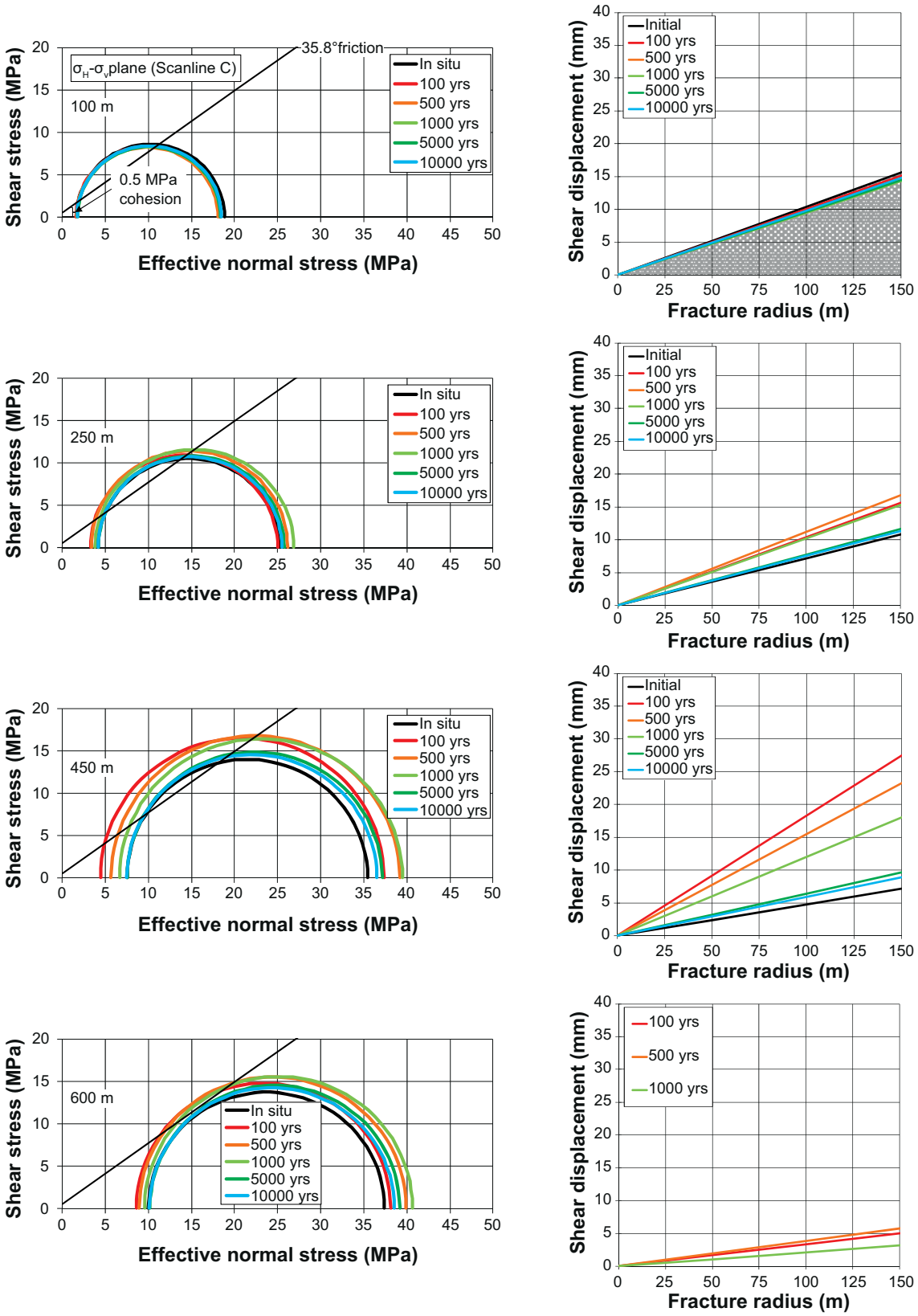

Figure E-7. *Left column: Mohr circle representations of the stress state at given depths along Scanline C in the σH–σv-plane. Right column: Corresponding estimates of the maximum slip at the centre of a fracture dipping 27.1°. Curves drawn in the grey shaded area represent instants of time when the stability is higher than under in situ conditions.*

Appendix F

Simplifications and approximations used in the near-field modelling work

F1 Near field heat load

In the large-scale models (cf. Chapter 6) given loss of canister positions is taken into account, e.g. 13% at the Forsmark site, and mirror heat sources are positioned and equivalent distance above the ground surface to ensure that the temperature at the ground surface remains constant at 0°C over the course of time. However, in the near-field models, the temperature effects due to mirror sources are not considered. This will overestimate the temperatures at repository depth by about 2°C after 10,000 years, cf. Figure F-1. However, during the first 1,000 years the temperatures at repository depth are not affected and the small increase in temperature after 10,000 years is judged to have only a minor influence on the results. For example, the tangential stresses in the walls of a deposition hole reach their maximum values after about 50 years.

F2 Boundary conditions during glacial phase

Boundary conditions for the glacial phase are obtained from 3D ice/crust/mantle calculations by /Lund et al. 2009/. Although not strictly the case, the principal stress additions are assumed to be aligned with the model axes. Figure F-2 shows the error associated with aligning the horizontal principal stress additions with the model axes.

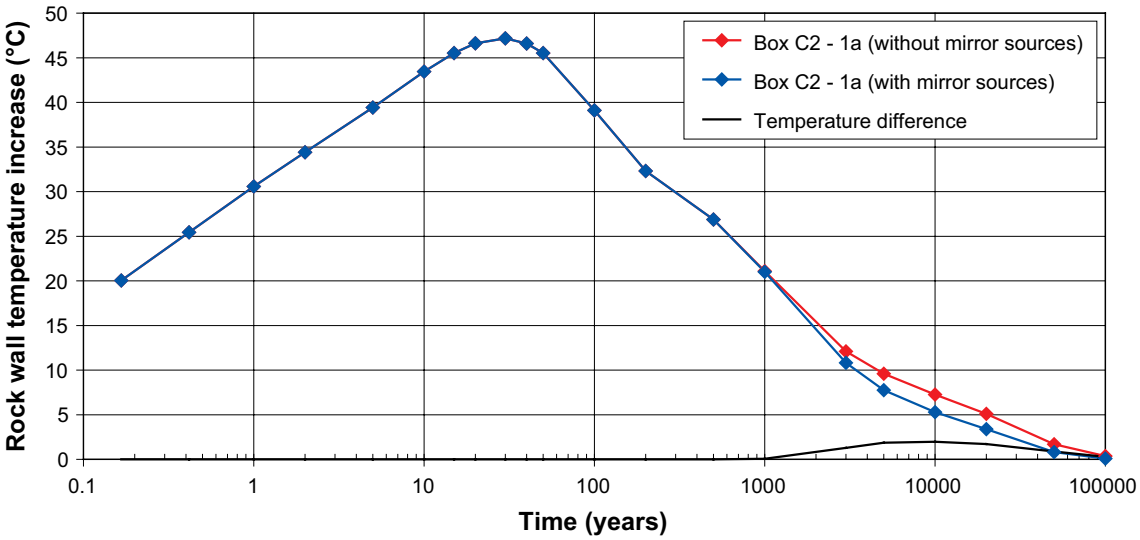

Figure F-1. *Influence on rock wall temperatures at repository depth at Forsmark due to negative mirror sources at 465 m above the ground surface. The ground surface influences the temperature increase between 1,000 and 100,000 years after deposition of the canisters; the maximum temperature difference is about 2°C. Note that the tangential stresses in the walls of the deposition holes reach their maximum after about 50 years.*

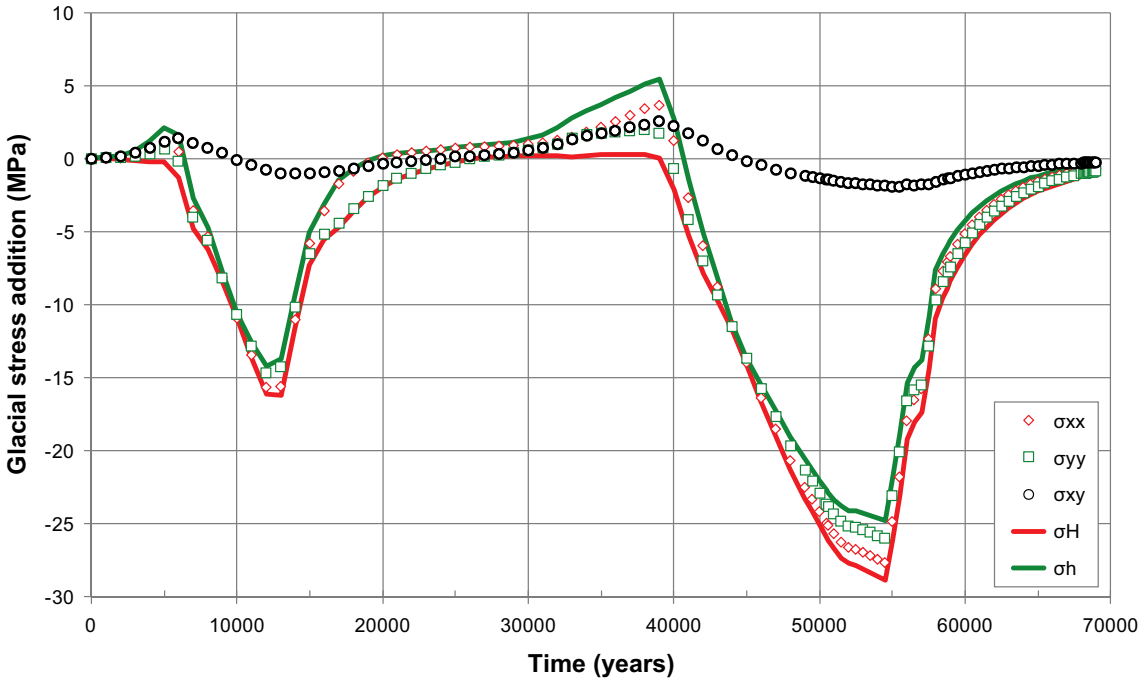

Figure F-2. *Glacial stress additions at Forsmark. Comparison between horizontal principal stresses (σH and σh) and stresses in the directions of the coordinate axes in the numerical models (σxx = along tunnel, σyy = across tunnel, σxy = shear stress in xy-plane).*

F3 Fractures

In the models the fractures are represented by planar features and extend to the model boundaries. The part of each fracture outside the 50 m radius is given fictitious properties with high strength, cf. Table F-1. Similarly to the modelling approach taken by /Fälth and Hökmark 2007/, the fractures' strength is ramped down from high strength to the intended strength value at every thermal time-step to ensure that the results are not influenced by non-physical movements due to thermal unbalanced forces.

Table F-1. Arbitrarily chosen high strength fictitious fracture properties.

Ficticious fracture properties	Unit	Value
Cohesion	MPa	500
Friction angle	°	63
Normal stiffness (JKN)	GPa/m	6,560
Shear stiffness (JKS)	GPa/m	340
Tensile strength	MPa	500

Appendix G

Effects of temperature reduction during permafrost conditions on transmissivity changes and shearing of near-field fractures

G1 General

In Chapter 7 only large-scale effects of the temperature reduction during permafrost conditions were considered without taking effects of near-field tunnels into account. The greatest effects of the horizontal stress reductions during permafrost conditions are found at shallow depths, cf. Figure 7-8 and Figure 7-10. At repository depth, the effects of a reduction in horizontal stress in addition to permafrost induced pore pressure are more moderate. In the following sections, corresponding near-field models to those described in Chapter 8, which take effects of temperature reduction during permafrost conditions into account, are provided.

G2 Description of 3DEC models

The *3DEC* models used here are identical to those described in Chapter 8 for the construction and operational phase and for the temperate phase. For the glacial phase, the pore pressure model that takes residual and permafrost induced excess pore pressures into account is used for reference: It is assumed that the excess pore pressure is about 98% of the glacially induced vertical load as the ice covers the site (at 12 ka and 54.5 ka), 0.74 MPa as the edge is passing at 15 ka, about 3.3 MPa in combination with proglacial permafrost (39 ka) and 1.11 MPa as the edge is passing at 58 ka.

The effects of the temperature reduction during permafrost conditions at 39 ka are represented by a reduction of the horizontal stress components by about 1.7 MPa and assuming the same pore pressure model as described above.

G3 Stress induced transmissivity changes

The vertical fractures (#1, #2 and #3) are in sufficiently high compression initially that the additional horizontal stress reduction does not result in any significant changes in the effective normal stress and corresponding relative transmissivity at the monitored points, cf. Figure G-1, Figure G-3 and Figure G-5.

Projections of the effective normal stress onto the vertical plane perpendicular to the deposition tunnel during the forebulge (39 ka) in combination with high pore pressures due to permafrost or high pore pressure and additional horizontal stress reductions due the temperature reduction are provided in Figure G-2, Figure G-4 and Figure G-6 (upper row in each figure) for each fracture #1–#3, respectively. In the bottom row of each figure, estimates of the relative transmissivity are given using the stress-transmissivity relation (A) shown in Figure 8-8. Similarly to the case where the temperature reduction is not considered, the transmissivity changes are concentrated to a limited region around the tunnel. For fractures #1 and #2, the region with a relative transmissivity increase greater than a factor 2 is increased by a distance of 2–2.5 m perpendicular to the tunnel.

The vertical stress is not affected by the temperature reduction during permafrost conditions. Therefore, additional stress induced transmissivity changes of the horizontal fracture (#4) are not expected, cf. Figure G-7 and Figure G-8.

Similarly to the vertical and horizontal fractures, the additional horizontal stress reduction does not result in any significant changes in the effective normal stress and corresponding relative transmissivity at the monitored points on the gently dipping fracture (#5), cf. Figure G-9.

Projections of the effective normal stress onto the vertical plane perpendicular to the deposition tunnel during the forebulge (39 ka) in combination with high pore pressures due to permafrost or high pore pressure and additional horizontal stress reductions due the temperature reduction is provided in Figure G-10 (upper row). The bottom row shows corresponding estimates of the relative transmissivity using the stress-transmissivity relation (A) shown in Figure 8-8. Similarly to the case where the temperature reduction is not considered, the transmissivity changes are concentrated to a limited region around the tunnel. The region with a relative transmissivity increase greater than a factor 2 is increased on average by a distance of about 2 m above and below the tunnel.

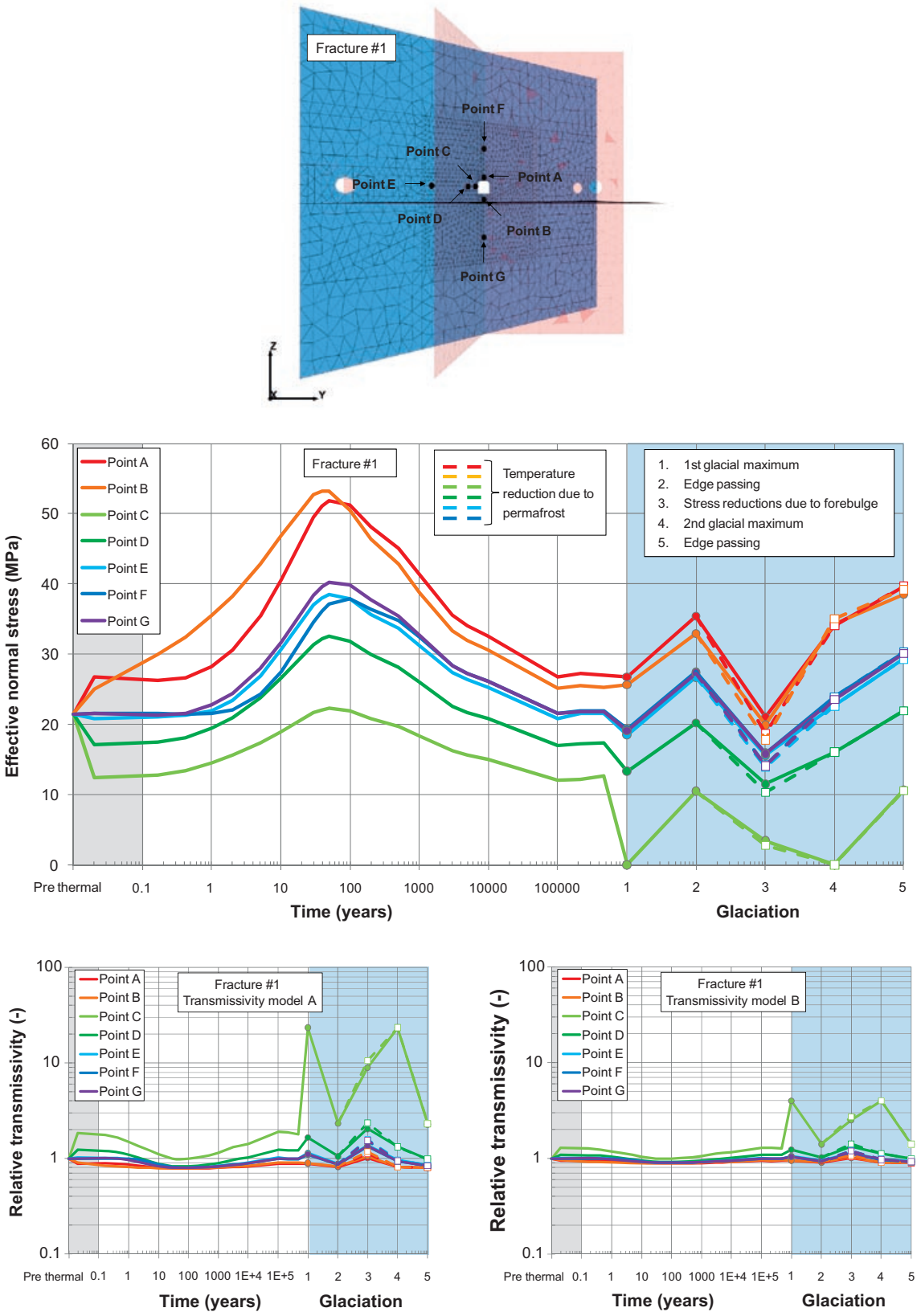

Figure G-1. *Locations of history points on Fracture #1 (top). Temporal evolution of the normal stress (including temperature reduction due to permafrost) at selected points (middle). Temporal evolution of the relative transmissivity based on the stress-transmissivity models in Figure 8-8 (bottom row). Grey and blue areas represent pre-thermal time and glaciation, respectively.*

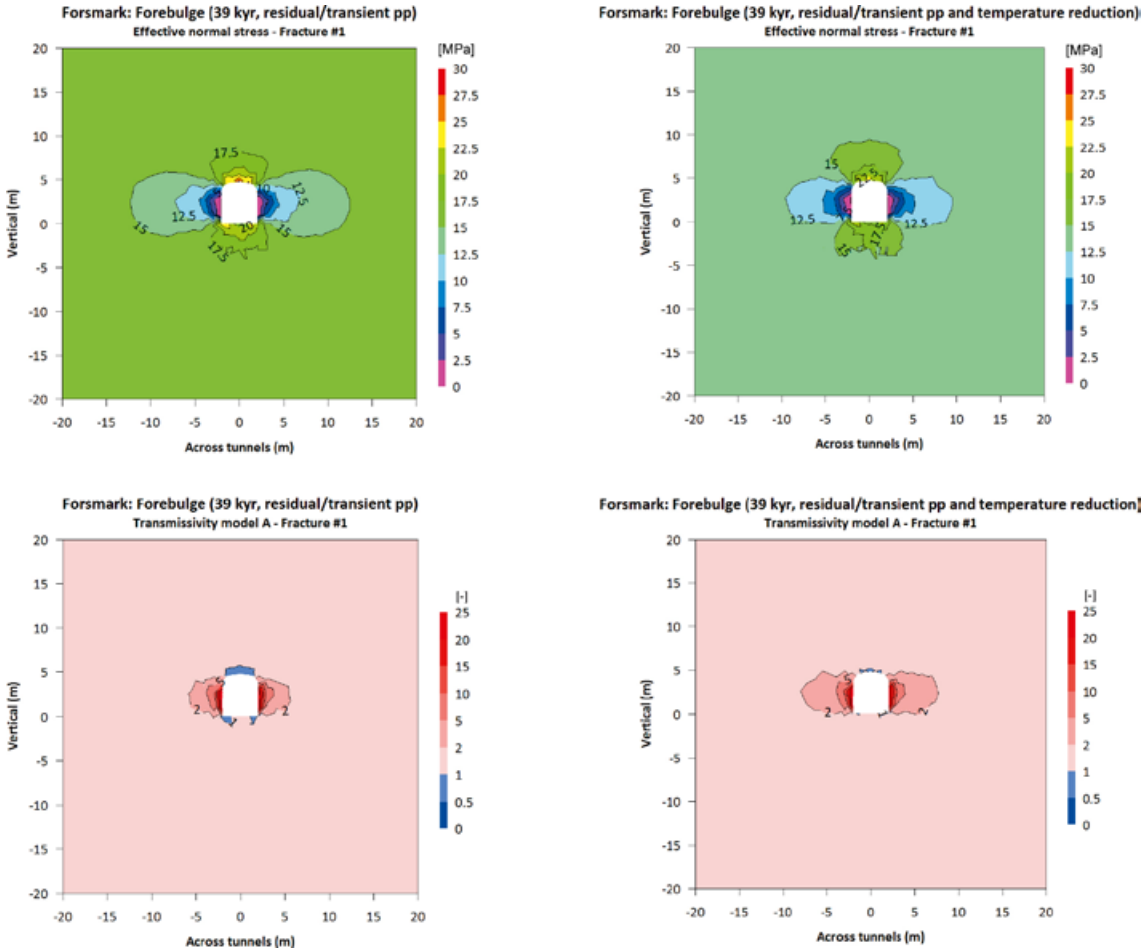

Figure G-2. *Projection of the effective normal stress (top row) and corresponding relative transmissivity (bottom row) on fracture #1 onto the vertical plane perpendicular to the deposition tunnel during the forebulge with permafrost induced pore pressure (left column) and with permafrost induced pore pressure and temperature induced stress reduction (right column).*

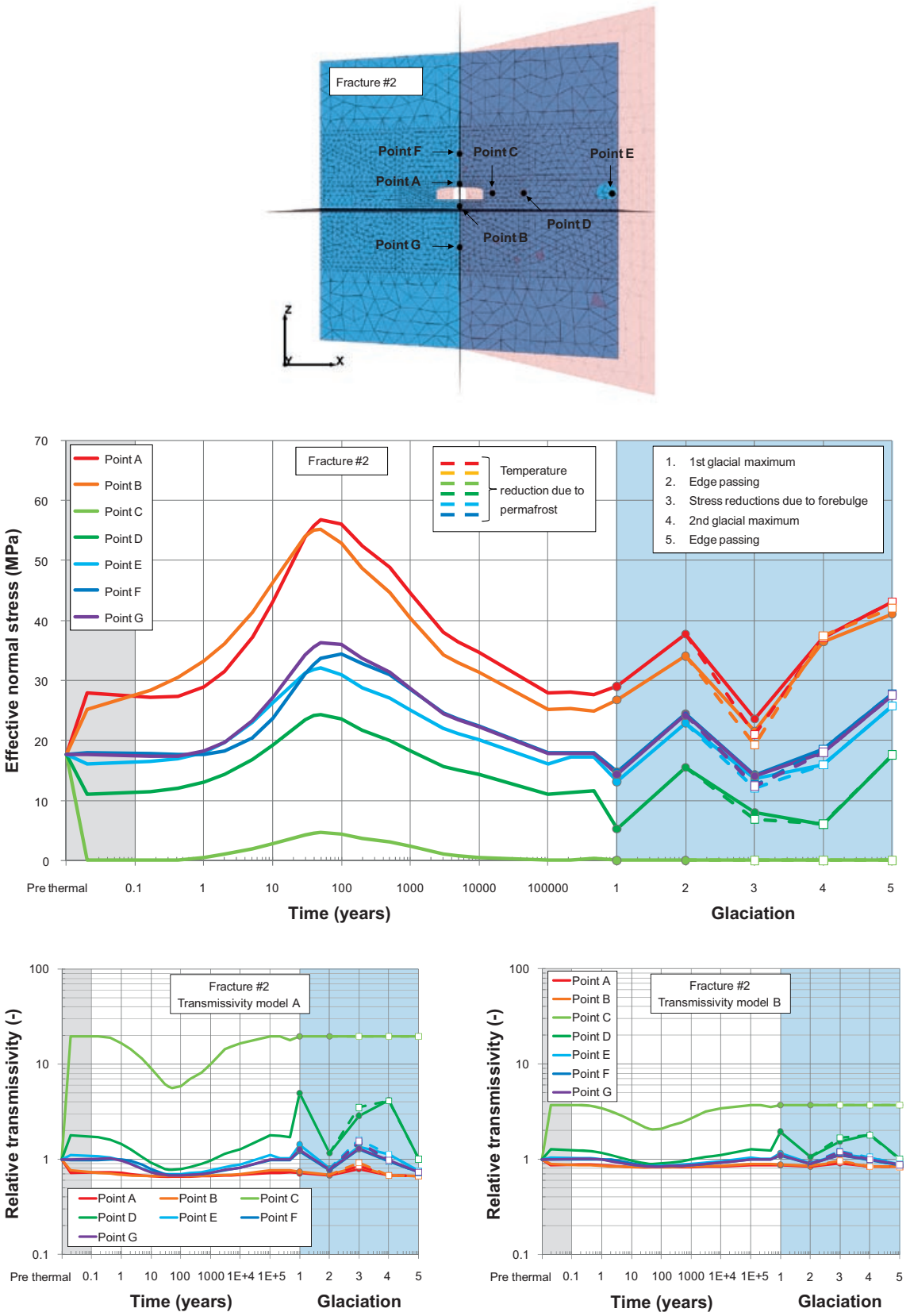

Figure G-3. *Locations of history points on Fracture #2 (top). Temporal evolution of the normal stress (including temperature reduction due to permafrost) at selected points (middle). Temporal evolution of the relative transmissivity based on the stress-transmissivity models in Figure 8-8 (bottom row). Grey and blue areas represent pre thermal time and glaciation, respectively.*

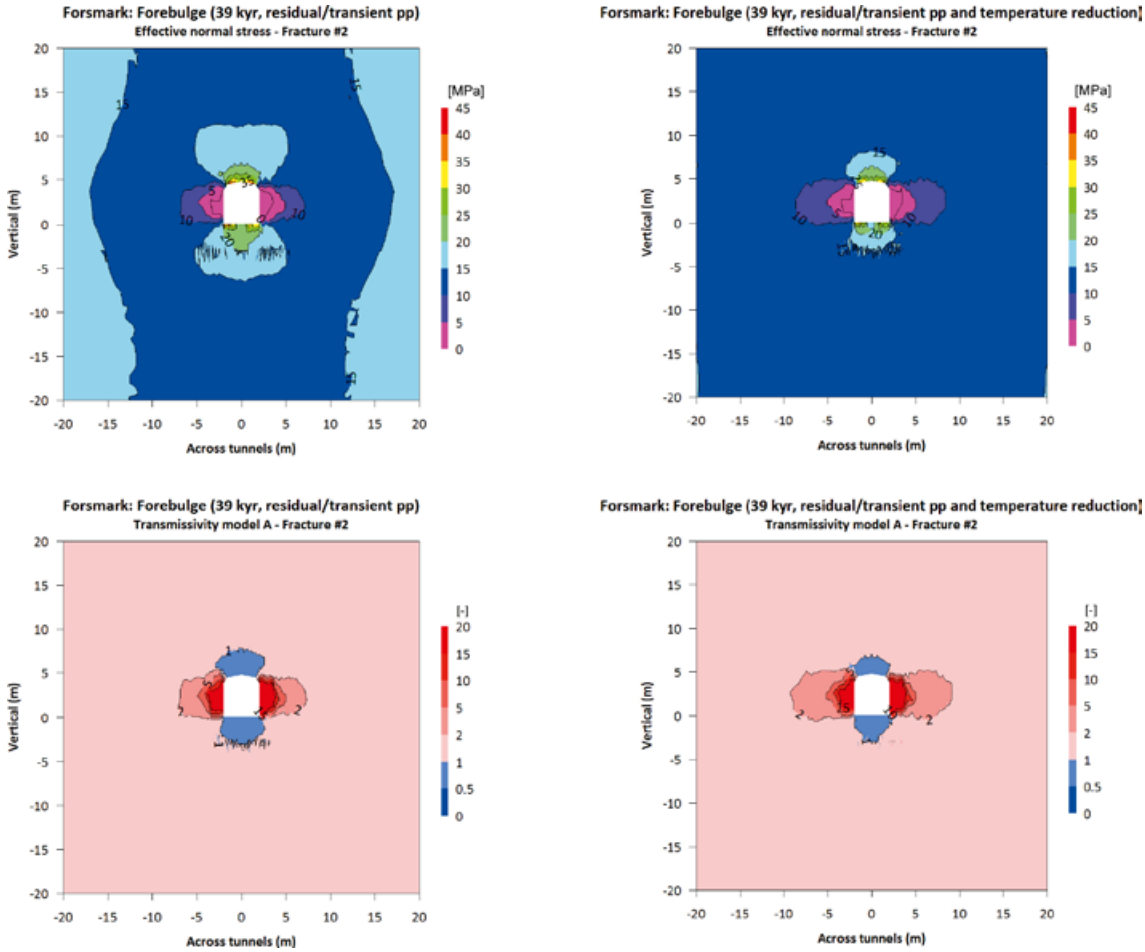

Figure G-4. *Projection of the effective normal stress (top row) and corresponding relative transmissivity (bottom row) on fracture #2 onto the vertical plane perpendicular to the deposition tunnel during the forebulge with permafrost induced pore pressure (left column) and with permafrost induced pore pressure and temperature induced stress reduction (right column).*

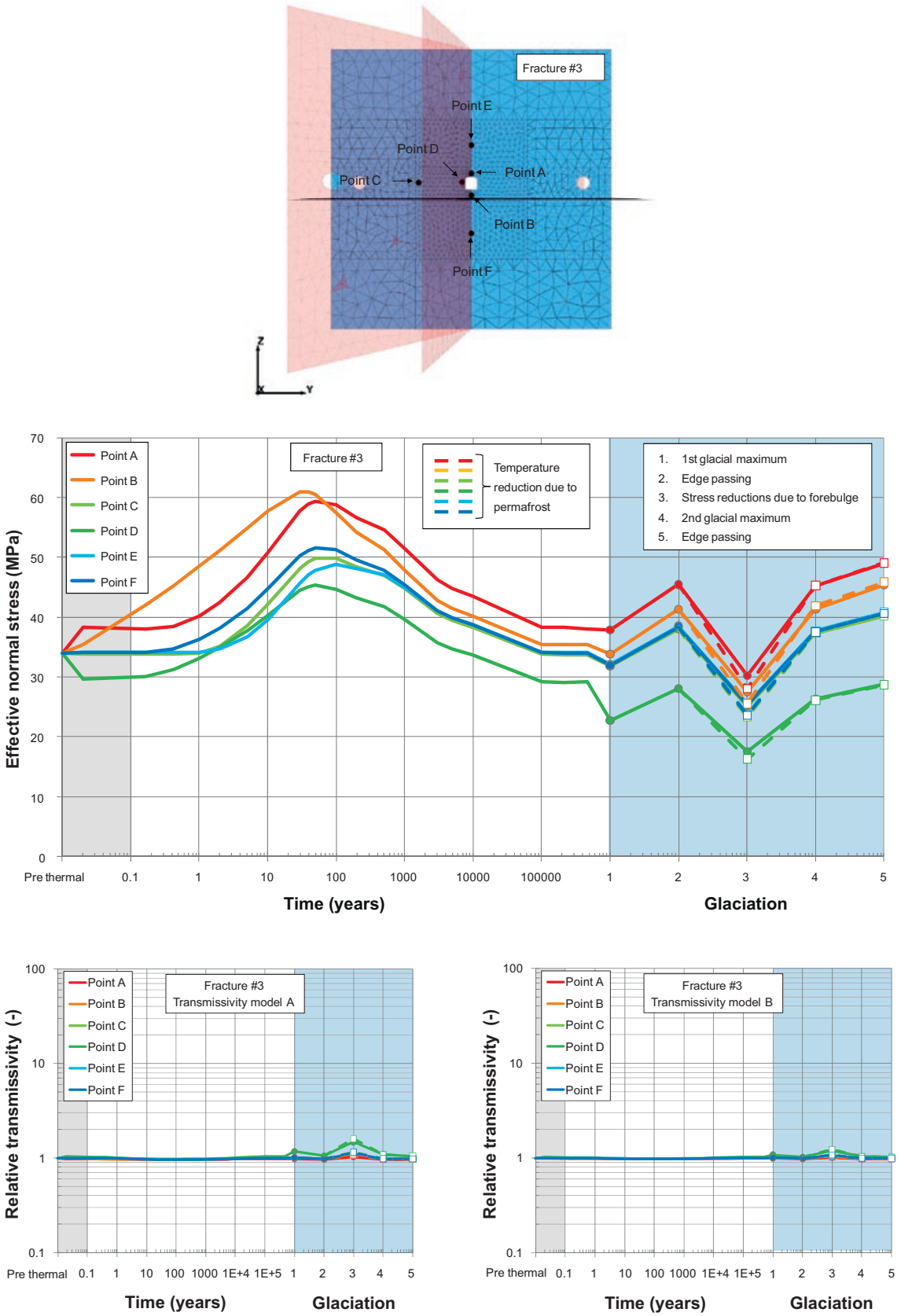

Figure G-5. *Locations of history points on Fracture #3 (top). Temporal evolution of the normal stress (including temperature reduction due to permafrost) at selected points (middle). Temporal evolution of the relative transmissivity based on the stress-transmissivity models in Figure 8-8 (bottom row). Grey and blue areas represent pre-thermal time and glaciation, respectively.*

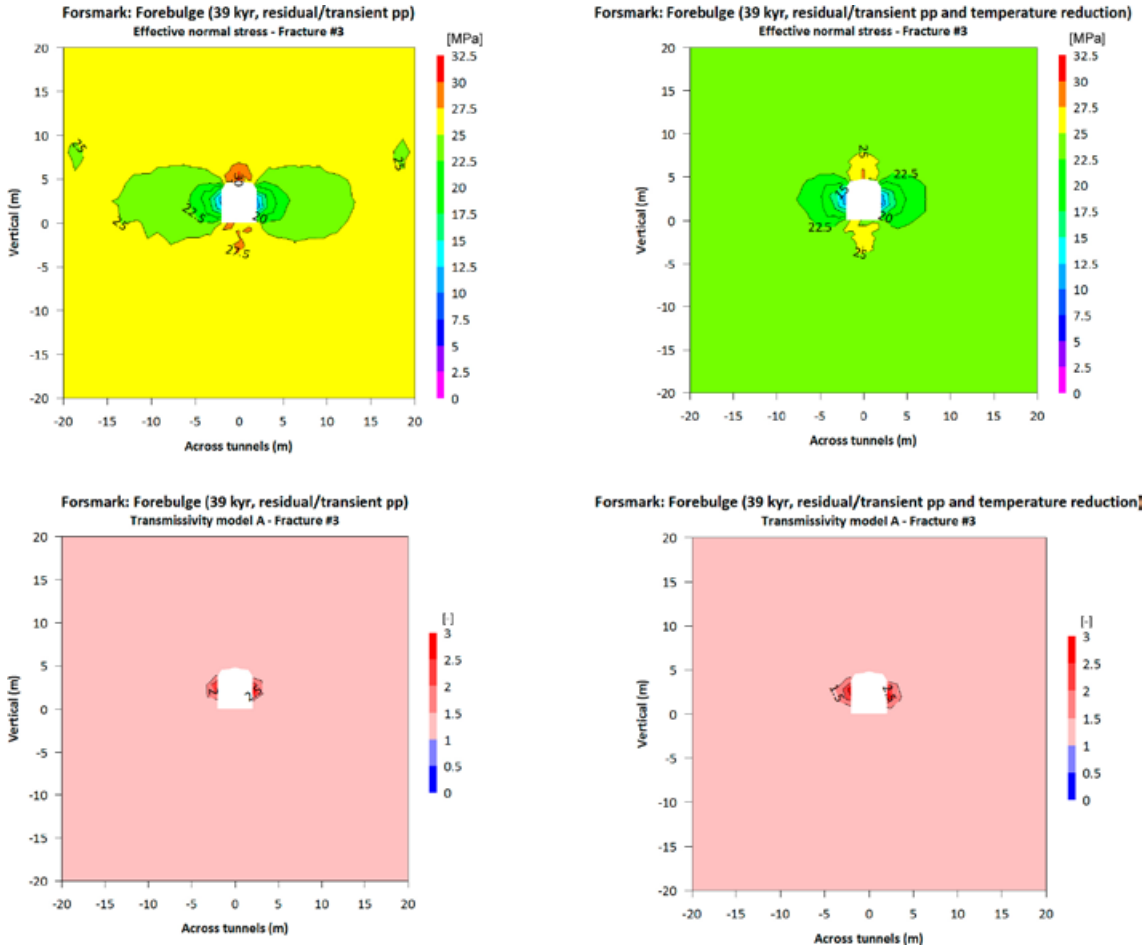

Figure G-6. *Projection of the effective normal stress (top row) and corresponding relative transmissivity (bottom row) on fracture #3 onto the vertical plane perpendicular to the deposition tunnel during the forebulge with permafrost induced pore pressure (left column) and with permafrost induced pore pressure and temperature induced stress reduction (right column).*

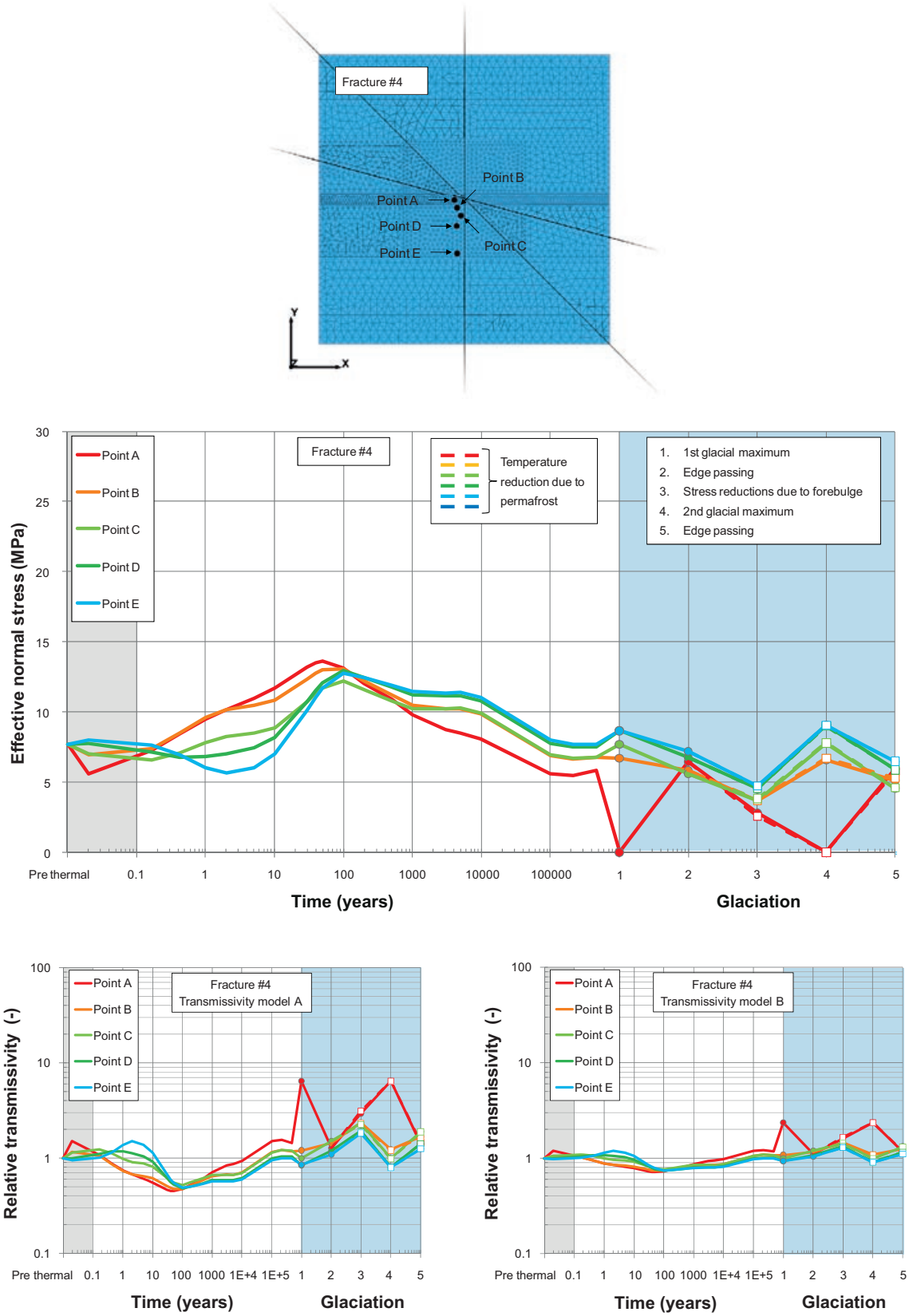

Figure G-7. *Locations of history points on Fracture #4 (top). Temporal evolution of the normal stress (including temperature reductions due to permafrost) at selected points (middle). Temporal evolution of the relative transmissivity based on the stress-transmissivity models in Figure 8-8 (bottom row). Grey and blue areas represent pre-thermal time and glaciation, respectively.*

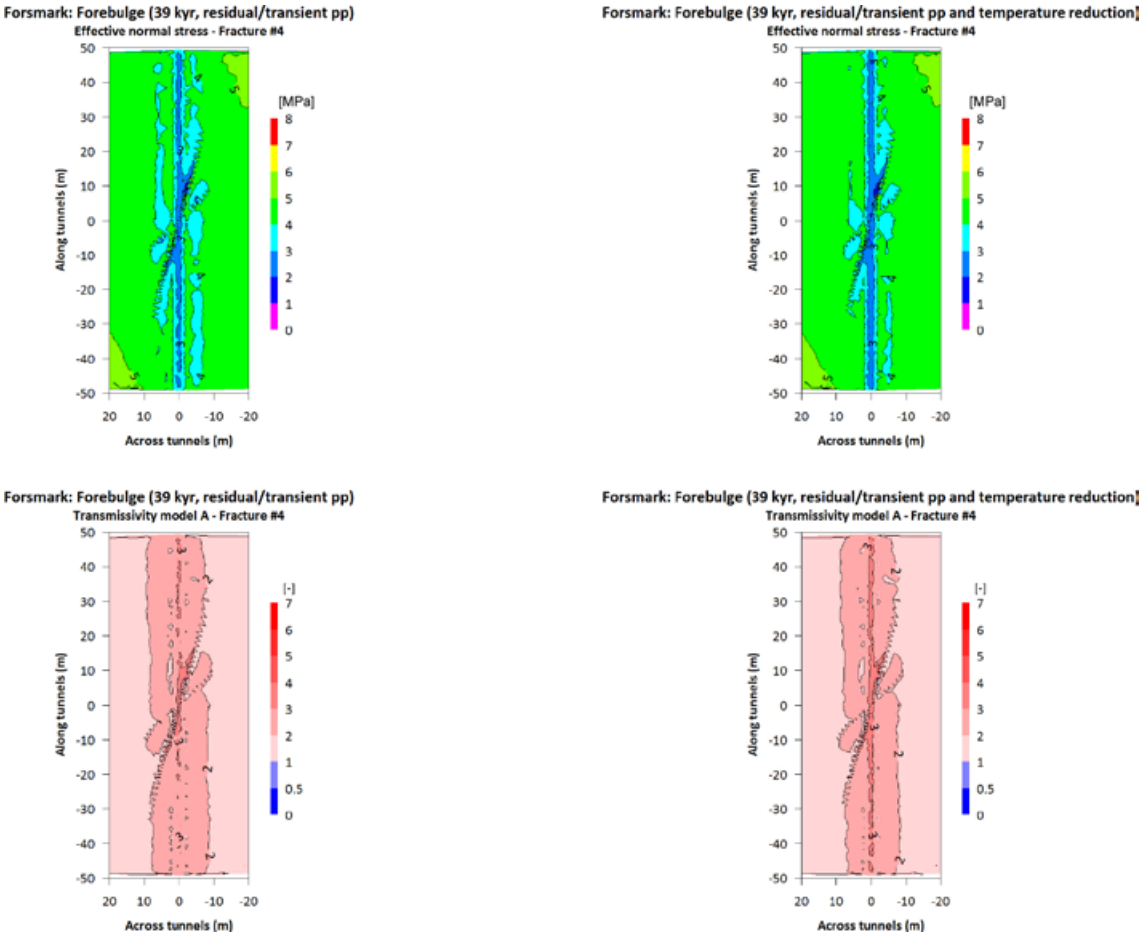

Figure G-8. *Effective normal stress (top row) and corresponding relative transmissivity (bottom row) on fracture #4 during the forebulge with permafrost induced pore pressure (left column) and with permafrost induced pore pressure and temperature induced stress reduction (right column).*

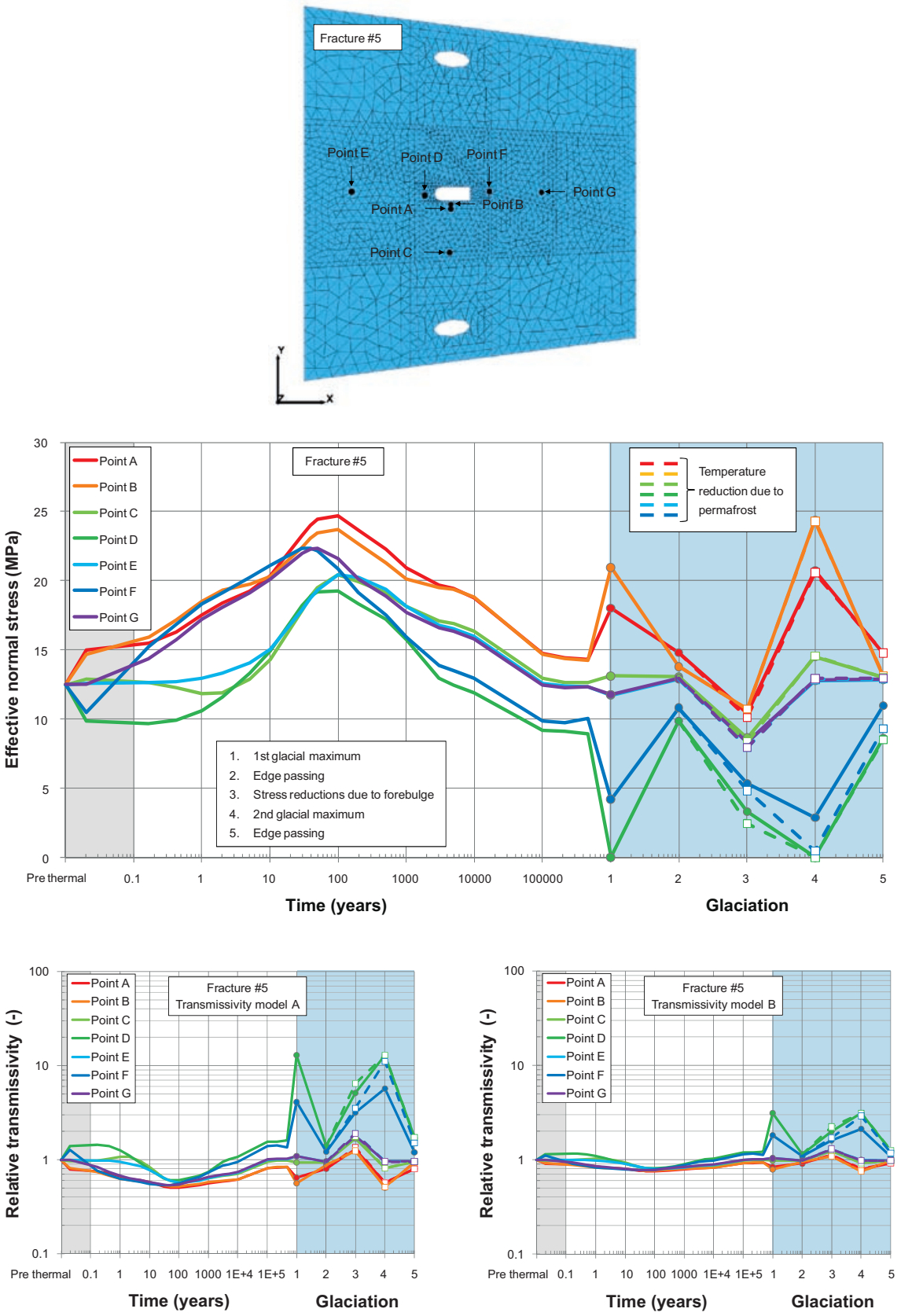

Figure G-9. *Locations of history points on Fracture #5 (top). Temporal evolution of the normal stress (including temperature reductions due to permafrost) at selected points (middle). Temporal evolution of the relative transmissivity based on the stress-transmissivity models in Figure 8-8 (bottom row). Grey and blue areas represent pre thermal time and glaciation, respectively.*

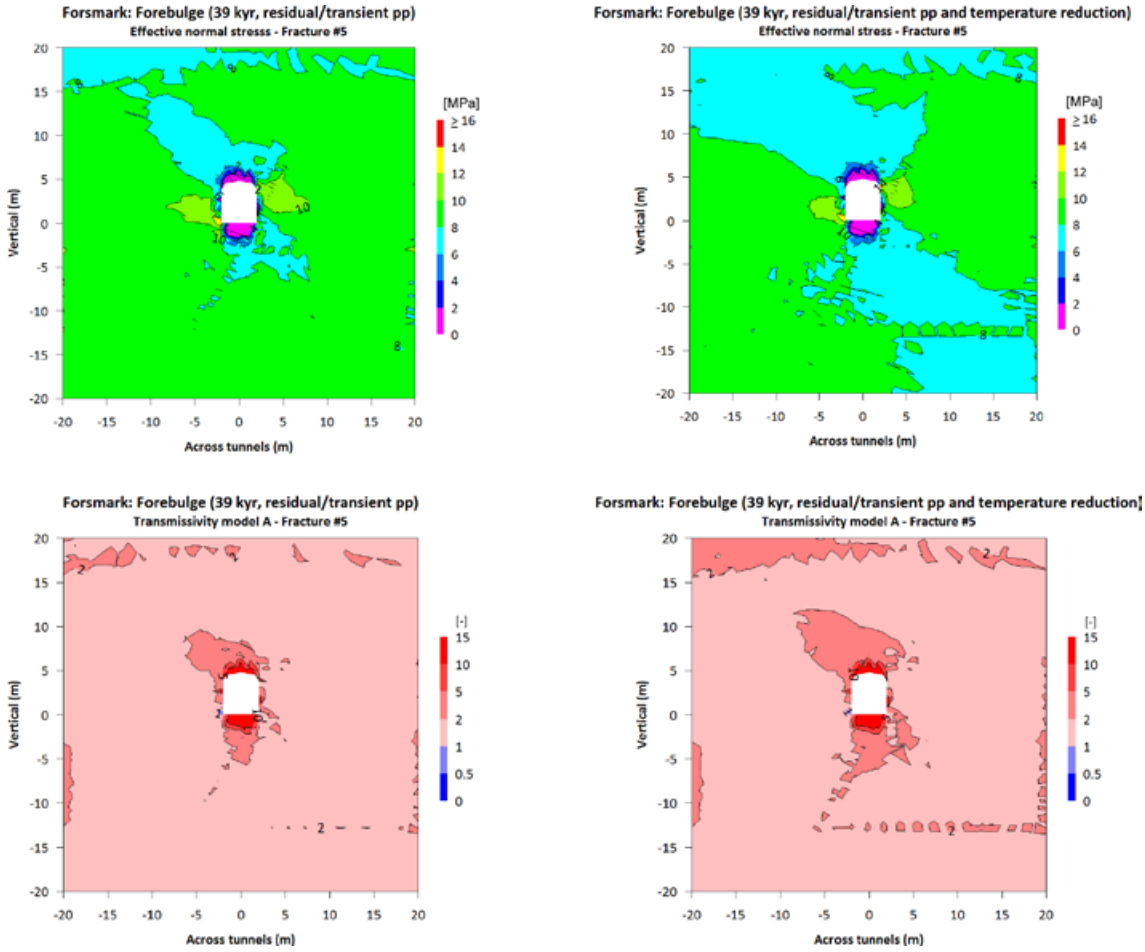

Figure G-10. *Projection of the effective normal stress (top row) and corresponding relative transmissivity (bottom row) on fracture #5 onto the vertical plane perpendicular to the deposition tunnel during the forebulge with permafrost induced pore pressure (left column) and with permafrost induced pore pressure and temperature induced stress reduction (right column).*

G4 Shearing

The shear displacements at the monitored points on the vertical fractures #1 and #2 are not affected by the additional stress reduction during permafrost conditions, cf. Figure G-11 and Figure G-12. This is verified by the contour plots of the accumulated shear displacement at the end of the glaciation (58 kyr). The maximum shear displacement on fracture #3 is less than 0.1 mm at all times.

For the horizontal fracture #4 (Figure G-13), the contour plots of the accumulated shear displacement at the end of the glaciation (58 kyr) show that, in the model with additional stress reduction during permafrost conditions, the sheared part of the fracture along the tunnel is more continuous, but the magnitude of the displacement is still less than 1 mm.

The monitored points on fracture #5 (Figure G-14, middle) are also not significantly affected by the additional stress reduction during permafrost conditions. As seen in the contour plots of the accumulated shear displacement at the end of the glaciation (Figure G-14, lower), the region around the tunnel with displacement magnitudes in the range 7–9 mm is only marginally increased.

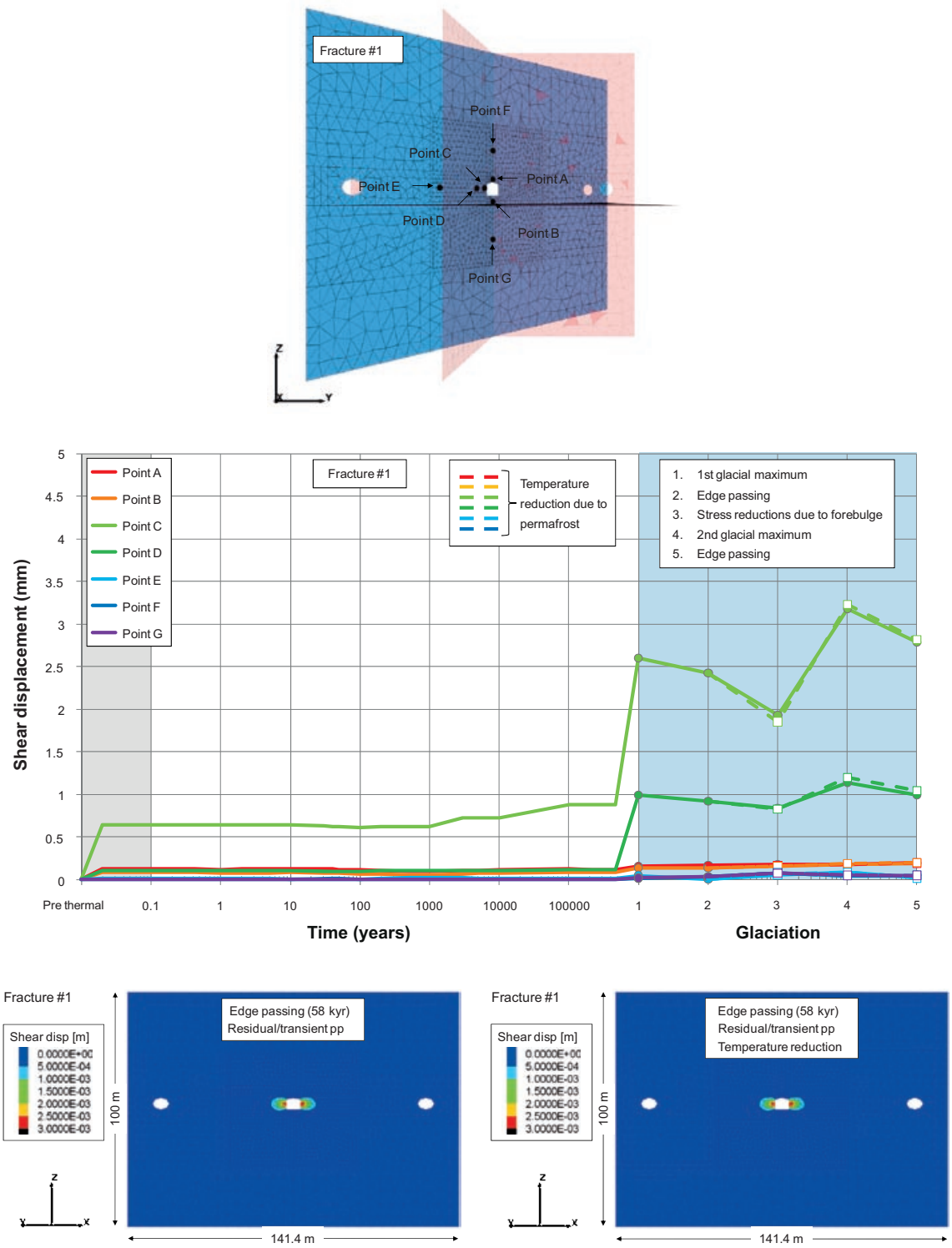

Figure G-11. *Locations of history points on fracture #1 (top). Temporal evolution of the shear displacement at selected points (middle). Grey and blue areas represent pre thermal time and glaciation, respectively. Lower: Shear displacement at the end of the glaciation with residual pore pressure (left) and with residual pore pressure in the model with temperature reduction during the forebulge (right).*

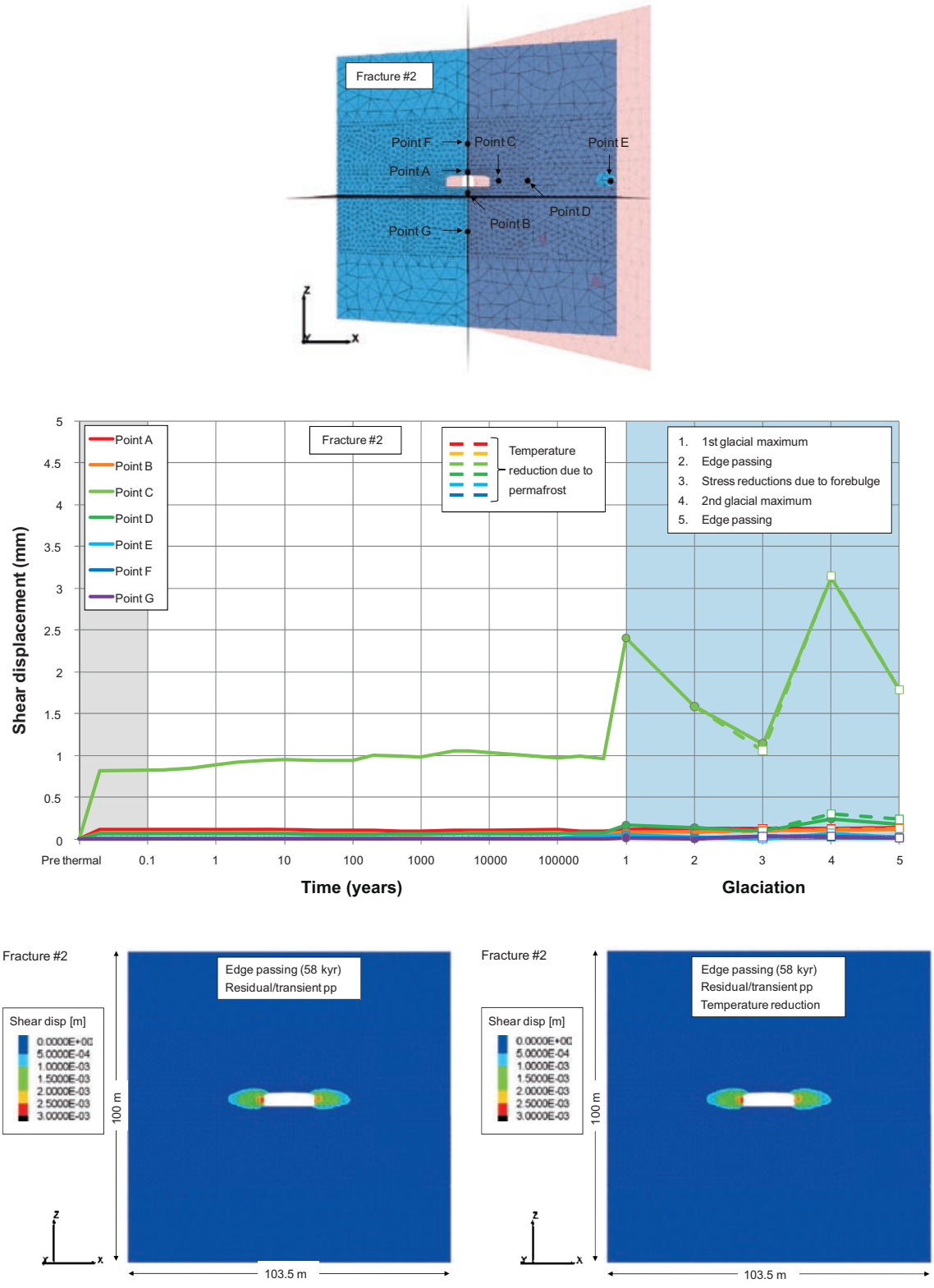

Figure G-12. *Locations of history points on fracture #2 (top). Temporal evolution of the shear displacement at selected points (middle). Grey and blue areas represent pre thermal time and glaciation, respectively. Lower: Shear displacement at the end of the glaciation with residual pore pressure (left) and with residual pore pressure in the model with temperature reduction during the forebulge (right).*

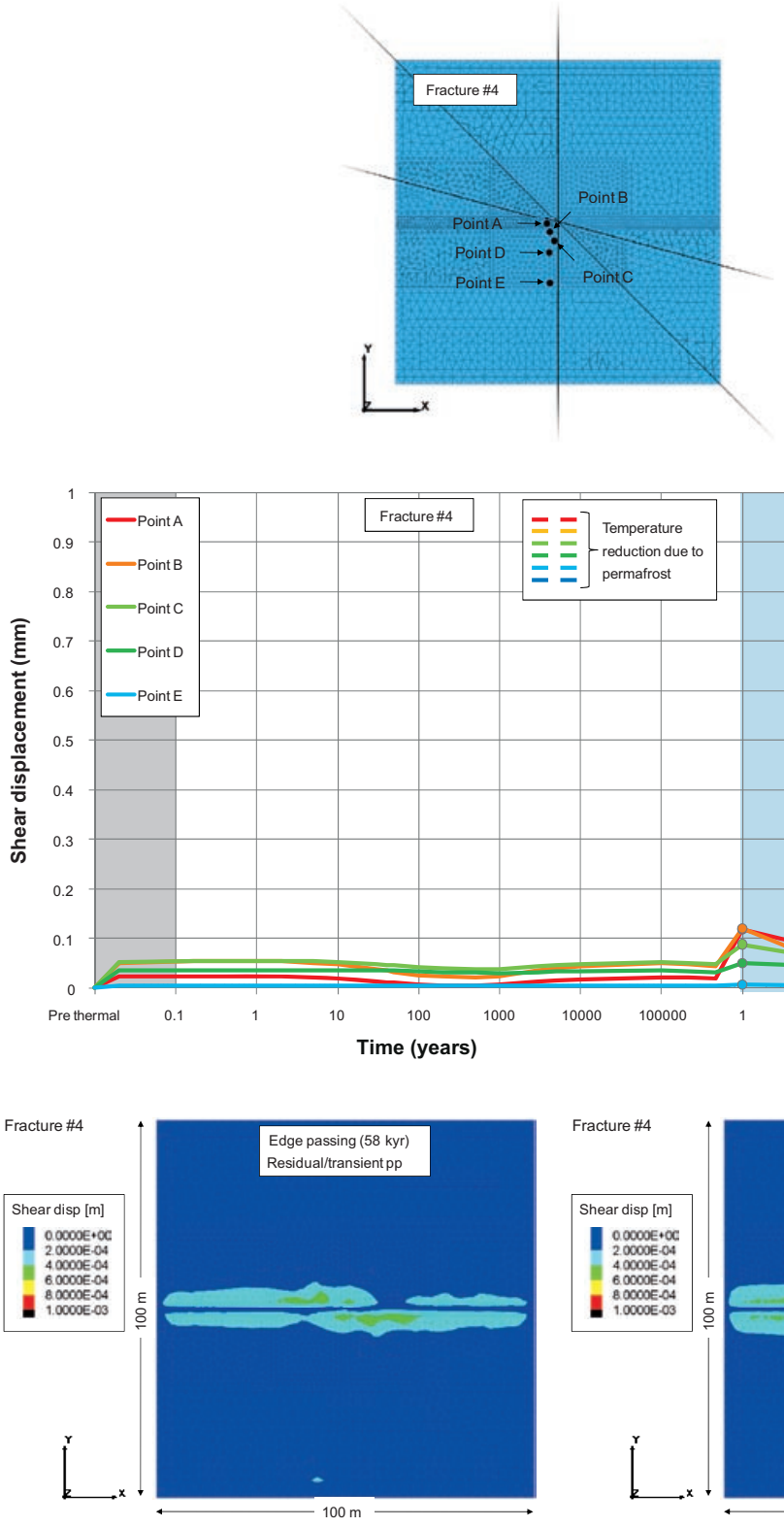

Figure G-13. *Locations of history points on fracture #4 (top). Temporal evolution of the shear displacement at selected points (middle). Grey and blue areas represent pre thermal time and glaciation, respectively. Lower: Shear displacement at the end of the glaciation with residual pore pressure (left) and with residual pore pressure in the model with temperature reduction during the forebulge (right).*

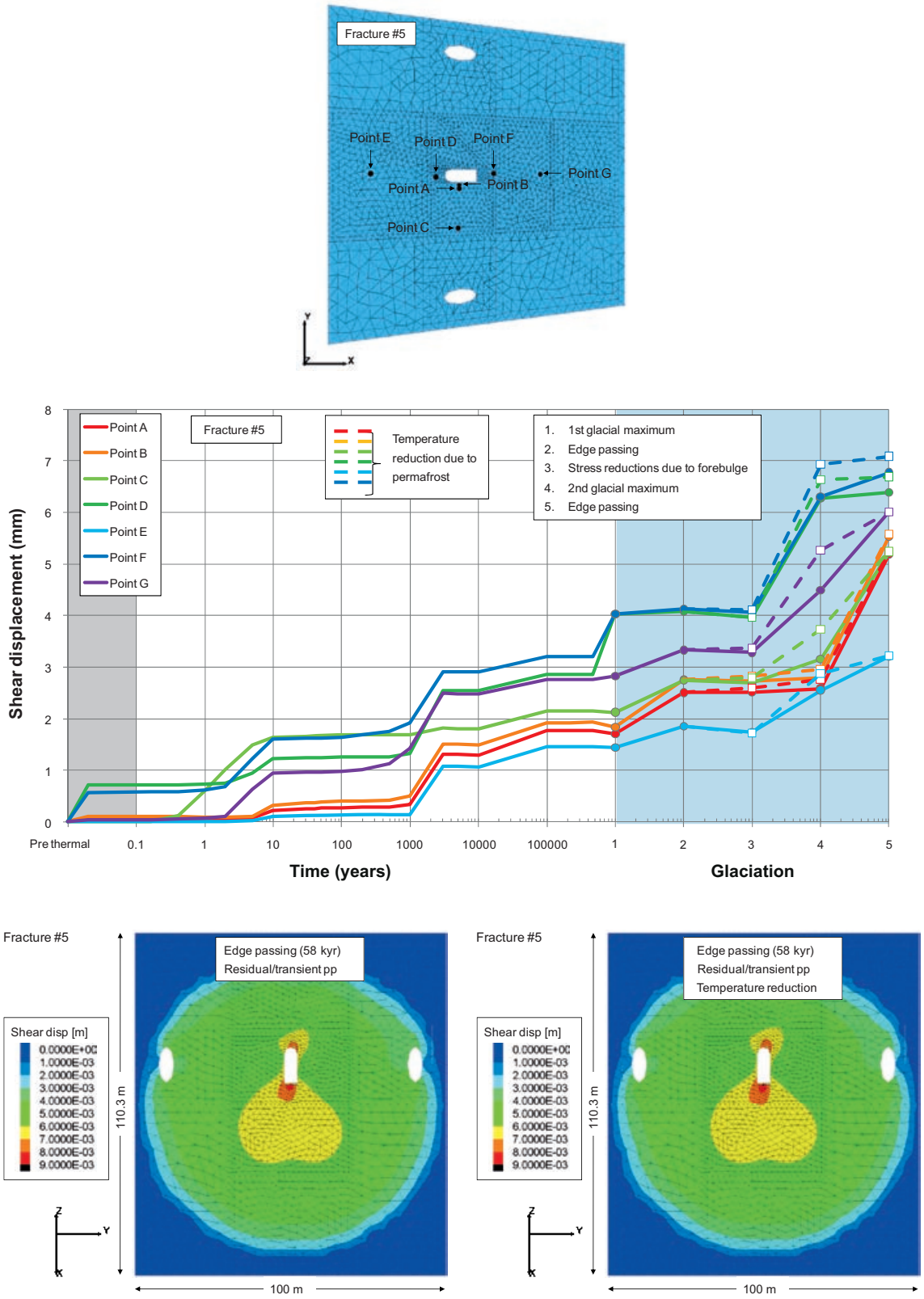

Figure G-14. *Locations of history points on fracture #5 (top). Temporal evolution of the shear displacement at selected points (middle). Grey and blue areas represent pre thermal time and glaciation, respectively. Lower: Shear displacement at the end of the glaciation with residual pore pressure (left) and with residual pore pressure in the model with temperature reduction during the forebulge (right).*

Appendix H

Complementary analyses of stresses in the near-field

H1 General

Results from the models giving the highest and lowest stresses are presented in the main text, cf. Chapter 9. Results from the remaining models are presented in the following sections.

H2 Forsmark

H2.1 Model overview

A model map for the linear elastic models is presented in Table H-1. The base case models with mean value properties are labelled ‘a’, whereas the models with dimensioning values of the heat transport properties are labelled ‘b’. Note that spalling assessments using results from models A1 (reference parameter values and uncertainty estimates) and B1 (reference parameter values only) are presented in the main text. Results from the remaining models (including parameter variations) are presented here.

H2.2 Material properties, initial conditions and boundary conditions

The mean values (and dimensioning values for the thermal conductivity) of the rock mass properties used in the modelling work are presented in Table 4-5. The reference values of the *in situ* stresses are presented in Table 4-2 with local deviation of the tunnel axis from the major horizontal *in situ* stress given in Table H-1.

In order to investigate the influence of uncertainties in Boxes B1 and C1, a further set of models are analyzed where uncertainties associated with Young’s modulus (expressed as ±1 std, cf. Table 4-7) and *in situ* stress magnitudes (Table 4-2) are accounted for. The orientation of the major horizontal *in situ* stress with respect to the tunnel axis for each of the five alternative stress states is given by the following:

- Stress state I, III, IV and V: 33° (Box C1).
- Stress state II: 0° (Box B1) and 3° (Box C1).

Table H-1. Model map for small near-field models at Forsmark.

Model code	Tunnel orientation with respect to major *in situ* stress	Description
A1	22°	BC from large-scale model Box A1.
1a		Mean heat conductivity in RFM029.
1b		Dimensioning value of heat conductivity in RFM029
B1	3°	BC from large-scale model Box B1.
1a		Mean heat conductivity in RFM029.
1b		Dimensioning value of heat conductivity in RFM029
C1	18°	BC from large-scale model Box C1.
1a		Mean heat conductivity in RFM045.
1b		Dimensioning value of heat conductivity in RFM045
C2	17°	BC from large-scale model Box C2.
1a		Mean heat conductivity in RFM029.
1b		Dimensioning value of heat conductivity in RFM029
D1	21°	BC from large-scale model Box D1.
1a		Mean heat conductivity in RFM029.
1b		Dimensioning value of heat conductivity in RFM029
D2	21°	BC from large-scale model Box D2.
1a		Mean heat conductivity in RFM029.
1b		Dimensioning value of heat conductivity in RFM029

H2.3 Stresses in walls of deposition holes

The tangential stress at the wall of the deposition hole as function of the azimuthal angle (cf. Figure H-1) at four depths below the tunnel floor is presented in Figure H-2 (Box C2), Figure H-3 (Boxes D1 and D2) and Figure H-4 (Box C1). The upper part of each figure shows the stresses after excavation of the deposition holes. The lower parts show the corresponding stresses after 50 years of heating for mean value properties (left) and dimensioning thermal properties (right). The temporal evolution of the major principal stress at canister mid-height in FFM06 and RFM045 is presented in Figure H-5.

Uncertainties

The tangential stress after excavation in Box C1 is presented in Figure H-6. If the high spalling strength assumed for fracture domain FFM06 (cf. Table 4-6) is relevant for typical rock in that domain, the spalling strength will not be exceeded in fracture domain FFM06 during excavation when uncertainties in the most likely *in situ* stresses and their orientations are considered. For the spalling strength to be exceeded in the upper metre of the deposition hole wall after excavation of the deposition holes, the stress magnitudes need to be of the order of the 'Proposed Maximum Stress Model' (Stress state V), cf. Table 4-2.

Figure H-7 and Figure H-8 show the thermally induced stresses at canister mid-height in Box B1 and C1, respectively. As shown previously, Box B1 has the most favourable tunnel orientation with respect to the major horizontal *in situ* stress. For the lower limit of the stress model (II) and assuming mean thermal properties and E = 62 GPa (mean value –1 std), 52% of the UCS will be exceeded during the thermal phase. The corresponding results for Box C1, i.e. for the lower limit of the stress model (II) and E = 57 GPa (mean value –1 std), show that the 52% of the UCS for FFM06 will not be exceeded during the thermal phase. With the exception of canisters placed in fracture domain FFM06, it is therefore unlikely that thermally induced spalling in the walls of the deposition holes can be avoided at Forsmark.

H2.4 Stresses in tunnel walls and roof

In the stress model given by /SKB 2005/ and used in SKI's review of SR-Can /Rutqvist and Tsang 2008/, the ratio between σ_{yy} (stress across tunnel) and σ_{zz} (vertical stress) is close to 3. Therefore, there is potential for tensile stresses to develop already after excavation. In the most recent stress model for the Forsmark site /Glamheden et al. 2007a/ the ratio between σ_{yy} and σ_{zz} is around 2, which implies that tensile stresses are unlikely to develop after excavation, cf. Figure H-9.

The major principal stress in the centre of the tunnel roof is presented in Figure H-10 (FFM06 and RFM045). As opposed to the stresses in the deposition hole walls (cf. previous section), the stresses in the tunnel roof will not exceed the spalling strength during the heated phase.

Uncertainties

Figure H-11 shows the thermally induced stresses in the centre of the roof of the deposition tunnel in Box C1 for the mean value and orientation of the *in situ* stress compared with the four more unfavourable stress assumptions (I, III, IV and V). As seen in the figures, not even for stress magnitudes and orientations as in the upper limit of the stress model are sufficient for the thermally induced stresses to exceed 52% of the UCS in FFM06.

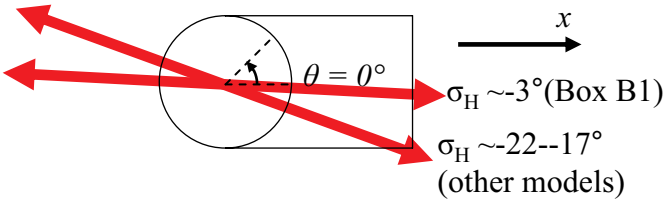

Figure H-1. *Definition of azimuthal angle and orientation major horizontal in situ stress with respect to the tunnel.*

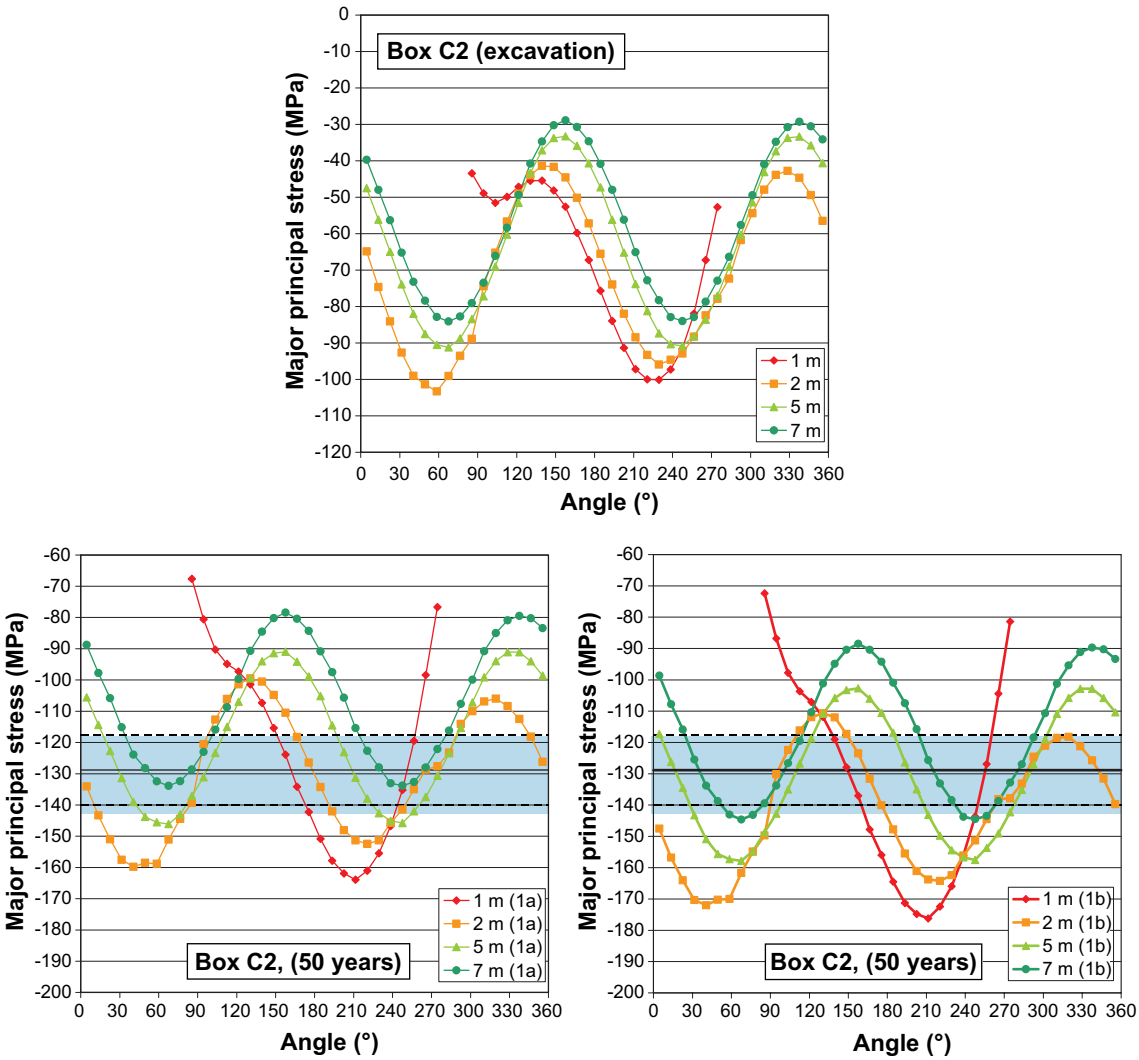

Figure H-2. *Tangential stress at different depths after excavation (top) and after 50 years of heating (bottom left and right) in Box C2 located in FFM01. Blue colour represents spalling strength (52–62% of UCS in FFM01).*

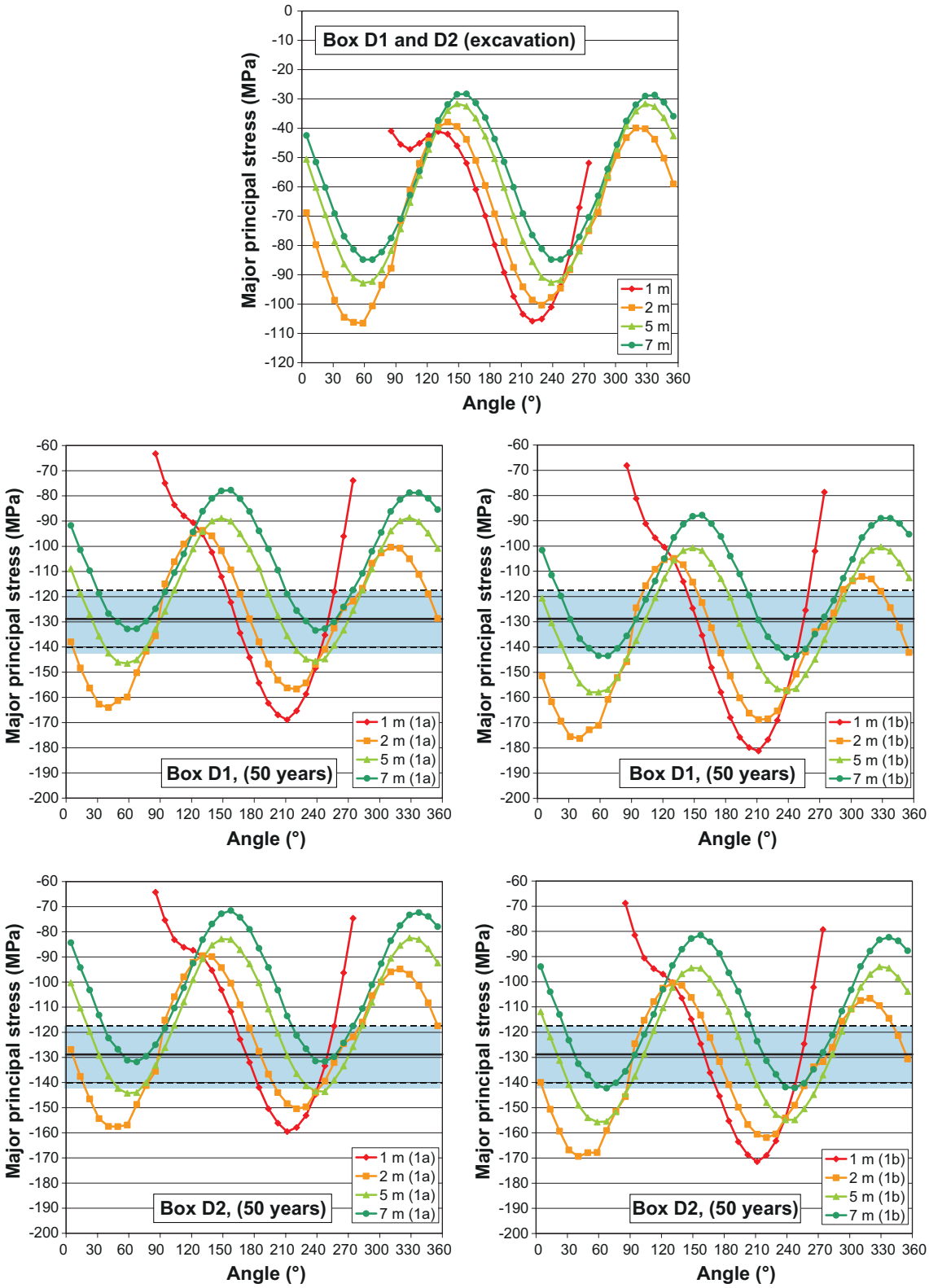

Figure H-3. *Tangential stress at different depths after excavation (top) and after 50 years of heating (bottom left and right) in Boxes D1 and D2 located in FFM01. Blue colour represents spalling strength (52–62% of UCS in FFM01).*

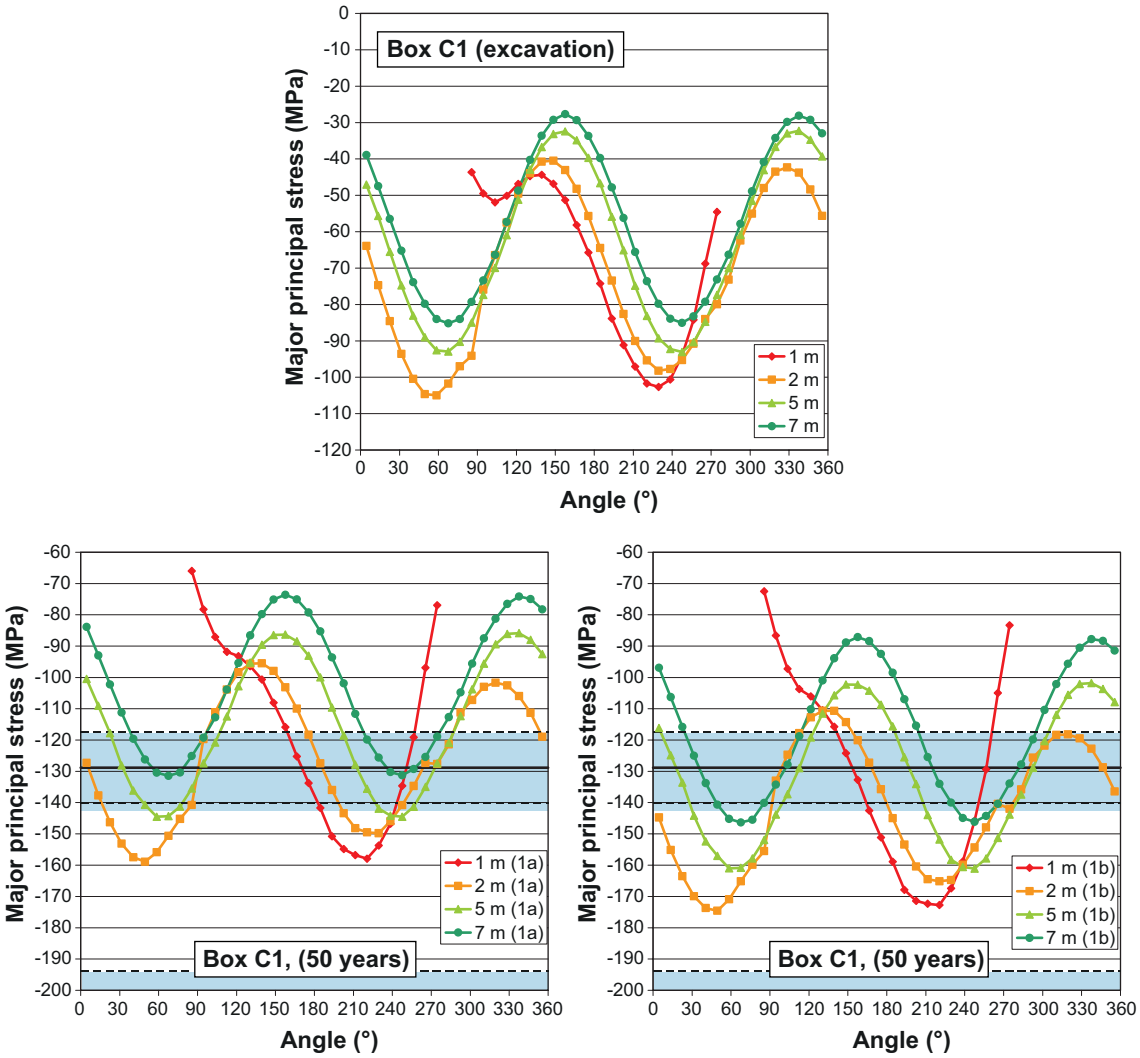

Figure H-4. *Tangential stress at different depths after excavation (top) and after 50 years of heating (bottom left and right) in Box C1 located in FFM06. Blue colour represents spalling strength (52–62% of UCS in FFM01 and FFM06).*

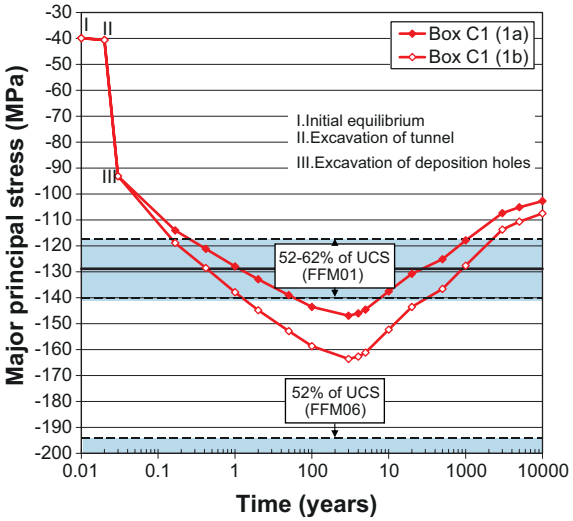

Figure H-5. *Temporal development of thermally induced stresses at canister mid-height on deposition hole wall in Box C1 in FFM06.*

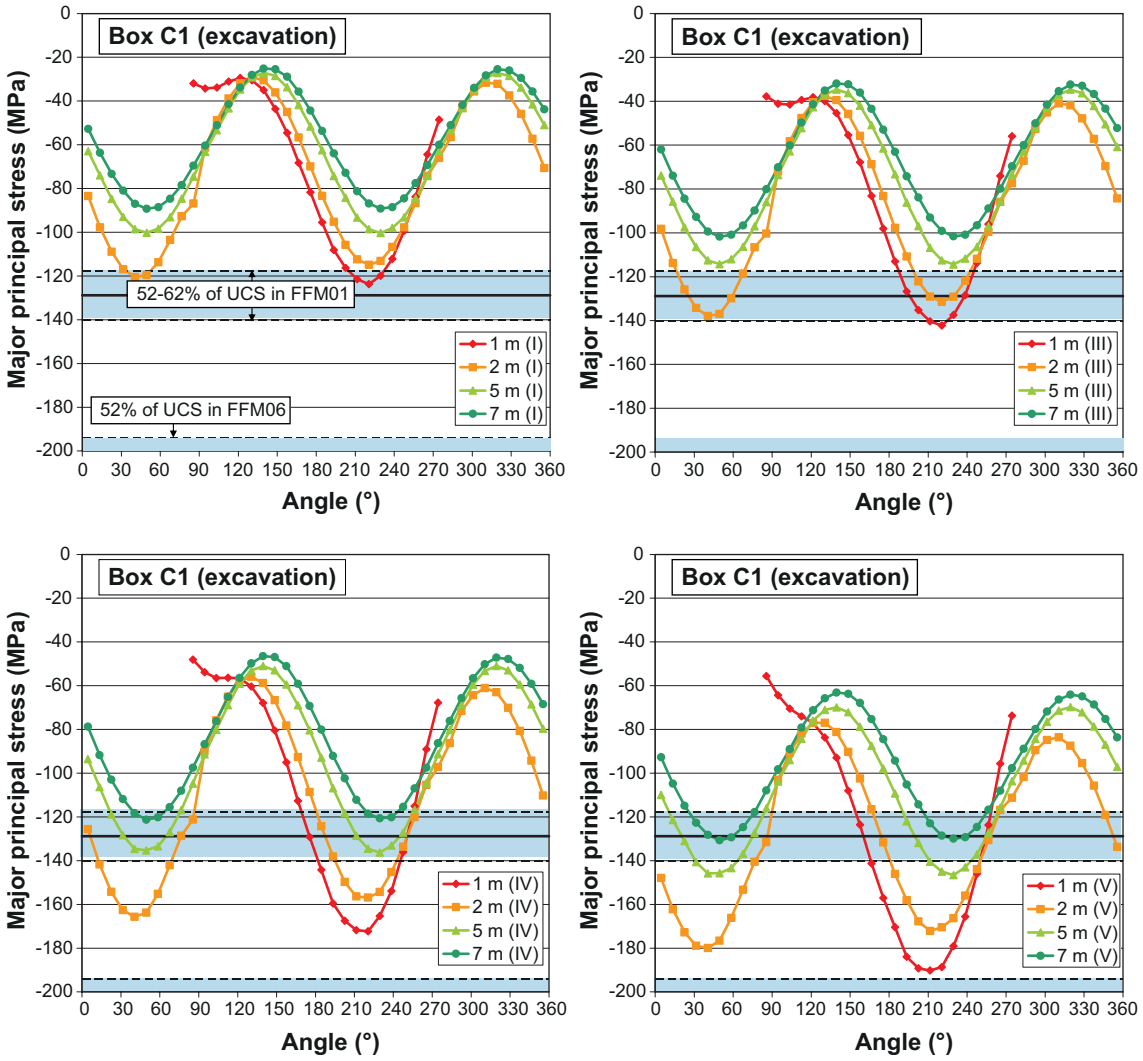

Figure H-6. *Tangential stress at different depths below the tunnel floor after excavation for different in situ stress assumptions (cf. Table 4-2) in Box C1 located in FFM06.*

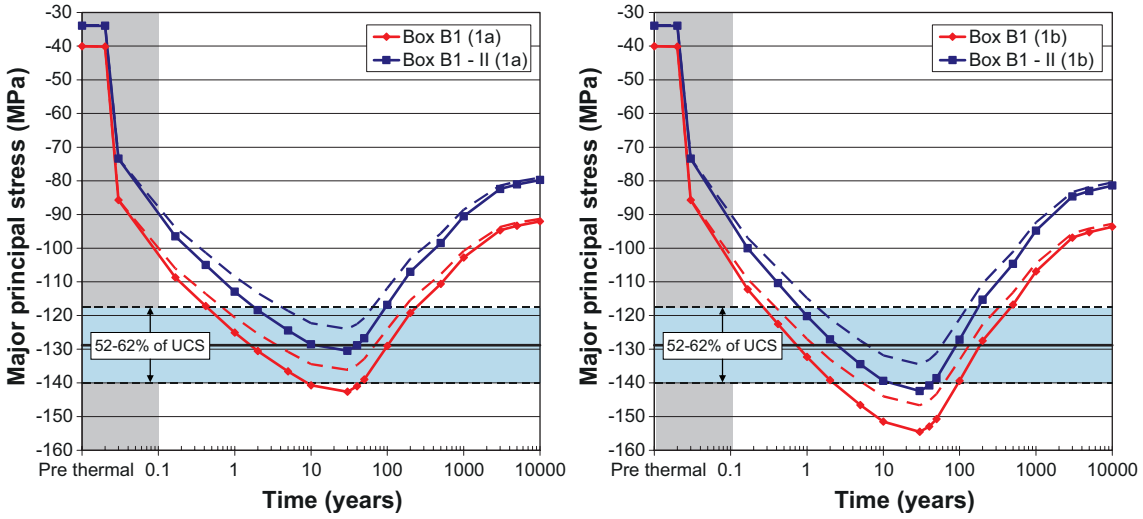

Figure H-7. *Temporal development of thermally induced stresses at canister mid-height in Box B1 in FFM01. Left: Mean heat transport properties. Right: Dimensioning value of heat transport properties. Plot symbols represent mean mechanical properties (E = 70 GPa), whereas dashed lines represent Young's modulus minus 1 standard deviation (E = 62 GPa).*

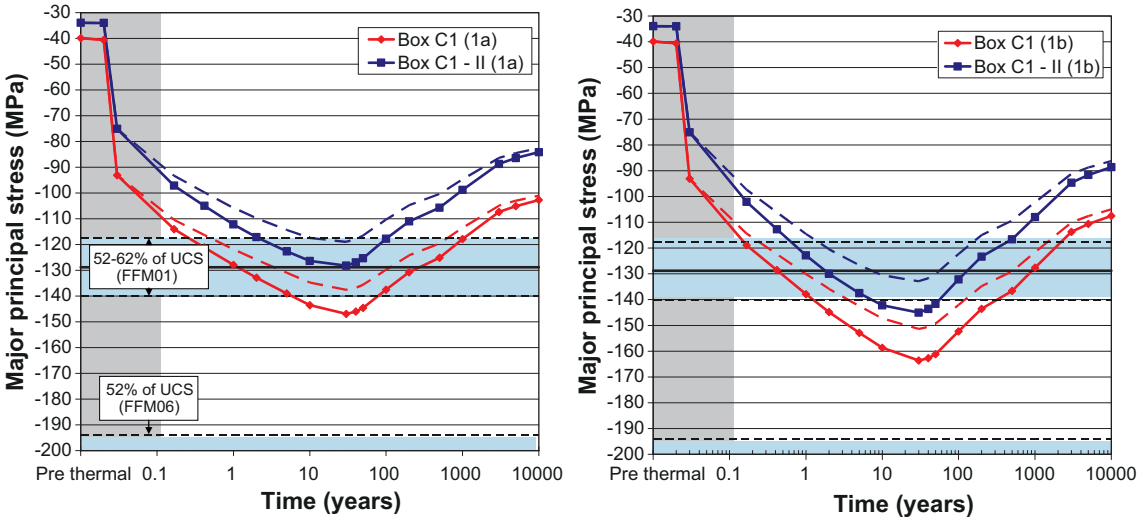

Figure H-8. *Temporal development of thermally induced stresses at canister mid-height in Box C1 in FFM06. Left: Mean heat transport properties. Right: Dimensioning value of heat transport properties. Plot symbols represent mean mechanical properties (E = 69 GPa), whereas dashed lines represent Young's modulus minus 1 standard deviation (E = 57 GPa).*

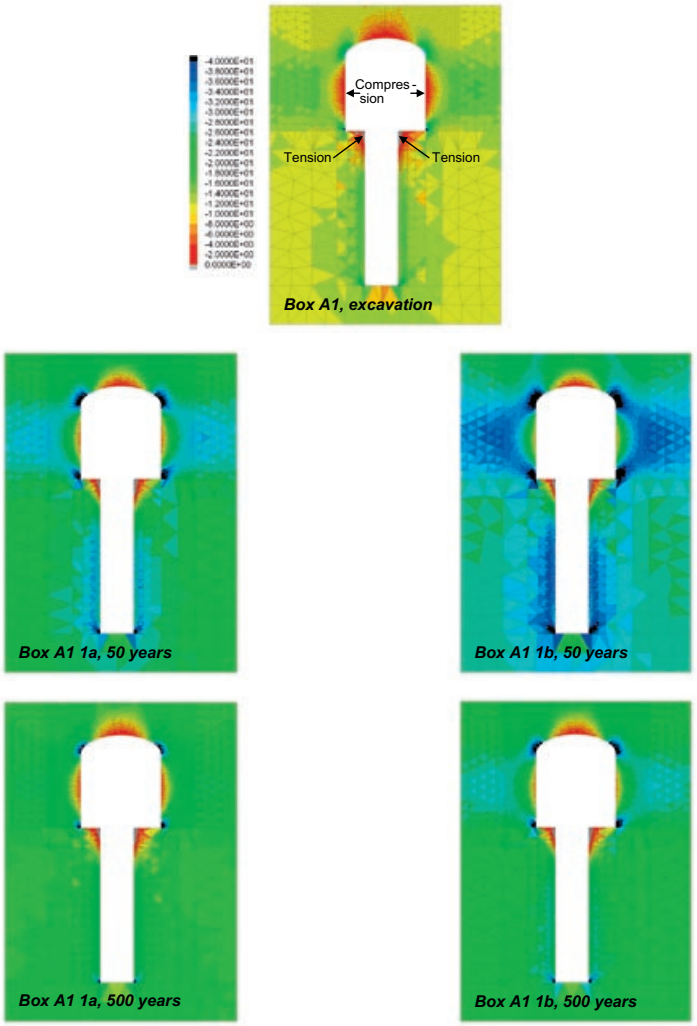

Figure H-9. *Contour plots of vertical stress component at Forsmark Box A1 after excavation (top), 50 years (middle) and 500 years (lower). Stresses range from –40 MPa (compression) to 0 MPa. Stresses outside the range are marked in black (compression) and light grey (tension).*

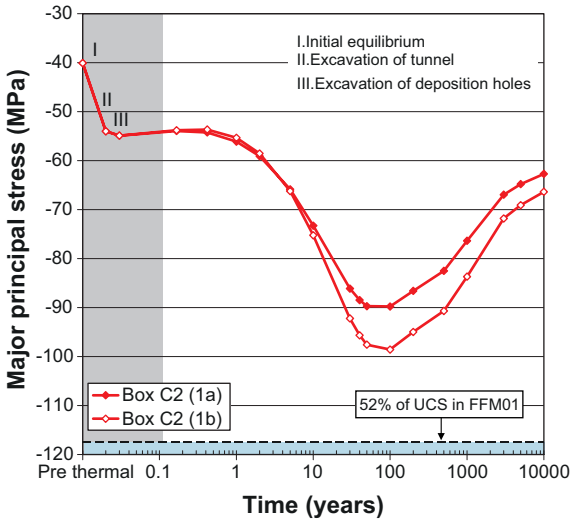

Figure H-10. *Temporal development of thermally induced stresses in tunnel roof in box in FFM06. Mean heat transport properties (1a) and dimensioning value of heat transport properties (1b).*

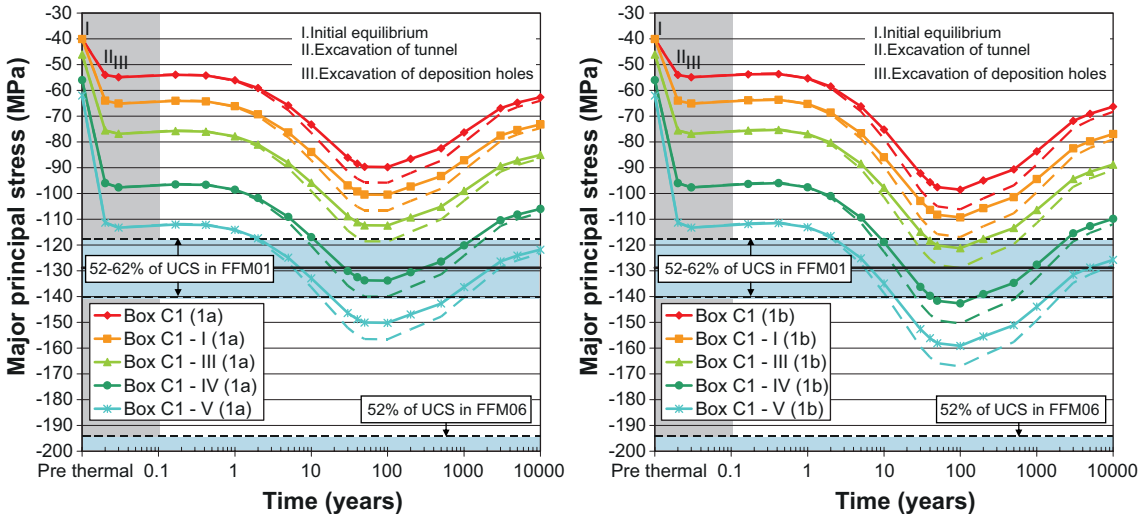

Figure H-11. *Temporal development of thermally induced stresses in tunnel roof in Box C1 in FFM06. Left: Mean heat transport properties. Right: Dimensioning value of heat transport properties. Plot symbols represent mean mechanical properties, whereas dashed lines represent Young's modulus plus 1 standard deviation.*

Appendix I

Laxemar

I1 Introduction

As Forsmark is the selected repository site, the main part of this report considers the THM evolution of the rock at that site. In this appendix, complementary analyses are provided for the Laxemar site.

The THM evolution of the rock mass at Laxemar is considered on two scales – the large scale and small scale – and during three of the repository phases (excavation and operational phase, the initial temperate phase and the glacial phase), cf. Table 2-1. The following scenarios studied during each of the considered repository phases, cf. Chapter 2, and the approach to evaluating the subsequent modelling results is described in Chapter 3.

- **The excavation and operational phase (Section 2.3):**
  - Potential of stress induced failure following from stress concentrations around deposition holes and tunnels (spalling), cf. Section I.6 (small scale).
- **The initial temperate phase (Section 2.4):**
  - Stress additions at different depths and accompanying transmissivity impact, cf. Section I.4 (large scale).
  - Increased stress concentrations around deposition holes and associated risk of stress induced failure in the walls (spalling), cf. Section I.6 (small scale).
- **The glacial phase (Section 2.6, without considering the impact of permafrost):**
  - Stress additions at different depths and accompanying transmissivity impact, cf. Section I.5 (large-scale).
  - Shearing, cf. Section I.5 (large-scale).
  - Pore pressure evolution.

The data used in the modelling work and the subsequent modelling results are described in the following sections. More detailed descriptions regarding the modelling approach can be found in the modelling chapters for Forsmark in the main text of this report, cf. Chapters 5, 6, 7 and 9.

I2 Data used in THM-modelling

I2.1 Overview of the Laxemar site

The locations of the three dominating rock domains (RSMA, RSMD and RSMM) at Laxemar site are presented in Figure I-1 (left). Within the local volume the rock mass is subdivided into six distinct fracture domains /Hakami et al. 2008/, FSM_C, FSM_W, FSM_NE005, FSM_N, FSM_EW007 and FSM_S, as shown in Figure I-1 (right). The repository is located in fracture domains FSM_C, FSM_W, FSM_NE005 and FSM_EW007. In the following subsections a summary of the relevant data used in the THM modelling on different scales of the repository rock mass are given with references to the primary sources of the data. More detailed descriptions of these data and discussions on uncertainties are provided in report ‘Comparative analysis of safety related site characteristics’ /SKB 2010b/.

I2.2 Layout

Layout D2 for the Laxemar site contains approximately 8,000 potential canister positions /SKB 2009d/, cf. Figure I-2, with about 44% of potential canister positions located in rock domain RSMD, 25% in rock domain RSMA and 31% in rock domain RSMM. The canister spacing in the three rock domains is 8.1 m in RSMD, 9 m in RSMA and 10.5 in RSMM, respectively /SKB 2010g/. All deposition tunnels are oriented approximately 130° with respect to North.

The repository depth at Laxemar is prescribed such that the roofs of the deposition tunnels are at or below an elevation of –500 m /SKB 2010g/. In the modelling work at all scales the repository depth is set to 500 m.

To meet the criterion of 6,000 deposited canisters, it is assumed that the loss of canister positions is 25%. There are uncertainties associated with the spatial distribution of fracturing, which means that the rejected canister positions cannot be identified in the layout /SKB 2010g/. In the large-scale modelling (Sections I.3 and I.4) every 4th canister is removed uniformly across the repository region order to achieve the given loss of canister positions, *i.e.* the average power density. In the near-field modelling every canister position is assumed to be filled (Section I.6).

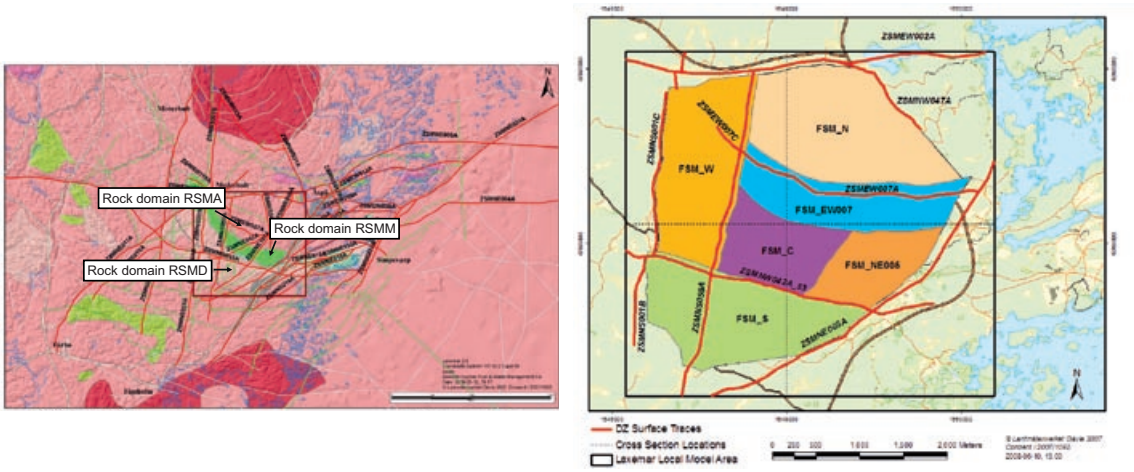

Figure I-1. *Left: Dominating rock domains in the local volume at Laxemar site. Modified from /Hakami et al. 2008/. Right: View of fracture domains (FSM_x) and major deterministic fracture zones (ZSM_x) at the ground surface at the Laxemar site, from /Hakami et al. 2008/.*

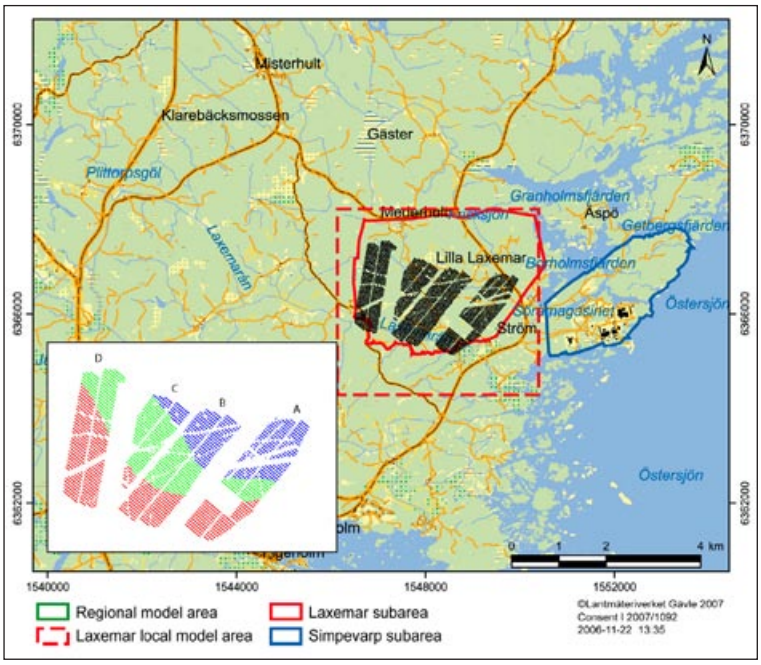

Figure I-2. *Map of the Laxemar area with the repository layout superimposed in black. Inset shows the layout with the three rock domains RSMD (canister spacing 8.1 m) marked in red, RSMA (canister spacing 9 m) marked in blue and RSMM (canister spacing 10.5 m) marked in green. Map of Laxemar area from /Hakami et al. 2008/.*

I2.3 State of stress

Figure I-3 shows stress vs. depth relations suggested for the region around the target area at Laxemar (depth interval 400–700 m) in the site model for Laxemar /Hakami et al. 2008/ – here extrapolated to depths between 0–1 km. In the large-scale modelling work, the most likely stress magnitudes and orientations (without account of the uncertainty spans) are used at all depths, cf. Table I-1. Note that, similarly to the large-scale modelling for the Forsmark site, *in situ* stresses are not explicitly included in the models. Where total stresses are required, the stresses presented in Table I-1 are added to the modelled thermally induced stresses (Section I.4) or glacial stresses (Section I.5).

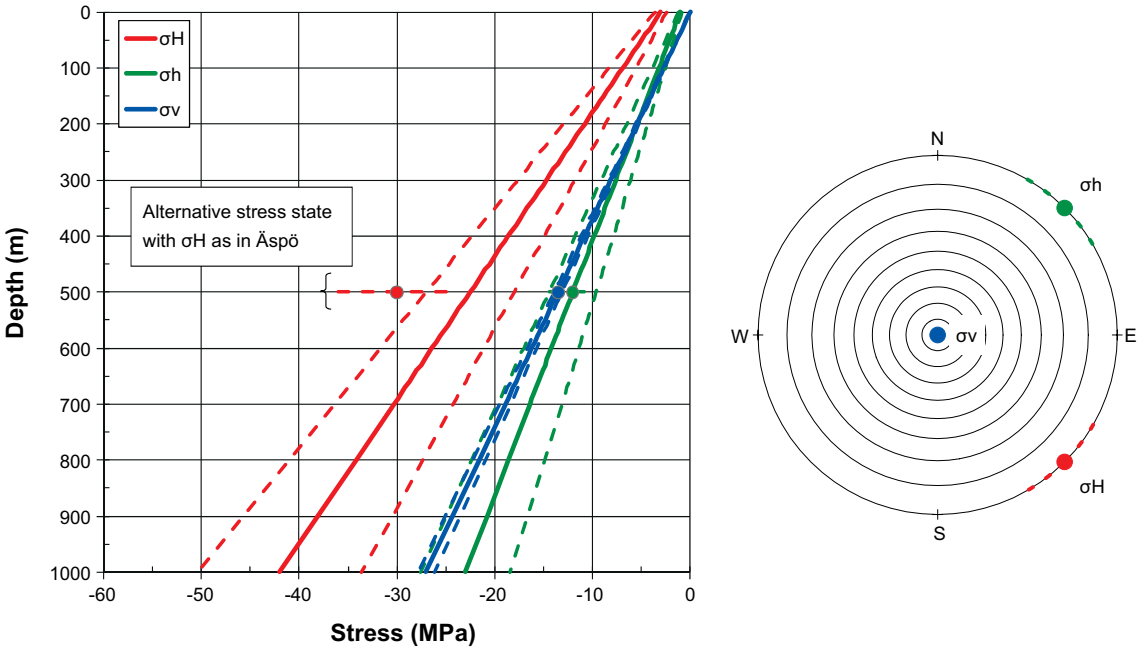

Figure I-3. *Left: In situ stress model (valid at 400–700 m depth – here extrapolated to depths between 0–1 km) with associated uncertainty spans /Hakami et al. 2008/ for the region around the target area at Laxemar (fracture domains FSM_C, FSM_W and FSM_NE005). The stress ranges in a modified stress state such that the major horizontal stress is increased to the level reported for Äspö /Andersson 2007/ are marked with plot symbols. Right: Mean value orientations (plot symbols) and ranges in uncertainty (dashed lines) of the principal in situ stress components.*

Table I-1. Stress-depth relations used in large-scale modelling work for Laxemar, based on suggestion for the region around the target area in the site model for Laxemar /Hakami et al. 2008/. The orientation of the major horizontal in situ stress is given with respect to North.

Depth range (m)	σH (MPa)	σH, orientation (°)	σh (MPa)	σv (MPa)
0–1,000	–3–0.039 z	135	–1–0.022 z	–0.027 z

In the small-scale (Section I.6) near-field modelling, two assumptions regarding the state of stress at repository depth (500 m) are made, cf. Table I-2:

- The most likely value of stress magnitudes and orientations at repository depth (500 m) in the stress model for Laxemar.
- The *in situ* stress orientations and magnitudes of the minor horizontal and vertical *in situ* stresses as in the stress model for Laxemar, whereas the magnitude of the major horizontal *in situ* stress is given by that at Äspö /Andersson 2007/.

The orientation of the major principal stress with respect to the deposition tunnels is determined from the layout presented in Figure I-2. All tunnels have the same orientation (130° with respect to North), which corresponds to a deviation of the major horizontal *in situ* stress from the tunnel axis by about 5° at all near-field model locations considered here.

Table I-2. Reference in situ stress magnitudes and orientation (with respect to North) at repository depth (500 m) used in near-field modelling work for Laxemar (upper two rows). Alternative stress magnitudes and orientations used for spalling assessment (lower two rows).

Stress model	σH (MPa)	Orientation (°)	σh (MPa)	σv (MPa)
Laxemar stress model	–22.5	135	–12	–13.5
Äspö σH	–30	135	–12	–13.5
Laxemar – I	–22.5	150	–12	–13.5
Äspö σH – III	–36	150	–14.4	–13.9

In addition to the most likely stress magnitudes and orientation of the major horizontal *in situ* stress, the following stress states are used to assess the potential for spalling (Section I.6) at the Laxemar site, cf. Table I-2 (following the same nomenclature as for Forsmark). For both additional stress states the most unfavourable orientation of the major horizontal *in situ* stress with respect to the local tunnel orientation is chosen, i.e. 20° for the near-field models considered here.

- **Stress state Laxemar I:** Most likely stress magnitudes at repository level (500 m) of the Laxemar stress.
- **Stress state Äspö III:** Upper limit stress magnitudes at repository level of the Äspö stress (500 m) assuming that the uncertainty span in the magnitude and orientation of the major horizontal stress at Äspö is the same as in the stress model for Laxemar.

I2.4 Fractures and fracture zones

Similarly to the large-scale modelling work for Forsmark (cf. Chapters 6 and 7), fractures are not modelled explicitly. Instead, estimates of transmissivity changes and shear displacements are presented:

- as functions of depth on hypothetical fracture planes with orientations perpendicular to the *in situ* stress components, i.e. vertical or horizontal planes.
- at repository depth on vertical fractures striking 27.1° (= 45°–35.7°/2) with respect to the major horizontal *in situ* stress. This is the fracture orientation with the largest possible instability, given the Mohr-Coulomb fracture strength (Table I-3) and the stress state (Table I-2), cf. Figure I-4.

The Mohr-Coulomb strength properties of the fractures are provided in Table I-3. These values are based on results from direct shear tests reported by /Hakami et al. 2008/ and given as the average value of their mean laboratory-determined peak and residual values.

Table I-3. Average fracture strength properties at Laxemar based on /Hakami et al. 2008/.

Property	Unit	Value
Cohesion	MPa	0.6
Friction angle	°	35.7

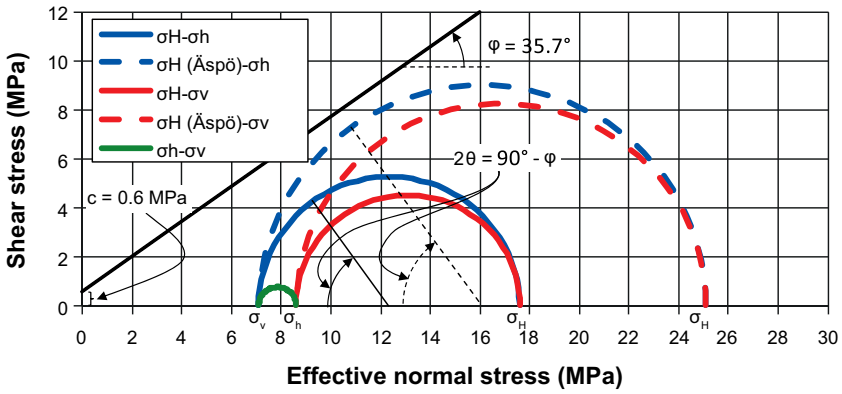

Figure I-4. Mohr circle representation of the in situ stress state at repository (500 m) depth (Table I-2). Given the Mohr-Coulomb fracture strength properties (Table I-3) and the stress state, the fracture orientation with the largest possible instability is vertical and strikes at an angle of 27.1° relative to the major horizontal stress.

I2.5 Thermal, thermo-mechanical and mechanical properties of the rock

The reference values of the thermal parameters chosen for the modelling work in the three dominating rock domains at Laxemar (RSMA1, RSMM01 and RSMD01) are presented in Table I-4.

- The heat capacity is represented by its mean value in each rock domain. For the large-scale models (Sections I.3 and I.4), the mean value heat capacity in rock domain RSMD01 is selected to represent the heat capacity on a large scale.
- Two values of the thermal conductivity are chosen: The mean value in each rock domain and the dimensioning value (*i.e.* the effective thermal conductivity for the hottest canisters) in each rock domain. Similarly as for the Forsmark site (Chapter 5), dimensioning values for the thermal conductivity can be obtained by use of nomographic charts, cf. Figure I-5. For the large-scale models (Sections I.3 and I.4), the mean value thermal conductivity in rock domain RSMD01 is selected to represent the thermal conductivity on a large scale.

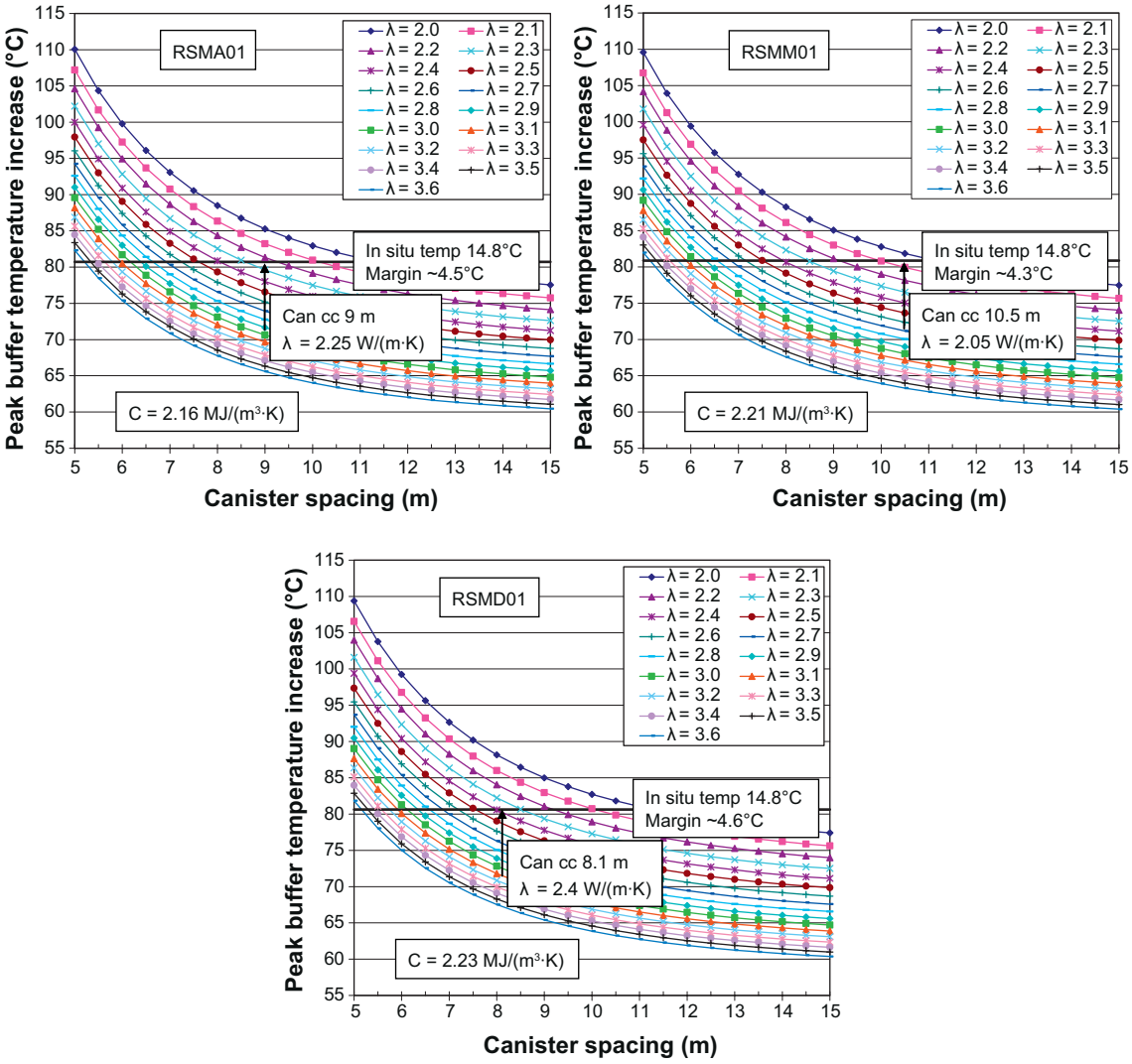

Figure I-5. *Nomographic charts for rock domains RSMA01 (top left), RSMM01 (top right) and RSMD01 (bottom) at Laxemar. The dimensioning thermal conductivity, for a given canister spacing, is defined as the effective thermal conductivity value that gives a peak buffer temperature of 100°C with account of in situ temperature and uncertainty margin. The uncertainty margin is estimated from /Hökmark et al. 2010/. Here the dimensioning conductivities are 2.25, 2.05 and 2.4 W/(m·K) in rock domains RSMA01, RSMM01 and RSMD01, respectively.*

Table I-4. Thermal properties of the rock mass /Sundberg et al. 2008a/. Dimensioning values of the thermal conductivity are obtained from the nomographic charts in Figure I-5.

Parameters	Unit	RSMA01	RSMM01	RSMD01
Heat capacity (*C*)	MJ/(m^3·K)	2.16	2.21	2.23
Mean thermal conductivity (λ_m)	W/(m·K)	2.93	2.65	2.76
Dimensioning thermal conductivity (λ_d)	W/(m·K)	2.25	2.05	2.4

The *in situ* temperatures at 400, 500 and 600 m depth at the Laxemar site are presented in Table I-5. Note that the *in situ* temperature does not influence the thermo-mechanical calculations and is only use here to obtain the values for the dimensioning thermal conductivity at repository depth (500 m) presented in Figure I-5 and Table I-4.

Table I-5. Mean in situ temperatures at different depths at Laxemar /Sundberg et al. 2008a/.

400 m	500 m	600 m
13.3°C	14.8°C	16.3°C

The reference mechanical parameter values chosen for the modelling work in fracture domains FSM_C, FSM_W, FSM_NE005, FSM_N and FSM_EW007 are presented in Table I-6.

- The value given for the density of rock is a generic value used in all modelling work to be compatible with the vertical stress gradient, cf. e.g. Table I-1.
- The elastic properties of the rock mass (Young's modulus and Poisson's ratio) are represented by their mean values in each fracture domain. For the large-scale models (Section I.4) an average value of Young's modulus of 55 GPa is used to represent the rock mass on a large scale.

Table I-6. Mean value mechanical properties of the rock mass at Laxemar /Hakami et al. 2008/.

Parameters	Unit	FSM_C, FSM_W and FSM_NE005	FSM_N and FSM_EW007
Density (ρ)	kg/m^3	2,700	2,700
Young's modulus (*E*)	GPa	59	50
Poisson's ratio (ν)	–	0.3	0.3

The reference thermo-mechanical /Sundberg et al. 2008a/ and strength /Hakami et al. 2008/ parameter values of the rock in the three dominating rock domains at Laxemar (RSMA1, RSMM01 and RSMD01) are presented in Table I-7.

- The heat expansion coefficient in all rock domains is that of *Ävrö granodiorite* /Sundberg et al. 2008a/.
- The spalling strength of the rock is assumed to be in the range 52–62% of the laboratory determined uniaxial compressive strength (*UCS*) of intact rock in each rock domain. Spalling analyses are conducted for near-field models located in all three rock domains (Section I.6).

Table I-7. Mean value strength and thermo-mechanical properties of intact rock at Laxemar /Hakami et al. 2008, Sundberg et al. 2008a/.

Parameters	Unit	RSMA01	RSMM01	RSMD01
Uniaxial compressive strength (*UCS*)	MPa	193	187	187
Heat expansion coefficient (α)	K^{-1}	$7.3 \cdot 10^{-6}$	$7.3 \cdot 10^{-6}$	$7.3 \cdot 10^{-6}$

I2.6 Hydraulic properties

The two stress-transmissivity relations proposed for the Forsmark site (cf. Figure 4-9) are based on average fracture normal stiffness estimates and one "worst case" option based on lower bound fracture normal stiffness estimates. Corresponding normal stiffness estimates for the Laxemar site and parameter values for the CY-model (Equation 3-5) are compiled in the report 'Comparative analysis of safety related site characteristics' /SKB 2010b/. The initial mechanical aperture, E_0, is estimated to 42 µm by use of Equation 3-4 assuming the corresponding hydraulic aperture at repository depth to be 20 µm /Rhén et al. 2008, Table 9-12/ and the joint roughness coefficient to be 6 /Hakami et al. 2008, Table 4-3/. Two sets of CY-model parameters are chosen based on the data shown in Figure I-6 (left) – the Laxemar average (*JKN* = 367 MPa/mm, *JEN* = 0.86) and a "worst case" option based on lower bound fracture normal stiffness estimates (*JKN* = 150 MPa/mm, *JEN* = 0.6). Figure I-6 (right) shows estimates of the hydraulic aperture based on the CY-model together with exponential fits assuming the residual aperture at high normal stress to be 20 µm. These estimates apertures are compared with the proposed models for Forsmark (cf. subsection 4.7.1). As seen in the figure, there are not sufficiently large differences between the two sites to warrant separate transmissivity-relations for the Laxemar site. Therefore, the same two stress-transmissivity relations proposed for the Forsmark site (cf. Figure 4-9) are used to represent stress induced transmissivity changes at Laxemar.

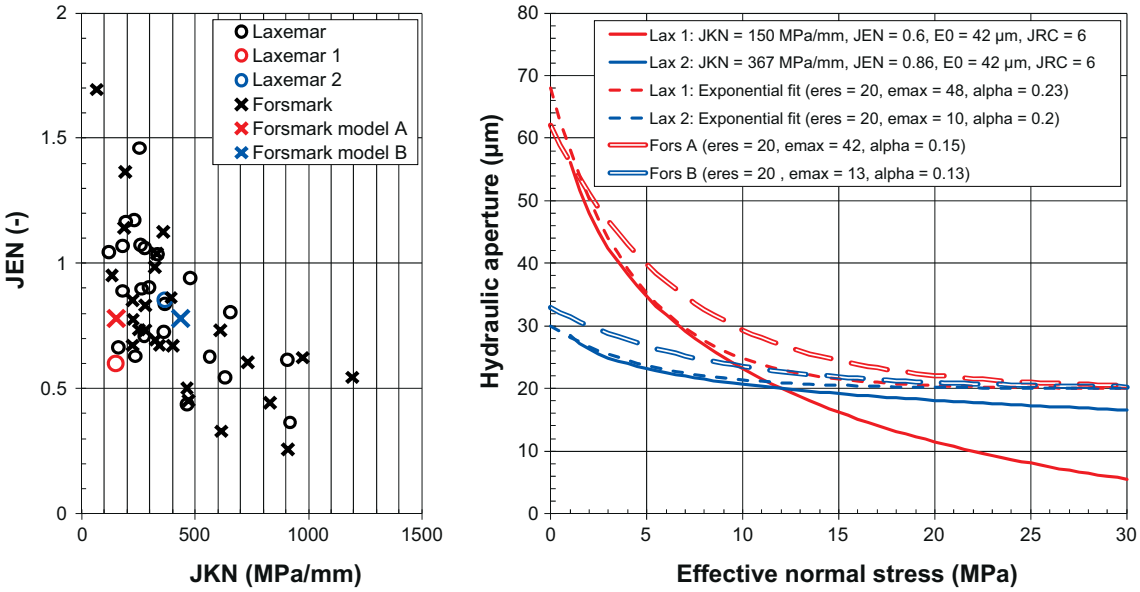

Figure I-6. *Left: CY-model parameters obtained from cyclic compression tests of samples from different boreholes at Laxemar (circles) and at Forsmark (marked with 'x'). Right: Hydraulic apertures estimated from the CY-model and Equation 3-4 for two sets of parameters from the left figure (see main text) together with exponential fits to the apertures. Fors A and B are the two proposed stress-transmissivity relations for Forsmark given in Figure 4-9. Both figures from /SKB 2010b/.*

I2.7 Glaciation

SKB's reference glacial cycle is based on a reconstruction of the Weichselian glaciation /e.g. SKB 2006a/, cf. Figure 2-2 (left). For the purpose of the modelling work, only the two major (*i.e.* the two latest) advance and retreat cycles are considered. Time zero denotes the time when the first mechanical effects of an approaching ice occur (cf. Figure 1-2). Therefore, the time-scale in figures showing the evolution of glacially induced stresses or ice sheet thickness in the following sections has no significance other than showing the time-frame of the two major advance and retreat cycles, *i.e.* it does not represent time after present (or deposition of the canisters). In this section, only data specific for the glacial phase are given. All other data used in the modelling of the glacial phase are the same as those in the previous sections.

Figure I-7 shows the temporal development of the glacially induced principal stresses obtained from ice-crust-mantle analyses performed by /Lund et al. 2009/ at 500 m depth at Laxemar during this glacial cycle. Similarly to the Forsmark site, there are only marginal variations in stress magnitudes with depth. For the purpose of the modelling work, the stress magnitudes given for 500 m depth are assumed to be valid at all depths in the upper 1 km of the rock.

Six points in time are selected for modelling work: The first glacial maximum (12 ka), edge passing (14 ka), stress reduction due to forebulge (42 ka), second glacial maximum (51 ka, vertical stress maximum), second glacial maximum (54.5 ka, horizontal stress maximum) and edge passing (55.5 ka), cf. Figure I-8. For the Laxemar site, the glacially induced excess pore pressure is assumed to be 98% of the glacially induced excess vertical stress at all times and at all depths, cf. Figure I-8. A more detailed pore pressure model (similar to that derived for Forsmark, cf. Appendix D) during periods of glacial retreat and in combination with proglacial permafrost is not considered.

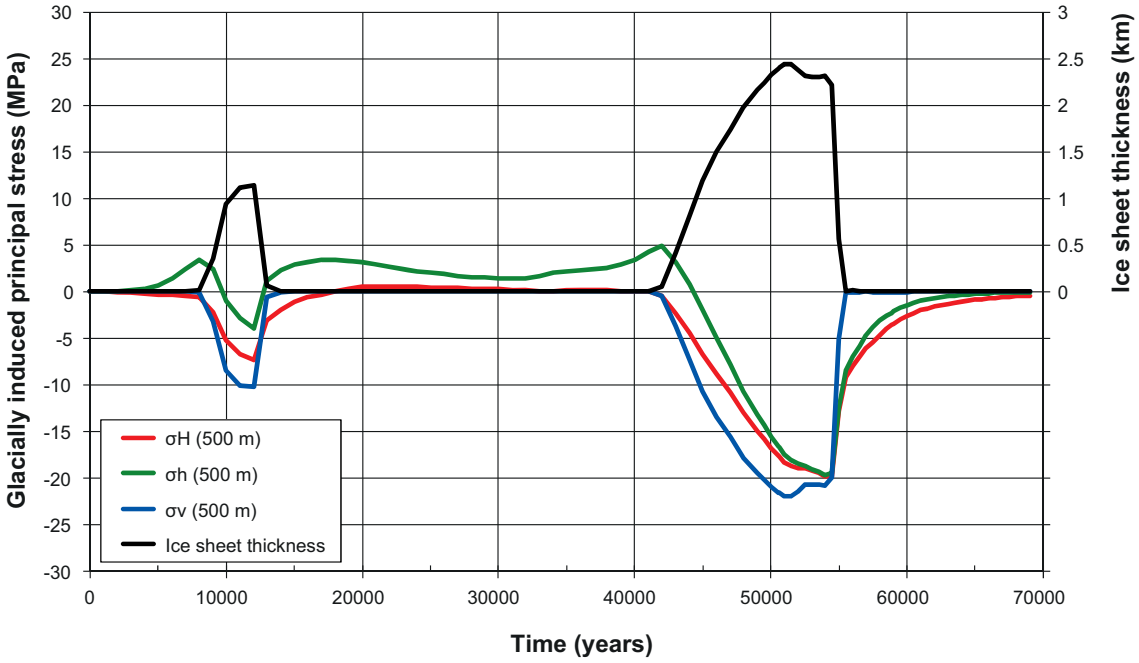

Figure I-7. *Temporal development of the glacially induced principal stresses (in excess of in situ conditions) at 500 m depth based on data from ice-crust-mantle analyses performed by /Lund et al. 2009/ and estimate of the ice sheet thickness during the reference glacial cycle at Laxemar.*

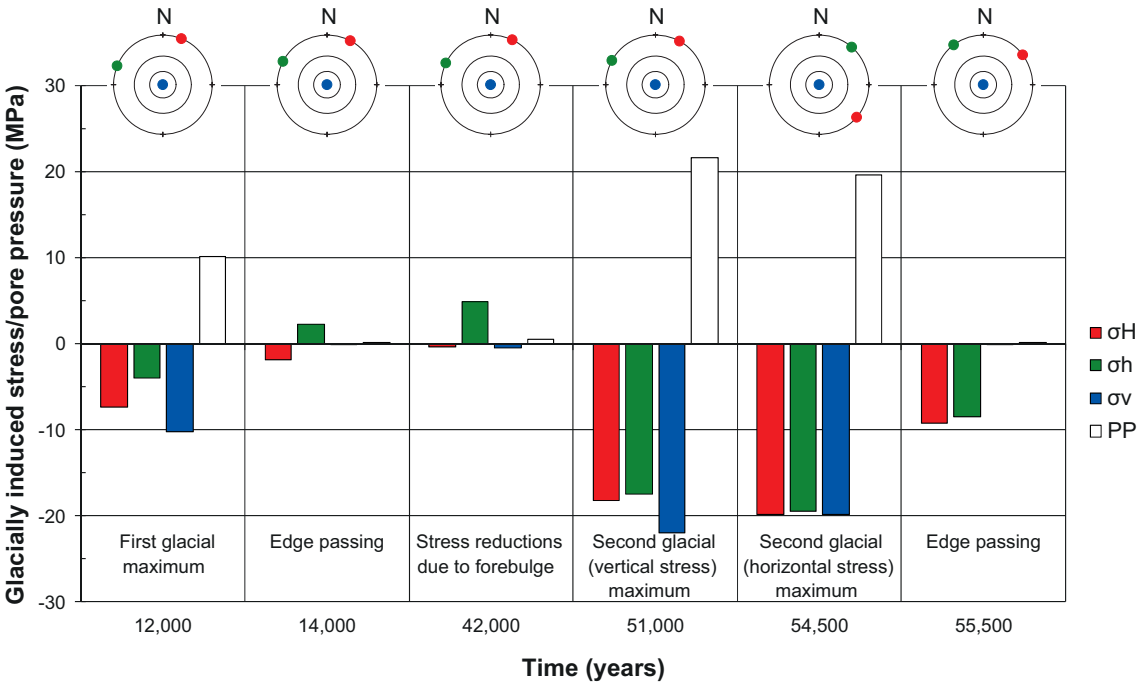

Figure I-8. *Glacially induced principal stress magnitudes, orientations of horizontal principal stress components and pore pressure assumptions (PP) used in the modelling work at all depths.*

I3 Large-scale thermal evolution

Layout D2 for the Laxemar site contains approximately 8,000 canister positions, cf. Figure I-9 (top), with canister spacings set in each rock domain (8.1 m in RSMD, 9 m in RSMA and 10.5 m in RSMM) in accordance with specifications in the Site Engineering Report (SER) for the Laxemar site /SKB 2010g/. The differences in spacing are a consequence of differences in rock thermal conductivities. Here, every 4th canister is removed uniformly across the repository region order to achieve the given loss of canister positions, *i.e.* the average power density. In all temperature calculations, as well as subsequent thermo-mechanical calculations for Laxemar in Sections I.4 and I.6, the tunnel floor is set at an elevation of –500 m in all areas of the repository. Point sources representing the heat generating canisters are positioned 5 m below the tunnel floor.

Figure I-9 shows the increase in rock temperature along two vertical scanlines at Laxemar – A (through a deposition area) and B (between two deposition areas). Here, the temperatures are calculated using mean value properties in rock domain RSMD, cf. Table I-4.

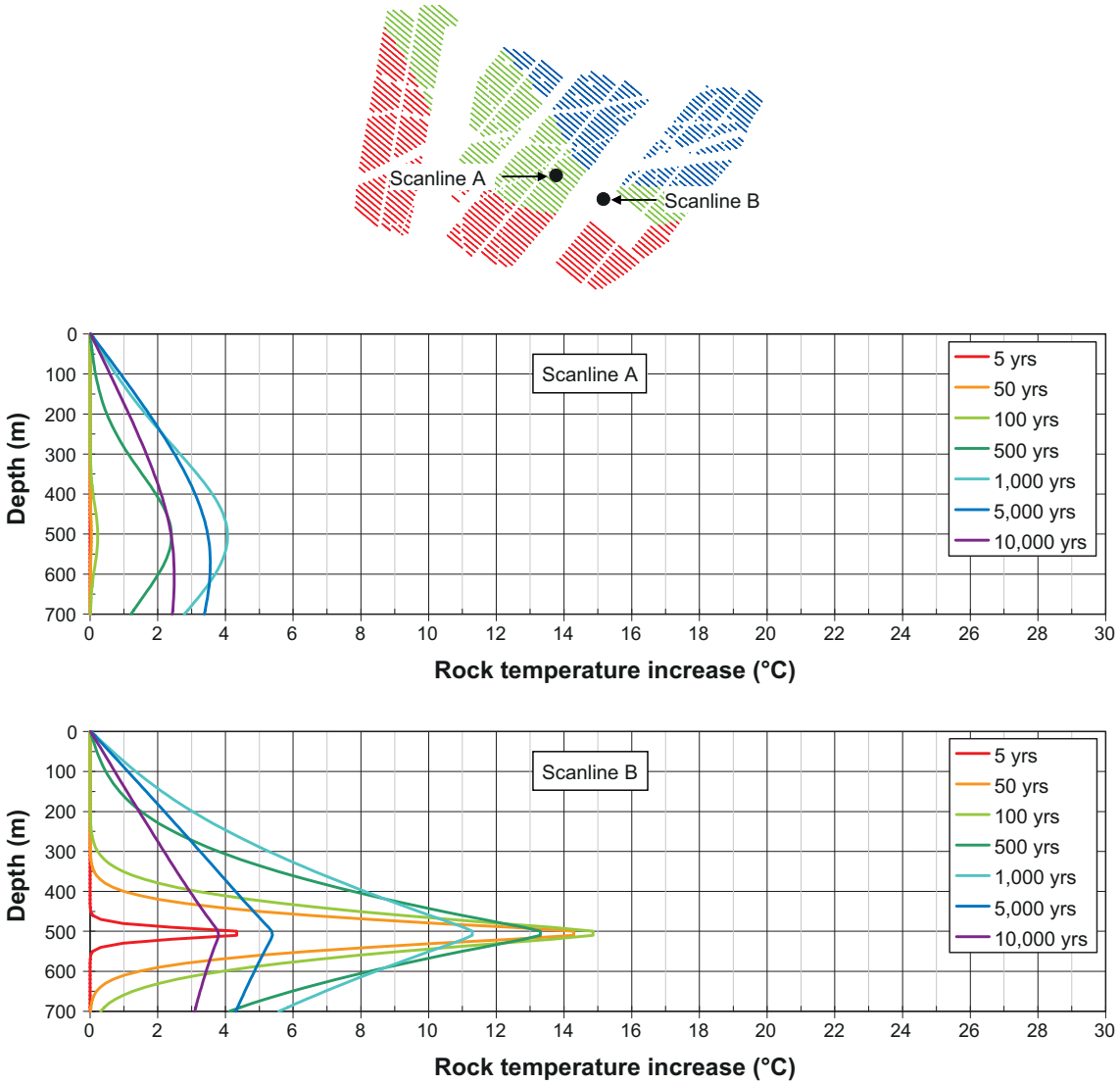

Figure I-9. *Increase in rock temperature as functions of depth along the vertical scanlines through the repository region marked in the uppermost figure. The colour scheme in the repository layout represents parts of the repository region with different canister spacing associated with each of the three rock domains (RSMx): Red colour represents 8.1 m canister spacing (RSMD), blue colour represents 9 m canister spacing (RSMA) and green colour represents 10.5 m canister spacing (RSMM).The repository is at 500 m depth.*

I4 Assessment of large-scale THM evolution: temperate phase

I4.1 Description of modelling approach

Objectives

The large-scale *3DEC* models are used to investigate/determine the following:

- Boundary conditions for near-field models.
- Stress evolution and associated transmissivity changes at different locations within the repository region.

Estimates of stress induced transmissivity changes

Similarly to the large-scale modelling work conducted for Forsmark in Chapter 6, the thermally induced stresses are obtained from the large-scale *3DEC* model and variations in relative transmissivity are estimated from the numerically obtained stress by use of the two stress-transmissivity models (A and B) presented in Figure 4-9 (see subsection 6.3.2 for details).

I4.2 Overview of 3DEC models

Layout D2 for the Laxemar site contains approximately 8,000 canister positions with an expected loss of 25%. As no information is given regarding the distribution of the loss of canister positions across the repository region, it is assumed to be uniform. In order to achieve the average thermal load on a large scale, every 4th canister is removed uniformly across the repository region. The locations of heat sources in the large-scale model are presented in Figure I-10 (left) together with the locations chosen for near-field modelling in Section I.6.

The modelled rock mass is represented by a linear elastic rectangular block with isotropic and homogeneous properties, cf. Section I.2.5. Its dimensions are 8 km×7.4 km×~3 km. An outline of the large-scale model is shown in Figure I-11. An average value of the deformation modulus based on /Hakami et al. 2008/ (E = 55 GPa), thermal and thermo-mechanical properties as in rock domain RSMD /Sundberg et al. 2008a/ are judged to be relevant in all modelled domains, cf. Section I.2.5 (Table I-4, Table I-6 and Table I-7). Where total stresses are required, the *in situ* stresses are added to the thermally induced stresses in a post processing step. The *in situ* stresses and initial temperature do not influence the calculations and are set to zero.

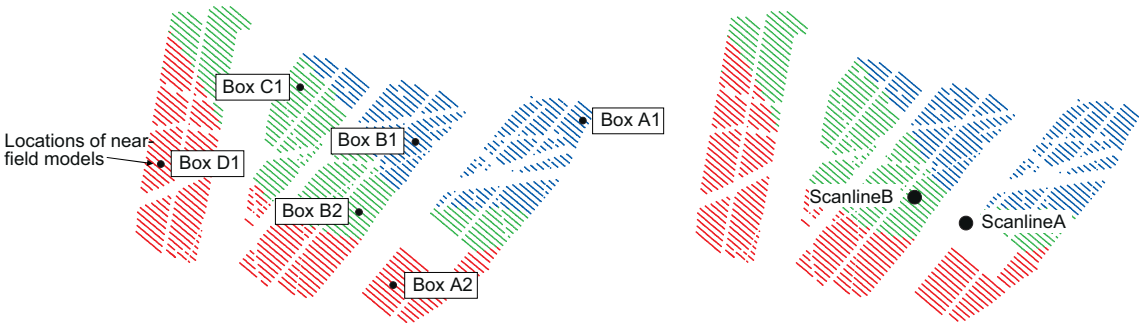

Figure I-10. *Laxemar Layout D2. Red colour represents parts of the repository region with 8.1 m canister spacing, blue colour represents parts of the repository region with 9 m canister spacing and green colour represents parts of the repository region with 10.5 m canister spacing. Left: Locations of near-field models, cf. Section I.6. Right: Locations of Scanlines A and B within the repository region.*

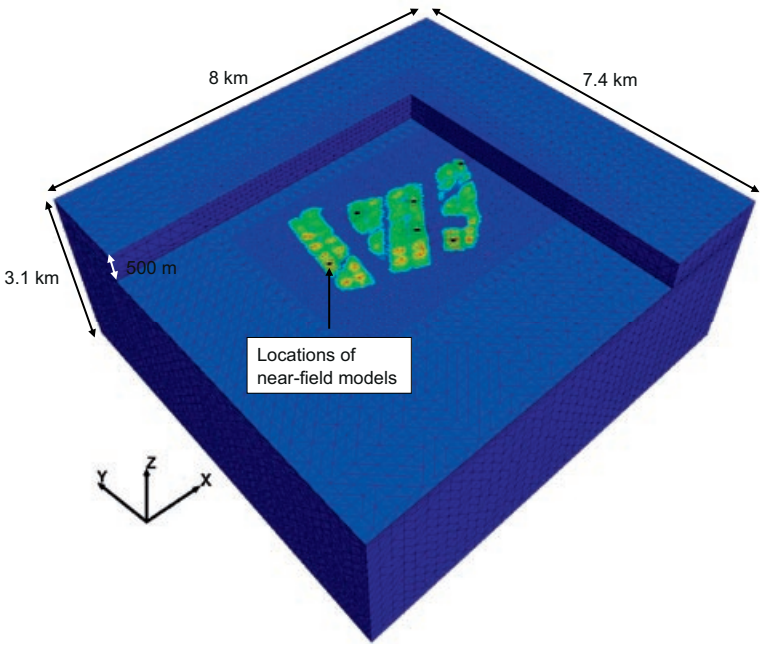

Figure I-11. *Outline of Laxemar large-scale 3DEC model. Note that parts of the model are hidden from view.*

I4.3 Boundary conditions for Laxemar near-field models

Similarly to the boundary conditions for the near-field models analysed for Forsmark, cf. Section 6.5, the boundary conditions for the Laxemar models are obtained from the displacements on pre-defined cut-planes representing the near-field model boundaries. Each near-field model consists of one tunnel segment with seven canisters. The model dimensions are 40 m (across tunnels) and 50 m (vertically) with the dimension in the along-tunnel-direction determined by the local canister spacing. The boundary conditions, which are evaluated as the relative expansion/contraction to the centre of the near-field model as functions of time, are presented in Figure I-12. Near-field analyses for the Laxemar site are conducted in Section I.6.

I4.4 Effects on fractures and fracture zones

Transmissivity changes

The transmissivity effects on large fractures are presented as functions of depth on planes perpendicular to the present-day major horizontal *in situ* stress (σ_H), minor horizontal *in situ* stress (σ_h) and the vertical *in situ* stress (σ_v) at the positions labelled A and B presented in Figure I-10 (right). Scanline A intersects the repository region between two deposition areas whereas Scanline B passes through the central parts of a deposition area.

Examples of transmissivity changes during the thermal phase along the two scanlines are presented in Figure I-13, Figure I-14, Figure I-15, Figure I-16, Figure I-17 and Figure I-18.

Along Scanline A, the following can be observed.

- **Vertical fractures striking perpendicular to the major horizontal *in situ* stress (σ_H, i.e. striking 45° with respect to North), cf. Figure I-13:** Close to the ground surface, the reductions in effective normal stress result in an increase in relative transmissivity by a factor around 1.3 (model A). At larger depths, there are only marginal variations in relative transmissivity. For model B, there are only negligible variations in relative transmissivity at all depths.
- **Vertical fractures striking perpendicular to the minor horizontal *in situ* stress (σ_h, i.e. striking 135° with respect to North), cf. Figure I-14:** The reductions in effective normal stress in the upper 200 m of rock result in an increase in relative transmissivity by up to around a factor 1.5 (model A). At larger depths, the relative transmissivity is reduced to (at minimum) a factor 0.7 (model A). For model B, there is an increase in relative transmissivity by a factor about 1.2 near the ground surface. Elsewhere the variations in relative transmissivity are negligible.
- **Horizontal fractures, cf. Figure I-15:** At shallow depths (<150 m), there are only negligible variations in relative transmissivity. At larger depths (with a maximum around repository depth), the reduction in effective normal stress results in an increase in relative transmissivity by a factor less than 1.5 (model A) and 1.2 (model B), respectively.

Along Scanline B, the following can be observed.

- **Vertical fractures striking perpendicular to the major horizontal *in situ* stress (σ_H, i.e. striking 45° with respect to North), cf. Figure I-16:** The reductions in effective normal stress in the upper 200 m of rock result in an increase in relative transmissivity by a factor of about 1.8 (model A). At larger depths, the effective stress is increased resulting in a reduction in relative transmissivity to (at minimum) a factor 0.8 (model A). For model B, there is an increase in relative transmissivity by a factor about 1.2 near the ground surface. Elsewhere the variations in relative transmissivity are negligible.
- **Vertical fractures striking perpendicular to the minor horizontal *in situ* stress (σ_h, i.e. striking 135° with respect to North), cf. Figure I-17:** In the upper 200 m of rock the effective normal stress decreases, resulting in an increase in relative transmissivity by up to a factor 2 (model A) and 1.4 (model B), respectively. At larger depths, the effective normal stress increases, with a maximum at repository depth. Here, the relative transmissivity is reduced to 0.4 (model A) and 0.7 (model B), respectively.
- **Horizontal fractures, cf. Figure I-18:** The increase in effective vertical stress results in only marginal reductions in relative transmissivity for both stress-transmissivity models.

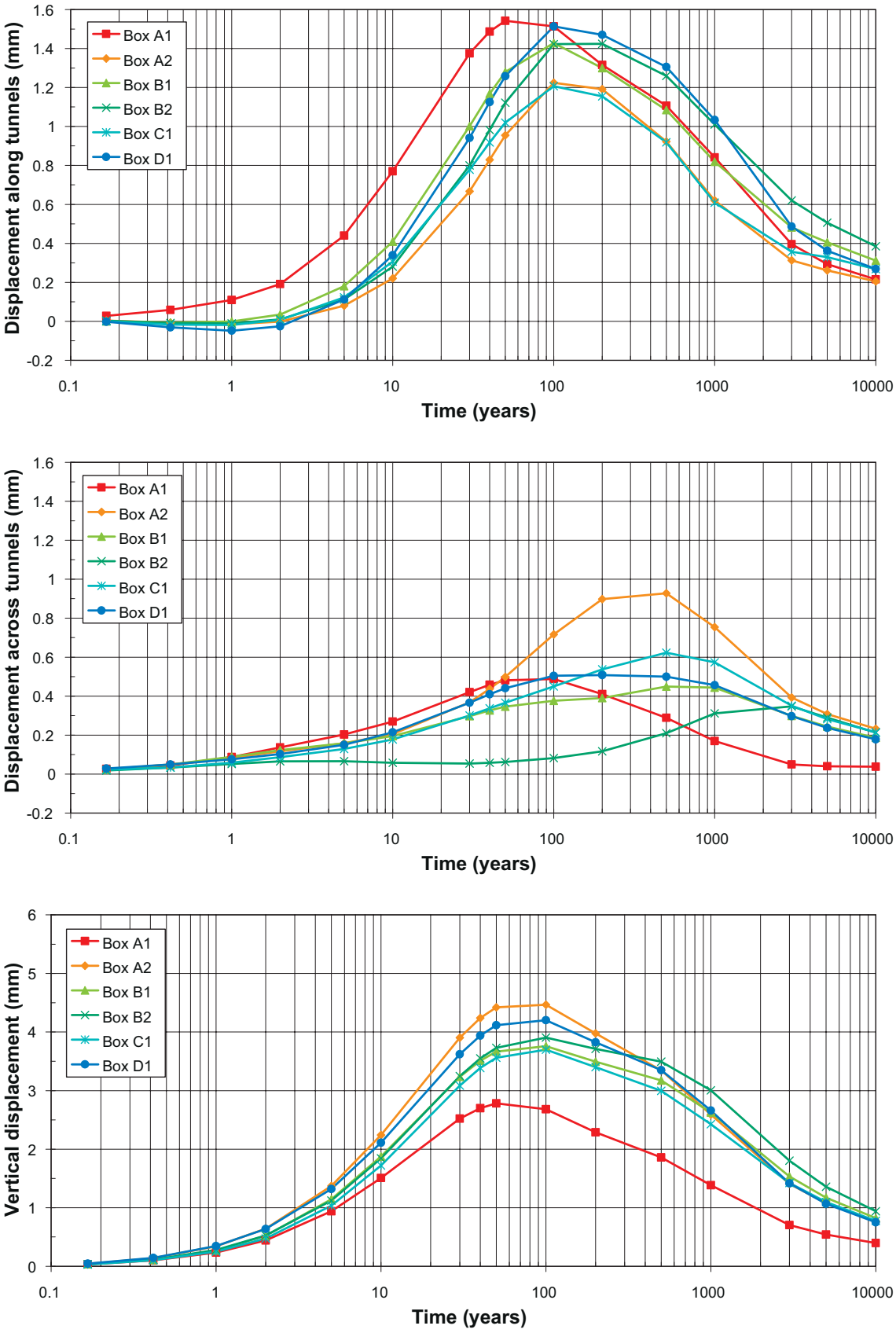

Figure I-12. *Boundary conditions for near-field models at Laxemar. Top: Horizontal displacement in the direction along tunnels. Middle: Horizontal displacement in the direction across tunnels. Lower: Vertical displacement.*

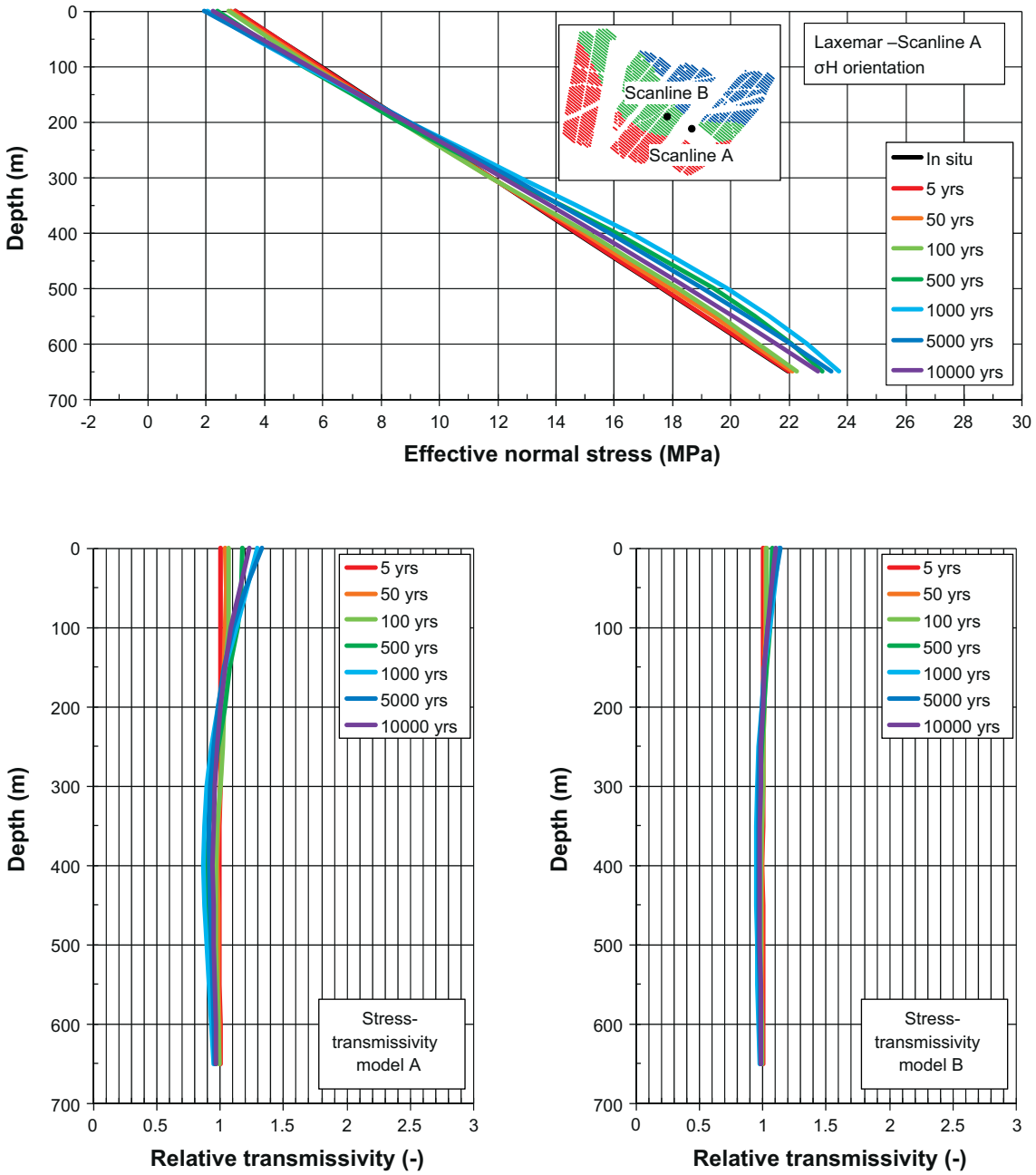

Figure I-13. *Top: Effective stress as a function of depth along Scanline A in the direction of the present-day σH. Bottom: Relative transmissivity of vertical fractures striking perpendicular to the present-day σH.*

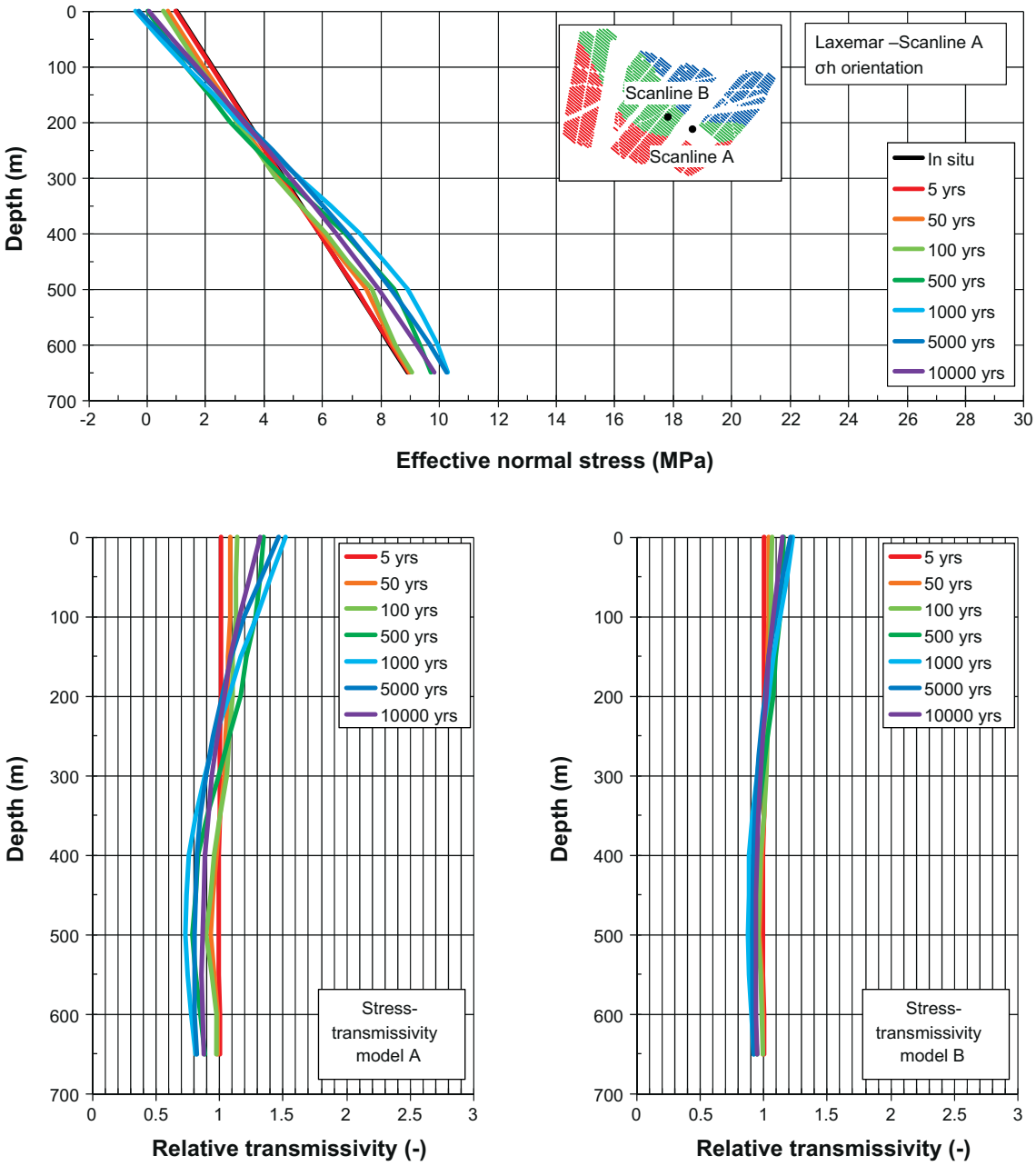

Figure I-14. Top: Effective stress as a function of depth along Scanline A in the direction of the present-day σh. Bottom: Relative transmissivity of vertical fractures striking perpendicular to the present-day σh.

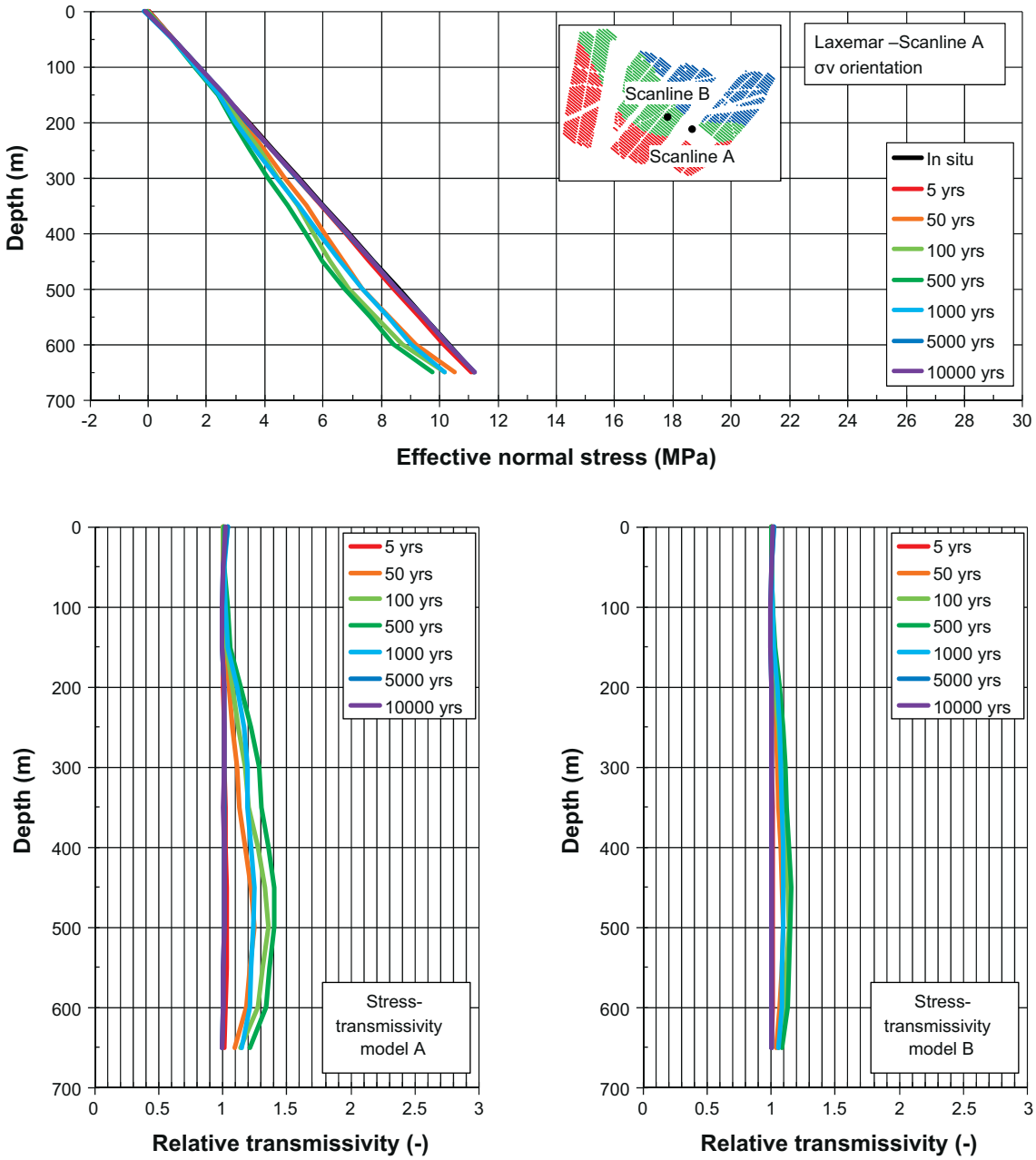

Figure I-15. *Top: Effective stress as a function of depth along Scanline A in the direction of σv. Bottom: Relative transmissivity of horizontal fractures perpendicular to σv.*

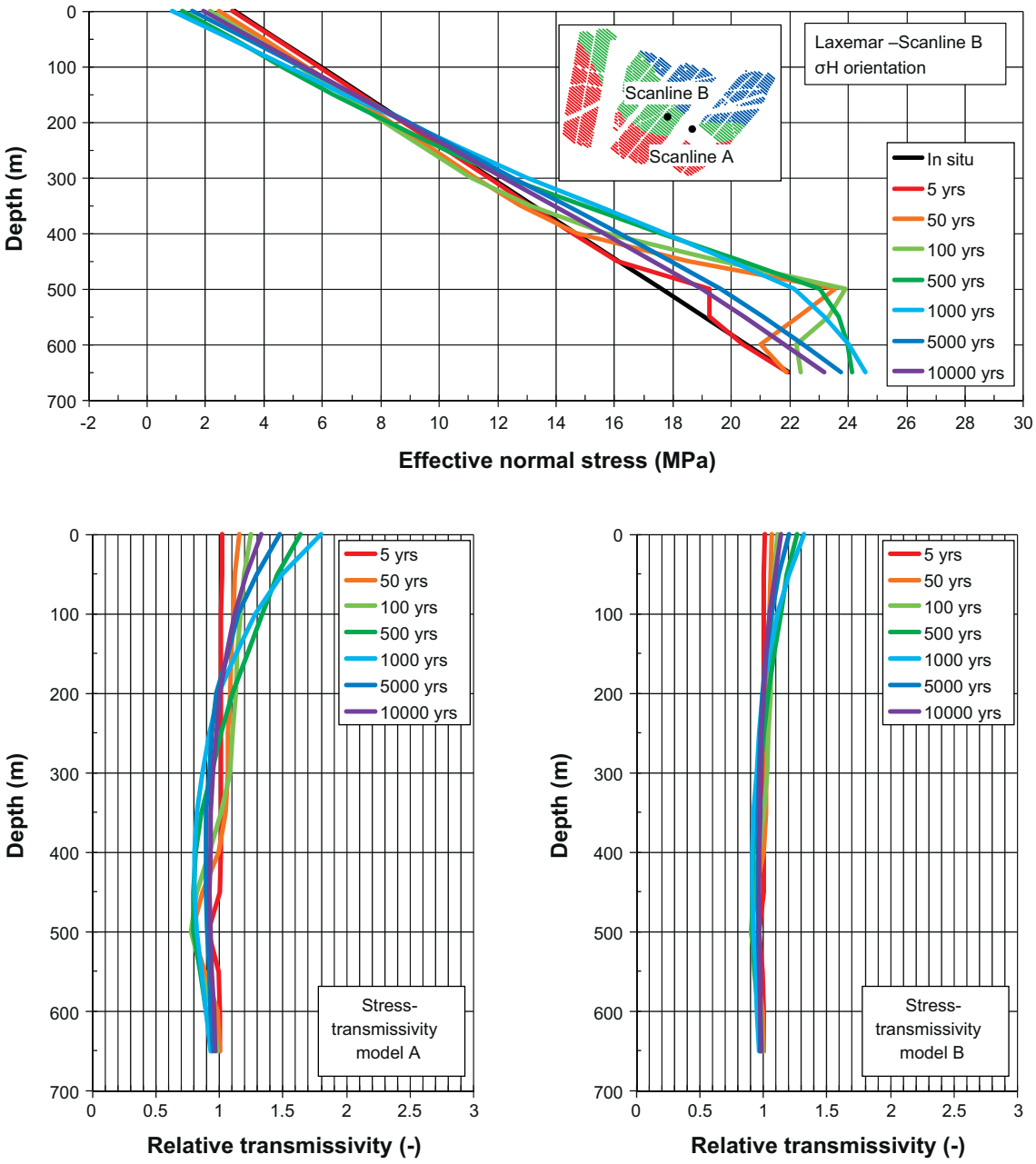

Figure I-16. Top: Effective stress as a function of depth along Scanline B in the direction of the present-day σH. Bottom: Relative transmissivity of vertical fractures striking perpendicular to the present-day σH.

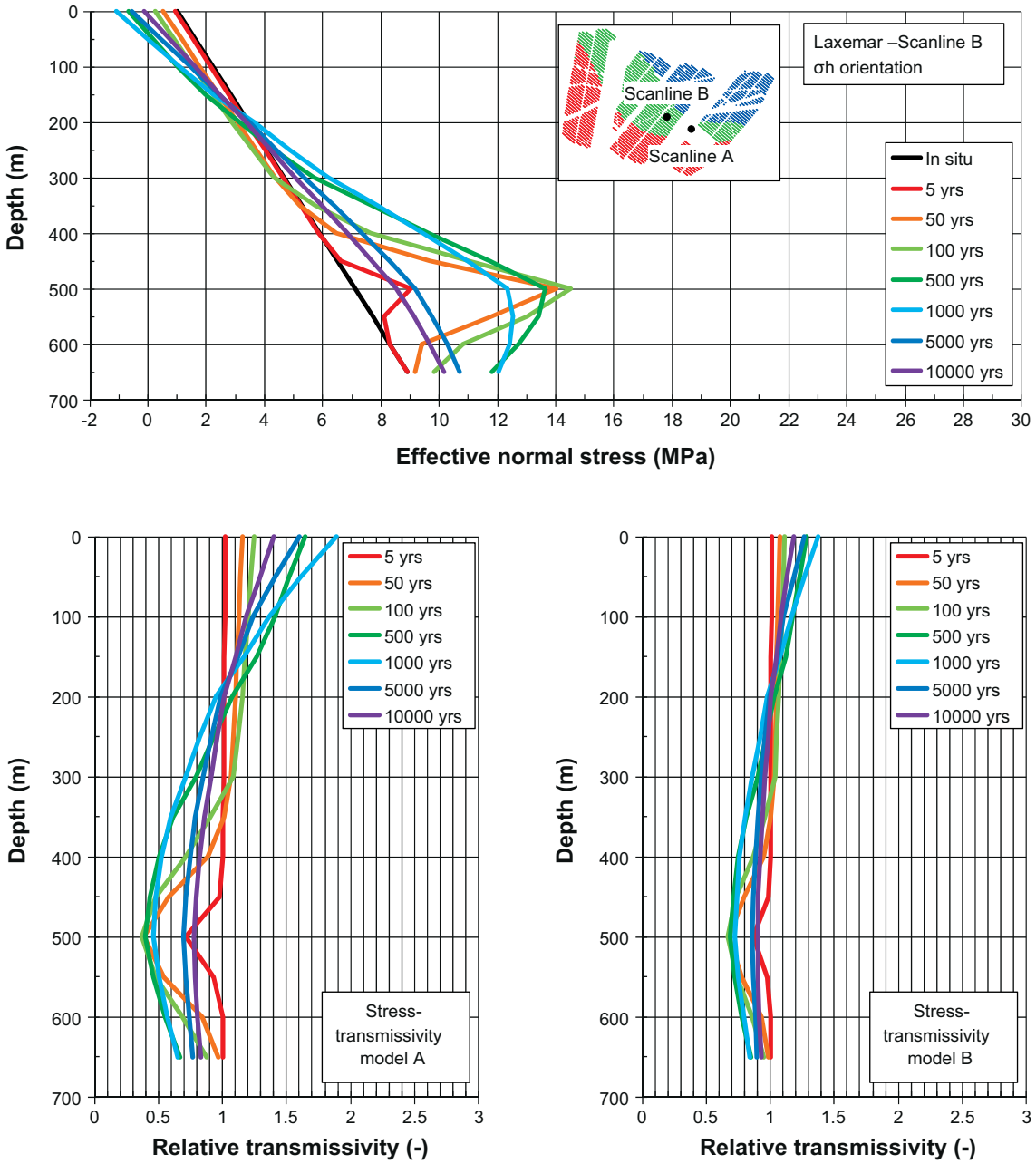

Figure I-17. *Top: Effective stress as a function of depth along Scanline B in the direction of the present-day σh. Bottom: Relative transmissivity of vertical fractures striking perpendicular to the present-day σh.*

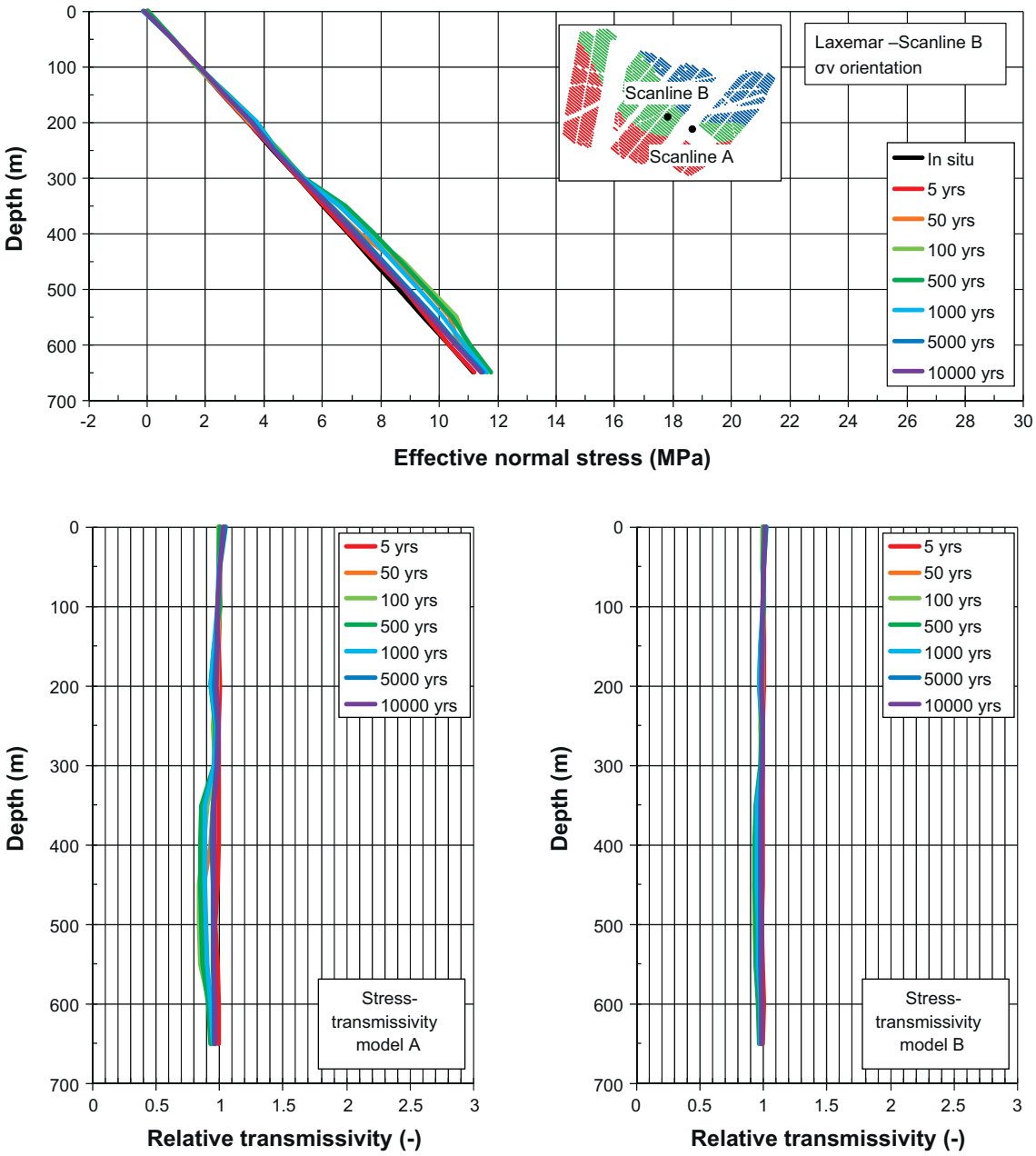

Figure I-18. *Top: Effective stress as a function of depth along Scanline B in the direction of σv. Bottom: Relative transmissivity of horizontal fractures.*

I4.5 Summary

Stresses

Depending on position in relation to the heated deposition areas, the following general observations regarding the thermally induced stresses can be made.

- The horizontal stresses increase below a depth of 150–200 m (thermally induced increased compression).
- The vertical stress increases along scanlines passing through the heated deposition areas (thermally induced increased compression).
- At shallow depths, there is a reduction in the horizontal stresses (thermally induced reduced compression). The most significant stress reductions are found directly above the heated deposition areas.
- Outside and between deposition areas, particularly around repository depth, there is a reduction in vertical stress (thermally induced reduced compression).

Transmissivity changes

The following observations can be made regarding the impact of the effective normal stress on relative transmissivity.

- **Vertical fractures striking perpendicular to *in situ* σ_H, i.e. striking 45° with respect to North:**
  - Insignificant transmissivity changes at all depth below 200 m, regardless of stress-transmissivity model.
  - Transmissivity increase, at shallow depths, by at most a factor 1.8 for fractures intersecting the heated deposition areas. For fractures between or outside the deposition areas the effects are smaller.
- **Vertical fractures striking perpendicular to *in situ* σ_h, i.e. striking 135° with respect to North:**
  - Unchanged or reduced transmissivities at all depths below 200 m.
  - Transmissivity increase, at shallow depths, by a factor 2 for fractures intersecting the heated deposition areas. For fractures between or outside the deposition areas the effects are smaller.
- **Horizontal fractures:**
  - Transmissivity increase by at most at most a factor 1.5 for parts of fracture that pass through non-heated regions of the repository horizon.

I5 Assessment of large-scale THM-evolution: glacial phase

I5.1 Description of modelling approach

Objectives

The objectives are as follows.

- Estimate effective stresses and accompanying transmissivity impacts at different depths during the glacial cycle.
- Estimate the potential for shearing at different depths and magnitude of the shear displacement of optimally oriented fractures.

Estimates of stress induced transmissivity changes

Similarly to the large-scale modelling of the temperate phase and corresponding analyses for Forsmark site in Chapters 6 and 7, fractures are not modelled explicitly. Instead, stress-induced transmissivity changes are evaluated on hypothetical fracture planes with orientations perpendicular to the present-day *in situ* stress components, *i.e.* vertical or horizontal planes. The two stress-transmissivity models proposed for the Forsmark site (Figure 4-9) are selected to estimate changes in relative transmissivity due to normal stress variations.

Hydraulic shearing

Similarly to the analyses for the Forsmark site, slip estimates are here assessed on optimally oriented fractures by use of the analytical solution, described in subsection 6.3.3, for the shear displacement at the centre of a circular fracture, cf. Equation 6-1. It should be reiterated that this expression gives only an approximation as in reality there is a variation in stress along the fracture.

I5.2 Glacial stresses

Figure I-19 (left) shows the temporal evolution of the glacially induced stresses at 500 m depth at Laxemar in the orientations of the present-day *in situ* stresses. As, similarly to the Forsmark site, there are only marginal variations in the glacially induced stresses in the upper 1.5 km of the rock, the glacial stresses obtained at 500 m are used at all depths and added to the *in situ* stresses, cf. Figure I-19 (right).

Six points in time during the glacial cycle, cf. Figure I-19 (left), are selected for further investigation. These correspond to present-day conditions (*in situ*), the first glacial maximum (12 ka), the ice margin passing over the site (14 ka), stress reductions due to the forebulge (42 ka), the second glacial maximum: vertical stress maximum (51 ka) and horizontal stress maximum (54.5 ka) and the ice margin passing over the site (55.5 ka).

In the modelling work for Laxemar, it is assumed that the excess pore pressure is 98% of the mechanical load at all times, *i.e.* the excess pore pressure is approximately zero when the ice margin is passing over the site and during permafrost conditions as the ice is advancing.

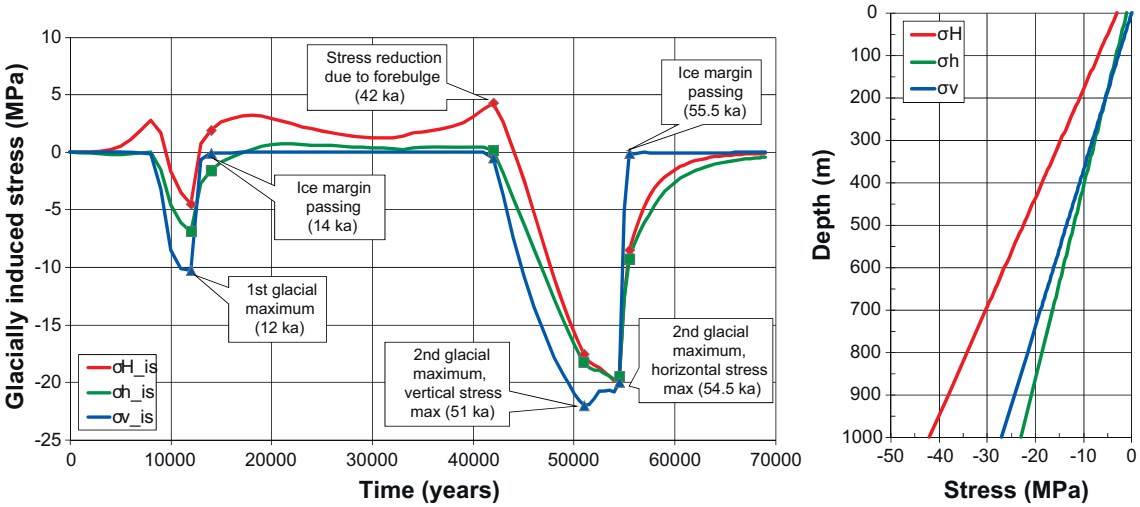

Figure I-19. *Left: Glacially induced stress components in the orientations of the present-day in situ stresses (cf. Figure I-7 and Figure I-8). Plot symbols mark the points in time used in the modelling work. Right: Present-day in situ stresses (Table I-1) as functions of depth.*

I5.3 Effects on fracture transmissivities

The effective normal stress and accompanying transmissivity effects on large fractures are calculated as functions of depth on vertical planes perpendicular to the present-day major horizontal (σ_H) and minor horizontal (σ_h) *in situ* stresses and on horizontal planes at the selected points in time shown in Figure I-19 (left).

Examples of normal stress and transmissivity changes during the glacial phase of vertical fractures striking perpendicular to the present-day major and minor horizontal *in situ* principal stresses as functions of depth are shown in Figure I-20 and Figure I-21, respectively. Corresponding results for horizontal fractures are presented in Figure I-22.

Assuming that the excess pore pressure is 98% of the mechanical load at all times (*i.e.* approximately zero as ice margin is passing over the site and during both advance and retreat phases, here at 14, 42 and 55.5 ka), the following can be observed.

- **Vertical fractures striking perpendicular to the major horizontal *in situ* stress (σ_H, i.e. striking 45° with respect to North), cf. Figure I-20:** The effective normal stress is reduced compared with *in situ* stress levels during the first glacial maximum (12 ka), the ice margin passing over the site (14 ka), the forebulge (42 ka) and the second glacial maximum (51 ka, vertical stress maximum). At the point in time with the largest reduction in effective normal stress (12 ka), the maximum increase in relative transmissivity is a factor around 5 (model A) at shallow depths – at repository depth (500 m) the corresponding increase in relative transmissivity is a factor 1.6. During the remaining points in time (54.5 and 55.5 ka), the effective normal stress is increased compared with *in situ* conditions resulting in reduced relative transmissivity.
- **Vertical fractures striking perpendicular to the minor horizontal *in situ* stress (σ_h, i.e. striking 135° with respect to North), cf. Figure I-21:** The effective normal stress is reduced during the first glacial maximum (12 ka), the forebulge (42 ka) and during the second glacial maximum (51 ka, vertical stress maximum). During the remaining points in time (14, 54.5 and 55.5 ka), the effective normal stress is either increased or unaffected compared with *in situ* conditions. The largest reductions effective normal stress occur during the first glacial maximum (12 ka) and the second glacial maximum (51 ka, vertical stress maximum). These reductions result in an increase in relative transmissivity (model A) by a factor close to 3 at shallow depths and a factor 2 at repository depth (500 m). During the remaining points in time, there are either negligible variations or reductions in relative transmissivity.
- **Horizontal fractures, cf. Figure I-22:** The effective vertical stress is unaffected or marginally increased at all times and at all depths, resulting in only negligible variations in the relative transmissivity.

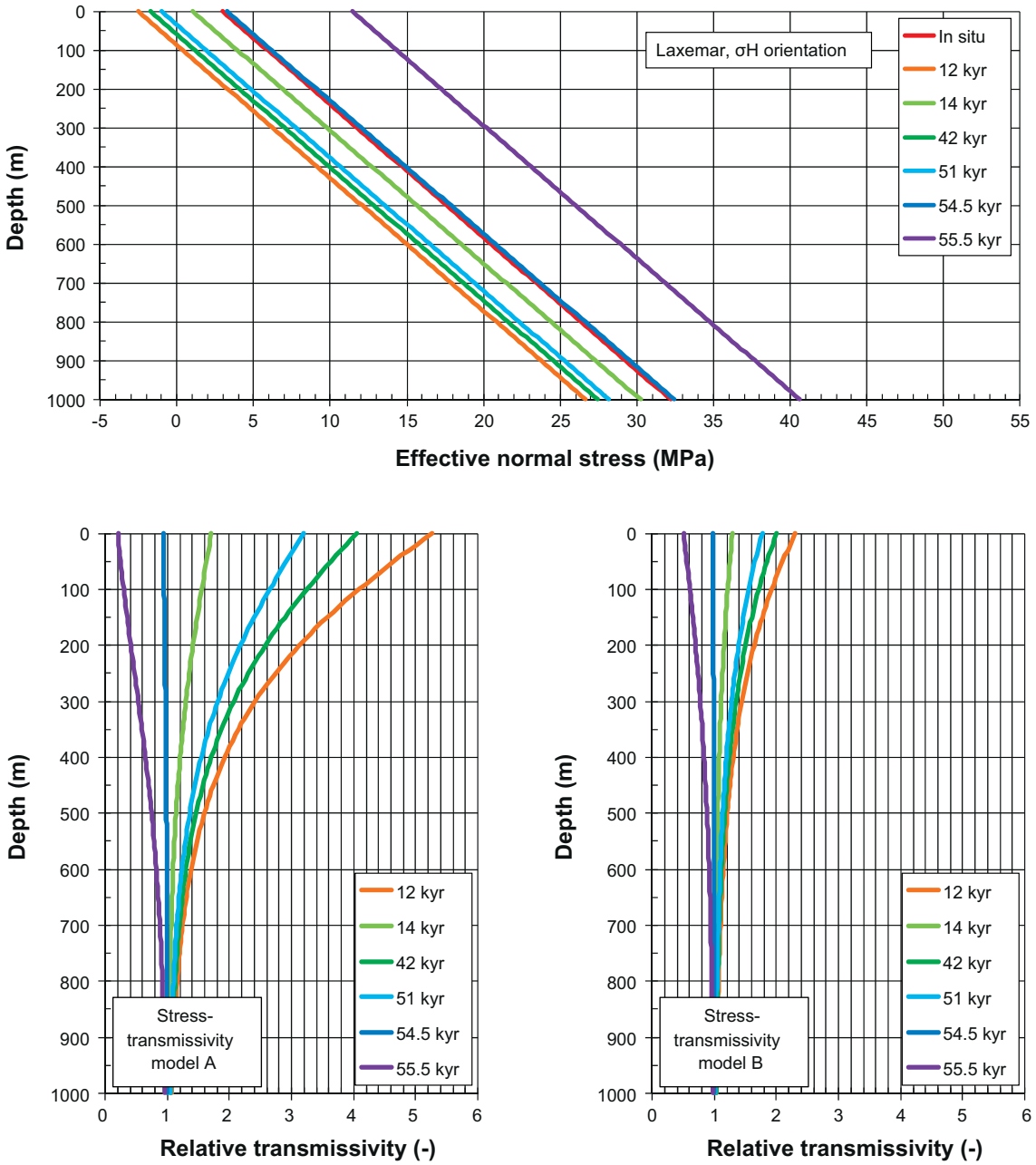

Figure I-20. *Top: Effective stress as a function of depth in the direction of the present-day σH. Bottom: Relative transmissivity of vertical fractures striking perpendicular to the present-day σH.*

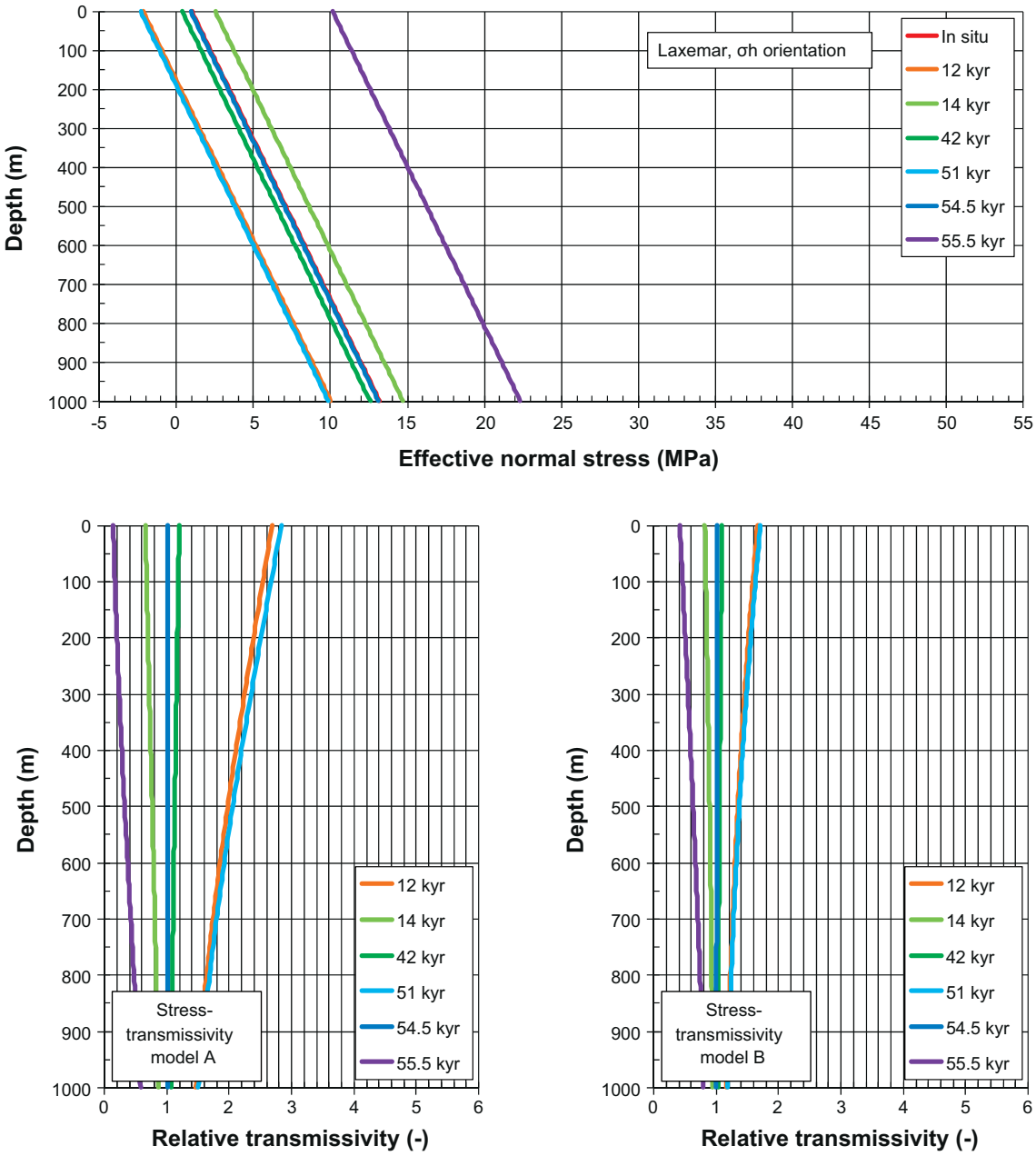

Figure I-21. Top: Effective stress as a function of depth in the direction of the present-day σh. Bottom: Relative transmissivity of vertical fractures striking perpendicular to the present-day σh.

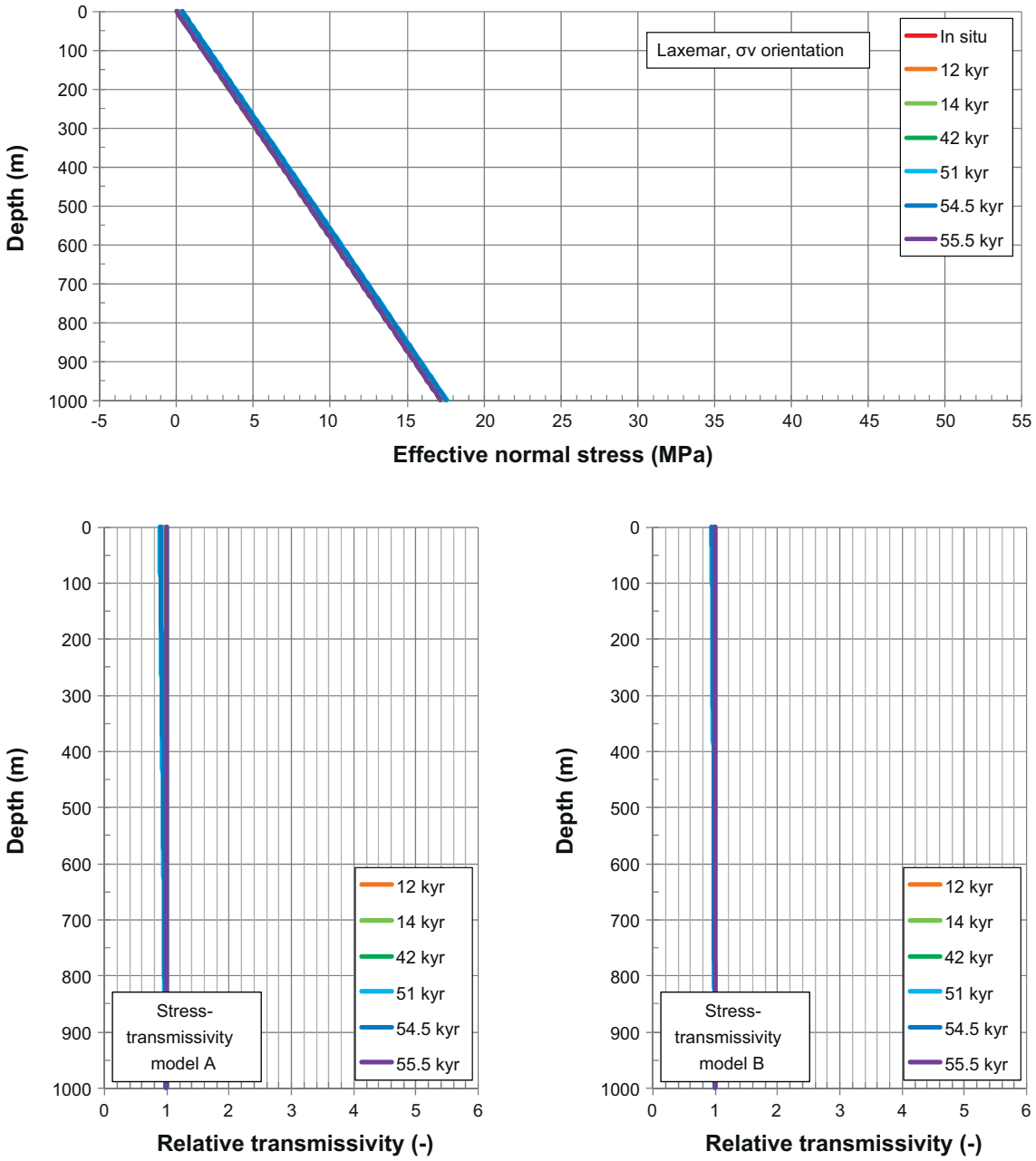

Figure I-22. *Top: Effective stress as a function of depth in the direction of σv. Bottom: Relative transmissivity of horizontal fractures.*

I5.4 Shearing under hydro-mechanical load

Estimates of the maximum shear displacement are made on vertical fractures striking 27.1° with respect to the major horizontal *in situ* stress, cf. Section I.2.4. This is the fracture orientation with the largest possible instability, given the Mohr-Coulomb fracture strength and the stress state, cf. Table I-3 and Table I-2. The elastic properties of the rock mass are given in Table I-6.

Figure I-23 shows the temporal evolution of the total principal stresses and the orientation of the major principal stress at repository depth (500 m) during the glacial phase at Laxemar for two assumptions regarding the *in situ* stress, cf. Table I-2:

- The *in situ* stresses are obtained from the Site Descriptive Model /Hakami et al. 2008/.
- The major horizontal *in situ* stress is assumed to be that at Äspö /Andersson 2007/ whereas the minor horizontal and vertical *in situ* stresses are obtained from the Site Descriptive Model /Hakami et al. 2008/.

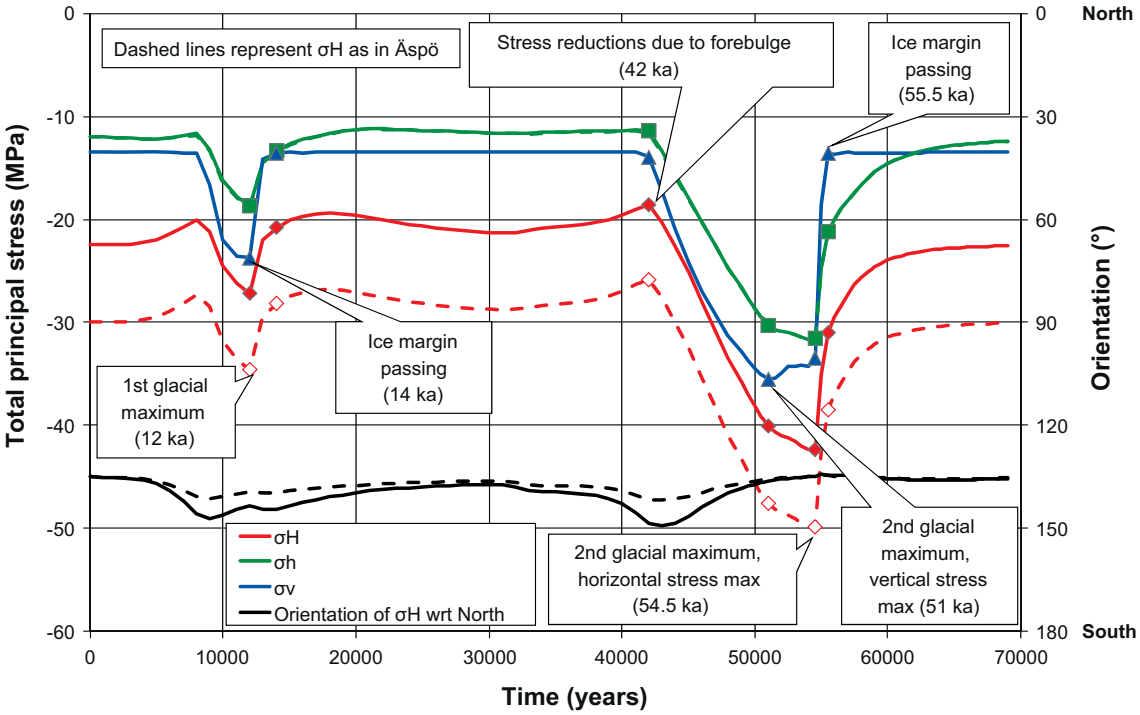

Figure I-23. *Total principal stresses at repository depth during the glacial phase at Laxemar compared with the orientation with respect to North of the major horizontal stress. Glacially induced stresses at 500 m depth from /Lund et al. 2009/. The in situ stresses at repository depth (500 m) are obtained from the Site Descriptive Model (dashed lines represent the major horizontal stress component as in Äspö), cf. Table I-2.*

During the glacial cycle, the orientation of the major horizontal principal stress is in the range 134–149° with respect to North. For the Äspö stress, the corresponding range in orientations is 135–142° with respect to North.

The corresponding Mohr circle representation of the stress state at repository depth is presented in Figure I-24. Note that, for the assumptions regarding the excess pore pressure made here, i.e. 98% of the mechanical load at all times and at all depths, and given the stress model for Laxemar /Hakami et al. 2008/, all fracture orientations at repository depth are stable during the glacial cycle. For the Äspö stress (marked with dashed lines in the figure), steeply dipping fractures are unstable during the first glacial maximum (12 ka) and during vertical stress maximum at the second glacial maximum (51 ka).

Figure I-25 shows estimates of slip at the centre of a vertical fracture striking 27.1° with respect to σ_H (note that the orientation of σ_H varies with time, cf. Figure I-23) as functions of the fracture radius during the first glacial maximum and second glacial maximum at maximum vertical stress. Depending on the value of the deformation modulus in the different fracture domains (50–59 GPa, cf. Table I-6), the maximum slip for a fracture with a radius of 100 m is in the range 3.3–6.4 mm.

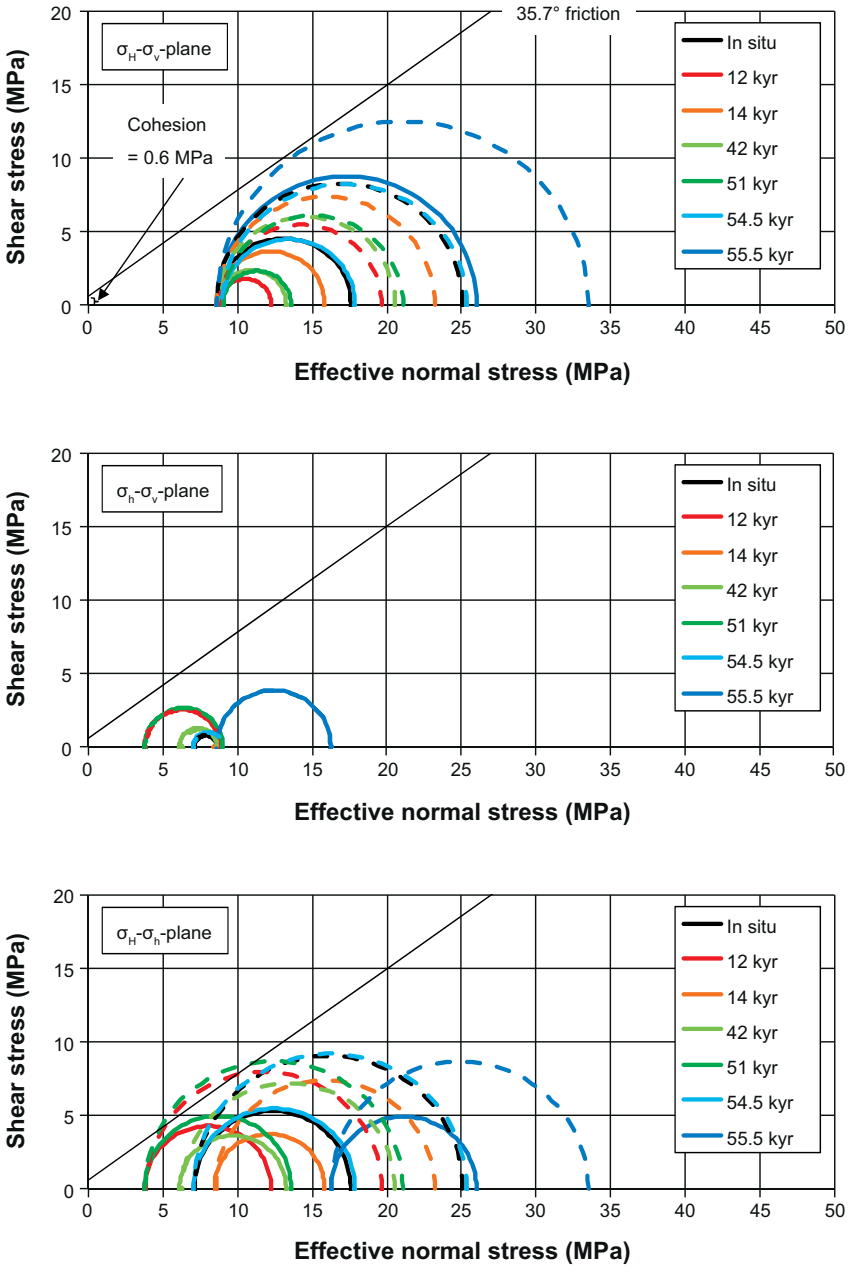

Figure I-24. *Mohr circle representations of stresses at repository depth at Laxemar (stress state with the major horizontal stress as in Äspö is marked with dashed lines) at present day conditions (in situ), first glacial maximum (12 kyr), ice margin passing (14 kyr), stress reductions due to forebulge (42 kyr), second glacial maximum, vertical stress maximum (51 kyr), second glacial maximum horizontal stress maximum (54.5 kyr) and edge passing at the end of the glacial cycle (55.5 kyr).*

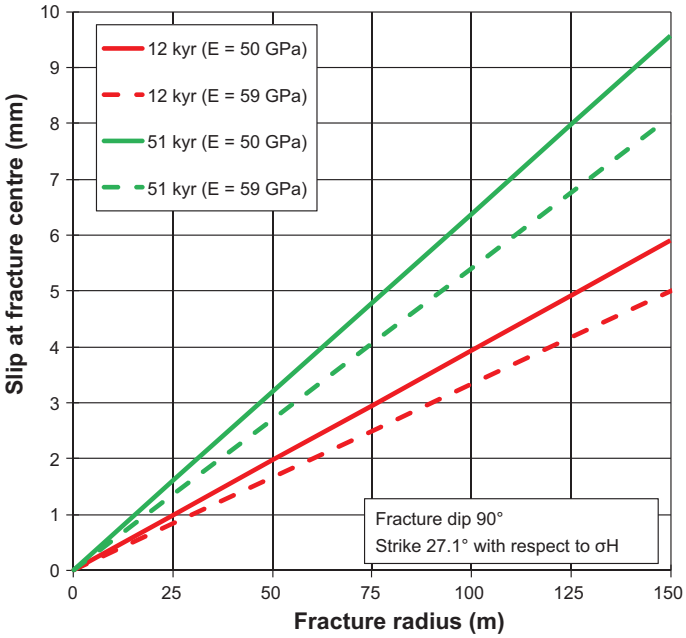

Figure I-25. *Estimate of the maximum slip at the centre of a fracture during the first glacial maximum (12 ka) and second glacial maximum at maximum vertical stress (51 ka) at repository level. The in situ stress model is given by the Site Descriptive Model with the major horizontal stress component as in Äspö, cf. Table I-2. The two values of Young's modulus (E) relate to variations between the rock domains at Laxemar, cf. Table I-6.*

I5.5 Summary

Fracture stability

The following can be concluded regarding the potential for fracture instability at the site.

- The magnitude of the major horizontal *in situ* stress is crucial. All fracture orientations at repository depth are stable during the glacial cycle if the stress magnitude reported by /Hakami et al. 2008/ can be assumed to be relevant.
- If the maximum horizontal stress is as reported for Äspö, the largest shear displacements occur in connection with the second glacial maximum (time of maximum vertical stress). An optimally oriented fracture with a radius of 100 m might slip at maximum around 6.5 mm, cf. Figure I-25.
- A more detailed pore pressure model (similar to that derived for Forsmark) during periods of glacial retreat and in combination with proglacial permafrost would result in more fracture orientations becoming unstable at these points in time.

Transmissivity changes

Normal stress variations

As seen in the analyses conducted for the Forsmark site in Section 7.4, the results are sensitive to assumptions regarding the magnitude of glacially induced pore pressures. For the Laxemar site, the effective normal stress impact on relative transmissivity (model A) during the glacial phase is provided below for the assumption that the excess pore pressure is 98% of the mechanical load at all times and at all depths (i.e. approximately zero as the ice margin passes over the site at 15 and 58 kyr).

- **Vertical fractures striking perpendicular to *in situ* σ_H, i.e. striking 45° with respect to North:** Transmissivity increase, at shallow depths, by a factor around 5. At repository depth the maximum increase is a factor 1.6.
- **Vertical fractures striking perpendicular to *in situ* σ_h, i.e. striking 135° with respect to North:** Transmissivity increase, at shallow depths, by a factor around 3. At repository depth the maximum increase is a factor 2.
- **Horizontal fractures:** Insignificant transmissivity changes at all times and at all depths.

Shearing

The following can be concluded regarding transmissivity effects due to shearing at the site.

- For the stress state as in the site report /Hakami et al. 2008/, all fractures are stable at repository depth during the entire glacial cycle when residual and permafrost induced excess pore pressures are not considered.
- If the maximum horizontal stress is as reported for Äspö, optimally oriented steeply fractures may slip during both glacial maxima. At these points in time, there would not be any additional residual pore pressures, which mean that the effective normal stress is about 6–7 MPa (cf. Figure I-24), i.e. above the highest normal stresses applied in the lab-scale transmissivity tests performed by /Olsson 1998/. Furthermore, the normalised slip magnitudes are less than 6.5 mm per 100 m fracture radius, cf. Figure I-25. Therefore the additional increase in transmissivity caused by shearing is likely to be modest.

I6 Assessment of spalling potential in the near-field

I6.1 General

The potential for spalling at the Laxemar site is assessed here only for deposition holes during the two first repository phases considered here, cf. Section 1.2:

- the construction and operational phase (mechanical impact), i.e. excavation of tunnels and deposition holes,
- the temperate phase (thermo-mechanical impact).

I6.2 Description of 3DEC models

Repository layout and model overview

The layout at Laxemar site (Layout D2) is presented in Figure I-26. The canisters are positioned 8.1 m (RSMD), 9 m (RSMA) and 10.5 m (RSMM) apart in parallel tunnels with a spacing of 40 m. As opposed to the Forsmark site (cf. Section 4.3), all tunnels at the Laxemar site have the same orientation – about 130° with respect to North. This corresponds to a deviation of the major horizontal *in situ* stress from the tunnel axis by about 5°.

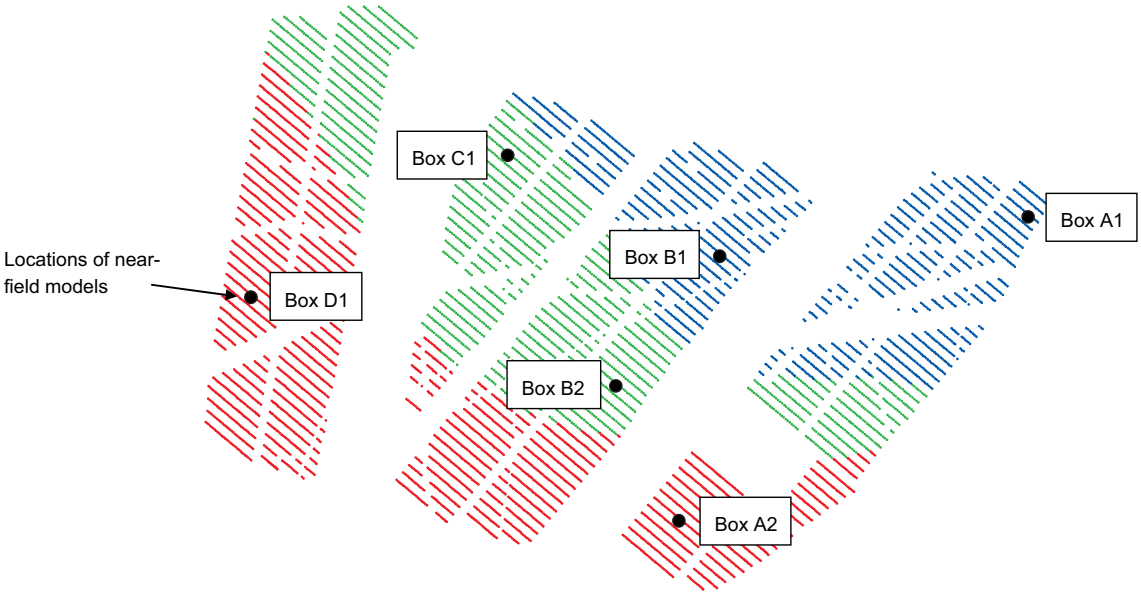

Figure I-26. *Laxemar Layout D2 and locations of near-field models. Red colour represents 8.1 m canister spacing (coincides with rock domain RSMD), blue colour represents 9 m canister spacing (coincides with rock domain RSMA) and green colour represents 10.5 m canister spacing (coincides with rock domain RSMM).*

Six locations (cf. Figure I-26) within the repository region have been selected for near-field thermo-mechanical modelling in order to determine the potential for thermally induced spalling in the walls of deposition holes.

Two models are located in each rock domain: Boxes A1 and B1 in RSMA, Boxes A2 and D1 in RSMD and Boxes B2 and C1 in RSMM. The models are analysed with respect to variations in thermo-mechanical properties and overall position within repository region. The base case models with mean value properties (labelled 1a) are presented in Table I-8 together with an additional set of models with dimensioning values of the heat transport properties (labelled 1b).

Model geometry

The near-field models for the Forsmark and Laxemar sites have identical geometries except for canister spacing, which is both site-dependent and varies between rock domains at the sites, cf. subsection 9.2.2.

Input data

The rock mass properties used in the modelling are presented in Table I-4 (thermal properties), Table I-6 (mechanical properties) and Table I-7 (thermo-mechanical and strength properties).

The reference *in situ* stress magnitudes and orientations with respect to North are presented in Table I-2. In all parts of the repository region, the major horizontal *in situ* stress deviates by about 5° from the tunnel axis. Each near-field model is analyzed with two different stress magnitudes, cf. Table I-2:

- Stress model for the Laxemar site.
- Major horizontal *in situ* stress as in the Äspö area with the minor horizontal and vertical stress components the same as in the stress model for Laxemar.

In order to investigate the influence of uncertainties, a further set of models where uncertainties *in situ* stress magnitudes and orientations (Table I-2) are accounted for are also analysed.

Calculation sequence

The calculation sequences for the construction and operational phase and the subsequent temperate phase are as described in subsection 9.2.4 for the Forsmark site but with boundary conditions for the temperate phase obtained from Figure I-12.

Table I-8. Model map for near-field models.

Model code	Mechanical properties	Description
A1	FSM_N and FSM_EW007	BC from large-scale model Box A1.
1a		Mean heat conductivity in RSMA.
1b		Dimensioning value of heat conductivity in RSMA
A2	FSM_NE005	BC from large-scale model Box A2.
1a		Mean heat conductivity in RSMD.
1b		Dimensioning value of heat conductivity in RSMD
B1	FSM_EW007	BC from large-scale model Box B1.
1a		Mean heat conductivity in RSMA.
1b		Dimensioning value of heat conductivity in RSMA
B2	FSM_C	BC from large-scale model Box B2.
1a		Mean heat conductivity in RSMM.
1b		Dimensioning value of heat conductivity in RSMM
C1	FSM_EW007	BC from large-scale model Box C1.
1a		Mean heat conductivity in RSMM.
1b		Dimensioning value of heat conductivity in RSMM
D1	FSM_W	BC from large-scale model Box D1.
1a		Mean heat conductivity in RSMD.
1b		Dimensioning value of heat conductivity in RSMD

I6.3 Results

The tangential stress at the wall of the deposition hole as function of the azimuthal angle (cf. Figure I-27) at four depths below the tunnel floor is presented in Figure I-28 (Box A1), Figure I-29 (Box A2), Figure I-30 (Box B1), Figure I-31 (Box B2), Figure I-32 (Box C1) and Figure I-33 (Box D1). The upper part of each figure shows the stresses after excavation of the deposition holes. The lower parts show the corresponding stresses after 50 years of heating for mean value properties (left) and dimensioning thermal properties (right).

The major horizontal *in situ* stress deviates by about 5° from the tunnel axis in all parts of the repository region. As seen in the figures below, the highest stresses (for both stress models) are found about 2–5 m below the tunnel floor.

The spalling strength (here assumed to be in the range 52–62% of the UCS) is not exceeded anywhere after excavation of the deposition holes. Depending on the stress model used in the numerical analyses, the stresses are:

- within about 50 MPa of the lower limit of the spalling strength (Laxemar stress model).
- within about 25 MPa of the lower limit of the spalling strength (major horizontal *in situ* stress as in the Äspö area).

As seen in the figures above, the highest stresses are found in rock domain RSMD (Box A2). Figure 9-8 and Figure I-35 show the maximum tangential stress in Box A2 after excavation and after 50 years along the deposition hole wall for the Laxemar *in situ* stress model and the corresponding stress model with the major horizontal *in situ* stress as in the Äspö area, respectively.

The temporal evolution of the major principal stress at canister mid-height is presented in Figure I-36 (Boxes A1 and B1), Figure I-37 (Boxes A2 and D1) and Figure I-38 (Boxes B2 and C1). Assuming the Laxemar *in situ* stress model and mean value thermal properties, the lower limit of the spalling strength (52% of the UCS) is only reached during the thermal phase in the models located in rock domain RSMD (Box A2 and D1). However, for the Äspö *in situ* stress and mean value thermal properties, the lower limit of the spalling strength is reached in all models within 5 months to 2 years. Furthermore, the upper limit of the spalling strength (62% of the UCS) is reached within 5–10 years in Boxes A2 and D1. In Box B2 the maximum stress is close to 62% of the *UCS* after 30 years.

For the dimensioning value of the thermal conductivity and the Laxemar *in situ* stress model, the lower limit of the spalling strength is reached in models A2, B2 and D1 after about 5 years. The upper limit of the spalling strength is not reached in any of the models. For the Äspö *in situ* stress and dimensioning values of the thermal conductivity, the lower limit of the spalling strength is reached within 5 months to 1 year in all models. The upper limit is reached after 2–5 years in Boxes A2, B2 and D1. In Boxes B1 and C1, the stresses are close to the upper limit after about 30 years.

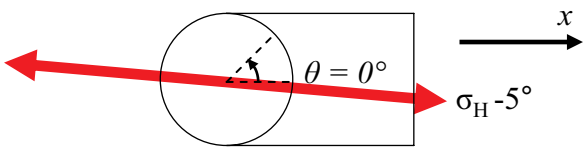

Figure I-27. *Orientation of the major horizontal in situ stress with respect to the tunnel and definition of azimuthal angle.*

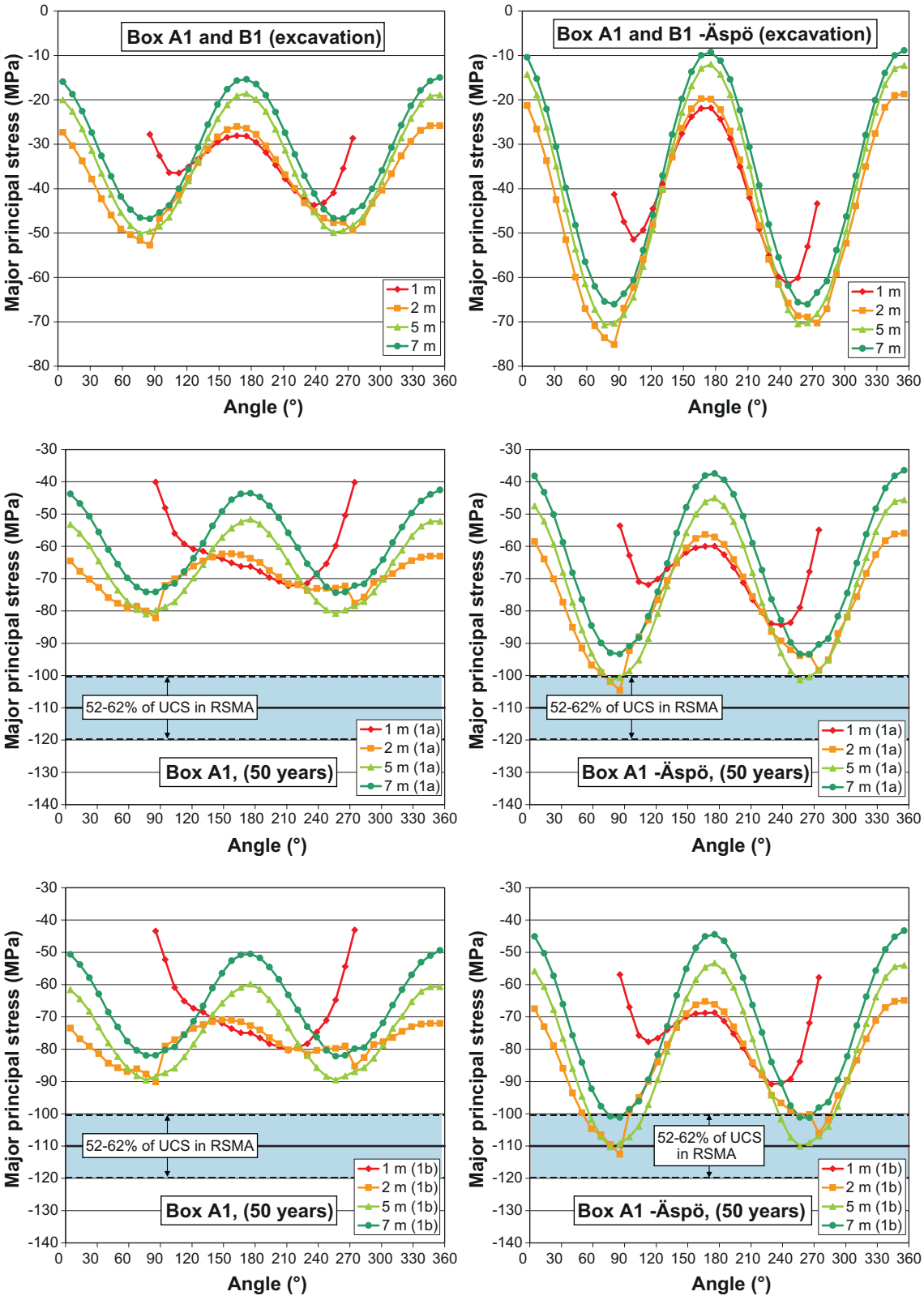

Figure I-28. *Tangential stress at different depths after excavation (top) and after 50 years of heating (middle and bottom) in Box A1. Blue colour represents spalling strength. Left: Laxemar in situ stress model /Hakami et al. 2008/. Right: Major horizontal in situ stress as in the Äspö area /Andersson 2007.*

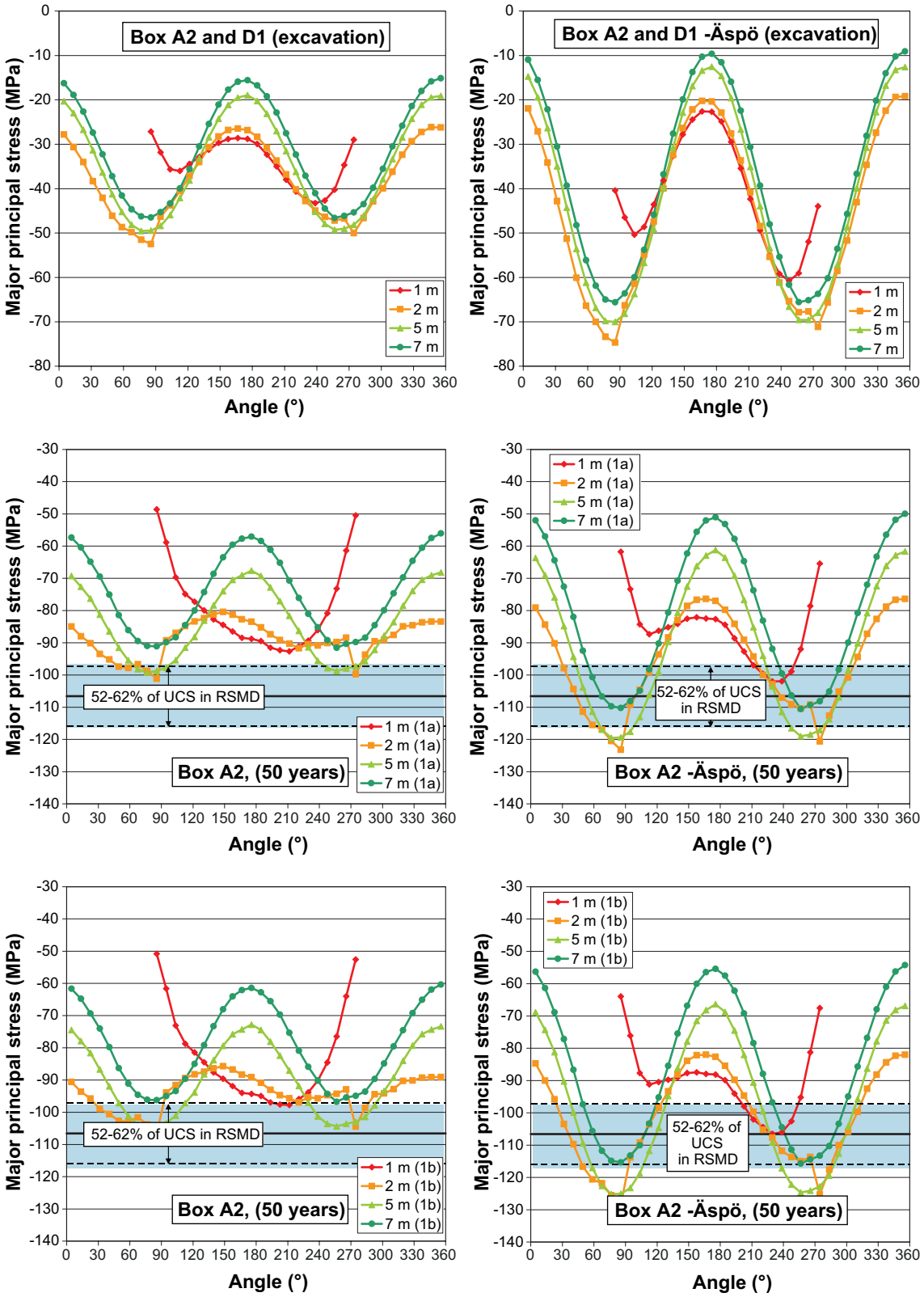

Figure I-29. *Tangential stress at different depths after excavation (top) and after 50 years of heating (middle and bottom) in Box A2. Blue colour represents spalling strength. Left: Laxemar in situ stress model /Hakami et al. 2008/. Right: Major horizontal in situ stress as in the Äspö area /Andersson 2007/.*

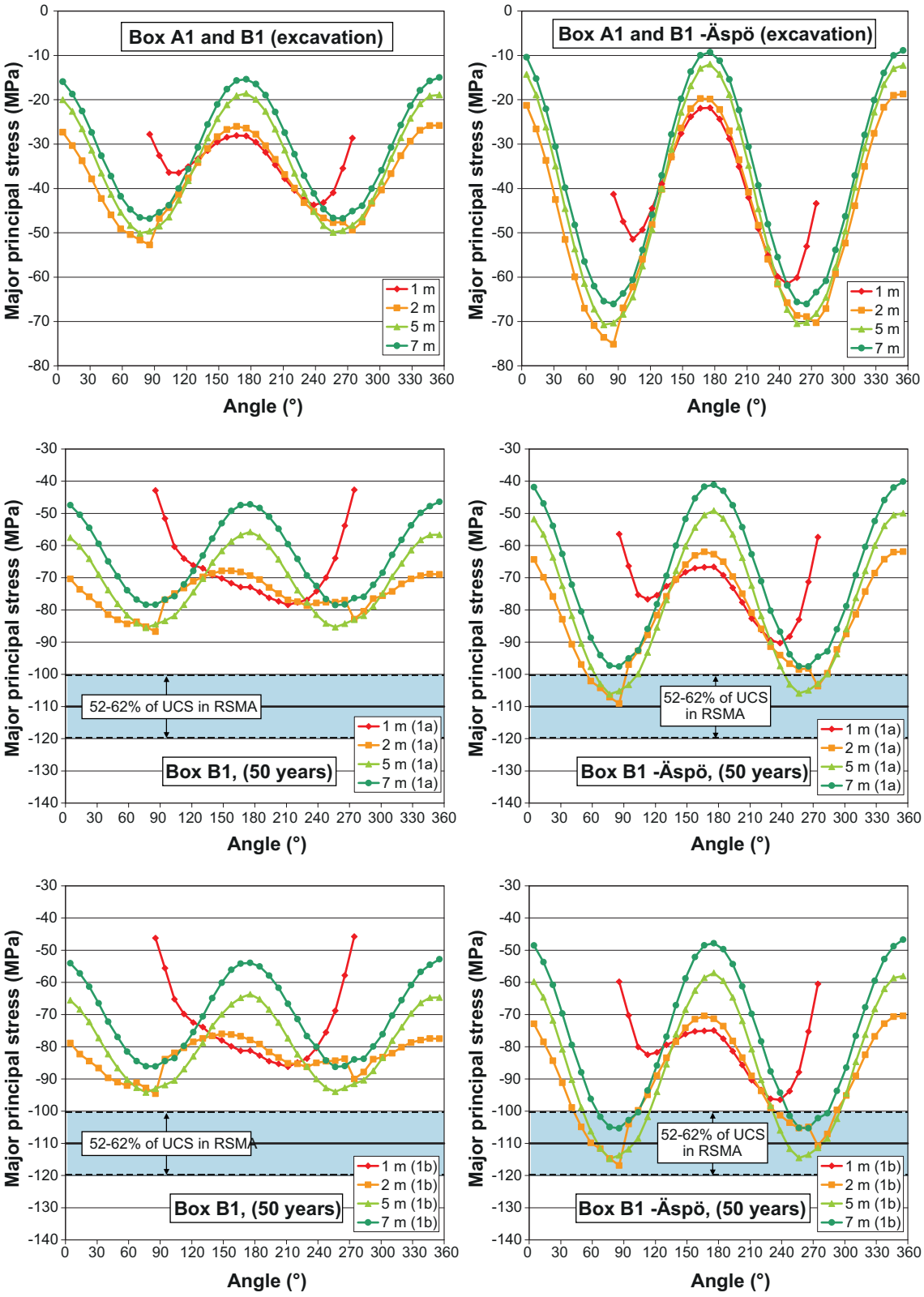

Figure I-30. *Tangential stress at different depths after excavation (top) and after 50 years of heating (middle and bottom) in Box B1. Blue colour represents spalling strength. Left: Laxemar in situ stress model /Hakami et al. 2008/. Right: Major horizontal in situ stress as in the Äspö area /Andersson 2007/.*

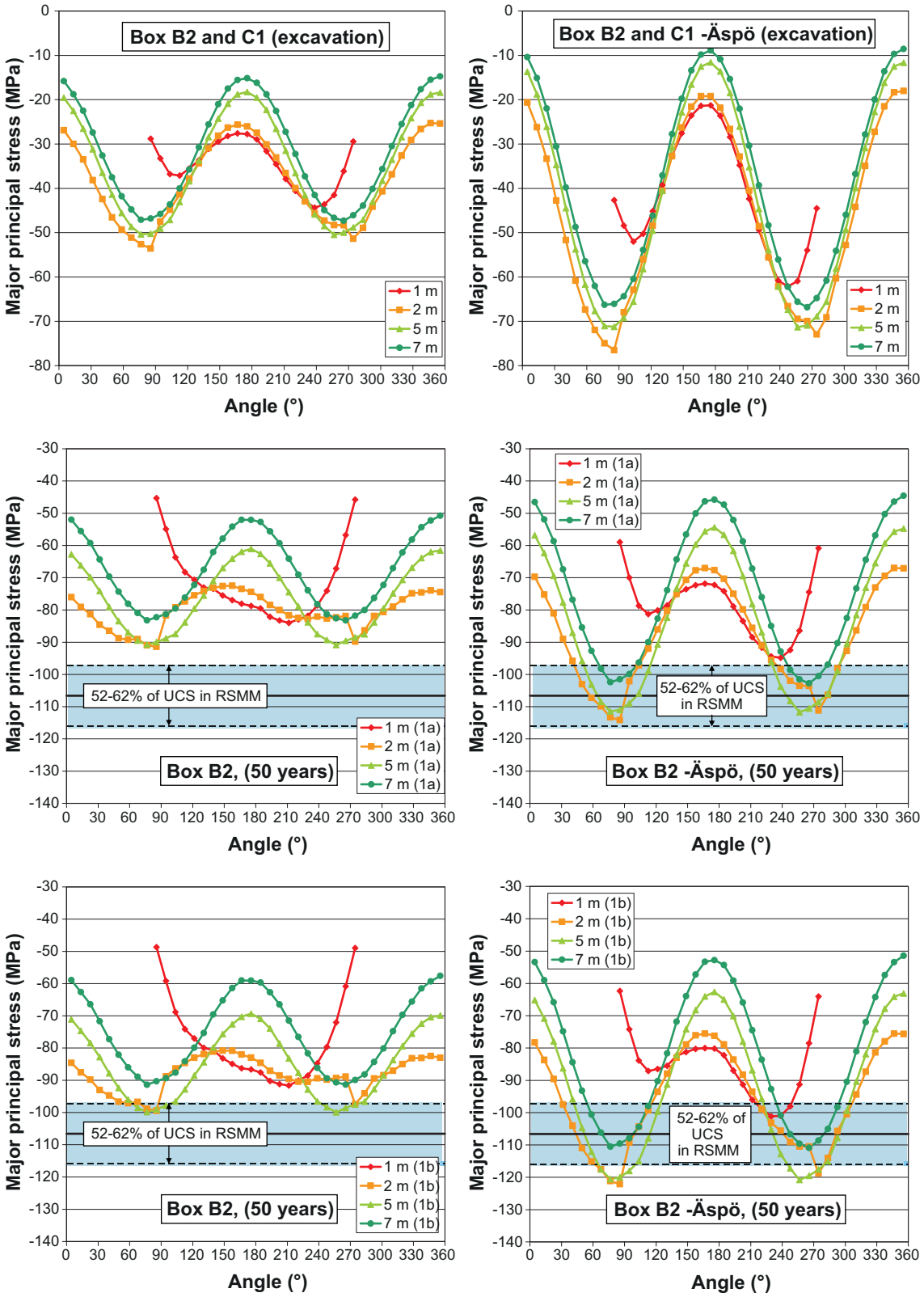

Figure I-31. *Tangential stress at different depths after excavation (top) and after 50 years of heating (middle and bottom) in Box B2. Blue colour represents spalling strength. Left: Laxemar in situ stress model /Hakami et al. 2008/. Right: Major horizontal in situ stress as in the Äspö area /Andersson 2007/.*

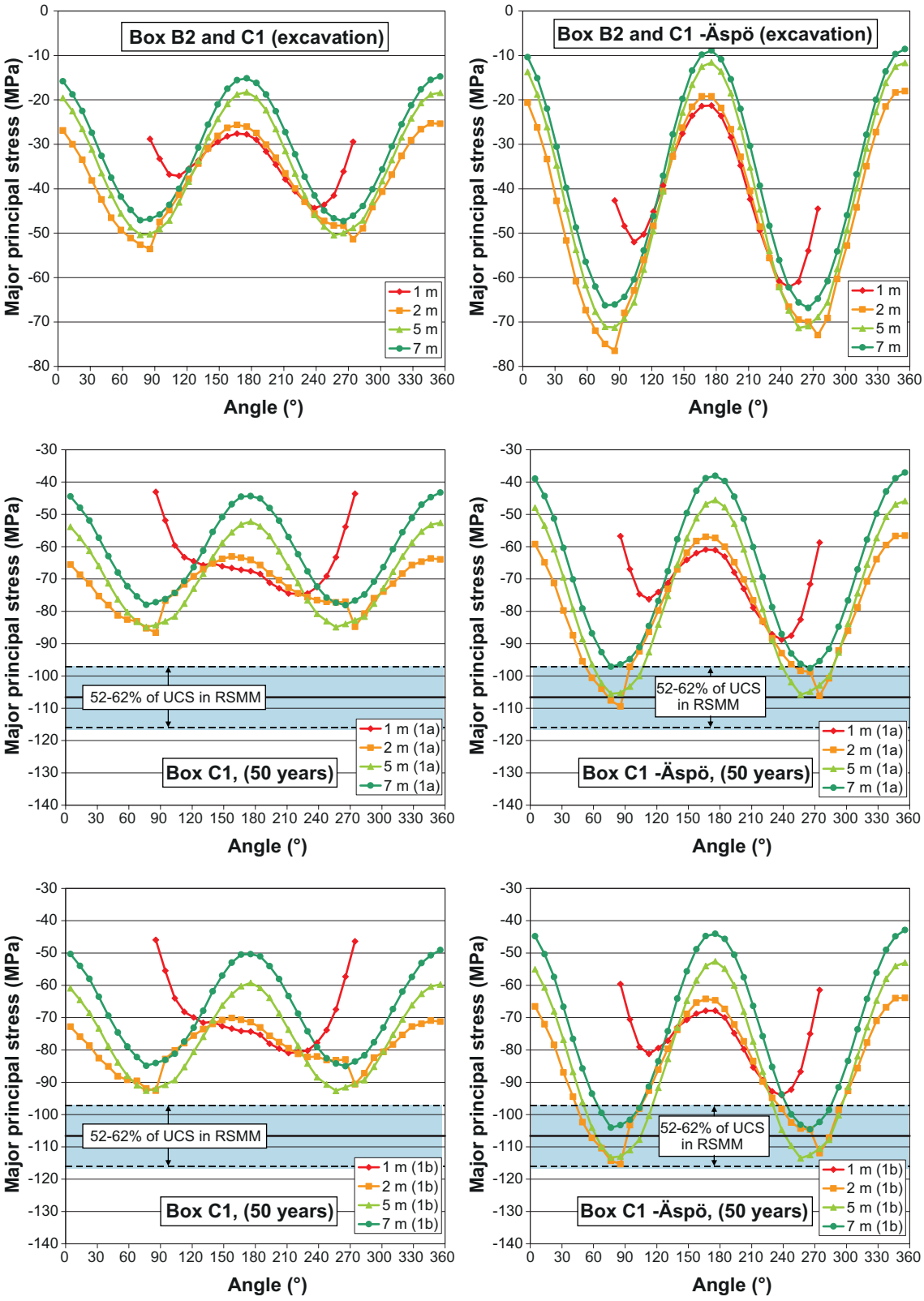

Figure I-32. *Tangential stress at different depths after excavation (top) and after 50 years of heating (middle and bottom) in Box C1. Blue colour represents spalling strength. Left: Laxemar in situ stress model /Hakami et al. 2008/. Right: Major horizontal in situ stress as in the Äspö area /Andersson 2007/.*

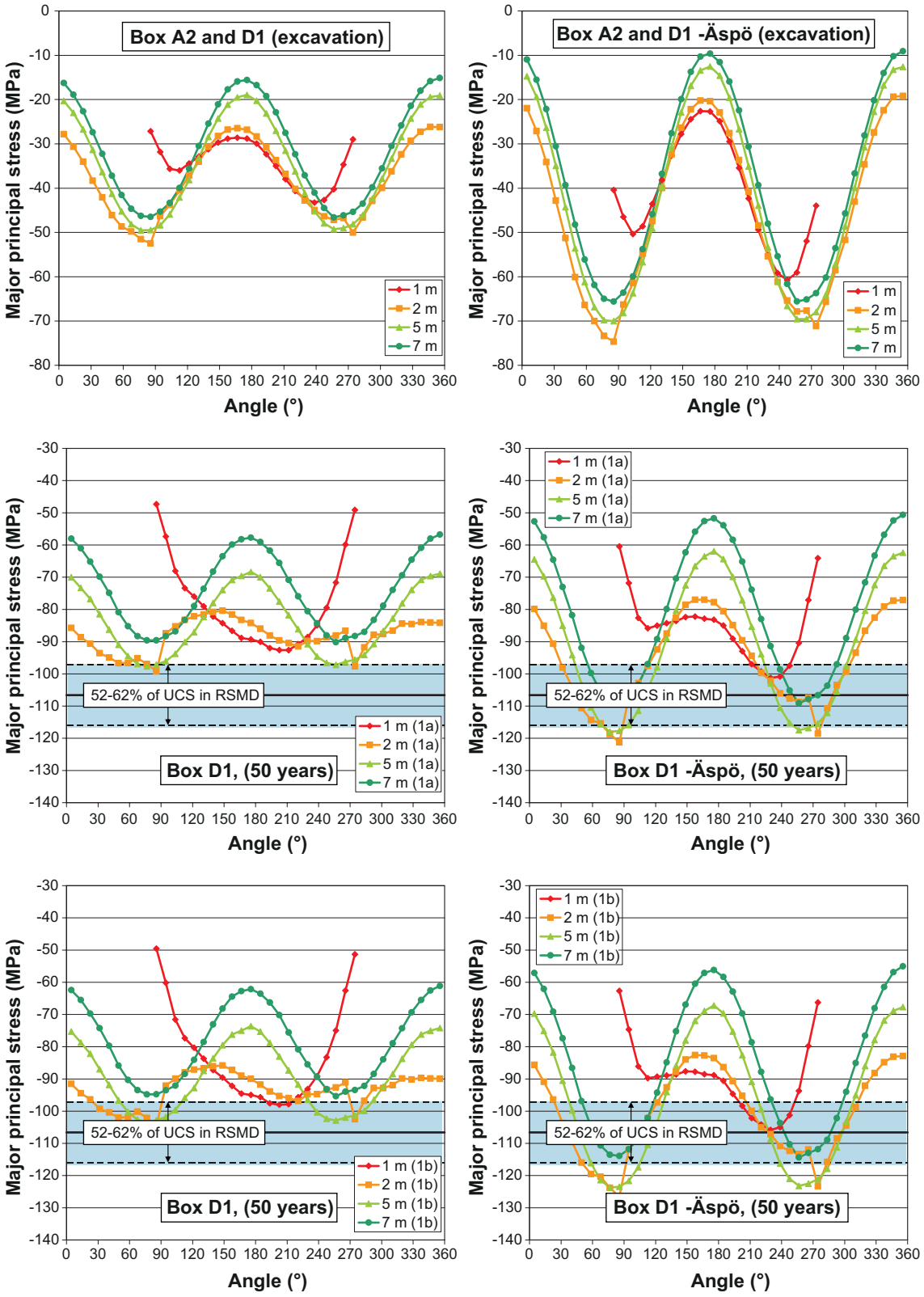

Figure I-33. *Tangential stress at different depths after excavation (top) and after 50 years of heating (middle and bottom) in Box D1. Blue colour represents spalling strength. Left: Laxemar in situ stress model /Hakami et al. 2008/. Right: Major horizontal in situ stress as in the Äspö area /Andersson 2007/.*

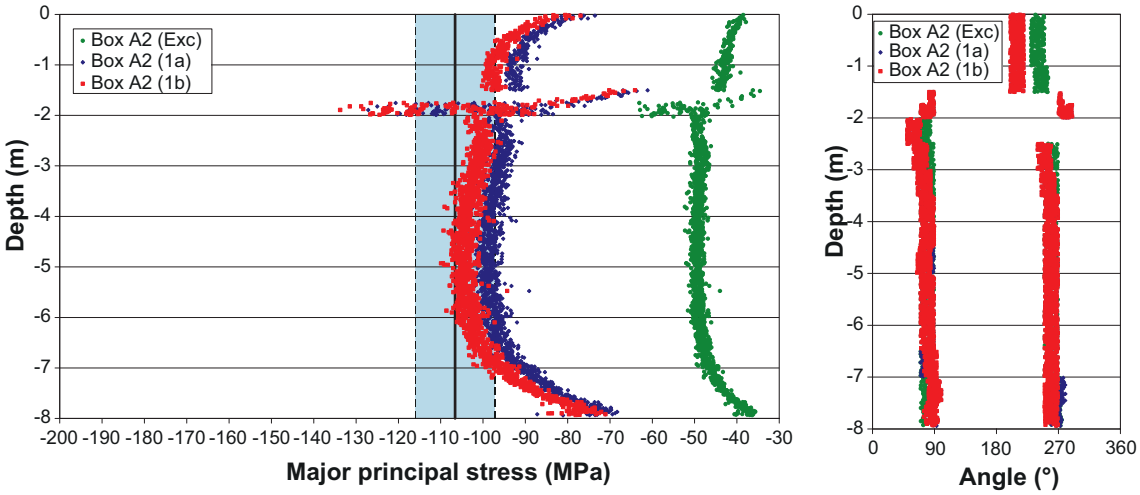

Figure I-34. *Left: Maximum tangential stress (Laxemar in situ stress model (cf. Table I-2) in Box A2 after excavation and 50 years (1a and 1b) along the deposition hole wall. Right: Location of maximum stress on deposition hole perimeter. Blue area represents spalling strength in rock domain RSMD (52–62% of UCS).*

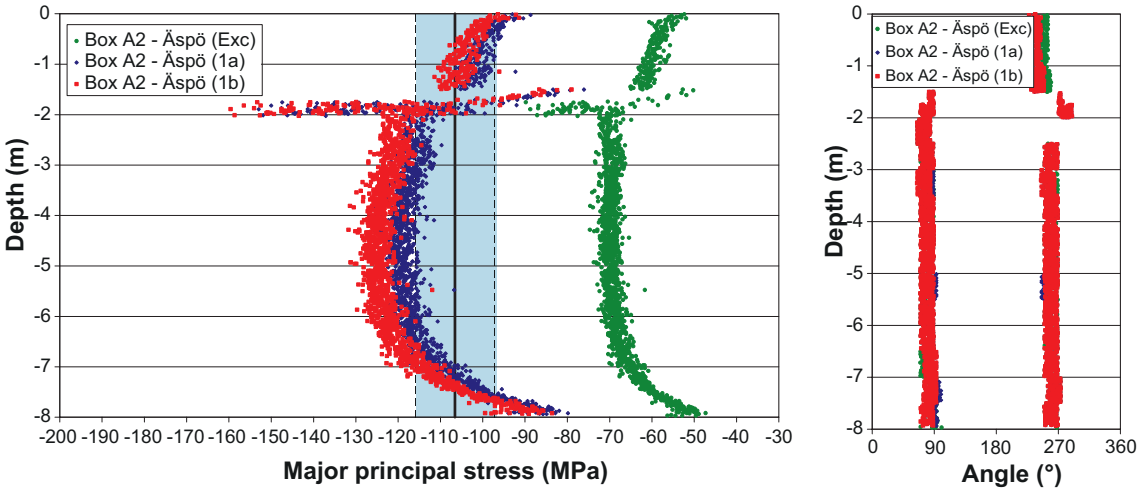

Figure I-35. *Left: Maximum tangential stress (major horizontal in situ stress as in Äspö (cf. Table I-2) in Box A2 after excavation and 50 years (1a and 1b) along the deposition hole wall. Right: Location of maximum stress on deposition hole perimeter. Blue area represents spalling strength in rock domain RSMD (52–62% of UCS).*

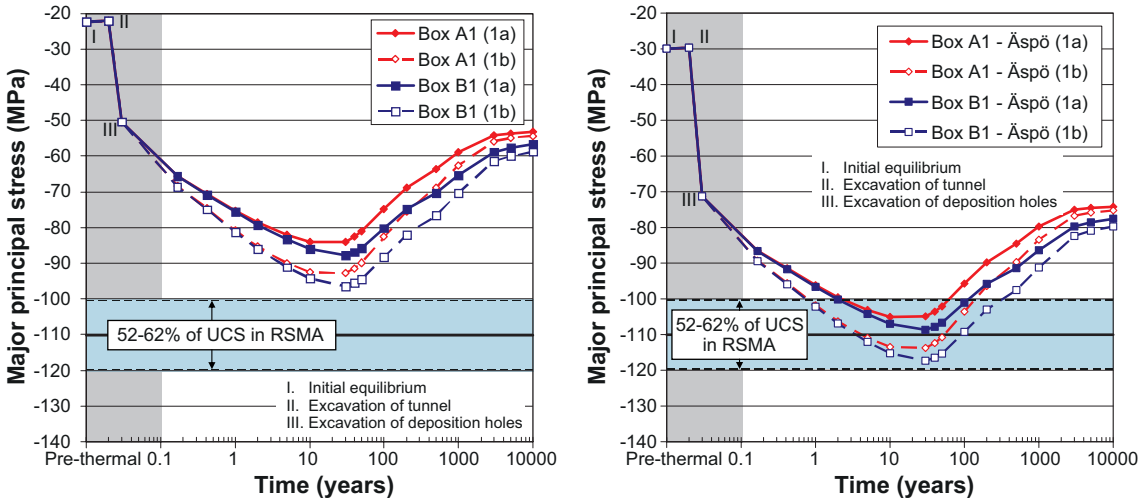

Figure I-36. Temporal development of thermally induced stresses at canister mid-height (5 m) in deposition hole walls in near-field models in RSMA. Left: Laxemar in situ stress model. Right: Major horizontal in situ stress as in the Äspö area.

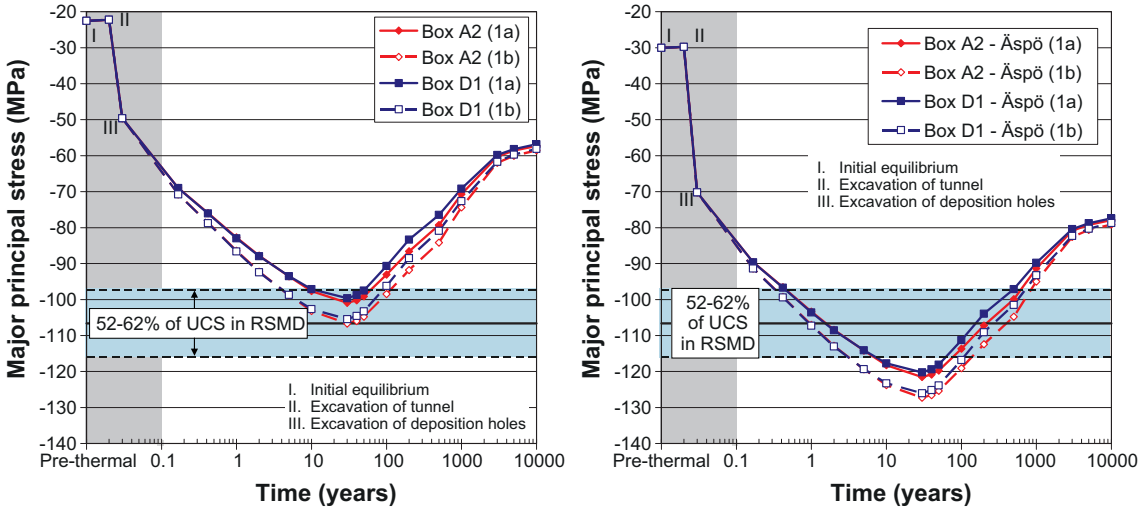

Figure I-37. Temporal development of thermally induced stresses at canister mid-height (5 m) in deposition hole walls in near-field models in RSMD. Left: Laxemar in situ stress model. Right: Major horizontal in situ stress as in the Äspö area.

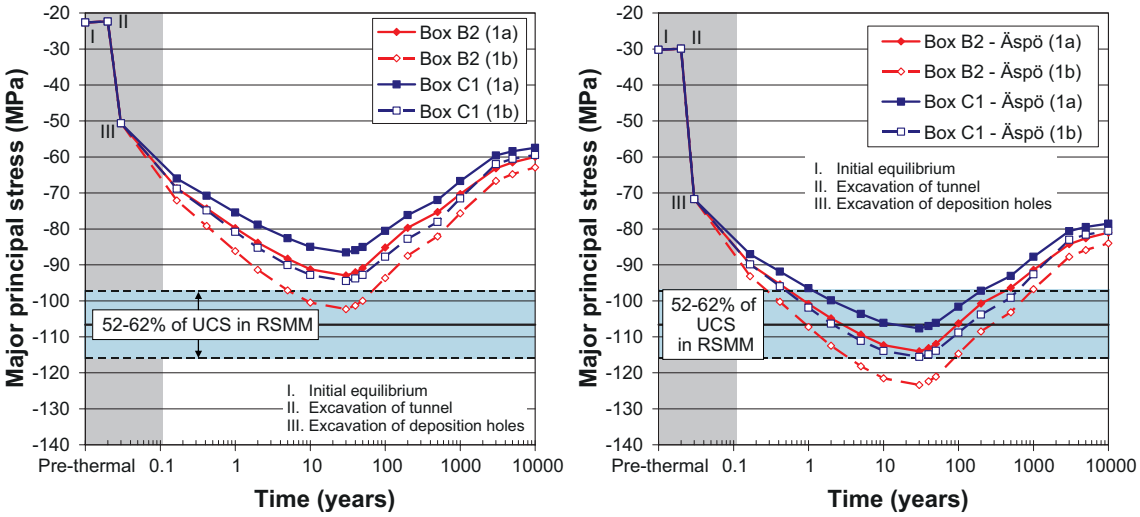

Figure I-38. *Temporal development of thermally induced stresses at canister mid-height (5 m) in deposition hole walls in near-field models in RSMM. Left: Laxemar in situ stress model. Right: Major horizontal in situ stress as in the Äspö area.*

I6.4 Uncertainties

The models in the previous section have been analysed with mean values of the mechanical properties and *in situ* stress orientations. The uncertainty of the orientation of the major horizontal *in situ* stress (Laxemar stress model) is ±15° /Hakami et al. 2008/. This corresponds to a maximum deviation of the major horizontal *in situ* stress from the tunnel orientation by 20°, cf. Table I-2.

The resulting tangential stresses after excavation at different depths are presented in Figure I-39. At canister mid-height (5 m) the differences in maximum stress are small – about 3 MPa. In the upper parts of the deposition hole, the differences are larger – 12–13 MPa at the 1 m-level and 6–7 MPa at the 2 m-level. At the time of maximum stress (30 years), the difference in tangential stress at canister mid-height is about 3 MPa (cf. Figure I-40).

An upper limit on the stress magnitudes and orientations at Äspö, assuming that the major horizontal *in situ* stress at Äspö has the same uncertainty span as the stress model for Laxemar (i.e. ±20% in magnitude and ±15° in orientation /Hakami et al. 2008/), are presented in Table I-2. Figure I-41 shows the maximum tangential stress in Box A2 after excavation and after 50 years along the deposition hole wall for the upper limit on the stress model with the major horizontal *in situ* stress as in the Äspö area.

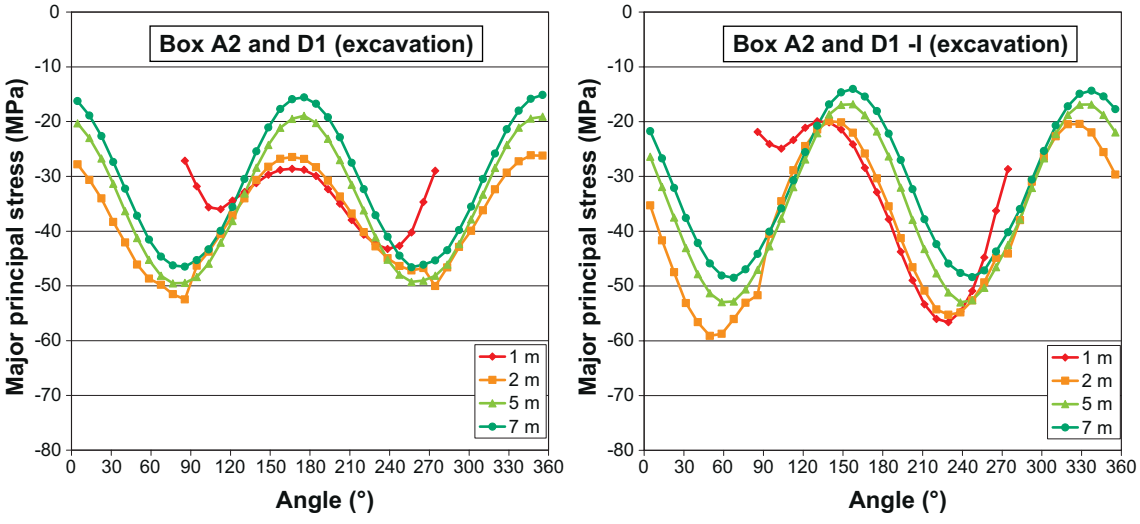

Figure I-39. *Tangential stresses in the walls of a deposition hole after excavation. Left: Mean in situ stress orientation. Right: Most unfavourable in situ stress orientation (20° with respect to tunnel orientation).*

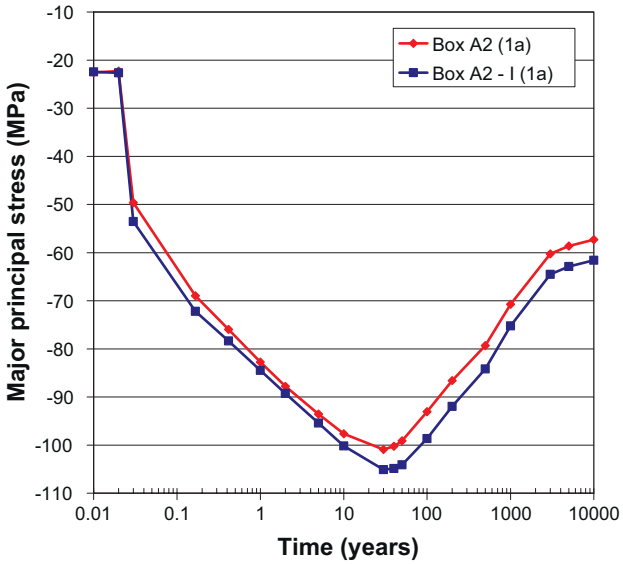

Figure I-40. *Temporal development of thermally induced stresses at canister mid-height (5 m) in deposition hole walls in Box A2 in RSMD. Mean stress orientation (red curve) and most unfavourable (20° with respect to tunnel orientation) in situ stress orientation (dark blue curve labelled I).*

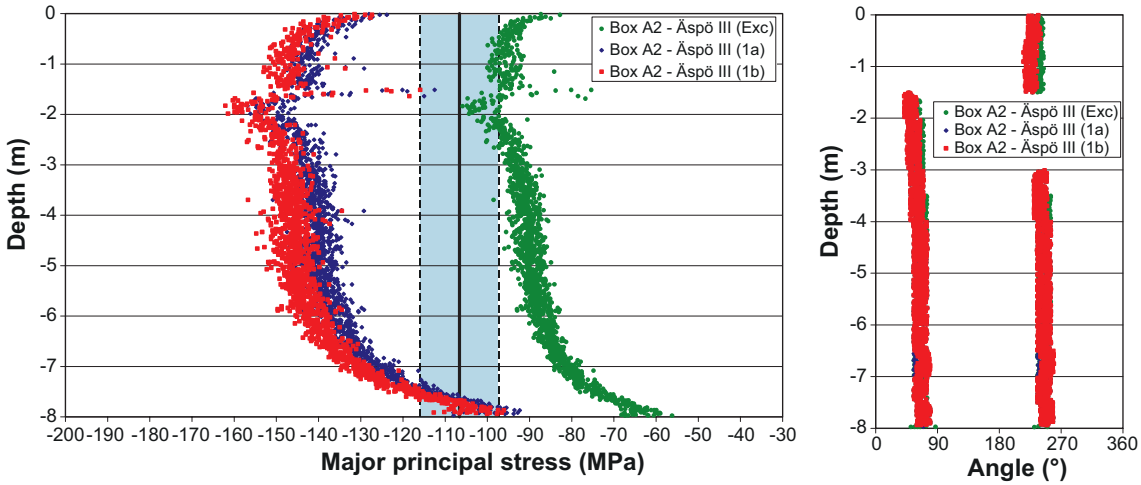

Figure I-41. *Left: Maximum tangential stress (upper limit on major horizontal in situ stress as in Äspö, cf. Table I-2) in Box A2 after excavation and 50 years (1a and 1b) along the deposition hole wall. Right: Location of maximum stress on deposition hole perimeter. Blue area represents spalling strength in rock domain RSMD (52–62% of UCS).*

I6.5 Summary

It is assumed that the spalling strength is 52–62% of the mean value uniaxial compressive strength (UCS) of intact rock, *i.e.* approximately 100–120 MPa in rock domain RSMA and 97–116 MPa in rock domains RSMM and RSMD, cf. Table I-7.

Construction and operational phase

For models with mean value *in situ* stress magnitudes and orientations, the following conclusion can be drawn.

- The spalling strength is not exceeded in the walls of the deposition holes.

When uncertainties in *in situ* stresses and their orientations are taken into account, the following conclusions can be drawn.

- The spalling strength is not exceeded in the walls of the deposition holes for the Laxemar stress model (σ_H = 22.5 MPa, σ_h = 12 MPa, σ_v = 13.5 MPa, σ_H orientation 20° with respect to tunnel orientation).
- For the Äspö stress model (σ_H = 36 MPa, σ_h = 14.4 MPa and σ_v = 13.9 MPa, σ_H orientation 20° with respect to tunnel orientation), the lower limit (52%) of the spalling strength is exceeded from about 0.5 m below the tunnel floor to about 2.5 m below the tunnel floor in the model with the highest stresses (Box A2). The upper limit spalling strength is not exceeded at any depth.

Temperate phase

For models with mean values of thermo-mechanical and mechanical properties, *in situ* stresses and their orientations, the following conclusions can be drawn.

- Models located within rock domain RSMA.
  - The spalling strength is not exceeded at canister mid-height (5 m) for the Laxemar stress model.
  - For the major horizontal *in situ* stress as in Äspö, the lower limit of the spalling strength (52%) is exceeded at canister mid-height (5 m) within 2 years (mean thermal conductivity) and within 1 year (dimensioning thermal conductivity). The upper limit spalling strength (62%) is not exceeded at canister mid-height.
- Models located within rock domain RSMD.
  - For the Laxemar stress model, the lower limit of the spalling strength (52%), but not the upper limit (62%), is exceeded at canister mid-height (5 m) for both values of the thermal conductivity.
  - In the model with the highest stresses (Laxemar stress model) after 50 years (Box A2) the lower limit of the spalling strength (52%) is exceeded from about 2 m to 6.5 m below the tunnel floor (mean thermal conductivity) and from about 0.5 m to 7 m below the tunnel floor (dimensioning thermal conductivity).
  - The spalling threshold is exceeded at canister mid-height for both values of the thermal conductivity (major horizontal *in situ* stress as in Äspö). In the model with the highest stresses (major horizontal *in situ* stress as in Äspö) after 50 years (Box A2), the lower limit of the spalling strength (52%) is exceeded from the tunnel floor to a depth of about 7.5 m (both values of the thermal conductivity). The upper limit of the spalling strength (62%) is exceeded from about 2 m to 6.5 m below the tunnel floor (mean thermal conductivity) and from about 2 m to 7 m below the tunnel floor (dimensioning thermal conductivity).
- Models located within rock domain RSMM.
  - For the Laxemar stress model and mean thermal conductivity, the spalling strength is not exceeded at canister mid-height (5 m). For the dimensioning thermal conductivity, the lower limit of the spalling strength (52%) is exceeded at canister mid-height in one model within about 5 years. The upper limit spalling strength (62%) is not exceeded at canister mid-height.
  - For the major horizontal *in situ* stress as in Äspö, the lower limit of the spalling strength (52%) is exceeded at canister mid-height (5 m) within 6 months to 1 year (mean thermal conductivity) and within a few months (dimensioning thermal conductivity). The upper limit of the spalling strength (62%) is exceeded at canister mid-height within 5–30 years (dimensioning thermal conductivity). The upper limit spalling strength is not exceeded for the mean value of the thermal conductivity.

For the models with upper limit *in situ* stress magnitudes (σ_H = 36 MPa, σ_h = 14.4 MPa and σ_v = 13.9 MPa), and orientations (20°), using major horizontal *in situ* stress as in Äspö, the following conclusion can be drawn:

- In the model with the highest stresses after 50 years (Box A2), the spalling strength is exceeded from the tunnel floor to a depth of about 7.4–7.8 m (mean thermal conductivity) and 7.5–7.9 m (dimensioning thermal conductivity), respectively.